NAM

LNEC-BUILD-3 - An incremental shake-table test on a Dutch URM detached house with Chimneys

Stylianos Kallioras, António Araújo Correia, Ana Isabel Marques, Vasco Bernardo, Paulo Xavier Candeias and Francesco Graziotti

IUSS Pavia, LNEC Portugal, EUCENTRE Italy, University of Pavia

L'Istituto Universitario di Studi Superiori di Pavia (University School for Advanced Studies Pavia)

Laboratório Nacional de Engenharia Civil Portugal (National Laboratory for Civil Engineering Portugal)

European Centre for Training and Research in Earthquake Engineering, Italy

Università degli studi di Pavia (University of Pavia)

Date October 2018

Editors Jan van Elk & Dirk Doornhof

General Introduction

Many of the buildings in the Groningen field area are unreinforced masonry buildings. A program to assess the response of these building to earthquakes was therefore initiated. This program built on the experimental and modelling program into the properties of URM building materials, wall elements and wall units.

A typical Groningen terraced house, built using materials from the Groningen area by builders from the Groningen area, was tested at the shake-table of Eucentre in Pavia, Italy (Ref. 1). Although at the end of this test program the building was seriously damaged, the building had not collapsed. This left questions on the remaining capacity of the structure and its ability to resist larger seismic movements before (partially) collapsing. The test in Eucentre was therefore followed-up with further tests at the laboratory of LNEC in Lisbon, Portugal (Ref. 2 to 5). Here the upper floors of the building tested in Eucentre were re-built in the LNEC laboratory and subjected to movements measured at the base of the upper floors in Eucentre. Additionally, the roof structure was tested separately.

Next, a detached house was tested in EUCentre at the shake-table (Ref. 6 and 7). This detached house represents a typical pre-1940 Dutch single-storey residential building constructed of double wythe clay brick masonry walls with timber floor diaphragms and a timber roof supported by timber trusses.

This report describes the testing of a house with a typical Dutch gambrel roof that allowed for living space above the attic floor. These high gables are potentially vulnerable to out-of-plane excitation. The floor was made of timber joists and planks, resulting in a flexible diaphragm.

A study was also initiated into falling objects like chimneys, gables and parapets (Ref. 8 and 9), using a very practical approach. To investigate the performance of falling non-structural masonry elements in earthquakes, two clay-brick chimneys were included in the detached house to be tested.

An incremental dynamic test was carried out up to collapse conditions of the specimen, using input ground motions compatible with induced-seismicity scenarios for the examined region. Structural and non-structural damage was surveyed in detail at the end of every earthquake simulation.

References

1. Eucentre Shake-table Test of Terraced House Modelling Predictions and Analysis Cross Validation, staff from ARUP, Eucentre (Pavia) and TU Delft, November 2015 [this document also includes; (1) Instruments full-scale test-house Eucentre Laboratory, (2) Protocol for Shaking Table Test on Full Scale Building (Eucentre) V_1, and (3) Selection of Acceleration Time-Series for Shake Table Testing of Groningen Masonry Building at the EUCENTRE, Pavia, all three by staff from Eucentre (Pavia)],
2. Collapse shake-table testing of terraced house (LNEC-BUILD1), Eucentre and LNEC (U. Tomassetti, A. A. Correia, F. Graziotti, A.I. Marques, M. Mandirola, P.X. Candeias), 1st September 2017.
3. LNEC-BUILD1: Modelling predictions and analysis cross-validation, ARUP, TU Delft, Eucentre and Mosayk (several staff members from all four institutions), 8th September 2017.
4. Using the Applied Element Method to model the collapse shake-table testing of a URM cavity wall structure (LNEC-BUILD1), Mosayk (D. Malomo, R. Pinho), 31st October 2017.
5. Using the Applied Element Method to model the collapse shake-table testing of a terraced house roof substructure (LNEC-BUILD2), Mosayk (D. Malomo, R. Pinho), 31st October 2017.
6. Experimental campaign on a clay URM full-scale specimen representative of the Groningen building stock (EUC-BUILD2), Eucentre (F. Graziotti, U. Tomassetti, A. Rossi, B. Marchesi, S. Kallioras, M. Mandirola, A. Fragomeli, E. Mellia, S. Peloso, F. Cuppari, G. Guerrini, A. Penna, G. Magenes, G), 20th July 2016.
7. EUC-BUILD2: Modelling predictions and analysis cross-validation of detached single-storey URM Building, ARUP, TU Delft, Eucentre and Arcadis (several staff members from all four institutions), 30th September 2016
8. Risk Assessment of Falling Hazards in Earthquakes in the Groningen region, Tony Taig and Florence Pickup (TTAC Ltd.), March 2016.
9. Risk Assessment of Falling Hazards in Earthquakes in the Groningen region (Appendices), Tony Taig and Florence Pickup (TTAC Ltd.), March 2016.

NAM

Title	**LNEC-BUILD-3 - An incremental shake-table test on a Dutch URM detached house with Chimneys**	**Date**	October 2018
		Initiator	NAM
Autor(s)	**Stylianos Kallioras, António Araújo Correia, Ana Isabel Marques, Vasco Bernardo, Paulo Xavier Candeias and Francesco Graziotti**	**Editors**	Jan van Elk and Dirk Doornhof
Organisation	IUSS Pavia, LNEC Portugal, EUCENTRE Italy, University of Pavia L'Istituto Universitario di Studi Superiori di Pavia (University School for Advanced Studies Pavia), Laboratório Nacional de Engenharia Civil Portugal (National Laboratory for Civil Engineering Portugal), European Centre for Training and Research in Earthquake Engineering, Italy, Università degli studi di Pavia (University of Pavia)	**Organisation**	NAM
Place in the Study and Data Acquisition Plan	<u>Study Theme:</u> Seismic Response of Buildings (URM) <u>Comment:</u> Many of the buildings in the Groningen field area are unreinforced masonry buildings. A program to assess the response of these building to earthquakes was therefore initiated. This program built on the experimental and modelling program into the properties of URM building materials, wall elements and wall units. A typical Groningen terraced house, built using materials from the Groningen area by builders from the Groningen area, was tested at the shake-table of Eucentre in Pavia, Italy (Ref. 1). Although at the end of this test program the building was seriously damaged, the building had not collapsed. This left questions on the remaining capacity of the structure and its ability to resist larger seismic movements before (partially) collapsing. The test in Eucentre was therefore followed-up with further tests at the laboratory of LNEC in Lisbon, Portugal (Ref. 2 to 5). Here the upper floors of the building tested in Eucentre were re-built in the LNEC laboratory and subjected to movements measured at the base of the upper floors in Eucentre. Additionally, the roof structure was tested separately. Next, a detached house was tested in EUCentre at the shake-table (Ref. 6 and 7). This detached house represents a typical pre-1940 Dutch single-storey residential building constructed of double wythe clay brick masonry walls with timber floor diaphragms and a timber roof supported by timber trusses. This report describes the testing of a house with a typical Dutch gambrel roof that allowed for living space above the attic floor. These high gables are potentially vulnerable to out-of-plane excitation. The floor was made of timber joists and planks, resulting in a flexible diaphragm.		

	A study was also initiated into falling objects like chimneys, gables and parapets (Ref. 8 and 9), using a very practical approach. To investigate the performance of falling non-structural masonry elements in earthquakes, two clay-brick chimneys were included in the detached house to be tested. An incremental dynamic test was carried out up to collapse conditions of the specimen, using input ground motions compatible with induced-seismicity scenarios for the examined region. Structural and non-structural damage was surveyed in detail at the end of every earthquake simulation.
Directliy linked research	(1) Shake table tests (2) Fragility curves for building typologies (URM) (3) Falling Objects (4) Risk Assessment
Used data	Experiments
Associated organisation	NAM
Assurance	Eucentre

EUCENTRE Research Report

LNEC-BUILD-3: AN INCREMENTAL SHAKE-TABLE TEST ON A DUTCH URM DETACHED HOUSE WITH CHIMNEYS

Authors

Stylianos Kallioras

IUSS Pavia

EUCENTRE, Italy

António Araújo Correia

LNEC, Portugal

Ana Isabel Marques

LNEC, Portugal

Vasco Bernardo

LNEC, Portugal

Paulo Xavier Candeias

LNEC, Portugal

Francesco Graziotti

University of Pavia,

EUCENTRE, Italy

OCTOBER 5, 2018

EUC203/2018U

LNEC-BUILD-3: AN INCREMENTAL SHAKE-TABLE TEST ON A DUTCH URM DETACHED HOUSE WITH CHIMNEYS

Authors

Stylianos Kallioras

IUSS Pavia

EUCENTRE, Italy

António Araújo Correia

LNEC, Portugal

Ana Isabel Marques

LNEC, Portugal

Vasco Bernardo

LNEC, Portugal

Paulo Xavier Candeias

LNEC, Portugal

Francesco Graziotti

University of Pavia,

EUCENTRE, Italy

October 5, 2018

Lisbon - Pavia

EUC203/2018U

prodotto e distribuito da:

produced and distributed by:

EUCENTRE Foundation

Via Adolfo Ferrata, 1 - 27100 Pavia, Italy

Phone (+39) 0382.5169811 - Fax (+39) 0382.529131

E-mail: info@eucentrepress.it - Web: www.eucentrepress.it

Protocol EUC203/2018U

SUMMARY

With the aim of investigating the seismic behaviour and failure modes of residential unreinforced masonry construction of the Groningen region in the Netherlands, a unidirectional shake-table test was performed on a full-scale building model up to collapse conditions. The tests were carried out at the testing facilities of the Structural Dynamics Laboratory of LNEC in Lisbon, Portugal.

The specimen embodied construction details representative of old detached single-storey houses of the Groningen region of the Netherlands, without any specific seismic detailing. The house featured a typical Dutch gambrel roof that allowed for living space above the attic floor, with high gables that were vulnerable to out-of-plane excitation. The floor was made of timber joists and planks, resulting in a flexible diaphragm. Two clay-brick chimneys were included to investigate the performance of falling non-structural masonry elements in earthquakes. An incremental dynamic test was carried out up to collapse conditions of the specimen, using input ground motions compatible with induced-seismicity scenarios for the examined region. Structural and non-structural damage was surveyed in detail at the end of every earthquake simulation. Low-intensity random vibration tests were additionally performed to assess the effect of the cumulative damage on the dynamic properties of the structure. The specimen was sufficiently instrumented with sensors that recorded the dynamic response at various locations. The mechanical properties of the employed masonry were determined through complementary strength tests on small masonry assemblies.

This report describes the key characteristics of the specimen, including the as-built geometry, the construction details and the mechanical characteristics of the materials, as well as the adopted instrumentation plan, the seismic input and the testing protocol. It also summarises the observations from the shake-table tests, illustrating the evolution of the structural and non-structural damage, and the global and by-parts dynamic response of the building. The attainment of significant damage limit states is correlated with experimentally defined engineering demand parameters and ground-motion intensity measures for the performance-based assessment of URM buildings. The tests produced experimental data that constitutes a valuable addition to the current state of knowledge on the seismic response of masonry building chimneys and the global structural masonry collapse. All data, including photographs and video recordings taken during the construction and the testing phases, are available upon request on www.eucentre.it/nam-project. The authors make this information available to assist in the development of analytical and numerical models to simulate the earthquake response of unreinforced masonry buildings and chimneys.

Cite as:

Kallioras S, Correia AA, Marques AI, Bernardo V, Candeias PX, Graziotti F. *LNEC-BUILD-3: An incremental shake-table test on a Dutch URM detached house with chimneys*. EUCENTRE Technical Report EUC203/2018U, EUCENTRE, Pavia, Italy; 2018. Available at www.eucentre.it/nam-project.

ACKNOWLEDGEMENTS

The experimental campaign described in the present report is part of the project “Study of the vulnerability of masonry buildings in Groningen” within the research framework programme on hazard and risk of induced seismicity in the Groningen region, sponsored by the Nederlandse Aardolie Maatschappij BV (NAM). The authors would like to express their deepest appreciation to the Dutch construction team of Ronda BV and the local Portuguese carpenters for their diligent work and enthusiasm in building the test house and the complementary specimens. The relentless commitment of the contractor was essential to the realisation of the building specimen and is gratefully acknowledged. Many thanks also go to J. Klement-Kroezen from NAM for her valuable assistance during the first week of the construction works, and to L. Grottoli for his generous help in performing the tests. The technical staff at LNEC provided constant support and practical solutions in dealing with challenges on laboratory issues; therefore, we would like to extend our sincere gratitude to all of them.

TABLE OF CONTENTS

LIST OF TABLES

LIST OF FIGURES

LIST OF SYMBOLS

a_T	=	Shake-table acceleration (in the longitudinal direction)
a_g	=	Base acceleration (foundation beam / “ground”)
$a_{1,S}$	=	South wall acceleration at the floor level
$a_{1,N}$	=	North wall acceleration at the floor level
$a_{1,D}$	=	Average floor-diaphragm acceleration
a_R	=	Roof ridge acceleration
$a_{C,W}$	=	West chimney acceleration at the top
$a_{t,C,S}$	=	South chimney acceleration at the top
$a_{m,C,S}$	=	South chimney acceleration at mid-height of the free-standing stack
$a_{1,C,S}$	=	South chimney acceleration at the floor level
$a_{C,S}$	=	South chimney acceleration at the centre of mass of the free-standing stack
$a'_{C,S}$	=	South chimney acceleration at the centre of mass of the part above the flashing
$a_{C,S,ro}$	=	Theoretical acceleration to initiate rocking of the entire South chimney stack
$a'_{C,S,ro}$	=	Theoretical acceleration to initiate rocking of the part of South chimney above the flashing
$a_{C,S,u}$	=	Theoretical acceleration to cause flexural cracking at the base of the South chimney stack
$AMP_{1,S}$	=	South wall acceleration amplification at the floor level
$AMP_{1,N}$	=	North wall acceleration amplification at the floor level
$AMP_{1,D}$	=	Average floor-diaphragm acceleration amplification
AMP_R	=	Roof ridge acceleration amplification
$AMP_{t,C,W}$	=	West chimney acceleration amplification at the top
$AMP_{t,C,S}$	=	South chimney acceleration amplification at the top
BSC_S	=	South wall base-shear coefficient
BSC^0_S	=	South wall base-shear coefficient without non-oscillatory mass
BSC_N	=	North wall base-shear coefficient
BSC^0_N	=	North wall base-shear coefficient without non-oscillatory mass
BSC_{TOT}	=	Overall base-shear coefficient
BSC^0_{TOT}	=	Overall base-shear coefficient without non-oscillatory mass
b_w	=	Outer width of the rectangular box section of the chimneys
CAV	=	Cumulative absolute velocity
E_{mortar}	=	Elastic modulus of mortar (28 days)
E_{m1}	=	Masonry Young’s modulus in compression
f	=	Vibration frequency
F_R	=	Gables-roof assembly inertia force
F^0_R	=	Inertia force for the top half portion of the gables-roof assembly
f_b	=	Brick standard compressive strength
f_{bt}	=	Brick flexural strength
f_c	=	Mortar compressive strength (28 days)

f_t	=	Mortar flexural strength (28 days)
$f_{m,w}$	=	Masonry compressive strength
f_{x3}	=	Masonry flexural in-plane strength
f_{x2}	=	Masonry flexural out-of-plane strength
f_w	=	Masonry flexural bond strength
f_{v0}	=	Masonry (bed-joint) initial shear strength
$f_{v0,tor}$	=	Masonry (bed-joint) initial shear strength in torsion
$G_{xy_i}(f)$	=	Cross-spectral density estimate between input and output signals
$G_{xx}(f)$	=	Auto-spectrum density estimate of the input signal
$G_{y_iy_i}(f)$	=	Auto-spectrum density estimate of the response signal
h_1	=	First inter-storey height
h_R	=	Roof inter-storey height
HI	=	Housner spectrum intensity (in the period window 0.1-2.5 s)
I_A	=	Arias intensity
$l_{0,S}$	=	Distance of the South lower plate from midspan of the floor
$l_{0,N}$	=	Distance of the North lower plate from midspan of the floor
mHI	=	Modified Housner spectrum intensity (in the period window 0.1-0.5 s)
m_{TOT}	=	Overall building mass
$m^0{}_{TOT}$	=	Overall building mass without the non-oscillatory mass
m_N	=	North side building mass
$m^0{}_N$	=	North side building mass without the non-oscillatory mass
m_S	=	South side building mass
$m^0{}_S$	=	South side building mass without the non-oscillatory mass
m_R	=	Gables-roof assembly mass
$m^0{}_R$	=	Mass of the top half portion of the gables-roof assembly
PS_A	=	Pseudo-spectral acceleration (for 5% damping ratio)
$PS_A(T_1)$	=	Pseudo-spectral acceleration at the fundamental vibration period (for 5% damping ratio)
$PS_A(T_{1,i})$	=	Pseudo-spectral acceleration at $T_{1,i}$ (for 5% damping ratio)
$PS_A(T_{1,und})$	=	Pseudo-spectral acceleration at $T_{1,und}$ (for 5% damping ratio)
$PS_A(T_{1,dam})$	=	Pseudo-spectral acceleration at $T_{1,dam}$ (for 5% damping ratio)
$PS_{A,avg}$	=	Geometric mean of pseudo-acceleration spectrum from $T_{1,und}$ to $T_{1,dam}$ (for 5% damping)
PGA	=	Peak ground acceleration
RSC	=	Roof-shear coefficient
RSC^0	=	Roof-shear coefficient for the top half portion of the gables-roof assembly
S_d	=	Spectral displacement (for 5% damping ratio)
t	=	Time
T	=	Vibration period
T_1	=	Fundamental vibration period
$T_{1,und}$	=	Fundamental vibration period of the undamaged structure
$T_{1,i}$	=	Fundamental vibration period of the structure after the i^{th} test (see ID No. in Table 4.1)
$T_{1,dam}$	=	Fundamental vibration period of the fully-damaged structure (*i.e.*, after the SC2-500% test)
$V_{b,S}$	=	South wall base shear

$V^0_{b,S}$	=	South wall base shear without non-oscillatory mass
$V_{b,N}$	=	North wall base shear
$V^0_{b,N}$	=	North wall base shear without non-oscillatory mass
$V_{b,TOT}$	=	Overall base shear
$V^0_{b,TOT}$	=	Overall base shear without non-oscillatory mass
$\gamma_{xyi}(f)$	=	Coherence function
Δ_x	=	Displacement in the longitudinal building direction (w.r.t. the shake table)
Δ_g	=	Base displacement (shake table / foundation beam)
$\Delta_{1,S}$	=	South floor-diaphragm displacement
$\Delta_{1,N}$	=	North floor-diaphragm displacement
$\Delta_{1,E}$	=	East floor-diaphragm displacement
$\Delta_{1,W}$	=	West floor-diaphragm displacement
$\Delta_{1,AVG}$	=	Average floor-diaphragm displacement
Δ_R	=	Roof ridge displacement
δ_R	=	Relative roof ridge displacement (w.r.t. the average floor displacement, $\Delta_{1,AVG}$)
$\Delta_{t,C,W}$	=	West chimney displacement at the top
$\Delta_{t,C,S}$	=	South chimney displacement at the top
$\Delta_{m,C,S}$	=	South chimney displacement at mid-height of the free-standing stack
$\Delta_{1,C,S}$	=	South chimney displacement at the floor level
$\delta_{C,S}$	=	Normalised differential displacement of the free-standing part of the South chimney
$\delta'_{C,S}$	=	Normalised differential displacement of the part of the South chimney above the flashing
ρ_{mortar}	=	Density of mortar
ρ_b	=	Density of bricks
$\rho_{m,w}$	=	Density of masonry (from double-wythe wallettes tested in compression)
$\rho_{m,t,bw}$	=	Density of masonry (from triplets tested in bond wrench)
$\rho_{m,t,s}$	=	Density of masonry (from triplets tested in shear)
μ	=	Masonry (bed-joint) shear friction coefficient
μ_{tor}	=	Masonry (bed-joint) shear friction coefficient in torsion

1 INTRODUCTION

1.1 Scope Statement

In recent years, the Groningen region of the Netherlands has been hit by small-magnitude earthquakes induced by natural-gas extraction and consequent reservoir depletion (Bourne *et al.*, 2015; Van Elk *et al.*, 2017). Low-intensity ground shakings occasionally act on the local building stock that mostly consists of unreinforced masonry (URM) buildings, designed without any seismic considerations. Due to the lack of empirical data on the earthquake performance of Dutch masonry buildings, an experimental campaign was launched in 2014, aimed at investigating the seismic behaviour of structural components, assemblies, and entire building systems (Graziotti *et al.*, 2018).

A new test series was designed for 2017-2018 to investigate aspects of the seismic response of URM structures that were not fully explored in previous tests and to reinforce the initial findings from the experimental activities of the past few years. Given the scarcity of experimental research regarding the collapse of masonry buildings at full scale, the emphasis was put on designing shake-table tests that induce collapse (Tomassetti *et al.*, 2018; Correia *et al.*, 2018). Moreover, due to the limited available experimental information on the seismic response of non-structural masonry elements, such as chimneys and gables (Giaretton *et al.*, 2017), investigating their role in the overall building performance was deemed essential to the project.

In that regard, an incremental shake-table test was recently performed on a full-scale building model up to collapse conditions at the experimental facilities of LNEC in Lisbon, Portugal, in collaboration with the research group for Masonry Structures of EUCENTRE. The specimen, named LNEC-BUILD-3, embodied features of typical Dutch detached houses dating to before World War II (Figure 1.1), such as large openings, a timber floor diaphragm, a gambrel roof with tall gables, two high clay-brick chimneys, and several other construction details that mostly affect the seismic vulnerability of these buildings. Among other aspects, the new tests targeted mainly towards:

i) improving analytical models for the prediction of URM damage with the focus on both in-plane and out-of-plane failure modes;

ii) refining the definition of damage limit states for clay-URM walls;

iii) correlating the observed damage with quantitative engineering parameters for the performance assessment of URM buildings;

iv) validating numerical models to predict the collapse of URM structures using macroelement and discrete element modelling strategies;

v) investigating the effect of flexible diaphragms on the in-plane and out-of-plane response of walls and entire façades;

vi) assessing the seismic performance and collapse of non-structural masonry elements such as chimneys and gables;

vii) evaluating the mechanical properties of clay-brick masonry walls.

The tests provided a large dataset that captures at full scale the in-plane and out-of-plane response of clay-URM walls, and the influence of various construction details on the dynamic global response of entire buildings. Interpretation of the experimental results will constitute the basis for the development of analytical and numerical models, to estimate the dynamic response and the parameters for the performance-based seismic assessment of URM buildings.

Figure 1.1 Building example of the typology in question: (a) North-East view; (b) South-East view. Street Nieuwstratt 8, Loppersum, Groningen.

1.2 Motivation in Test Design

The design of the test building was partially guided by the simulation results of a numerical reference model generated with the Extreme Loading for Structures (ELS) software using the applied element method (AEM)[1] (Pinho *et al.*, 2017). The highly detailed model simulated the earthquake response of a pre-1940 Dutch detached building in Groningen, made of clay-URM walls, with a timber gambrel roof and a flexible timber-floor diaphragm (Figure 1.2). Openings were present in three out of the four building façades, while a vertical chimney was attached to one of the transverse building walls (*i.e.*, West), at midspan. The floor was composed by a system of timber joists spanning discontinuously between the longitudinal, South and North walls: a central timber girder provided intermediate support to the joists. The girder was embedded at one end into the masonry of the East wall, while at the other end it was supported by an interior wall.

The numerical reference model was built based on real dimensions, and in reality, the transverse East and West walls of the reference building are longer than the proposed geometry of the building specimen. Driven by the limiting dimensions of the shake table, the length of the East and West façades had to be shorter (by approximately 20-30%), reducing the effects on the OOP vulnerability of the walls. As a way to counterbalance the favourable effects of shortening the length of the East façade, it was decided to build it as a single-wythe wall. Contrary to the East wall, the West façade was designed as double-wythe. The latter is due to the presence of the chimney, since otherwise: i) the part of the wall at the location of the chimney would result too much stiffer compared to the rest of the wall; ii) the interlocking would be less realistic, in contradiction with information provided by local practitioners from Groningen.

A second chimney was introduced in the specimen design with the purpose to investigate the dynamic response of building chimneys with different free-standing lengths above the roofline, at locations in the building plan characterised by dissimilar expected displacement and acceleration demands. Both chimneys were designed based on typical Dutch URM building chimneys found in Loppersum of Groningen, such as those shown in Figure 1.3.

It is important to stress that in designing the building specimen at full-scale, it was not intended to replicate a real building from the Groningen area. That was neither possible, due to the limiting dimensions and payload limit of the shake table, nor desirable, as even buildings of the same typology often exhibit diversity in building geometry, employed materials and structural detailing

[1] Applied Element Method is a modelling approach that combines traits of both the Finite Element Method (FEM) and the Discrete Element Method (DEM). With more than two decades of continuous research and development AEM is considered a promising method that can track structural collapse behavior passing through all stages of response: elastic; crack initiation and propagation; element separation (Meguro and Tagel-Din, 2000; ASI, 2017).

that limit the value of the acquired information. Instead, the main aim was to carry out tests on a generic structure with typical characteristics of the systems in question that could provide plenty of data for the development and tuning of numerical models. Therefore, the building prototype included many construction details found in the typology in question, but rarely someone would see all of them in a single real building.

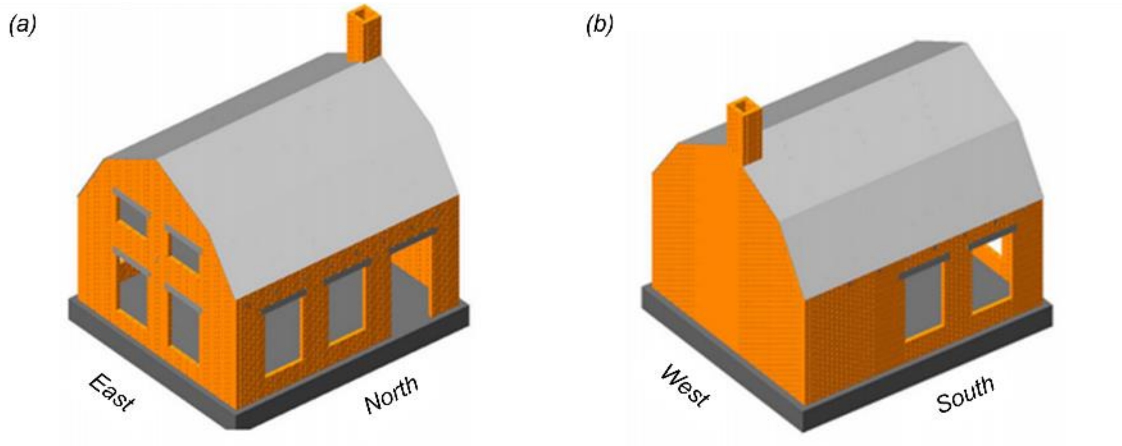

Figure 1.2 Numerical model of a building resembling the LNEC-BUILD-3 prototype developed on Extreme Loading for Structures software: (a) East-North view; (b) West-South view (Pinho et al., 2017).

Figure 1.3 Examples of typical Dutch building chimneys in Loppersum, Groningen. Streets: (a) Kruisweg 2; (b) Kruisweg 16; (c) Badweg 49; (d) Molenweg 7; (e) Singelweg 22; (f) Wirdumerweg 2.

2 SPECIMEN OVERVIEW

2.1 Specimen Geometry

The prototype building was characterised by a 2.72-m floor height (measured to the top of the attic floorboards) and a 2.50-m-high symmetrical gambrel roof extending over tall gable walls that were weakly connected to the roof framing. Such gables are generally more vulnerable when subjected to out-of-plane excitation. Hence, the unidirectional shake-table tests were performed in the direction perpendicular to the gables, as shown by the arrows in Figure 2.1.

The overall footprint dimensions were 5.66 m in the shaking direction, 5.44 m in the transverse one, and the walls were constructed in a rectangular layout (Figure 2.2a). The load-bearing structural system consisted of 208-mm-thick, double-wythe clay-URM walls in three out of the four perimeter walls. The East façade, built orthogonal to the shaking direction, was made of a single, 100-mm-thick wythe with openings both in the first storey and the roof. Large asymmetrical openings were also present on the North and South façades, resulting in varying wall areas in the longitudinal direction with the intent to magnify differential wall displacements under uniaxial seismic excitation (Figure 2.2b and Figure 2.3).

A 100-mm-thick interior wall was built parallel to the direction of shaking, longwise the centreline of the building plan (Figure 2.2). The wall was 1.98-m long, including two symmetric 0.75-m-wide flanges, and did not extend over the floor. Two openings were foreseen to avoid interference with the beams of a steel frame installed in the interior of the building: a 57×55 cm window at the height of 0.72 m, and a smaller one, with dimensions 57×31 cm, at 2.04 m (Figure 2.4a; section B-B').

Figure 2.1 Full-scale building specimen: (a) North-West view; (b) South-East view. Arrows indicate the direction of shaking.

The floor was made of timber joists and planks, resulting in a flexible diaphragm spanning discontinuously between the longitudinal walls; the interior wall and a timber girder provided intermediate support to the floor joists. The girder was located at midspan of the transverse building direction, supported by the East façade and the interior wall. There was no connection of the floor diaphragm to the West wall, which was restrained only at its vertical edges, *i.e.*, at the intersections with the North and South walls.

The specimen included two vertical chimneys: one was interlocked with the West wall, while the second one was built together with the squat South pier (Figure 2.3). Both chimneys were of brick construction. They were designed to have the same flue (34×34 cm) and a total height of 5.28 m, reaching slightly higher than the roof ridge (5.22 m). The chimney stack in the South façade was sensibly slender, extending about 2.3 m above the roofline, while the West chimney was squatter as it penetrated the pitched roof very close to the ridge, extending about 0.9 m above the roofline.

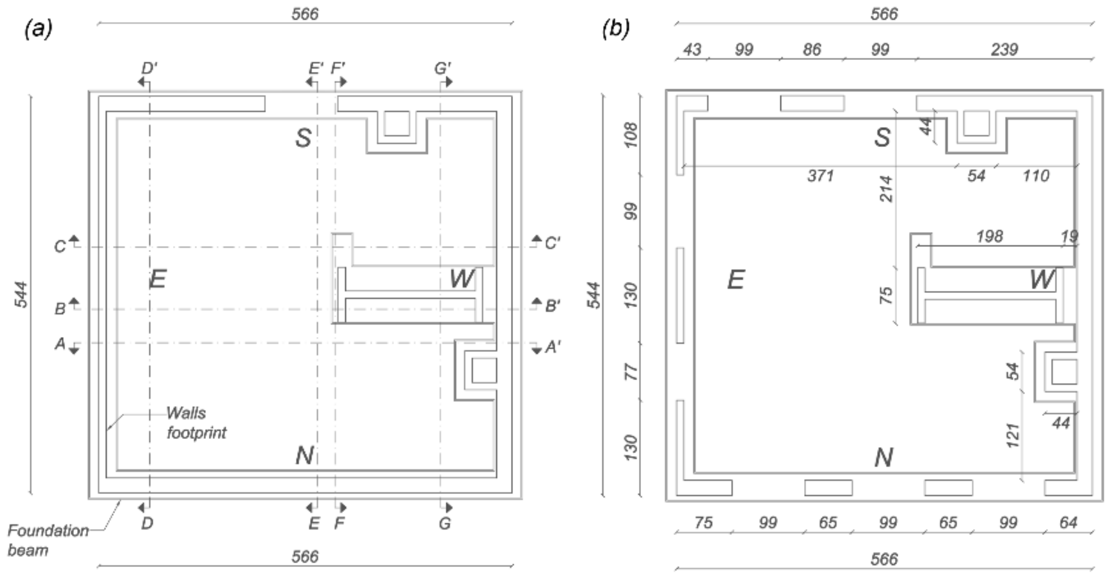

Figure 2.2 Plan of the building specimen: (a) walls footprint; (b) section at 1 m from the base. Units of cm.

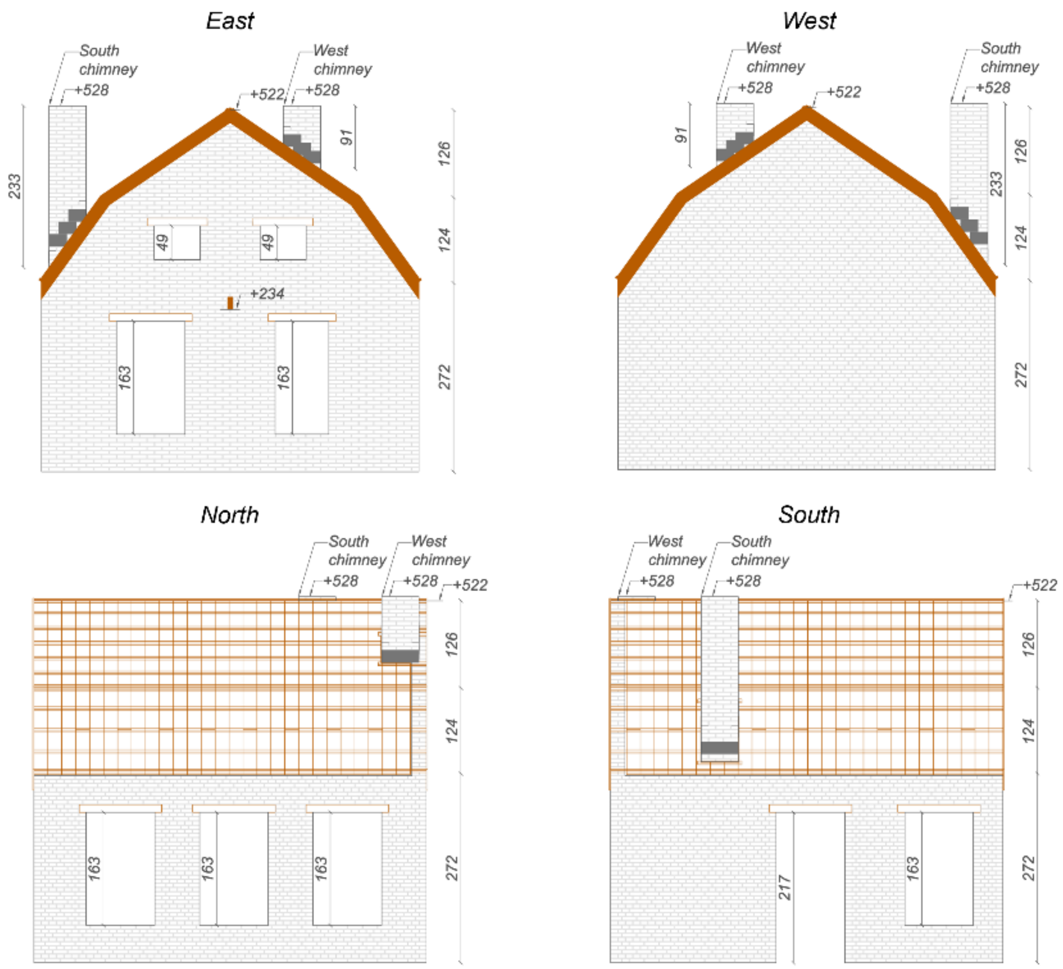

Figure 2.3 Elevation views of the building specimen. Units of cm.

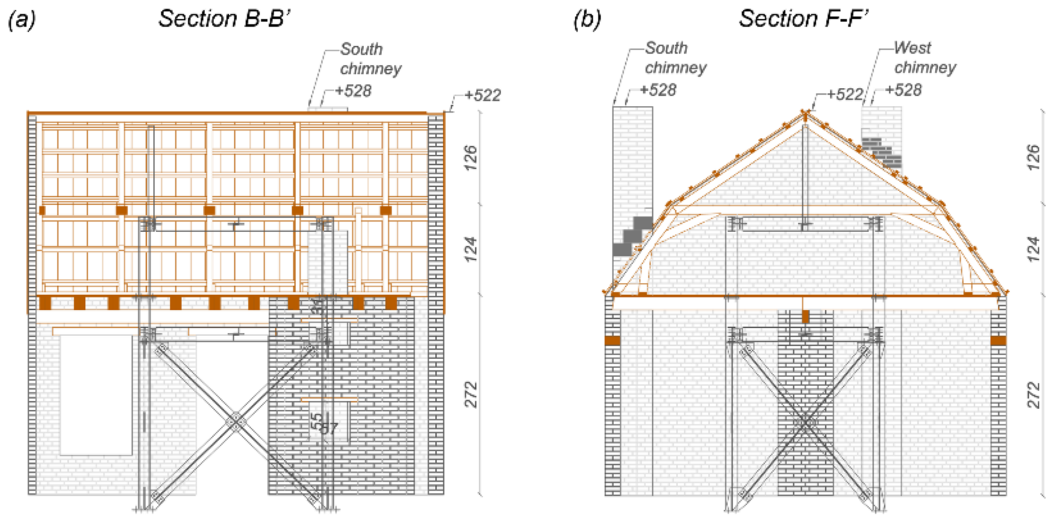

Figure 2.4 Sections in elevation of the building specimen: (a) section B-B'; (b) section F-F'. Units of cm.

All walls were supported by a composite steel-concrete foundation rigidly fixed to the shake table (Figure 2.5a). A rigid steel frame was installed inside the building specimen (Figure 2.5b). This structure served as a safety system, protecting the shake table against impact due to structural collapse, and constituted a rigid reference system for direct measurement of the floor, wall, and roof displacements. The frame was not in contact with the building since its columns ran through four holes in the floor diaphragm.

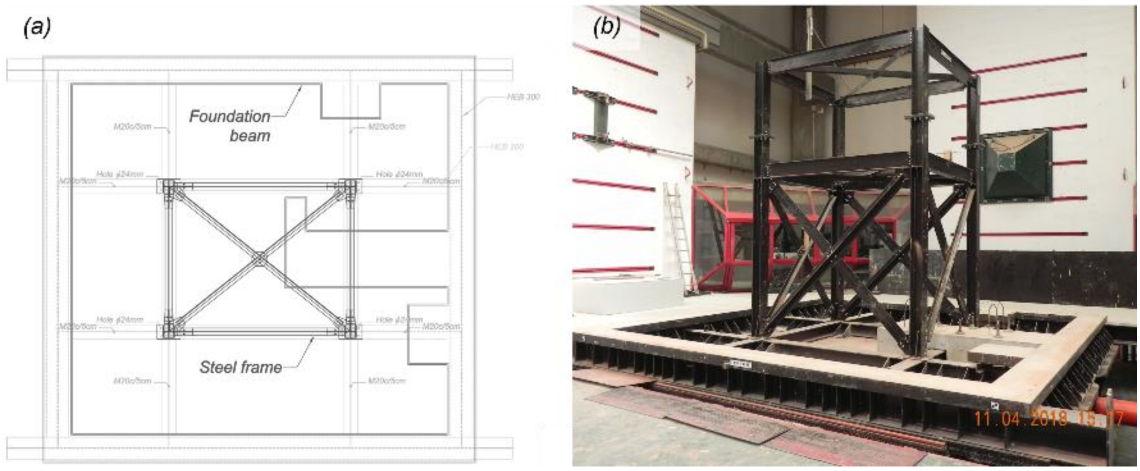

Figure 2.5 Building foundation and safety frame: (a) foundation plan; (b) North-West view of the steel frame.

2.2 Construction Details

Even though not expected to be exhaustive of all possible geometric variations of the local building stock, the building prototype included several characteristics representative of pre-1940s clay-brick detached URM houses of the Groningen region. A firm of builders from the province of Groningen built the masonry walls, using materials shipped from the Netherlands. Portuguese contractors undertook the construction of the gambrel roof following indications provided by Dutch practitioners. The specimen was built at full scale directly on the shake table of the LNEC laboratory to avoid possible damage during transportation.

2.2.1 Masonry walls and lintels

The *Dutch cross* brickwork bond was adopted for the double-wythe bearing walls, with 208×100×50 mm solid clay bricks and 10-mm-thick, fully mortared head and bed joints (Figure 2.6). This bond is slightly different from the *English cross* bond in generating the lap at the quoins (Mitchell, 1956): in Dutch bond, all quoins are three-quarter bats, placed in alternately stretching and heading orientation with successive courses (hence, there is no need of placing queen closers). The characteristics of this type of bond are readily appreciated in Figure 2.7 that illustrates four successive courses of brickwork above the windows apron (*i.e.*, from the 13th to the 16th course of bricks). The East façade and the interior wall were built with the standard stretcher bond (sometimes termed as the half-running bond), where bricks in successive courses were staggered by half a stretcher.

Lintels were placed above all openings (Figure 2.8): they consisted of a 110-mm-deep timber beam with a width equal to the thickness of the wall, extending into the masonry 100 mm on each side of the opening for support. Most masonry buildings in Groningen include lintels made of reinforced concrete (RC). In the case of the test building, adhering to the local practices would require casting the RC elements several days before the beginning of the construction. Due to the short period intervening between the design of the specimen and the scheduled beginning of the construction works, the idea of placing RC lintels was quickly abandoned. Instead, timber lintels were used to span the space between the piers of the building walls.

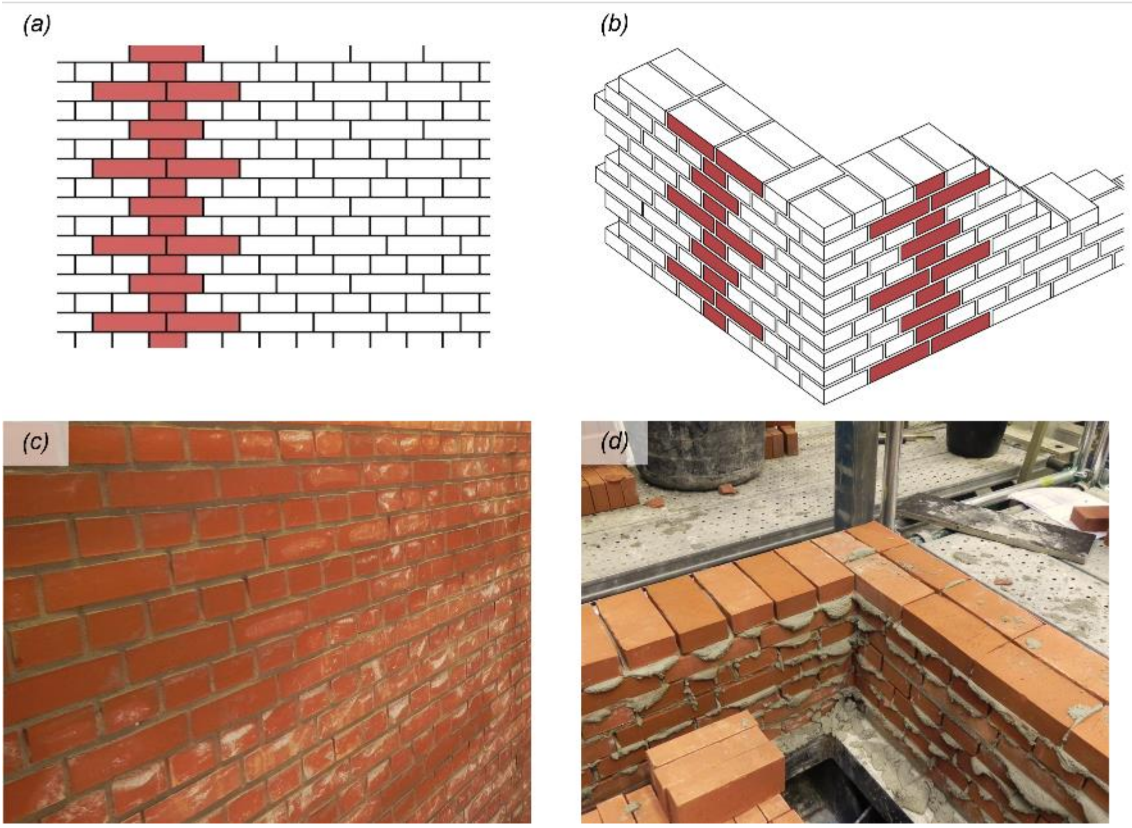

Figure 2.6 Construction details of the building specimen: (a, b) Dutch cross bond scheme; (c) brickwork bond of the West building façade; (d) interlocking of walls at the South-West corner.

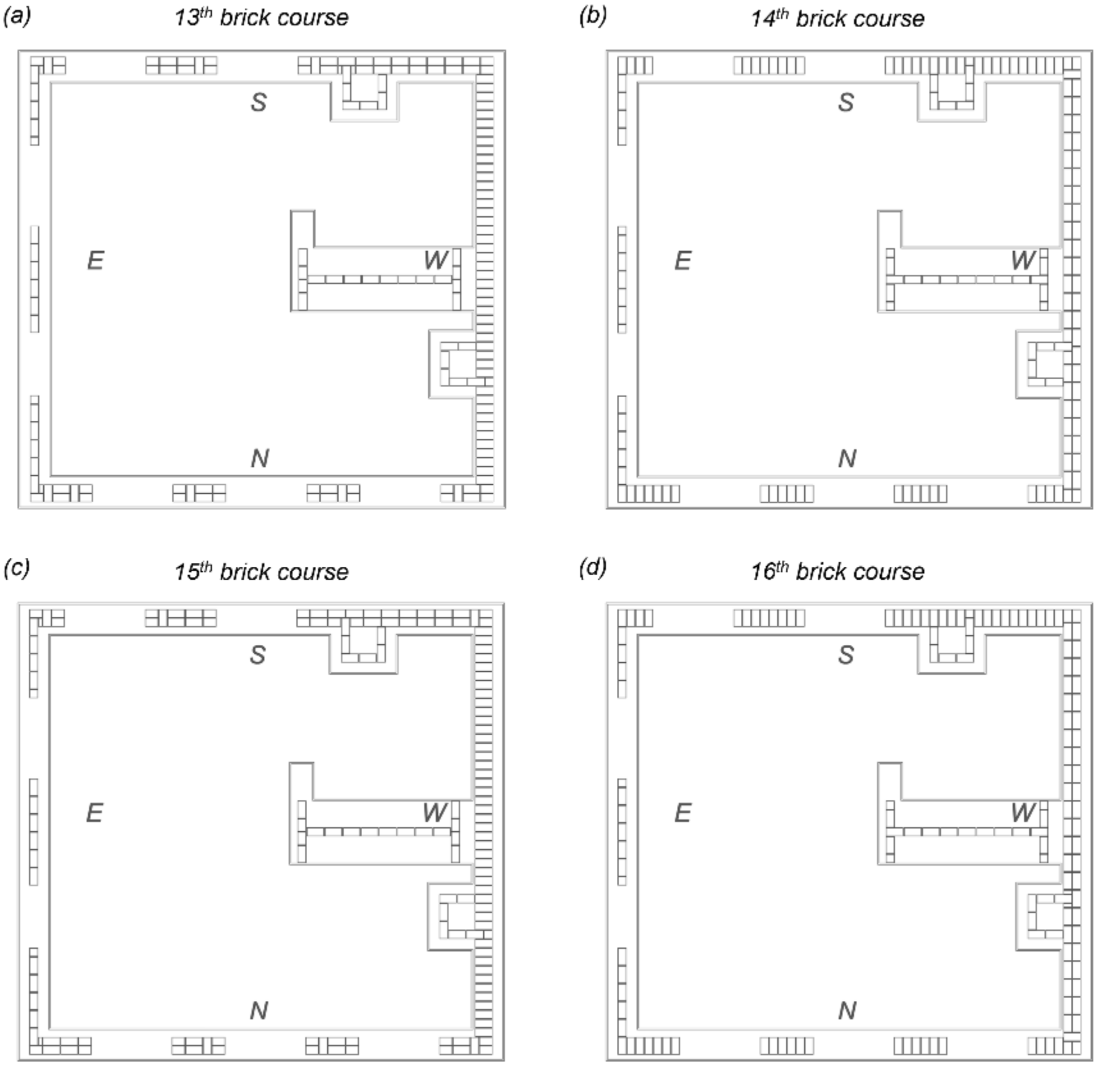

Figure 2.7 Successive courses of bricks in the Dutch cross bond: (a) 13th; (b) 14th; (c) 15th; (d) 16th brick layers (above the level of the windows apron).

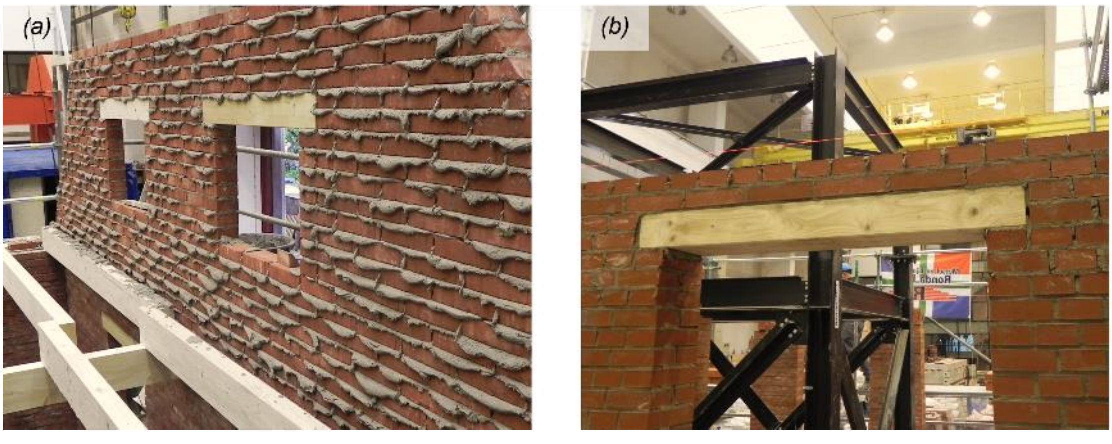

Figure 2.8 Construction details of the building specimen: (a) timber lintels above the openings of the East gable wall; (b) lintel placed above the window of the South façade.

2.2.2 Floor diaphragm

The floor diaphragm consisted of 190-mm-wide×24-mm-thick straight-edge timber (pine) floorboards, nailed perpendicularly to 9 pairs of single-span timber joists of section 75-mm wide and 180-mm deep, stretching across the North-South direction (Figure 2.9a and b). The joists were lapped over the interior wall and a central 75-mm-wide×180-mm-deep timber girder that divided the distance between the longitudinal walls in two 2.6-m-long spans. The girder was supported at one end on the full thickness of the East wall (Detail A; Figure 2.10a and b), while at the other end it was embedded into the eastern flange of the interior wall (Detail B; Figure 2.10c and d).

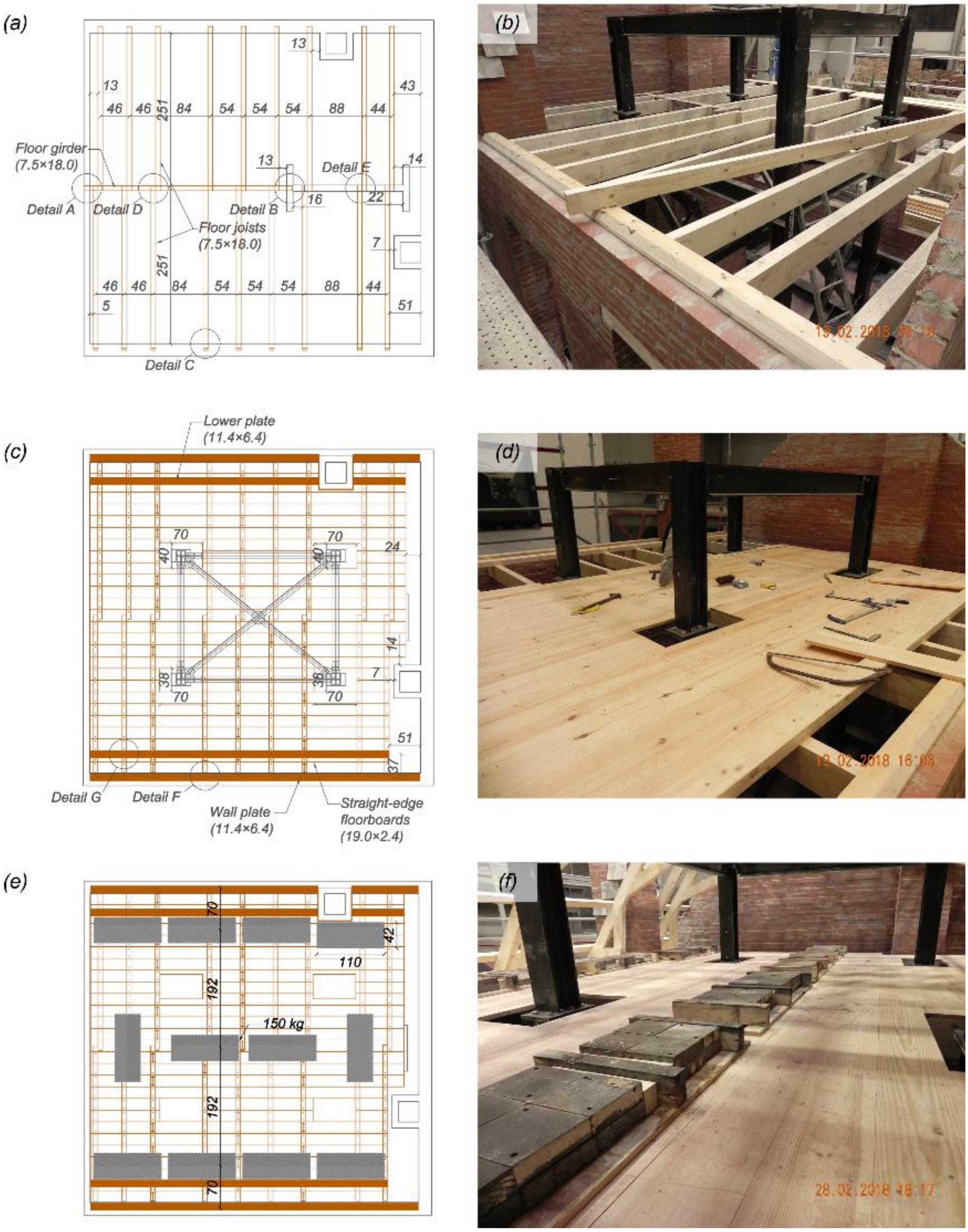

Figure 2.9 Floor framing: (a) floor framing plan; (b) floor joists during construction; (c) floorboards layout; (d) floor sheathing during construction; (e, f) additional masses on top of the floor. Units of cm.

The wood joists were supported on the inner wythe (~100-mm wide) of the longitudinal walls at height 2.52 m above the foundation. The ends of the joists inserted into the masonry were cut at an 80° angle (Detail C; Figure 2.11a and b); no extra devices were provided to stiffen the connection. All beams were laid directly on the bricks: there was no bed-joint, but only joints filled with mortar on the two vertical sides of each section. At the other ends, the joists merely rested on the full width of the floor girder, without any mechanical connection (Detail D; Figure 2.11c and d). The joists laying on the top of the interior wall were embedded into the full thickness of the wall, in pocket connections and absence of mortar around the timber sections (Detail E; Figure 2.11e and f).

Two 114-mm-wide×64-mm-deep timber wall plates were placed above the longitudinal South and North walls. They were screwed to the floor joists at the locations where the latter were recessed into the masonry using 100-mm-long screws of 4.0 mm diameter. There was no mortar above the bricks, consequently the plates were not in direct contact with the top of the walls (Detail F; Figure 2.12a and b). Two 114-mm-wide×64-mm-deep longitudinal timber beams, termed as lower plates, were additionally fastened on top of the floor joists at a short distance parallel to the wall plates (Detail G; Figure 2.12c and d). These timber plates were installed to transfer loads from the roof trusses to the floor and the top of the walls.

The floorboards were nailed to the joists with two nails at each intersection. The nails were 65 mm long and 3.1 mm in diameter (see Detail H; Figure 2.15a and c). Four small openings (approximately 70×40 cm) were foreseen in the floor sheathing so that the columns of the safety frame could run through the diaphragm, oversized to accommodate the lateral displacements of the specimen. The net floor area was 24 m^2, and the exact layout of the floorboards is illustrated in Figure 2.9c and d. An additional mass of 1.8 t was provided to the floor by twelve 150-kg-heavy blocks of steel plates, evenly distributed over the diaphragm to account for superimposed dead and live loads (Figure 2.9e and f).

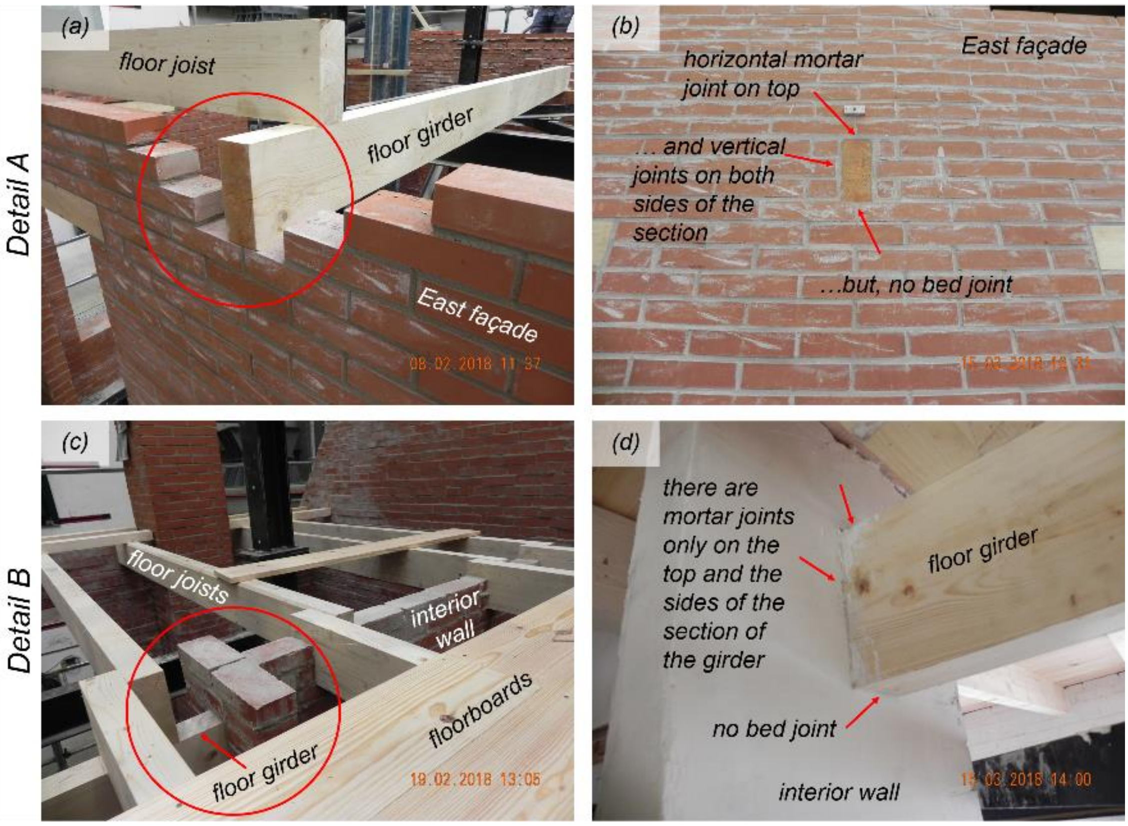

Figure 2.10 Construction details of the floor: (a, b) connection of the floor girder to the East wall; (c, d) support of the floor girder on the interior wall.

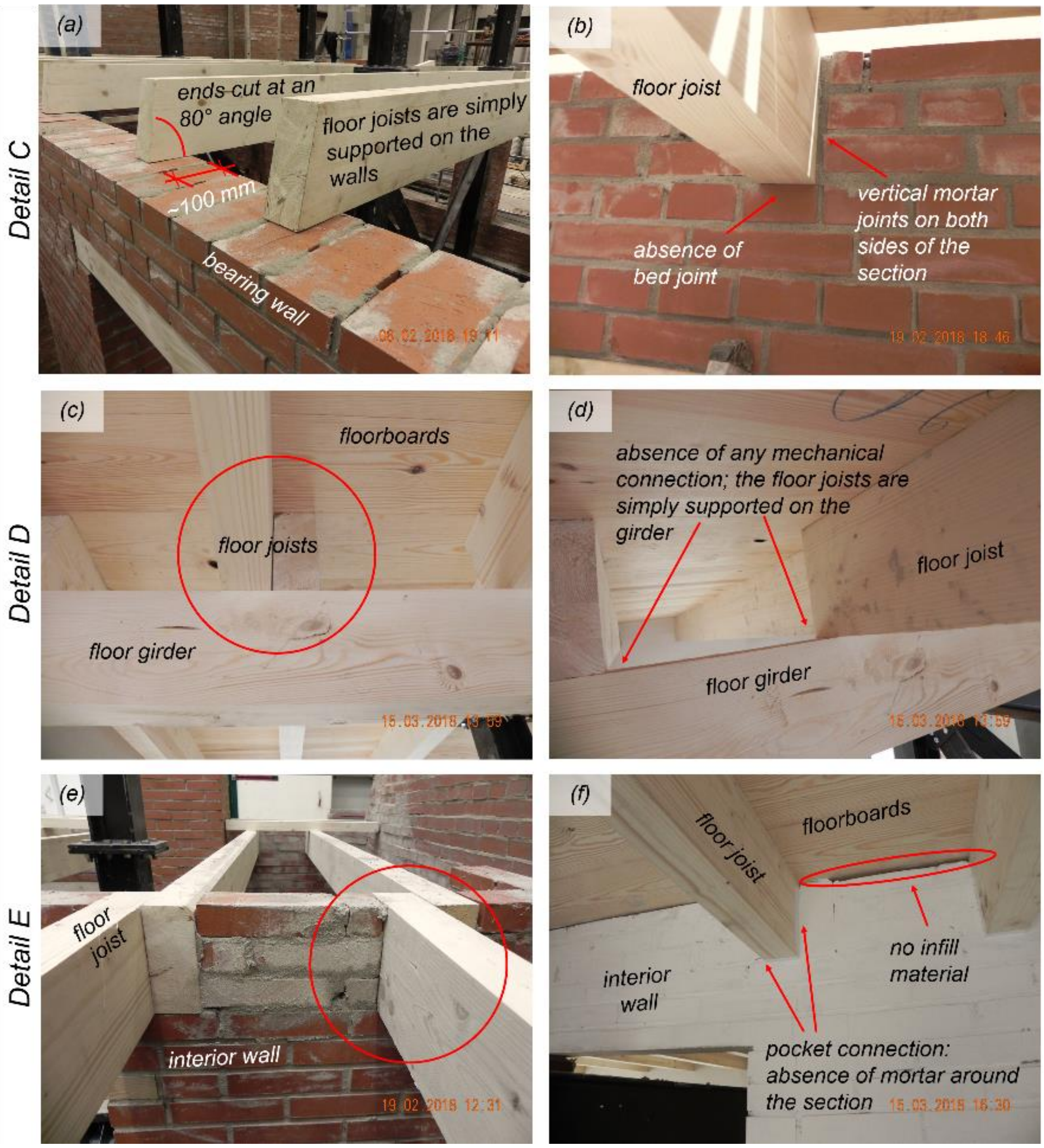

Figure 2.11 Construction details of the floor: (a, b) support of the floor joists on the perimeter walls; (c, d) support of the floor joists on the central girder; (e, f) connection of the floor joists with the interior wall.

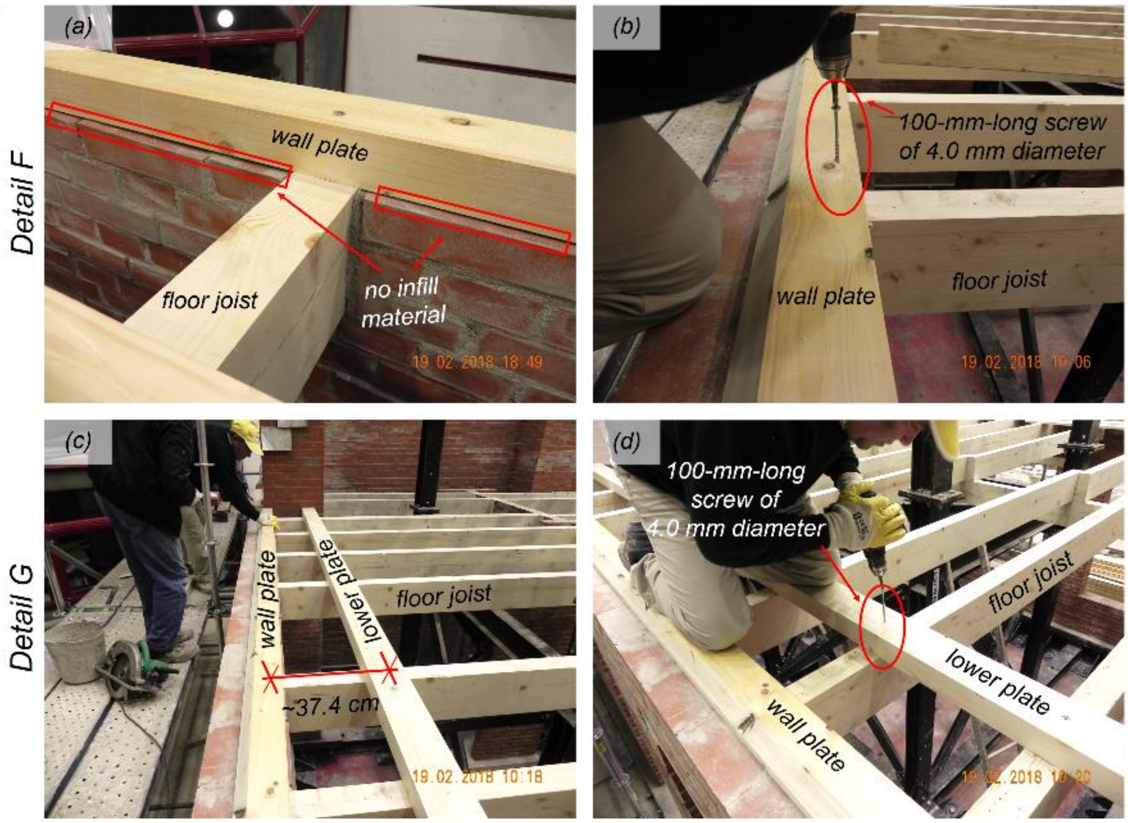

Figure 2.12 Construction details of the floor: (a, b) connection of the wall plates to the floor joists; (c, d) connection of the lower plates to the floor joists.

2.2.3 Gambrel roof

The prototype building had a 2.5-m-high symmetrical gambrel roof (measured from the top of the floorboards to the ridge of the roof sheathing). The external roof shape was designed to combine two slopes, 54° and 34° for the lower and the upper gambrel pitch, respectively (Figure 2.13). The structure consisted of five South-North timber trusses, supporting fourteen 64-mm-wide×44-mm-deep purlins and a 38-mm-wide×120-mm-deep ridge beam (Figure 2.14a and b).

The truss rafters were connected to timber wall plates placed above the longitudinal, South and North walls. The plates were screwed to the floor joists at the locations where the latter were recessed into the masonry. Screws were used to ensure the robustness of these connections. Struts were additionally provided to support the rafters and transfer loads of the roof to the floor frame through longitudinal timber beams, termed as lower plates, fastened perpendicularly to the joists. The area was further reinforced with short tie beams (Detail H; Figure 2.15). Horizontal rafter-tie beams were also placed at mid-height of each truss, intended to function as tension ties that resist the outward thrust of opposing rafters. A pair of tie beams were provided, one for each side of the truss to confine the rafters' knee in a lap joint that involved notching of the tie beams only. Details of the joint between the tie beams and the gambrel rafters are illustrated in Figure 2.16 (Detail I). Additional oblique struts were installed to strengthen the joint (Details J and K; Figure 2.17). All connections of the wooden roof trusses were crafted at the construction site (Figure 2.18).

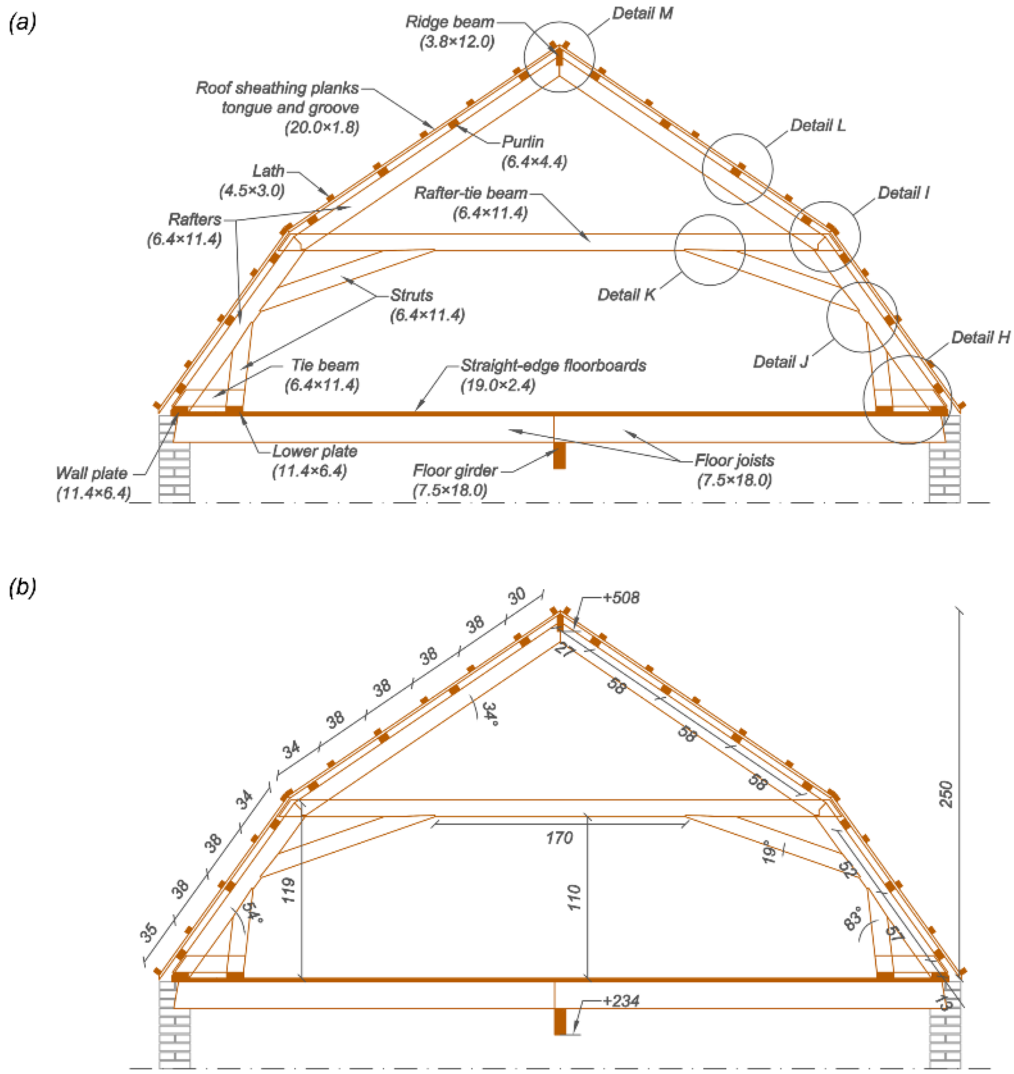

Figure 2.13 Elevation view of the roof structure (Truss A; section D-D'): (a) component elements of the timber truss; (b) truss key dimensions. Units of cm.

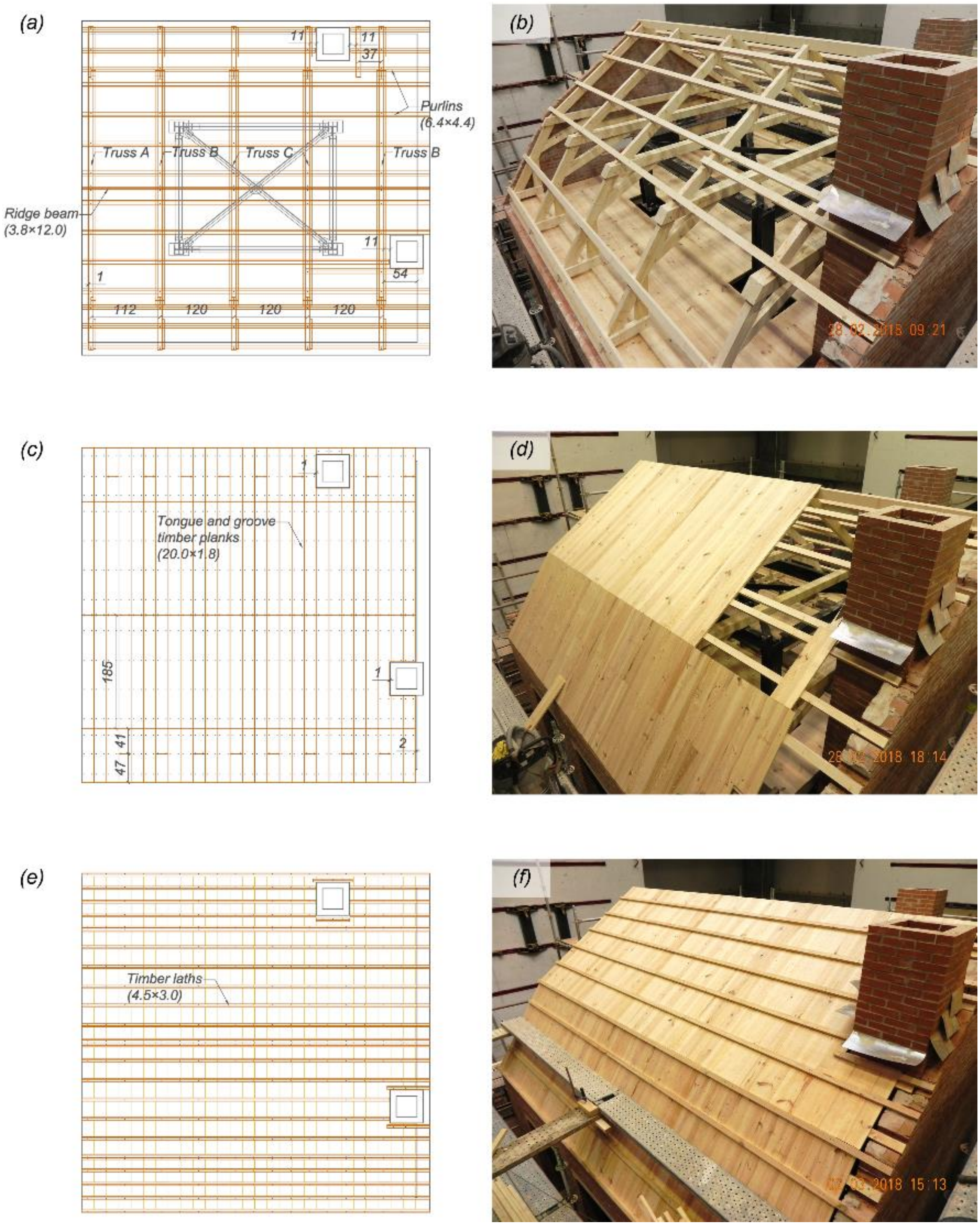

Figure 2.14 Roof framing: (a) roof framing plan; (b) roof trusses spanning between the South and North walls; (c) roof planks layout; (d) roof sheathing during construction; (e, f) strips of laths installed to fasten the tiles. Units of cm.

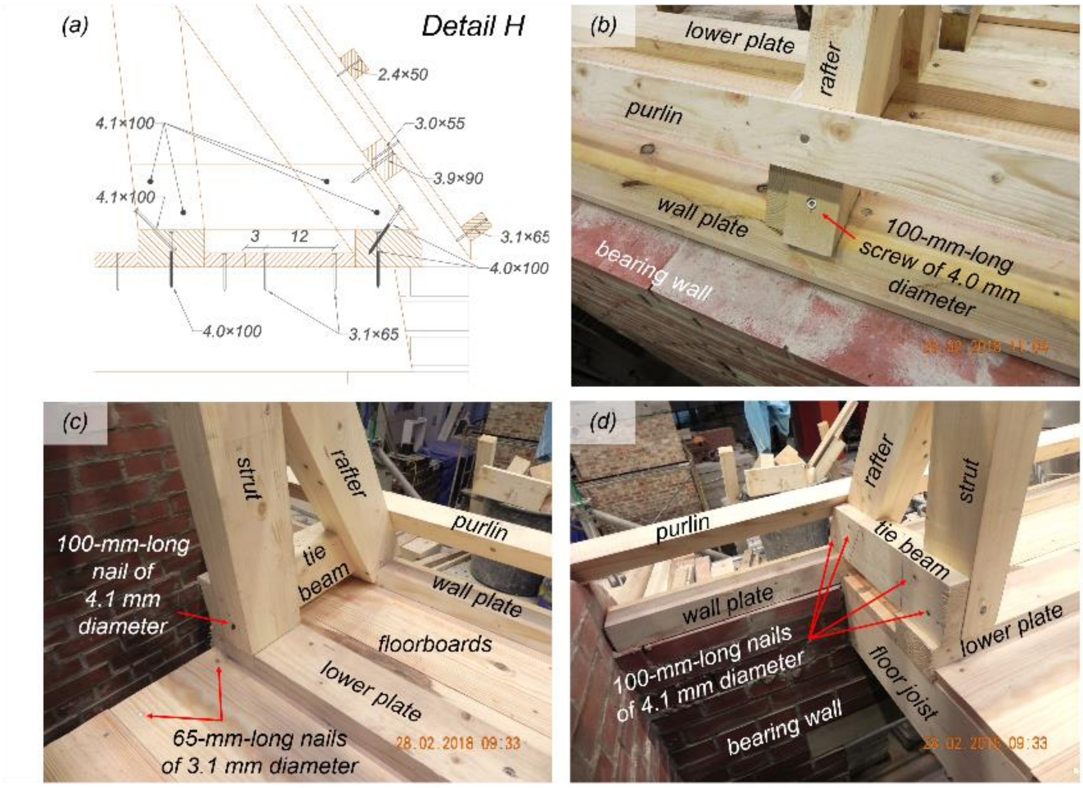

Figure 2.15 Construction details of the roof truss supports: (a) detail drawing of the truss supports; (b) connection of the truss rafter to the wall plate; (c, d) connection details at the lower ends of the truss.

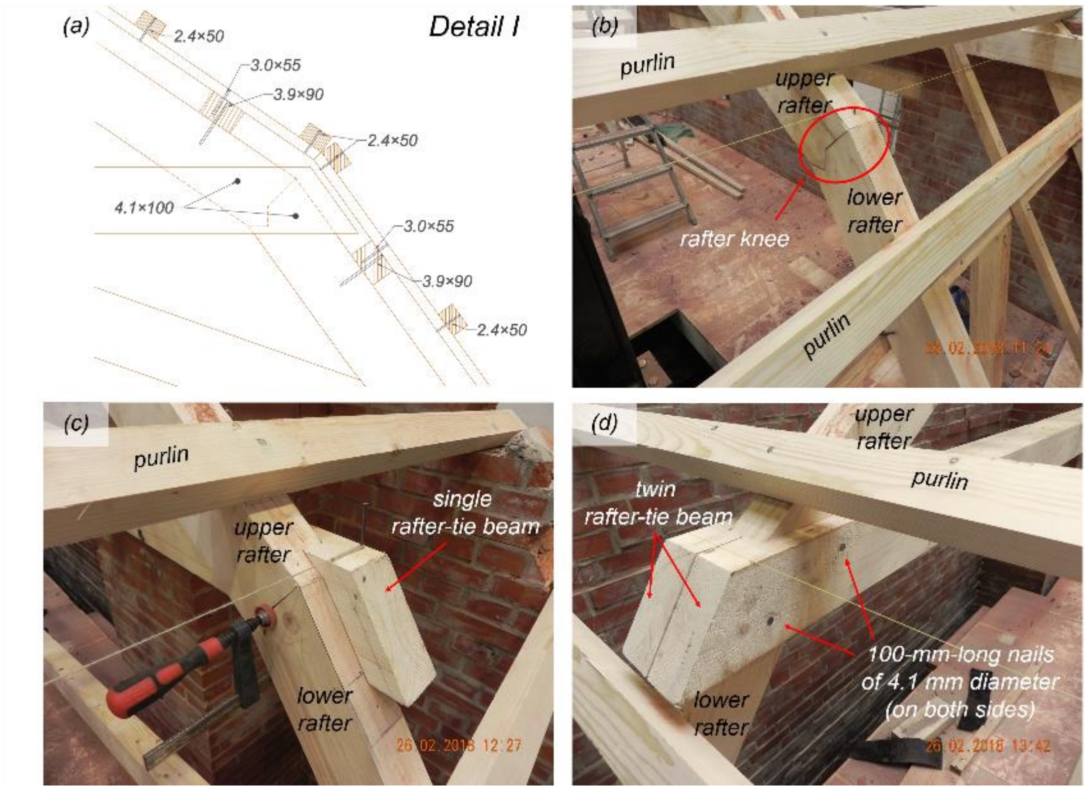

Figure 2.16 Construction details of the rafters' knee: (a) detail drawing of the joint; (b) contact point of the gambrel rafters; (c) realisation of the lap joint; (d) completion of the joint with a double tie-beam.

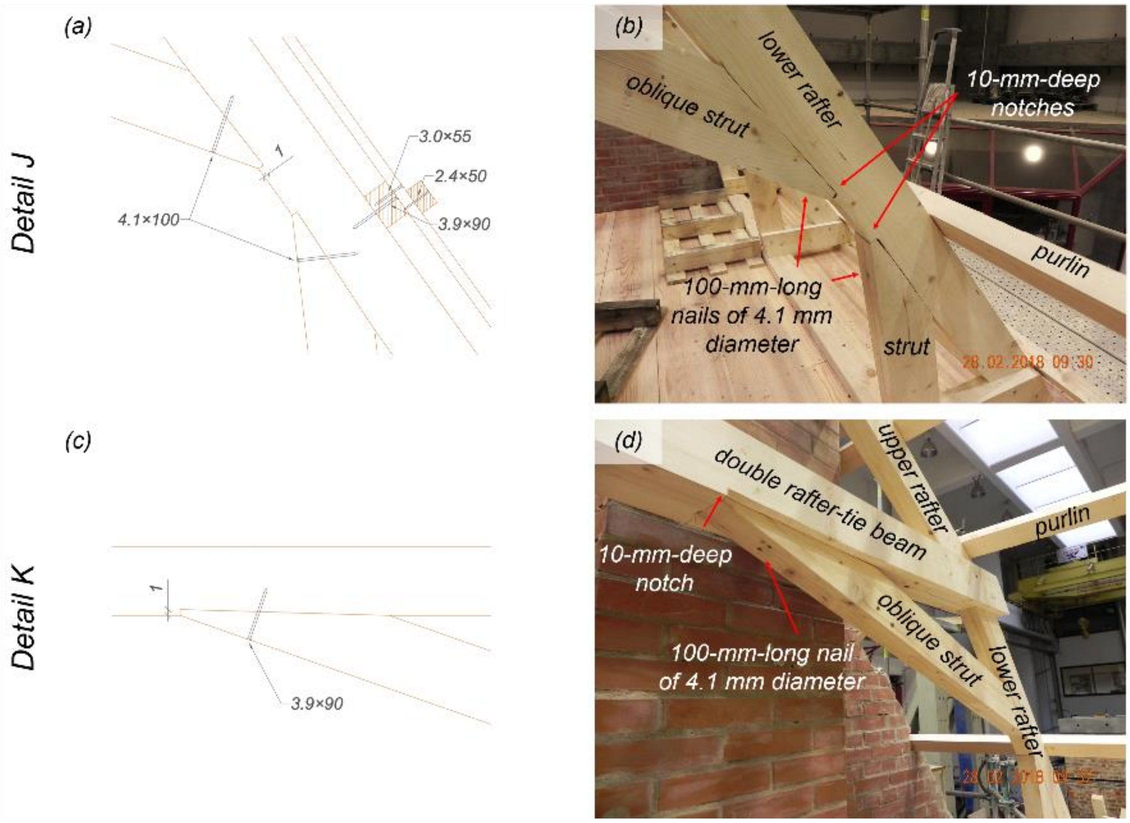

Figure 2.17 Construction details of the roof trusses: (a, b) connection of the struts to the lower gambrel rafter; (c, d) connection of the struts to the double tie-beam.

The roof trusses were installed at nearly equal spaces: the bay between the easternmost truss, termed Truss A, and the next one, Truss B, was 1.12 m, while the succeeding trusses occurred at intervals of 1.20 m (Figure 2.14a). Truss A and Truss B differed in that the former included a single rafter-tie beam that allowed to place the truss almost back to back with the East gable wall, while the latter consisted of a pair of tie beams. A narrow gap of 1 cm was left between Truss A and the East gable wall to avoid pounding of the roof frame on the wall during the construction of the timber structure (Figure 2.19a). On the West side, Truss B was located at a distance approximately 11 cm from the chimney, or 54 cm from the gable wall with the aim to accommodate relative displacements between the roof and the chimney. Truss C was built with the diagonal struts at a slightly higher angle compared to Truss B (*i.e.*, an angle 25° instead of 19°) to prevent interference with the steel safety frame installed inside the building specimen (Figure 2.19b and Figure 2.20).

The purlins extended through both gables but were supported exclusively by the timber trusses; openings were cut on the walls only after their erection and the gaps between purlins and masonry were grouted with mortar (Figure 2.21a and b). This configuration resulted in a very small fraction of gravity load being transmitted to the gables under static conditions. 200-mm-wide×18-mm-thick tongue and groove timber boards were nailed perpendicularly to the purlins above the roof framing (Figure 2.14c and d). The roof was completed with clay tiles, supported by strips of laths nailed above the timber boards, running along the length of the roof (Figure 2.14e and f). Four planks were nailed to the purlins, outside each gable wall (Figure 2.21c and d), forming an end-plate which restrained the relative displacement between gables and roof due to gable out-of-plane response. In particular, 18-mm-thick×190-mm-wide timber boards were attached perpendicularly to the section of the roof purlins using 60-mm-long screws at each connection; the planks were not connected to the ridge beam. These plates proved to be one of the main determinants of the behaviour of the gables, as evident in the damage observed during the last tests: high stresses were developed at the top of the West gable wall that resulted in detaching of the plates from the roof purlins.

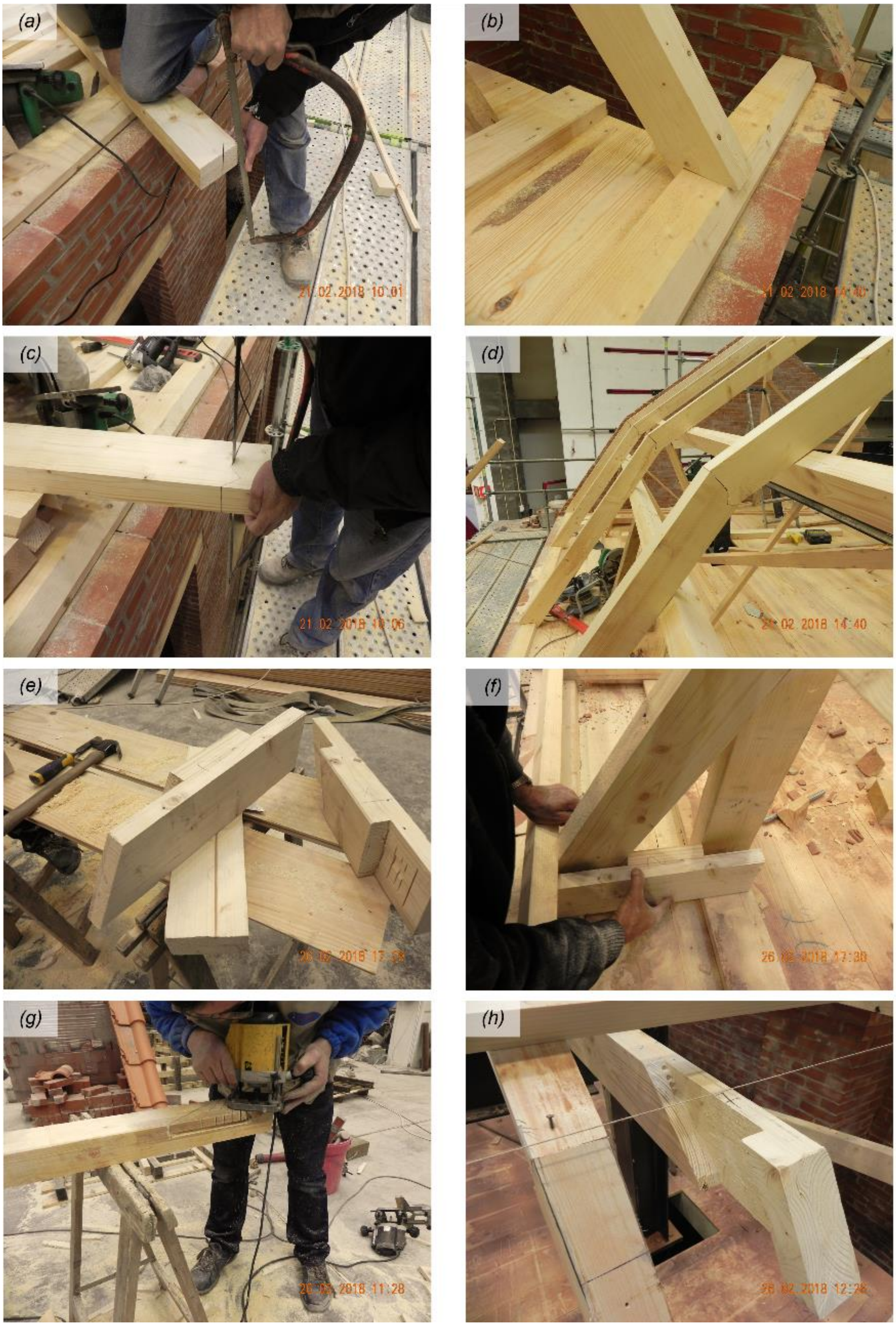

Figure 2.18 Crafting the connections of the timber roof trusses: (a, b) rafters toe; (c, d) rafters knee; (e, f) lower tie beams; (g, h) mortise joint.

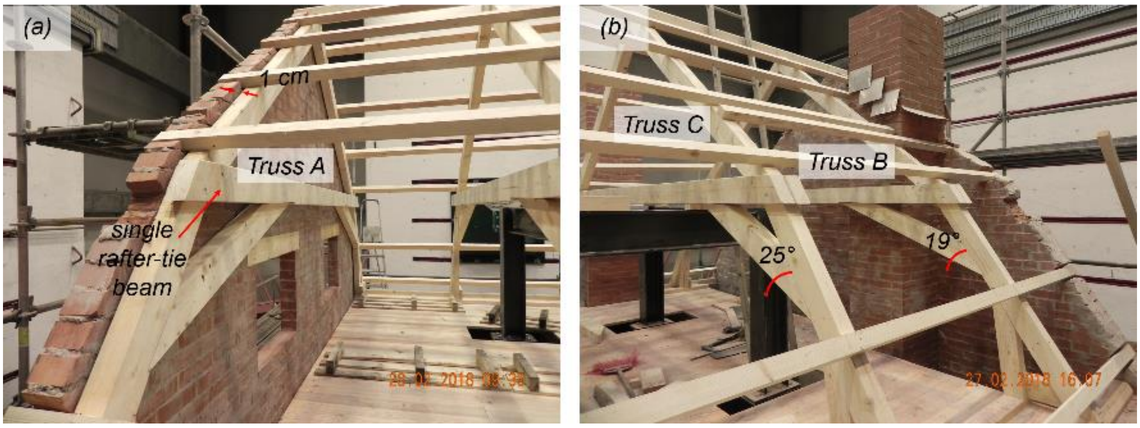

Figure 2.19 Construction details of the roof trusses: (a) Truss A and East gable; (b) Truss B and Truss C.

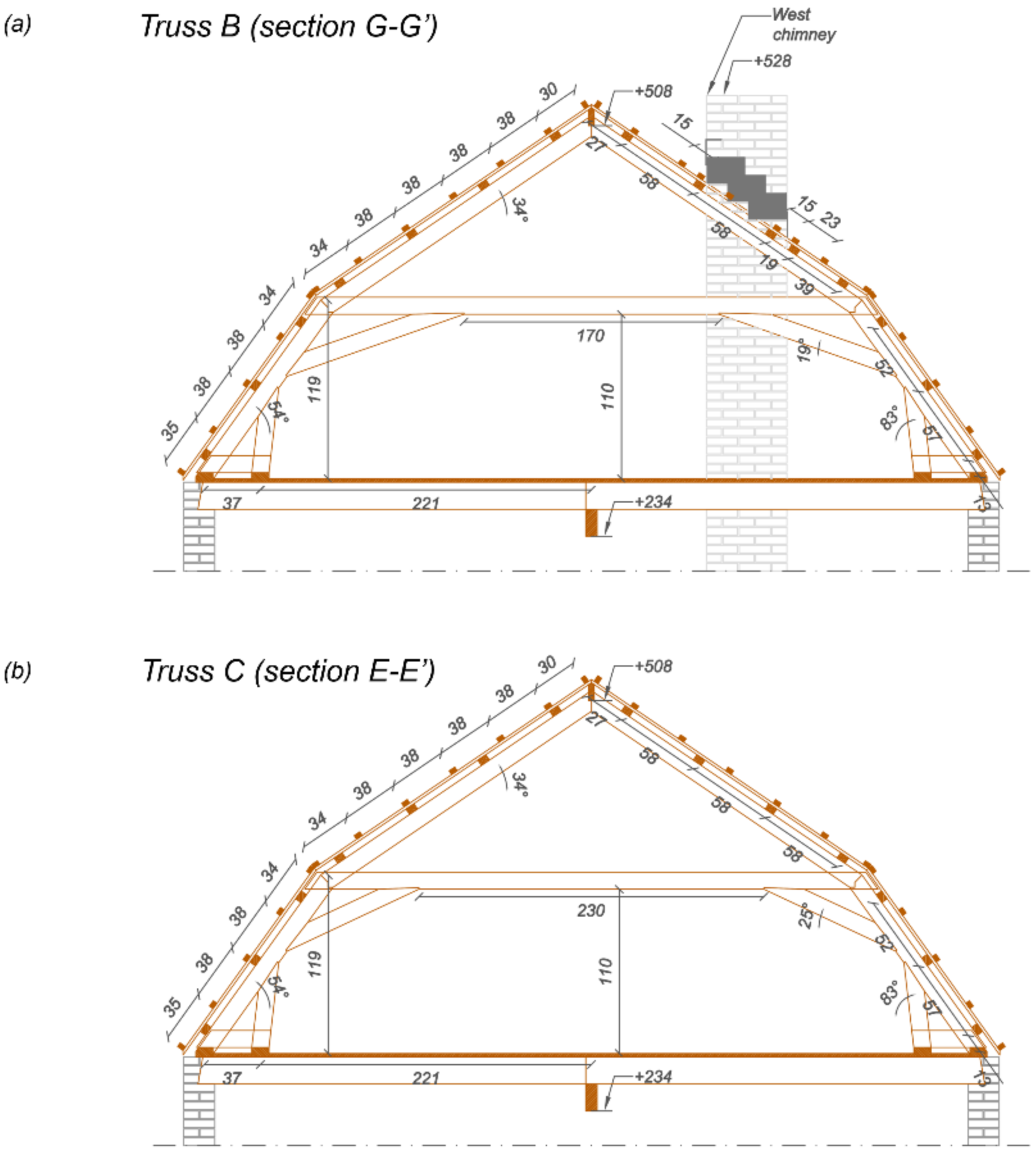

Figure 2.20 Elevation views of the roof trusses: (a) Truss B (section G-G'); (b) Truss C (section E-E'). Units of cm.

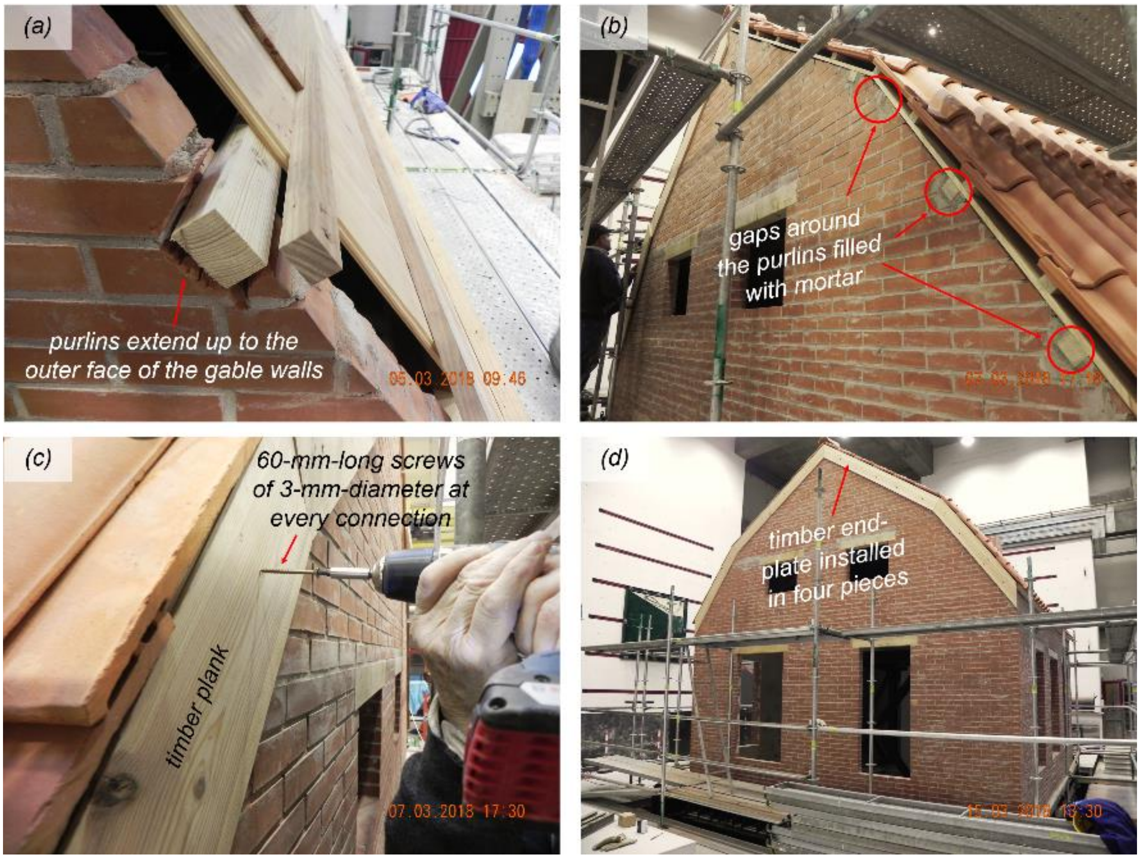

Figure 2.21 Construction details of the roof: (a, b) connections between the purlins and the East gable; (c, d) planks blocking the purlins outside the East gable wall.

Nails were used to realise the connections between the timber elements of the roof, as shown in the detail drawings of Figure 2.22 (Details L and M). The roof boards were fastened to the purlins using two nails at each intersection. The nails were 55 mm long and 3.0 mm in diameter. The in-plane stiffness of the diaphragm was essentially provided by the nailed connections and the effectiveness of the tongue and groove joints of the boards. Screws were used to attach the tiles onto the laths and hold them in place during the dynamic test (Figure 2.23). Special long screws were employed to secure the ridge tiles that were used to cap the top from falling. Some tiles were inevitably cut to fit tight spots, such as the areas around the chimneys.

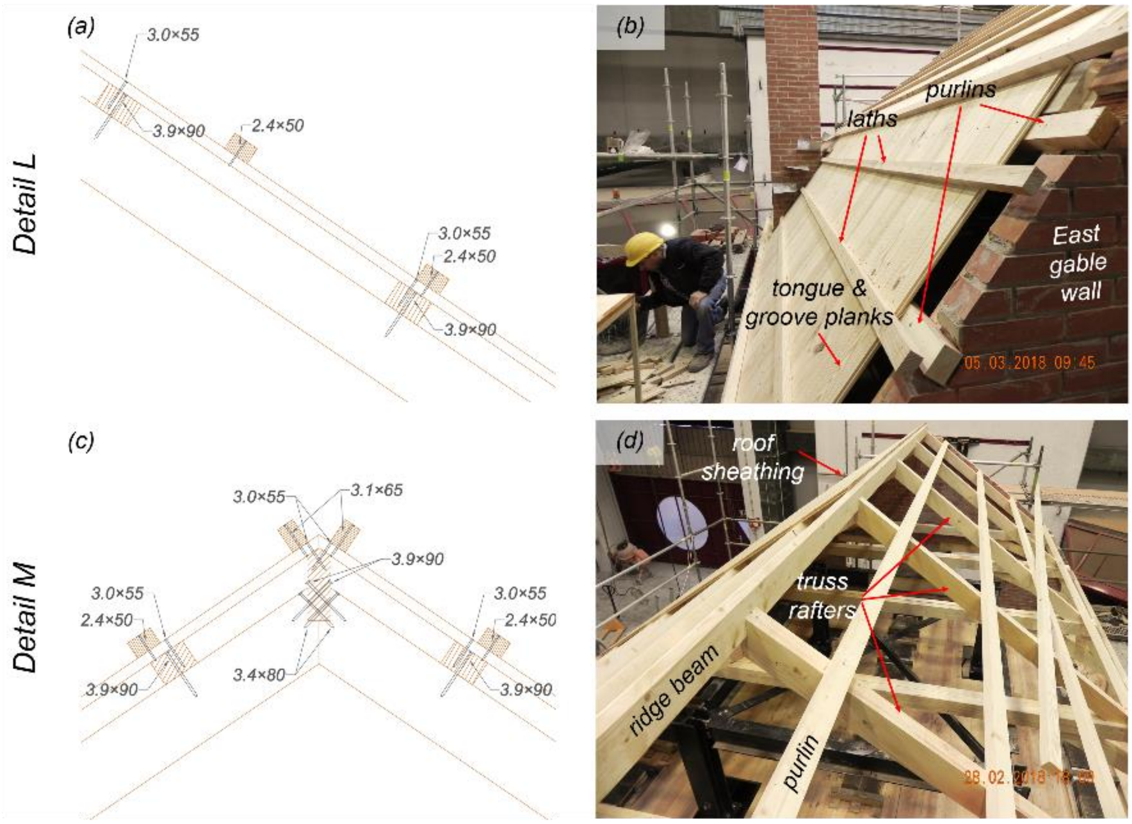

Figure 2.22 Construction details of the roof: (a, b) connections among purlins, planks, and laths; (c, d) realisation of the nail connections at the ridge.

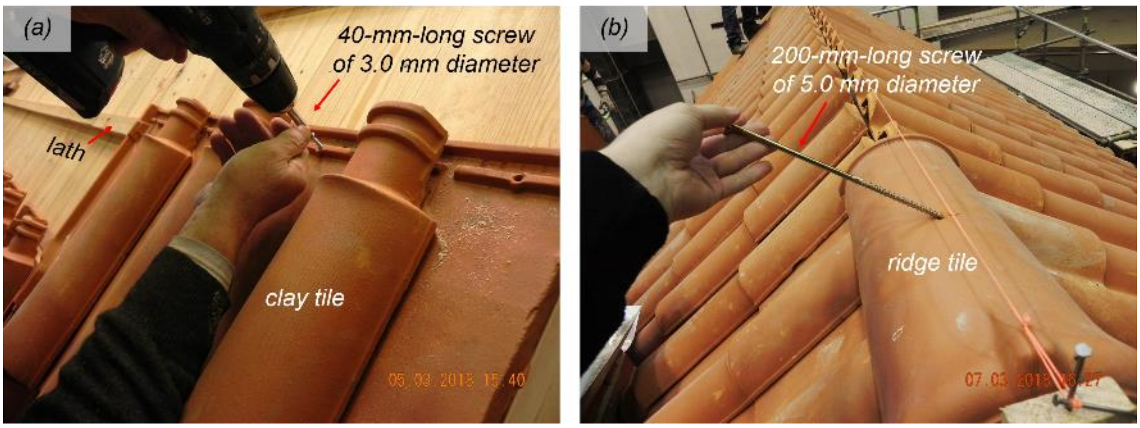

Figure 2.23 Roof finishing with clay tiles: (a) fastening of the tiles on timber laths; (b) attachment of the ridge tiles to the ridge beam.

2.2.4 Chimney flashing

At the locations where the chimneys penetrated the pitched roof, flashing was used to seal up the joints. Although someone could argue that water penetration should not be a problem in laboratory environment conditions, waterproofing seams between the chimneys and the roof were intended to simulate the reduced bond area due to the flashing material being introduced into the mortar joints of the brickwork in real building chimneys. This practice results in chimneys particularly prone to overturning during an earthquake as little cohesion exists between the parts of the stack on either side of the interfering material.

For building chimneys found in the province of Groningen, builders in the past were usually using metal flashing materials based on lead. Lead is preferred to date when meant to remain exposed over the long term due to its extreme durability compared to modern materials that can fail within a few years. For the flashing applications of the chimneys of the test building, soft zinc was used instead, as an environmentally friendly alternative to lead. Zinc was an excellent material because of its smooth texture that is like that of lead, and its workability since it delivers easy folding. Wide pieces of zinc were installed at the head and the apron of the chimneys, while the sides received step flashing (Figure 2.24). Since the material was not intended to minimise water penetration, the sheets of zinc were not cut long enough to be placed underneath the roof tiles. Details of the installation of the pieces of zinc are illustrated in Figure 2.25.

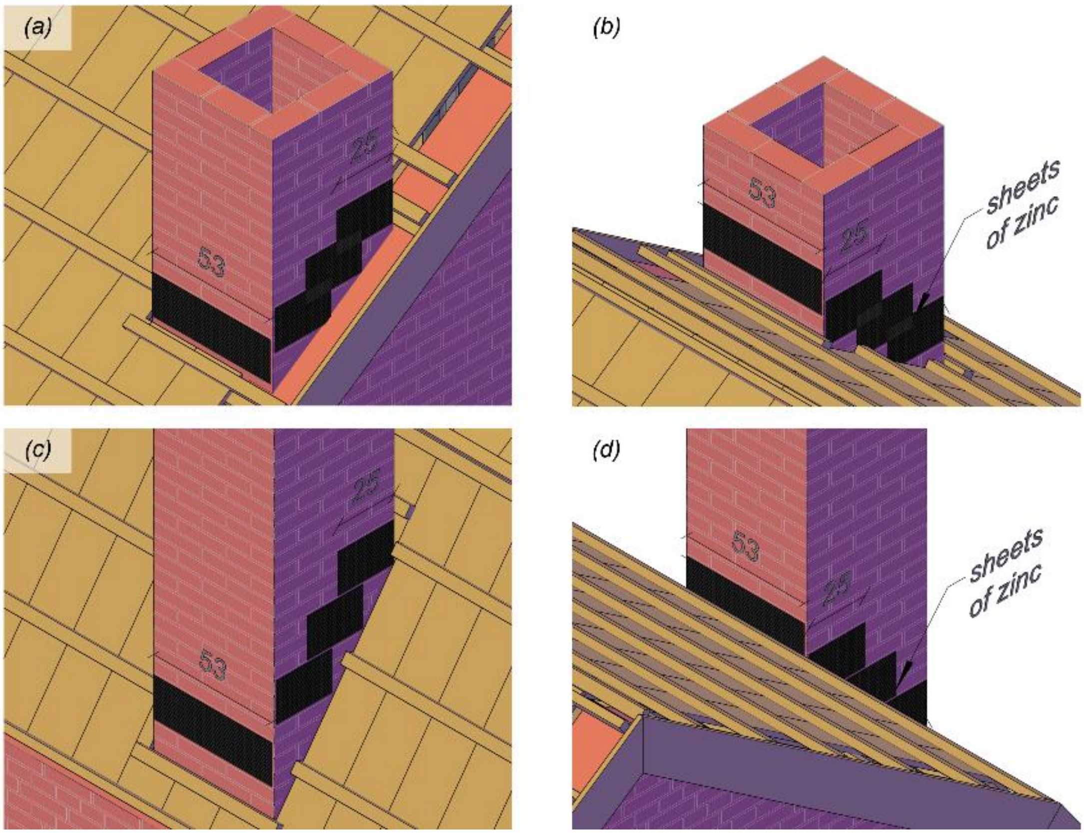

Figure 2.24 Chimney flashing: (a) North-West view of West chimney; (b) South-East view of West chimney; (c) South-East view of South chimney; (d) North-West view of South chimney.

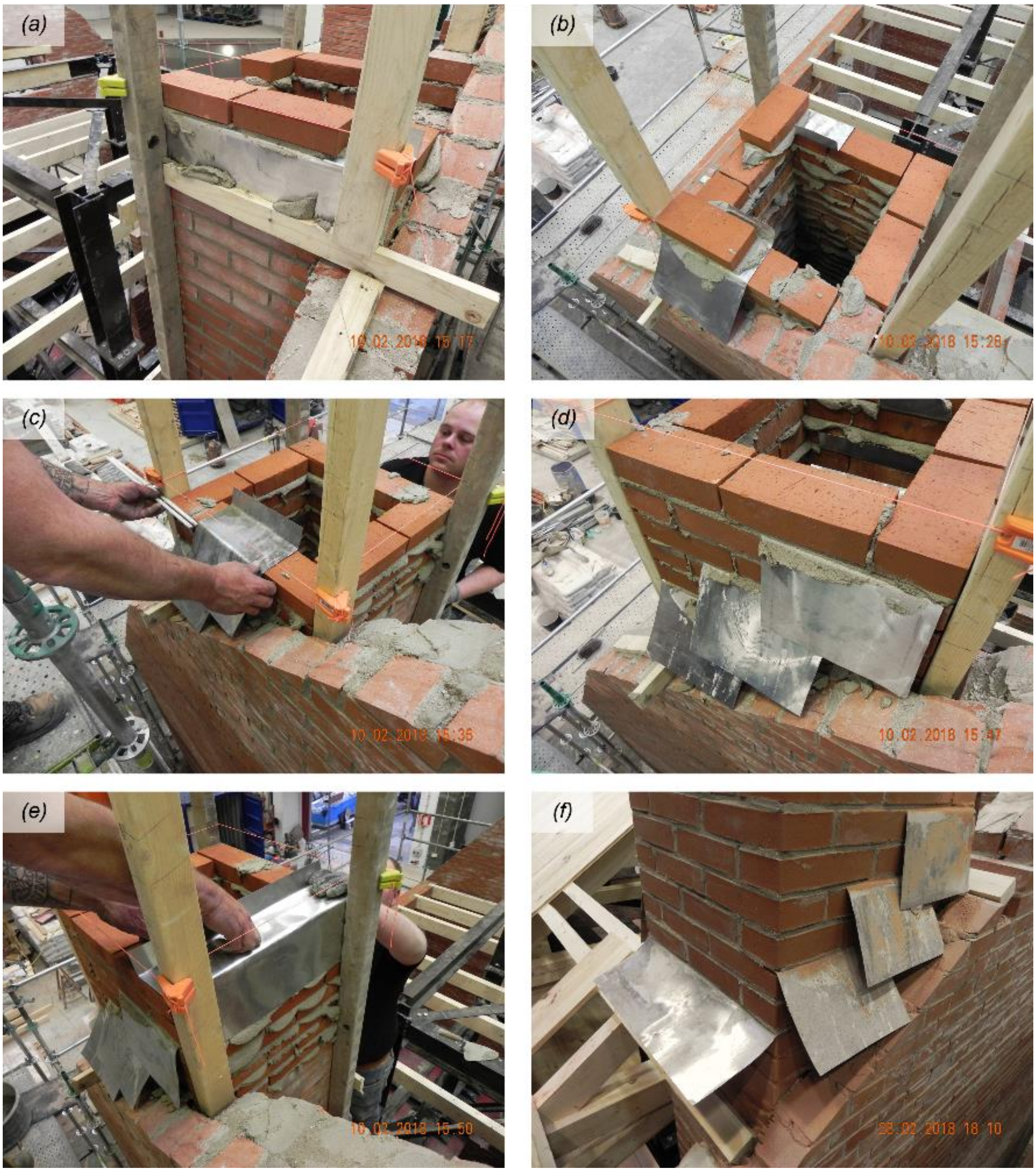

Figure 2.25 Construction details of the West chimney flashing: (a) wide piece of zinc at the chimney apron; (b) bottom layer of step flashing; (c) installing sheets of zinc in mortar joints; (d) step flashing on the chimney side; (e) piece of zinc at the chimney head; (f) finished flashing.

2.2.5 Building finishing

The walls of the southern part of the first storey were covered with plaster, and the room was equipped with a timber floor and typical house furniture. The aim was to investigate the effects of the shaking on the building content and to refine the definition of damage limit states when reference is made to serviceability (*i.e.*, when structural wall damage and cracking of the plaster are not readily distinguished).

Plaster was applied on the entire South wall, on half of the East and West walls, as well as on the South face of the interior wall (Figure 2.26 and Figure 2.27a). All walls were later painted white to facilitate detecting the cracks during the post-test surveys (Figure 2.27b). A timber floor that covered most of the plan area was built just above the foundation level (Figure 2.27c), and a set of furniture was placed close to the South-East corner of the room (Figure 2.27d). The furnishing included a bookcase placed back to back with the central pier of the South wall (but not attached to the wall), two tables, a chair, and a floor lamp. Items sensitive to acceleration were installed on the walls and the ceiling (*e.g.*, photo frames, lighting).

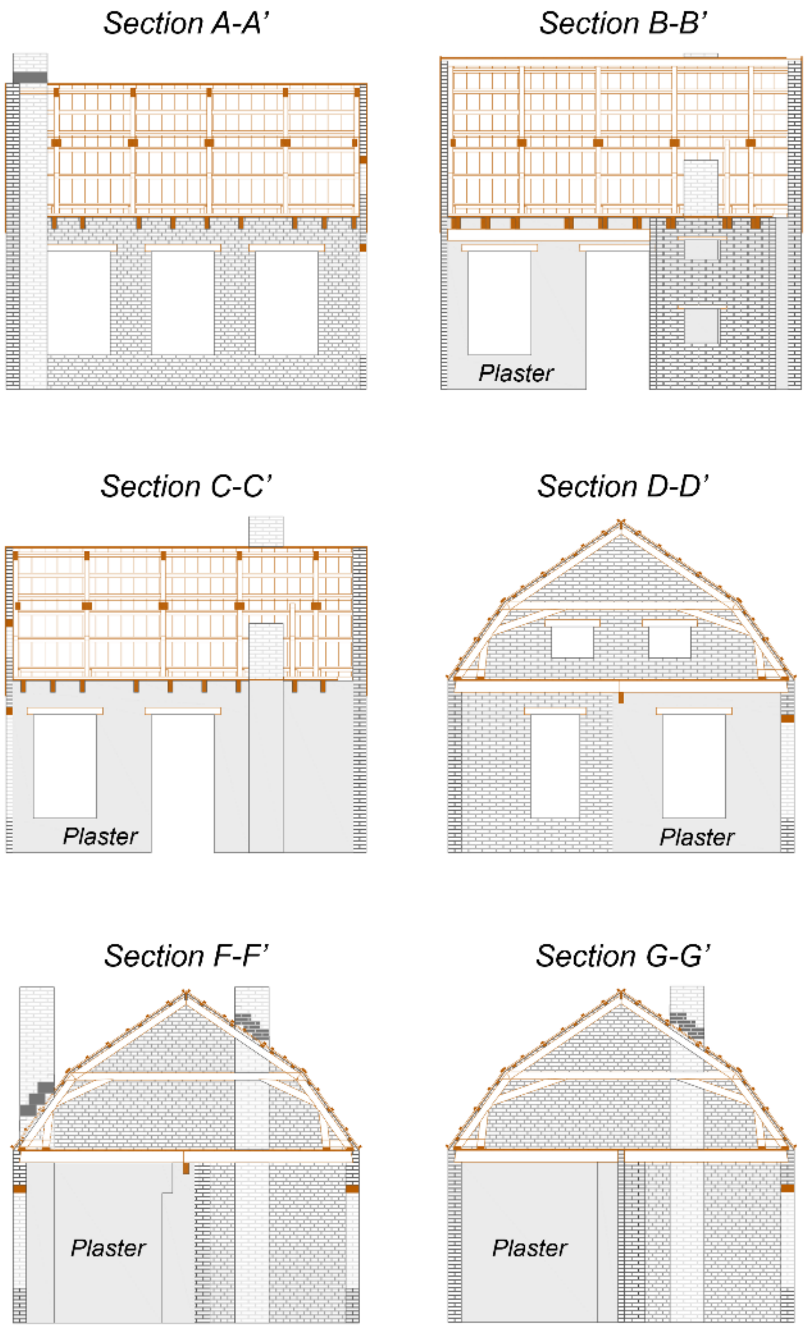

Figure 2.26 Sections in elevation of the building specimen: wall rendering with plaster.

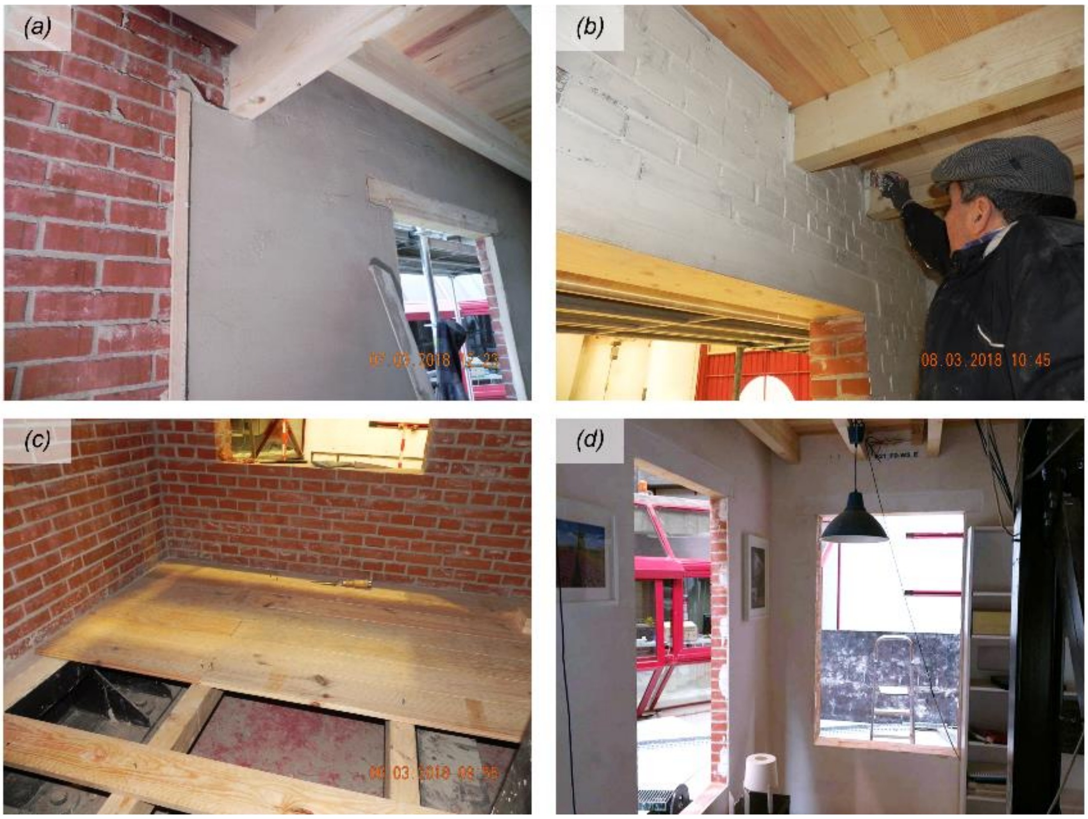

Figure 2.27 Building finishing: (a) rendering of the East wall; (b) painting of the interior side of the walls; (c) timber floor above the foundation; (d) furnishing.

2.2.6 Mortar and timber contraction cracking

The building prototype suffered slight damage during the construction period: minor cracking was detected around most lintels, due to the contraction of both the timber lintels and the early-age mortar and the weak cohesion developed between mortar and timber (Figure 2.28a). Cracks also developed at the locations where the floor joists were inserted into the masonry, presumably due to the vibrations caused by the construction works on the attic floor and the roof. These cracks were often extended to the corner of the openings (Figure 2.28b to d). On the North side, where the lintels were placed at a short in-between distance, cracks propagated along the top of the piers to form a long crack that extended throughout the length of the façade (Figure 2.28e). Similarly, in the East gable wall, a hairline crack was developed that connected the two cracks formed initially above the two windows (Figure 2.28f).

Figure 2.29 illustrates the cracks detected in the building prototype after the end of the construction works. In several cases, the cracks in the mortar joints were wide, often penetrating the entire wall thickness. Thus, the old pointing was partially restored: the joints were repaired up to a depth of 1.5 to 2 cm (on both exterior and interior sides when necessary) to make them solid, durable, and good looking (Figure 2.30a and b). Of course, all cracks were reopened once the specimen was subjected to shaking. However, this only happened after several tests had been completed and not from the early stages of the test (see Section 6.4).

Figure 2.28 Damage detected prior to the testing: (a) cracking at the mortar-timber interface; (b, c) cracking due to floor joists-wall interaction; (d) crack propagation from the corner of an opening; (e) crack propagation between two lintels of the North façade; (f) crack propagation between the lintels of the East gable wall.

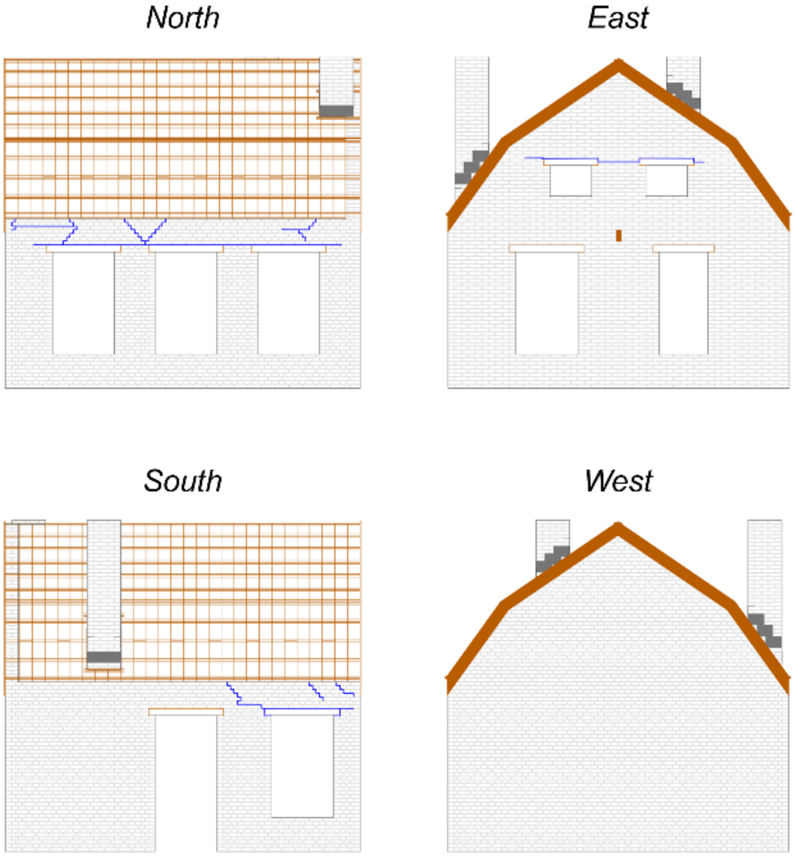

Figure 2.29 Observed crack pattern on the perimeter walls of the prototype building after the end of the construction (exterior view).

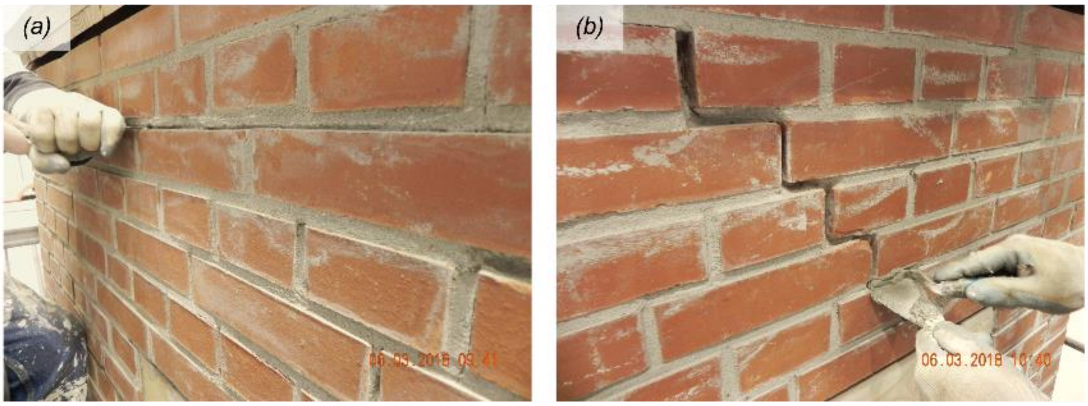

Figure 2.30 Mortar joints repointing: (a) removal of the old mortar joint; (b) filling with new mortar.

2.3 Masses

The masonry had a mean density of 1912 kg/m^3. Masonry walls, floor diaphragm, and finished roof provided masses of 24.8 t, 0.71 t, and 3.01 t, respectively. An additional mass of 1.8 t was provided to the attic floor by twelve 150-kg-heavy blocks of steel plates, evenly distributed over the diaphragm to account for superimposed dead and live loads (corresponding to approximately 67 kg/m^2). The total mass of the building specimen thus added to 30.3 t (Table 2.1).

Table 2.1 Summary of structural and additional masses.

Component			Mass [t]
Masonry walls	North side	below floor	8.54
	South side	below floor	8.65
		chimney above floor	0.86
	Gables (including the West chimney)		5.18
	Interior wall		1.53
Floor	Timber structure		0.71
	Additional floor mass		1.80
Roof	Timber structure		0.99
	Clay tiles		2.02
Total			**30.3**

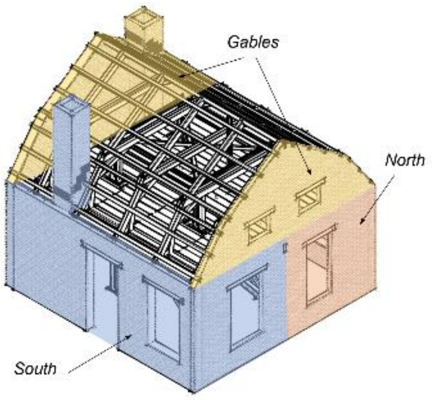

3 INSTRUMENTATION

3.1 Instrumentation Plan

The instrumentation consisted of 40 accelerometers (A), eight wire potentiometers (WPs), and 16 linear variable displacement transducers (LVDTs), mounted on the specimen to capture its response during the dynamic tests (Figure 3.1 and Figure 3.2). The steel safety frame inside the building served as a rigid reference system for the direct measurement of displacements of the floor, the walls, and the roof. Additional accelerometers and LVDTs were installed below the shake table to record the applied table accelerations and displacements. The earthquake-simulation tests were covered by high-definition video cameras installed around but also inside the specimen.

Accelerometers (Figure 3.3) were installed on the foundation beam, on the walls and the chimneys, on the floor diaphragm, and on the roof at the locations shown in Figure 3.1. Most of the sensors were mounted in the shaking direction, while some were also oriented transversely or vertically to gain insight into the vibration modes of the structure.

LVDTs recorded the longitudinal displacements of the floor diaphragm and the top of the interior wall with respect to the rigid steel frame (Figure 3.4a and b). Such sensors also monitored possible differential displacements between the floor and the top of the North and South walls (Figure 3.4c), sliding of the principal floor girder on its supporting walls (Figure 3.4d), and relative displacements between the roof ridge and the East and West gables (Figure 3.4e). Additional LVDTs were placed at the bottom of the squat South pier and the interior wall to record possible sliding at the base of the walls with respect to the foundation (Figure 3.4f). Failure with sliding at the base of such a squat pier was observed in the final run of the shake-table test on specimen EUC-BUILD-2 (Graziotti *et al.*, 2016; Kallioras *et al.*, 2018).

Wire potentiometers recorded the out-of-plane deflections of the East and West façades, the translations of the ridge beam, and the displacements at the top of the two chimneys (Figure 3.5). All potentiometers installed in the interior of the building were measuring displacements relative to the steel reference frame, consequently relative to the shake-table surface (*i.e.*, the foundation beam and the steel frame were tightly fastened on the shake table). In the case of the two chimneys, however, the measurements were done with reference to the strong reaction wall of the laboratory, found on the West side of the specimen.

Several instruments were removed while approaching the ultimate limit state of the building to secure them from damage caused by potential falling objects. In most cases, the precautionary measures regarded accelerometers; therefore, tributary structural masses of the affected sensors were distributed accordingly to those instruments that remained as were on the specimen. In only a few cases, displacement transducers were removed, while in some others, they provided discontinuous readings due to exceedance of their measuring stroke length (instrument saturation). Where video recordings were available, the displacement histories of key points were retrieved by tracking the motion of the related components using an application-specific software. For a thorough discussion of the acquired data and the post-processing assumptions, the reader is referred to Section 5. A detailed description of the instrument locations, the corresponding measuring quantities, and the mass distribution to accelerometers are provided in Table 5.3.

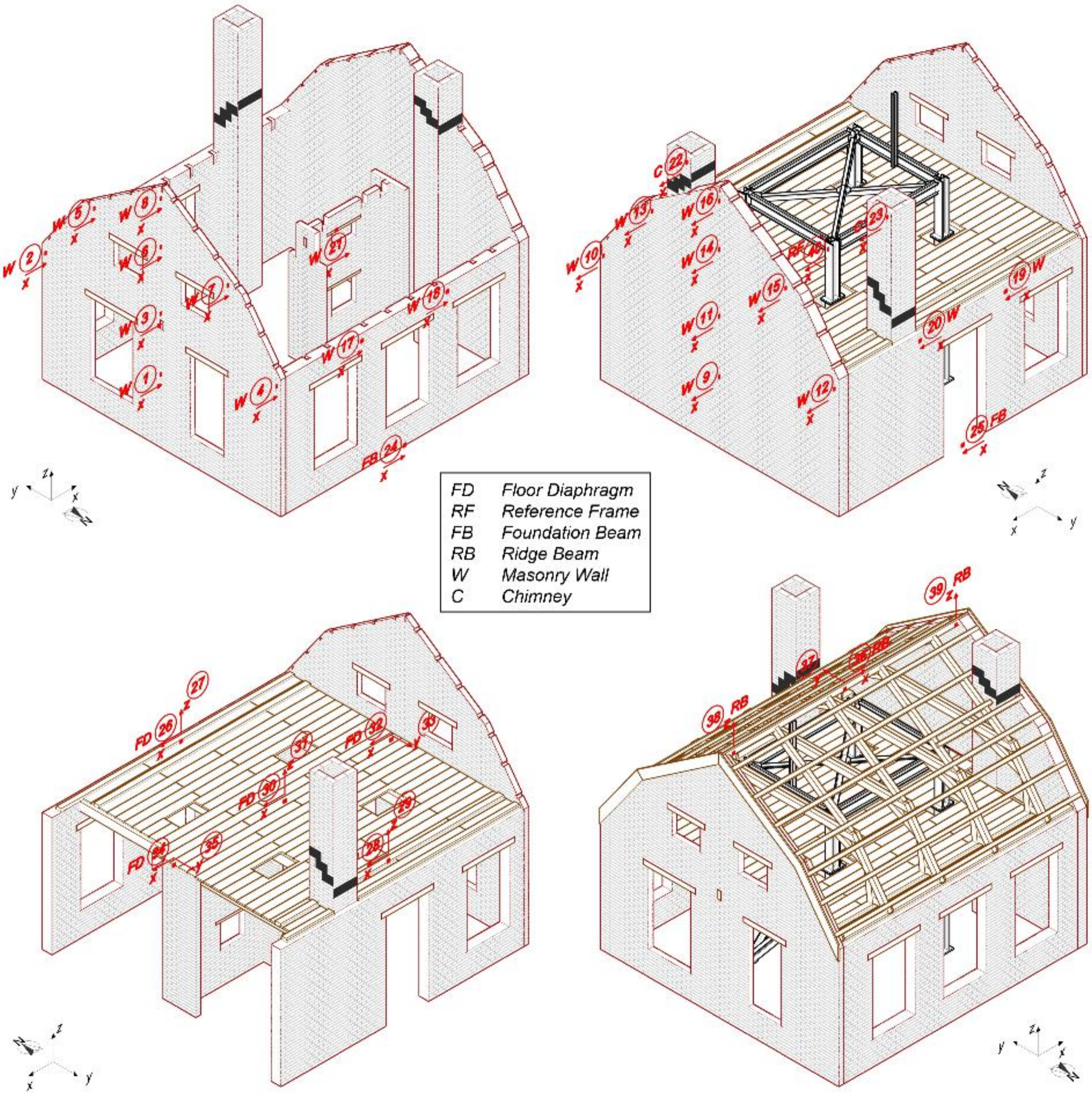

Figure 3.1 Instrumentation plan: 1D accelerometers. Letters indicate the component on which each instrument is mounted.

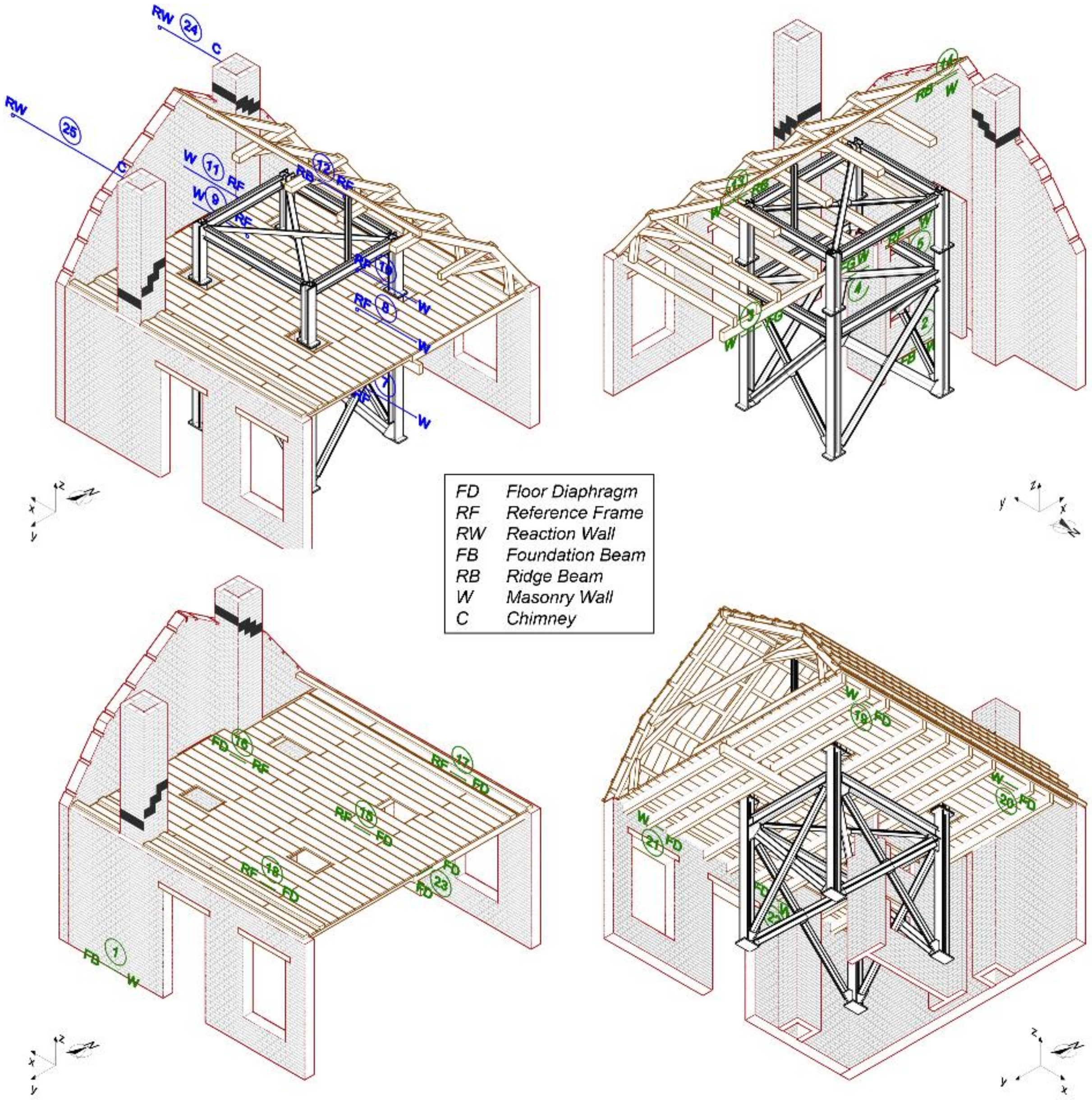

Figure 3.2 Instrumentation plan: wire potentiometers (blue) and LVDTs (green). Letters indicate the component on which each instrument is mounted.

Figure 3.3 Accelerometers mounted on (a) the East façade; (b) the West façade; (c) the foundation beam; (d) the South façade; (e) the floor diaphragm; (f) the roof ridge beam.

Figure 3.4 LVDTs monitoring differential displacements between (a) reference frame-floor diaphragm; (b) reference frame-interior wall; (c) longitudinal walls-floor diaphragm (i.e. lower plates); (d) floor girder-East wall; (e) gable wall-ridge beam; (f) foundation beam-South squat pier.

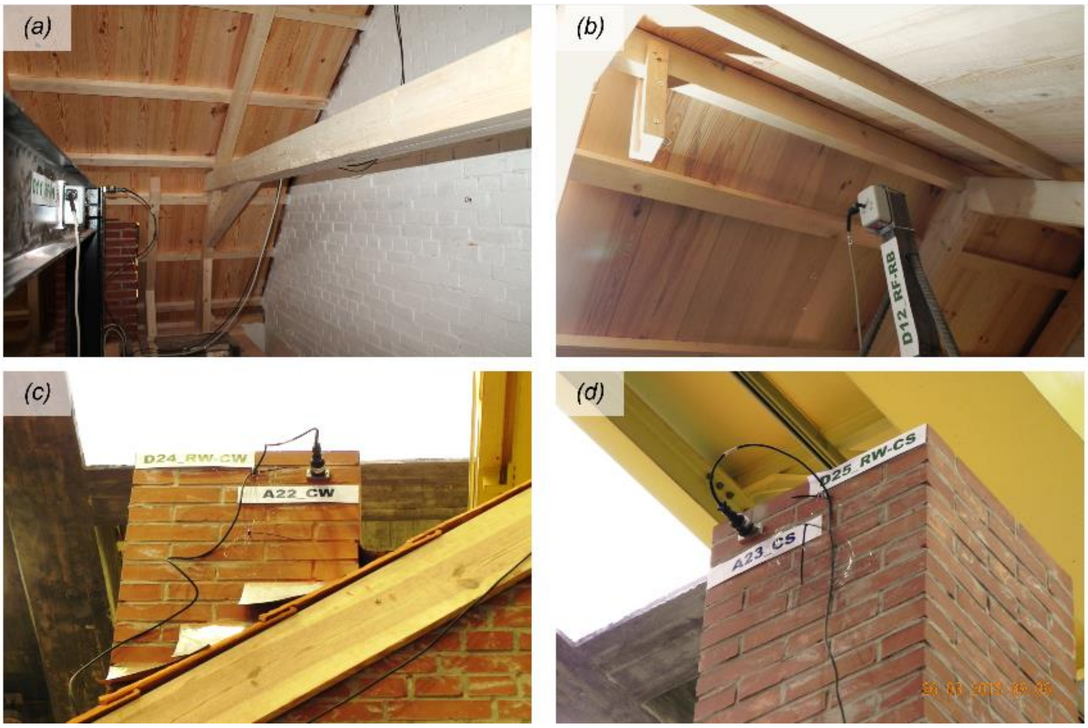

Figure 3.5 Wire potentiometers recording displacements at (a) the mid-height of the West gable wall (w.r.t. the reference frame); (b) the roof ridge beam (w.r.t. the reference frame); (c) the top of the West chimney (w.r.t. the reaction wall); (d) the top of the South chimney (w.r.t. the reaction wall).

4 TESTING PROTOCOL

The specimen was subjected to incremental unidirectional dynamic tests, applying a series of shake-table motions of increasing intensity to assess progressive damage, failure modes, and ultimate capacity of the building. The increments were initially defined based on the testing experience of specimen EUC-BUILD-2 (Graziotti *et al.*, 2016; Kallioras *et al.*, 2018), while in later stages the intensity of the input motions was decided by engineering judgment based on the observed damage.

4.1 Input Motions

The selected input motions should necessarily reflect the seismic hazard characteristics of the Groningen gas field. Production-induced earthquakes are typically characterised by short duration, owing to the nature of the causative focal mechanism and the short source-to-site distance (*i.e.*, due to the shallow depth of the rupture). Moreover, cumulative damage in a poorly designed masonry building is likely to exhibit significant sensitivity to ground motion duration that is more pronounced when the structure enters higher levels of inelasticity. As such, selection criteria should consider the ground motion duration in addition to the spectral shape and the magnitude of possible earthquakes. The adopted input motions should also be compatible with the requirements of the testing, meaning: i) to offer greater control of the shake table, allowing the optimum matching between input and feedback signals; ii) to be simple enough to facilitate the interpretation of the acquired response quantities and the application in numerical modelling; and iii) to allow the comparison of the obtained data with past test results.

Under the above considerations, two single-component, pulse-like earthquake accelerograms with smooth response spectra were adopted: a first record, labelled SC1, with peak ground acceleration PGA = 0.096 g; and a second record, termed SC2, with PGA = 0.155 g. The SC1 record had 5-75% significant duration ($D_{s,5\text{-}75\%}$) equal to 0.38 s, while in the case of signal SC2, $D_{s,5\text{-}75\%}$ was 1.72 s. The two ground motions were representative of earthquake scenarios with return periods of 50 and 475 years based on the V1 hazard model for the Groningen region (Bourne *et al.*, 2015). The model has been revised since then, and the two records do not correspond to events with these return periods anymore. The signals were used for the shake-table tests of specimen EUC-BUILD-2; thus, their use offered the additional advantage for direct comparison of the new data with the results of the tests performed in Pavia. Figure 4.1 shows the theoretical acceleration histories of the two input signals and their elastic pseudo-acceleration response spectra at 5% viscous damping ratio. Details on the development of the protocol are included in the report of Bommer *et al.* (2015).

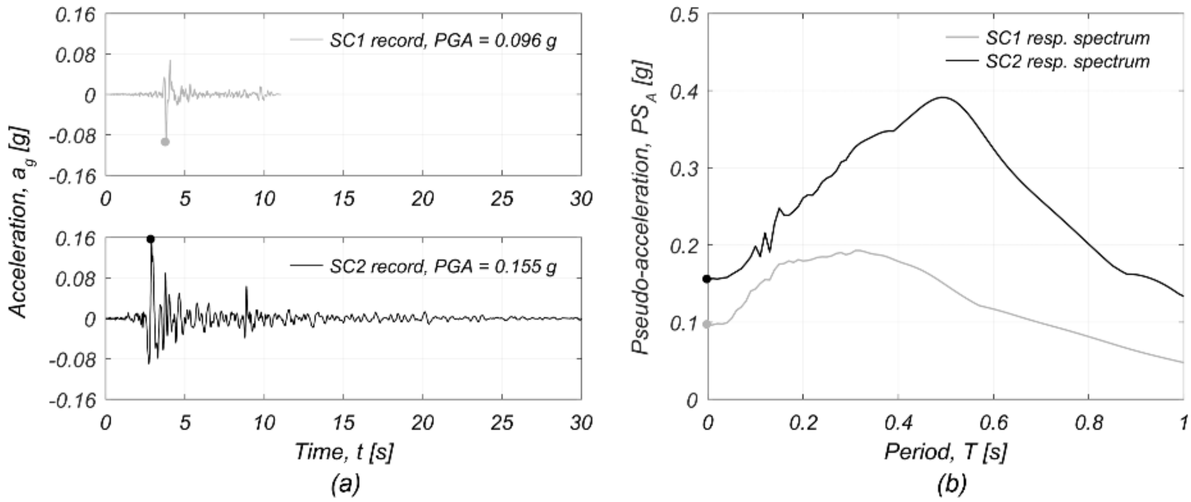

Figure 4.1 SC1 and SC2 signals: (a) acceleration histories; (b) elastic pseudo-acceleration response spectra for 5% viscous damping ratio.

4.2 Testing Sequence

The two selected records were scaled in acceleration amplitude to obtain the desired incremental test protocol, consisting of the 15 earthquake simulations highlighted in

Table 4.1. In-between those tests, the specimen was subjected to 14 low-amplitude random excitations covering a wide frequency band (0.1-40 Hz) with consistent energy content for the dynamic characterisation of the specimen. These tests allowed assessing the effect of cumulative damage on the evolution of the global dynamic properties of the building. The fundamental period of the undamaged structure was $T_{1,und}$ = 0.147 s, while by the end of all tests it shifted to $T_{1,dam}$ = 0.314 s.

Table 4.1 illustrates the applied testing sequence specifying: the test identification number; the test name; the input signal used; the nominal amplitude scale factor; and the date and time of execution. For more details on the dynamic identification of the structure, the reader is referred to Section 6.1.

Table 4.1 Summary of the testing sequence.

Test ID No.	Test name	Input signal	Nominal scale factor	Date	Time
1	CHAR#0	RNDM	-	26 Mar 2018	15:28
2	CHAR#0-bis	RNDM	-	26 Mar 2018	15:37
3	SC1-50%	SC1	50%	26 Mar 2018	15:48
4	SC1-50%-rev	SC1	-50%	26 Mar 2018	16:02
5	SC1-100%	SC1	100%	26 Mar 2018	16:06
6	CHAR#1	RNDM	-	26 Mar 2018	16:34
7	SC1-150%	SC1	150%	26 Mar 2018	16:42
8	CHAR#2	RNDM	-	26 Mar 2018	16:57
9	SC2-50%	SC2	50%	26 Mar 2018	17:10
10	SC2-100%	SC2	100%	26 Mar 2018	17:20
11	CHAR#3	RNDM	-	26 Mar 2018	17:36
12	SC2-150%	SC2	150%	26 Mar 2018	17:45
13	CHAR#4	RNDM	-	26 Mar 2018	18:09
14	SC2-200%	SC2	200%	26 Mar 2018	18:15
15	CHAR#5	RNDM	-	26 Mar 2018	18:44
16	CHAR#6	RNDM	-	27 Mar 2018	12:06
17	SC2-100%-bis	SC2	100%	27 Mar 2018	12:09
18	SC2-200%-bis	SC2	200%	27 Mar 2018	12:52
19	CHAR#7	RNDM	-	27 Mar 2018	13:30
20	SC2-250%	SC2	250%	27 Mar 2018	13:44
21	CHAR#8	RNDM	-	27 Mar 2018	13:58
22	SC2-300%	SC2	300%	27 Mar 2018	16:58
23	CHAR#9	RNDM	-	27 Mar 2018	17:03
24	SC2-350%	SC2	350%	27 Mar 2018	18:58
25	CHAR#10	RNDM	-	27 Mar 2018	19:04
26	SC2-400%	SC2	400%	27 Mar 2018	19:49
27	CHAR#11	RNDM	-	27 Mar 2018	20:04
28	SC2-500%	SC2	500%	27 Mar 2018	20:09
29	CHAR#12	RNDM	-	27 Mar 2018	20:32

5 DATA ACQUISITION AND PROCESSING

This section provides information related to the sensor measurements from the 15 earthquake simulations and the 14 random vibration tests performed on the building specimen. Some limitations regarding the acquired data are first reported, then the assumptions in deriving useful response quantities from the recorded acceleration and displacement histories are thoroughly discussed. All datasets have been organised in distributable data files that can be requested online on the EUCENTRE Foundation repository at the URL www.eucentre.it/nam-project by referring to LNEC-BUILD-3. The authors make this information available to encourage the development of analytical and numerical models that simulate the dynamic response of unreinforced masonry buildings with characteristics similar to the LNEC-BUILD-3 specimen. Interpretation of the sensor measurements and a detailed discussion on the seismic performance of the building are provided in Sections 6 and 7.

5.1 Missing Instrument Recordings

Several instruments were removed while approaching the ultimate limit state of the building to secure them from collateral damage due to partial or total collapse. Of the sensors that remained mounted on the specimen, a few accelerometers exhibited intermittent or spurious readings due to different reasons including attachment to collapsed structural or non-structural components (*e.g.*, chimneys and gable end plates), impact with falling objects, or instrument malfunction. Moreover, due to the large displacement demands that the building underwent during the final shaking runs, several displacement transducers reached their stroke-length capacity, affecting the recorded histories in ranges around the peak displacement responses. Table 5.1 summarises all sensors that exhibited recording problems or were merely dismounted to prevent their failure.

Table 5.1 List of sensors that were removed or exhibited problems during the testing sequence.

Sensor type	Sensor ID No.	Test	Cause of dysfunction
Accelerometers	5, 7, 10, 12, 15, 17, 19, 27, 29, 31, 33, 35, 37, 38, 39	SC2-350%, SC2-400%, SC2-500%; CHAR#10, CHAR#11, CHAR#12	Removal to prevent damage
	22	SC2-400%, SC2-500%; CHAR#11, CHAR#12	Attachment to collapsed component
	13	SC2-350%, SC2-400%, SC2-500%	Impact with falling object
	18	Observed during several tests	Sensor intermittent fault
Wire potentiometer	24	SC2-350%	Instrument saturation
	24, 25	SC2-400%, SC2-500%; CHAR#11, CHAR#12	Removal prior to imminent saturation
	7	SC2-350%, SC2-400%, SC2-500%; CHAR#10, CHAR#11, CHAR#12	Relocation to another measuring point
	10, 11	SC2-500%	Instrument saturation
LVDT	19, 20, 21	SC2-350%, SC2-400%, SC2-500%; CHAR#10, CHAR#11, CHAR#12	Removal to prevent damage
	17	SC2-500%	Instrument saturation

5.1.1 Instrument removal or relocation

In total, 15 accelerometers were uninstalled before the SC2-350% test (Table 5.1), in particular:

i) five accelerometers recording the acceleration response at different locations of the transverse, East and West façades (A 5, 7, and A 10, 12, 15, respectively);

ii) two accelerometers placed on the longitudinal, South and North walls (A 17 and 19, respectively);

iii) five sensors placed on the floor diaphragm (A 27, 29, 31, 33 and 35), monitoring accelerations in the *y* (transverse) and *z* (vertical) building directions;

iv) three sensors mounted on the roof ridge beam (A 37, 38 and 39), recording accelerations in *y* and *z* directions.

For the same reason, three LVDTs, installed on the South and North walls, LVDTs 19, 20 and 21, were also uninstalled: they monitored the relative displacements of the timber lower plates (running close and parallel to the South and North edges of the floor diaphragm), with respect to the walls. The corresponding recorded deformations seemed negligible up to that phase of testing, while in the following tests, no damage was observed at the locations of connection of the floor joists to the walls. Therefore, the displacements at the top of the longitudinal walls were reasonably assumed equal to those recorded at the lower plates of the floor.

The wire potentiometers that measured the displacements at the top of the two chimneys, WP 24 and 25, were also dismounted during the final two tests (*i.e.*, SC2-400% and SC2-500%). It was decided to do so because WP 25 had been quite close to reaching its stroke-length capacity, while WP 24 had already saturated during the SC2-350% test (Figure 5.2a). In the absence of real measurements, the displacement histories at the top of the chimneys were retrieved from analysing the video recordings (see Section 5.2).

Measuring the displacement at the roof ridge was critical, therefore during the last three tests (SC2-350% and thenceforth) the WP 12 wire potentiometer was adjusted to offer greater stroke length for measuring deformations towards the positive direction (*i.e.*, towards West). For measuring the displacement in the negative direction, WP 7 was employed (shown in red in Figure 5.1a). The instrument initially recorded the out-of-plane deflection of the East central pier at mid-height of the first storey (see Figure 3.2). Consequently, displacement recordings from the latter location are missing from the final dataset from test SC2-350% until the end; the corresponding columns are filled with “not-a-number” (*NaN*) elements.

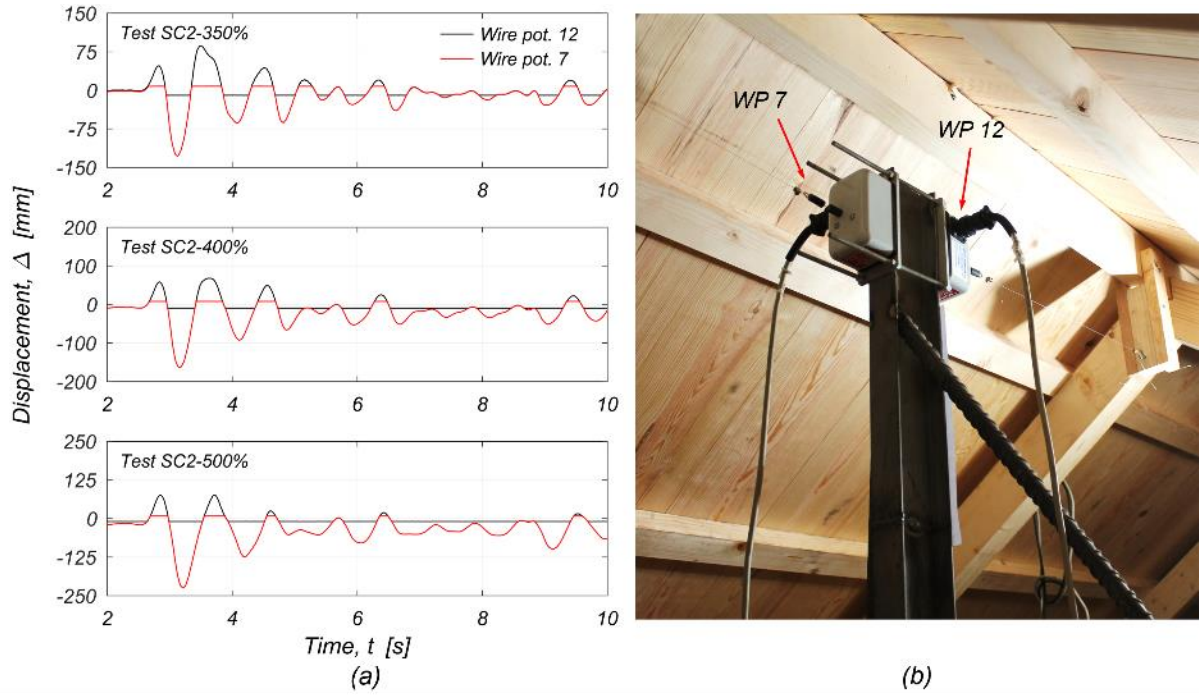

Figure 5.1 Measuring the displacement of the roof ridge during tests SC2-350%, SC2-400% and SC2-500%: (a) displacement recordings by WP 12 and WP 7 in the time window 2-10 s; (b) location of wire potentiometers WP 12 and WP 7.

5.1.2 Instrument saturation

When the building experienced large displacement responses, several displacement transducers reached their measuring length limits (Table 5.1). In particular:

i) WP 24, which measured the displacement at the top of the West chimney, reached its stroke-length capacity during testing under SC2-350% (Figure 5.2a);

ii) LVDT 17 that measured the relative displacement of the lower plate (found on the North side of the floor) with respect to the steel reference frame, saturated during the SC2-500% test (Figure 5.2);

iii) WP 10 and WP 11, measuring the out-of-plane displacements at mid-height of the East and West gable walls, respectively, saturated during the SC2-500% shaking run (Figure 5.2c and d).

The missing segments of the affected displacement readings were retrieved from the analysis of the video recordings of the tests (see Section 5.2).

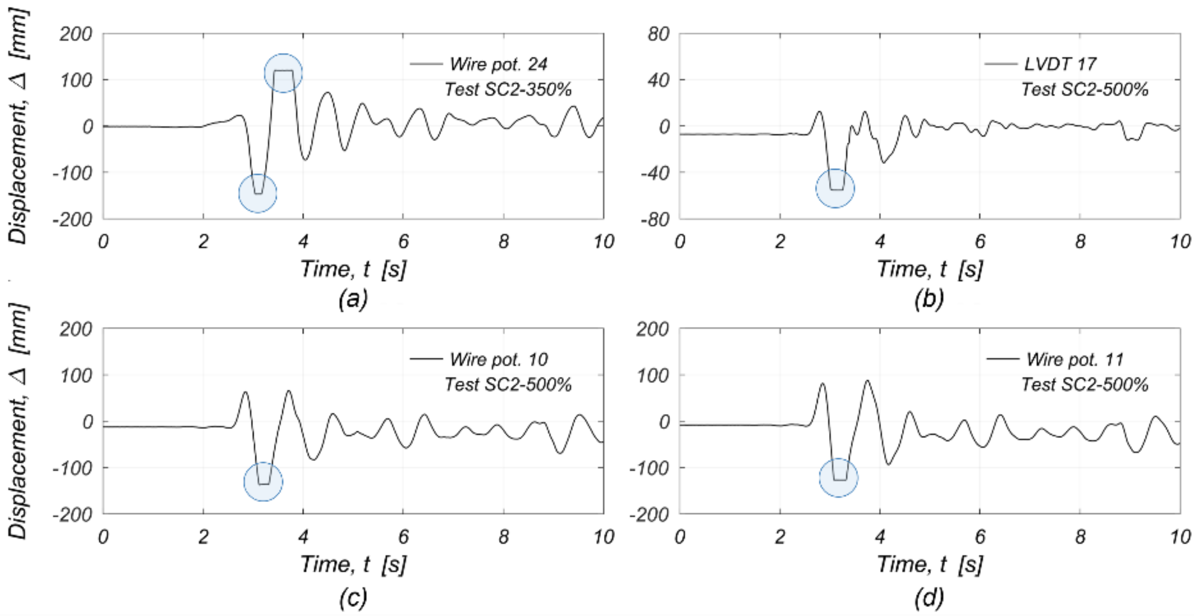

Figure 5.2 Saturated displacement transducers: (a) wire potentiometer at the top of the West chimney; (b) LVDT on the North side of the floor; (c) wire potentiometer at mid-height of the East gable; (d) wire potentiometer at mid-height of the West gable.

5.1.3 Instrument malfunction

Accelerometer A 18 was mounted on the specimen during all test runs. For unknown reasons, the sensor exhibited malfunctions, recording acceleration histories with spurious spikes during several test runs, hence, the instrument readings were removed from the distributed dataset. Several accelerometers near sensor A 18 were removed in the last three test runs to prevent them from being damaged, including accelerometer A 17, also attached to the North masonry wall (see Figure 3.1). Consequently, when it comes to computing the developed inertia forces, accelerations at the top of the North wall were taken equal to the readings of accelerometer A 17 for testing up to SC2-300%, while they were assumed equal to the accelerations recorded on the North side of the floor diaphragm during tests SC2-350% to SC2-500%.

Problems were also noticed in the functioning of accelerometer A 13 during test SC2-350%. From then onwards, the instrument recordings included spurious spikes followed by periods of unstable readings. The sensor was mounted at mid-height of the West gable wall, on the northernmost side. The effect was attributed to the impact caused by the collapse of the timber plank that was placed on the face of the West gable wall, attached to the roof purlins. The mass associated with the instrument location was redistributed to accelerometer A 14, found at the same elevation, at midspan of the gable wall.

5.2 Data Post-Processing

The section discusses assumptions made in deriving the inertia forces and the critical displacement histories.

5.2.1 Acceleration recordings – inertia forces

For the computation of inertia forces, the building mass was distributed to zones around the accelerometer locations. In the absence of several accelerometers during the last test runs, which were either removed to protect them from damage or exhibited recording problems due to extensive damage to the specimen, some degrees of freedom were not sufficiently monitored. Thus, structural masses were necessarily redistributed. The masses initially associated with accelerometers A 5 and A 7, mounted on the East gable wall, were assigned to the A 6 sensor for tests SC2-350%, SC2-400%, and SC2-500%. Similarly, on the West side, the masses at the location of accelerometers A 13 (only for the tests displaying malfunction, *i.e.*, from SC2-350% onwards) and A 15 were attributed to A 14, which was mounted at midspan of the gable. On the same building façade, instruments A 10 and A 12, found at the wall edges, were also removed before the SC2-350% test run; after that, their tributary masses were associated with accelerometers A 18 and A 20, respectively, found on the return walls of the North and South sides. Finally, the wall masses linked to accelerometers A 17 and A 19, which were installed at the top of the North and South building façades, were associated to the adjacent sensors A 18 and A 20, respectively. The masses attributed to each accelerometer location (before any assumed redistribution for the last tests) are listed in the rightmost column of Table 5.3 in Section 5.3.

As discussed in Section 5.1.3, the A 18 accelerometer exhibited recording problems during several tests. Consequently, accelerations at that location were taken equal to the readings of accelerometer A 17 for testing stages up to SC2-300%, while they were assumed equal to the accelerations recorded by A 26 on the North side of the floor diaphragm during tests SC2-350% to SC2-500%. This assumption affected all calculated inertia forces for the masses of the accelerometers depending on A 18, according to the associations above (meaning, instruments A 10 and A 17).

5.2.2 Displacement recordings

Displacement records are provided including the residual deformations reached during previous test runs. Residuals at the end of every test were computed by averaging the displacement amplitudes in the time window 1.5 to 0.5 s before the end of each recording.

Several displacement-recording instruments reached their stroke-length capacity or were simply removed before imminent saturation (see Table 5.1). The missing segments of the displacement readings were retrieved from the analysis of the video recordings of the tests, with the use of Tracker (Brown, 2018), a free Java video analysis tool developed by the Open Source Physics Project (available by OSP online at https://www.compadre.org/osp). An example of such analysis is shown in Figure 5.3a for obtaining the displacement history at the top of the West chimney during SC2-300% test. The displacement histories obtained from the video recordings were matching sufficiently well the parts of the records acquired by the laboratory acquisition system, as evident in Figure 5.3b and c.

The Tracker video analysis program allows users to track the motion of an object in a digital video recording, after calibrating the scale and defining appropriate coordinate axes just as for traditional video analysis. The video recordings that were processed are projected with a frequency between 24 and 30 frames per second. Hence, users of the data should keep in mind that the recovered displacement recordings should not contain information for vibration periods below 0.042 s.

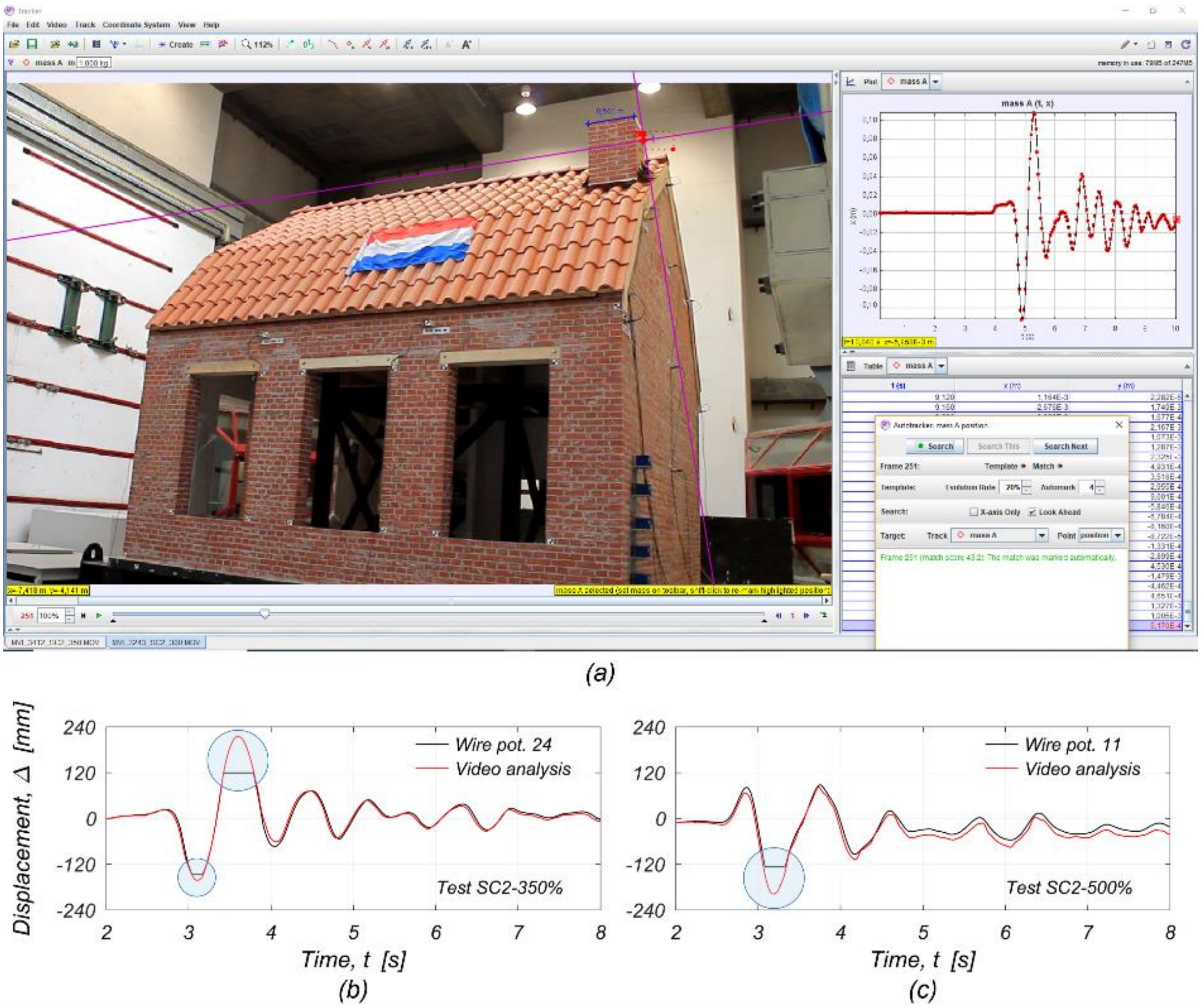

Figure 5.3 Retrieval of the missing data using software Tracker: (a) example of video analysis for the West chimney in test SC2-300%; (b) displacement histories for the West chimney in test SC2-350%; (c) displacement histories for the West gable wall, at mid-height, in test SC2-500%.

5.3 Data Distribution

The datasets from the earthquake simulations are provided in 15 *.txt* files, named after the corresponding shake-table test, as listed (shaded in light blue) in Table 5.2. Each file is a two-dimensional matrix of 105 columns, where each column contains the history of a measured or derived physical quantity. The lines of the *.txt* files correspond to individual instants of the time series. Similarly, the data from the random-vibration tests are organised in 14 *.txt* files. However, those matrices have just 75 columns as they provide only the direct acceleration and displacement measurements obtained by the data acquisition system.

Table 5.2 Shake-table test data: file names.

Test ID No.	Test name	Data file name	Matrix size (rows No. × columns No.)
1	CHAR#0	#1_CHAR#0	35990 × 75
2	CHAR#0-bis	#2_CHAR#0-bis	35990 × 75
3	SC1-50%	#3_SC1-50%	3990 × 105
4	SC1-50%-rev	#4_SC1-50%-rev	3990 × 105
5	SC1-100%	#5_SC1-100%	3990 × 105
6	CHAR#1	#6_CHAR#1	35990 × 75
7	SC1-150%	#7_SC1-150%	3990 × 105
8	CHAR#2	#8_CHAR#2	35990 × 75
9	SC2-50%	#9_SC2-50%	9990 × 105
10	SC2-100%	#10_SC2-100%	9990 × 105
11	CHAR#3	#11_CHAR#3	35990 × 75
12	SC2-150%	#12_SC2-150%	9990 × 105
13	CHAR#4	#13_CHAR#4	35990 × 75
14	SC2-200%	#14_SC2-200%	9990 × 105
15	CHAR#5	#15_CHAR#5	35990 × 75
16	CHAR#6	#16_CHAR#6	35990 × 75
17	SC2-100%-bis	#17_SC2-100%-bis	9990 × 105
18	SC2-200%-bis	#18_SC2-200%-bis	9990 × 105
19	CHAR#7	#19_CHAR#7	35990 × 75
20	SC2-250%	#20_SC2-250%	9990 × 105
21	CHAR#8	#21_CHAR#8	35990 × 75
22	SC2-300%	#22_SC2-300%	9990 × 105
23	CHAR#9	#23_CHAR#9	35990 × 75
24	SC2-350%	#24_SC2-350%	9990 × 105
25	CHAR#10	#25_CHAR#10	35990 × 75
26	SC2-400%	#26_SC2-400%	9990 × 105
27	CHAR#11	#27_CHAR#11	35990 × 75
28	SC2-500%	#28_SC2-500%	9990 × 105
29	CHAR#12	#29_CHAR#12	35990 × 75

Table 5.3 describes the content of the first 75 columns of the data matrices for both earthquake simulations and dynamic identification tests. The columns correspond to quantities directly measured by the sensors. The table lists from left to right: the column number in the data matrix; the sensor identification number; a brief description of the measured quantity and the instrument location; the recorded degree of freedom; the measurement units; the mass attributed to the accelerometer location. Displacement measurements are expressed in units of mm and accelerations in units of g. The data is organised in each file as follows:

i) Column1 contains the time at a sampling rate of 200 Hz;

ii) Columns 2 to 9 contain the displacement and acceleration histories recorded by the two displacement transducers and the six accelerometers permanently mounted on the shake table;

iii) Columns 10 to 33 contain the displacement histories measured by wire potentiometers and LVDTs. Note that six in-between instruments, shown in grey in the table, were removed or relocated during the last tests (for details see Table 5.1), so the corresponding time-series were substituted by a “not-a-number” (*NaN*) flag;

iv) Columns 34 and 35 provide the forces measured by the load cell of the horizontal (longitudinal) and vertical actuators of the shake table (expressed in units of kN);

v) Columns 36 to 75 contain the acceleration histories recorded by the 40 accelerometers. Note that 16 in-between sensors, shown in grey in the table, were removed or were attached to elements that collapsed in later steps of the testing; consequently, the corresponding columns were filled with *NaN* flags (see Table 5.1).

Positive displacements and accelerations are for motion towards the West building side. All acceleration and displacement recordings were filtered using a low-pass filter set to a frequency of 35 Hz. The displacement time series obtained from the earthquake simulations include residuals accumulated during previous tests runs, while in the case of the random vibrations, the displacement recordings are offset to zero.

The three displacement transducers that saturated during the SC2-500% test (*i.e.*, WP 10, WP 11, and LVDT 17) are highlighted with red in the table and the corresponding displacement histories are substituted with *NaN* flags in the data matrix. Similarly, the displacement history of potentiometer WP 24, which was affected by instrument saturation during test SC2-350%, was replaced by *NaN* flags. All displacement recordings fully retrieved or complemented with information from the analysis of the video recordings are included in columns 76 to 80, described in Table 5.4. The West chimney collapsed during testing at SC2-400%, so the corresponding acceleration and displacement responses (columns 57 and 80, respectively) are cut at 4.22 s (line 845).

The accelerometers that recorded spurious accelerations (*i.e.*, A 13 from SC2-350% to the end, and A 18 during all tests) are also highlighted with red in Table 5.3.

Table 5.3 Accelerometer and displacement transducer recordings: matrix columns 1 to 75. Letters indicate the measuring instrument: A, accelerometer; WP, wire potentiometer; LVDT, linear variable displacement transducer.

Col. No.	Sensor ID	Measured quantity - Instrument location	Rec. DOF	UM	Associated mass (in *x* dir.) [kg]
1	-	Time	-	[s]	-
2	-	Shake-table longitudinal displacement	*x*	[mm]	-
3	-	Shake-table transverse displacement	*y*	[mm]	-
4	-	Shake-table longitudinal acceleration (sensor mounted on the South side of the table)	*x*	[g]	-
5	-	Shake-table vertical acceleration	*z*	[g]	-
6	-	Shake-table transverse acceleration	*y*	[g]	-
7	-	Shake-table longitudinal acceleration (sensor mounted at the N-E corner of the table)	*x*	[g]	-
8	-	Shake-table vertical acceleration (sensor mounted at the N-E corner of the table)	*z*	[g]	-
9	-	Shake-table vertical acceleration (sensor mounted at the S-W corner of the table)	*z*	[g]	-
10	LVDT 1	Sliding at the base of the squat pier of the South façade (w.r.t. the foundation)	*x*	[mm]	-
11	LVDT 2	Sliding at the base of the interior wall (w.r.t. the foundation)	*x*	[mm]	-
12	LVDT 3	Sliding of the floor girder at East end (w.r.t. the East wall)	*x*	[mm]	-
13	LVDT 4	Sliding of floor girder at West end (w.r.t. the interior wall)	*x*	[mm]	-
14	LVDT 5	Displacement at the top of the interior wall (w.r.t. the reference frame)	*x*	[mm]	-
15	WP 8	OOP deflection of the East wall at the floor level (w.r.t. the reference frame)	*x*	[mm]	-

16	WP 9	OOP deflection of the West wall at the floor level (w.r.t. the reference frame)	*x*	[mm]	-
17	WP 10	OOP deflection of the East gable wall at mid-height (w.r.t. the reference frame); ***for test SC2-500%, see col. 76***	*x*	[mm]	-
18	WP 11	OOP deflection of the West gable wall at mid-height (w.r.t. the reference frame); ***for test SC2-500%, see col. 77***	*x*	[mm]	-
19	WP 12	Roof-ridge beam displacement (w.r.t. the reference frame)	*x*	[mm]	-
20	LVDT 13	OOP displacement of the East gable wall at the ridge level (w.r.t. the ridge beam)	*x*	[mm]	-
21	LVDT 14	OOP displacement of the West gable wall at the ridge level (w.r.t. the ridge beam)	*x*	[mm]	-
22	WP 25	Displ. at the top of the South chimney (w.r.t. the West reaction wall); ***for tests SC2-400% and SC2-500%, see col. 78***	*x*	[mm]	-
23	LVDT 23	Floor separation along the transverse direction of the East façade (from joist to joist)	*y*	[mm]	-
24	LVDT 18	Floor-diaphragm displacement on the South side (w.r.t. the reference frame)	*x*	[mm]	-
25	LVDT 17	Floor-diaphragm displacement on the North side (w.r.t. the reference frame); ***for test SC2-500%, see col. 79***	*x*	[mm]	-
26	LVDT 19	North wall top displacement at the N-E corner (w.r.t. the North lower plate – below the floor)	*x*	[mm]	-
27	LVDT 20	North wall top displacement at the N-W corner (w.r.t. the North lower plate – below the floor)	*x*	[mm]	-
28	LVDT 21	South wall top displacement at the S-E corner (w.r.t. the South lower plate – below the floor)	*x*	[mm]	-
29	LVDT 22	South wall top displacement at the location of the chimney (w.r.t. the South lower plate – below the floor)	*x*	[mm]	-
30	WP 7	OOP deflection of the East wall at mid-height of the first storey (w.r.t. the reference frame)	*x*	[mm]	-
31	WP 24	Displ. at the top of the West chimney (w.r.t. the West reaction wall); ***for tests SC2-350% and SC2-400%, see col. 80***	*x*	[mm]	-
32	LVDT 15	Floor-diaphragm displacement on the East side, at midspan (w.r.t. the reference frame)	*x*	[mm]	-
33	LVDT 16	Floor-diaphragm displacement on the West side, at midspan (w.r.t. the reference frame)	*x*	[mm]	-
34	-	Force measured by the load cell of the horizontal (longitudinal) actuators of the shake table	*x*	[kN]	-
35	-	Force measured by the load cell of the vertical actuators of the shake table	*z*	[kN]	-
36	A 1	East wall acceleration at mid-height of the first storey (at wall midspan)	*x*	[g]	405
37	A 2	East wall acceleration at the level of the floor (at the S-E corner)	*x*	[g]	621
38	A 3	East wall acceleration at the level of the floor (at wall midspan)	*x*	[g]	395
39	A 4	East wall acceleration at the level of the floor (at the N-E corner)	*x*	[g]	807
40	A 5	East wall acceleration at mid-height of the gable (at the S-E corner)	*x*	[g]	200
41	A 6	East wall acceleration at mid-height of the gable (at midspan)	*x*	[g]	279
42	A 7	East wall acceleration at mid-height of the gable (at the N-E corner)	*x*	[g]	200
43	A 8	East wall acceleration at the level of the ridge	*x*	[g]	167
44	A 9	West wall acceleration at mid-height of the first storey (at wall midspan)	*x*	[g]	1626
45	A 10	West wall acceleration at the level of the floor (at the N-W corner)	*x*	[g]	1599
46	A 11	West wall acceleration at the level of the floor (at wall midspan)	*x*	[g]	1133

47	A 12	West wall acceleration at the level of the floor (at the S-W corner)	*x*	[g]	1210
48	A 13	West wall acceleration at mid-height of the gable (at the N-W corner)	*x*	[g]	711
49	A 14	West wall acceleration at mid-height of the gable (at midspan)	*x*	[g]	674
50	A 15	West wall acceleration at mid-height of the gable (at the S-W corner)	*x*	[g]	462
51	A 16	West wall acceleration at the level of the ridge	*x*	[g]	369
52	A 17	North wall acceleration at the level of the floor (at the top of the Eastward central pier)	*x*	[g]	656
53	A 18	North wall acceleration at the level of the floor (at the top of the Westward central pier)	*x*	[g]	657
54	A 19	South wall acceleration at the level of the floor (at the top of the central pier)	*x*	[g]	765
55	A 20	South wall acceleration at the level of the floor (at the top of the squat pier)	*x*	[g]	1919
56	A 21	Interior wall acceleration at the level of the floor (at wall midspan)	*x*	[g]	751
57	A 22	Acceleration at the top of the West chimney	*x*	[g]	267
58	A 23	Acceleration at the top of the South chimney	*x*	[g]	497
59	A 24	Foundation beam acceleration on the North side (at midspan)	*x*	[g]	4106
60	A 25	Foundation beam acceleration on the South side (at midspan)	*x*	[g]	4282
61	A 26	Floor-diaphragm longitudinal acceleration on the North side (at the middle)	*x*	[g]	1381
62	A 27	Floor-diaphragm vertical acceleration on the North side (at the middle)	*z*	[g]	-
63	A 28	Floor-diaphragm longitudinal acceleration on the South side (at the middle)	*x*	[g]	1381
64	A 29	Floor-diaphragm vertical acceleration on the South side (at the middle)	*z*	[g]	-
65	A 30	Floor-diaphragm longitudinal acceleration (at the center)	*x*	[g]	419
66	A 31	Floor-diaphragm vertical acceleration (at the center)	*z*	[g]	-
67	A 32	Floor-diaphragm longitudinal acceleration on the East side (at midspan)	*x*	[g]	419
68	A 33	Floor-diaphragm transverse acceleration on the East side (at midspan)	*y*	[g]	-
69	A 34	Floor-diaphragm longitudinal acceleration on the West side (at midspan)	*x*	[g]	419
70	A 35	Floor-diaphragm transverse acceleration on the West side (at midspan)	*y*	[g]	-
71	A 36	Longitudinal acceleration at midspan of the ridge beam	*x*	[g]	1504
72	A 37	Transverse acceleration at midspan of the ridge beam	*y*	[g]	-
73	A 38	Vertical acceleration at the East end of the ridge beam	*z*	[g]	-
74	A 39	Vertical acceleration at the West end of the ridge beam	*z*	[g]	-
75	A 40	Longitudinal acceleration at the top S-W corner of the steel reference frame	*x*	[g]	-

Table 5.4 Displacement histories retrieved from video analysis for the recording instruments that exhibited problems: matrix columns 76 to 80.

Col. No.	Sensor ID	Measured quantity - Instrument location	Rec. DOF	UM	Test
76	WP 10	OOP deflection at mid-height of the East gable wall (w.r.t. the shake table); ***for tests up to SC2-400%, see col. 17***	*x*	[mm]	SC2-500%
77	WP 11	OOP deflection at mid-height of the West gable wall (w.r.t. the shake table); ***for tests up to SC2-400%, see col. 18***	*x*	[mm]	SC2-500%
78	WP 25	Displacement at the top of the South chimney (w.r.t. the laboratory floor); ***for tests up to SC2-350%, see col. 22***	*x*	[mm]	SC2-400%; SC2-500%
79	LVDT 17	Floor-diaphragm displacement on the North side (w.r.t. the shake table); ***for tests up to SC2-400%, see col. 25***	*x*	[mm]	SC2-500%
80	WP 24	Displacement at the top of the West chimney (w.r.t. the laboratory floor); ***for tests up to SC2-300%, see col. 31***	*x*	[mm]	SC2-350%; SC2-400%

Table 5.5 describes the quantities provided in columns 81 to 103 of the earthquake-simulation *.txt* data files, which were not directly measured by the acquisition system, but were derived after post-processing. Quantities such as inertia forces (*e.g.*, base shear and gables-roof inertia forces) were computed after the assumptions mentioned in Section 5.2 and further discussed in Section 6.6. Accelerations and displacements are provided in units of g and mm, respectively, while forces are expressed in units of kN.

The authors suggest that readers who wish to make use of the data for modelling the dynamic response of the building specimen should refer to column No. 82 for the input base accelerations (*i.e.*, accelerations recorded on the building foundation). Accelerations recorded by the sensors installed on the shake table were at a considerable distance from the foundation beam; hence they might exhibit differences in amplitude. Such differences are not attributed to relative displacements of the building foundation with respect to the shake table, but to amplification caused by the presence of spurious rotational components that cannot be fully eliminated when controlling a tri-dimensional shake-table system under high-intensity input.

Table 5.5 Accelerometer and displacement transducer derived data: matrix columns 81 to 103.

Col. No.	Recorded / computed quantity	DOF	UM	Description / Derivation
81	Shake-table acceleration, a_T	x	[g]	Average of col. 4 and 7
82	Base acceleration (foundation beam), a_g	x	[g]	Average of col. 59 and 60
83	South wall acceleration (at the floor level), $a_{1,S}$	x	[g]	Average of col. 54 and 55 until test SC2-300%; equal to col. 55 for test SC2-350% and thereafter
84	North wall acceleration (at the floor level), $a_{1,N}$	x	[g]	Equal to col. 52 until test SC2-300%; equal to col. 61 for test SC2-350% and thereafter
85	Average floor diaphragm acceleration, $a_{1,D}$	x	[g]	Average of col. 61, 63, 65, 67 and 69
86	Roof ridge acceleration, a_R	x	[g]	Equal to col. 71
87	West chimney acceleration (at the top), $a_{t,C,W}$	x	[g]	Equal to col. 57
88	South chimney acceleration (at the top), $a_{t,C,S}$	x	[g]	Equal to col. 58
89	Base displacement (shake table / foundation beam), Δ_g	x	[mm]	Equal to col. 2
90	South floor-diaphragm displacement, $\Delta_{1,S}$	x	[mm]	Equal to col. 24
91	North floor-diaphragm displacement, $\Delta_{1,N}$	x	[mm]	Equal to col. 25 until test SC2-400%; equal to col. 79 for test SC2-500%
92	Average floor-diaphragm displacement, $\Delta_{1,AVG}$	x	[mm]	Average of col. 24, 25, 32 and 33 until test SC2-400%; substitution of col. 25 with col. 79 for test SC2-500%
93	Roof-ridge displacement (w.r.t. the shake table), Δ_R	x	[mm]	Equal to col. 19
94	West chimney displacement (at the top, w.r.t. the shake table), $\Delta_{t,C,W}$	x	[mm]	Equal to col. 31 until test SC2-300%; equal to col. 80 for tests SC2-350% and SC2-400%
95	South chimney displacement (at the top, w.r.t. the shake table), $\Delta_{t,C,S}$	x	[mm]	Equal to col. 22 until test SC2-350%; equal to col. 78 for test SC2-400% and thereafter
96	South wall base shear, $V_{b,S}$	x	[kN]	Inertia force of South wall plus half of the inertia force of E/W and interior walls
97	North wall base shear, $V_{b,N}$	x	[kN]	Inertia force of North wall plus half of the inertia force of E/W and interior walls
98	Overall base shear, $V_{b,TOT}$	x	[kN]	Sum of the products of each accelerometer reading with the associated mass
99	Gables-roof assembly inertia force, F_R	x	[kN]	Sum of the products of each acc. reading with the associated mass above the floor (excluding the South chimney)
100	South wall base shear, $V^0_{b,S}$ (inertia force without non-oscillatory mass)	x	[kN]	Col. 96 minus the product of column 60 times mass 4106 kg
101	North wall base shear, $V^0_{b,N}$ (inertia force without non-oscillatory mass)	x	[kN]	Col. 97 minus the product of column 59 times mass 4282 kg
102	Overall base shear, $V^0_{b,TOT}$ (inertia force without non-oscillatory mass)	x	[kN]	Col. 98 minus the sum of products of columns 60 and 59 with masses 4106 and 4282 kg, respectively
103	Inertia force for top half portion of the gables-roof assembly, F^0_R	x	[kN]	Sum of the products of acc. reading with the associated mass above the gables mid-height only (excluding the South chimney)

Table 5.6 Displacement and acceleration histories retrieved from video analysis for the South chimney at the level of fracture above the roofline (+3.78 m): matrix columns 104 and 105.

Col. No.	Measured quantity - Instrument location	Rec. DOF	UM	Test
104	South chimney displacement at mid-height of the free-standing stack (+3.78 m) after the fracture (w.r.t. the shake-table), $\Delta_{m,C,S}$	x	[mm]	SC2-350%; SC2-400%; SC2-500%
105	South chimney acceleration at mid-height of the free-standing stack (+3.78 m) after the fracture (w.r.t. the shake-table), $a_{m,C,S}$	x	[g]	

6 TEST RESULTS

The building specimen did not suffer any visible damage up to test SC2-150% (*PGA* = 0.21 g), began showing minor cracks for shaking under SC2-200% (*PGA* = 0.29 g), and was considered at near-collapse state after test SC2-400% (*PGA* = 0.68 g) when the West chimney collapsed, and the rest of the structure underwent substantial degradation. During test SC2-500% (*PGA* = 1.0 g), debris from the West chimney fell in the interior of the building and portions of the East and North façades displaced as rigid bodies by sliding. Excessive residual deformations were measured at the end of the shaking. A considerable percentage of the walls had lost their load-bearing capacity, and the structure was barely in equilibrium. The building would not survive further shaking; therefore, tests were stopped to prevent collateral damage to the instrumentation and the shake table. Videos of the testing sequence are available on the EUCENTRE YouTube channel (EUCENTRE, 2018).

Before every earthquake-simulation test, the building was subjected to low-amplitude random excitations for assessing the progressive effect of the cumulative damage on its dynamic structural properties: the fundamental period of the undamaged structure was $T_{1,und}$ = 0.15 s, while by the end of the testing sequence it shifted to $T_{1,dam}$ = 0.31 s. Initially, the response was dominated by the out-of-plane deflection of the gables-roof assembly. Changes in the deformed modal shapes were not seen before testing under SC2-250% (*PGA* = 0.58 g), when a global building response was triggered.

The following paragraphs illustrate the analysis results for the identification of the building dynamic characteristics and the major observations from the earthquake simulations, including the description of the damage evolution and the developed failure mechanisms, the hysteretic response, the overall displacement demands and the performance of the chimneys.

6.1 System Dynamic Identification

6.1.1 Introduction and methodology

Several types of signals are available for use in experimental modal analysis, such as random vibrations or impulsive signals. For estimating the frequency response functions (FRFs), the choice depends upon the characteristics of the system, the theory underlying the parameter estimation, and the expected use of the data. Different kinds of excitation signals have their specific characteristics, and some are more suitable for certain applications than others. For testing the LNEC-BUILD-3 specimen, a white-noise signal was adopted, characterised by frequency content in the range of 0.1-40 Hz, nominal peak-to-peak amplitude 4 mm, and duration 160 s, while the FRFs were computed based on the input-output relationships.

The excitation was applied with a dual purpose: (i) to characterise the entire test system (*i.e.*, shake table plus building specimen) during the adaptive tuning process for the desired target signals; (ii) to identify the dynamic response properties of the specimen. In the latter case, the FRFs were used to quantify the effect of the damage evolution on the dynamic characteristics of the specimen, *i.e.*, to monitor the decrease in natural frequencies and to compute the increase in modal damping. For the comparison of the analysis results, it was essential always to use input signals of the same type and amplitude.

The dynamic identification of the building was performed using the acceleration response-histories recorded by the sensors mounted on the structure (Figure 6.1). The FRFs were computed with the LNEC-SPA software (Mendes and Campos Costa, 2007) accounting for the single-input-to-multi-output (SIMO) relationships between the acceleration recordings. Figure 6.2 shows one of those functions that was obtained considering the table acceleration as the input signal and the ridge beam acceleration as the response.

The calculation of the complex FRF $H_i(f)$ was performed according to Bendat and Piersol (2010), by considering the following relationship:

$$H_i\left(f\right)=\frac{G_{xyi}\left(f\right)}{G_{xy}\left(f\right)} \tag{1}$$

where: x stands for the input shake-table acceleration in each direction independently; y_i, is a recorded acceleration response at any location of the structure; $G_{xyi}(f)$, is the cross-spectral density estimate between input and output signals; $G_{xx}(f)$ is the auto-spectrum density estimate of the input signal. The coherence function that quantifies the quality of the transfer function was computed as:

$$\gamma_{xy_i}^2\left(f\right)=\frac{\left|G_{xy_i}\left(f\right)\right|^2}{G_{xx}\left(f\right)G_{y_iy_i}\left(f\right)} \tag{2}$$

where, $G_{y_iy_i}(f)$ is the auto-spectrum density estimate of the output signal. For a given frequency, f, the closer to the unit the coherency function is, the better is the correlation between the input and the output signals.

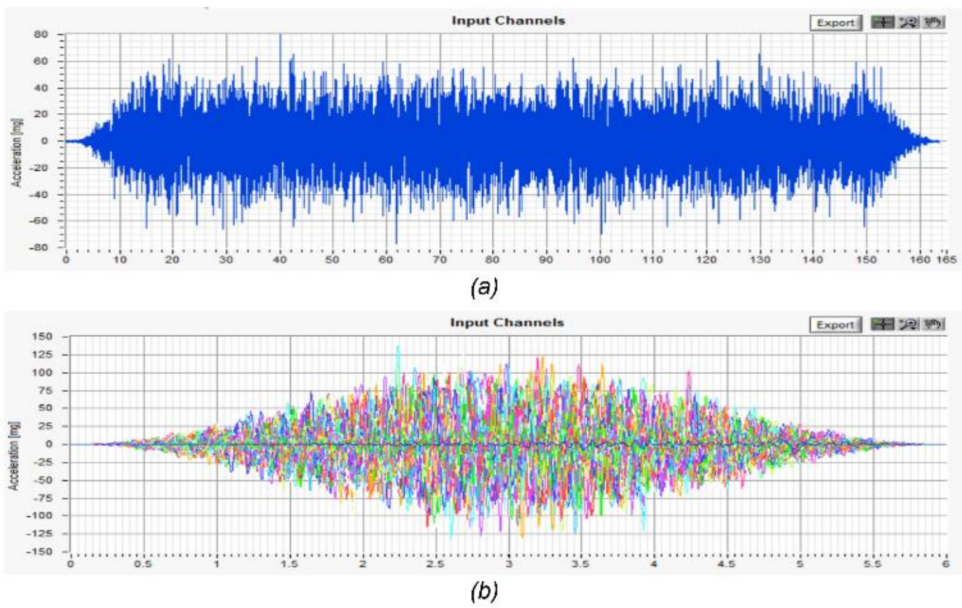

Figure 6.1 Specimen dynamic identification: (a) input acceleration history; (b) windowed average input.

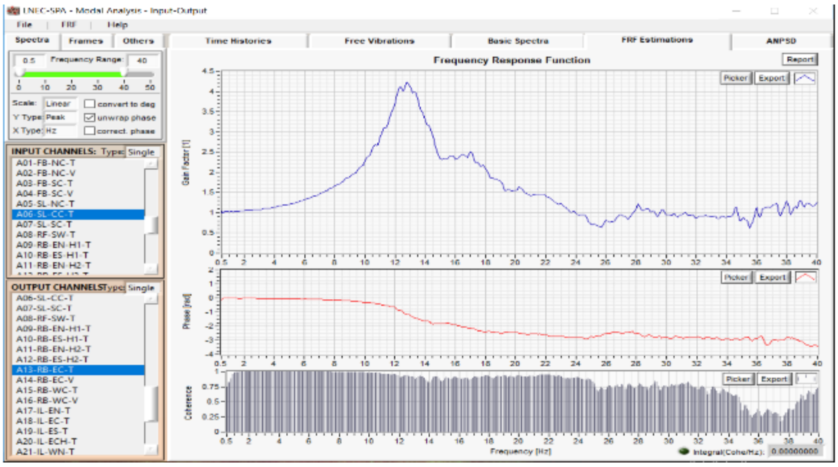

Figure 6.2 Specimen dynamic identification: frequency response function from the accelerations recorded in the longitudinal direction of the specimen.

The following paragraphs describe briefly the methods used to estimate the natural frequencies, the modal damping values, and the mode shapes of the building specimen through random-vibration tests.

6.3.1.1 The FDD method

The frequency-domain decomposition (FDD) method is based on the diagonalisation of the spectral response density matrices for their decomposition into the modal contributions at each frequency. The diagonalisation is done through the singular value decomposition (SVD) for each of the datasets. This decomposition corresponds to a single-degree-of-freedom (SDOF) identification of the system for each singular value. The method can be summarised in the following steps:

i) The structural response is expressed as the sum of the contributing modes of vibration:

$$y(t) = \Phi q(t) \tag{3}$$

where $\mathbf{\Phi}$ is the matrix of the deflected shape and $\boldsymbol{q}$ is the time-variant vector.

ii) The matrix of auto-correlation response functions is computed as:

$$C_{yy}(\tau) = E\left\{ y(t+\tau) y(t)^T \right\} \tag{4}$$

iii) By introducing Eq. (6.3) to Eq. (6.4), the latter becomes:

$$C_{yy}(\tau) = E\left\{ \Phi q(t+\tau) q(t)^H \Phi^H \right\} = \Phi C_{qq}(\tau) \Phi^H \tag{5}$$

where $(\cdot)^H$ represents the conjugate transposed operator for Hermitian matrices. Eq. (6.5) expresses the matrices of the auto-correlation functions in modal coordinates.

iv) Application of the Fourier transform to Eq. (6.5) yields:

$$G_{yy}(f) = \Phi G_{qq}(f) \Phi^H \tag{6}$$

v) For uncorrelated modal coordinates, $\boldsymbol{G_{qq}}$ is a diagonal matrix and the modes of vibration expressed in $\boldsymbol{\Phi}$ are orthogonal. This leads to the conclusion that the above expression is similar to that resulting from the decomposition into singular values:

$$SVD(A) = U(f)SU(f)^H = \left[\{u_i(f)\},\ldots\right]\begin{bmatrix} \ddots & & \\ & S_i & \\ & & \ddots \end{bmatrix}\left[\{u_i(f)\},\ldots\right]^H \tag{7}$$

where $\boldsymbol{S}$ is a real diagonal matrix with the singular values in descending order and a representation of the various frequencies as shown in Figure 6.3. It presents peaks coincident with the system vibration frequencies or other dynamic phenomena that may cause vibrations at those frequencies (*e.g.*, rotary machines). The $\boldsymbol{U}$ matrix includes complex numbers that represent the modal shapes for the identified vibration modes. When using the SVD algorithm, the $\boldsymbol{U}$ matrix depends on the frequency due to the rearranging of the singular values involved in the algorithm.

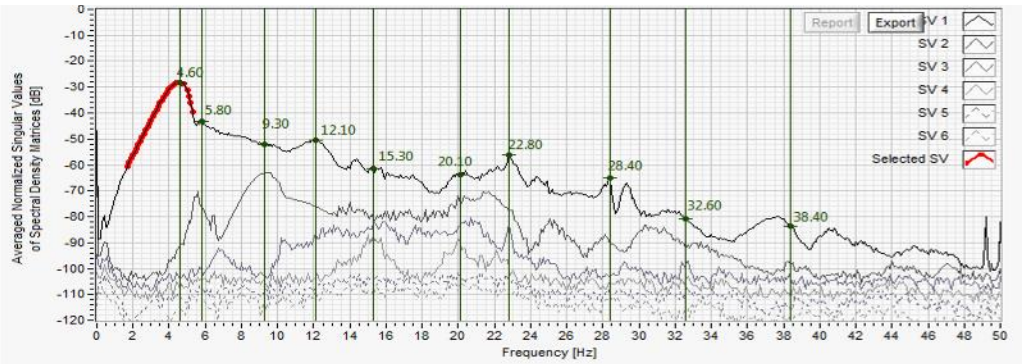

Figure 6.3 Representation of the singular values matrix.

6.3.1.2 The EFDD method

The enhanced frequency-domain decomposition (EFDD) method, proposed by Brincker *et al.* (2001), was additionally employed. The approach provides improved estimates of the vibration frequencies compared to the FDD method, while it also gives estimates of the modal damping. The method consists in making adjustments to the auto-correlation functions of a SDOF system, obtained from the functions of spectral density by selecting through a chosen criterion, weighing a set of points in the vicinity of each resonance, and finally applying the inverse of the Fourier transform. The employed criteria consist in defining a limit value of the modal assurance criterion (MAC) coefficient which receives values in the range of 0 to 1: unit when the vibration modes have the same configuration; null when they are orthogonal.

This method allows a more accurate estimation of the vibration frequencies, because it is based on the adjustment to the zero crossings of the auto-correlation function and not only on the peaks, which can be influenced by several factors, such as the frequency resolution. The modal damping is obtained from the logarithmic decrement of the impulse response function, as shown in Figure 6.4.

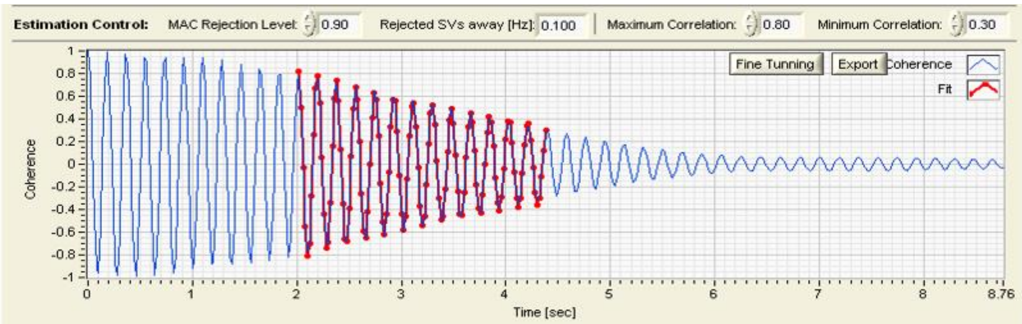

Figure 6.4 Frequency estimate (zero-crossings) and damping (logarithm decrement) of the impulse response estimate.

The numerical correlation of the mode-shape vectors of the undamaged state of the model and the subsequent damaged states can also be obtained by computing the MAC coefficient as described in the following equation:

$$MAC_{u,d} = \frac{\left|\sum_{i=1}^{n} \varphi_i^u \varphi_i^d\right|^2}{\sum_{i=1}^{n}\left(\varphi_i^u\right)^2 \sum_{i=1}^{n}\left(\varphi_i^d\right)^2} \quad (8)$$

where φ^u is the mode-shape vector corresponding to the undamaged condition of the model, φ^d is the mode-shape vector corresponding to the damaged condition of the model, and n is the number of the estimated degrees of freedom (Allemang *et al.*, 1982). The product of the above expression is a scalar value in the range of 0 and 1 that indicates the extent of correlation between the two cases.

6.1.2 Modal analysis results

6.3.2.1 Test CHAR#0 (on undamaged structure)

A dynamic identification test was performed before proceeding with the earthquake simulations to obtain an image of the dynamic properties of the building in its undamaged state. Figure 6.5a depicts the set of the accelerometers considered for visualisation of the mode shapes. Frequencies and damping values for the first nine modes were evaluated through the application of both FDD and EFDD methods (Table 6.1). Figure 6.5b shows the FDD analysis results: a frequency around 6.8 Hz characterised the fundamental vibration mode of the building. The shapes of the first, third and ninth modes are visualized in Figure 6.6.

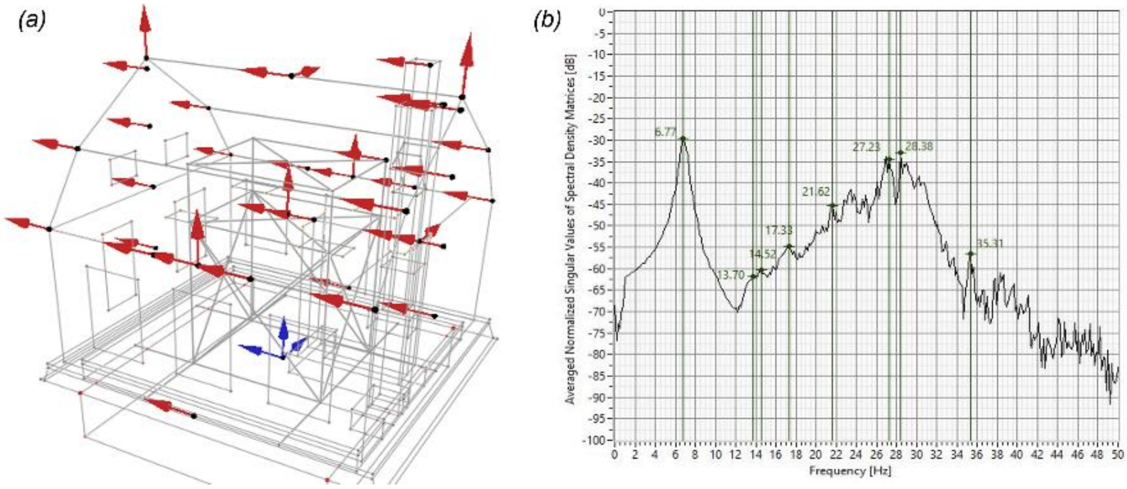

Figure 6.5 Dynamic identification test CHAR#0: (a) accelerometers location; (b) FDD analysis results.

Table 6.1 Dynamic identification test CHAR#0: summary of the modal analysis results with application of both FDD and EFDD analysis methods.

Vibration mode	FDD method		EFDD method		Damping
	Frequency	Period	Frequency	Period	
	[Hz]	[s]	[Hz]	[s]	[%]
1	6.77	0.148	6.82	0.147	4.04
2	13.70	0.073	13.73	0.073	2.46
3	14.52	0.069	14.53	0.069	2.36
4	17.33	0.058	17.38	0.058	1.70
5	21.62	0.046	21.66	0.046	0.41
6	23.43	0.043	23.43	0.043	1.00
7	27.23	0.037	27.12	0.037	1.04
8	28.38	0.035	28.39	0.035	0.22
9	35.31	0.028	35.26	0.028	0.24

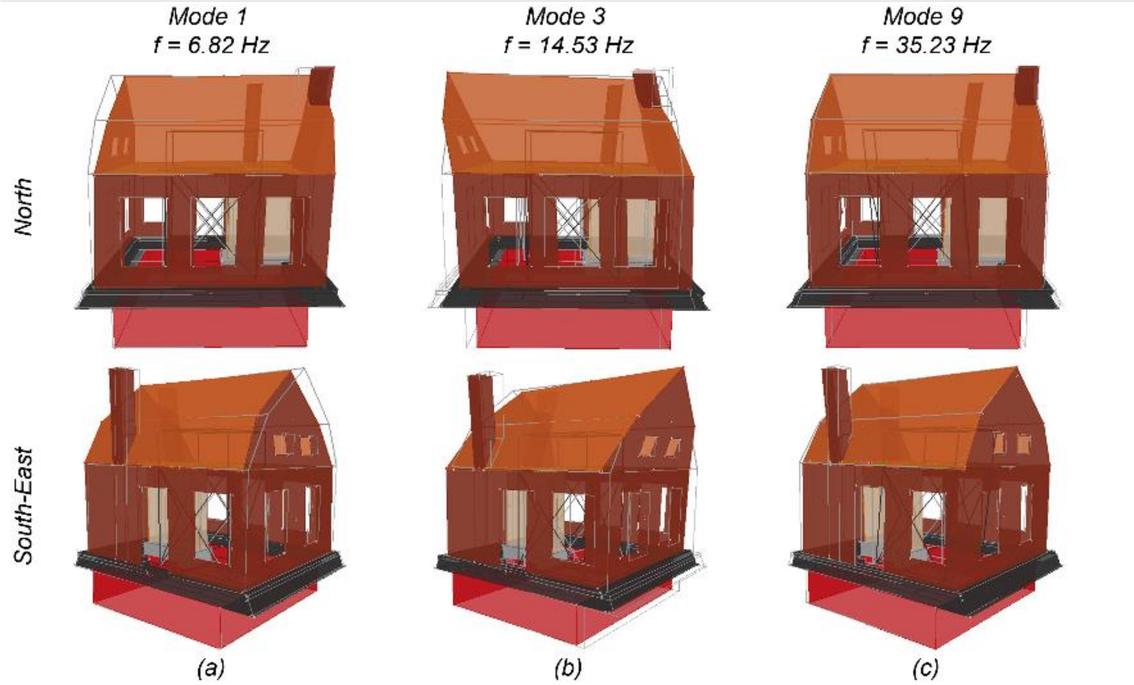

Figure 6.6 Dynamic identification test CHAR#0: vibration-mode shapes.

6.3.2.2 Test CHAR#9 (after test SC2-300%)

Low-intensity random-vibration tests were consistently performed before every earthquake test (see

Table 4.1 for the exact applied testing sequence): no significant change in the modal properties of the building specimen was noticed until before the SC2-250% test (see appendix A). The analysis results of the CHAR#8 test (following the shaking under SC2-250%) showed a decrease in vibration frequencies of the building model and an increase of the modal damping values. Further decrease in the frequencies and increase in the damping was seen in the CHAR#9 test, as illustrated in Figure 6.7b. Table 6.2 lists the frequencies of the first nine vibration modes; Figure 6.8 shows the deformed shapes of the first, third and ninth vibration modes.

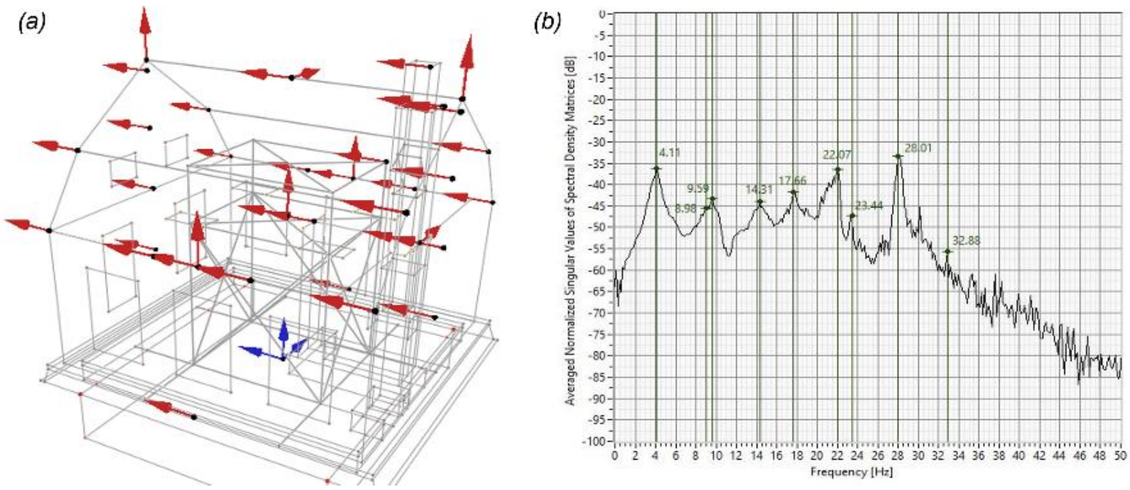

Figure 6.7 Dynamic identification test CHAR#9: (a) accelerometers location; (b) FDD analysis results.

Table 6.2 Dynamic identification test CHAR#9: summary of the modal analysis results with application of both FDD and EFDD analysis methods.

Vibration mode	FDD method		EFDD method		Damping
	Frequency	Period	Frequency	Period	
	[Hz]	[s]	[Hz]	[s]	[%]
1	4.11	0.243	3.99	0.251	3.44
2	8.98	0.111	9.03	0.111	3.35
3	9.59	0.104	9.57	0.104	3.11
4	14.31	0.070	14.36	0.070	0.59
5	17.66	0.057	17.68	0.057	1.65
6	22.07	0.045	22.09	0.045	0.49
7	23.44	0.043	23.37	0.043	0.51
8	28.01	0.036	28.11	0.036	0.70
9	32.88	0.030	32.69	0.031	0.55

Figure 6.8 Dynamic identification test CHAR#9: vibration-mode shapes.

After test CHAR#9 (after the SC2-300% test), several accelerometers were removed from the specimen. In the subsequent random-vibration tests, a continuous decrease in the modal frequencies was identified as further damage was cumulated (Table 6.3). Besides, some significant changes were also seen in the mode shapes.

Table 6.3 Evolution of the frequencies of vibration modes of the building. Tests performed after the removal of the accelerometers are highlighted in red.

Modal frequencies [Hz] (EFDD method)									
Test ID name	Vibration modes								
	First (Period [s])	Second	Third	Forth	Fifth	Sixth	Seventh	Eighth	Ninth
CHAR#0	6.82 (0.147)	13.73	14.53	17.38	21.66	23.43	27.12	28.39	35.26
CHAR#1	6.80 (0.147)	13.70	14.46	17.23	21.64	23.44	27.25	28.29	35.54
CHAR#2	6.69 (0.149)	13.70	14.45	17.13	21.59	23.18	27.14	28.05	35.63
CHAR#3	6.67 (0.150)	13.70	14.44	16.97	21.60	22.85	26.83	27.30	35.29
CHAR#4	6.59 (0.152)	13.72	14.45	16.99	21.31	22.94	26.65	26.85	35.42
CHAR#5	6.44 (0.155)	13.70	14.46	16.92	21.07	22.87	26.60	26.82	35.54
CHAR#6	6.24 (0.160)	13.27	14.20	16.49	20.19	22.82	26.56	26.71	35.60
CHAR#7	6.33 (0.158)	13.13	14.20	16.19	19.28	22.78	26.46	26.61	34.98
CHAR#8	5.20 (0.192)	9.51	10.53	15.71	16.97	22.19	24.65	28.24	34.31
CHAR#9	3.99 (0.251)	9.03	9.57	14.36	17.68	22.09	23.37	28.11	32.69
CHAR#10	3.58 (0.279)	8.55	9.56	13.38	17.20	21.61	23.06	28.16	32.73
CHAR#11	3.18 (0.314)	7.66	9.39	12.99	16.93	21.65	23.08	28.16	32.70
CHAR#12	3.18 (0. 314)	7.91	9.55	12.39	17.02	21.87	23.26	27.98	32.29

The evolution of the modal damping ratio is reported in Table 6.4. It should be stressed that estimating the modal damping involves significantly higher uncertainty than evaluating the vibration frequencies. However, there is a generally increasing trend in the damping estimates as damage is spreading.

Table 6.4 Evolution of the modal damping ratio of the building. Tests performed after the removal of the accelerometers are highlighted in red.

Modal damping ratio [%] (EFDD method)									
Test ID name	Vibration modes								
	First	Second	Third	Forth	Fifth	Sixth	Seventh	Eighth	Ninth
CHAR#0	4.04	2.46	2.36	1.70	0.41	1.00	1.04	0.22	0.24
CHAR#1	3.95	2.39	2.15	1.57	0.38	0.89	0.96	0.27	0.74
CHAR#2	3.97	2.21	2.03	1.52	0.61	0.74	0.97	0.37	0.50
CHAR#3	4.46	2.21	2.05	1.58	0.60	0.36	1.07	0.67	0.08
CHAR#4	4.19	2.23	2.13	1.56	0.37	0.60	1.14	0.94	0.36
CHAR#5	3.90	2.41	2.05	1.77	0.81	1.09	1.15	1.02	0.33
CHAR#6	4.68	2.26	2.17	1.89	1.31	1.27	0.96	1.15	0.49
CHAR#7	4.04	2.35	2.16	1.96	1.09	1.08	0.98	1.13	0.17
CHAR#8	4.42	2.64	2.97	1.99	1.54	0.18	0.88	0.41	0.59
CHAR#9	3.44	3.35	3.11	0.59	1.65	0.49	0.51	0.70	0.55
CHAR#10	2.41	3.53	3.20	0.99	1.46	0.80	0.36	0.60	0.62
CHAR#11	5.38	2.66	1.89	2.08	1.73	0.78	0.36	0.61	0.51
CHAR#12	5.44	1.68	3.14	1.44	0.76	0.23	0.68	0.81	0.81

6.2 Shake-Table Performance

The performance of the shake-table test was in general satisfactory in terms of response spectra of the actual table motions within the period range of the building specimen (Figure 6.9 to Figure 6.11). Comparisons between the target response spectra (in grey) and those obtained from the actual table motions (in black) demonstrate that the controller well reproduced the ground motion for low-intensity shakings (*i.e.*, for SC1 earthquakes). During application of the strong motion SC2 scaled at amplitudes equal to or higher than 200%, an average undershoot of the order of 10-20% was generally observed for spectral ordinates between 0.15 s and 0.32 s periods (*i.e.*, between $T_{1,und}$ and $T_{1,dam}$). A deep undershoot of nearly 35% at the fundamental period of the building was only noticed when targeting at 300% of SC2. This shortfall was partially compensated by the amplification observed in the accelerations recorded at the level of the building foundation; the corresponding acceleration spectra are shown in blue in the figures below.

The values of the fundamental building period, $T_{1,i}$, reported in Figure 6.9 to Figure 6.11 refer to the estimates coming from analysis results of the dynamic identification test (see Section 6.1.2) performed before the annotated earthquake simulation.

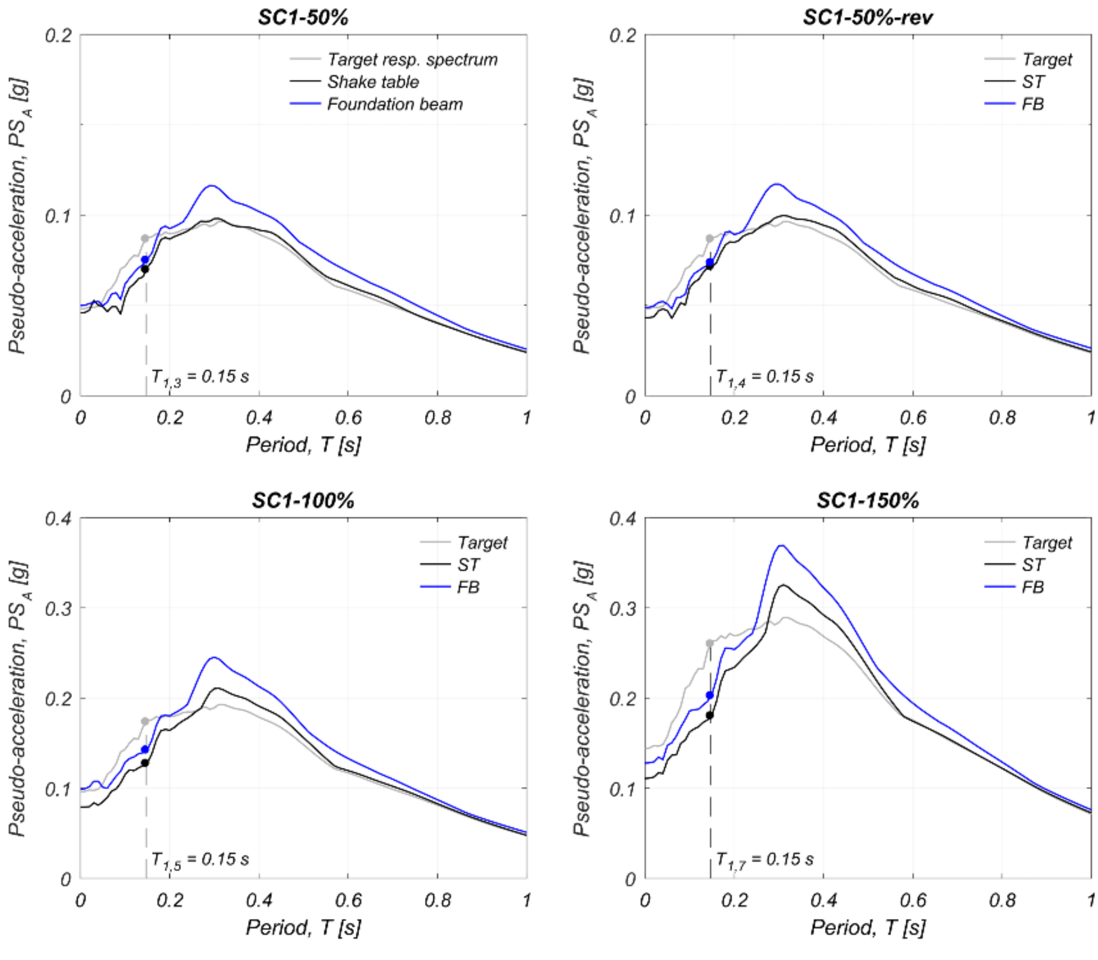

Figure 6.9 Comparison between elastic 5%-damped pseudo-acceleration response spectra of the actual input signals and target spectra for SC1 motions.

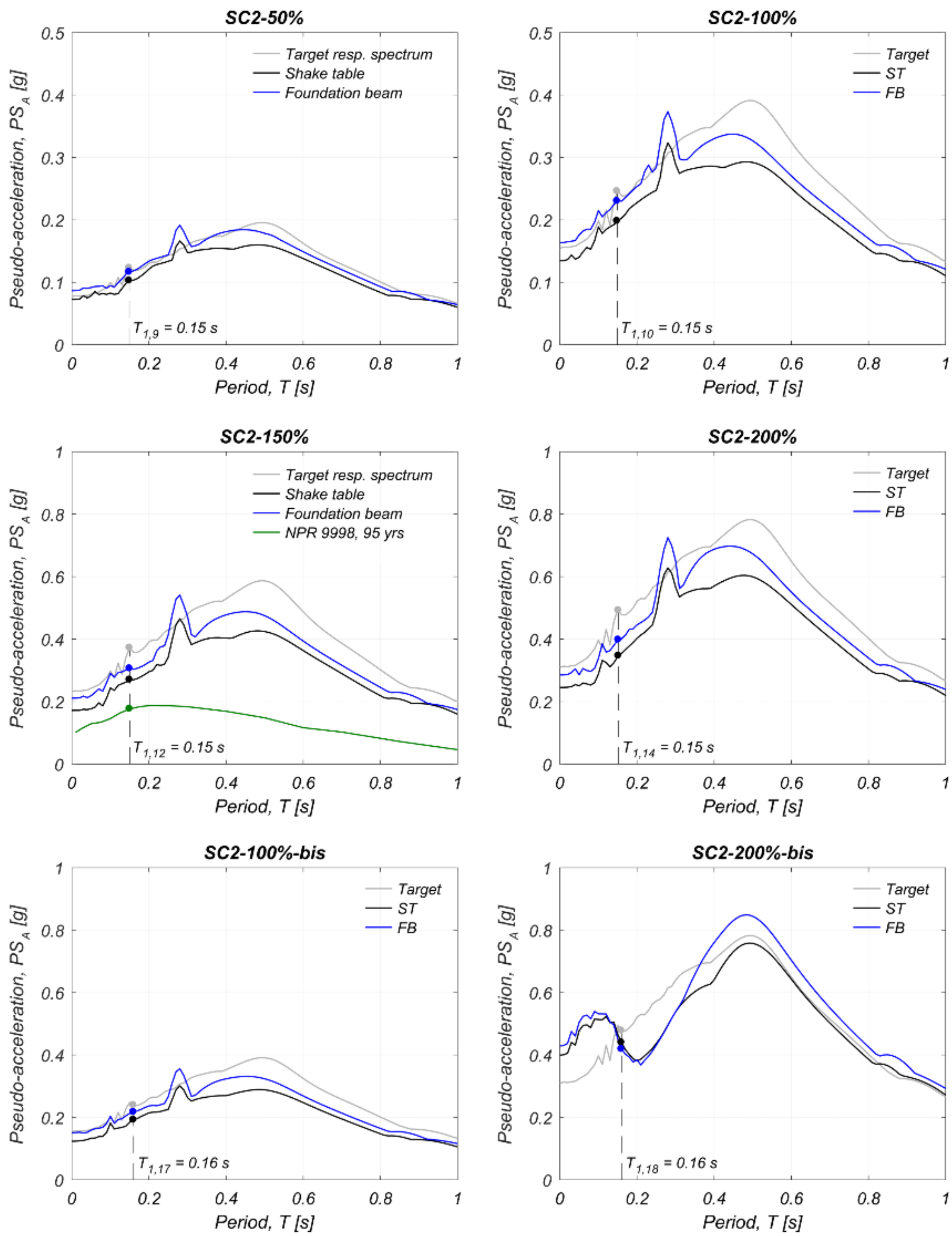

Figure 6.10 Comparison between elastic 5%-damped pseudo-acceleration response spectra of the actual input signals and target spectra for SC2 motion scaled up to 200%-bis. Comparison against the NPR 9998 (2017) elastic spectrum for events with return period of 95 years for the area of Loppersum, Groningen (lat. 53.330115, long. 6.747205).

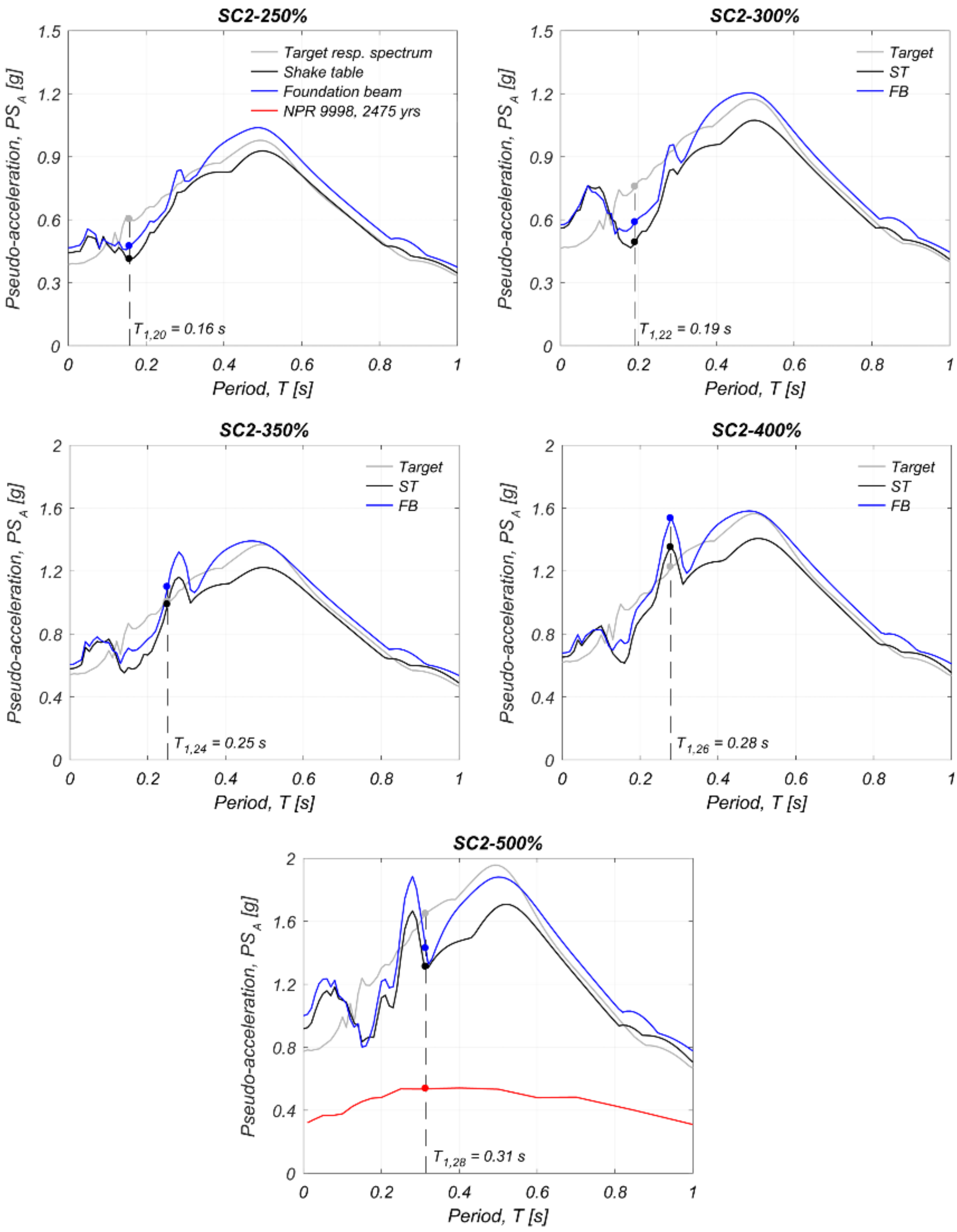

Figure 6.11 Comparison between elastic 5%-damped pseudo-acceleration response spectra of the actual input signals and target spectra for SC2 motion scaled from 250% to 500%. Comparison against the NPR 9998 (2017) elastic spectrum for events with return period 2475 years for the area of Loppersum, Groningen (lat. 53.33, long. 6.75)

Discrepancies between the target and the feedback table motions are always expected due to the evolution of the dynamic characteristics of the specimen, caused by the cumulative structural damage. Observed discrepancies could also be attributed to the difficulty in controlling a shake-table system with so many degrees of freedom. In fact, accelerations recorded on the foundation beam were higher than accelerations recorded by the accelerometers installed below the shake table. The reported difference is due to the mild presence of a vertical acceleration component and the slight rotation around the y-axis of the table (*i.e.*, transverse to the direction of motion). The sensors mounted on the shake table and the foundation were at an in-between distance around 0.8 m, and a small rotation around the transverse table axis could cause considerable amplification to the accelerations recorded on the building foundation.

Figure 6.10 and Figure 6.11 additionally compare the response spectra of the applied SC2-150% and SC2-500% motions with the elastic spectra defined in the Dutch code (NPR 9998, 2017) for seismic actions with mean return periods of 95 and 2475 years, respectively. Earthquake SC2-150% did not result in any visible structural or non-structural damage, despite being almost twice as demanding as the hazard level that a practitioner would reasonably consider when verifying the structure against damage that affects building functionality and aesthetics. Moreover, the structure reached collapse conditions only after testing at SC2-500%, when the applied motion was 2.5 times stronger (in terms of $PS_{A,avg}$ in the period range of interest) than the code spectrum used for the performance assessment of buildings at near-collapse conditions (2475 years return period).

6.3 Input-Motion Characteristics

Several intensity measures (IMs) were evaluated to characterise the input shake-table motions. Table 6.5 lists some of the ground-motion intensity measures that are commonly used in seismic risk studies for correlation with the structural performance. In particular, from left to right the table provides: the nominal and recorded peak ground accelerations, *PGA*; the peak ground velocity (*PGV*); the actual pseudo-spectral acceleration, PS_A, and spectral displacement, S_D, at the fundamental period of the undamaged ($T_{1,und}$) and damaged ($T_{1,i}$) state of the prototype for 5% damping ratio; the geometric mean of the pseudo-acceleration spectral ordinates, $PS_{A,avg}$, in the period window from $T_{1,und}$ = 0.147 s to $T_{1,dam}$ = 0.314 s; the cumulative absolute velocity, *CAV*; the Arias intensity, I_A; and the Housner intensity (*HI*) in its classical and a modified definition (*mHI*). For the calculation of all intensity measures the accelerations recorded on the building foundation beam were used (*i.e.*, column No. 82 of the data matrix).

The values of the fundamental building period, $T_{1,i}$, which were used to estimate the spectral ordinates reported in Table 6.5 refer to the estimates coming from the analysis results of the dynamic identification test (see Section 6.1.2) performed before the annotated earthquake simulation.

The average pseudo-spectral acceleration was calculated according to Bianchini *et al.* (2009), taking the geometric mean of the pseudo-acceleration spectrum for 5% viscous damping ratio between $T_{1,und}$ and $T_{1,dam}$:

$$\ln PS_{A,avg} = \frac{1}{T_{1,dam} - T_{1,und}} \int_{T_{1,und}}^{T_{1,dam}} \ln PS_A(T)\, dT \tag{9}$$

Eq. (9) computes merely the arithmetic mean of the logarithm of pseudo-spectral accelerations. The above representation is usually convenient because ground-motion prediction models usually quote the results of regression analyses in terms of the natural logarithm of pseudo-spectral accelerations. While the geometric and arithmetic mean values are generally very similar (in this case, they differ by less than 4%), the former is less sensitive to extreme spectral ordinates (Eads *et al.*, 2015).

The cumulative absolute velocity (*CAV*) was introduced by the Electric Power Research Institute (EPRI; 1991); it is defined as:

$$CAV = \int_0^{D_{tot}} |a(t)|\, dt \tag{10}$$

where $|a(t)|$ is the absolute value of the acceleration at time t, and D_{tot} is the total duration of the ground-motion record. Since its introduction, *CAV* has been extensively studied for use as potential damage-related ground-motion IM (Campell and Bozorgnia, 2010).

The Arias intensity, I_A, (Arias, 1970) is defined as the integral of the square of the ground acceleration over the entire length of the time-series:

$$I_A = \frac{\pi}{2g} \int_0^{D_{tot}} a^2(t)\,dt \tag{11}$$

The I_A can simultaneously reflect multiple attributes, such as the frequency content, the duration, and the amplitude of the ground motion; Travasarou *et al.* (2003) have demonstrated that structural damage has a stronger correlation with I_A than that with *PGA*.

The Housner intensity (*HI*) in its classical (Housner, 1952) and a modified definition (*mHI*) for short-period masonry structures (Magenes *et al.*, 2014) were also evaluated. The modified version was redefined as the integral of the pseudo-velocity spectrum (for 5% viscous damping) over the period range 0.1-0.5 s, rather than in the range 0.1-2.5 s as in its classical definition. In symbols:

$$mHI = \int_{0.1s}^{0.5s} PS_V(T)\,dT \tag{12}$$

This parameter has proven to better-correlate with the nonlinear displacement demand on short-period URM structures (Graziotti *et al.*, 2016).

The significant durations, $D_{5\text{-}75}$ and $D_{5\text{-}95}$, are provided to characterise the ground-motion duration (Kempton and Stewart, 2006; Bradley, 2011), defined as the time intervals between the development of 5% and 75% of I_A, and between 5% and 95% of I_A, respectively. As each signal was linearly scaled in acceleration amplitude, its significant duration remained unchanged. The actual unscaled input record SC1 (*i.e.* at 100%) had $D_{s,5\text{-}75\%}$ = 0.37 s and $D_{s,5\text{-}95\%}$ = 5.05 s; record SC2-100% had instead $D_{s,5\text{-}75\%}$ = 2.05 s and $D_{s,5\text{-}95\%}$ = 10.21 s.

Table 6.5 Summary of input-motion characteristics.

Test input	Nom. *PGA*	Rec. *PGA*	*PGV*	$PS_A(T_{1,und})$	$S_D(T_{1,und})$	$PS_A(T_{1,i})$	$S_D(T_{1,i})$	$PS_{A,avg}$	*CAV*	I_A	*HI*	*mHI*
	[g]	[g]	[m/s]	[g]	[mm]	[g]	[mm]	[g]	[m/s]	[mm/s]	[mm]	[mm]
SC1-50%	0.048	0.050	0.028	0.075	0.40	0.075	0.40	0.099	0.30	5.8	71	17
SC1-50%-rev†	0.048	0.049	0.028	0.073	0.39	0.073	0.39	0.098	0.29	5.8	70	17
SC1-100%	0.096	0.099	0.058	0.14	0.76	0.14	0.76	0.20	0.57	24	140	35
SC1-150%	0.14	0.13	0.086	0.20	1.1	0.20	1.1	0.28	0.85	53	210	53
SC2-50%	0.077	0.087	0.057	0.12	0.62	0.12	0.64	0.14	1.3	31	150	28
SC2-100%	0.16	0.16	0.10	0.23	1.2	0.23	1.3	0.28	2.3	110	280	53
SC2-150%	0.23	0.21	0.15	0.30	1.6	0.30	1.7	0.38	3.3	230	410	76
SC2-200%	0.31	0.29	0.22	0.39	2.1	0.40	2.3	0.51	4.7	450	560	110
SC2-100%-bis*	0.16	0.15	0.11	0.21	1.1	0.22	1.4	0.26	2.3	110	270	51
SC2-200%-bis*	0.31	0.43	0.26	0.46	2.5	0.42	2.7	0.43	5.2	550	690	110
SC2-250%	0.39	0.47	0.33	0.46	2.5	0.47	2.9	0.62	7.0	980	880	140
SC2-300%	0.46	0.58	0.38	0.55	3.0	0.59	5.4	0.69	8.1	1300	1000	170
SC2-350%	0.54	0.61	0.45	0.70	3.8	1.1	17	0.93	9.5	1800	1200	200
SC2-400%	0.62	0.68	0.51	0.76	4.1	1.5	30	1.1	11	2400	1400	230
SC2-500%	0.77	1.0	0.62	0.84	4.5	1.4	35	1.3	13	3600	1700	270

Values are provided with the significance of two digits
† The input motion was applied with reversed sign
* The running simulation was repetition of previous test

6.4 Damage Evolution

After every earthquake simulation, structural and non-structural damage was surveyed in detail and cracks were accurately mapped. Figure 6.12 and Figure 6.13 show the evolution of the overall damage pattern as seen from the external side of the prototype building. Figure 6.14 illustrates the cracks appeared on the interior wall (visualised without the plaster coat). Cracks marked in red were observed at the end of the annotated test, while cracks shown in black had already been detected after previous shaking runs.

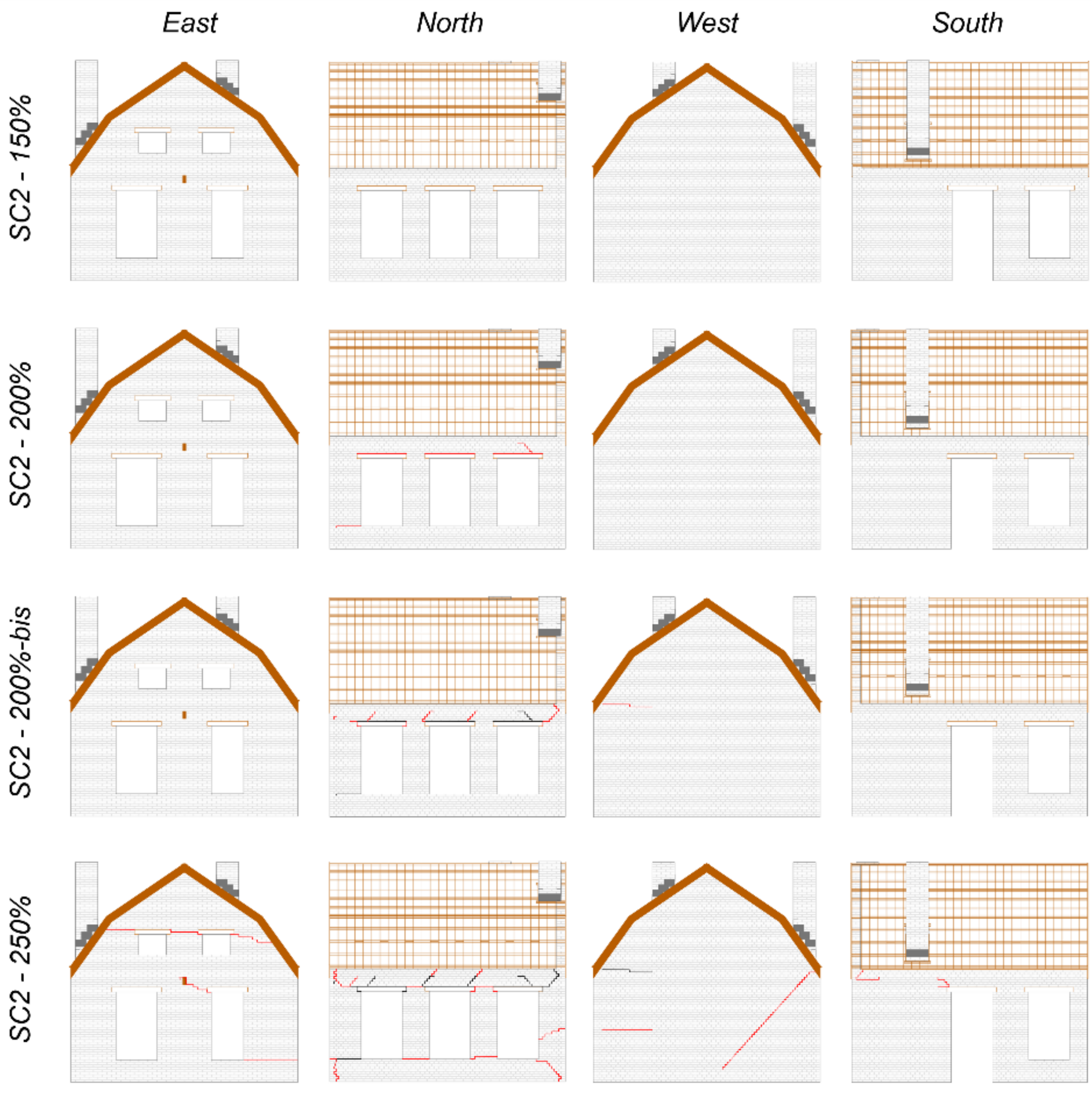

Figure 6.12 Evolution of the specimen crack pattern: tests SC2-150% to SC2-250%. Cracks marked in red were observed at the end of the annotated test run. Cracks marked in black were already detected in previous test runs.

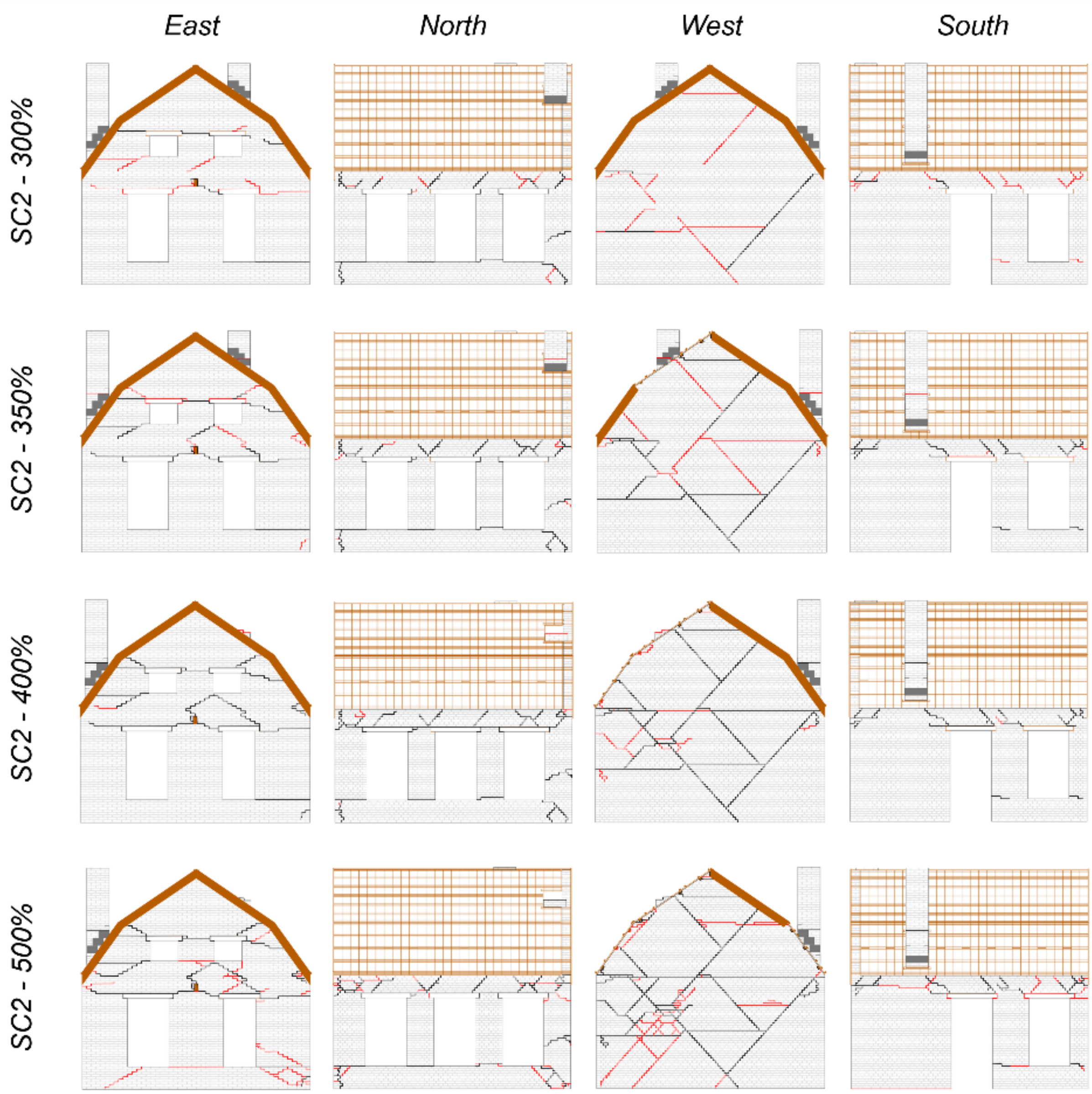

Figure 6.13 Evolution of the specimen crack pattern: tests SC2-300% to SC2-500%. Cracks marked in red were observed at the end of the annotated test run. Cracks marked in black were already detected in previous test runs.

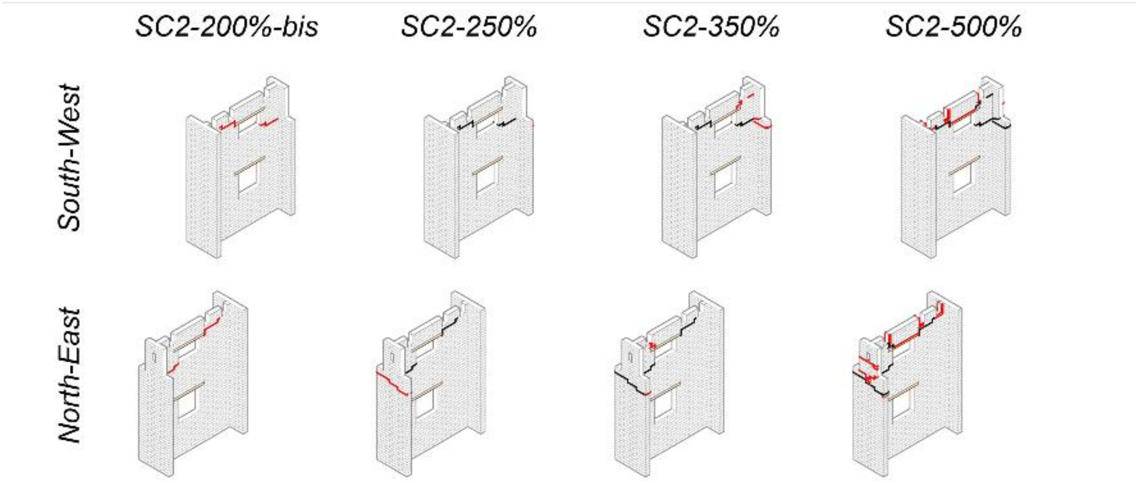

Figure 6.14 Evolution of the crack pattern of the interior wall. Cracks marked in red were observed at the end of the annotated test run. Cracks marked in black were already detected in previous test runs.

6.4.1 Damage after test SC2-150%

During testing under SC1 input motions, scaled from 50% to 150% (recorded *PGA* from 0.050 g to 0.13 g), the building did not experience any visible damage. Similarly, the SC2 signal scaled from 50% to 150% (*PGA* from 0.087 g to 0.21 g) did not induce any detectable crack.

6.4.2 Damage after test SC2-200%

Minor damage became visible on the North building façade for testing at SC2-200% (*PGA* = 0.29 g). A diagonal crack was observed above the westernmost opening, propagating from the mortar-lintel interface to one of the floor joists through a joint that had been repointed after the construction (Figure 6.15a). A horizontal hairline flexural crack was also noticed at the bottom end of the easternmost pier (Figure 6.15b).

Figure 6.15 Damage on the North wall after test SC2-200%: (a) diagonal crack above the opening; (b) flexural crack at the base of the pier.

6.4.3 Damage after test SC2-200%-bis

The damage did not evolve for testing under SC2-100%-bis (*PGA* = 0.15 g). The SC2-200%-bis test (*PGA* = 0.43 g) resulted in the opening of stair-stepped cracks in some mortar joints that had been repaired after the construction, and the formation of a few new minor cracks on the North façade, spreading from the lintels towards the top of the wall at the locations where the floor joists were inserted into the masonry (Figure 6.16a). A new hairline horizontal crack was also revealed on the West façade at the floor level, running from the North-West corner towards the interconnection with the chimney (Figure 6.16b). Cracks were additionally detected on the plaster of the interior wall, around the corners of the upper window (Figure 6.16c and d). No damage was detected on the South and East walls until this intensity level.

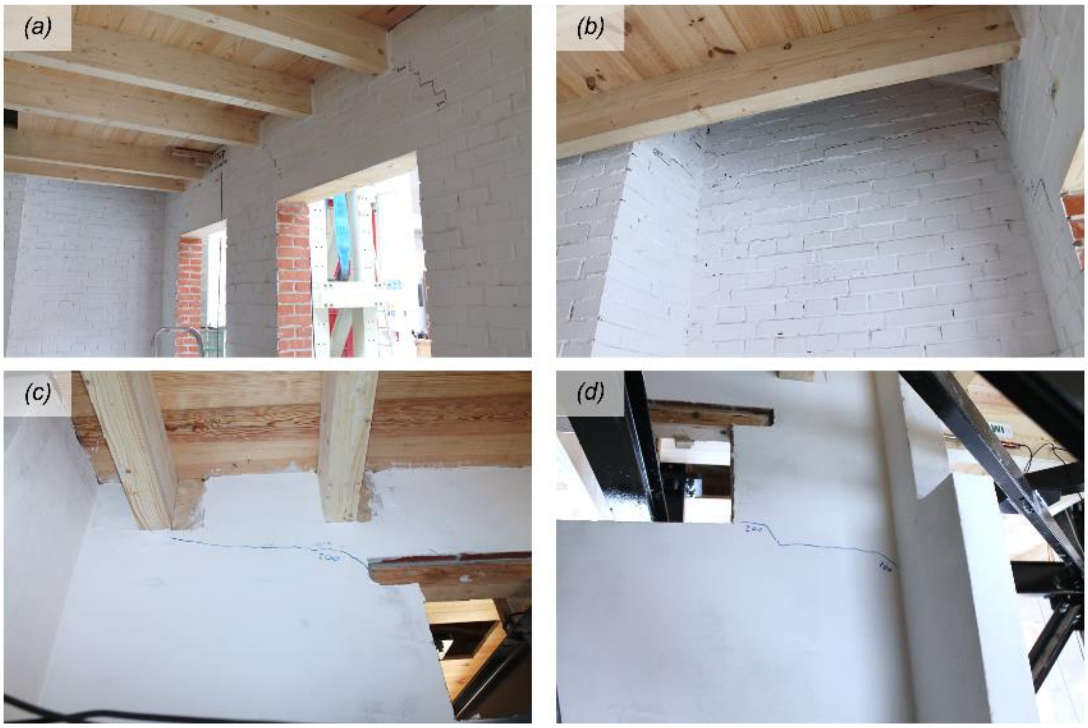

Figure 6.16 Damage after test SC2-200%-bis: (a) diagonal cracks above the openings of the North wall; (b) horizontal crack on the West façade; (c, d) cracks on the plaster of the interior wall.

6.4.4 Damage after test SC2-250%

During shaking under SC2-250% (*PGA* = 0.47 g), a global response of the structure was triggered, as evidenced by the formation of new cracks and the propagation of pre-existing ones in all building walls. In-plane mechanisms developed in all piers of the North façade, with prevailing flexural-rocking behaviour as suggested by the formation of thin horizontal cracks at their top and bottom ends (Figure 6.17). Wider cracks were found at the top of the corner piers, with permanent openings of 0.2-0.4 mm; they were extended to the transverse façades, due to the interaction between in-plane and out-of-plane responses of the intersecting walls (Figure 6.18a). Similar cracks were formed at the top of the squat pier on the South side, at the intersection with the West façade (Figure 6.18b). Characteristic examples of cracks formed due to the interaction between intersecting walls were the horizontal cracks found at the mid-height of the West wall (Figure 6.18c) and the bottom of the northernmost pier of the East façade (Figure 6.18d): they were both propagating from the wall edges, at the intersections with the corner piers of the North façade. A 45°-diagonal hairline crack appeared on the West wall that was visible only on the internal side due to the rendering (Figure 6.19a); it was compatible with incipient activation of a two-way out-of-plane bending mechanism involving the entire façade. Some damage was also noticed at the weak connections between the roof purlins and the gable wall, but the width of those cracks was very small (Figure 6.19b). On the East side, cracks were made visible just above the openings of the gable wall, extending throughout the entire length (Figure 6.20): they were associated with the onset of an out-of-plane overturning mechanism of the upper portion of the gable. On the same façade, a hairline stair-stepped crack was developed at the support of the floor girder, due to the interaction between the floor and the wall. The interior wall suffered some minor damage in one of the flanges (Figure 6.14) because of the high displacement demands from the floor diaphragm (Figure 6.21); measured permanent openings were about 0.5-0.8 mm wide. Overall, the structure had suffered only slight damage and was deemed fully operational with just minor repairs (for a thorough discussion on the seismic performance of the building prototype, the reader is referred to

Section 7). The shaking did not affect the building content other than a few books on the shelves that fell on their side.

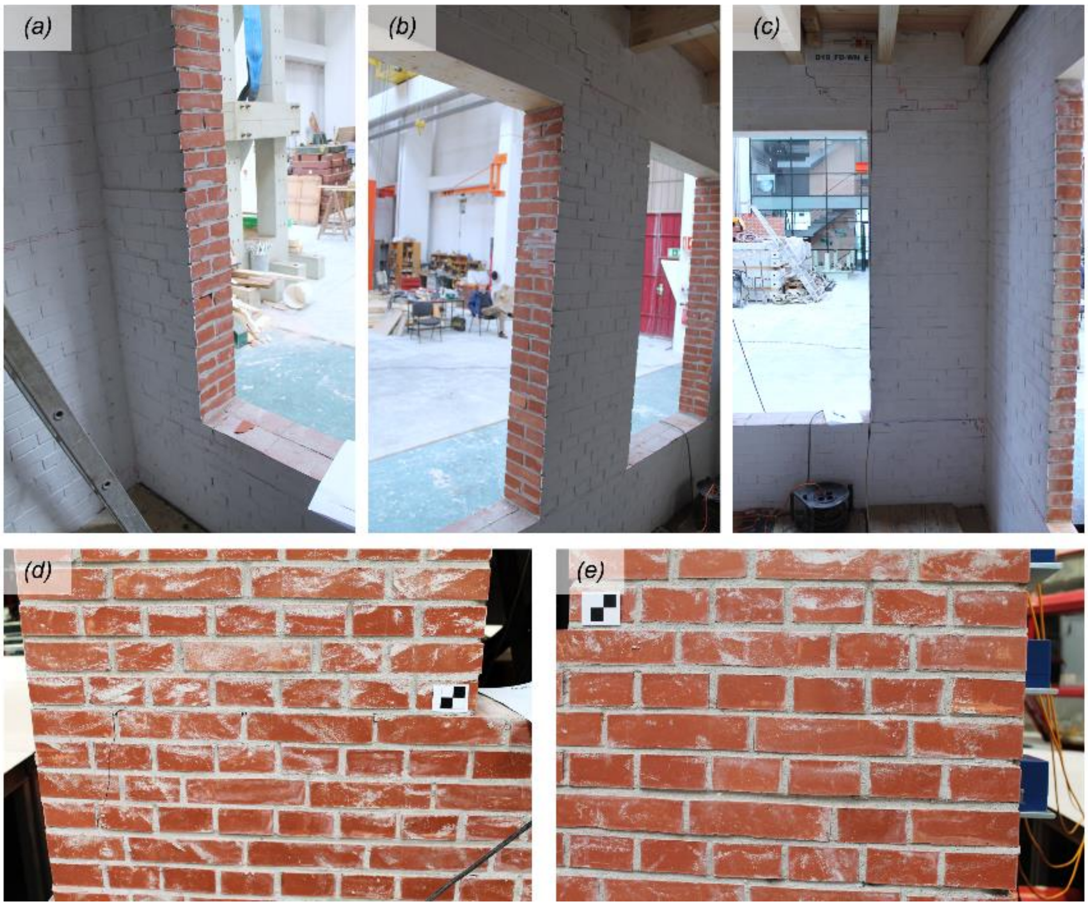

Figure 6.17 Damage on the North façade after test SC2-250%: (a, b, c) hairline flexural cracks at the top and bottom ends of all piers; (d, e) cracks at the base of the corner piers.

Figure 6.18 Damage due to interaction between in-plane and out-of-plane wall responses after test SC2-250%: (a, b) vertical cracks at the top of the longitudinal corner piers; (c) horizontal crack at mid-height of the West façade; (d) horizontal crack along the base of a pier of the East façade.

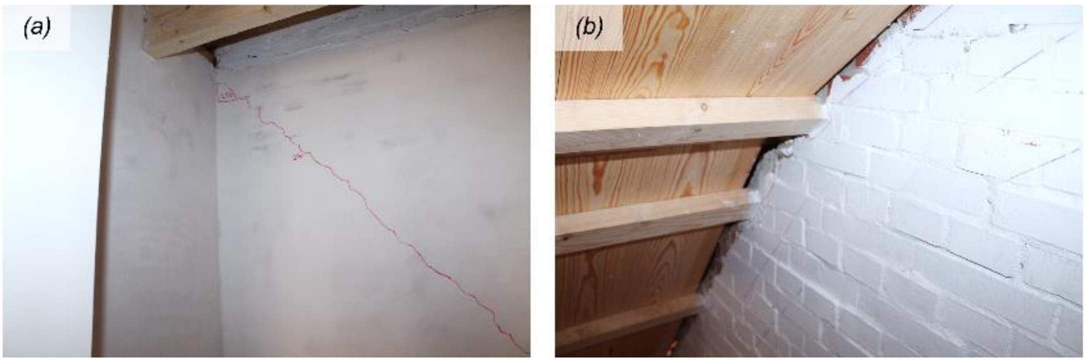

Figure 6.19 Damage on the West façade after test SC2-250%: (a) stair-stepped crack visible from the interior side; (b) damage to the connections between the roof purlins and the gable.

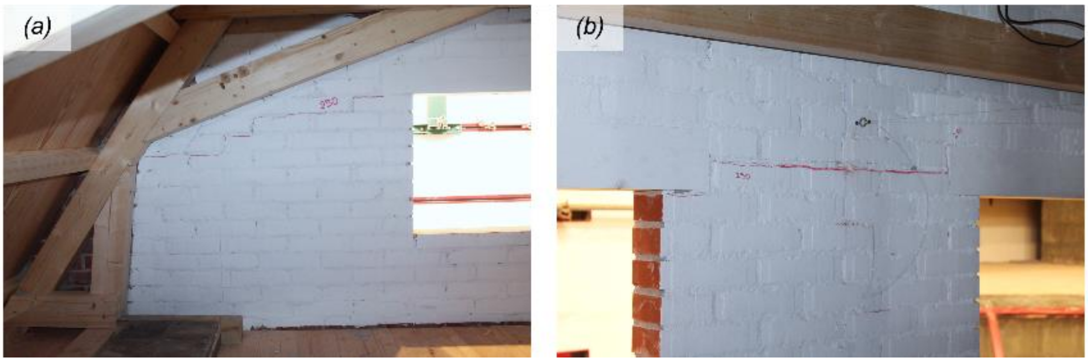

Figure 6.20 Damage on the East gable wall after test SC2-250%: (a) stair-stepped crack starting from the lintel; (b) horizontal crack between the lintels.

Figure 6.21 Damage on the interior wall after test SC2-250%.

6.4.5 Damage after test SC2-300%

For testing at 300% of motion SC2 (*PGA* = 0.58 g), new cracks were formed on both transverse, East and West façades owing to out-of-plane response. On the West side, the observed damage was mostly attributed to unequal out-of-plane displacements at the intersections with the longitudinal piers. Cracks were observed at mid-height of the first story and the chimney, and on the gable wall (Figure 6.22), but crack residual widths did not exceed 0.5 mm. On the East side, diagonal cracks were developed around the corners of the openings of the gable (Figure 6.23a and b). Horizontal cracks were also formed above the lintels of the first-storey windows and at the support of the principal floor girder, with a residual opening of 0.1 mm (Figure 6.23c and d). Participation of part of the North wall in the out-of-plane response of the East façade was manifested through the damage induced to the North-East corner piers: pre-existing stair-stepped and vertical cracks in the upper areas reached approximately 5-mm-wide openings (Figure 6.24a and b), while permanent sliding of 7 mm occurred at the lower parts (Figure 6.24c and d). The slender South piers exhibited cracks characteristic of flexural behaviour that were detectable mostly on the internal side of the wall due to the plaster (Figure 6.25a and b). Failure also occurred in the South chimney: a horizontal crack cut through the entire chimney a few centimetres below the floor diaphragm (Figure 6.25c and d), involving permanent translation of the upper part equal to 0.3 mm, with a residual crack width of 1.5 mm. The extent of damage to the interior wall did not evolve significantly in this test, but pre-existing openings reached residuals of 1.5-2.0 mm. During testing under SC2-300%, the building in overall was brought to a moderate structural damage condition, requiring extensive repairs and possible disruption of its functionality.

Figure 6.22 Damage on the West façade after test SC2-300%: (a, b) cracks at mid-height of the first storey; (c, b) cracks on the gable wall.

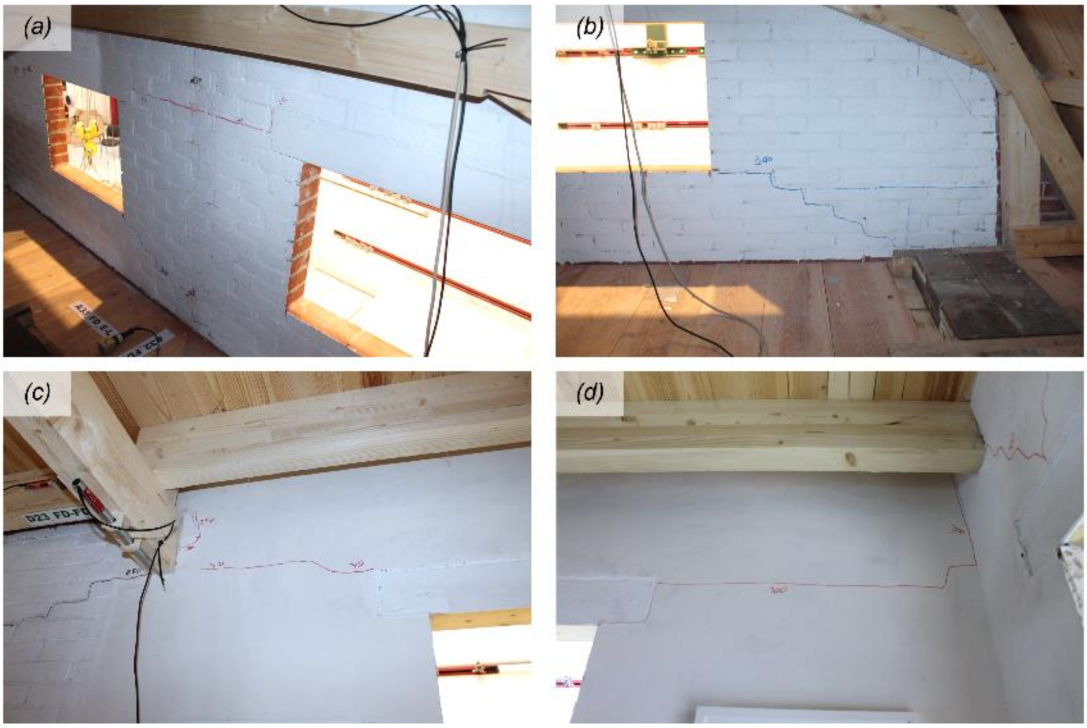

Figure 6.23 Damage on the East façade after test SC2-300%: (a, b) cracks on the gable wall; (c) cracks around the support of the floor girder; (c) horizontal cracking above the level of the windows.

Figure 6.24 Damage on the intersecting piers of North and East façades at the end of test SC2-300%.

Figure 6.25 Damage on the South building façade after test SC2-300%: (a, b) cracks at the top and bottom ends of the central pier; (c, d) flexural crack at the base of the chimney stack.

6.4.6 Damage after test SC2-350%

In the SC2-350% test (*PGA* = 0.61 g), both chimneys suffered considerable damage: horizontal cracks were developed in joints where flashing material was inserted. The West chimney exhibited a hybrid flexural/shear failure above the roofline and dislocation of the order of a few centimetres (Figure 6.26a and b). The South chimney, due to its higher slenderness, responded with excessive rocking, followed by an offset of a few millimetres at the new base point of rocking (Figure 6.26c). A 2-mm residual sliding was recorded across the plane of fracture that occurred during the SC2-300% test, and permanent openings up to 14 mm were observed on both lateral sides of the chimney due to toe-crushing failure that mostly affected the plaster cover (Figure 6.26d).

Further damage was accumulated in the transverse building façades. On the East gable wall, new cracks run from the lintels to the connections between the roof purlins and the wall (Figure 6.27a and b). Sliding of the floor girder on top of the East central pier was recorded for the first time during this test, equal to nearly 2 mm. Diffuse cracks were also observed on the West wall: a horizontal crack was developed along the base of the gable (Figure 6.27c); diagonal cracks were formed and connected with pre-existing ones in the first story and the gable (Figure 6.27d). Extensive cracking was observed from the interior at the interlocking of the chimney with the wall (Figure 6.27e and f). One of the timber boards installed on the outer face of the West gable was detached due to the differential displacements of the masonry and the roof purlins (as seen in Figure 6.26a). As discussed in Section 5.1.3, this collapse caused problems to the function of one of the accelerometers attached to the external side of the West façade (*i.e.*, A 13; Figure 3.1). Only a few new cracks appeared on the North and South façades; deformations were accommodated mainly by pre-existing cracks that resulted in residual widths of about 7-8 mm.

Figure 6.26 Damage to the chimneys during test SC2-350%: (a) failure in the West chimney at the location of flashing; (b) permanent sliding of the West at the level of the roofline; (c) fracture at mid-height of the South chimney stack; (d) residual displacement at the base of the South chimney stack.

Figure 6.27 Damage on the transverse walls after test SC2-350%: (a, b) diagonal cracks propagating from the lintels to the supports of the purlins on the East gable wall; (c, d) new horizontal and diagonal cracks in both stories of the West wall; (e, f) damage at the connection of the chimney to the West building façade.

6.4.7 Damage after test SC2-400%

When the building was subjected to the SC2 motion scaled at 400% (*PGA* = 0.68 g), the West chimney collapsed soon after the arrival of the pulse (Figure 6.28). After the shaking, widespread damage was observed throughout the building, which was deemed to have reached near-collapse conditions. An out-of-plane rigid-body mechanism involved great portion of the West façade; damage included mortar-joint sliding with a maximum residual displacement approximately 35 mm (Figure 6.29a and b). An out-of-plane mechanism fully activated also on the East façade: pre-existing stair-stepped cracks were further widened at midspan of the wall due to the floor girder, which forced the area into high displacement demands; the girder sustained permanent sliding of about 3 mm (Figure 6.30a). Sliding of the East-North intersecting piers across the pre-existing horizontal crack at their bottom, running around the corner, increased to 10 mm (Figure 6.30b). On the North side, cracks in the upper areas of the corner piers exhibited residual widths that in some cases exceeded 10 mm (Figure 6.31). No new cracks were detected on the interior wall, but residuals reached up to 8 mm.

In the interior of the building, worrisome was the motion of some objects such as the hanging photo frames, which lost contact with the walls, and the bookcase, which exhibited intense rocking response and permanent translation of several centimetres. The orientation of the bookcase was parallel to the direction of the input ground motion preventing overall overturning or books falling off the shelves.

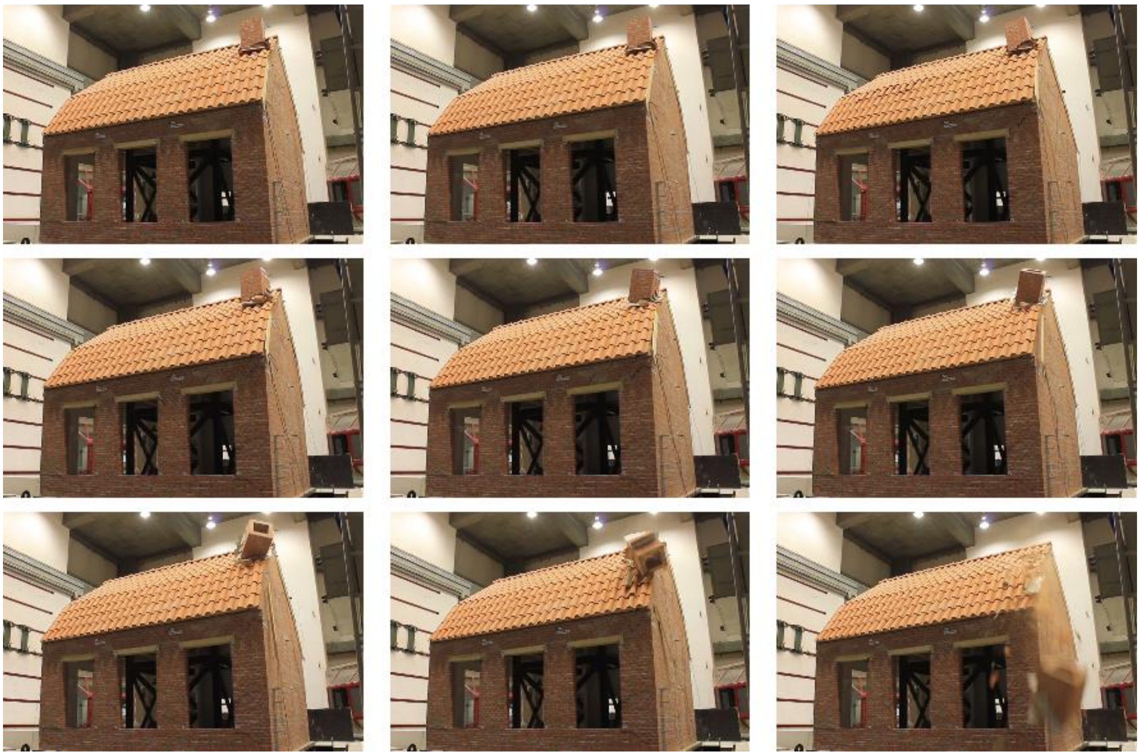

Figure 6.28 Collapse of the West chimney during testing under SC2-400%.

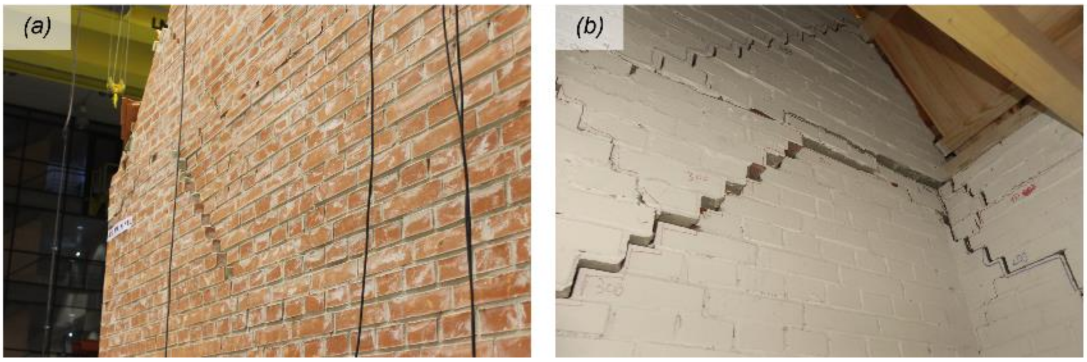

Figure 6.29 Damage on the West façade after test SC2-400%: mortar-joint sliding due to rigid-body out-of-plane mechanism.

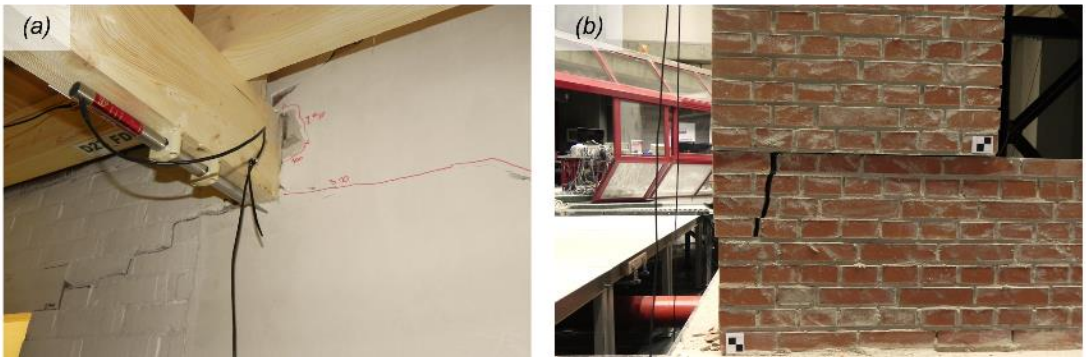

Figure 6.30 Damage on the East façade after test SC2-400%: (a) cracking around the support of the floor girder; (b) permanent sliding at the North-East corner.

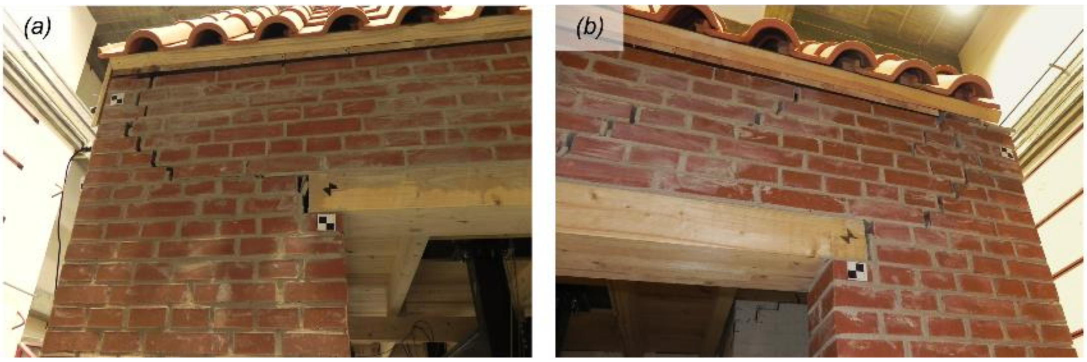

Figure 6.31 Damage on the North façade after test SC2-400%: wide permanent openings at the top of the corner piers.

6.4.8 Damage after test SC2-500%

The SC2-500% test (recorded *PGA* = 1.0 g; nominal *PGA* = 0.77g) was the final test that induced the failure of a big part of the West chimney at mid-height of the first story. Due to the collapse, debris fell in the interior of the house (Figure 6.32b). With the end of the test, the rest of the building was brought to a state where the load-bearing structure was hardly standing. All North piers exhibited pronounced rocking failure mechanism: pre-existing horizontal cracks opened at their top and bottom, reaching residual widths up to 10 mm (Figure 6.32c). The corner piers and the spandrels of the North façade displayed large permanent openings with widths in the range of 10-20 mm (Figure 6.32d and e). The North-East portion of the building was translated as a rigid body by sliding; the residual displacement reached nearly 100 mm (Figure 6.32f and g). Further permanent dislocation was also noticed at the support of the floor girder on the East wall that reached 6 mm (Figure 6.32h). In the East gable wall, new cracks were formed at the windows apron, while previous cracks at the top of the openings became wider, penetrating the entire wall thickness (Figure 6.32i).

Separation of the floorboards at midspan of the floor diaphragm occurred due to the activation of the out-of-plane mechanisms of the East and West building façades (Figure 6.32j). The developed mechanisms forced, in turn, the longitudinal walls to move towards opposite directions, causing enlargement of their in-between distance by approximately 12 mm by the end of test SC2-500%. Floor separation was monitored between two of the floor joists laying on the East side of the diaphragm by LVDT 23 (see Figure 3.2); the measurements showed that residuals started cumulating since testing under SC2-250%.

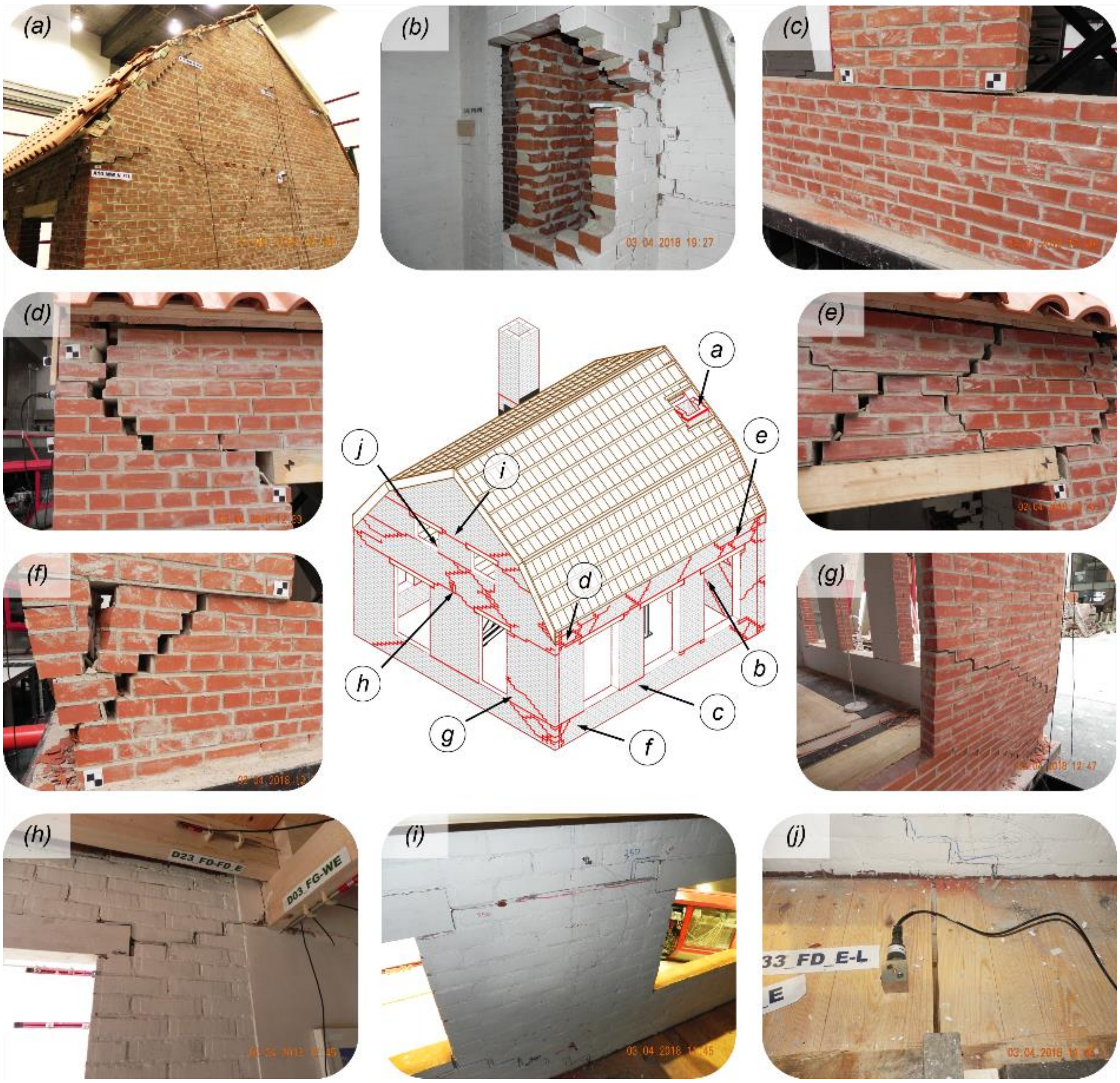

Figure 6.32 Observed damage after test SC2-500% (North-East building view): (a) collapse of chimney and timber plates of the West façade; (b) collapse of the West chimney in the interior of the building; (c) flexural crack at the base of a North pier; (d) cracks at the top of the North wall due to out-of-plane mechanism of the East façade; (e) large permanent openings on the North spandrels; (f) near-collapse state of the North-East corner piers; (g) near-collapse state of the East façade; (h) sliding of the floor girder on the supporting pier of the East façade; (i) horizontal cracks on the East gable due to out-of-plane overturning mechanism; (j) separation of floorboards at midspan of the floor.

Visible cracking formed on the squat South pier only at this final stage of the test (Figure 6.33a). Sliding at the foundation beam-wall interface was monitored by LVDT 1 (see Figure 3.2): peak sliding reached 0.6 mm during test SC2-500%, and permanent opening of about 0.4 mm was noticed all along the wall base. However, residual sliding was first recorded during test SC3-300% (0.2 mm), and then in test SC2-350% (0.35 mm), but cracks were not detectable. The rest of the façade suffered limited cracking, mostly developed around the lintels, while wide cracks were only seen in the upper portions of the corners, which followed the large displacements of the transverse building façades (Figure 6.33b). Damage was seen at two locations in the chimney of the South façade: below the level of the floor and at the level of flashing (Figure 6.33c and d). Large residual deformations due to mortar-joint sliding and brick de-cohesion were observed on the entire West building façade (Figure 6.33e and f). The wall was heavily damaged, on the verge of experiencing partial or total collapse. Severely damaged also ended up the interior wall that reached peak displacements approximately 55 mm and suffered large deformations with residuals of about 30 mm at the top due to dislocation of the floor joists (Figure 6.33g). No sliding or significant differential displacements were noticed across the interfaces between wall plates and longitudinal walls. Damage was not evident neither at the nailed connections between the timber elements of the roof trusses or the connections between the trusses and the wall plates. Some damage was only seen at the change of inclination in the roof sheathing due to excessive deflection of the upper part of the roof structure (Figure 6.33h).

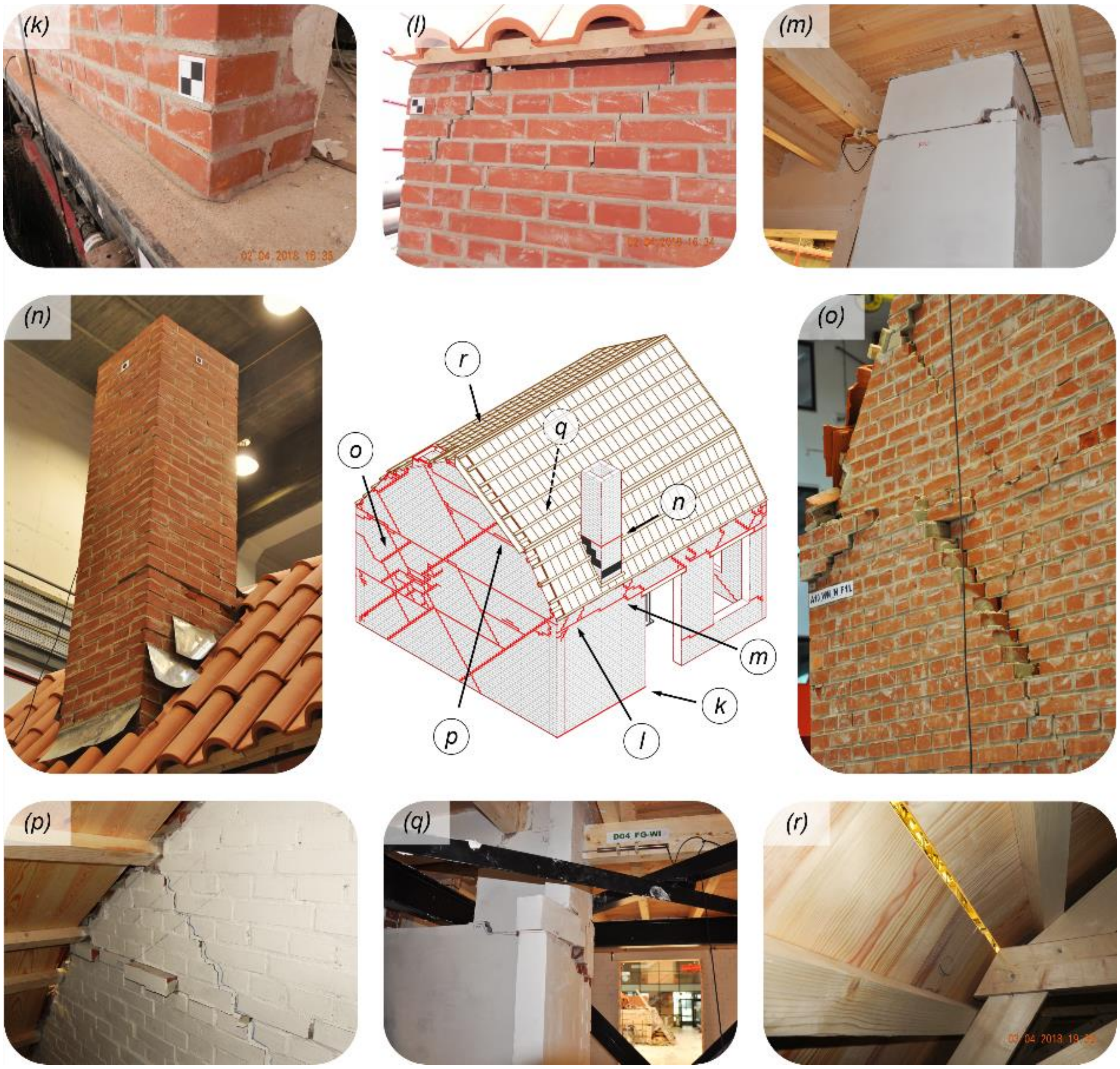

Figure 6.33 Observed damage after test SC2-500% (South-West building view): (a) crack due to sliding at the base of the squat South pier; (b) cracks at the top of the South wall due to out-of-plane mechanism of the West façade; (c) horizontal crack at the base of the South chimney stack; (d) cracking of the South chimney above the roofline; (e) mortar-joint sliding on the West façade; (f) brick de-cohesion on the West gable; (g) damage with residual deformations in the interior wall; (h) damage to the timber sheathing at the change of inclination of the roof.

6.5 Deformed Shapes

Figure 6.34 and Figure 6.35 depict the effects of the activated damage mechanisms on the deformed shapes of the prototype building at different stages of the dynamic test. The annotated displacements refer to measurements on the floor diaphragm with respect to the steel reference frame at the instant of maximum in-plane shear deformation of the diaphragm. Displacements were monitored at four locations: $\Delta_{1,N}$ and $\Delta_{1,S}$ were recorded on the lower plates, running parallel to the longitudinal, North and South walls, at about 30 cm from them (see Figure 3.4); $\Delta_{1,E}$ and $\Delta_{1,W}$ were measured at midspan of the diaphragm, near the East and West edges of the floor (see Figure 13). Due to the discontinuity of the floor joists and the presence of the interior wall, the diaphragm exhibited non-uniform deformation along its spanning direction. Therefore, shear deformations, $\gamma_{f,N}$ and $\gamma_{f,S}$, were defined individually for the North and South parts of the diaphragm, respectively. In absolute values:

$$\gamma_{f,N} = \left| \frac{\Delta_{1,N} - \dfrac{\Delta_{1,E} + \Delta_{1,W}}{2}}{l_{0,N}} \right| \quad \text{and} \quad \gamma_{f,S} = \left| \frac{\Delta_{1,S} - \dfrac{\Delta_{1,E} + \Delta_{1,W}}{2}}{l_{0,S}} \right| \tag{13}$$

where $l_{0,N}$ = $l_{0,S}$ = 2.21 m is the distance of the lower plates from the floor midspan. The peak diaphragm shear deformation, $\gamma_{f,max}$, was taken as the maximum between the distortions of the North and South parts:

$$\gamma_{f,\max} = \max\left\{\gamma_{f,N}, \gamma_{f,S}\right\} \tag{14}$$

The North side, consisting of slender piers with rocking behaviour, exhibited larger displacements than the South façade, which included a stiffer and stronger squat pier. Displacements recorded at midspan of the floor were limited by the restraining effect of the interior wall and increased only at final stages of the test when the wall suffered extensive damage. Consequently, the floor diaphragm underwent significant shear deformation, initially concentrated mainly in the North span. For instance, for testing under SC2-300%, at the instant of peak shear deformation of the floor diaphragm, the North span was distorted by $\gamma_{f,N}$ = $\gamma_{f,max}$ = 1.0%, about 3.5 times more than the South span that underwent $\gamma_{f,S}$ = 0.29%. The deformation became uniform along the full span in the last test runs, following the opening of new cracks in the interior wall and the South façade. The peak diaphragm shear deformation reached 1.7% during test SC2-500% when the maximum differential displacement between the interior wall and the South wall was about 39 mm. As a result of the high in-plane flexibility of the floor diaphragm, the building did not exhibit overall torsional response.

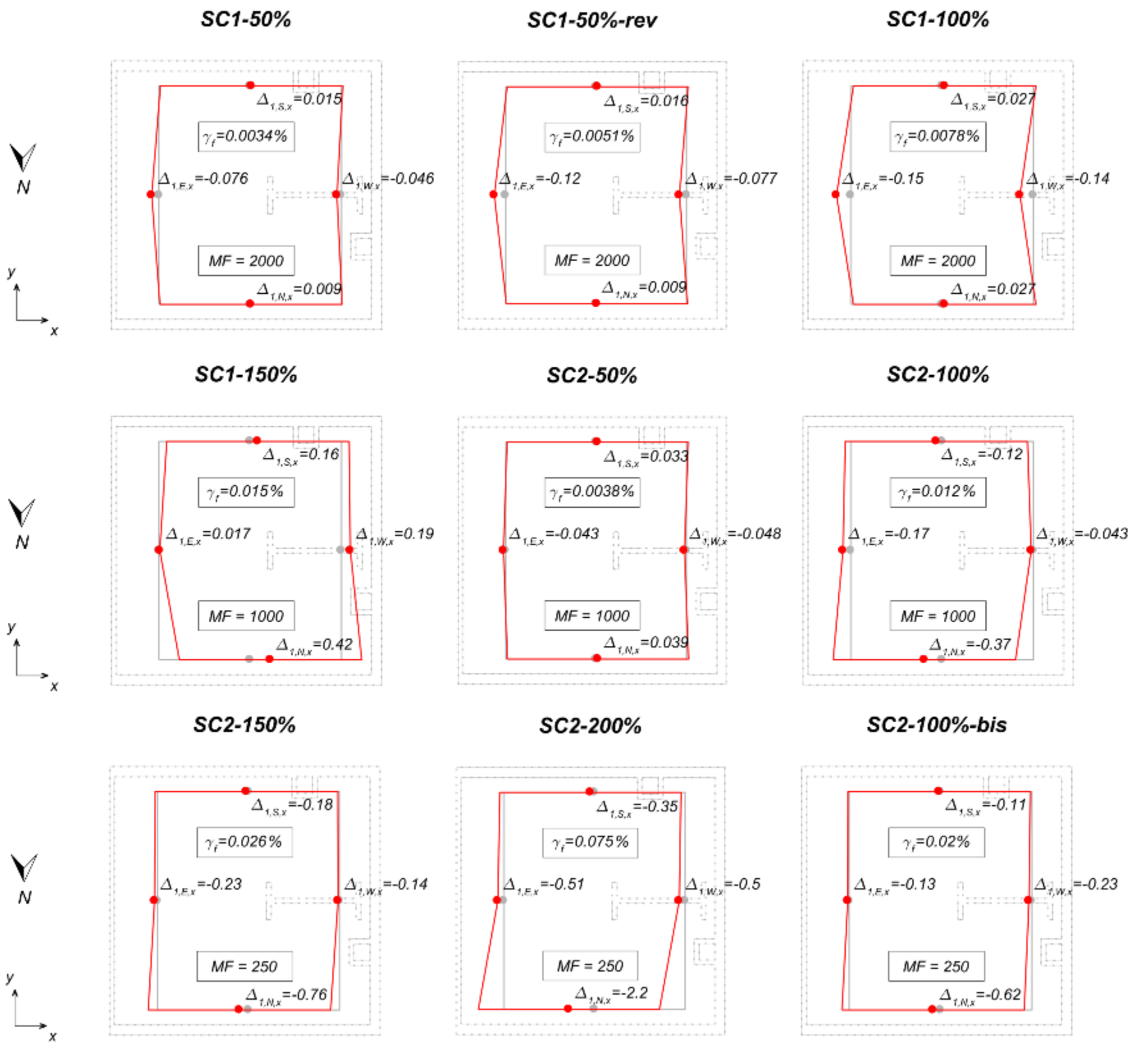

Figure 6.34 Deformed shapes of the floor at the instants of maximum diaphragm shear deformations: test runs SC1-50% to SC2-100%-bis. MF is the displacement magnification factor on the figure. Units of mm unless otherwise specified.

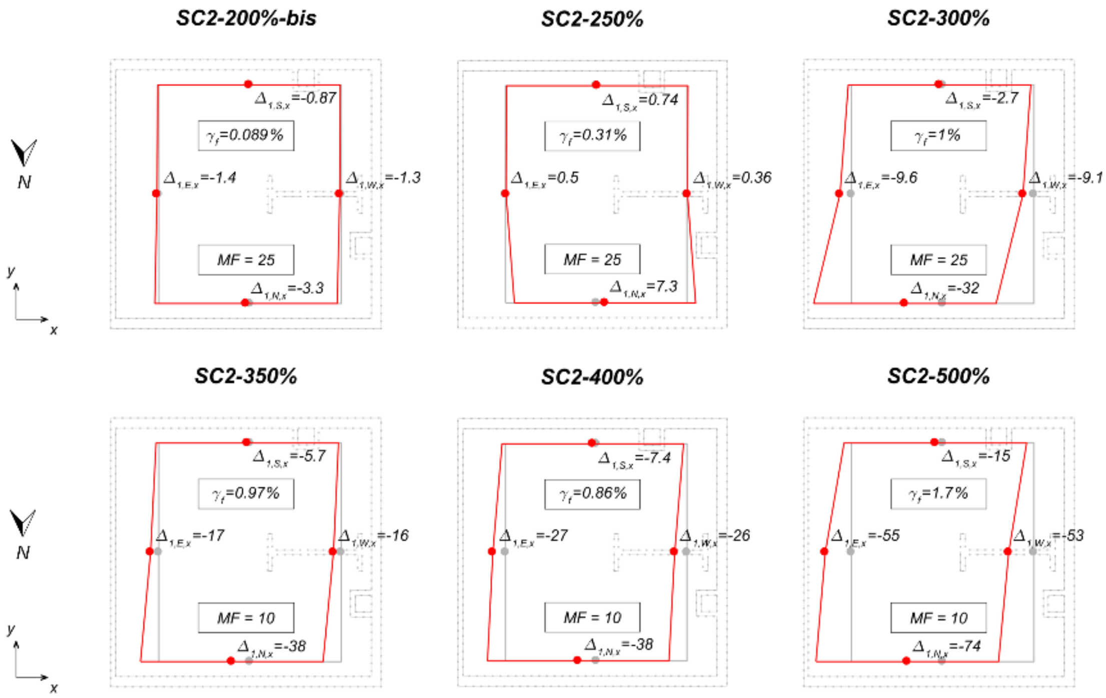

Figure 6.35 Deformed shapes of the floor at the instants of maximum diaphragm shear deformations: test runs SC2-200%-bis to SC2-500%. MF is the displacement magnification factor on the figure. Units of mm unless otherwise specified.

Figure 6.36 and Figure 6.37 show displacement profiles at midspan of the East and West façades at the instants of maximum ridge displacements. Displacements were measured on the internal side of the walls. The deflected shapes show initial inter-story deformation concentrations between the first floor and the roof ridge, in a response that was mostly dominated by the out-of-plane deflection of the gables-roof system. During test SC2-300%, over the height of the East façade, the roof-drift ratio reached nearly 3.0%, about 5.5 times the first-story drift ratio, which was 0.55%. Apparently, the presence of the floor girder proved crucial in mitigating the out-of-plane deflections of the East wall. The effect can be easily appreciated given the almost 3-time higher displacements observed during the same test at the floor level of the West façade, which was unrestrained in overturning. At the final shaking test, the structure exhibited similar inter-story drift demands in the two stories, 4.4% and 4.2% for the roof and the first story, respectively.

Figure 6.36 and Figure 6.37 also depict the deflected shapes of the two chimneys at the same instants (projected on the vertical plane of the roof ridge). The West chimney was initially deflected together with the West building façade to which it was attached; significant differential displacements were recorded only after the SC2-300% test. On the South side, the chimney was initially translated almost as rigid with the squat South pier. Significant deflections were noticed during test SC2-300% when the first flexural crack opened at the location where the chimney penetrated the floor, and the free-standing part began rocking over a height of about 2.8 m.

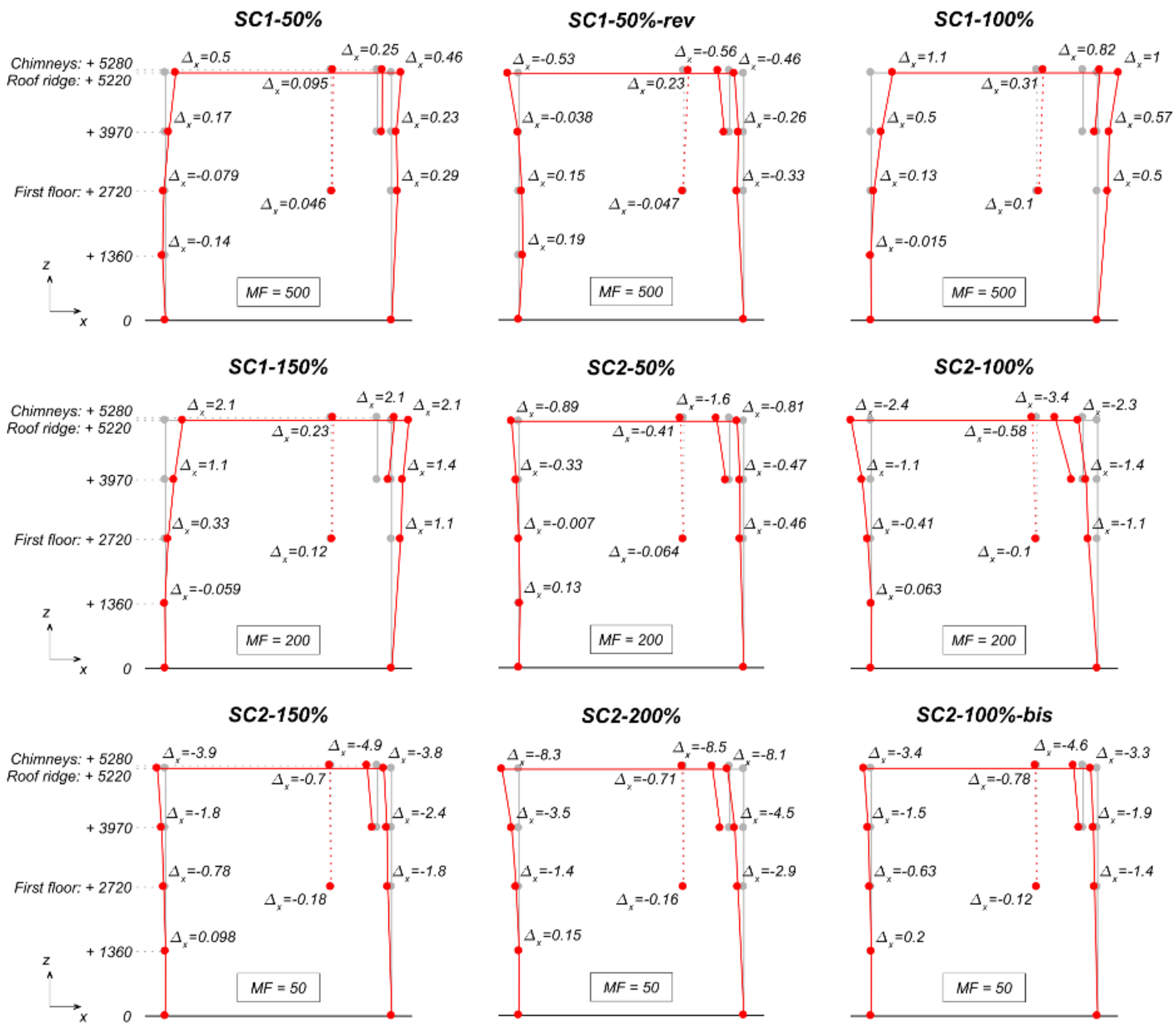

Figure 6.36 Displacement profiles at midspan of the transverse walls, at the instants of maximum roof ridge displacements: test runs SC1-50% to SC2-100%-bis. MF is the displacement magnification factor on the figure. Units of mm.

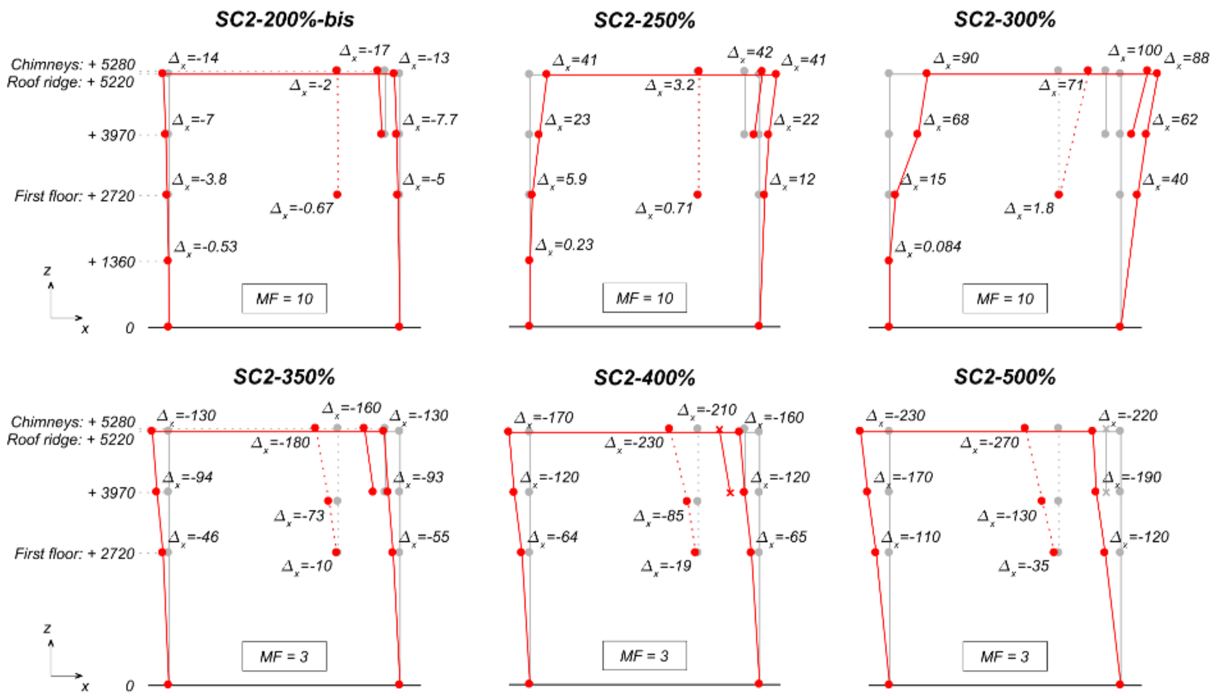

Figure 6.37 Displacement profiles at midspan of the transverse walls, at the instants of maximum roof ridge displacements: test runs SC2-200%-bis to SC2-500%. MF is the displacement magnification factor on the figure. Units of mm.

6.6 Hysteretic Response

Due to the different geometries of the longitudinal, North and South walls, combined with the flexibility of the floor and roof diaphragms, the hysteretic response of the building specimen is provided considering three separate subsystems, namely, North wall, South wall, and gables-roof assembly, in addition to the overall building response. Figure 6.38 to Figure 6.42 depict the hysteretic response in terms of normalised base shear versus inter-story drift ratio for all test runs. Westward displacements and forces are positive.

Inter-story drift ratios $\theta_{1,N}$ and $\theta_{1,S}$ are defined individually for the North and South walls, respectively, as:

$$\theta_{1,N} = \frac{\Delta_{1,N}}{h_1} \quad \text{and} \quad \theta_{1,S} = \frac{\Delta_{1,S}}{h_1} \tag{15}$$

where h_1 = 2720 mm is the first-floor height above the foundation, while $\Delta_{1,N}$, and $\Delta_{1,S}$ are the displacements measured on the North and South sides of the floor diaphragm with respect to the foundation. In particular, the displacements were measured on the lower plates found near the top of the two longitudinal walls. No damage was observed at the connections of the floor joists to the walls; therefore, the displacements at the top of the longitudinal walls were reasonably assumed equal to those recorded on the lower plates of the floor.

The average first-floor drift ratio, $\theta_{1,AVG}$, was taken as the mean between all normalised displacements recorded on the diaphragm. The average includes, in addition to the drifts defined in Eq. (15), the drift ratios $\theta_{1,E}$ and $\theta_{1,W}$ coming of the measurements acquired at midspan of the diaphragm, on the East and West sides, $\Delta_{1,E}$, and $\Delta_{1,W}$, so that:

$$\theta_{1,AVG} = \frac{\theta_{1,N} + \theta_{1,S} + \theta_{1,E} + \theta_{1,W}}{4} \tag{16}$$

The base-shear coefficient, *BSC*, is defined as the base-shear force, V_b, normalised by the weight of the mass that contributes to the same force. Shear forces were computed as the sum of the products of each accelerometer measurement times the tributary mass, lumped at the instrument location. Considering the overall building and its North and South subsystems, these coefficients can be expressed as:

$$BSC_{TOT} = \frac{V_{b,TOT}}{g \cdot m_{TOT}} = \frac{\sum a_i \cdot m_i}{g \cdot m_{TOT}} \tag{17}$$

$$BSC_N = \frac{V_{b,N}}{g \cdot m_N} = \frac{\sum a_{i,N} \cdot m_{i,N}}{g \cdot m_N} \tag{18}$$

$$BSC_S = \frac{V_{b,S}}{g \cdot m_S} = \frac{\sum a_{i,S} \cdot m_{i,S}}{g \cdot m_S} \tag{19}$$

where a_i represents the acceleration recorded by accelerometer *i*, and m_i is the tributary mass associated with the instrument. Subscripts *TOT*, *N* and *S* identify quantities related to the overall structure or its subsystems. The mass distribution illustrated in Table 2.1 was used to determine the total masses: $m_{TOT} = \sum m_i = 30.3$ t, $m_N = \sum m_{i,N} = 14.7$ t, and $m_S = \sum m_{i,S} = 15.6$ t. For the calculation of the subsystem shear forces, half of the inertia of transverse walls, interior wall, floor, and the roof was allocated to each of them, in agreement with what was done for specimen EUC-BUILD-2 (Kallioras *et al.*, 2018).

The base-shear forces determined with Eq. (17) to (19) include the inertia of the lower half of the first-story walls, which accelerate together with the shake table. This mass is about 8.4 t and represents 28% of the total for the prototype building. When using equivalent frames or other simplified numerical models of lumped-mass systems, the mass of lower half of the first-story walls is often assumed concentrated at the base and is supposed to move with the ground, without contributing to the seismic response of the structure. Therefore, base-shear coefficients BSC^0 can be determined excluding the contribution of the lower parts of the masonry walls:

$$BSC^0_{TOT} = \frac{V^0_{b,TOT}}{g \cdot m^0_{TOT}} = \frac{\sum a_i \cdot m^0_i}{g \cdot m^0_{TOT}} \tag{20}$$

$$BSC^0_N = \frac{V^0_{b,N}}{g \cdot m^0_N} = \frac{\sum a_{i,N} \cdot m^0_{i,N}}{g \cdot m^0_N} \tag{21}$$

$$BSC^0_S = \frac{V^0_{b,S}}{g \cdot m^0_S} = \frac{\sum a_{i,S} \cdot m^0_{i,S}}{g \cdot m^0_S} \tag{22}$$

where m^0_i is the tributary mass associated with each instrument excluding the portions accelerated with the table, $m^0_{TOT} = \sum m^0_i = 21.9$ t, $m^0_N = \sum m^0_{i,N} = 10.6$ t, and $m^0_S = \sum m^0_{i,S} = 11.3$ t.

The response of the gables-roof assembly is presented in terms of roof-story drift ratio, θ_R, and roof-shear coefficient, *RSC*. The roof-story drift ratio is defined as the ratio of the relative displacement between the ridge and the first floor, to the ridge height above the floor, $h_R = 2500$ mm:

$$\theta_R = \frac{\Delta_R - \Delta_{1,AVG}}{h_R} \quad (23)$$

where Δ_R and $\Delta_{1,AVG}$ represent the roof-ridge and average first-floor displacements with respect to the foundation. Two definitions were adopted for the *RSC*, as for the base shear. In one case, *RSC* is taken as the ratio between the story shear at the roof base (F_R) and the weight of the mass above the first floor that contributes to that force. Following the second approach, only the lateral inertia of the masses located above half the roof-story height (F^0_R) and the corresponding weights were considered to calculate RSC^0. In symbols:

$$RSC = \frac{F_R}{g \cdot m_R} = \frac{\sum a_{i,R} \cdot m_{i,R}}{g \cdot m_R} \quad (24)$$

$$RSC^0 = \frac{F_R^0}{g \cdot m_R^0} = \frac{\sum a_{i,R} \cdot m_{i,R}^0}{g \cdot m_R^0} \quad (25)$$

where a_i and $m_{i,R}$ are the acceleration time-series and the tributary mass of accelerometer *i*, mounted on the gables-roof assembly, $m_R = \sum m_{i,R}$ = 8.2 t (see Table 2.1), and $m^0_R = \sum m^0_{i,R}$ = 3.2 t. The inertia forces developed by the part of the South chimney extending above the floor were not accounted in the calculation of F_R and F^0_R (and in turn, of *RSC* and RSC^0), due to its independent response from the rest of the roof structure. Consequently, the corresponding mass of that portion of the chimney is excluded from the sums m_R and m^0_R, as well.

Inelastic response was initially observed in the North subsystem during the SC2-200% test (*PGA* = 0.29 g), associated with the formation of hairline flexural cracks in the slender longitudinal piers; the wall inter-storey drift demand was $\theta_{1,N}$ = 0.08% for attained base-shear coefficient, BSC_N = 0.32. In the following tests, the system exhibited an increasingly nonlinear hysteretic response, due to its hybrid rocking-sliding behaviour, that culminated in remarkable strength and stiffness degradation at final stages, due to the concentration of damage. The response of the South subsystem remained elastic up to test SC2-250% (*PGA* = 0.47 g) when light damage appeared for the first time at the top of the slender piers of the South façade and at its intersections with the transverse walls. The shaking forced the subsystem into drifts up to $\theta_{1,S}$ = 0.1%, with a BSC_S of 0.44. This part of the structure demonstrated mostly narrow hysteresis loops that became wider only during the application of motion SC2-500% (*PGA* = 1.0 g) when peak inter-storey drift demands reached $\theta_{1,S}$ = 0.65%, and residuals increased to 0.18%.

The hysteretic response of the specimen during the last three earthquake simulations, SC2-350% to SC2-500%, is repeated in Figure 6.43. Overall, the maximum attained base-shear coefficients were $BSC_{TOT,max}$ = 0.59 and $BSC^0_{TOT,max}$ = 0.57, while the maximum recorded average first-floor drift ratio was $\theta_{1,AVG,max}$ = 1.9%, observed for shaking at SC2-500%. Ultimately, the prototype building was found at a very heavily damaged condition. This is readily perceived when looking at the force-displacement relationship of Figure 6.43d for the final shaking test: the response lays on the second quadrant, where maximum displacements and average accelerations occurred with the same sign, as the masonry walls were extensively cracked and masses oscillated asynchronously. The noticeable asymmetry in the response of the specimen is mainly attributed to the almost single-sided pulse of the applied input signal SC2.

Figure 6.38 to Figure 6.43 show only the *BSC-θ* and *RSC-θ* (or, V_b-*θ* and F_R-*θ*) dynamic relationships obtained with the first definition of the normalised shear forces. The shape of the hysteretic responses is significantly affected by the spatial distribution in the amplitude of the acting inertia forces that was more pronounced when the structure experienced extensive damage, and the masses along the building height were mobilised with a phase difference. This effect is illustrated through the comparison of the backbone curves obtained with both definitions in Figure 6.44; therein, the force-displacement relationships are plotted considering responses in the negative direction of motion only (*i.e.*, towards East).

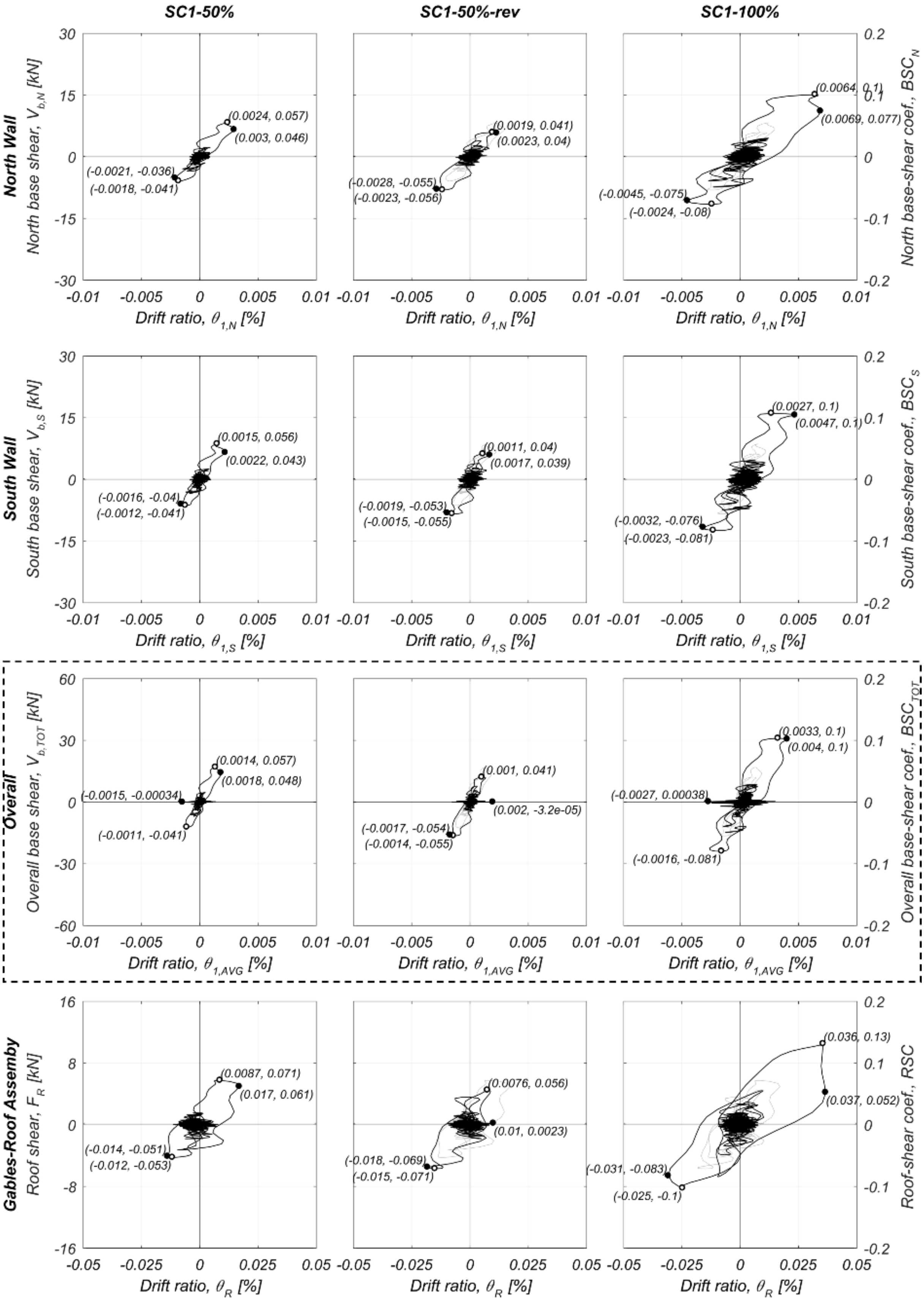

Figure 6.38 Specimen hysteretic responses: test runs SC1-50%, SC1-50%-rev and SC1-100%.

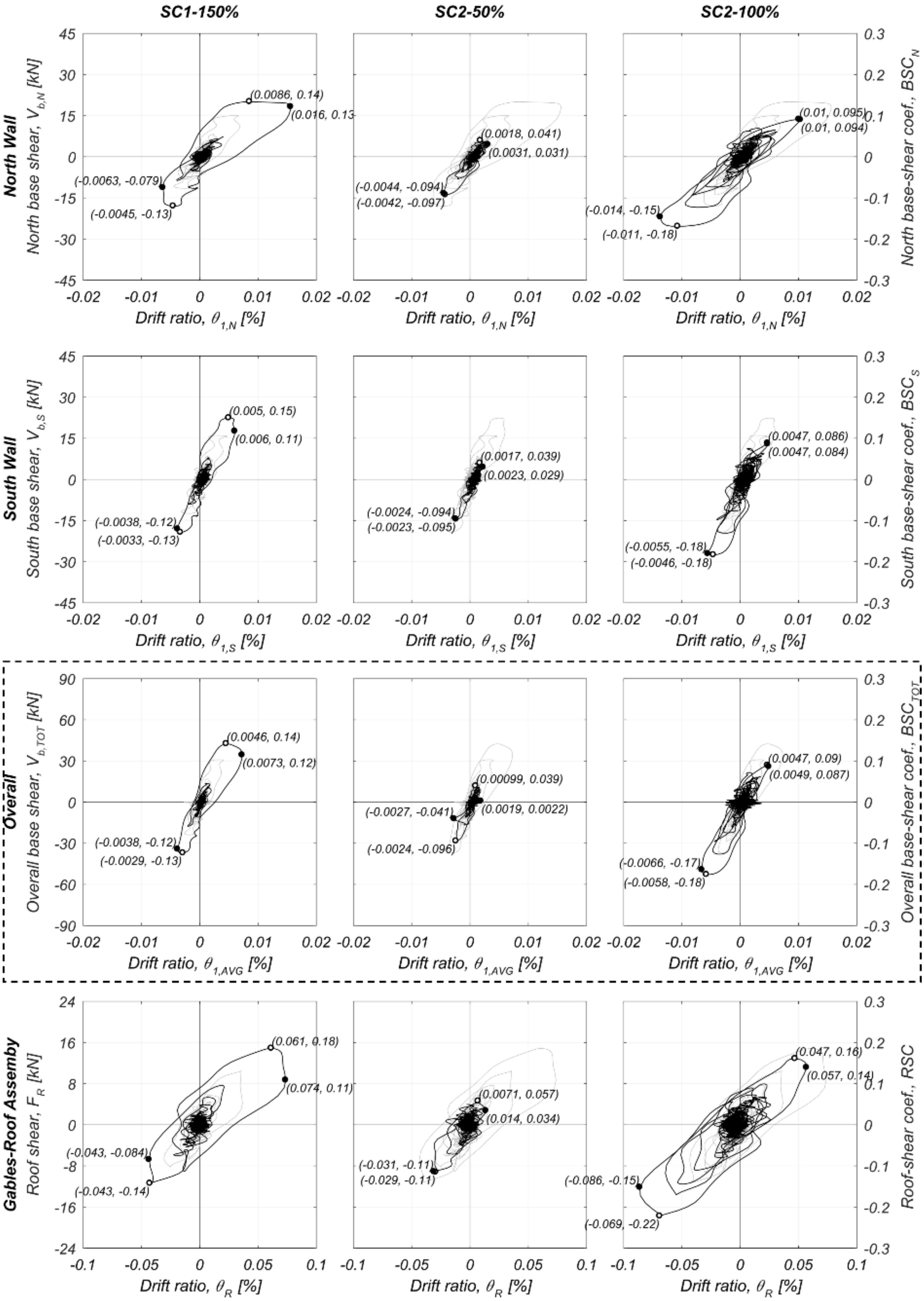

Figure 6.39 Specimen hysteretic responses: test runs SC1-150%, SC2-50% and SC2-100%.

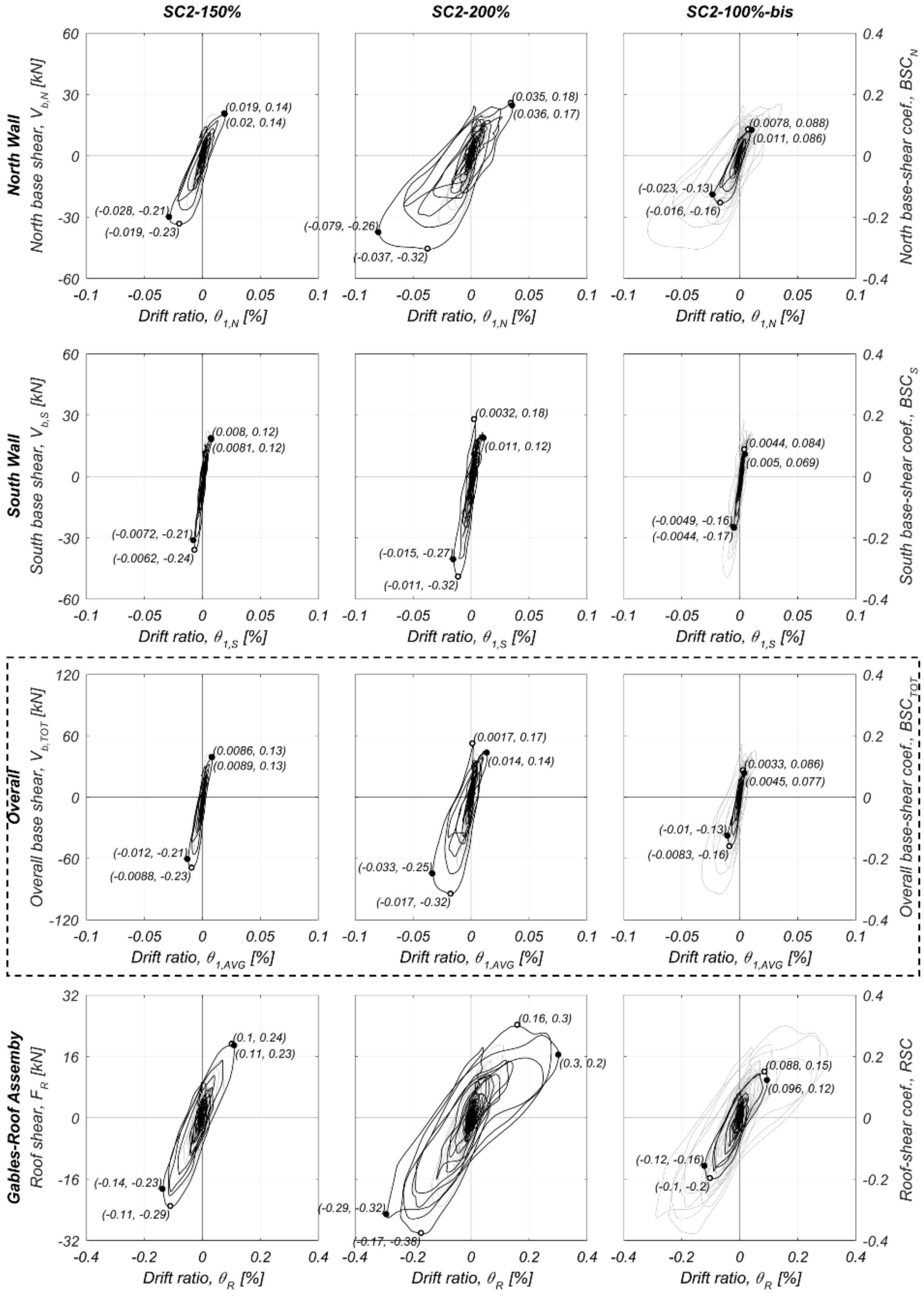

Figure 6.40 Specimen hysteretic responses: test runs SC2-150%, SC2-200% and SC2-100%-bis.

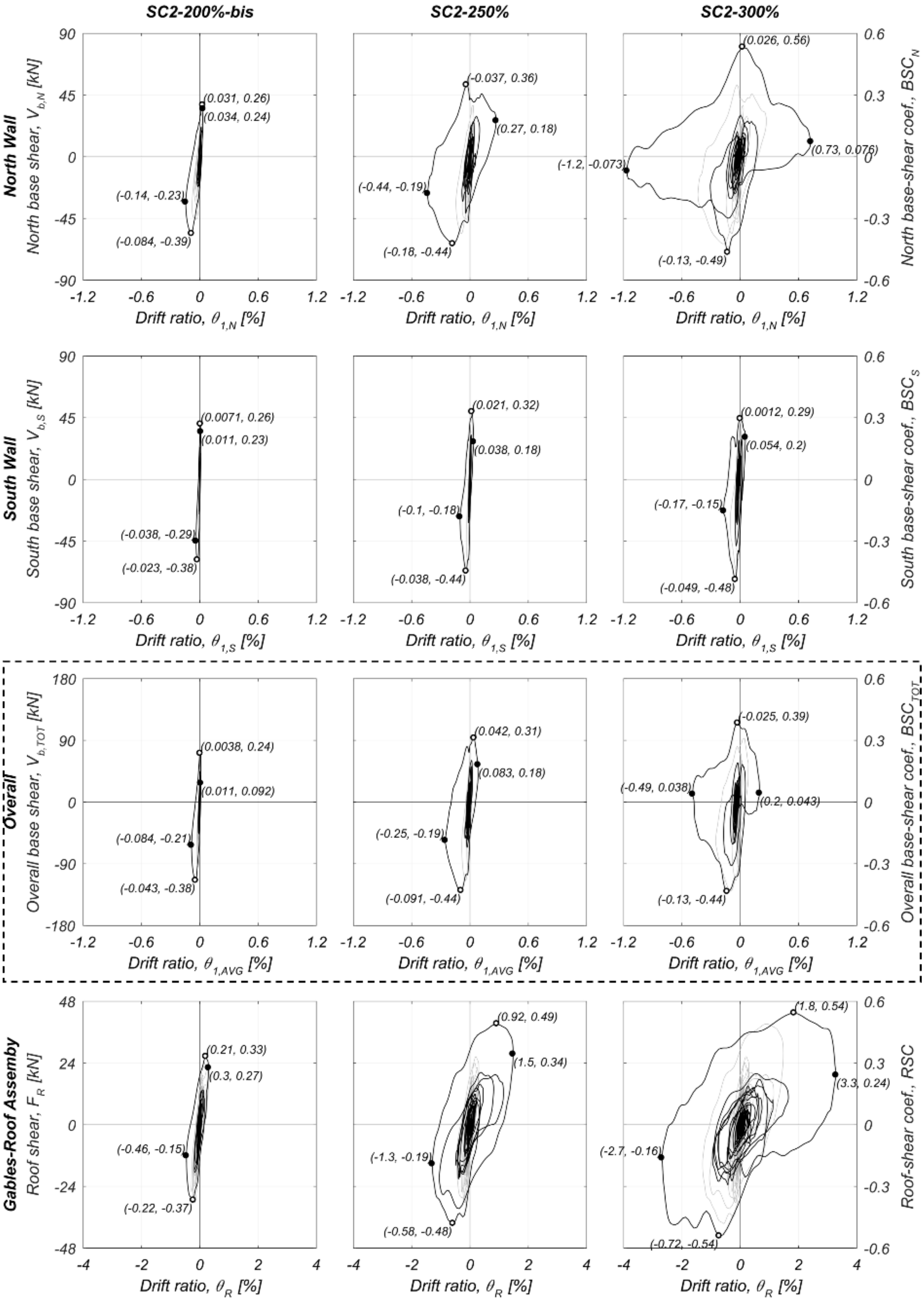

Figure 6.41 Specimen hysteretic responses: test runs SC2-200%-bis, SC2-250% and SC2-300%.

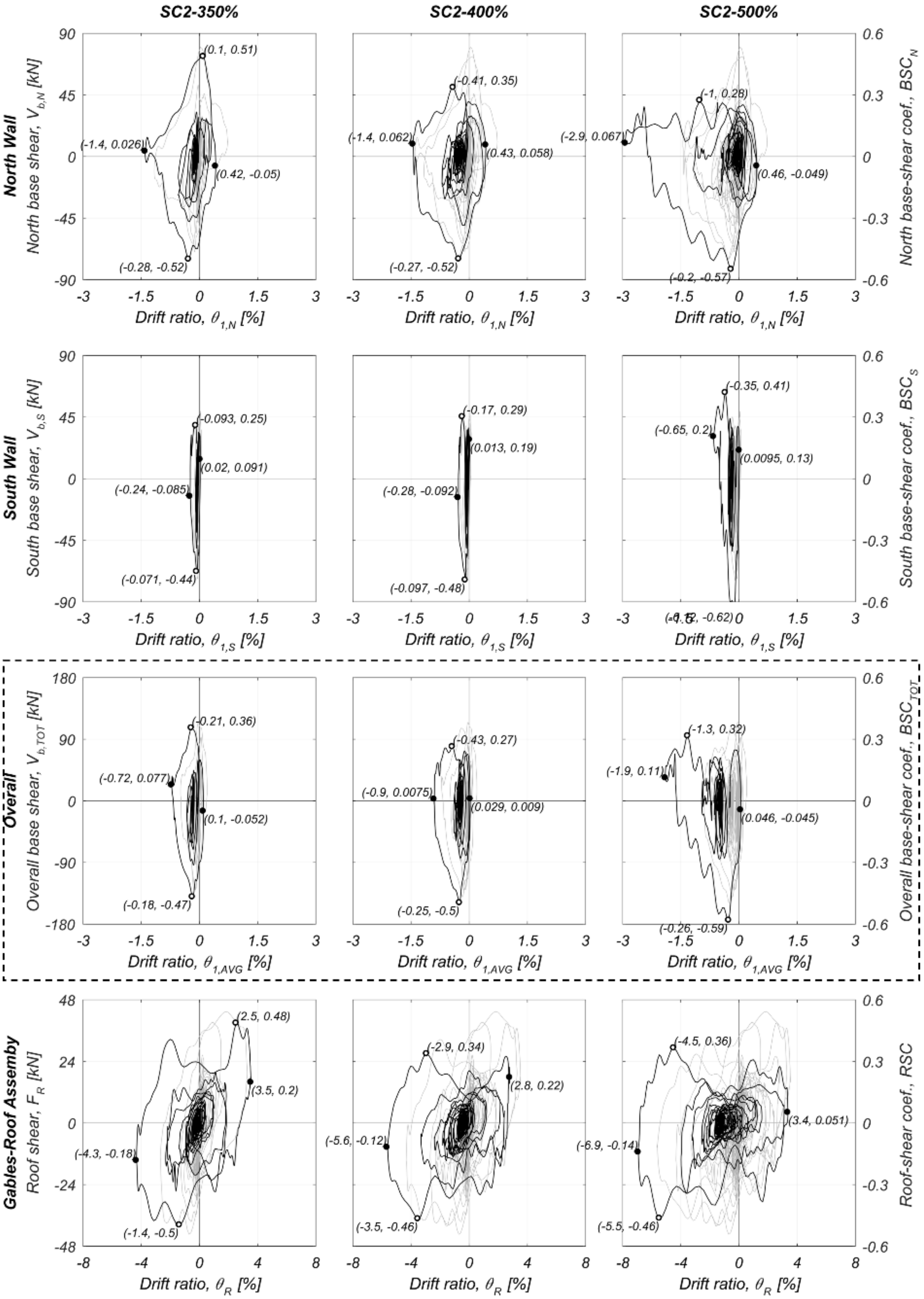

Figure 6.42 Specimen hysteretic responses: test runs SC2-350%, SC2-400% and SC2-500%.

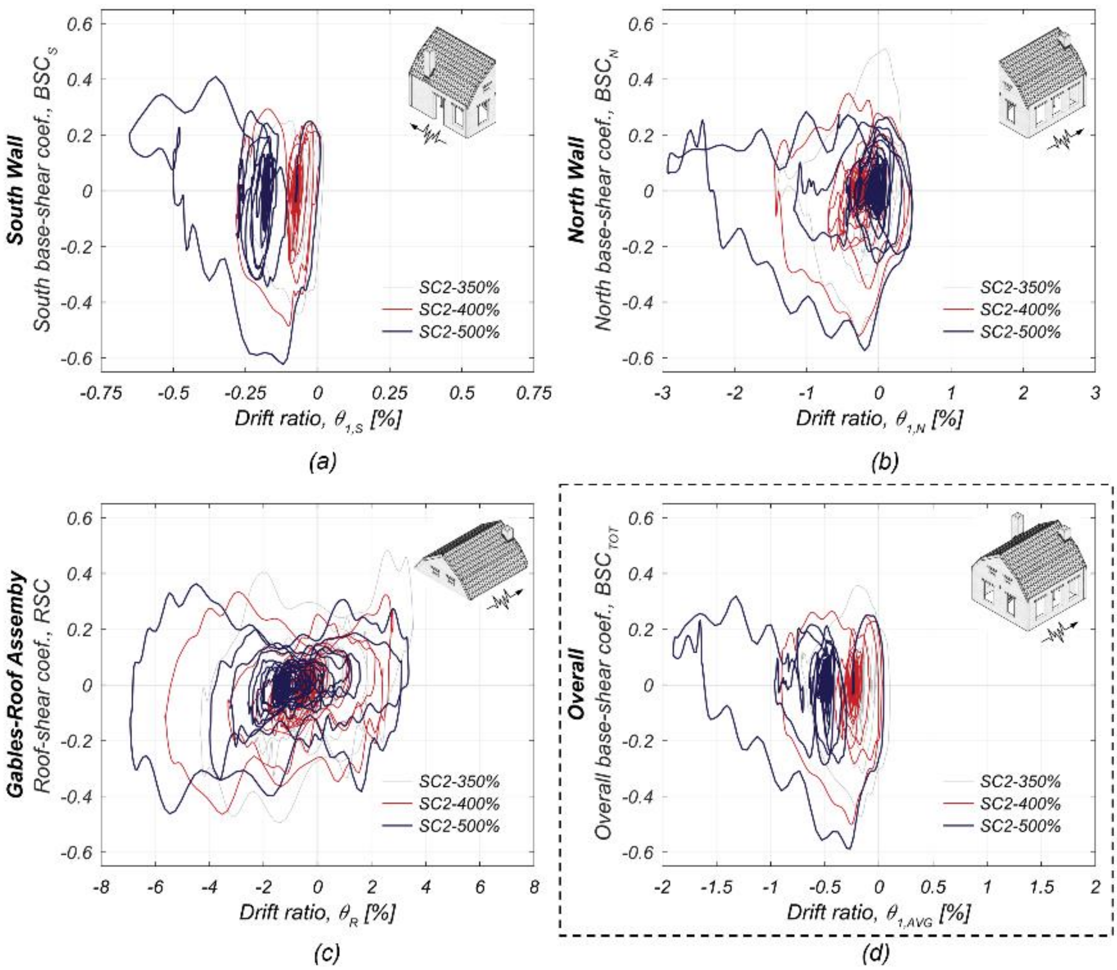

Figure 6.43 Specimen hysteretic responses during the last three earthquake simulations: (a) South subsystem; (b) North subsystem; (c) gables-roof subsystem; (d) Overall structure.

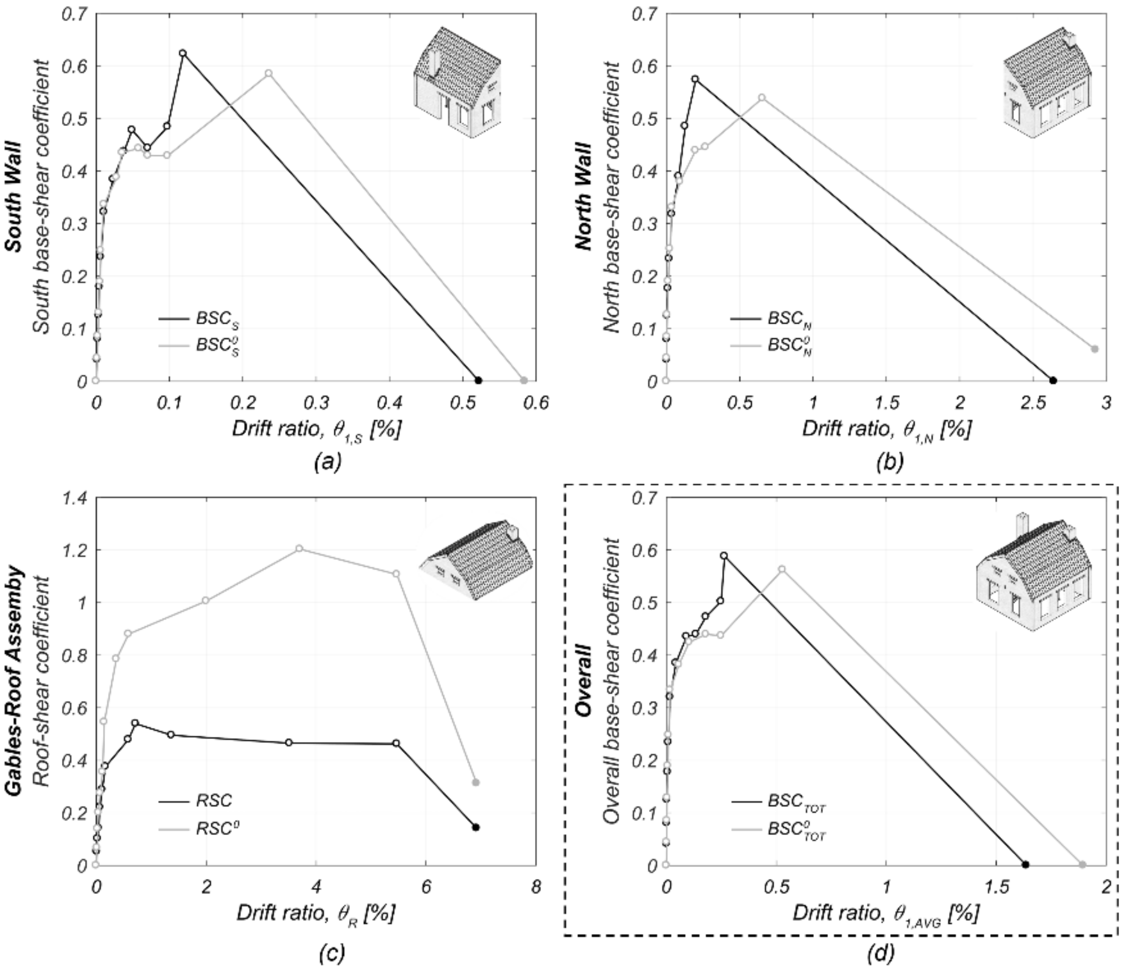

Figure 6.44 Specimen backbone curves: (a) South subsystem; (b) North subsystem; (c) gables-roof subsystem; (d) Overall structure.

6.7 Performance of Chimneys

The two chimneys exhibited disparate dynamic performance and ultimate failure mechanism, due to their different geometry and location in the prototype building.

On the West building side, the displacement profile of the chimney was coupled with that of the façade, while there was no discernible difference between accelerations recorded at the top of the chimney and the roof ridge up to test SC2-250% (Figure 6.45a and b). It was only under motion SC2-300% when responses first started to deviate, and the chimney exhibited higher accelerations mainly due to the formation of a horizontal crack at the top part of the gable, which forced accelerations to level off. During test SC2-350% (*PGA* = 0.61 g), fracture of the chimney occurred at the roofline, followed by permanent sliding across a joint where the bond was weaker due to the flashing. The brittle failure caused acceleration amplification of the order of 6.5-7. Shaking at SC2-400% (*PGA* = 0.68 g) resulted in the collapse of the chimney stack that rolled down the North pitch of the roof without causing substantial damage but fragmenting of some tiles (Figure 6.45c). Accelerations continued increasing at mid-height of the first story, leading to further damage to the chimney and partial collapse in the interior of the building during test SC2-500% (*PGA* = 1.0 g).

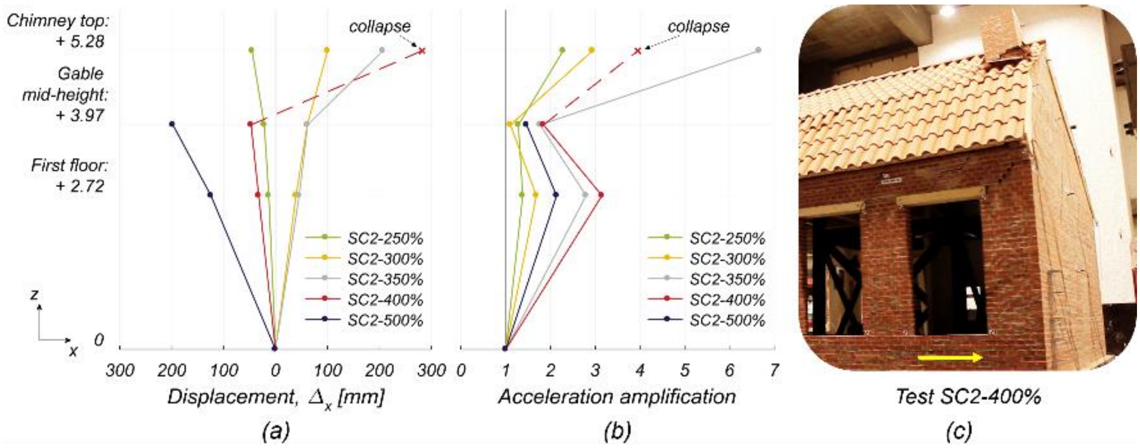

Figure 6.45 Dynamic response of the West chimney: (a) deflected shape at the instant of peak displacement at the top; (b) acceleration amplification profile; (c) snapshot at the instant of collapse for shaking at SC2-400%.

On the South side, the chimney was initially translated almost as rigid together with the squat pier, with which was interlocked (Figure 6.46a). Significant deflections that reached 77 mm at the top were noticed for the first time during test SC2-300% (*PGA* = 0.58 g): a flexural crack formed about the level where the chimney penetrated the floor (~ 2.52 m) and the stack began rocking over a height of 2.8 m. During test SC2-350% (*PGA* = 0.61 g), the crack migrated several centimetres above the roofline, following a possible collision between the chimney stack and the roof sheathing. Horizontal cracking took place at a joint around the mid-height of the free-standing part, where flashing material was inserted (~ 3.78 m), and consequently, the bond was liable to fail. The upper portion of the chimney stack was separated from the lower one and initiated an independent rocking response around a new pivot axis. At the top, the lateral displacement rocketed to a peak of about 210 mm, while the recorded accelerations were remarkably amplified (Figure 6.46b) due to the impact occurring either between the lower block and the top of the squat pier or between the two rocking blocks. In the following tests, the chimney stack demonstrated pure rocking oscillations as a two-rigid-block system, with quasi-stable displacement amplitude that reached a maximum of nearly 290 mm (Figure 6.46c).

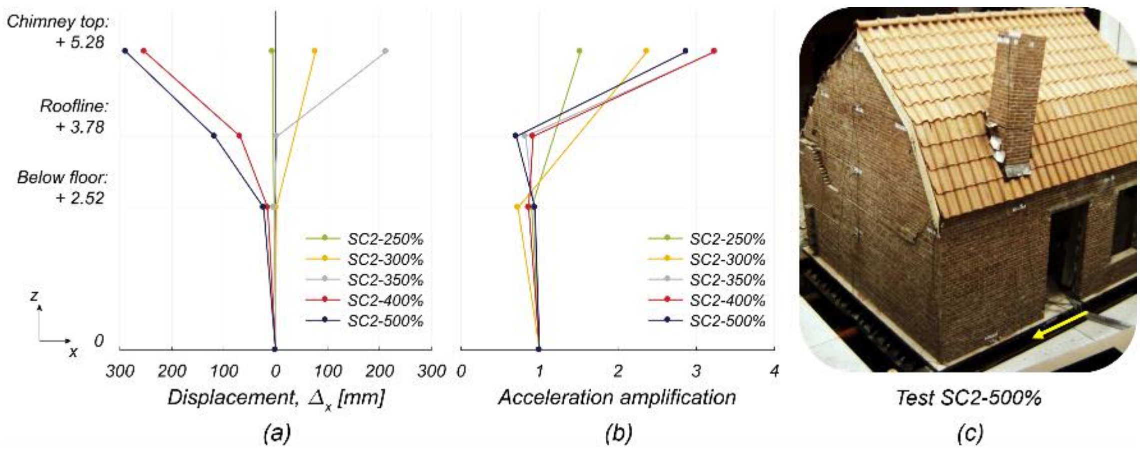

Figure 6.46 Dynamic response of the South chimney: (a) deflected shape at the instant of peak displacement at the top; (b) acceleration amplification profile; (c) snapshot at the instant of peak top displacement during test SC2-500%.

Figure 6.47 illustrates the dynamic hysteretic response of the South chimney in terms of acceleration versus displacement for the last five tests, SC2-250% to SC2-500%. The two plots distinguish between the rocking response of the entire free-standing stack and the short upper portion resulting after cracking at mid-height. Further superimposed onto the plots are analytical predictions of the initial linear-elastic branch (solid line) and ultimate strength (solid dot), as well as the post-cracking residual strength from rigid-body rocking (dashed line). Displacements are treated in a normalised form, $\delta_{C,S}$ and $\delta^{'}_{C,S}$, defined as:

$$\delta_{C,S} = \frac{\Delta_{t,C,S} - \Delta_{1,C,S}}{b_w} \quad \text{and} \quad \delta^{'}_{C,S} = \frac{\Delta_{t,C,S} - \Delta_{m,C,S}}{b_w} \tag{26}$$

where $\Delta_{t,C,S}$, $\Delta_{1,C,S}$ and $\Delta_{m,C,S}$ are the lateral displacements at the top and at the two base points of rocking (*i.e.*, at the floor and mid-height level, respectively), while b_w = 540 mm is the outer width of the rectangular box section of the chimney. Quantities $a_{C,S}$ and $a^{'}_{C,S}$ are referring to the centre of mass of the two rocking systems. Accelerations were considered to vary linearly along the height of the two blocks, so that:

$$a_{C,S} = \frac{a_{1,C,S} + a_{t,C,S}}{2} \quad \text{and} \quad a^{'}_{C,S} = \frac{a_{m,C,S} + a_{t,C,S}}{2} \tag{27}$$

where $a_{t,C,S}$, $a_{1,C,S}$ and $a_{m,C,S}$ represent the acceleration response-histories at the top, the base and mid-height of the chimney.

As shown by the *a-δ* relationships of Figure 6.47a, the response of the as-yet uncracked chimney stack (green line) was linear up to $\delta_{C,S}$ = 0.005 (~ 2.8 mm relative displacement), reached during test SC2-250%. The first cracking occurred at the base of the 2.8-m-high stack for accelerations at the centre of mass equal to 0.44 g (empty dot) in the test that followed. In theory, the acceleration required to induce flexural cracking at the base of the slender stack is approximately $a_{C,S,u}$ = 0.72 g, calculated assuming flexural bond strength equal to 0.36 MPa (taken from Table 8.1 of Section 8). This estimate is about 65% higher than the actual acceleration capacity; the difference is presumably attributed to the fact that cracks appear in the weakest joints where the strength can be significantly lower than the average bond strength. Once fully cracked, the chimney underwent rocking-type response that was triggered for lower acceleration, approximately 0.36 g, significantly higher than the theoretical acceleration to initiate rocking, $a_{C,S,ro}$ = 0.2 g (estimated considering pure rigid-body rocking motion).

The theoretical acceleration to cause cracking above the roofline was $a^{'}_{C,S,u}$ = 1.8 g (accounting for a reduced bond area due to the flashing), a value which is multiple times higher than the recorded accelerations. This seems to confirm the hypothesis that the new fracture occurred because of impact between the roof and the chimney rather than exceedance of the latter's flexural capacity. The predicted capacity envelope, shown in Figure 6.47b by the dashed line, was defined by the points of maximum attainable acceleration, $a^{'}_{C,S,ro}$ = 0.36 g, and displacement, $\delta^{'}_{C,S,ro}$ = 1 (for $\Delta_{t,C,S}$ - $\Delta_{m,C,S}$ = b_w), after considering simple rigid-body stability mechanics for the upper portion of the chimney. Based on the analytical calculations, it was rather obvious that even during the final shaking run, the chimney stack was far from reaching overturning instability.

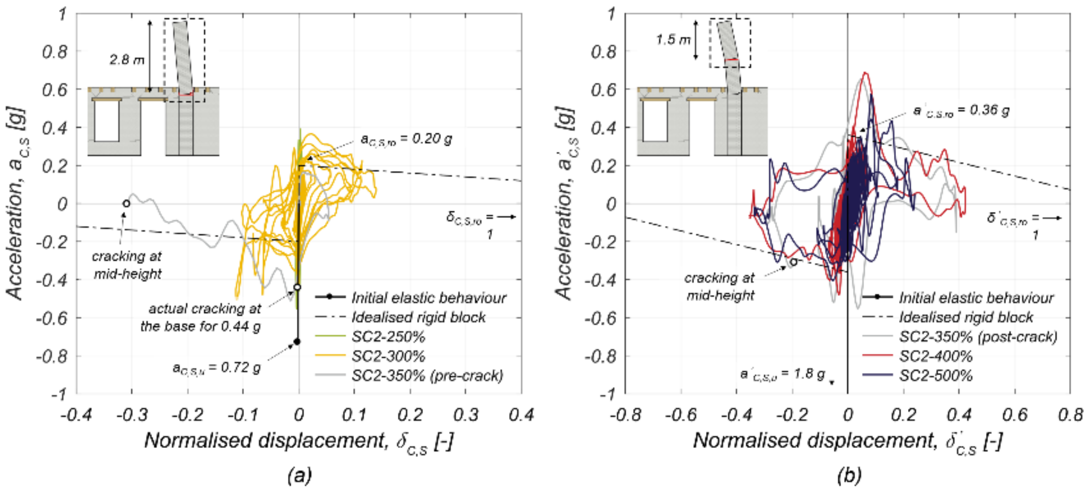

Figure 6.47 Hysteretic response of the South building chimney: (a) rocking over the entire height of the chimney stack; (b) rocking of the upper portion of the chimney after the fracture above the roofline.

7 BUILDING SEISMIC PERFORMANCE

This section proposes the qualitative definition of damage states (DS) for the clay-URM building specimen, with reference to the post-earthquake damage observations from the shake-table experiment. Thresholds between the damage states, termed damage limits (DL), are subsequently identified and related to quantitative engineering demand parameters.

7.1 Identification of Damage Limits

Five damage states were considered in accordance with the EMS-98 damage classification (Grünthal, 1998): DS0-DS1, no structural or non-structural damage; DS2, minor structural damage (or moderate non-structural damage); DS3, moderate structural damage (or heavy non-structural damage); DS4, heavy structural damage (or very heavy non-structural damage); and DS5, very heavy structural damage with partial or total collapse (Figure 7.1).

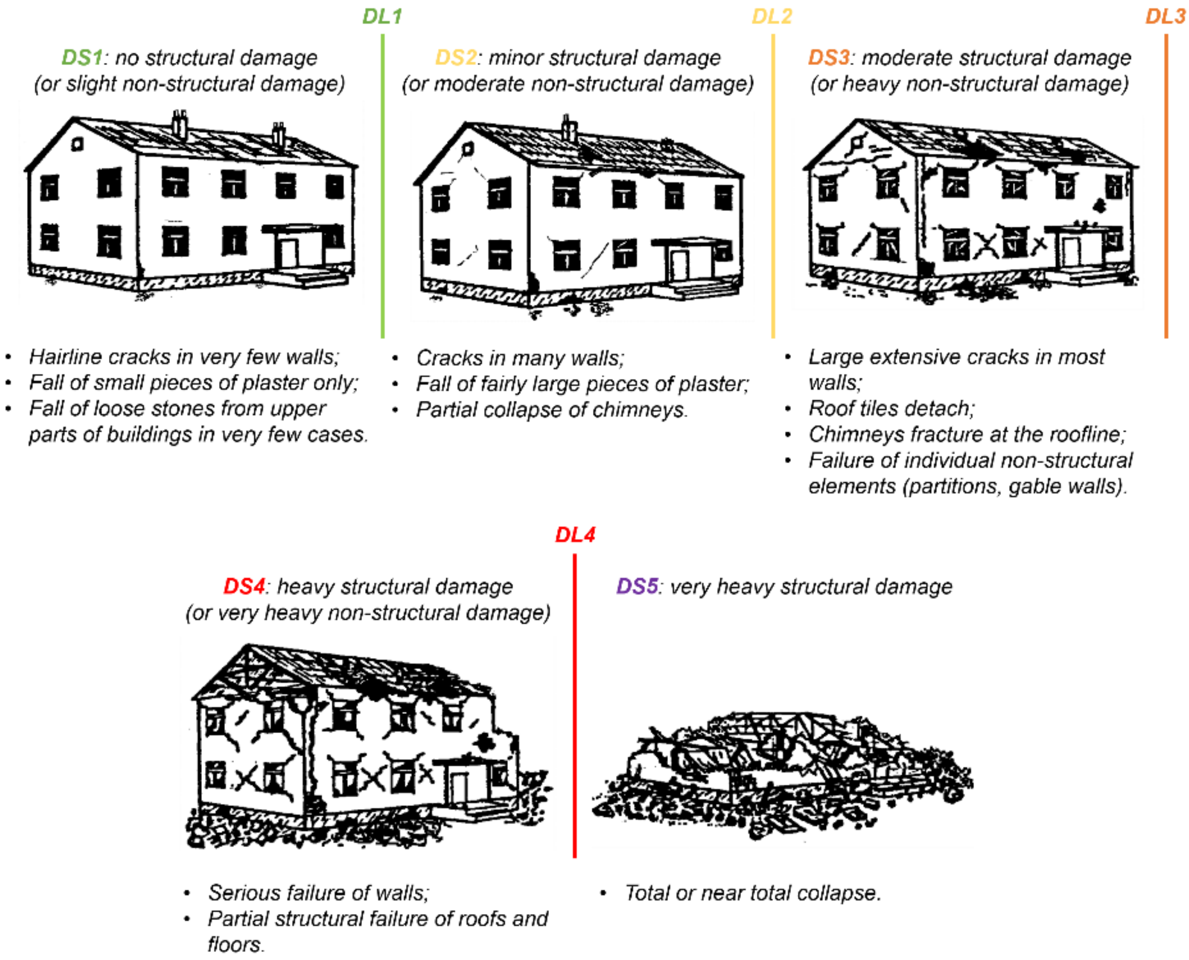

Figure 7.1 Classification of damage to masonry buildings (adapted from Grünthal, 1998).

Low-level non-structural damage was not easily distinguished from the structural damage, being mostly associated with damage to the plaster. Overall, structural damage was first observed after test SC2-200% in the slender piers of the North building wall (Figure 7.2), which was not covered with plaster. Damage to walls finished with plaster, meaning to the interior wall and the walls of the South first-storey room, occurred only in later phases of the testing when the North subsystem and the roof had already undergone substantial structural damage. Therefore, delimiting a state where the building was free of structural damage but exhibited minor non-structural damage was not feasible. As such, limit states DS0 and DS1 were unified.

Four damage limits were consequently defined where DL1 constitutes the limit condition at which no damage was visible, DL4 is the limit condition at which heavy structural (or very heavy non-structural) damage was reported, before entering the near-collapse conditions, while DL2 and DL3 denote the attainment of intermediate levels of damage. Near-collapse conditions mean that the building is so gravely damaged that re-occupancy is not an option in any case. The level of damage sustained by structural elements is such that the building is beyond repair and most probably would be demolished in practice, as posing a threat to life and limb due to falling hazards. Such damage to the load-bearing masonry had already occurred in test SC2-400% when the building exhibited significant degradation in stiffness and strength, and one chimney collapsed. The structure was still standing even after the SC2-500% test but was on the verge of falling, and aftershock activity could induce partial or total collapse.

Each DL was associated with an earthquake input: specifically, DL(*i*) was associated with the last run that caused overall building damage classified as DS(*i*). The maximum average inter-storey drift ratio induced to the structure by this run was taken as the reference engineering demand parameter corresponding to DL(*i*), in agreement with what was done for specimen EUC-BUILD-2. Due to the considerable number of executed test-runs and the accumulation of damage, the definition of more severe damage limits is deemed to be more punishing relatively to lower-damage thresholds. Table 7.1 lists the tests runs when the structure reached each threshold.

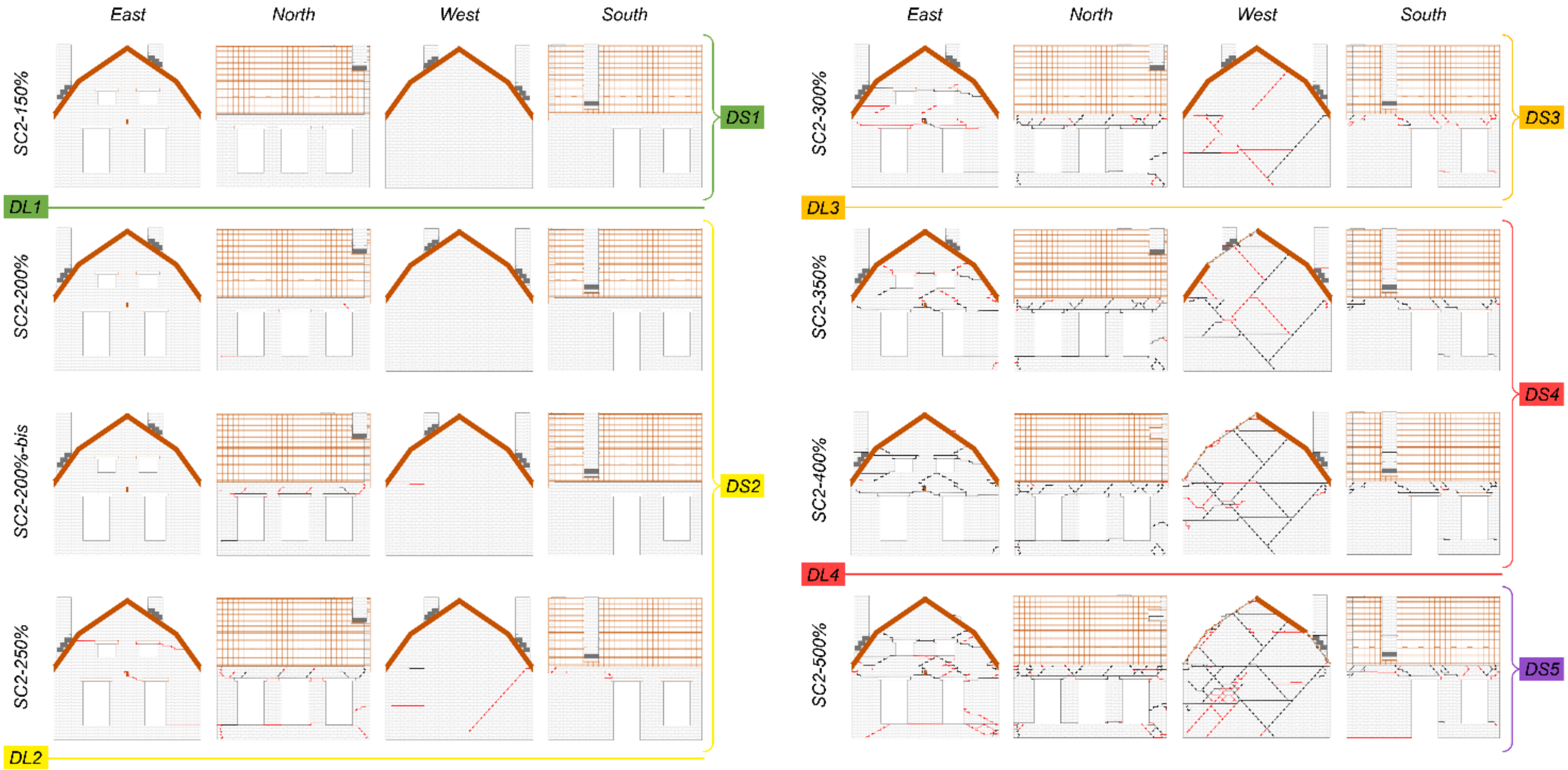

Figure 7.2 Evolution of specimen crack pattern and identification of global damage states and damage limits.

Table 7.1 Summary table of global damage limit states for the building specimen.

DL1	DL2	DL3	DL4
Maximum demand with no evident structural damage	Maximum demand with only minor structural damage	Maximum demand with only moderate structural damage	Maximum demand with heavy structural damage before developing near-collapse conditions
• *No visible damage.*	• *Hairline flexural/rocking cracks at top and bottom of all North piers.* • *Hairline cracks on both transverse façades due to incipient out-of-plane mechanisms.* • *Crack residual widths did not exceed 1 mm (Baggio et al., 2007).*	• *Diagonal cracks and sliding in the North wall due to interaction with the East façade; permanent openings reached 5-7 mm.* • *Fracture at the base of the South chimney stack.* • *Cracks on the interior wall had residual widths of 1.5-2 mm.*	• *Collapse of the West chimney above the roofline.* • *Out-of-plane rigid-body mechanism of the West façade and sliding with residuals up to 35 mm.* • *Permanent openings on the interior wall reached 8 mm.*
SC2-150% (*PGA* = 0.21 g)	SC2-250% (*PGA* = 0.47 g)	SC2-300% (*PGA* = 0.58 g)	SC2-400% (*PGA* = 0.68 g)
$\theta_{1,AVG,DL1}$ = 0.012%	$\theta_{1,AVG,DL2}$ = 0.25%	$\theta_{1,AVG,DL3}$ = 0.49%	$\theta_{1,AVG,DL4}$ = 0.9%

Figure 7.3 illustrates the backbone curve of the building specimen, consisting in the peak structural responses of the incremental dynamic tests. In particular, the curve is constructed by the points of maximum force demands (empty dots) and the peak displacement demand in test SC2-500% (solid dot; truncated at zero force), considering only the response in the negative direction (towards East), where the nonlinear response was more pronounced. A comparison is provided against a definition of the curve that does not include residual deformations from previous tests, hence discards traces of spurious stiffness degradation. Vertical coloured lines in the figure denote the damage limits for the overall structure that account for residual deformations per se.

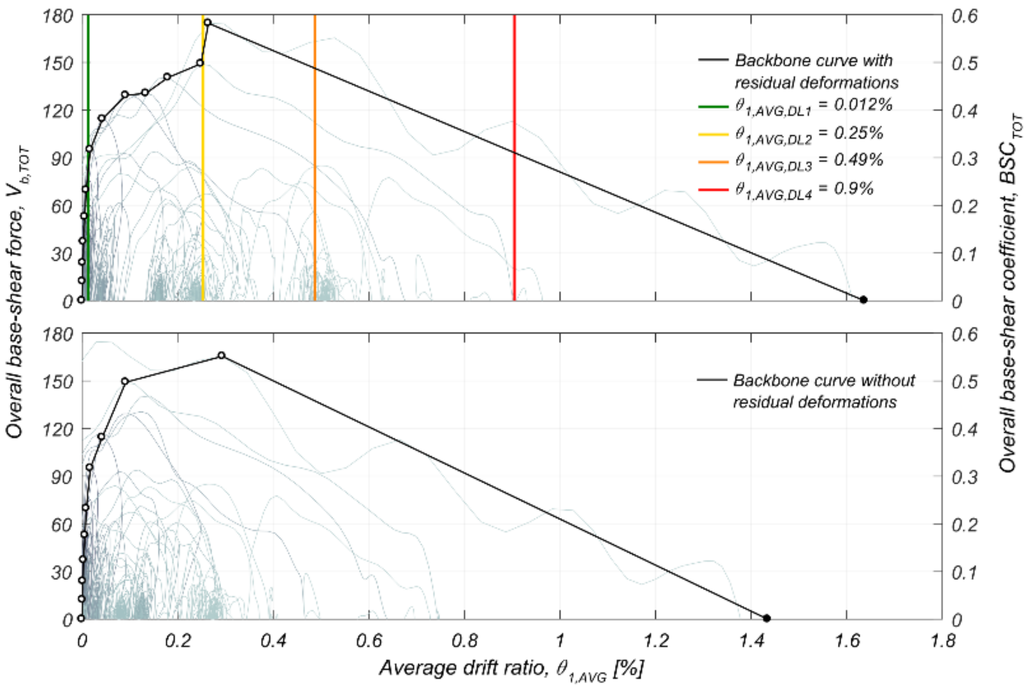

Figure 7.3 Backbone curves and damage limit states for the overall building response. Top: with the inclusion of residual deformations; bottom: without residuals from previous tests.

7.2 Summary of Specimen Seismic Performance

An overall summary of the response of the tested house is shown in Figure 7.4 and Figure 7.5, where peak lateral displacements, peak and residual drift ratios, peak acceleration amplification factors, and the first-mode period evolution are plotted for testing under scenario motions SC1 and SC2. The SC1 motions were sensibly weaker and did not put any significant strain on the structure.

All displacement quantities are measured horizontally, with reference to the shake-table surface. Peak and residual drift ratios are normalised displacements over different lengths; consequently, attention is required when compared to each other. For instance, the roof drift ratio is a measure of deformation concentrated within the roof inter-storey height, while the drift-ratio definition of the chimneys uses the total bottom-to-top height, even though deformations in the latter case were mostly concentrated above the floor level. Both displacements and drift ratios are provided in absolute values; however, all peaks were measured for building side sway to the negative direction that means towards the East. Accordingly, residual deformations were built up towards the East side of the building.

The acceleration amplification factors, *AMP*s, are defined as the ratios of peak acceleration response recorded at various building components to peak acceleration recorded at the foundation (*PGA*). Where more than one accelerometer was available, accelerations were defined as an average of the different readings weighted by the masses to the corresponding sensors. Interesting is the amplification trend exhibited by the two chimneys that experienced very high accelerations at the top. The maximum acceleration in the West chimney was recorded during its violent splitting in two parts at the top; however, high accelerations were also recorded at mid-height of the first storey, which led to the collapse of the structure inside the building. Acceleration amplifications at the top of the South chimney stabilised after cracking occurred, and the stack began rocking.

The first-mode period of the undamaged structure was $T_{1,und}$ = 0.147 s, while by the end of the testing sequence it shifted to $T_{1,dam}$ = 0.314 s. Initially, the response was dominated by the out-of-plane deflection of the gables-roof assembly. Changes in the modal shapes were not seen before testing at SC2-250% when a global building response was triggered, and the fundamental period increased to 0.19 s. Further significant elongation was noticed after test SC2-300% when the period reached 0.25 s. At the beginning of the testing, the apparent viscous damping ratio for the first mode was 4.0%, while by the end it had risen slightly to about 5.5%. More information on the applied random vibrations and modal analysis methods can be found in Section 6.1.

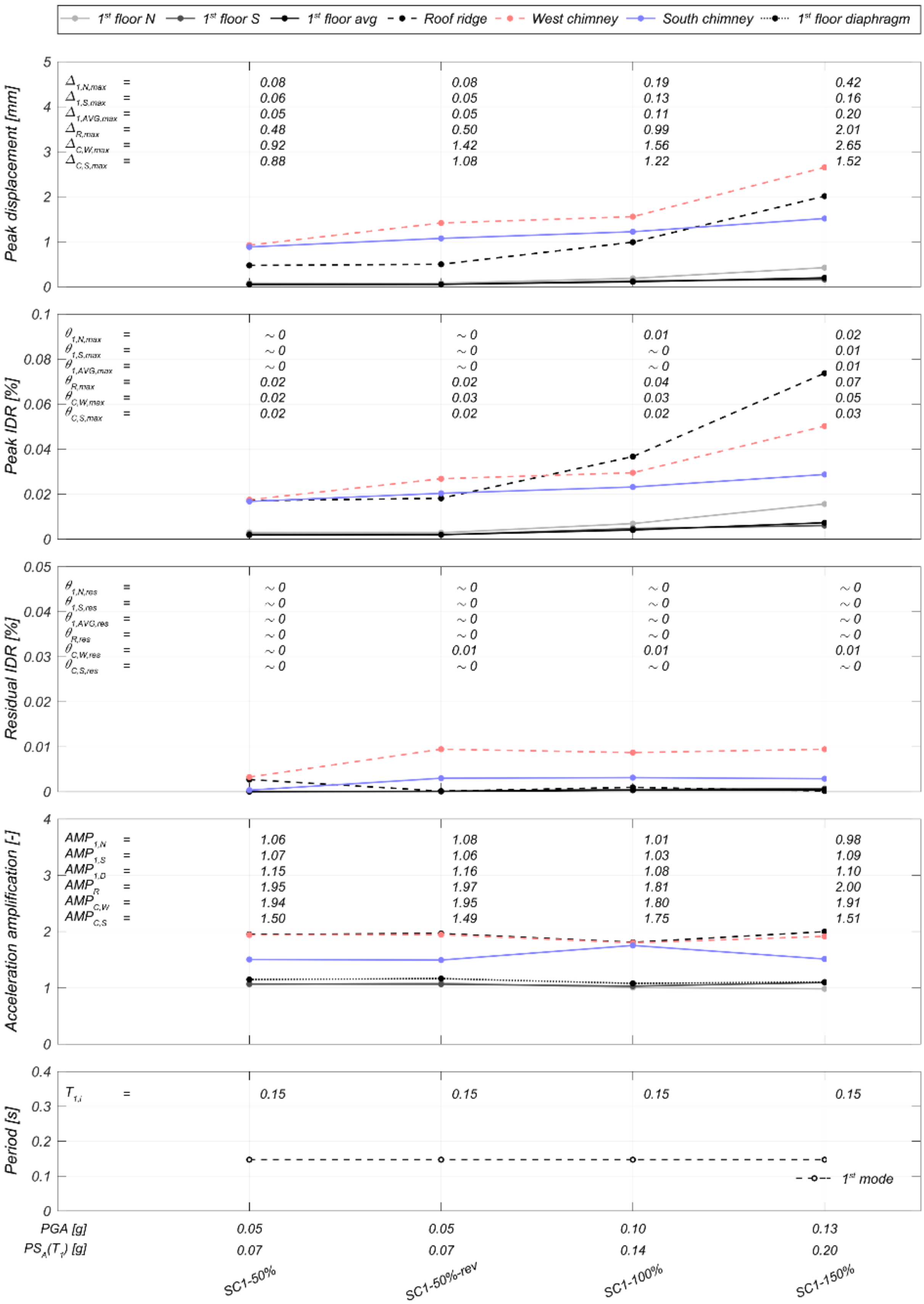

Figure 7.4 Summary of the performance of the building specimen under SC1 motions.

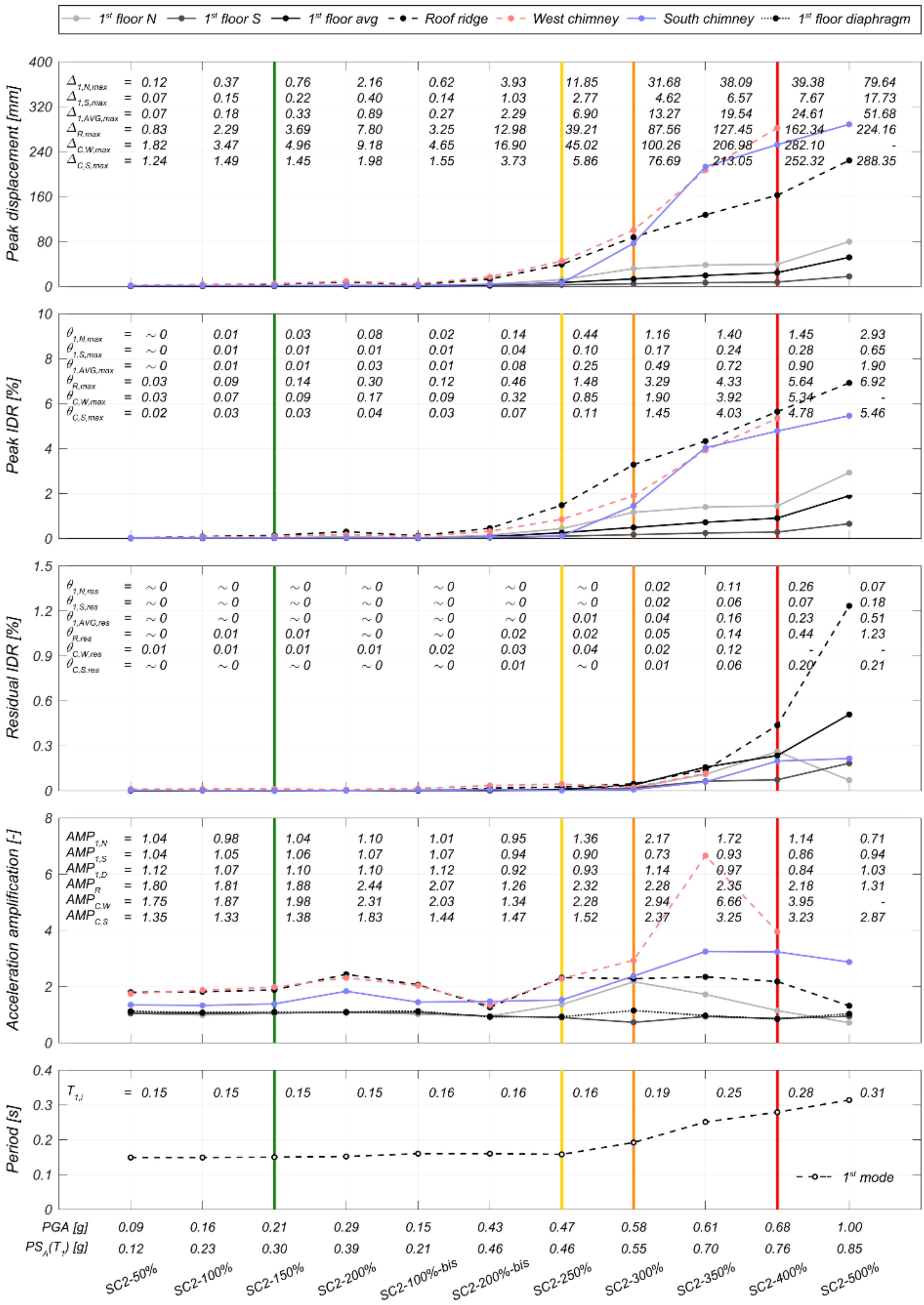

Figure 7.5 Summary of the performance of the building specimen under SC2 motions.

8 MECHANICAL PROPERTIES OF MATERIALS AND COMPONENTS

8.1 Test Overview and Summary of Results

A series of mechanical characterisation tests were conducted on the clay-brick masonry of the building specimen at the testing facilities of LNEC. The testing series comprised strength tests on mortar samples (Figure 8.1a) and clay units (Figure 8.1b), as well as compression and bending tests on small masonry assemblies (Figure 8.1c to e), bond wrench tests (Figure 8.1f), direct shear tests on triplets (Figure 8.1g), and torsional-shear tests on doublets (Figure 8.1h). All specimens were fabricated from the batches of units and mortar used to build the prototype building.

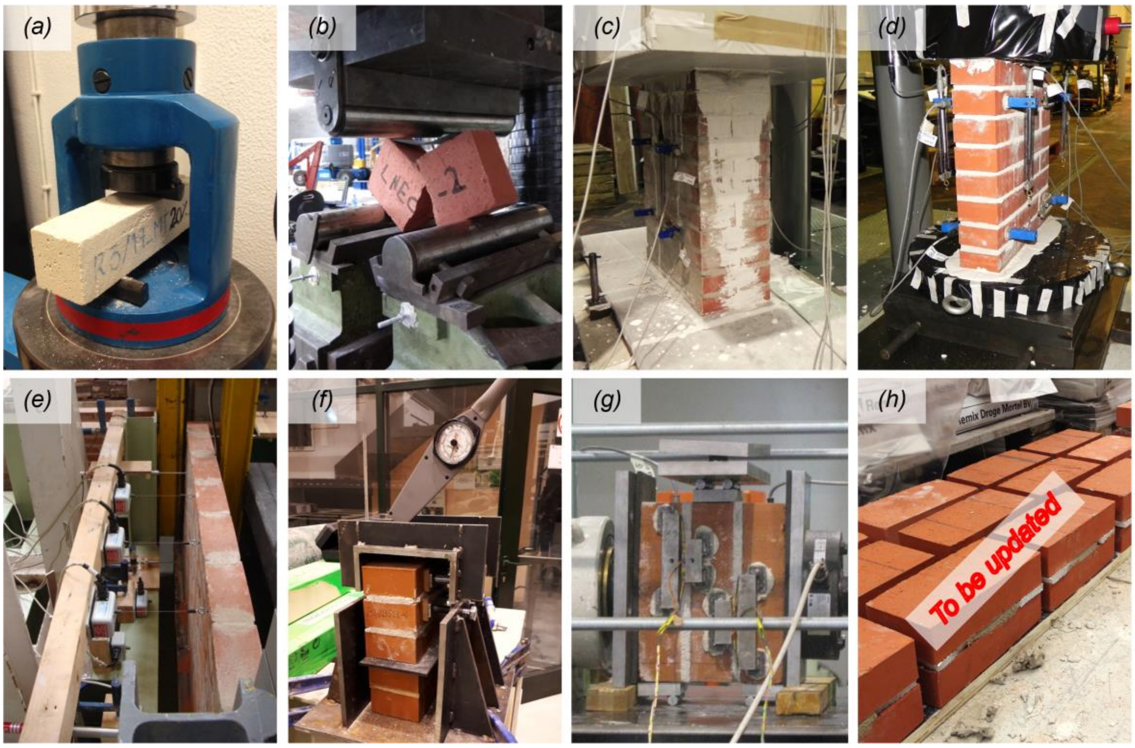

Figure 8.1 Mechanical characterization tests: (a) three-point bending test on a mortar specimen; (b) three-point bending test on a solid-clay brick; (c) compression test on a double-wythe masonry wallette; (d) compression test on a single-wythe masonry wallette; (e) four-point out-of-plane bending test; (f) bond wrench test; (g) direct shear test on a triplet; (h) shear test in torsion on a doublet.

The solid clay bricks had compressive strength f_b = 74 MPa (EN 772-1, 2011) and flexural-tensile strength f_{bt} = 6.5 MPa for bending in the strong axis. The compressive and flexural-tensile strengths of the mortar were f_c = 2.65 MPa and f_t = 1.22 MPa, respectively (EN 1015-11, 1999), at the testing age of 28 days.

Compression tests were performed on eight double-wythe masonry wallettes, with loading applied perpendicularly to the horizontal bed-joints (EN 1052-1, 1998), allowing an estimation of the masonry compressive strength, f_m = 11.45 MPa, and elastic modulus secant at 33% of the compressive strength, E_{m1} = 9120 MPa. Eight additional tests were performed on single-wythe wallettes built with the half-running bond, providing slightly higher estimates, f_m = 16.08 MPa and E_{m1} = 11508 MPa. Four-point out-of-plane bending tests on eight single-wythe wallettes (EN 1052-2, 1999) were carried out to evaluate the out-of-plane flexural strength of the masonry, f_{x2} = 2.13 MPa. Bond wrench tests on 13 specimens (EN 1052-5, 2005) were employed to determine the bond strength of masonry at the time of the shake table test, f_w = 0.365 MPa, while 16 masonry triplets were subjected to direct shear tests (EN 1052-3, 2002) to determine the masonry bed-joint cohesion, f_{v0} = 0.47 MPa, and shear friction coefficient, μ = 0.81.

A novel testing procedure will also be followed to evaluate the strength of the bed joints under combined torsion and compression. The bed-joint shear resistance in torsion is one of the most important parameters controlling the capacity of a wall subjected to out-of-plane two-way bending (Vaculik and Griffith, 2018). The reader who is interested in knowing more about the test setup and understanding how the obtained parameters affect the dynamic response of entire walls is referred to the experimental study of Graziotti *et al.* (2018).

The results of all complementary tests performed on materials for the prototype building are summarised in Table 8.1. There, the obtained average values and dispersions are compared with the estimates acquired from the experimental campaign of EUC-BUILD-2, and the data from in-situ tests on pre-1940s clay-brick masonry buildings in Groningen (Tondelli *et al.*, 2015). The comparison reveals that prototypes EUC-BUILD-2 and LNEC-BUILD-3 had similar masonry compressive strength and Young's modulus (the difference was less than 7%), but the two estimates were considerably higher than what was observed in the existing building stock. In particular, the masonry walls tested in the lab were on average 27% stronger and 77% stiffer in compression than the masonries found in the field. Meanwhile, masonry bed-joint cohesion and shear friction, and flexural bond strength resulted around 50% to 200% higher for specimen LNEC-BUILD-3 with respect to EUC-BUILD-2; nonetheless, the experimental values bracketed the values found in the in-situ tests. In general, the material strength estimates evaluated in situ exhibited higher dispersions than the strengths measured in the lab, as they were affected by the material variability from building to building.

Table 8.1 Summary of masonry mechanical properties of the building prototype. Comparison with estimates obtained from laboratory tests at the University of Pavia (EUC-BUILD-2) (Kallioras et al., 2018) and in-situ tests on pre-1940s clay-brick URM buildings in the Groningen region (Tondelli et al., 2015).

Material property [units]	LNEC-BUILD-3		EUC-BUILD-2		In situ tests	
	Avg.	C.o.V.	Avg.	C.o.V.	Avg.	C.o.V.
Density of mortar, ρ_{mortar} [kg/m^3]	1616	0.035	-	-	-	-
Density of bricks, ρ_b [kg/m^3]	2103	0.015	2101	0.02	-	-
Density of masonry, $\rho_{m,w}$ [kg/m^3] (from double-wythe wallettes tested in compression)	1959	0.009	1979	0.01	-	-
Density of masonry, $\rho_{m,t,bw}$ [kg/m^3] (from triplets tested in bond wrench)	1961	0.009				
Density of masonry, $\rho_{m,t,s}$ [kg/m^3] (from triplets tested in shear)	1992	0.005				
Brick standard compressive strength, f_b [MPa]	74.2	0.045	46.8	0.11	25.6	0.23
Brick flexural strength, $f_{bt}^{\dagger}$ [MPa]	6.50	0.09	8.50	0.05	6.43	0.64
Mortar compressive strength (28 days), f_c [MPa]	2.65 ^{M} 3.57 ^{C}	0.187 ^{M} 0.084 ^{C}	4.12	0.24	-	-
Mortar flexural strength (28 days), f_t [MPa]	1.22 ^{M} 1.40 ^{C}	0.164 ^{M} 0.115 ^{C}	1.20	0.33	-	-
Elastic modulus of mortar (28 days), E_{mortar} [MPa]	5162 ^{M} 6432 ^{C}	0.113 ^{M} 0.067 ^{C}	-	-	-	-
Masonry compressive strength, $f_{m,w}$ [MPa]	11.45 ^{D} 16.08 ^{S}	0.083 ^{D} 0.067 ^{S}	11.22	0.07	8.91	0.52
Masonry Young's mod. in compression, $E_{m1}^{\dagger\dagger}$ [MPa]	9120 ^{D} 11508 ^{S}	0.128 ^{D} 0.165 ^{S}	9833	0.25	5346	0.60
Masonry flexural in-plane strength, f_{x3} [MPa]	-	-	0.44	0.19	0.61	0.45
Masonry flexural out-of-plane strength, f_{x2} [MPa]	2.13	0.097	0.64	0.15	0.83	0.47
Masonry flexural bond strength, f_w [MPa]	0.365	0.360	0.23	0.60	0.33	0.69
Masonry (bed-joint) initial shear strength, f_{v0} [MPa]	0.47	-	0.15	-	0.28	0.26
Masonry (bed-joint) shear friction coefficient, μ [-]	0.81	-	0.55	-	0.66	0.18
Masonry (bed-joint) cohesion in torsion, $f_{v0,tor}$ [MPa]	TBD	TBD	-	-	-	-
Masonry (bed-joint) sh. friction coef. in torsion, μ_{tor} [-]	TBD	TBD	-	-	-	-

^{M} Value refers to the full-scale building specimen
^{C} Value refers to the tests on the small-scale specimens
† Estimate from bending tests in the strong axis of the units
†† Value equal to the slope of the secant at 33% $f_{m,w}$
^{D} Estimates from compression tests on double-wythe masonry wallettes (English/Dutch cross bond)
^{S} Estimates from compression tests on singe-wythe masonry wallettes (stretcher bond)

8.2 Mortar characterisation tests

8.2.1 Characterisation of the mortar materials

The bedding mortar used in the masonry is a pre-dosed cement and hydraulic lime mortar with the references shown in Figure 8.2.

Figure 8.2 Type of product used in bedding mortar.

On January 30, 2018, the materials that compose the mortar (mortar powder and aggregate) were received at the Building Wall Finishes Unit (URPa) of the Building Finishes and Thermal Insulation Division of the Buildings Department of LNEC. The aggregate was slightly damp, but as it was representative of the application that would be made, it was decided to make the tests under these conditions. After the conditioning of the material, the following tests were performed:

- Test to determine the water content of the aggregate;
- Test to determine the bulk density.

8.2.2 Test to determine the water content of aggregate

The water content of the aggregate was determined by the procedure described in standard NP EN 1097-5:2011 "Test for mechanical and physical properties of aggregates. Part 5: Determination of water content by drying in a ventilated oven (NP EN 1097-5, 2011). Three samples of the aggregate were chosen and placed in a pre-weighed tray, in order to calculate its initial mass. The tray was placed in an oven at 105 degrees Celsius until the mass of the aggregate became constant, which means that the difference between measurements was less than 0.1% on a 24 hour interval.

The water content is given by the following equation:

$$w = \frac{M_1 - M_3}{M_3} \times 100 \tag{1}$$

where:
M_1 is the initial aggregate mass [g], and M_3 is the constant aggregate mass after drying [g]. Table 8.2 shows the percentage of water content present in the aggregate samples.

Table 8.2 Percentage of water content present in the aggregate samples.

Identification of the sample	Water content [%]
WCS1	3.8
WCS2	3.7
WCS3	2.4
Average [MPa]	**3.3**
Standard deviation [MPa]	0.78
Coefficient of variation [-]	0.237

8.2.3 Test to determine the bulk density

The bulk density of the mortar powder and of the aggregate was determined by the procedure described in Cahier du CSTB 2669-4:1993 "Enduit monocouches d'imperméabilisation à base de liant hydraulique" (CSTB, 1993). Three samples of both products were prepared and homogenised in order to avoid the risk of segregation. Bulk density of the products was determined using the equipment shown in Figure 8.3 by filling the container, opening the shutter and, if necessary, helping the powder to go down using a spatula. When the container was full, the excess was removed by levelling the surface with the help of a ruler. The container and the product were weighted rounding to the nearest gram (M_1).

Mortar powder

Sand

Figure 8.3 Determination of the bulk density on each type of material used in mortar.

The bulk density is given by the following equation:

$$\gamma = \frac{M_2 - M_1}{V} \tag{2}$$

where:
M_1 is the empty container mass [g];
M_2 is the container with the product [g];
V is the empty container volume [dm^3].

Table 8.3 and Table 8.4 shows the results for all samples of the two products expressed in kg/m^3.

Table 8.3 Results of bulk density for the mortar powder.

Identification of the sample	Container		M_2 [g]	Bulk density [kg/m^3]
	Volume [dm^3]	M_1 [g]		
BDMP1	0.50	379.5	1094.8	1431
BDMP2	0.50	379.5	1098.4	1438
BDMP3	0.50	379.5	1093.2	1427
			Average [MPa]	**1432**
			Standard deviation [MPa]	5.33
			Coefficient of variation [-]	0.004

Table 8.4 Results of bulk density for the aggregate.

Identification of the sample	Container		M_2 [g]	Bulk density [kg/m^3]
	Volume [dm^3]	M_1 [g]		
BDS1	0.50	379.5	904.2	1049
BDS2	0.50	379.5	908.0	1057
BDS3	0.50	379.5	907.3	1056
			Average [MPa]	**1054**
			Standard deviation [MPa]	4.04
			Coefficient of variation [-]	0.004

8.2.4 Characterisation and identification of samples of study mortars before hardening

The study mortar samples were cast with varying composition depending on the use, or not, of sand: 0%, 20%, and 40%. The amount of water was defined by the manufacturer (3.4 litres per 25 kilograms of mortar powder).

Since it was necessary to choose the type of mortar to be used in the construction of the building prototype and to determine the behaviour of this mortar over time, the study mortars were divided into two groups: mortar test (MT) and mortar for maturation curve (MMC).

The designation of the study mortars is conformant with the following descriptions:

- MT_0% - mortar test without sand;
- MT_20% - mortar test with 20% added sand;
- MT_40% - mortar test with 40% added sand.

- MMC_0% - mortar for maturation curve without sand;
- MMC_20% - mortar for maturation curve with 20% added sand;
- MMC_40% - mortar for maturation curve with 40% added sand.

Table 8.5 shows the dates when the study mortars were cast, the number of specimens built, the tests performed for each and their age at the time of the tests.

Table 8.5 Study mortars composition.

Study mortars	Cast date	Number of specimens	Tests	Age
MT_0%	30-01-2018	3	Flexural and compressive strengths	6 days
MT_20%	30-01-2018	3	Flexural and compressive strengths	6 days
MT_40%	30-01-2018	3	Flexural and compressive strengths	6 days
MMC_0%	31-01-2018	9	Flexural and compressive strengths and dynamic modulus of elasticity	10, 20 and 28 days
MMC_20%	31-01-2018	9	Flexural and compressive strengths and dynamic modulus of elasticity	10, 20 and 28 days
MMC_40%	31-01-2018	9	Flexural and compressive strengths and dynamic modulus of elasticity	10, 20 and 28 days

The study mortars were produced in the URPa laboratory according to the dosages described in Table 8.6 using a mixer and moulded into standard moulds measuring 160 mm × 40 mm × 40 mm, as shown in Figure 8.4 and Figure 8.5.

Table 8.6 Study mortars composition

Mixture components	MT_0% and MMC_0%	MT_20% and MMC_20%	MT_40% and MMC_40%
	Weight [kg]	Weight [kg]	Weight [kg]
Mortar powder	3.1821	2.6035	2.3866
Sand	0	0.3833	0.7027
Water	0.433	0.406	0.420
Water / product ratio	13.6	13.6	13.6

Figure 8.4. Producing the study mortars

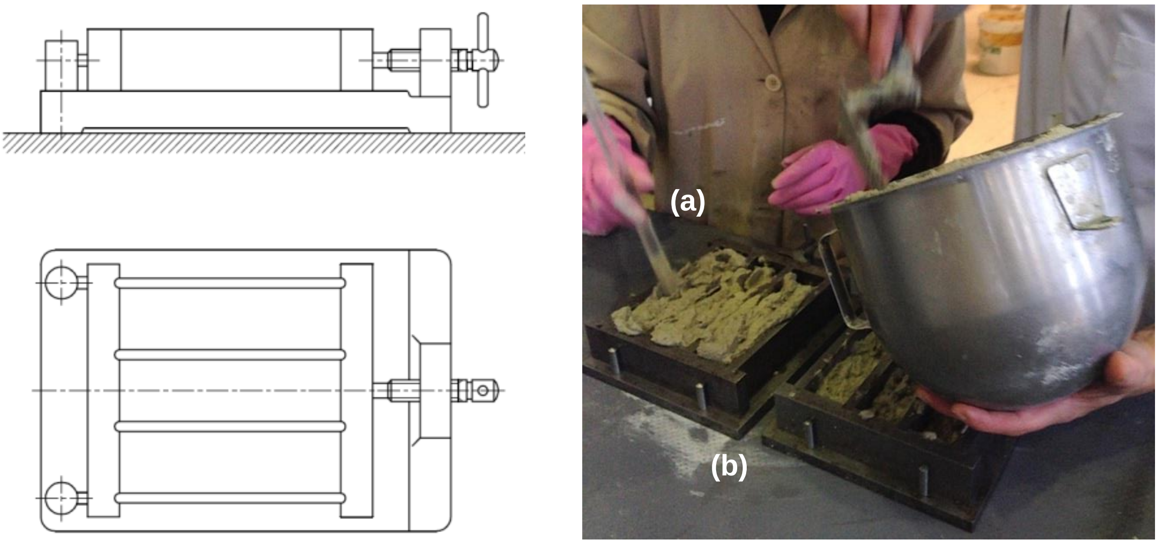

Figure 8.5 Moulding of mortar specimens: (a) pestle and (b) mould.

The tests considered adequate for the characterisation of these specimens were:

- Tests for the determination of the bulk density of fresh mortar;
- Tests for the determination of the consistence of fresh mortar (by flow table).

8.2.5 Tests for the determination of the bulk density of fresh mortar

The bulk density was determined by the quotient between the sample mass and its volume, for standard compaction conditions. The adopted methodology for this test is described in the standard EN 1015-6:1998 "Methods of test for mortar for masonry – Part 6: Determination of bulk density of fresh mortar" (EN 1015-6, 1998). The test starts by the pre-determination of the mass of the container (cylindrical cup), thus obtaining m_1. Then, using a spatula, the cylindrical cup is filled with a first layer up to approximately half of its capacity. The contents are then compacted with ten strokes carried out from the oscillation of the container on alternate sides. The process continues by filling the container a little over its capacity and repeating the same compaction process as described above. Finally, the surface is levelled with the aid of a spatula by removing the excess mortar so that the surface becomes flat and coincident with the upper edge of the container. The outer surface of the container is conveniently cleaned to remove any residual mortar and the assembly is weighed (thus obtaining m_2).

Considering that the mortar mass is given by the difference between the mass of the set m_2 and the mass of the empty container m_1, the bulk density of the mortar can be determined by the following equation.

$$D = \frac{m_2 - m_1}{V} \qquad (3)$$

where:
D is the bulk density [kg/m^3]
m_2 is the mass of the container with mortar [kg];
m_1 is the mass of the container [kg];
V is the volume of the container [m^3].

Figure 8.6 shows some phases of the test being performed, while the results obtained for the study mortars are given in Table 8.7.

Figure 8.6 Carrying out the determination of bulk density of fresh study mortars.

Table 8.7 Results on the determination of bulk density of fresh study mortars.

Identification of the specimen	m_1 [kg]	m_2 [kg]	Bulk density [kg/m^3]
MT_0%	0.4634	2.1203	1660
MT_20%	0.4634	2.0220	1560
MT_40%	0.4634	2.0109	1550
MMC_0%	0.4634	2.2264	1760
MMC_20%	0.4634	2.1365	1670
MMC_40%	0.4634	2.0874	1620

8.2.6 Tests for the determination of the consistence of fresh study mortars (by flow table)

The purpose of this test is to determine the consistency of the mortar in fresh state. The consistency is a measure of the fluidity of the fresh mortar, measuring the deformation of the mortar when subjected to external forces. The methodology adopted for this test is described in the standard EN 1015-3:1999 "Methods of test for mortar for masonry – Part 3: Determination of consistency of fresh mortar (by flow table)" (EN 1015-3, 1999). The test begins by moistening the table and the mould after ensuring that they are properly cleaned, then the mould is placed centred on the table and the mortar is introduced in two equal layers. Both layers are compacted with 25 strokes with the compaction bar, making sure that each stroke reaches the full thickness of the layer to ensure uniform filling of the mould. The excess mortar is then extracted with the spatula, removing it and wiping with a cloth to leave the table dry and clean. Approximately 15 seconds later, the mould is raised slowly, and 15 strokes are applied at a rate of 1 stroke per second to spread the mortar. The diameter (in millimetres) of the scattering is measured in two orthogonal directions (d_1, and d_2). The mortar spreading is expressed in millimetres and is the result of the average values d_1 and d_2.

Figure 8.7 (a) presents a schematic representation of the spreading table and in Figure 8.7 (b) some phases of the tests performed are illustrated. The results obtained for all mortar samples collected are given in Table 8.8.

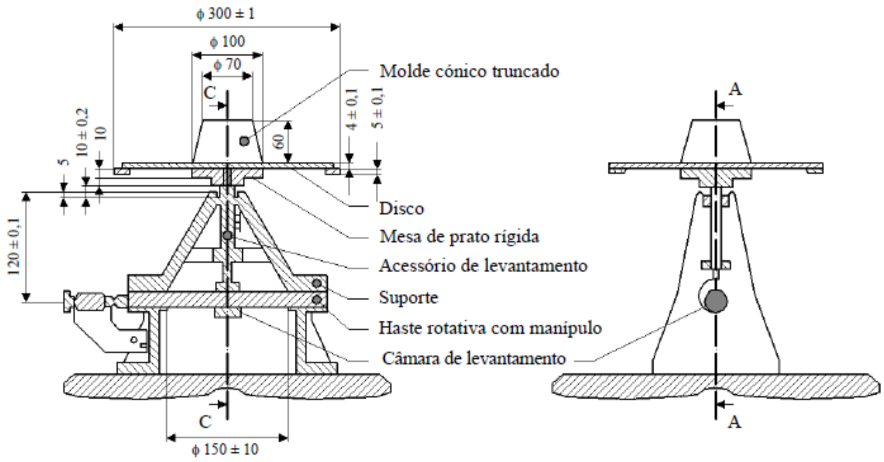

(a)

(b)

Figure 8.7 Determination of consistence of fresh study mortars by scattering: (a) schematic representation of equipment; (b) test run.

Table 8.8 Results on the determination of the consistency of fresh mortar.

Identification of the specimen	d_1 [mm]	d_2 [mm]	Consistency [mm]
MT_0%	160	161	161
MT_20%	169	168	169
MT_40%	170	175	173
MMC_0%	153	152	152
MMC_20%	159	162	160
MMC_40%	184	173	179

8.2.7 Characterisation and identification of specimens (hardened study mortars)

After the specimens were built, some were identified and selected to perform the physical and mechanical tests at different ages as shown in Figure 8.8. These tests consist on determining the dynamic modulus of elasticity and determining the bending and compressive strengths. The storage of the specimens in a controlled environment was performed according to the specifications of standard EN 1015-11:1999 "Methods of test for masonry – Part 11: Determination of flexural and compressive strength of hardened mortar" (EN 1015-11, 1999) which correspond to placing the mould in a plastic bag of polyethylene for two days, ensuring a relative humidity of 95 ± 5%, in a room conditioned at 20 ± 2 °C and with a relative humidity of 65 ± 5%. Subsequently, the mortar test specimens (MT_0%, MT_20% and MT_40%) were demoulded and kept under the aforementioned curing conditions for 4 days, instead of 5 days as described in the standard. This change was necessary because the test needed to be performed at 6 days in order to make a decision on which type of mortar test would be used in the construction of the model. The mortar for maturation curve specimens (MMC_0%, MMC_20% and MMC_40%) were demoulded and kept under the aforementioned curing conditions for 5 days as described in the standard. Figure 8.9 illustrates the reported curing conditions of some of the specimens.

Figure 8.8 Part of study mortar specimens.

Figure 8.9 Curing conditions of study mortar specimens.

The designation of the specimens is the same used in the samples, but with an underscore and a number identifying each specimen. The characteristics of the various specimens of all types of mortar are presented in Appendix F.

The bulk density average values for the study mortar specimens are given in Table 8.9, with additional details also provided in Appendix F.

Table 8.9 Bulk density for study mortar specimens selected for the tests.

Specimen	Average bulk density [kg/m^3]	Standard deviation [kg/m^3]	Coefficient of variation [-]
MT	1473.94	48.96	0.033
MCC	1523.08	87.33	0.057

Since the tests for the determination of the dynamic modulus of elasticity are non-destructive, the same specimens were also used for the bending and compression strength tests.

The selected tests for these samples were the following:

- Tests to determine the dynamic modulus of elasticity;
- Tests for determination of flexural and compression strengths.

8.2.8 Tests for the determination of dynamic modulus of elasticity of study mortars

The modulus of elasticity of a coating mortar is a property that translates its ability to absorb stresses and deformations. Thus, the quality and durability of a mortar coating are directly related to its modulus of elasticity. The dynamic modulus of elasticity was determined by the procedure described in standard NP EN 14146:2006 "Test methods for natural stone. Determination of dynamic modulus of elasticity (by measuring fundamental resonance frequency)" (NP EN 14146, 2006). This is a non-destructive test which consists in determining the resonance frequency of prismatic specimens through a vibration induced longitudinally to the test specimen. The specimen is attached to the measuring apparatus through its central part and is subsequently induced to vibrate at one of its extremities, with such vibration being received by a sensor placed at the other end of the specimen after having passed its entire length. In a frequency spectrum, we can observe the highest peak corresponding to the self-frequency of the specimen. Figure 8.10 shows one of the test specimens as well as the type of plot obtained.

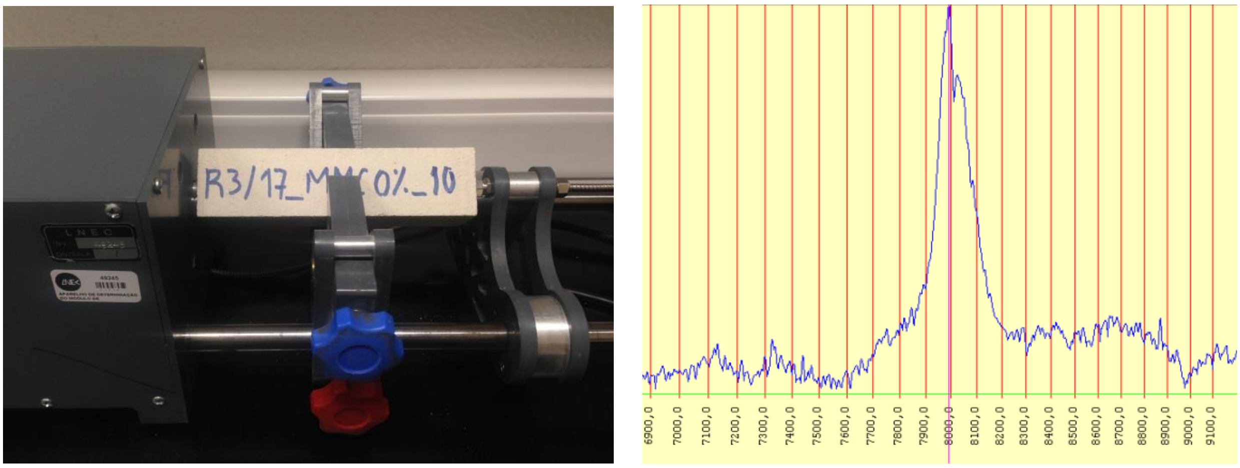

Figure 8.10 Performing the test to determine the dynamic modulus of elasticity and plot obtained.

From the observation of the frequency plot associated with each specimen it is possible to determine the fundamental resonance frequency (*F*) for each of them, which corresponds to the lowest frequency at which a maximum oscillation amplitude is obtained. After the specimens have been measured and weighed, and their resonance frequency determined, the dynamic modulus of elasticity was calculated using the following formula:

$$E_d = 4L^2 \times F^2 \times \rho \times 10^{-6} \tag{4}$$

where:
E_d is the dynamic modulus of elasticity [MPa];
L is the length of the specimen [m];
F is the longitudinal frequency of resonance [Hz];
ρ is the bulk density [kg/m^3].

In order to establish a relation between the days of maturation and the mechanical properties of the study mortars, the results of the tests for the determination of the dynamic modulus of elasticity of the mortar for maturation curve specimens (MMC) for 10, 20 and 28 days of age are presented in detail in Appendix F and shown in Figure 8.11 to Figure 8.13.

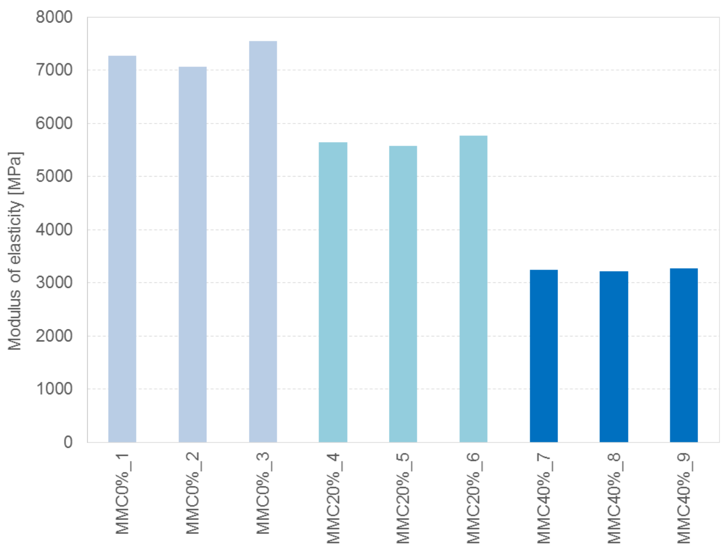

Figure 8.11 Test results for the determination of the dynamic modulus of elasticity of mortar for maturation curve (MMC_0%, MMC_20% and MMC_40%) after 10 days of age.

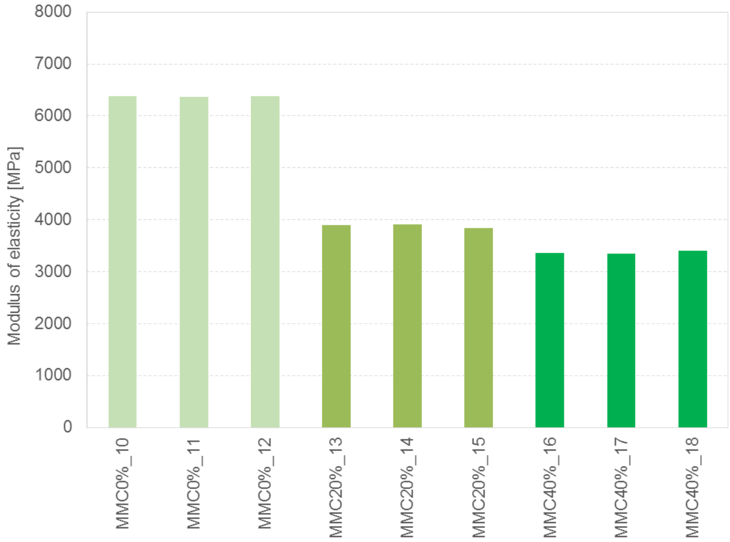

Figure 8.12 Test results for the determination of the dynamic modulus of elasticity of mortar for maturation curve (MMC_0%, MMC_20% and MMC_40%) after 20 days of age.

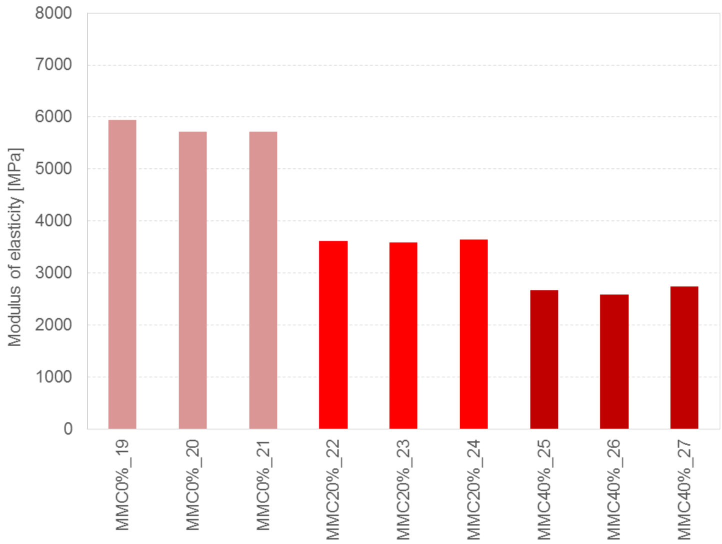

Figure 8.13 Test results for the determination of the dynamic modulus of elasticity of mortar for maturation curve (MMC_0%, MMC_20% and MMC_40%) after 28 days of age.

Table 8.10 presents a summary of the average dynamic modulus of elasticity obtained for mortar for maturation curve with 0% added sand and with 20% added sand (MMC_0% and MMC_20%). Table 8.11 presents a summary of the average dynamic modulus of elasticity obtained for mortar for maturation curve with 40% added sand (MMC_40%).

Table 8.10 Summary of the average dynamic modulus of elasticity obtained for the mortar for MMC_0% and MMC_20% for the different ages.

Age of study mortars	MMC_0%			MMC_20%		
	Average [MPa]	Standard deviation [MPa]	Coefficient of variation [-]	Average [MPa]	Standard deviation [MPa]	Coefficient of variation [-]
10 days	7294	242	0.033	5660	96	0.017
20 days	6377	8	0.001	3887	40	0.010
28 days	5792	129	0.022	3618	24	0.007

Table 8.11 Summary of the average dynamic modulus of elasticity obtained for the mortar for MMC_40% for the different ages.

Age of study mortars	MMC_40%		
	Average [MPa]	Standard deviation [MPa]	Coefficient of variation [-]
10 days	3246	28	0.009
20 days	3369	34	0.010
28 days	2668	75	0.028

Figure 8.14 shows the maturation curve over time for the dynamic modulus of elasticity of MMC mortars.

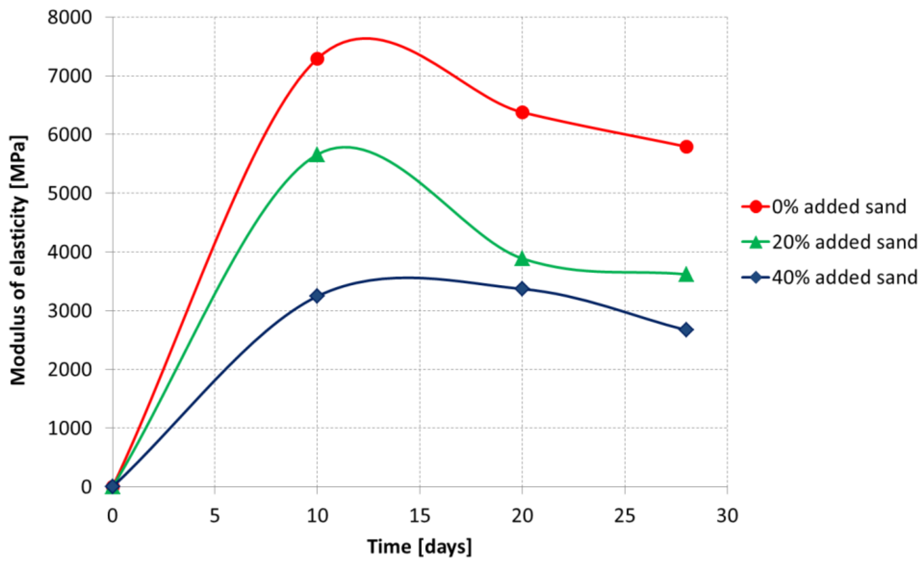

Figure 8.14 Maturation curve over time for the dynamic modulus of elasticity of MMC mortars.

8.2.9 Tests for the determination of flexural and compressive strengths of study mortars

Test for the determination of flexural strength

The test to determine the flexural strength was performed according to the standard EN 1015-11:1999 "Methods of test for masonry – Part 11: Determination of flexural and compressive strength of hardened mortar" (EN 1015-11, 1999). The purpose of this test is to obtain the flexural strength of the mortar (hardened mortar), by applying a half-span load to a simply supported prismatic specimen as depicted in Figure 8.15 (a). The specimen is placed on the test machine and is centred with the longitudinal axis perpendicular to the two supports, ensuring that one of the side moulding faces stays fixed on the supports. The load is applied at mid-span through an upper bearing point, and imposing a gradual force and increasing continuously, between 10 and 50 N/s, forcing the failure to occur in a range of time between 30 and 90 seconds. The maximum force supported by the specimen is recorded until failure and the flexural strength of the specimen is then calculated. In Figure 8.15 (b) one of the test specimens is shown.

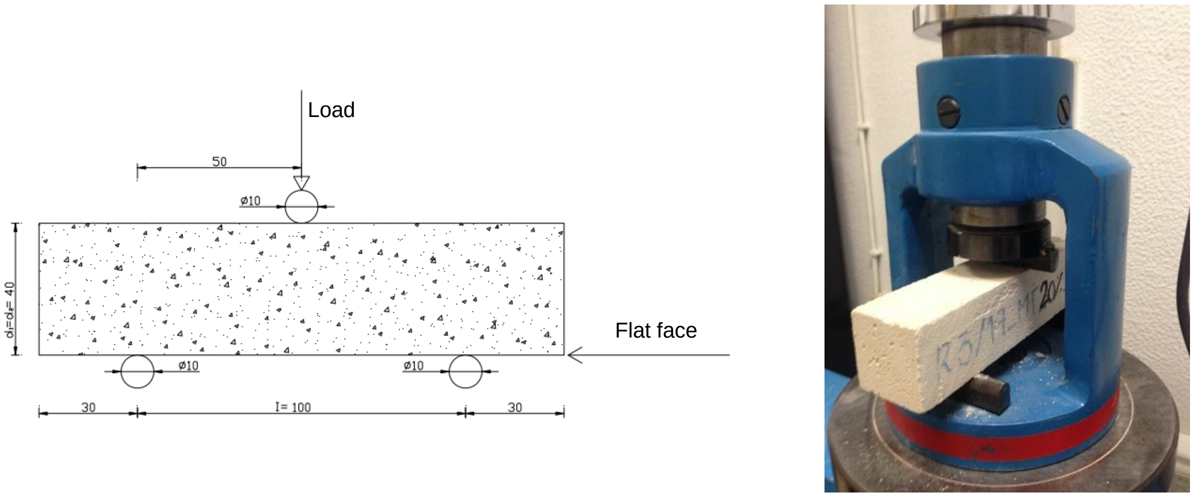

(a) (b)

Figure 8.15 Test for determination of flexural strength: (a) scheme of positioning of the specimen and (b) specimen being tested.

The flexural strength is given by the following equation:

$$f_t = 1.5 \times \frac{F_f \times l^2}{b \times d} \quad (5)$$

where:
f_t is the flexural strength [MPa];
F_f is the maximum flexural force applied to the specimen at the moment of rupture [N];
l is the distance between the bottom rollers [mm];
b is the width of the test specimen [mm];
d is the height of the test specimen [mm].

Test for the determination of compressive strength

The test to determine the compressive strength was performed in accordance with the standard EN 1015-11:1999 "Methods of test for masonry – Part 11: Determination of flexural and compressive strength of hardened mortar" (EN 1015-11, 1999). This test allows the determination of the compressive strength of mortar specimens (hardened mortar). This test is performed immediately after the flexural test, and on the prisms resulting therefrom, by applying a load until failure.

The specimen is placed centred on the lower plate of the machine test with the flat face in contact to the lower plate. The upper plate of the machine is lowered until it contacts the upper face of the specimen, as shown in Figure 8.16 (a). An increasing force is then applied gradually and without shock, to obtain the failure between 30 and 90 seconds until the failure of the specimen. The compressive strength values determined by this method are designated by f_c. The calculation is performed using the following formula:

$$f_c = \frac{F_c}{A_c} \quad (6)$$

where:
f_c is the compressive strength [MPa];
F_c is the maximum compressive force applied to the specimen at the moment of failure [N];
A_c is the area of the specimen in contact with the plates of the machine test [mm^2].

Figure 8.16 (b) depicts one of the specimens being tested.

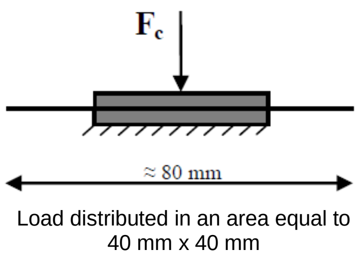

(a)

(b)

Figure 8.16 Test for compressive strength: (a) test scheme and (b) specimen being tested.

In order to obtain a relation between the maturation time and the mechanical properties of the study mortars, Figure 8.17 to Figure 8.20 show the test results on flexural and compressive strengths of mortar test specimens (MT) after 6 days of age and of mortar for maturation curve specimens (MMC) after 10, 20 and 28 days of age. Additional results are given in Appendix F. In the plots of Figure 8.21 to Figure 8.24, the compressive strength is represented with bars and the value of the modulus of elasticity for the corresponding specimens is represented by a line.

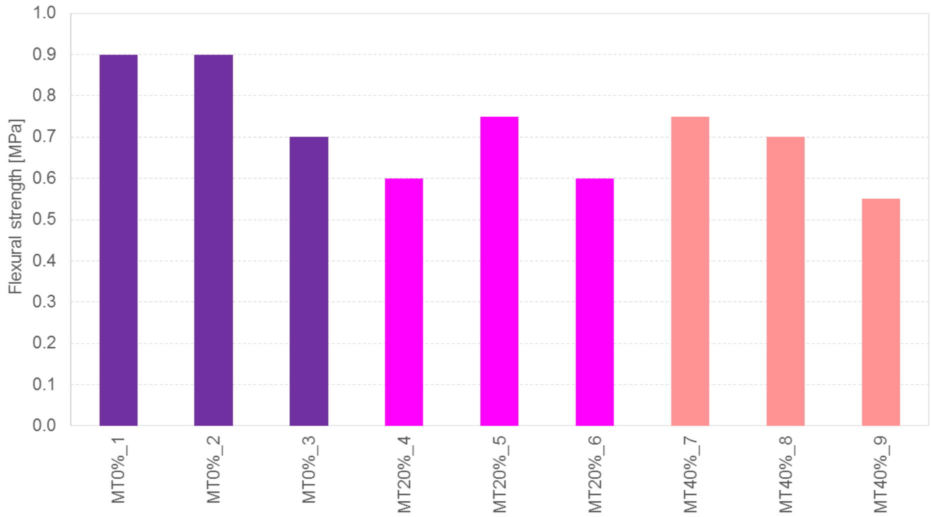

Figure 8.17 Flexural strength test results for mortar test (MT_0%, MT_20% and MT_40%) after 6 days of age.

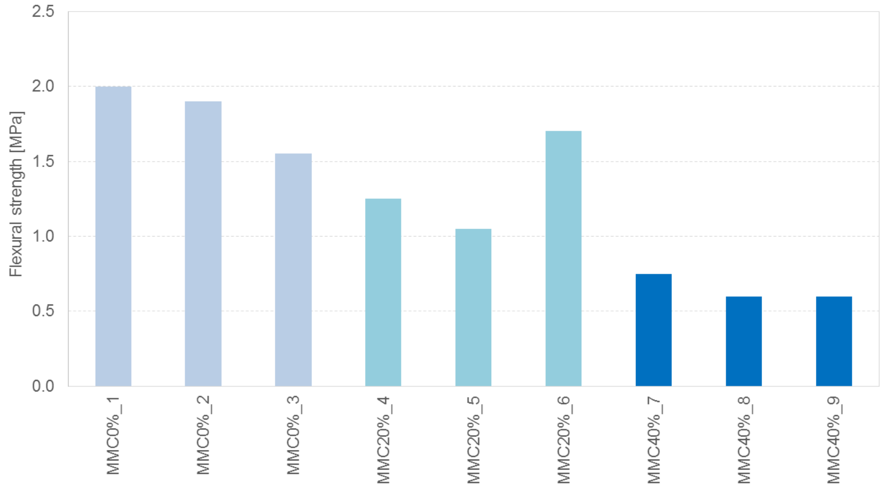

Figure 8.18 Flexural strength test results mortar for maturation curve (MMC_0%, MMC_20% and MMC_40%) after 10 days of age.

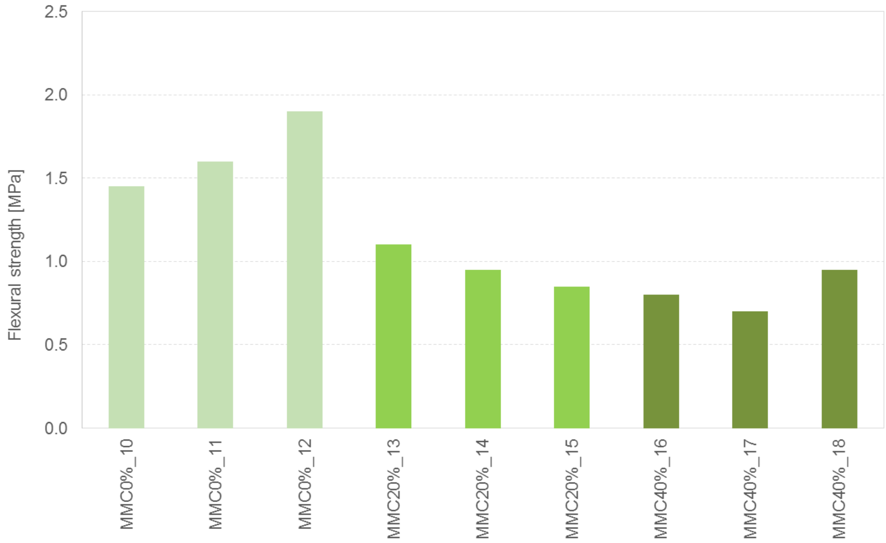

Figure 8.19 Flexural strength test results mortar for maturation curve (MMC_0%, MMC_20% and MMC_40%) after 20 days of age.

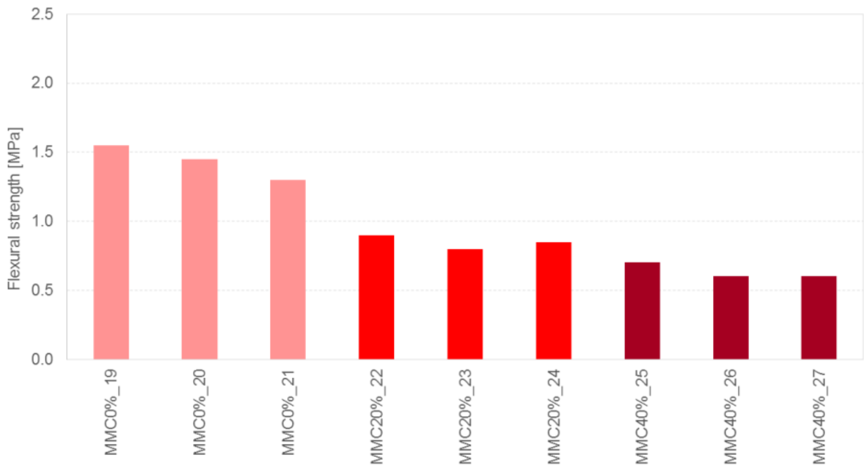

Figure 8.20 Flexural strength test results mortar for maturation curve (MMC_0%, MMC_20% and MMC_40%) after 28 days of age.

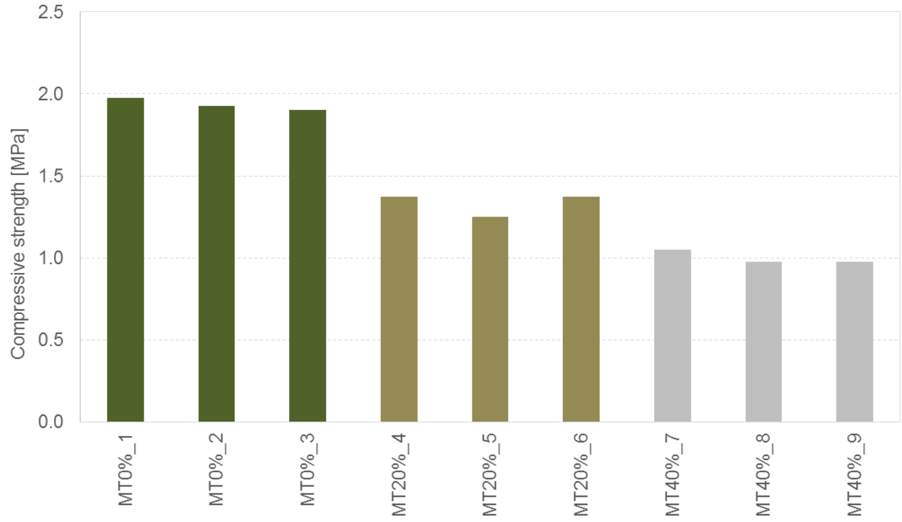

Figure 8.21 Compressive strength and modulus of elasticity test results for mortar test (MT_0%, MT_20% and MT_40%) after 6 days of age.

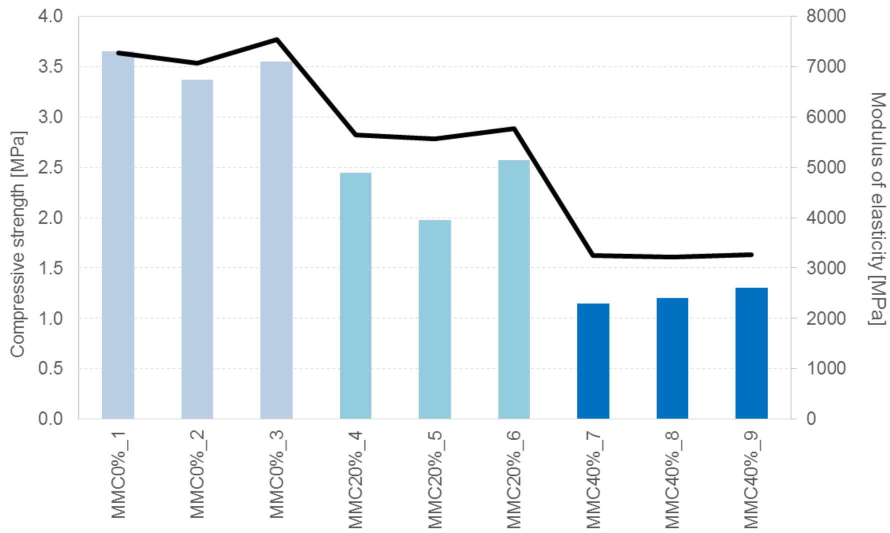

Figure 8.22 Compressive strength and modulus of elasticity test results for maturation curve (MMC_0%, MMC_20% and MMC_40%) after 10 days of age.

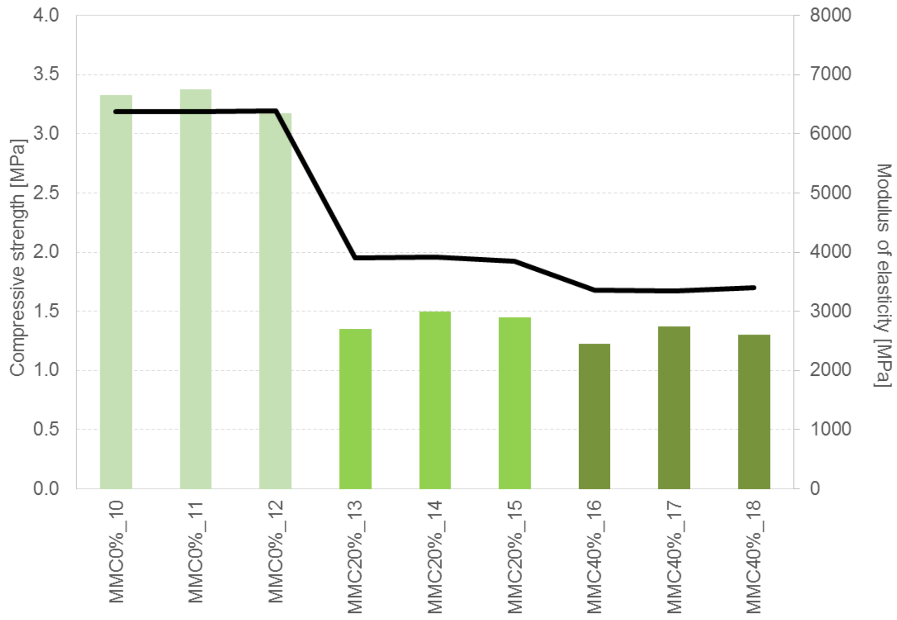

Figure 8.23 Compressive strength and modulus of elasticity test results for maturation curve (MMC_0%, MMC_20% and MMC_40%) after 20 days of age.

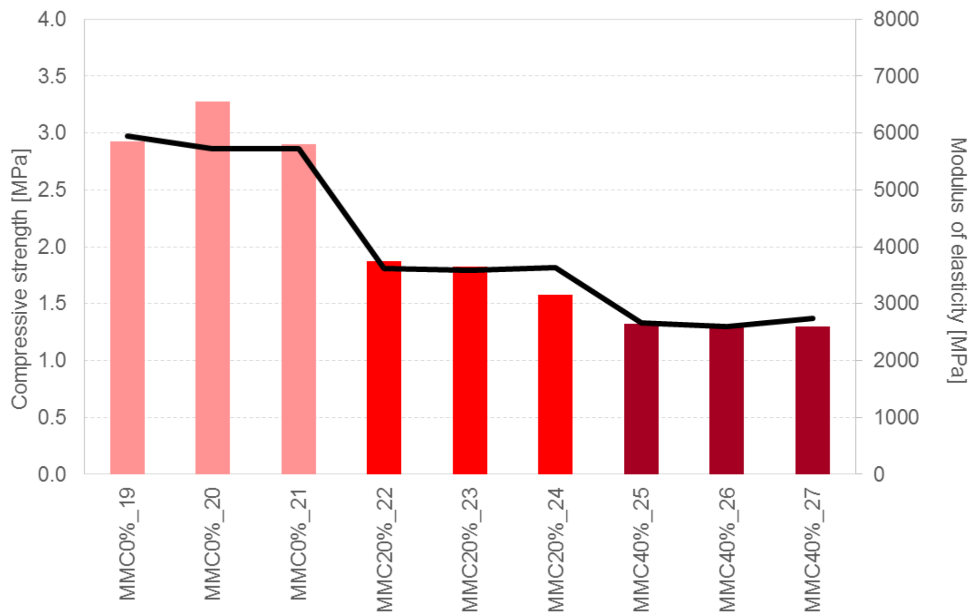

Figure 8.24 Compressive strength and modulus of elasticity test results for maturation curve (MMC_0%, MMC_20% and MMC_40%) after 28 days of age.

Table 8.12, Table 8.12 and Table 8.13 shows the summary of the averages of compressive and flexural strength obtained for the study mortars corresponding to 0%, 20% and 40% added sand.

Table 8.12 Summary of the compressive and flexural strength averages obtained for the study mortars with 0% added sand for different ages.

	Compressive strength of mortars with 0% added sand			Flexural strength of mortars with 0% added sand		
Age of study mortars	Average [MPa]	Standard deviation [MPa]	Coefficient of variation [-]	Average [MPa]	Standard deviation [MPa]	Coefficient of variation [-]
6 days (MT)	1.93	0.09	0.045	0.83	0.12	0.139
10 days (MMC)	3.53	0.19	0.055	1.82	0.24	0.130
20 days (MMC)	3.29	0.17	0.050	1.65	0.23	0.139
28 days (MMC)	3.03	0.28	0.094	1.43	0.13	0.088

Table 8.13 Summary of the compressive and flexural strength averages obtained for the study mortars with 20% added sand for different ages.

	Compressive strength of mortars with 20% added sand			Flexural strength of mortars with 20% added sand		
Age of study mortars	Average [MPa]	Standard deviation [MPa]	Coefficient of variation [-]	Average [MPa]	Standard deviation [MPa]	Coefficient of variation [-]
6 days (MT)	1.33	0.07	0.051	0.65	0.09	0.133
10 days (MMC)	2.33	0.37	0.158	1.33	0.33	0.250
20 days (MMC)	1.43	0.16	0.110	0.97	0.13	0.130
28 days (MMC)	1.76	0.15	0.087	0.85	0.05	0.059

Table 8.14 Summary of the compressive and flexural strength averages obtained for the study mortars with 40% added sand for different ages.

	Compressive strength of mortars with 40% added sand			Flexural strength of mortars with 40+% added sand		
Age of study mortars	Average [MPa]	Standard deviation [MPa]	Coefficient of variation [-]	Average [MPa]	Standard deviation [MPa]	Coefficient of variation [-]
6 days (MT)	1.00	0.05	0.055	0.67	0.10	0.156
10 days (MMC)	1.22	0.10	0.081	0.65	0.09	0.133
20 days (MMC)	1.30	0.12	0.091	0.82	0.13	0.154
28 days (MMC)	1.31	0.04	0.029	0.63	0.06	0.091

Figure 8.25 shows the maturation curve over time for the flexural strengths of MMC and MT mortars. Figure 8.26 shows the maturation curve over time for the compression strengths of MMC and MT mortars.

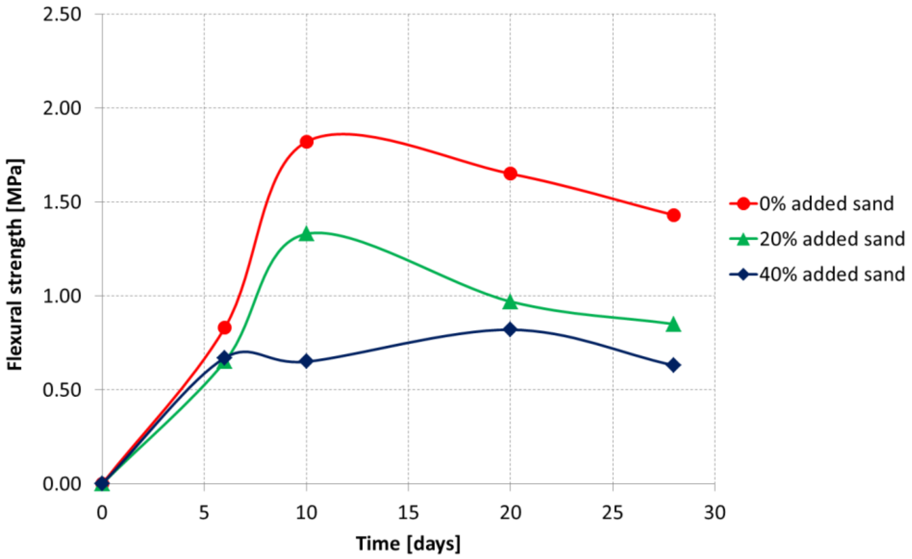

Figure 8.25 Maturation curve over time for the flexural strengths of MMC and MT mortars.

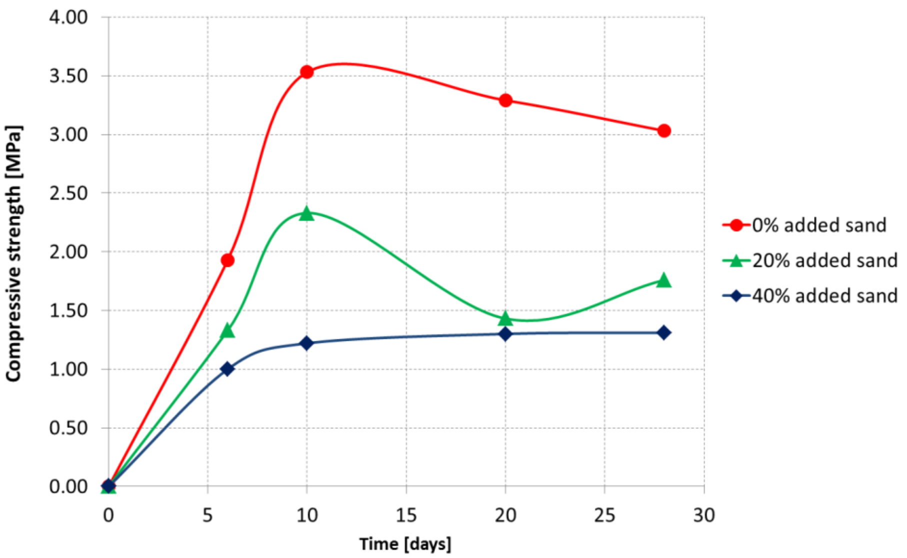

Figure 8.26 Maturation curve over time for the compressive strengths of MMC and MT mortars.

8.2.10 Characterisation and identification of samples of collected mortar before hardening

The study mortar samples were tested in the morning of the beginning of the process to evaluate mortar strength at the age of 6 days. In case the results were showing that the mortar was too strong to be used in the proportions given by the manufacturer, sand should have been added to control the strength of the product.

Based on the results at 6 days of the three types of mortar test previously studied (MT_0%, MT_20% and MT_40%) those responsible for the construction of the model decided which type of mortar to be used. It was pointed out that the results at 6 days may not faithfully reflect the mechanical properties since the hardening process is still at an early stage.

The selected mortar had the addition of 20% aggregate by volume of powder. Table 8.15**Error! Reference source not found.** shows the adopted percentage of water for the mortar. These values were measured by Dutch construction professionals that prepared the mortars and are presented in .

Table 8.15 Mortar composition adopted in the construction of the building prototype and the small assemblies

Mixture components	Quantity
Mortar powder	25.0 kg (1 bag)
Sand	3.7 kg
Water	3.9 kg
Water / powder mortar ratio	15.6 %

Samples of mortar were collected by LNEC technicians during the construction of the building prototype and the small specimens that were used in the characterization of the masonry joints (*wallettes* and *triplets*). The mixture was prepared *in situ* mixing mortar, water, and sand in the proportion given in Table 8.15. Figure 8.27 illustrates the construction of the building prototype in one of the phases in which the mortar samples were collected. Figure 8.28 illustrates the construction of masonry characterisation specimens.

Figure 8.27 Construction of the building prototype at the time of collection of mortar samples.

Figure 8.28 Construction of characterisation specimens at the time of mortar sampling.

Samples were collected from two different batches of the mixture every day during the construction week (duration six days). This resulted in a total of eleven collections (named as MC, followed by an identification number): nine from the mortar used to build the house and two from the construction of the masonry assemblies. The samples collected from the mortar mixed for the construction of the prototype correspond to the following building locations as presented in Figure 8.29:

- MC1 and MC2 were collected during the construction of the East facade and the easternmost portion of the South facade involving parts of the masonry walls below the openings and below the lintels, respectively;
- MC3 was taken from the mortar used for building the interior wall;
- MC4 was taken from the batch used to build the lower half of the squat pier and the chimney of the South wall and the low parts of the West wall;
- MC5 and MC6 were representative of the mortar used to build the masonry piers of the North façade and the rest of the West wall up to the level of the floor;
- MC8 mortar was used for the construction of the West gable wall;
- MC10 was the mortar used in building the East gable wall;
- MC11 was taken from the mortar used to build the South chimney.

Mortar samples MC7 and MC9 were collected during the building of the small masonry components as presented in Figure 8.30, in particular:

- MC7 was taken from a mortar batch prepared to build the 16 masonry *wallettes* to be subjected to compression and the 16 triplets to be tested in shear;
- MC9 was collected while building the eight *wallettes* for the out-of-plane bending tests and the doublets and triplets built for the torsional-shear tests and the bond wrench tests, respectively.

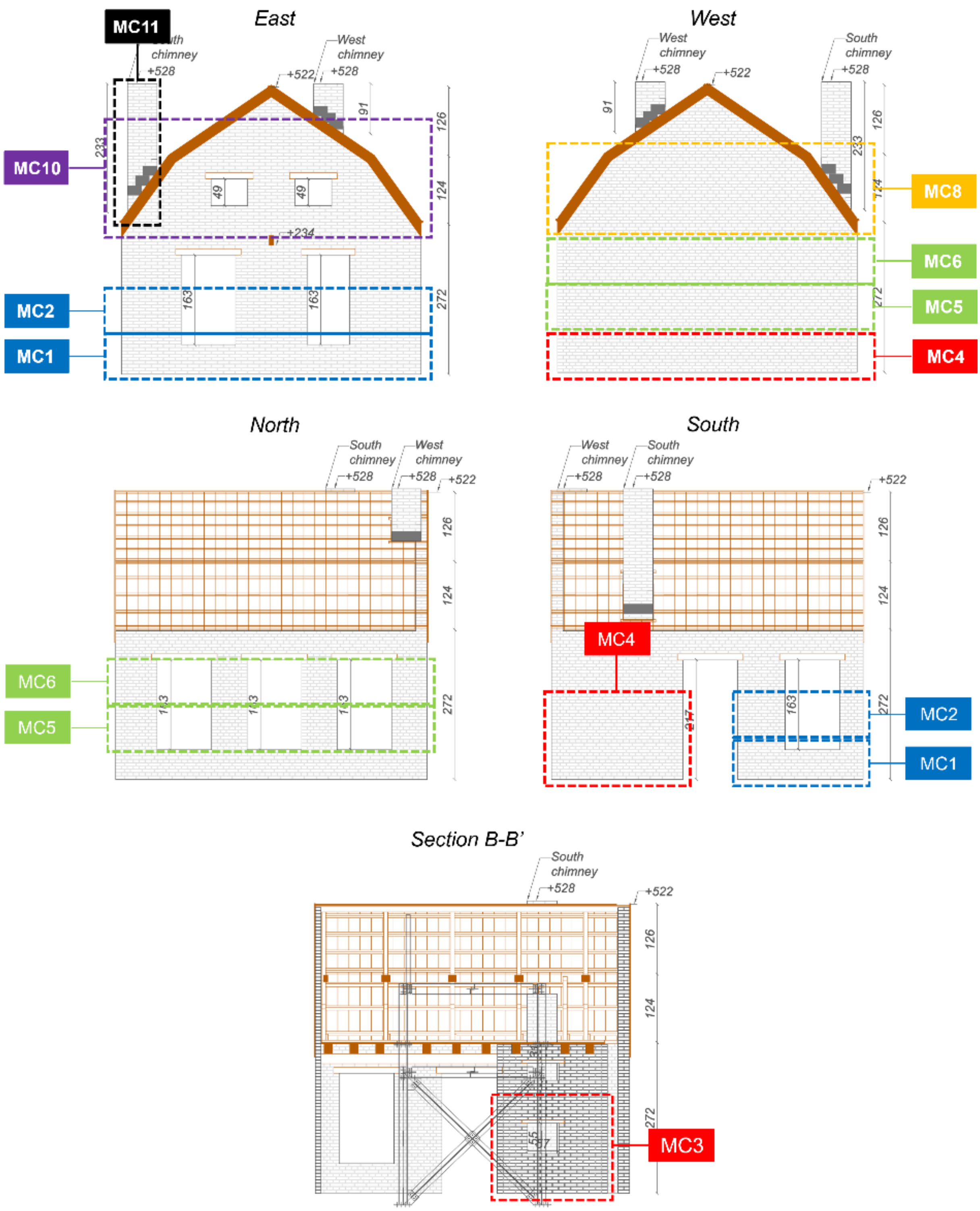

Figure 8.29 Mortar sampling from the construction of the building prototype

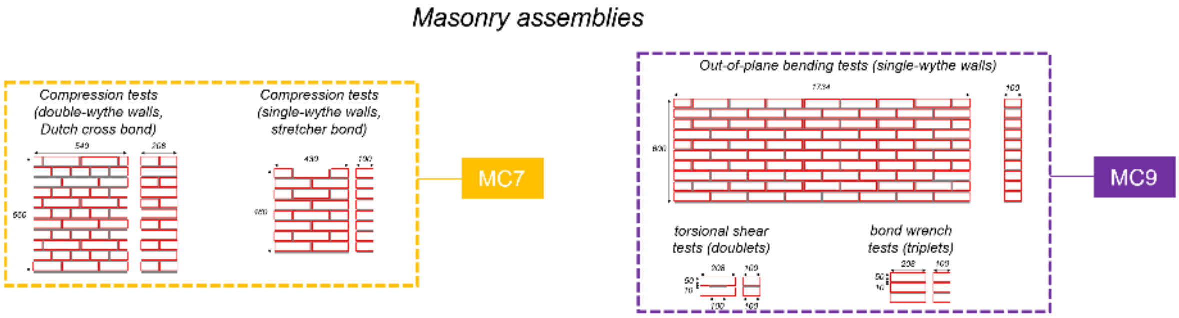

Figure 8.30 Mortar sampling from the construction of the small masonry assemblies

The samples were cast into standard moulds, and the resulting prisms had dimensions of 160 mm × 40 mm × 40 mm as presented in Figure 8.5 of sub-chapter 8.2.4. Four moulds were cast every time mortar was collected (i.e., twelve prisms). Tests were performed for one month to obtain estimates of the dynamic modulus of elasticity, flexural strength and compressive strength of mortar for three testing ages: 10, 20 and 28 days and during the seismic test of building prototype (approximately 50 days). With the remaining specimens flexural strength and compressive strength tests were performed for all collected mortars while the seismic test for the building prototype was being performed.

The tests considered adequate for characterising these samples were:

- Tests for the determination of the bulk density of fresh mortar;
- Tests for the determination of the consistence of fresh mortar (by flow table).

8.2.11 Tests for the determination of the bulk density of fresh collected mortars

The adopted methodology for the determination of bulk density of fresh collected mortars is already described in sub-chapter 8.2.5. The results obtained for this test are given in Table 8.16.

Table 8.16 Results obtained for the determination of bulk density of fresh mortar for all samples collected.

Identification of the sample	Date of collect	m_1 [kg]	m_2 [kg]	Bulk density [kg/m^3]
MC_1	2018-02-05	0.463	2.2833	1.8203
MC_2	2018-02-05	0.463	2.2306	1.7676
MC_3	2018-02-06	0.463	2.2330	1.7700
MC_4	2018-02-06	0.463	2.2747	1.8117
MC_5	2018-02-07	0.463	2.1800	1.7170
MC_6	2018-02-07	0.463	2.2425	1.7795
MC_7	2018-02-08	0.463	2.2964	1.8334
MC_8	2018-02-08	0.463	2.1793	1.7163
MC_9	2018-02-09	0.463	2.2626	1.7996
MC_10	2018-02-09	0.463	2.1695	1.7065
MC_11	2018-02-10	0.463	2.3040	1.8410
			Average MC	**1.7784**
			Standard deviation MC	**0.0482**
			Coefficient of variation [-]	**0.027**

8.2.12 Tests for the determination of the consistence of fresh collected mortar (by flow table)

The adopted methodology for the determination of the consistence of fresh collected mortar is already described in sub-chapter 8.2.6. The results obtained for this test are given in Table 8.17.

Table 8.17 Results on the determination of the consistency of fresh mortar for all samples collected.

Identification of the sample	Date of collect	d_1 [mm]	d_2 [mm]	Consistency [mm]
MC_1	2018-02-05	157	158	158
MC_2	2018-02-05	165	163	164
MC_3	2018-02-06	160	164	162
MC_4	2018-02-06	163	165	164
MC_5	2018-02-07	149	157	153
MC_6	2018-02-07	170	164	167
MC_7	2018-02-08	163	157	160
MC_8	2018-02-08	160	168	164
MC_9	2018-02-09	151	143	147
MC_10	2018-02-09	156	158	157
MC_11	2018-02-10	164	167	166
			Average MC	**160.09**
			Standard deviation MC	**6.037**
			Coefficient of variation [-]	**0.038**

8.2.13 Characterisation and identification of specimens (hardened collected mortar)

After the samples were collected, they were used in the construction of the specimens to perform the physical and mechanical tests at three different ages: 10 days, 20 days and 28 days. These tests consist on determining the dynamic modulus of elasticity and determining the bending and compressive strengths. The storage of the specimens in a controlled environment followed the specifications of standard EN 1015-11:1999 "Methods of test for masonry – Part 11: Determination of flexural and compressive strength of hardened mortar" (EN 1015-11, 1999) which correspond to placing the mould in a plastic bag of polyethylene for 2 days, ensuring a relative humidity of 95 ± 5%, in a room conditioned at 20 ± 2 °C and a relative humidity of 65 ± 5%, as shown in Figure 8.31. Subsequently, the specimens were demoulded and kept under the aforementioned curing conditions for 5 days, after which the specimens were removed from the bag and remained in the same room (at 20 ± 2 °C and at a relative humidity of 65 ± 5%) until the date of the test. Figure 8.32 illustrates the reported curing conditions of some of the specimens.

Figure 8.31 Part of mortar specimens.

Figure 8.32 Curing conditions of mortar specimens.

The designation of the specimens is the same used in the samples, but with an underscore and a number identifying each specimen. The characteristics of the various specimens are presented in Appendix F.

The bulk density average values for the collected mortar specimens are given in Table 8.18, with additional details also provided in Appendix F

Table 8.18 Bulk density for collected mortar specimens selected for the tests.

Specimen	Average bulk density [kg/m^3]	Standard deviation [kg/m^3]	Coefficient of variation [-]
MC	1616.17	55.97	0.035

Since the tests for the determination of the dynamic modulus of elasticity are non-destructive, the same specimens were also used for the bending and compression strength tests.

The selected tests for these samples were, thus:

- Tests to determine the dynamic modulus of elasticity;
- Tests for determination of flexural and compression strengths.

8.2.14 Tests for the determination of dynamic modulus of elasticity of collected mortar

The adopted methodology for the determination of dynamic modulus of elasticity of collected mortar is already described in sub-chapter 8.2.8. In order to establish a relation between the days of maturation and the mechanical properties of the mortar, the results of the tests for the determination of the dynamic modulus of elasticity for 10 days, 20 days, 28 days of age and during the seismic test of building prototype (approximately 50 days) are presented in detail in Appendix F. Figure 8.33 to Figure 8.36 show the mortars collected directly from the building prototype and Figure 8.37 to Figure 8.40 represent the mortars from the characterisation specimens, in which each colour represents a single mortar collection.

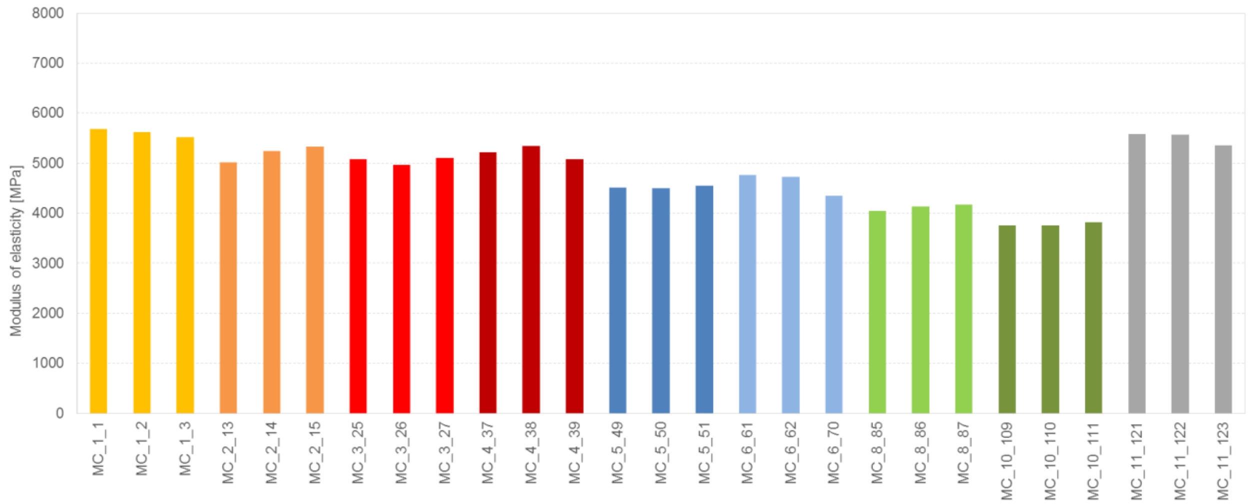

Figure 8.33 Test results for the determination of the dynamic modulus of elasticity for the mortars collected directly from the building prototype after 10 days of age.

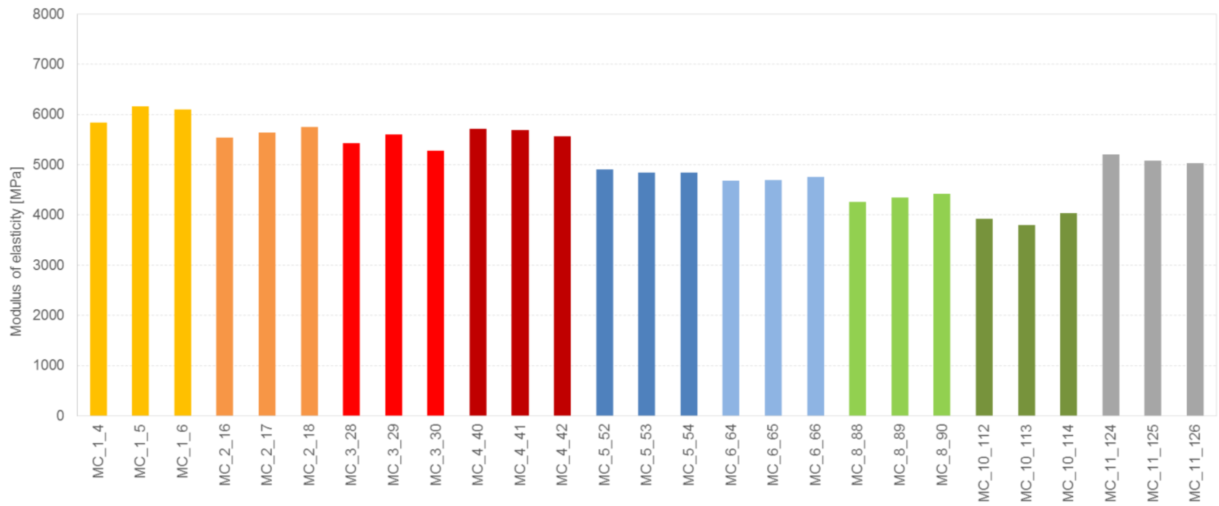

Figure 8.34 Test results for the determination of the dynamic modulus of elasticity for the mortars collected directly from the building prototype after 20 days of age.

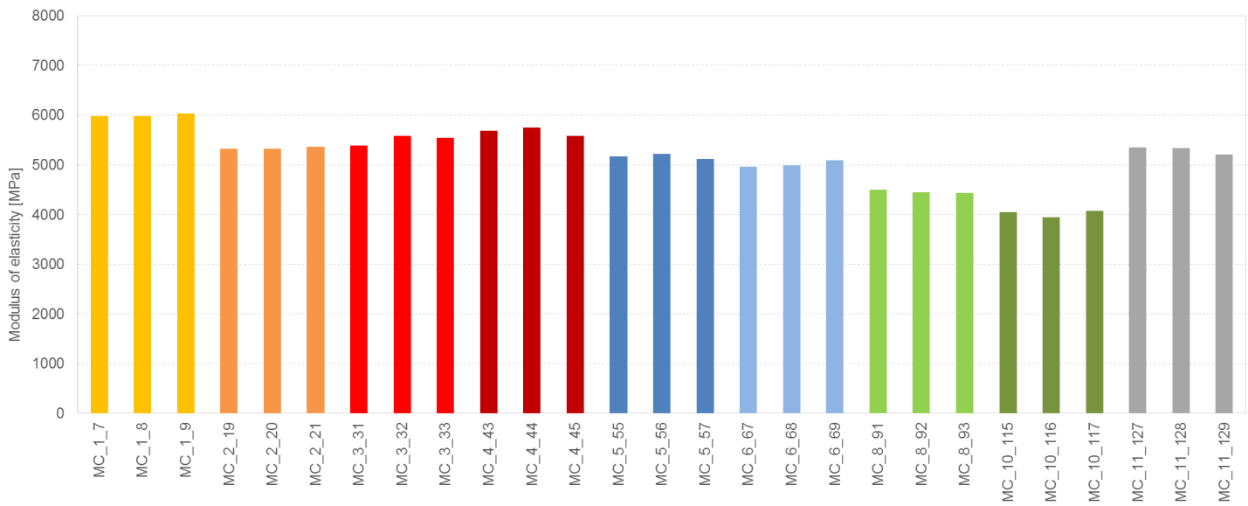

Figure 8.35 Test results for the determination of the dynamic modulus of elasticity for the mortars collected directly from the building prototype after 28 days of age.

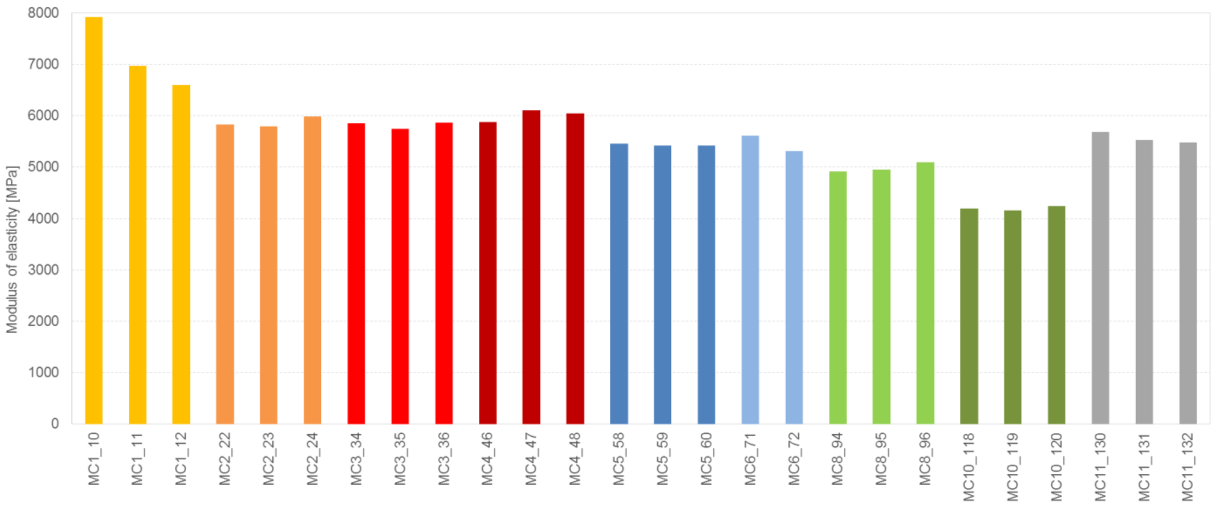

Figure 8.36 Test results for the determination of the dynamic modulus of elasticity for the mortars collected directly from the building prototype during the seismic test.

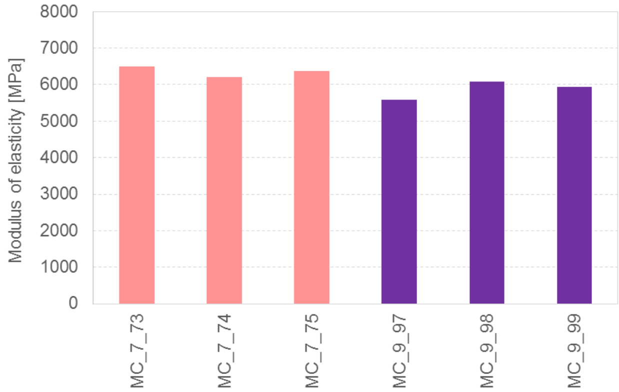

Figure 8.37 Test results for the determination of the dynamic modulus of elasticity for the mortars collected directly from the characterisation specimens after 10 days of age.

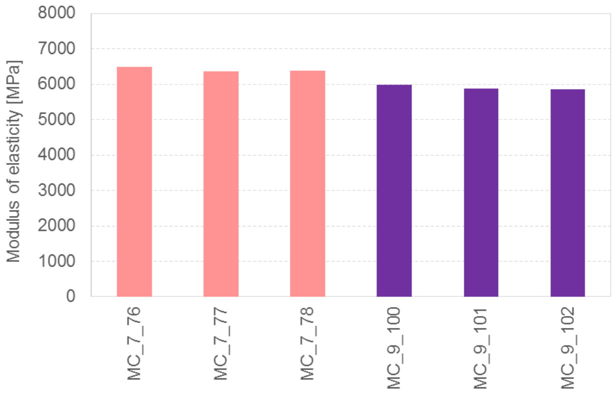

Figure 8.38 Test results for the determination of the dynamic modulus of elasticity for the mortars collected directly from the characterisation specimens after 20 days of age.

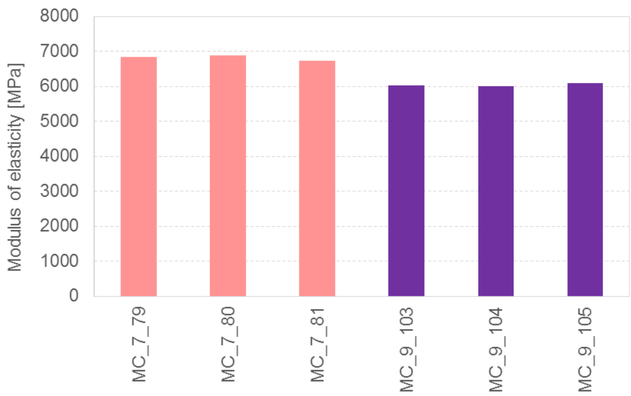

Figure 8.39 Test results for the determination of the dynamic modulus of elasticity for the mortars collected directly from the characterisation specimens after 28 days of age.

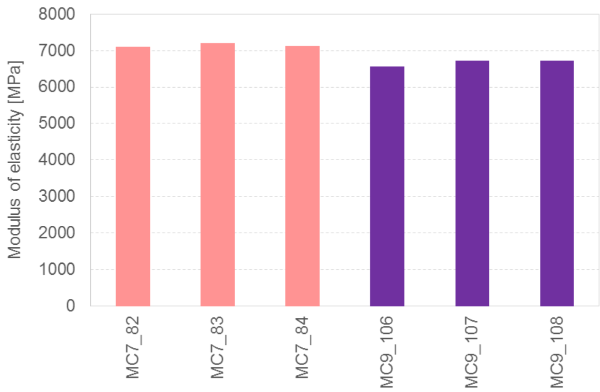

Figure 8.40 Test results for the determination of the dynamic modulus of elasticity for the mortars collected directly from the characterisation specimens during the seismic test.

Figure 8.41 presents the distribution of the dynamic modulus of elasticity of collected mortars after 28 days of age.

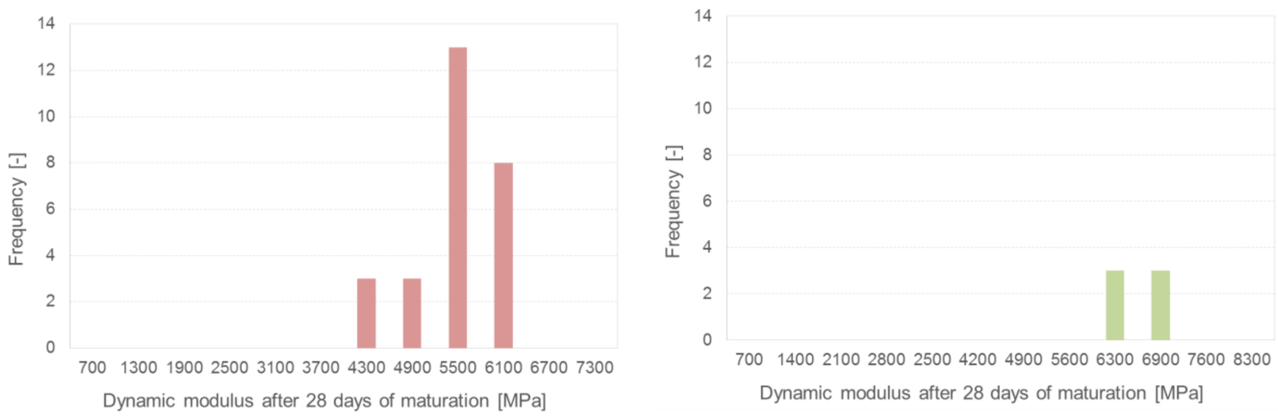

Specimens collected directly from building prototype

Specimens collected directly from characterisation specimens

Figure 8.41 Distribution of the dynamic modulus of elasticity of collected mortars after 28 days of age.

Table 8.19 presents a summary of the average dynamic modulus of elasticity obtained for the mortars collected directly from the building prototype and the characterisation specimens.

Table 8.19 Summary of the average dynamic modulus of elasticity obtained for the two types of bedding mortar collected directly from the full-scale model for the different ages.

Age of mortar	Dynamic modulus of elasticity of specimens collected directly from building prototype			Dynamic modulus of elasticity of specimens collected directly from characterisation specimens		
	Average [MPa]	Standard deviation [MPa]	Coefficient of variation [-]	Average [MPa]	Standard deviation [MPa]	Coefficient of variation [-]
10 days	4844	611	0.126	6114	326	0.053
20 days	5079	665	0.131	6155	283	0.046
28 days	5162	586	0.113	6432	428	0.067
50 days	5615	812	0.145	6903	266	0.038

The plot of Figure 8.42 shows the relation of the dynamic modulus of elasticity of the collected mortar as a function of maturation time. The dashed lines refer to the modulus of elasticity of the bedding mortars taken from the characterisation test specimens. The continuous lines refer to the dynamic modulus of elasticity of the bedding mortars taken from building prototype.

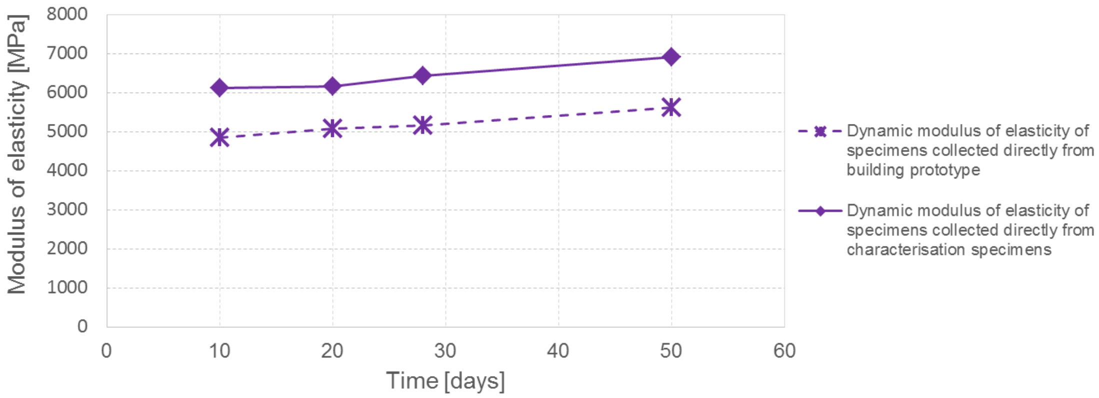

Figure 8.42 Relation between dynamic modulus of elasticity and maturation time for the bedding mortars removed from the building prototype and the characterisation test specimens.

8.2.15 Tests for the determination of flexural and compressive strengths of collected mortar

The adopted methodology for the determination of flexural and compressive strengths of collected mortar is already described in sub-chapter 8.2.9. In order to establish a relation between the days of maturation time and the mechanical properties of the mortars, Figure 8.43 to Figure 8.50 show the test results of flexural strengths of collected mortar for 10 days, 20 days, 28 days of age and during the seismic test of building prototype (approximately 50 days) in which each colour represents a single mortar collection. In the plots of Figure 8.51 to Figure 8.58 the compressive strength is represented with bars, in which each colour represents a single mortar collection, and the value of the modulus of elasticity for the corresponding specimens is represented by a line for all collected mortars. Additional results are given in Appendix F.

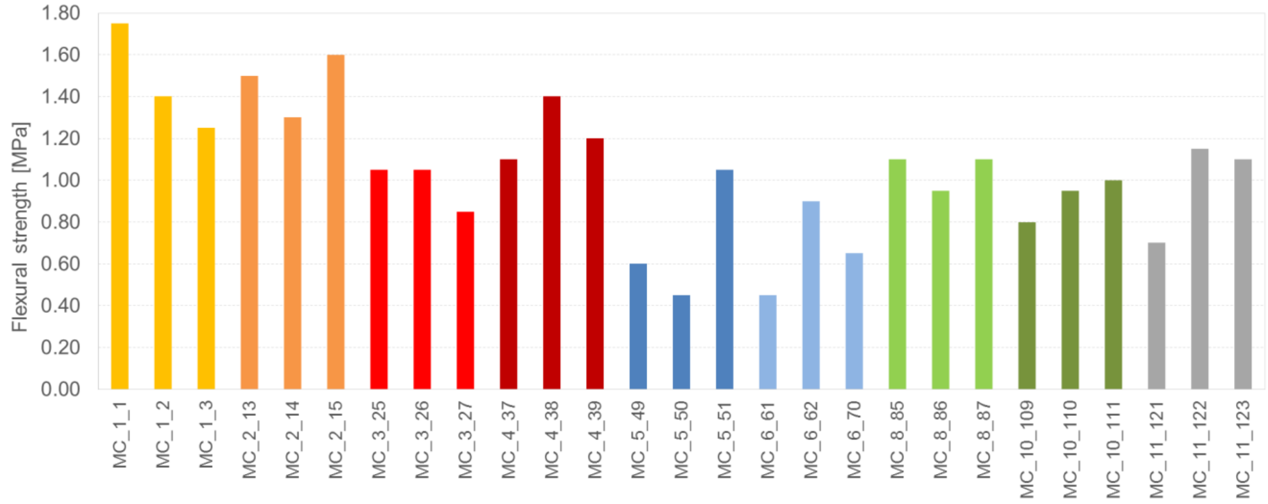

Figure 8.43 Flexural strength test results for the mortars collected directly from the building prototype after 10 days of age.

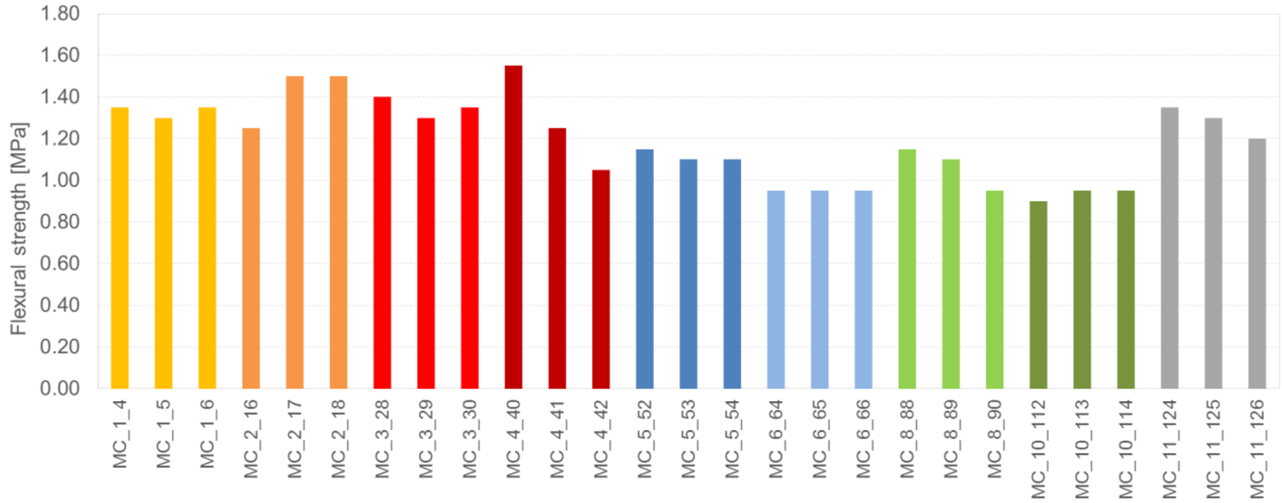

Figure 8.44 Flexural strength test results for the mortars collected directly from the building prototype after 20 days of age.

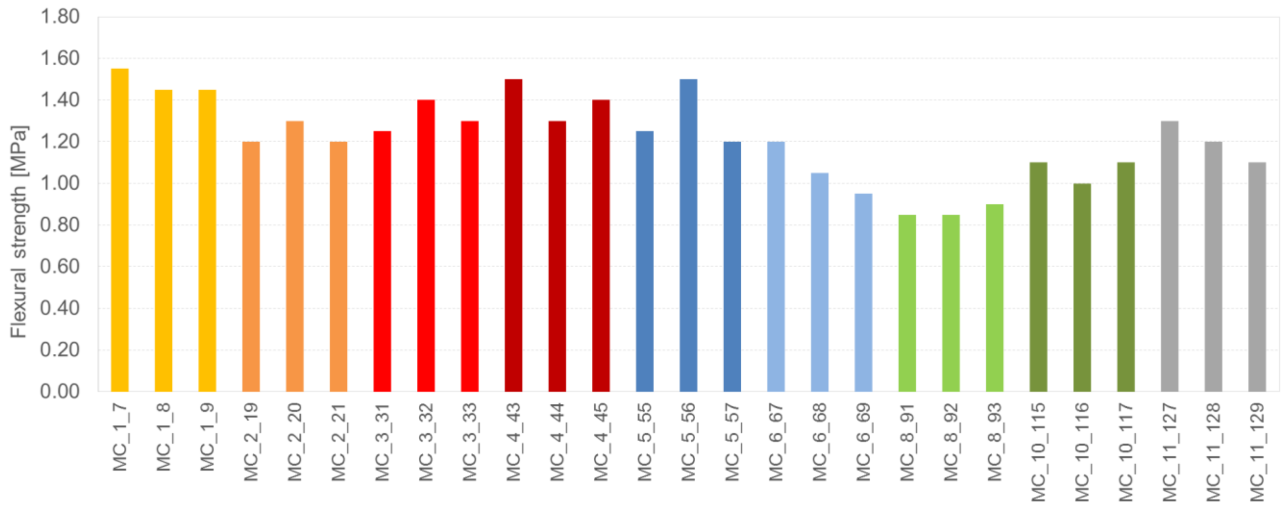

Figure 8.45 Flexural strength test results for the mortars collected directly from the building prototype after 28 days of age.

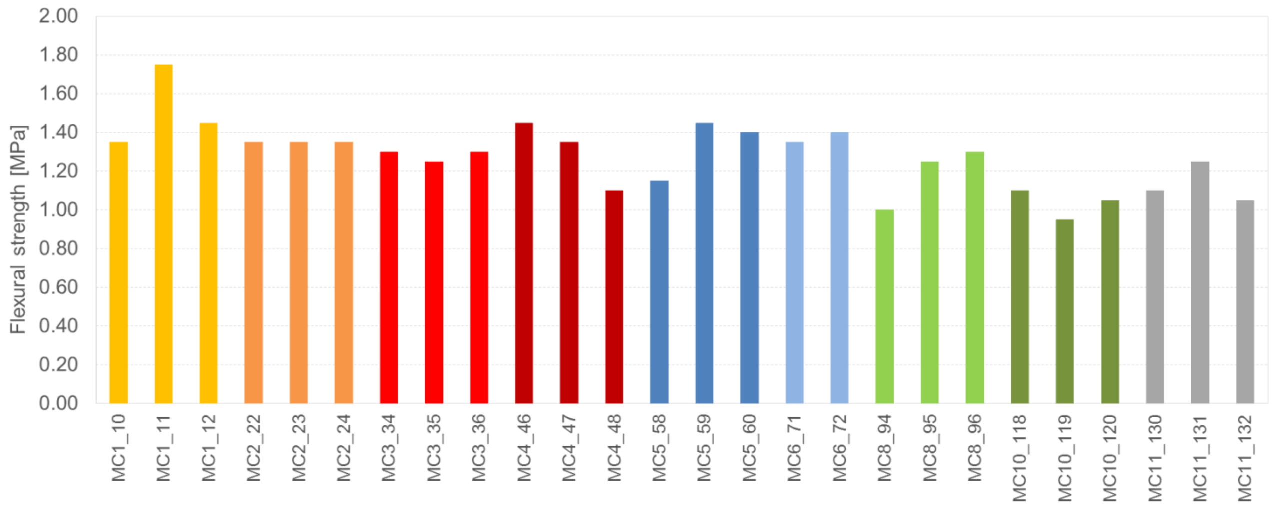

Figure 8.46 Flexural strength test results for the mortars collected directly from the building prototype during the seismic test.

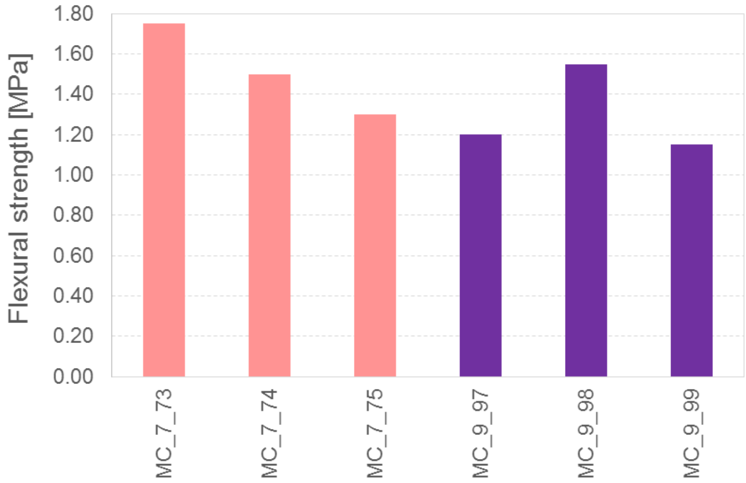

Figure 8.47 Flexural strength test results for the mortars collected directly from the characterisation specimens after 10 days of age.

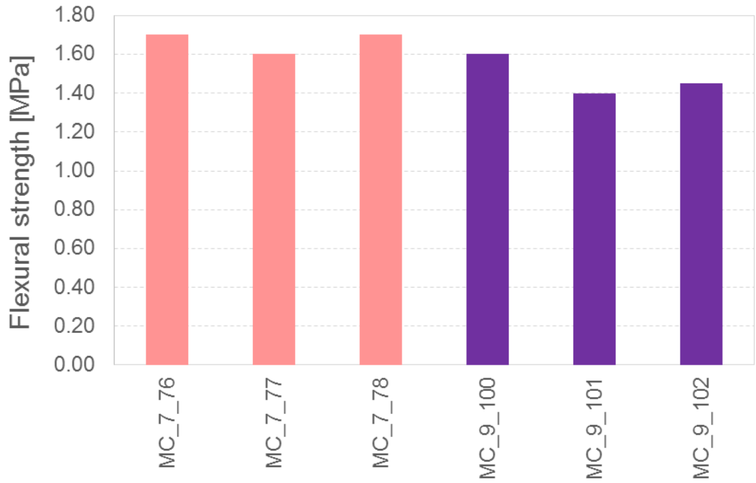

Figure 8.48 Flexural strength test results for the mortars collected directly from the characterisation specimens after 20 days of age.

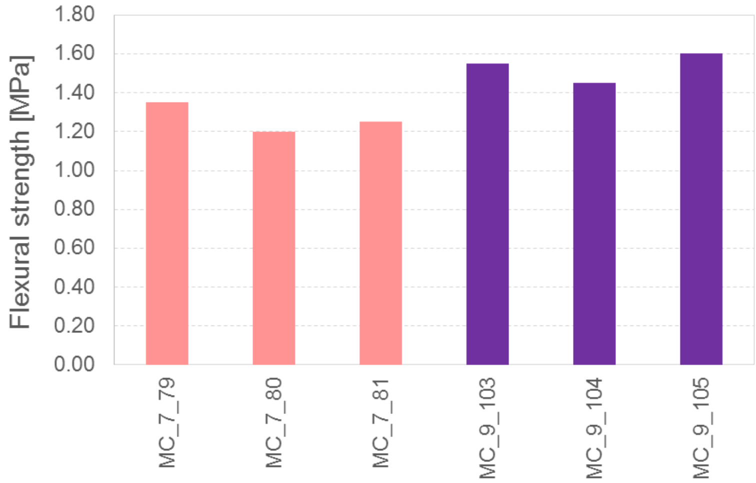

Figure 8.49 Flexural strength test results for the mortars collected directly from the characterisation specimens after 28 days of age.

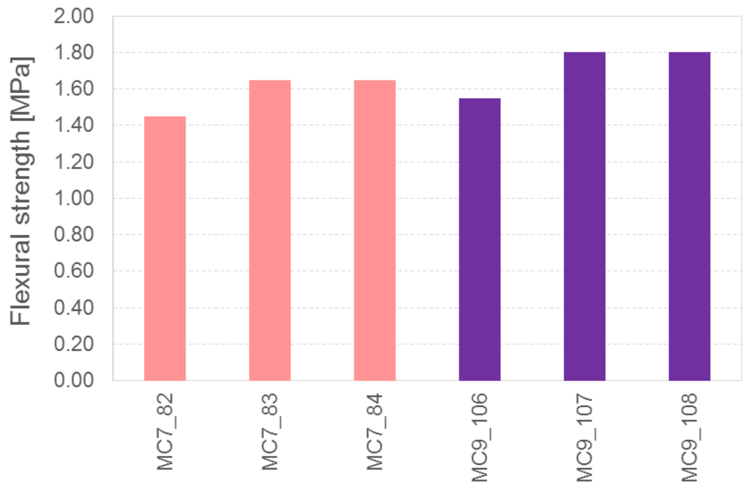

Figure 8.50 Flexural strength test results for the mortars collected directly from the characterisation specimens during the seismic test.

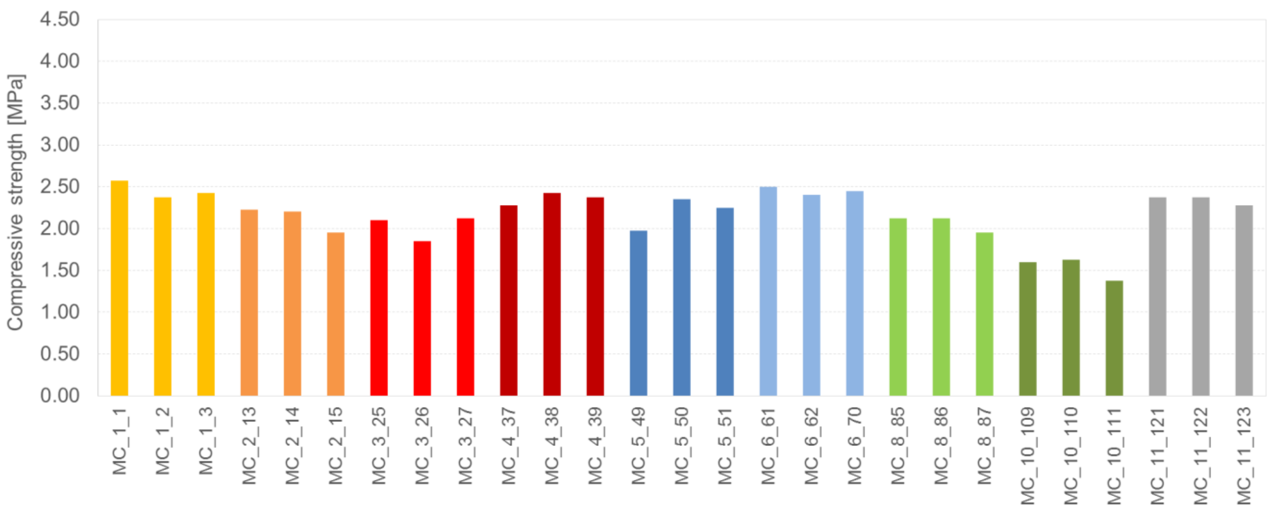

Figure 8.51 Compressive strength and modulus of elasticity test results for the mortars collected directly from the building prototype after 10 days of age.

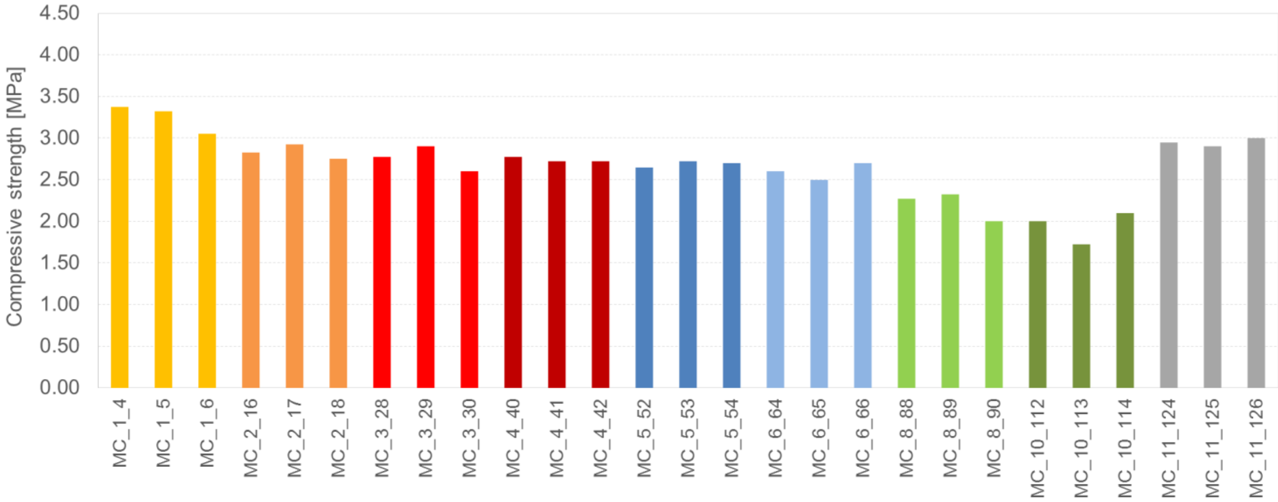

Figure 8.52 Compressive strength and modulus of elasticity test results for the mortars collected directly from the building prototype after 20 days of age.

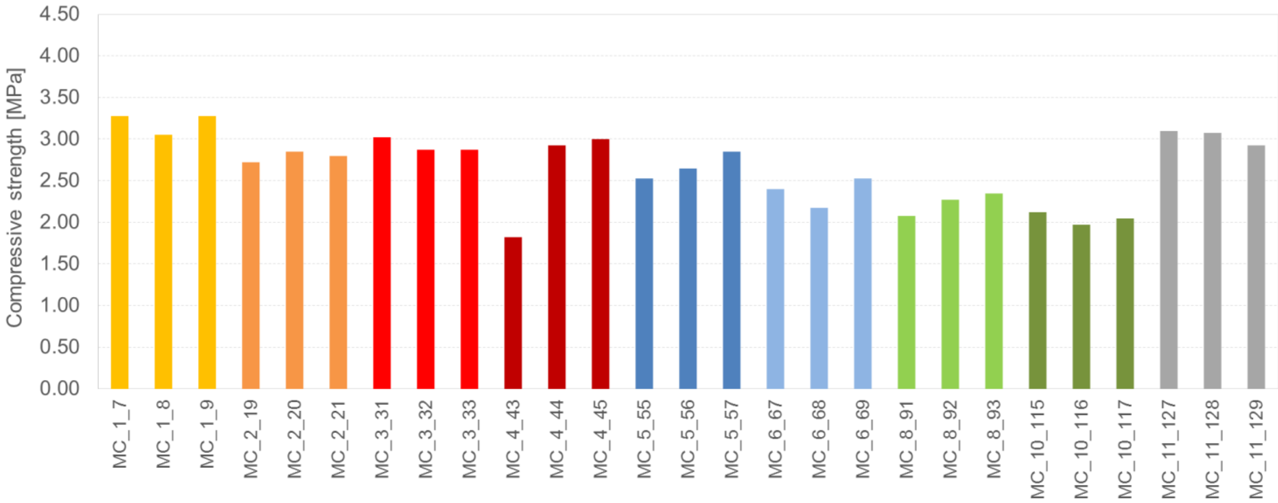

Figure 8.53 Compressive strength and modulus of elasticity test results for the mortars collected directly from the building prototype after 28 days of age.

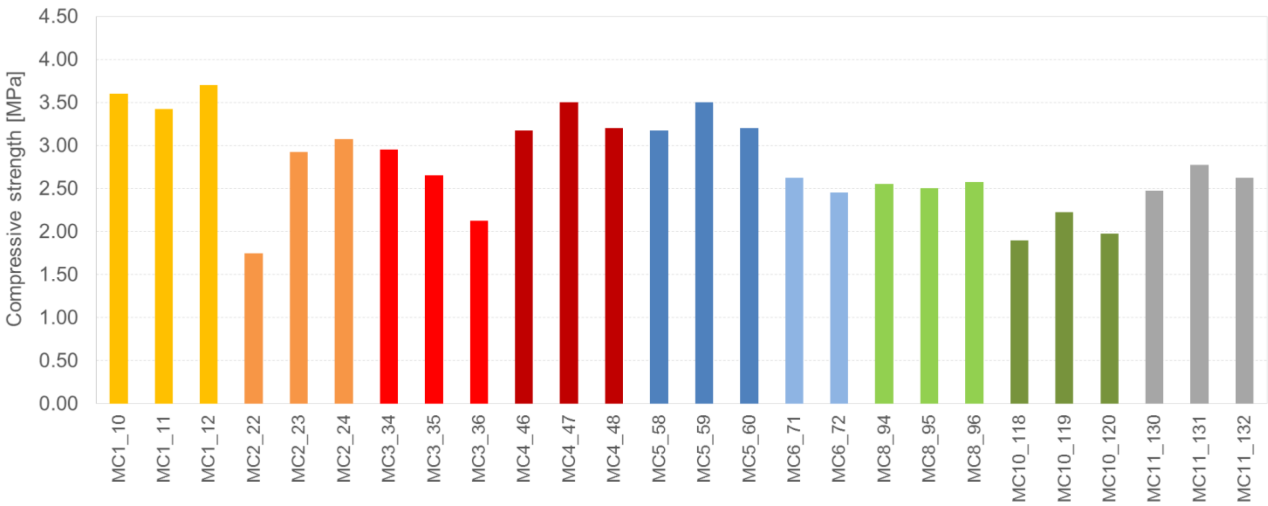

Figure 8.54 Compressive strength and modulus of elasticity test results for the mortars collected directly from the building prototype during the seismic test.

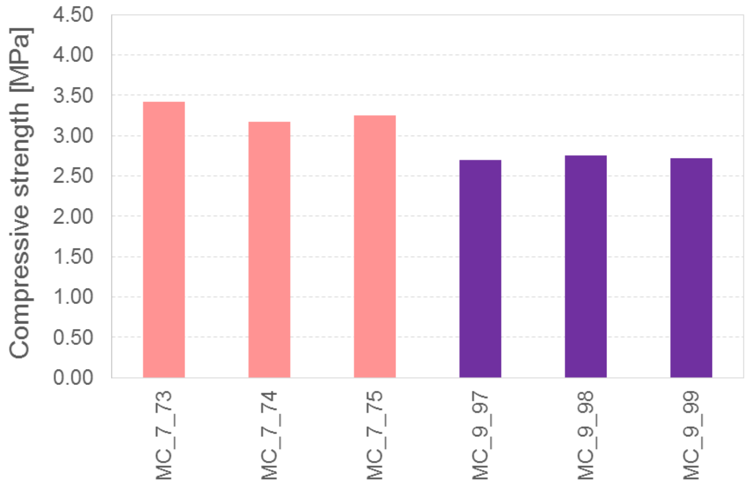

Figure 8.55 Compressive strength and modulus of elasticity test results for the mortars collected directly from the characterisation specimens after 10 days of age.

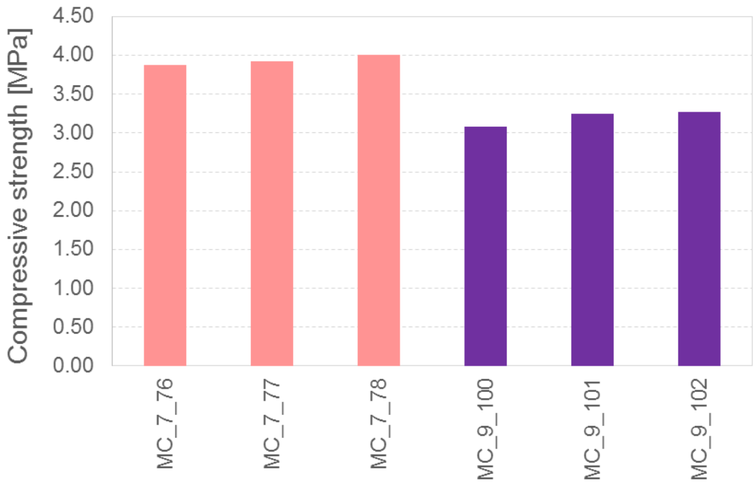

Figure 8.56 Compressive strength and modulus of elasticity test results for the mortars collected directly from the characterisation specimens after 20 days of age.

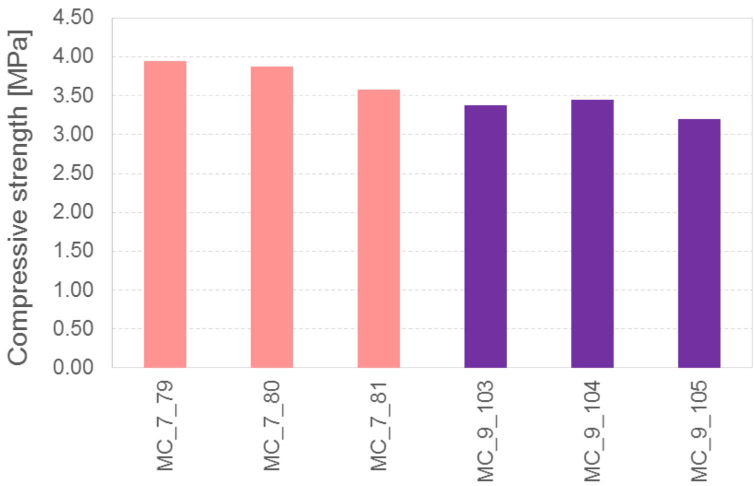

Figure 8.57 Compressive strength and modulus of elasticity test results for the mortars collected directly from the characterisation specimens after 28 days of age.

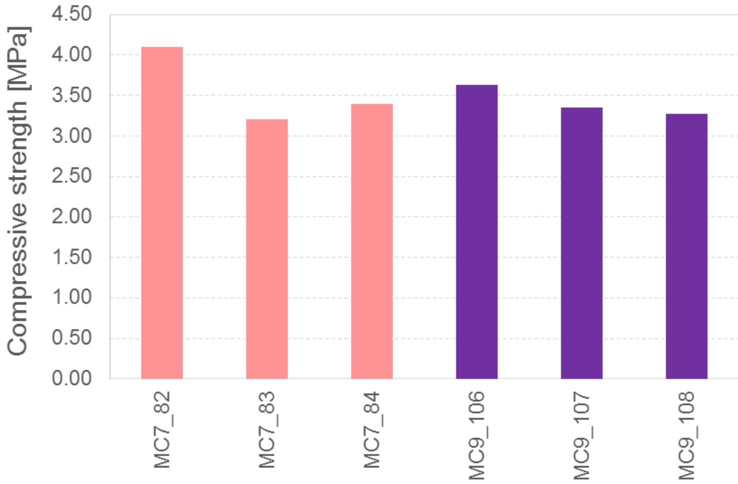

Figure 8.58 Compressive strength and modulus of elasticity test results for the *mortars collected directly from the characterisation specimens during the seismic test.*

Figure 8.59 and Figure 8.60 presents the distribution of the flexural and compressive strengths of collected mortars after 28 days of age.

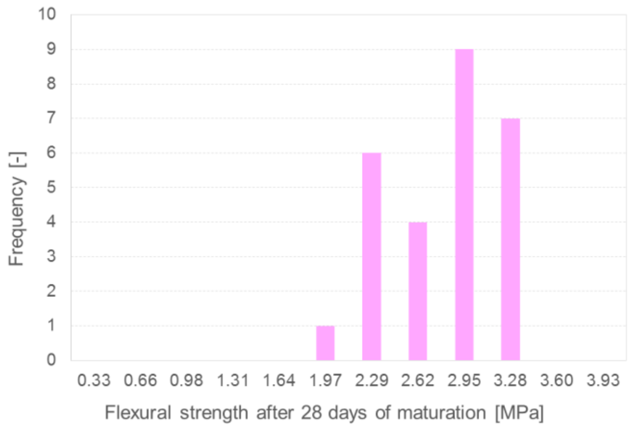

Specimens collected directly from building prototype

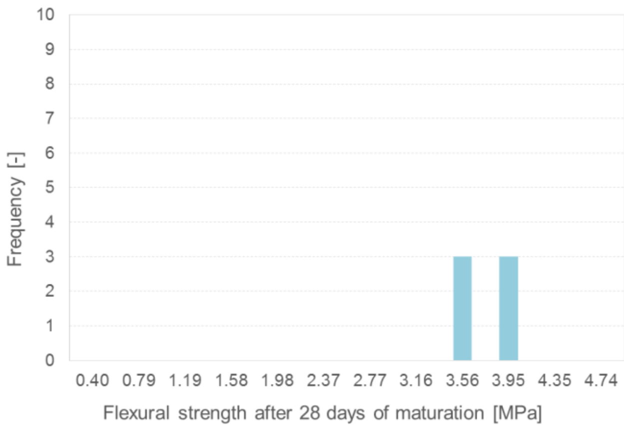

Specimens collected directly from characterisation specimens

Figure 8.59 Distribution of the flexural strength of collected mortars after 28 days of age.

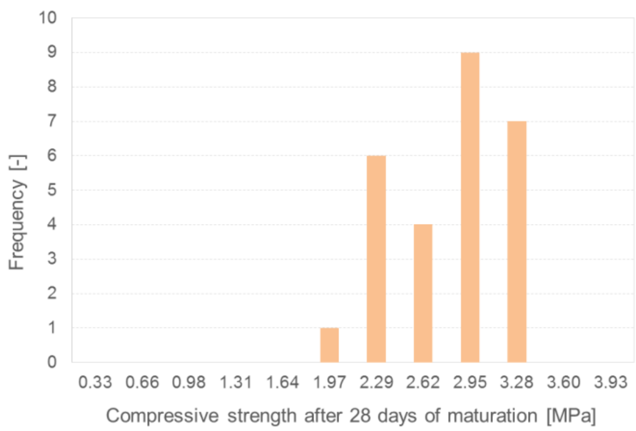

Specimens collected directly from building prototype

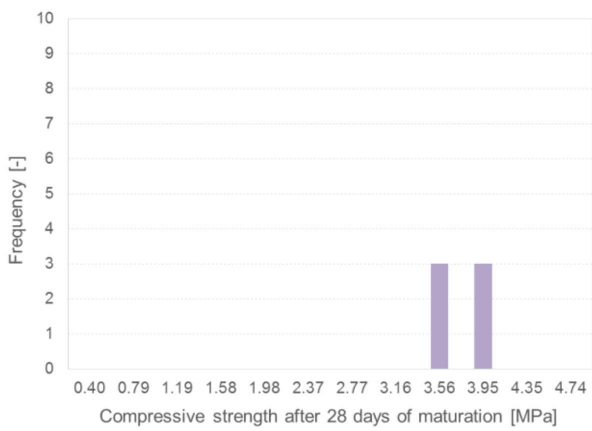

Specimens collected directly from characterisation specimens

Figure 8.60 Distribution of the compressive strength of collected mortars after 28 days of age.

Table 8.20 and Table 8.21 present a summary of the averages of compressive and flexural strength obtained for the mortars collected directly from the building prototype and the characterisation specimens.

Table 8.20 Summary of the flexural strength averages obtained for the bedding mortar collected directly from the full-scale model for the different ages.

Age of mortar	Flexural strength of specimens collected directly from building prototype			Flexural strength of specimens collected directly from characterisation specimens		
	Average [MPa]	Standard deviation [MPa]	Coefficient of variation [-]	Average [MPa]	Standard deviation [MPa]	Coefficient of variation [-]
10 days	1.05	0.32	0.308	1.41	0.23	0.164
20 days	1.19	0.19	0.163	1.58	0.13	0.080
28 days	1.22	0.20	0.164	1.40	0.16	0.115
50 days	1.28	0.18	0.138	1.65	0.14	0.084

Table 8.21 Summary of the compressive strength averages obtained for the bedding mortar collected directly from the full-scale model for the different ages.

Age of mortar	Compressive strength of specimens collected directly from building prototype			Compressive strength of specimens collected directly from characterisation specimens		
	Average [MPa]	Standard deviation [MPa]	Coefficient of variation [-]	Average [MPa]	Standard deviation [MPa]	Coefficient of variation [-]
10 days	2.17	0.33	0.151	3.00	0.31	0.104
20 days	2.66	0.40	0.151	3.57	0.41	0.114
28 days	2.65	0.50	0.187	3.57	0.30	0.084
50 days	2.79	0.60	0.214	3.49	0.54	0.154

The plot of Figure 8.61 and Figure 8.62 shows the relation of the compressive and flexural strength as a function of maturation time. The dashed lines refer to the flexural and compressive strength of the bedding mortars taken from the characterisation test specimens. The continuous lines refer to the flexural and compressive strengths of the bedding mortars taken from building prototype.

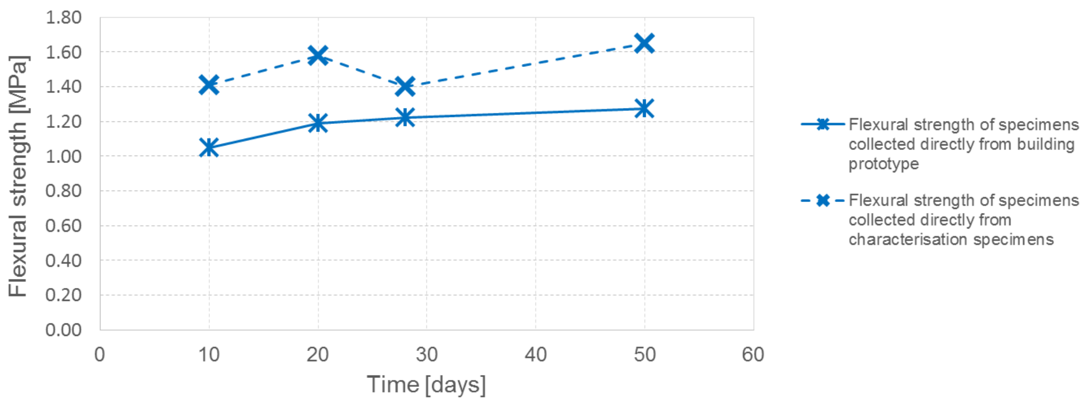

Figure 8.61 Relation between flexural strength and maturation time for the bedding mortars removed from the building prototype and the characterisation test specimens.

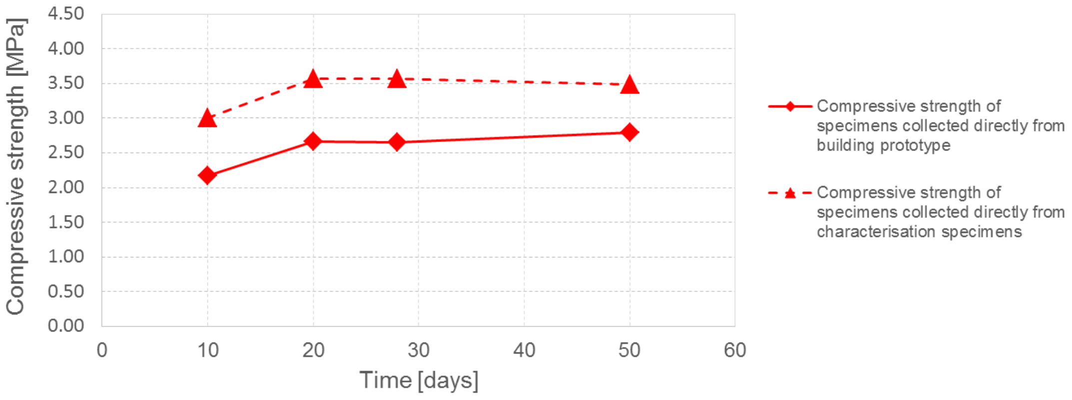

Figure 8.62 Relation between compressive strength and maturation time for the bedding mortars removed from the building prototype and the characterisation test specimens.

8.3 Solid clay bricks characterisation tests

8.3.1 Characterisation and identification of specimens

The masonry walls are composed of solid clay bricks with approximate dimensions of 210 mm long, 100 mm wide and 45 mm high, as illustrated in Figure 8.63.

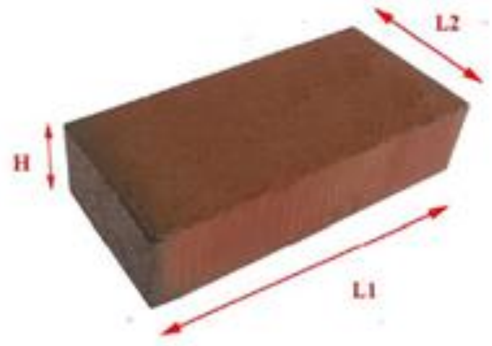

Figure 8.63 Solid clay unit used on masonry walls.

Several specimens were collected and selected from the material used for the construction of the building prototype and the characterisation specimens. The specimens collected were more than 30 days inside the premises of the laboratory units without specific packaging until the date of the test. The designation of the bricks is BSCL (Bricks Solid Clay).

In Table 8.22 the characteristics of the solid clay bricks specimens selected for the tests are presented, with additional details provided in Appendix G.

Table 8.22 Characteristics of the solid clay bricks selected for the tests.

Type of specimen	Average Mass [kg]	Average Length (L1) [mm]	Average Width (L2) [mm]	Average Height (H) [mm]
BSCL	2121.50	0.2126	0.1015	0.0467

The bulk density average values for the solid clay bricks are given in Table 8.23, with additional details also provided in Appendix G

Table 8.23 Bulk density for solid clay bricks selected for the tests.

Specimen	Average bulk density [kg/m^3]	Standard deviation [kg/m^3]	Coefficient of variation [-]
BSCL	2103.19	32.43	0.015

The following tests were performed:

- Test to determine the compressive strength;
- Test to determine the water absorption capillarity coefficient;
- Test to determine the moisture content.

8.3.2 Tests for the determination of compressive strength

To quantify the compressive strength of the bricks, the method described in EN 772-1 "Methods of test for masonry units; Part 1: Determination of compressive strength" (EN 772-1, 2011) was used. It basically consists in placing the specimen in the test machine for the application of the load without shock, that is, in a gradual manner and with a controlled speed. The load was applied in the direction of the smallest dimension of the specimen, equal to the loading status to which the elements under analysis are subjected when inserted into the walls of the buildings. Finally, the breaking force is recorded.

Tests were carried out on a test machine with a capacity of 5000 kN with force control and a test speed of 13 kN/s and 21.6 kN/s, according to the relation of Table 2 of EN 772-1 (2011), which presents the recommended values for the rate of application of the load according to the expected compressive strengths. Each test lasted approximately 180 seconds.

The compressive strength values determined by this method are designated as f_b and are calculated according to the following formula:

$$f_b = \frac{\mathrm{F}_c}{A_c} \tag{7}$$

where:
f_b is the collapse compressive strength [MPa];
F_c is the maximum compressive force applied to the specimen at the time of collapse [N];
A_c is the area of the specimen in contact with the plates of the test machine [mm^2].

The faces of bricks of the specimens were smoothed by wear, as shown in Figure 8.64. Considering that this process is carried out using a mechanical device cooled by water, the specimens were wetted. Afterwards they were heated in a ventilated oven at ± 105 ºC until a constant mass was reached, as shown in Figure 8.64.


Surfaces smoothed by wear


Drying of specimens

Figure 8.64 Preparation of bricks.

Figure 8.65 illustrates how the tests were performed to determine the compressive strength for the bricks. The compressive strength was calculated considering the average gross area of the two faces in contact with the press plates. To obtain the standard compressive strength, f_b, the compressive strength of each specimen is multiplied by a shape factor *d*, which depends on the width and height of the bricks according to the aforementioned standard.

Eleven solid clay bricks were tested in compression for the determination of the brick compression strength. This test was carried out on the solid clay bricks specimens designated as BSCL_1 to BSCL_11. In Table 8.24 the compressive strength results for solid clay bricks are presented.

Bricks on the test machine plate

Test machine used

Figure 8.65 Specimens subjected to compressive strength tests.

Table 8.24 Summary of the results from compression tests on solid clay brick specimens.

Specimen	Date of test	Length (L1) [mm]	Width (L2) [mm]	Average gross area [mm^2]	Speed rate [kN/s]	Maximum force [kN]	Compressive strength [MPa]	Shape factor [-]	Standard compressive strength [MPa]
BSCL_1	27-02-2018	0.2122	0.1014	21517.54	13.0	2088	97.04	0.725	70.35
BSCL_2	27-02-2018	0.2130	0.1021	21740.93	6.4	2211	101.70	0.725	73.73
BSCL_3	27-02-2018	0.2150	0.1018	21873.18	21.6	2281	104.28	0.725	75.61
BSCL_4	27-02-2018	0.2135	0.1014	21649.60	21.6	2273	104.99	0.725	76.12
BSCL_5	27-02-2018	0.2136	0.1012	21606.22	21.6	2221	102.79	0.725	74.53
BSCL_6	27-02-2018	0.2129	0.1018	21668.57	21.6	2273	104.90	0.725	76.05
BSCL_7	27-02-2018	0.2132	0.1016	21666.11	21.6	2127	98.17	0.725	71.17
BSCL_8	27-02-2018	0.2127	0.1015	21598.98	13.0	2199	101.81	0.725	73.81
BSCL_9	27-02-2018	0.2118	0.1023	21670.86	13.0	2333	107.66	0.725	78.05
BSCL_10	27-02-2018	0.2131	0.1019	21714.74	13.0	2031	93.53	0.725	67.81
BSCL_11	27-02-2018	0.2120	0.1018	21572.07	13.0	2352	109.03	0.725	79.05
	Average	**0.2130**	**0.1017**	**21661.71**	**-**	**2217**	**102.35**	**-**	**74.21**
	Standard deviation	0.0009	0.0003	94.84	-	101	4.63	-	3.36
	Coefficient of variation [-]	0.004	0.003	0.004	-	0.045	0.045	-	0.045

The average estimate of the compressive strength was f_b = 102.3 MPa, characterized by a low dispersion around the mean, σ = 4.6 MPa (C.o.V. = 0.045). The average estimate of the standard compressive strength was f_b = 74.21 MPa, characterized by a low dispersion around the mean, σ = 3.4 MPa (C.o.V. = 0.045). The test results show that the bricks were quite strong in compression, when compared to the average compressive strength obtained from compression tests on similar clay bricks tested in Pavia in 2016 (Graziotti *et al.*, 2016; Kallioras *et al.*, 2018): then, the bricks had an average strength in compression equal to 46.8 MPa (C.o.V. = 0.11).

Figure 8.66 presents a typical failure of bricks that were tested, while in Appendix G the figures with the obtained fractures are presented for all specimens.

Figure 8.66 Brick for the compressive strength test after failure.

8.3.3 Tests for determination of the water absorption capillarity coefficient

The test for determination of the capillarity coefficient was performed on six specimens of each type of block by the procedures described in EN 772-11 "Methods of test for masonry units Part 11: Determination of water absorption of aggregate concrete, autoclaved aerated concrete" (EN 772-11, 2011). To perform this test the specimens were initially dried at 105 ± 5 ° C until 0.1% of constant mass was obtained. After cooling, the faces that were immersed in water (2 measurements per dimension, near the edges) are measured and the area that is in contact with the water is determined. Subsequently the initial mass of the specimen was measured and the bricks inserted in a tray with elements that allow the passage of water under them, with the face to be submerged downwards, immersed in water up to 5 ± 1mm, as shown in Figure 8.67. After the specified period for the material concerned, which in this case is 60 ± 2 s, the specimen is removed and the surface water is removed with absorbent paper and the specimens are weighed.

Brick during the test

Weighing of brick

Figure 8.67 Determination of the water absorption coefficient by capillarity of the bricks.

The water absorption coefficient by capillarity determined by this method is designated by *C*. The calculation is done according to the following formula:

$$C = \frac{M_i - M_0}{A \times \sqrt{t_i}} \tag{8}$$

where:
C is the water absorption coefficient by capillarity [$kg/m^2.min^{0,5}$];
M_i is the mass of the dry specimen [kg];

M_f is the mass of the specimen after immersion in water for 60 seconds [kg];
A is the area of the specimen in contact with water [m^2];
t_i is the immersion time of the specimen in water (60 seconds in this specific case) [s].

This test was performed on the bricks specimens designated by BSCL_12 to BSCL_17. Table 8.25 shows the results of the water absorption coefficient by capillarity of the bricks.

Table 8.25 Results for the water absorption coefficient by capillarity for bricks.

Specimen	Area [m^2]	Initial Mass [g]	Final Mass [g]	Immersion time [s]	Coefficient of water absorption [$g/(m^2.s^{½})$]	Average [$g/(m^2.s^{½})$]	Average [$kg/(m^2.min^{½})$]
BSCL_12	0.0215	2102.32	2138.36	60	216.53	177.91	**1.38**
BSCL_13	0.0215	2087.76	2121.50		202.30		
BSCL_14	0.0215	2148.83	2176.64		166.93		
BSCL_15	0.0214	2128.15	2153.02		149.94		
BSCL_16	0.0215	2109.23	2138.22		174.23		
BSCL_17	0.0213	2123.93	2149.91		157.54		

8.3.4 Tests for the determination of moisture content

The test for determination of the moisture content was carried out on six specimens of each type based on the procedures described in EN 772-10:1999 "Methods of test for masonry units - Part 10: Determination of moisture content of calcium silicate and autoclaved aerated Concrete units" (EN 772-10, 1999) and in NP EN 1097-5 "Tests of the mechanical and physical properties of the aggregates. Part 5: Determination of the water content by drying in a ventilated oven" (NP EN 1097-5, 2011). This test has as its main objective to determine the moisture content by the thermogravimetric method.

To carry out this test, six solid clay bricks specimens were selected with the designation BSCL_18 to BSCL_23. After the selection of the specimens, they were individually weighed and placed in a ventilated oven at a constant temperature of 105 ± 5 ° C, as shown in Figure 8.68, and weighed every 24 hours. This procedure must be carried out until a constant weight is obtained, i.e. until two consecutive weighings correspond to a mass loss of less than 0.2% of the total mass. After the specimens had reached a constant mass, the test pieces were again weighed, according to Figure 8.69.

The moisture content is determined according to the following formula:

$$w_s = \frac{m_{0,s} - m_{dry,s}}{m_{dry,s}} \times 100 \tag{9}$$

where:
w_s is the percentage moisture content [%];
$m_{0,s}$ is the mass of the specimen before drying [g];
$m_{dry,s}$ is the mass of the specimen after drying [g].

Figure 8.68 Drying the blocks in a ventilated oven.

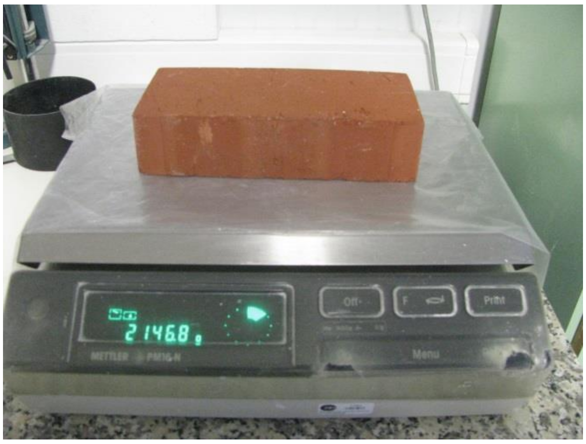

Figure 8.69 Weighing of blocks.

Table 8.26 shows the weighings carried out until a constant mass of 0.2% is reached for the bricks specimens.

Table 8.26 Weighing until constant mass is reached for the brick specimens.

Date	BSCL_18		BSCL_19		BSCL_20		BSCL_21		BSCL_22		BSCL_23	
	Mass [g]	Checking stopping criterion (0,2%)	Mass [g]	Checking stopping criterion (0,2%)	Mass [g]	Checking stopping criterion (0,2%)	Mass [g]	Checking stopping criterion (0,2%)	Mass [g]	Checking stopping criterion (0,2%)	Mass [g]	Checking stopping criterion (0,2%)
21-02-2018	2145.32	-	2146.2	-	2126.16	-	2105.15	-	2118.91	-	2114.68	-
22-02-2018	2144.53	Stop	2145.63	Stop	2125.5	Stop	2104.54	Stop	2118.4	Stop	2113.98	Stop
23-02-2018	2144.57	Stop	2145.62	Stop	2125.51	Stop	2104.57	Stop	2118.37	Stop	2113.95	Stop
24-02-2018	2144.38	Stop	2145.47	Stop	2125.38	Stop	2104.46	Stop	2118.21	Stop	2113.79	Stop
25-02-2018	2144.53	Stop	2145.66	Stop	2125.59	Stop	2104.61	Stop	2118.35	Stop	2113.93	Stop
26-02-2018	2144.59	Stop	2145.7	Stop	2125.59	Stop	2104.61	Stop	2118.38	Stop	2113.95	Stop
27-02-2018	2144.57	Stop	2145.67	Stop	2125.54	Stop	2104.62	Stop	2118.43	Stop	2113.91	Stop

Table 8.27 summarises the percentages of moisture content of brick specimens.

Table 8.27 Percentage of moisture content of the brick specimens.

Specimen	W_S [%]	Average [%]	Standard deviation [%]	Coefficient of variation [%]
BSCL_18	0.03	**0.03**	0.01	0.266
BSCL_19	0.02			
BSCL_20	0.03			
BSCL_21	0.03			
BSCL_22	0.02			
BSCL_23	0.04			

8.4 Masonry characterisation tests

8.4.1 Characterisation and identification of specimens

Sixteen *wallettes* were built (eight simple-wythe and eight double-wythe). The simple *wallettes* have eight layers with dimensions approximately 435 x 100 x 470 mm and the double *wallettes* have eleven layers with dimensions approximately 550 x 210 x 650 mm. These dimensions are according to the provisions of norm EN 1052-1 "Methods of test for masonry – Part 1: Determination of compressive strength" (EN 1052-1, 1998). Forty-two *triplet* specimens were tested, with approximately 210 x 100 x 165 mm. Figure 8.70 shows the *wallettes* (simple and double) and *triplets* that were constructed for the tests.

Simple *wallettes*

Double *wallettes*

Triplets

Figure 8.70 Types of masonry specimens (wallettes and triplets) built for testing.

The construction of the specimens for the characterisation tests (*wallettes* and *triplets*) took place in February, during the construction of the building prototype and was carried out by construction professionals from the Netherlands, as shown in Figure 8.71

Simple *wallettes*

Double *wallettes*

Triplets

Figure 8.71 Construction of wallettes and triplets.

The selected tests for these specimens were:

- Compressive strength tests (CTBSCL_#S and CTBSCL_#D);
- Shear tests (TBSCL_##);
- Bond wrench tests (BWBSCL_##).

The designation of the specimens is in accordance with the following descriptions: CTBSCL_S – Solid clay simple *wallettes* for the compressive strength tests; CTBSCL_D – Solid clay double *wallettes* for the compressive strength tests; TBSCL – Solid clay bricks *triplets* for the shear tests; BWBSCL – Solid clay bricks *triplets* for the bond strength tests. All of the specimens were measured with a calliper and weighed on a digital weighing-machine.

Figure 8.72 presents a schematic view with the various parameters measured in the test specimens, while in the Table 8.28 dimensions and masses of the two types of *wallettes* constructed for the compressive strength tests are summarised, with additional details provided in Appendix H.

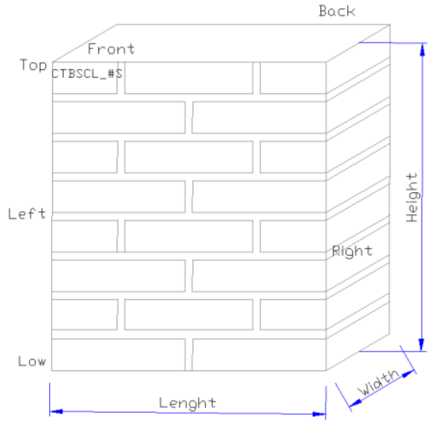

Single *wallettes* (CTBSCL_S)

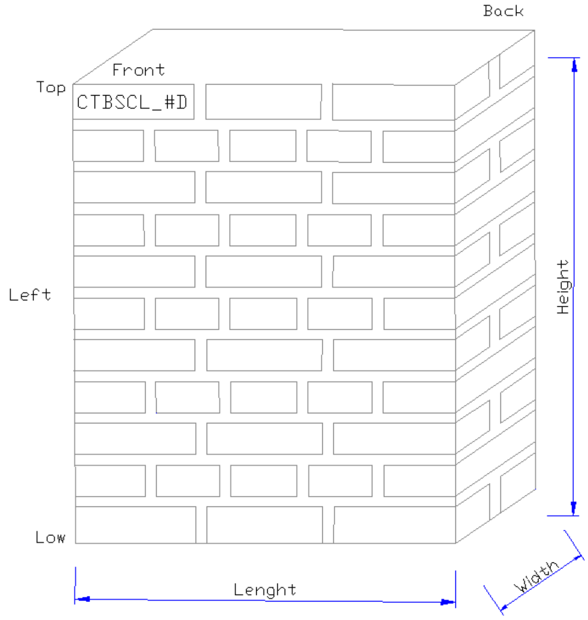

Double *wallettes* (CTBSCL_D)

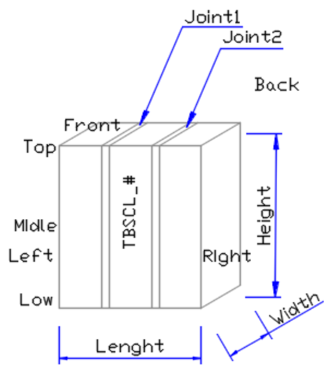

Triplets for shear tests (TBSCL)

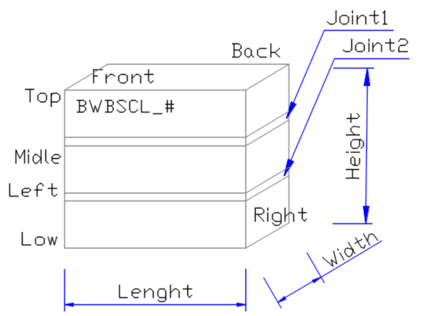

Triplets for bond wrench tests (BWBSCL)

Figure 8.72 Schematic with the identification of the parameters measured in the various specimens.

Table 8.28 Dimensions and masses of the two types of wallettes constructed for the compressive strength tests.

Specimen	Average Length [mm]	Average Width [mm]	Average Height [mm]	Average Mass [kg]
CTBSCL_S	436.06	100.16	472.13	40.760
CTBSCL_D	543.47	211.31	650.00	146.244

In Table 8.29, the dimensions and masses of the two types of *triplets* built for the bond strength tests and shear tests are shown. Additional details are provided in Appendix H.

Table 8.29 Dimensions and masses of the two types of triplets built for the bond wrench tests and shear tests.

Specimen	Average Height [mm]	Average Width [mm]	Average Length [mm]	Average Mass [kg]
TBSCL	166.57	101.51	211.59	7.015
BWBSCL	171.86	100.86	213.01	7.353

The bulk density values for the two types of *wallettes* and *triplets* built are summarised in Table 8.30, with additional results presented in Appendix H.

Table 8.30 Summary of the results of the bulk density for the all types of specimens built.

Specimen type	Bulk density		
	Average [kg/m³]	Standard deviation [kg/m3]	Coefficient of variation [-]
Single *wallettes* (CTBSCL_S)	1976.98	18.60	0.009
Double *wallettes* (CTBSCL_D)	1959.21	17.89	0.009
Triplets for bond wrench tests (BWBSCL)	1960.88	10.03	0.005
Triplets for shear tests (TBSCL)	1991.56	9.36	0.005

8.4.2 Tests for the determination of compressive strength

The test to determine the compressive strength was performed according to an adaptation of the standard method described in the standard EN 1052-1:1998 “Methods of test for masonry – Part 1: Determination of compressive strength” (EN 1052-1, 1998). The principle of this test is the determination of the compressive strength of masonry specimens and possible determination of the respective modulus of elasticity and *Poisson's* coefficient.

This test was performed on some of above mentioned *wallettes* specimens designated as CTBSCL_1S to CTBSCL_6S and CTBSCL_1D to CTBSCL_6D. *Wallettes* were not perfectly tiled at the time of construction, as shown in Figure 8.73. To fix this problem and due to the small irregularities of the lower and upper faces of the single *wallettes* (areas that would be in contact with the plates of the press), these faces were regularised with a thin layer of gypsum, as shown in Figure 8.74. After this regularisation a very fine layer of gypsum is placed on both sides already with the specimen on top of the testing machine, which are levelled by the plates of the press machine, as shown in Figure 8.74.

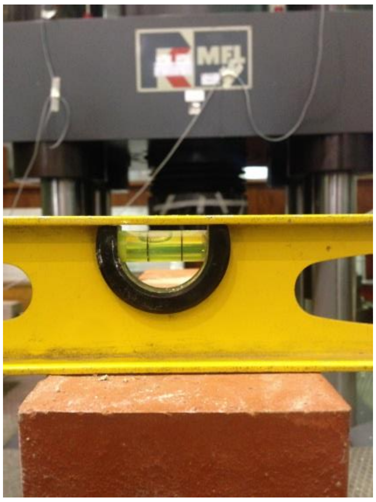

Figure 8.73 Wallettes with lack of orthogonality between them.

Preparation

During the process

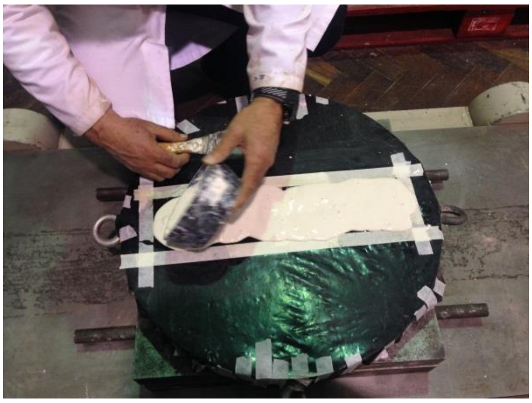

Layer of gypsum levelled by the plates of the press machine

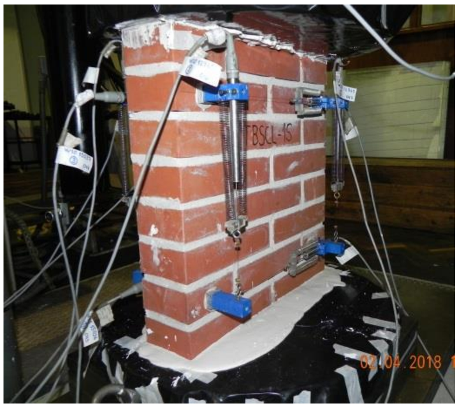

Wallette in the press machine

Figure 8.74 Regularisation of the wallettes faces.

Subsequently, the specimens were instrumented with four displacement transducers on each face, as shown in Figure 8.73. The vertical displacement transducers are of type W20 (with a measuring range of ± 20 mm) and measure strains for the determination of the modulus of elasticity (1, 2, 5 and 6) and two horizontal displacement transducers of type W10 (with a measuring range of ± 10 mm, since smaller deformations are expected) which measure deformations in the direction perpendicular to the force in order to provide an evaluation of *Poisson*'s coefficient (3, 4, 7 and 8).

The instrumentation was placed in the central area of the specimen so that the measurements are carried out in an area that is not affected by the boundary conditions, as illustrated in the schemes of Figure 8.75 and Figure 8.76 (the schematics with the instrumentation locations for all tested *wallettes* are shown in Appendix H). Additionally, two displacement transducers were placed that measure the deformation of the plates of the press so that the deformation of the specimen up to failure may be recorded. For example, Figure 8.77 and Figure 8.78 show the instrumentation performed on each face of the two types of *wallettes*. The displacement transducers and the testing machine were duly calibrated immediately prior to the start of the trials with the collaboration of the Metrological Quality Unit of LNEC's Scientific Instrumentation Centre.

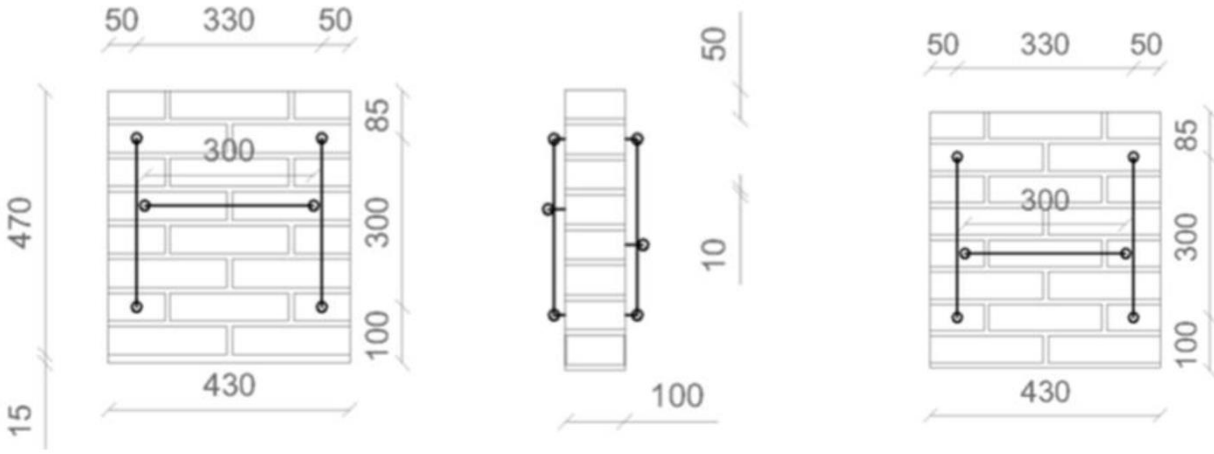

Front Side Back

Figure 8.75 Scheme and numbering of the transducers placed on each face of the single wallettes.

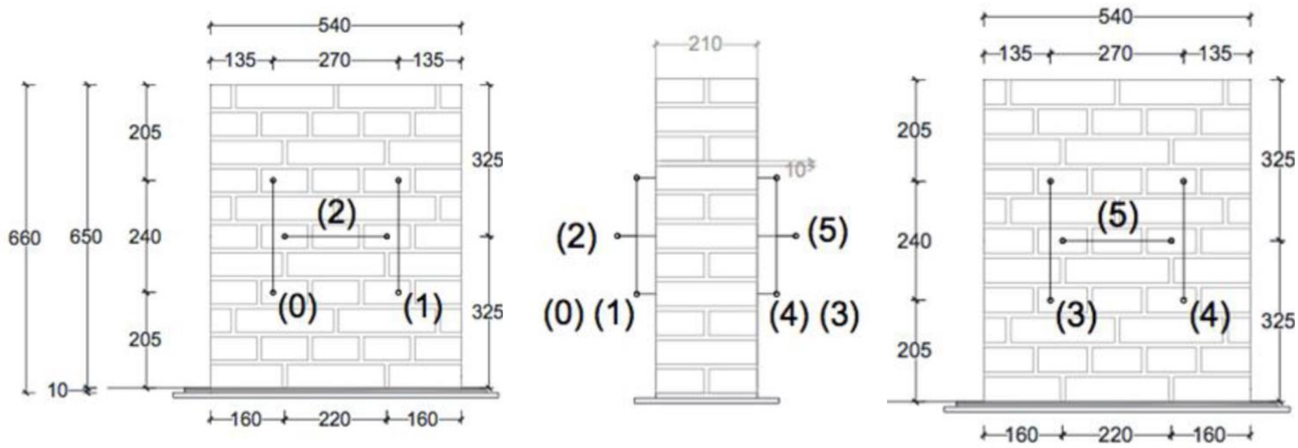

Front Side Back

Figure 8.76 Scheme and numbering of the transducers placed on each face of the double wallettes.

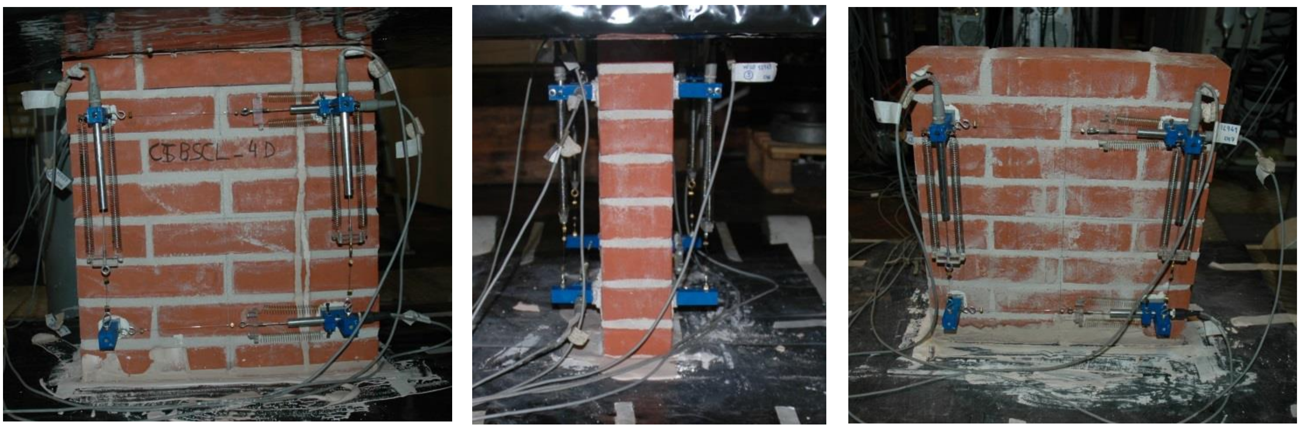

Front Side Back

Figure 8.77 Instrumentation placed on each face of the single wallettes.

Front Side Back

Figure 8.78 Instrumentation placed on each face of the double wallettes.

The test procedure for the *wallettes* consists essentially in placing the specimen in the test machine for load application without shock, i.e. in a gradual way and at a controlled speed until the failure of the specimen. Several increasing cycles of loading and unloading were carried out, with equal increments (at each load level three cycles were performed). In Table 8.31 the load values of these cycles for single and double *wallettes* are presented, while in Figure 8.79 and Figure 8.80 an example of one of these tests is presented as a plot showing the force as a function of time.

The tests were performed on a machine with a capacity of 5000 kN, with a control in force and a test speed of 3 kN/s for single *wallettes* and 4 kN/s for double *wallettes* in the first three cycles. In the collapse cycle the test was performed with a control in displacement and a test speed of 0.05 mm/s. A sampling frequency of 5 Hz was used, each run lasting approximately 60 minutes for each test. The load application was performed vertically to the specimen.

Table 8.31 Cyclic load values for single and double wallettes.

Specimen	Load values of 1st cycle [kN]	Load values of 2nd cycle [kN]	Load values of 3rd cycle [kN]
Single *wallettes* (CTBSCL_S)	150	300	450
Double *wallettes* (CTBSCL_D)	250	500	750

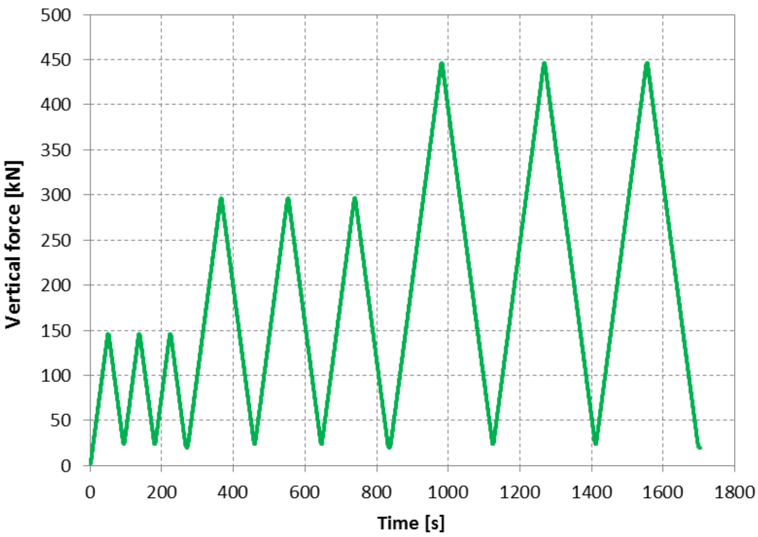

Figure 8.79 Application of force as a function of time for the single wallettes.

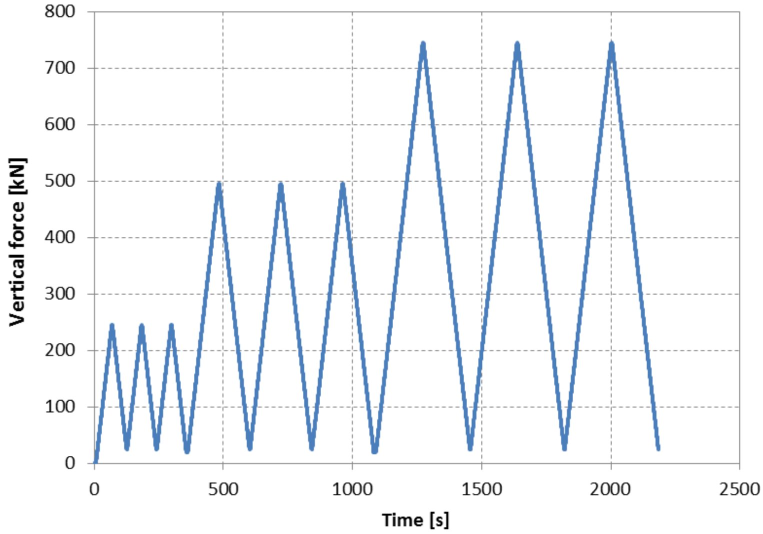

Figure 8.80 Application of force as a function of time for the double wallettes.

For the sake of safeguarding the equipment, the instrumentation was maintained up to the fourth load level, and after the last cycle at this load level the final loading was started until the specimen failure. For this final loading, the deformation until failure was measured using the transducers installed in the press plate. The first *wallette* tested was used to evaluate the compressive strength of the test specimens to define the loading threshold from which the instrumentation should be removed.

Figure 8.81 and Figure 8.82 present single and double *wallettes* after their failure, while in Appendix I the figures with the obtained fractures are presented for all specimens.

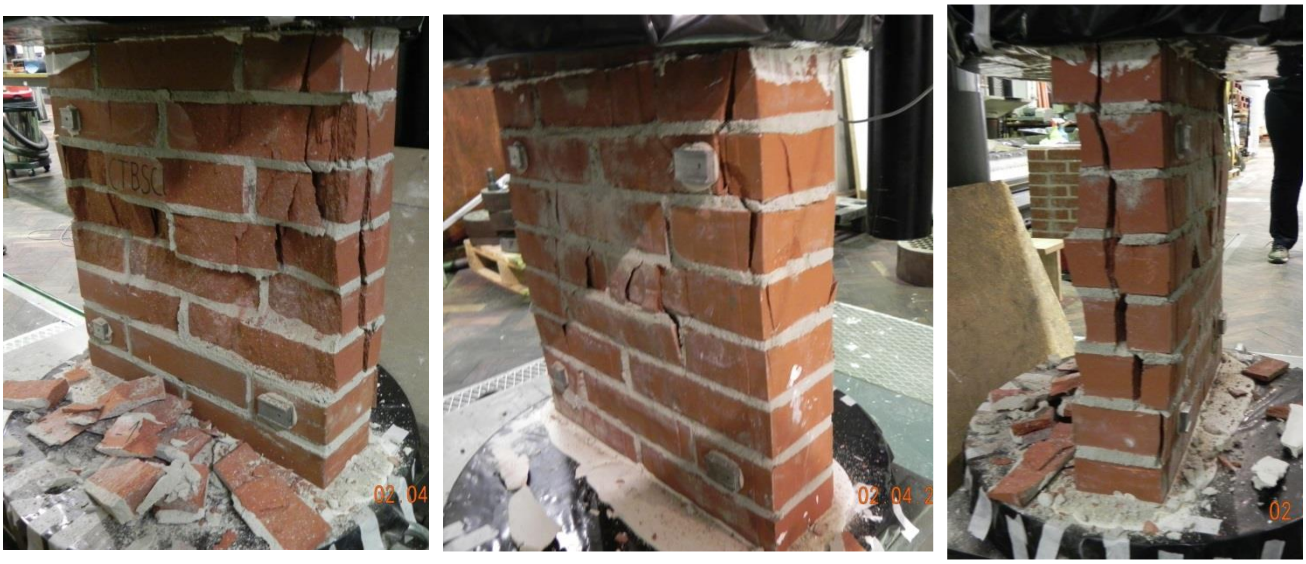

Failure front view | Failure back view | Failure lateral view

Figure 8.81 Single wallette during the test and after failure.

Failure front view Failure back view Failure lateral view

Figure 8.82 Double wallette during the test and after failure.

The results of the compressive strength obtained in the single and double *wallettes* are summarised in Table 8.32 and Table 8.33 respectively. In order to determine the modulus of elasticity of the *wallettes*, the average of the vertical deformations recorded by the displacement transducers 1, 2, 5 and 6 was computed and the modulus of elasticity (E_1), given by the secant line from the origin up to 33% of the failure load, was derived.

Table 8.32 Summary of the compressive strength for the single wallettes.

Specimen	Date of test	Average gross area [mm^2]	Maximum force [kN]	Compressive strength [MPa]
CTBSCL_1S	02-04-2018	43675	700	16.44
CTBSCL_2S	23-04-2018	43809	752	17.17
CTBSCL_3S	22-05-2018	43775	654	14.94
CTBSCL_4S	22-05-2018	43556	638	14.66
CTBSCL_5S	23-05-2018	43650	748	17.13
CTBSCL_6S	23-05-2018	43450	702	16.15
Average		**43653**	**699**	**16.08**
Standard deviation		134	47	1.07
Coefficient of variation [-]		0.003	0.067	0.067

Table 8.33 Summary of the compressive strength for the double wallettes.

Specimen	Date of test	Average gross area [mm^2]	Maximum force [kN]	Compressive strength [MPa]
CTBSCL_1D	23-03-2018	114480	1451	12.68
CTBSCL_2D	26-03-2018	114573	1439	12.56
CTBSCL_3D	26-03-2018	115257	1212	10.52
CTBSCL_4D	27-03-2018	114744	1277	11.13
CTBSCL_5D	27-03-2018	115091	1215	10.55
CTBSCL_6D	28-03-2018	115712	1301	11.24
Average		**114976**	**1316**	**11.45**
Standard deviation		468	106	0.96
Coefficient of variation [-]		0.004	0.081	0.083

Figure 8.83 to Figure 8.88 shows the plots that relate the vertical and horizontal deformations to the vertical load measured for each single *wallette* specimen.

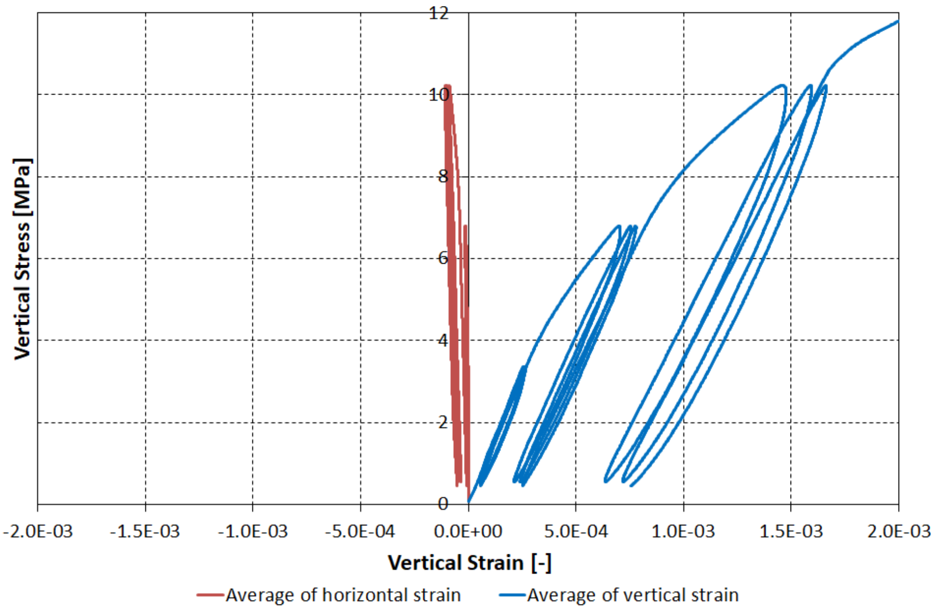

Figure 8.83 Vertical stress vs. vertical and horizontal strains for single wallette CTBSCL_1S.

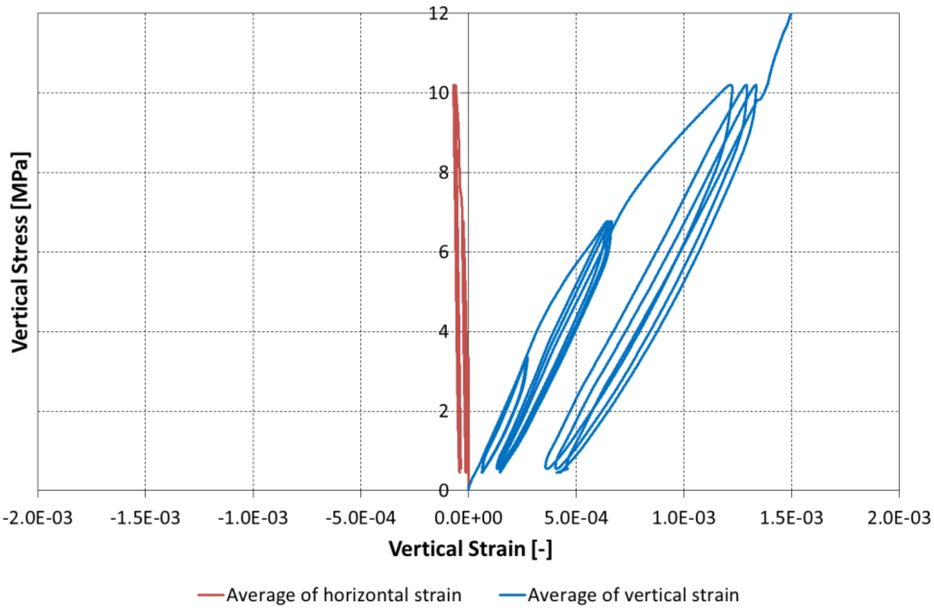

Figure 8.84 Vertical stress vs. vertical and horizontal strains for single wallette CTBSCL_2S.

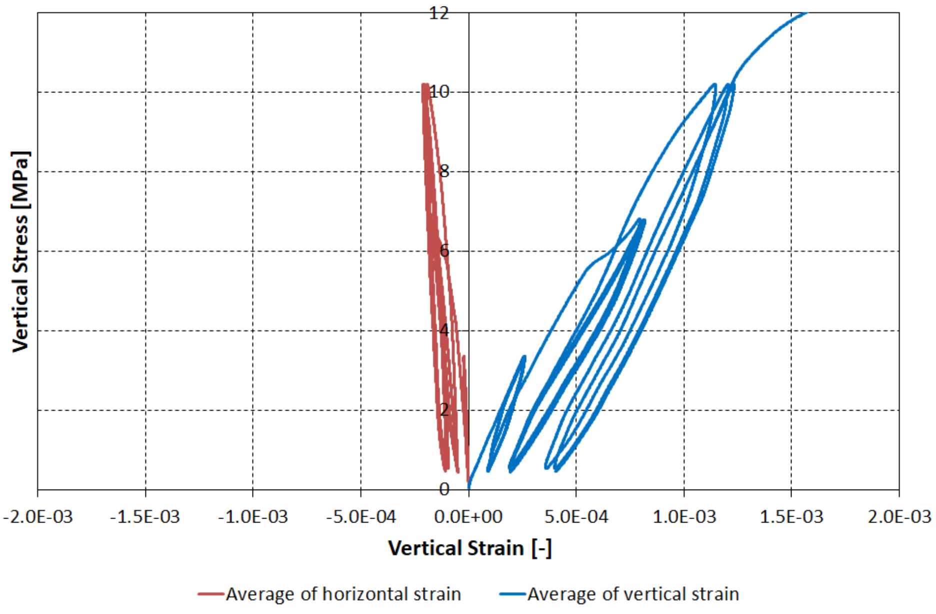

Figure 8.85 Vertical stress vs. vertical and horizontal strains for single wallette CTBSCL_3S.

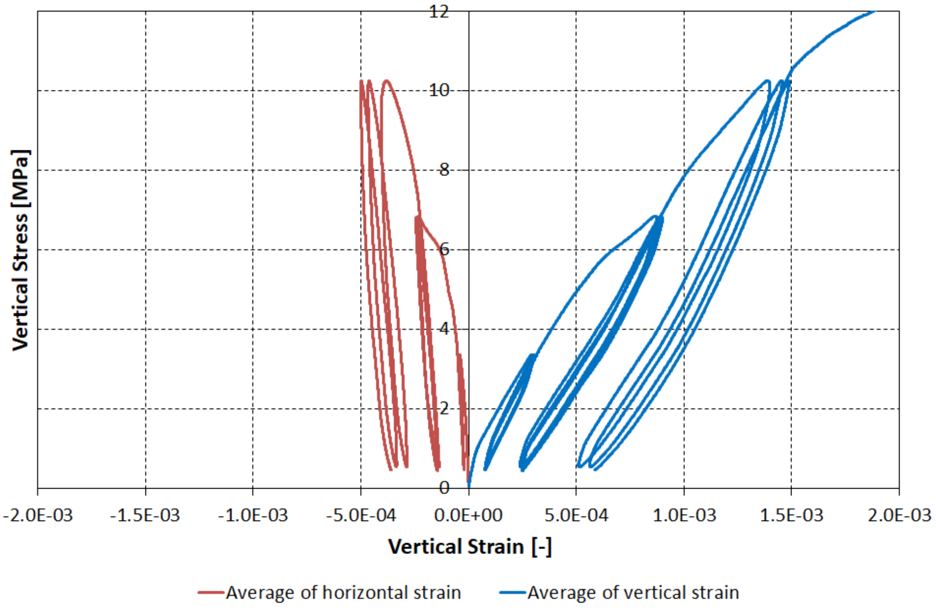

Figure 8.86 Vertical stress vs. vertical and horizontal strains for single wallette CTBSCL_4S.

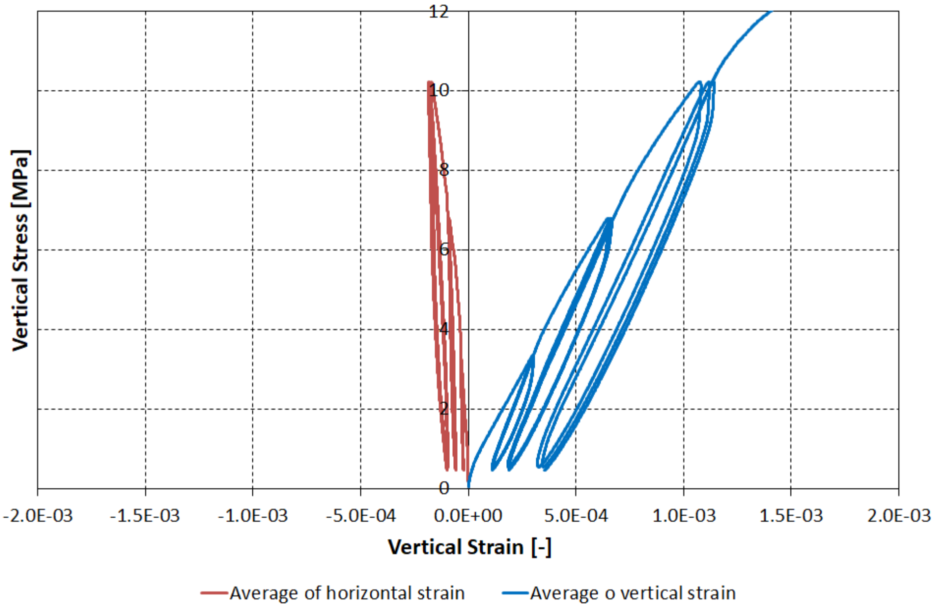

Figure 8.87 Vertical stress vs. vertical and horizontal strains for single wallette CTBSCL_5S.

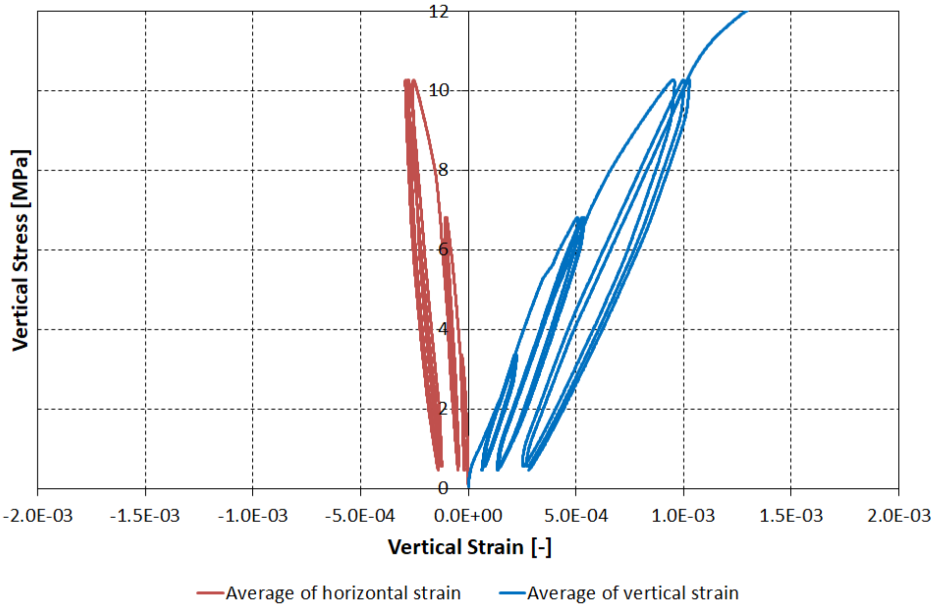

Figure 8.88 Vertical stress vs. vertical and horizontal strains for single wallette CTBSCL_6S.

Figure 8.89 to Figure 8.94 show the plots relating the vertical stress with the vertical strain measured for the single *wallettes*, as well as the corresponding modulus of elasticity.

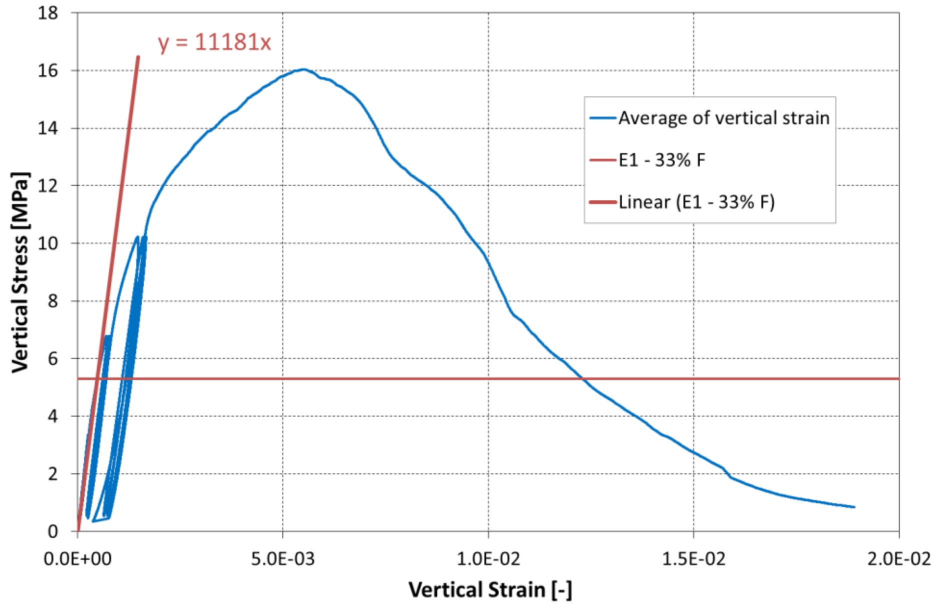

Figure 8.89 Vertical stress vs. vertical strain and determination of the modulus of elasticity for single wallette CTBSCL_1S.

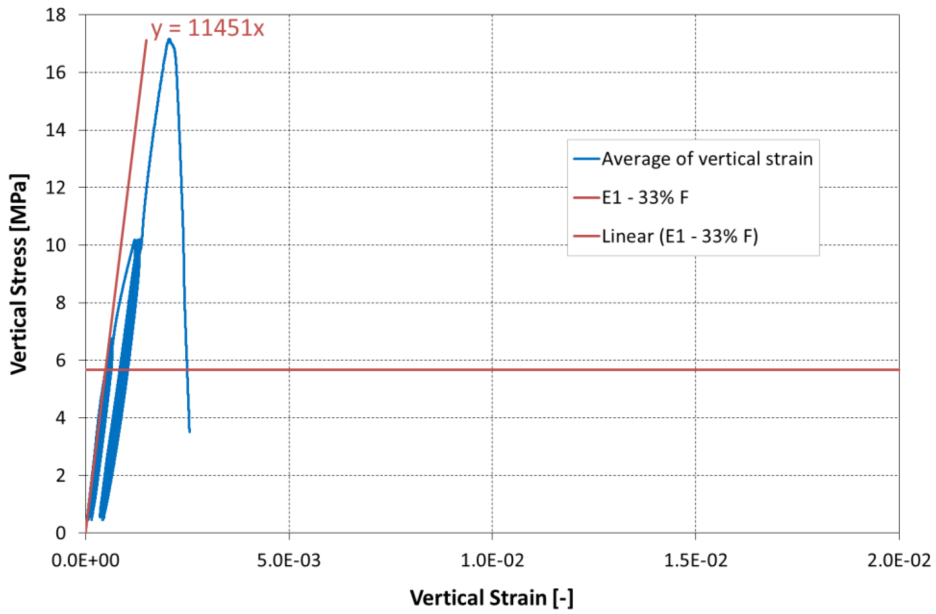

Figure 8.90 Vertical stress vs. vertical strain and determination of the modulus of elasticity for single wallette CTBSCL_2S.

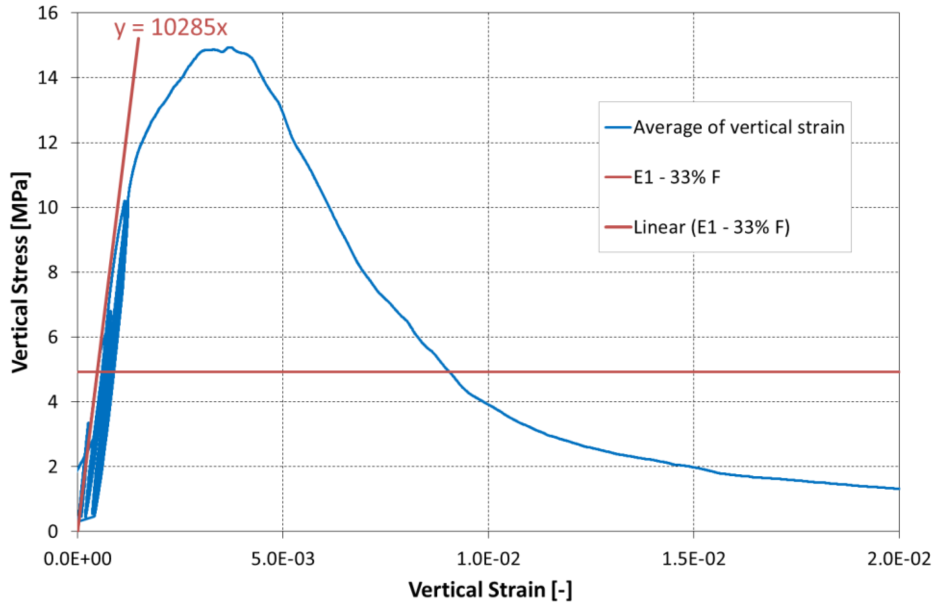

Figure 8.91 Vertical stress vs. vertical strain and determination of the modulus of elasticity for single wallette CTBSCL_3S.

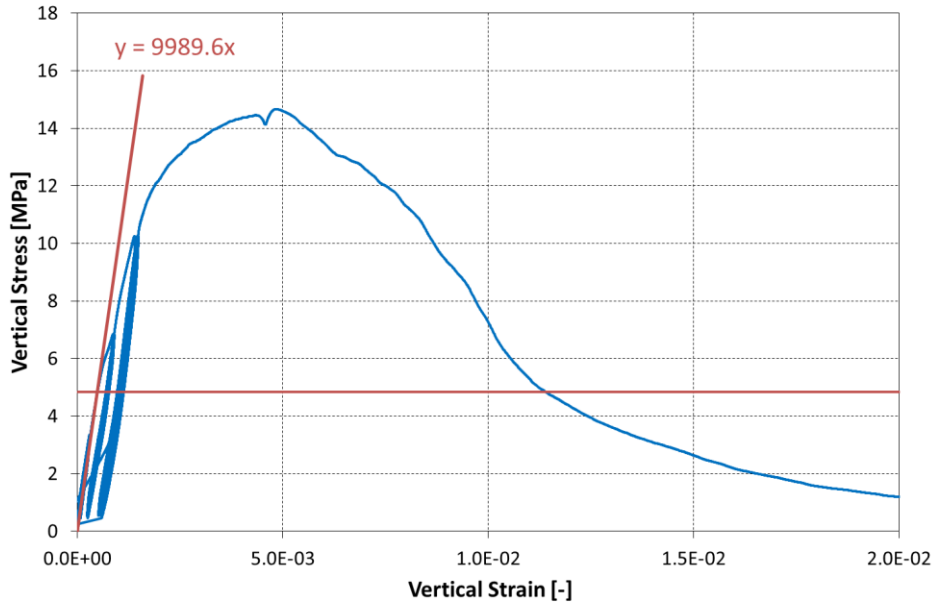

Figure 8.92 Vertical stress vs. vertical strain and determination of the modulus of elasticity for single wallette CTBSCL_4S.

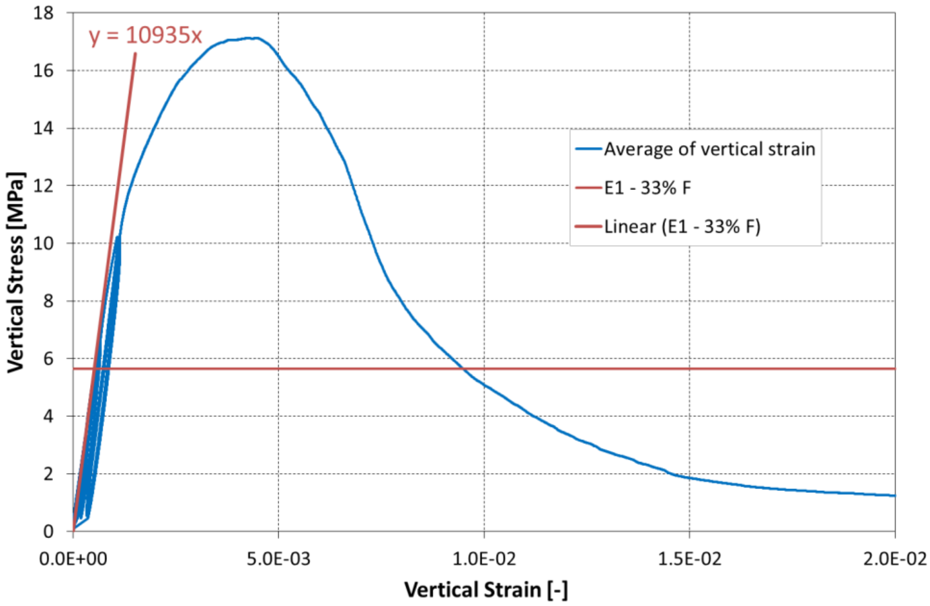

Figure 8.93 Vertical stress vs. vertical strain and determination of the modulus of elasticity for single wallette CTBSCL_5S.

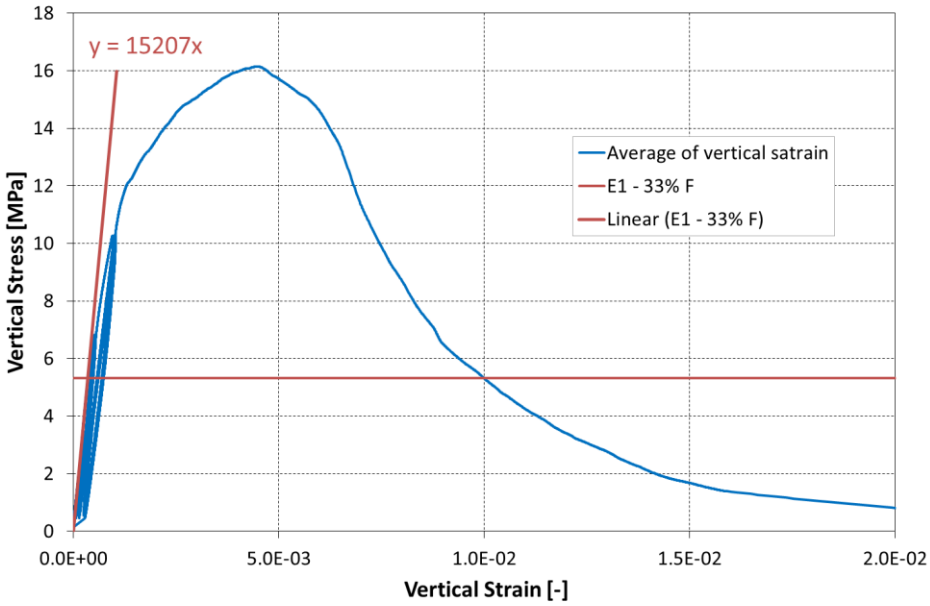

Figure 8.94 Vertical stress vs. vertical strain and determination of the modulus of elasticity for single wallette CTBSCL_6S.

The results obtained for the modulus of elasticity E_1 for each single *wallette* are summarised in Table 8.34, while Figure 8.95 shows the distribution of the moduli of elasticity obtained.

Table 8.34 Summary of the modulus of elasticity for single wallettes.

Specimen	Compressive strength [MPa]	E_1 (33% F_{max}) [MPa]
CTBSCL_1S	16.44	11181
CTBSCL_2S	17.17	11451
CTBSCL_3S	14.94	10285
CTBSCL_4S	14.66	9990
CTBSCL_5S	17.13	10935
CTBSCL_6S	16.15	15207
Average [MPa]	**16.08**	**11508**
Standard deviation [MPa]	1.07	1893
Coefficient of variation [-]	0.067	0.165

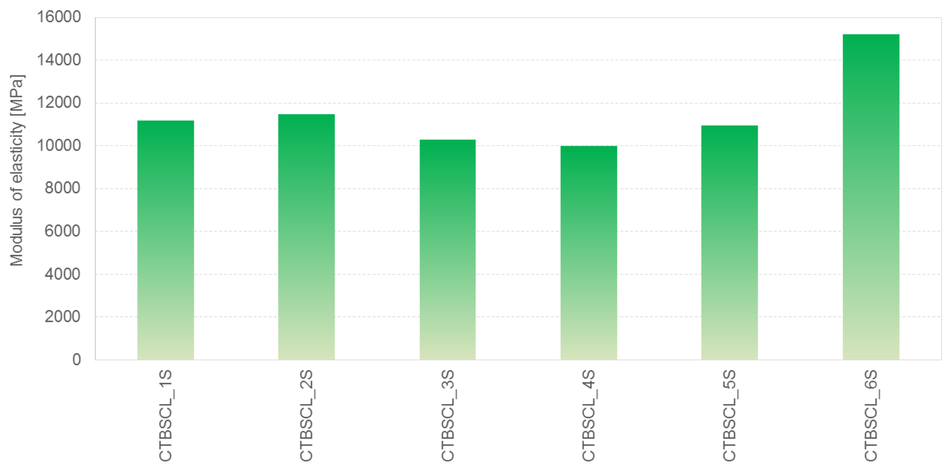

Figure 8.95 Distribution of moduli of elasticity obtained for single wallettes.

Figure 8.96 to Figure 8.101 shows the plots that relate the vertical and horizontal deformations to the vertical load measured for each double *wallette* specimen.

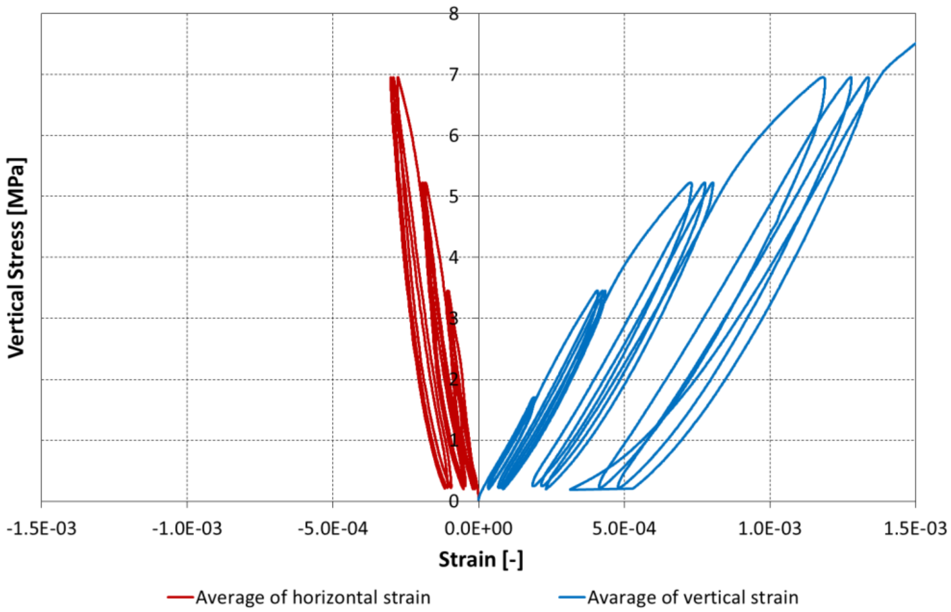

Figure 8.96 Vertical stress vs. vertical and horizontal strains for double wallette CTBSCL_1D.

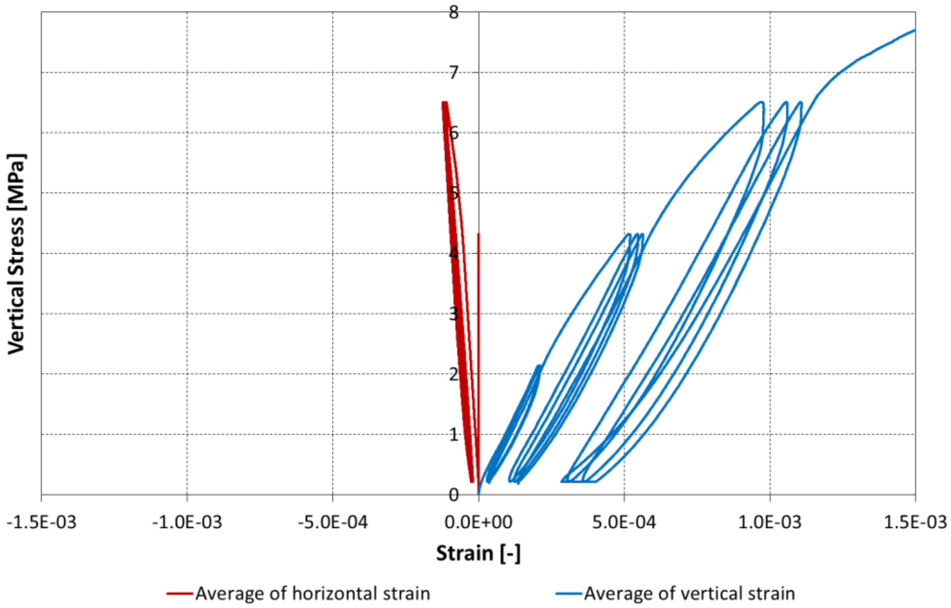

Figure 8.97 Vertical stress vs. vertical and horizontal strains for double wallette CTBSCL_2D.

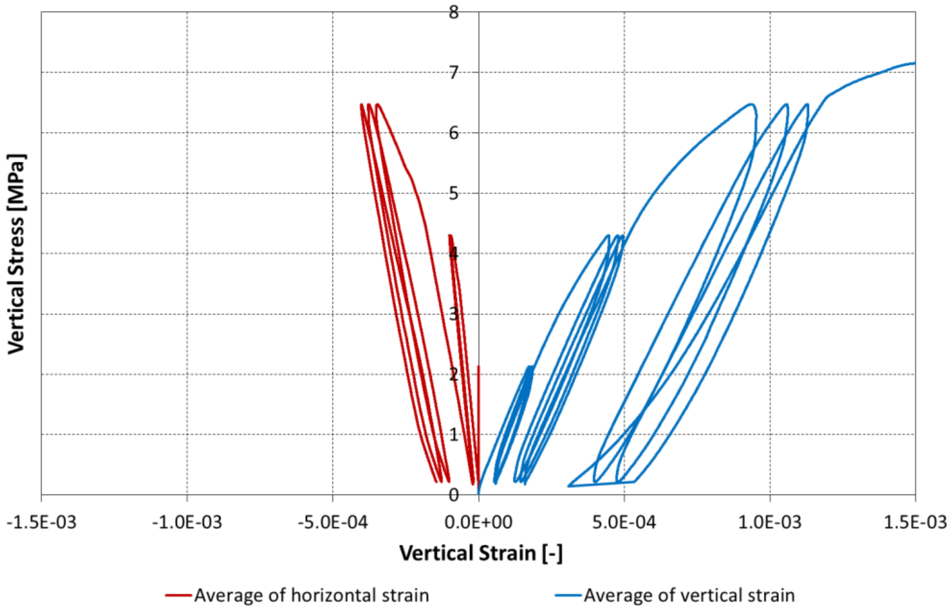

Figure 8.98 Vertical stress vs. vertical and horizontal strains for double wallette CTBSCL_3D.

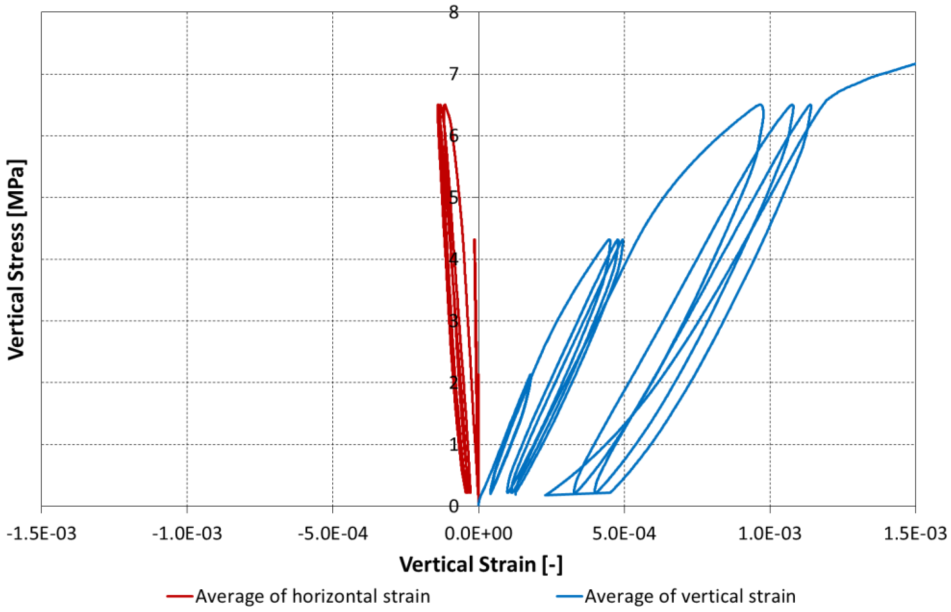

Figure 8.99 Vertical stress vs. vertical and horizontal strains for double wallette CTBSCL_4D.

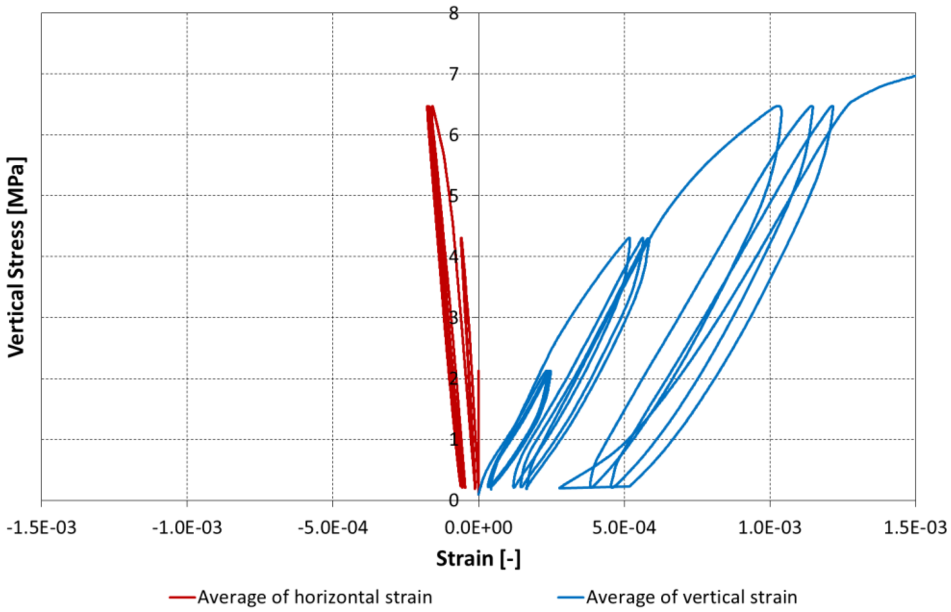

Figure 8.100 Vertical stress vs. vertical and horizontal strains for double wallette CTBSCL_5D.

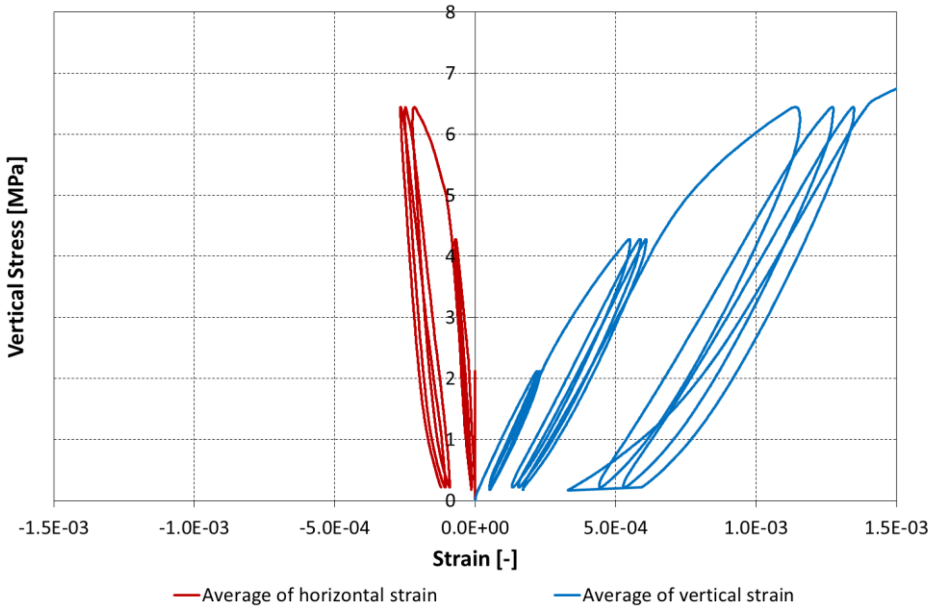

Figure 8.101 Vertical stress vs. vertical and horizontal strains for double wallette CTBSCL_6D.

Figure 8.102 to Figure 8.107 show the plots relating the vertical stress with the vertical strain measured for the double *wallettes*, as well as the corresponding modulus of elasticity.

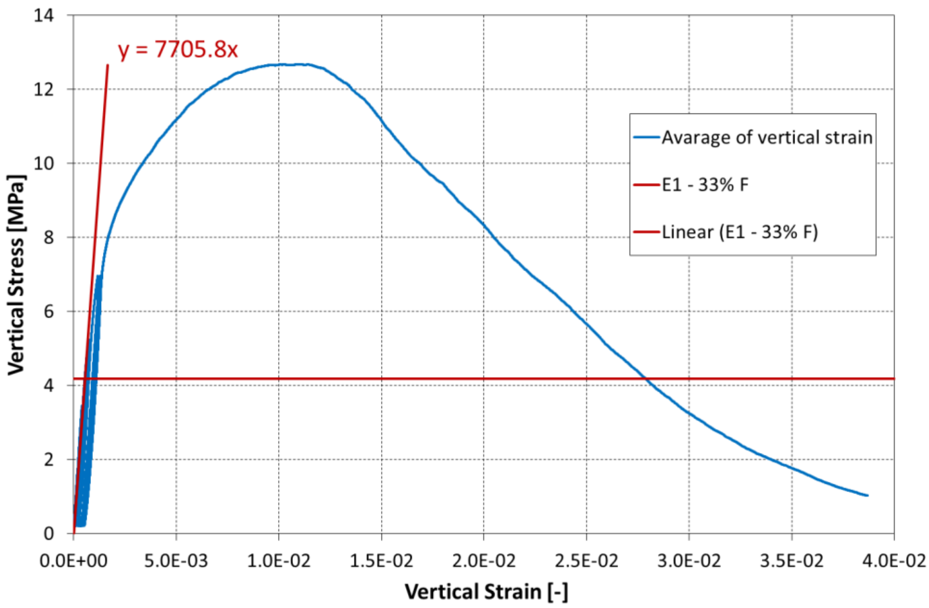

Figure 8.102 Vertical stress vs. vertical strain and determination of the modulus of elasticity for double wallette CTBSCL_1D.

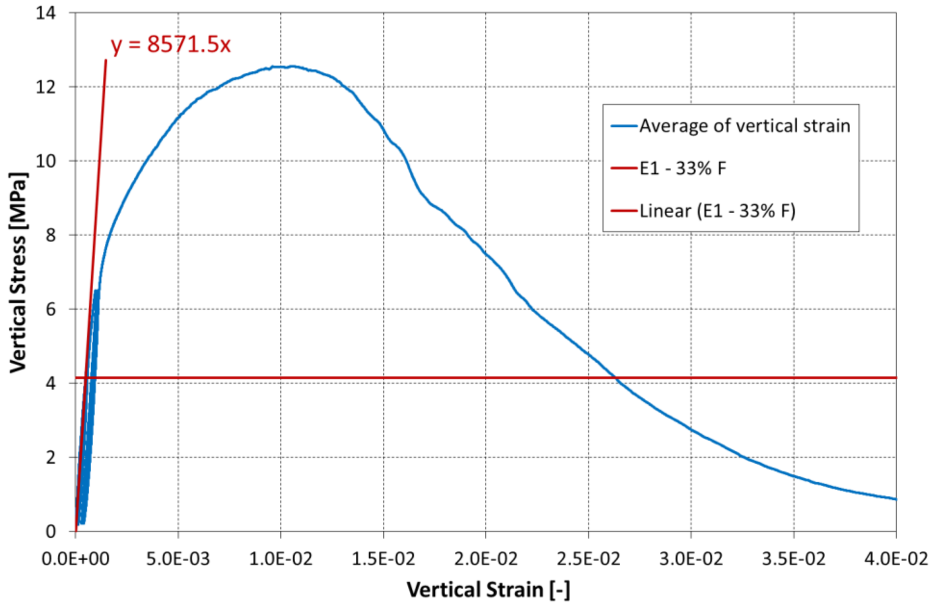

Figure 8.103 Vertical stress vs. vertical strain and determination of the modulus of elasticity for double wallette CTBSCL_2D.

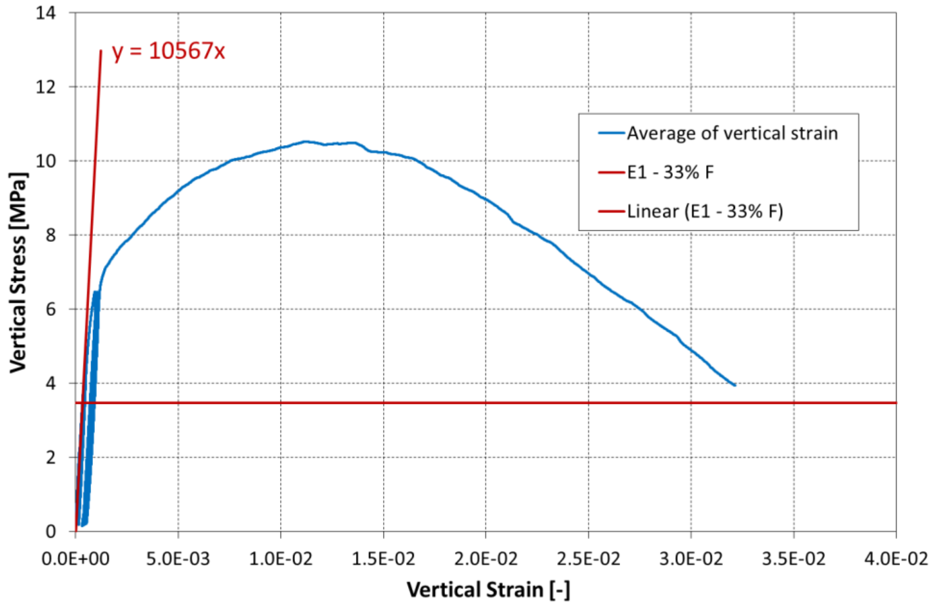

Figure 8.104 Vertical stress vs. vertical strain and determination of the modulus of elasticity for double wallette CTBSCL_3D.

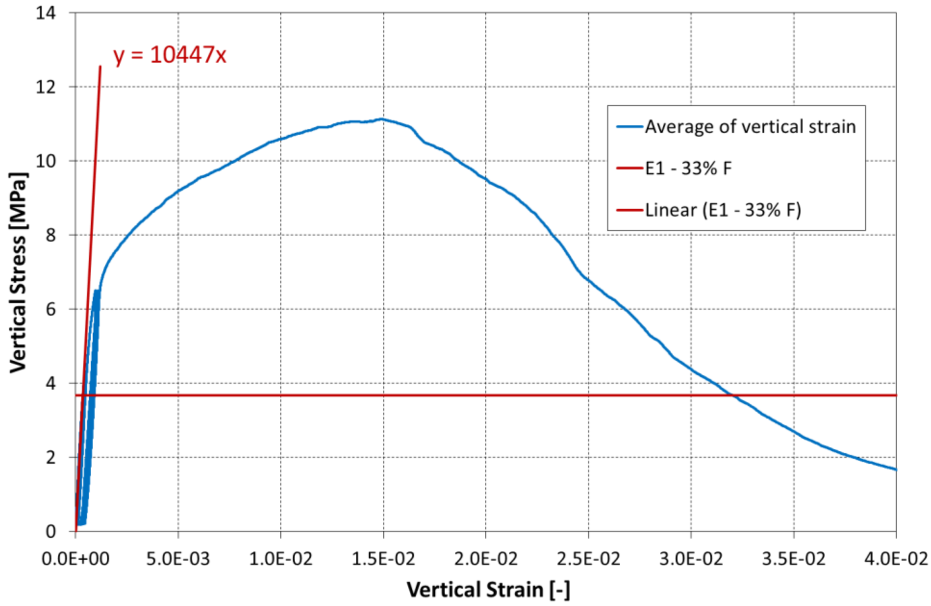

Figure 8.105 Vertical stress vs. vertical strain and determination of the modulus of elasticity for double wallette CTBSCL_4D.

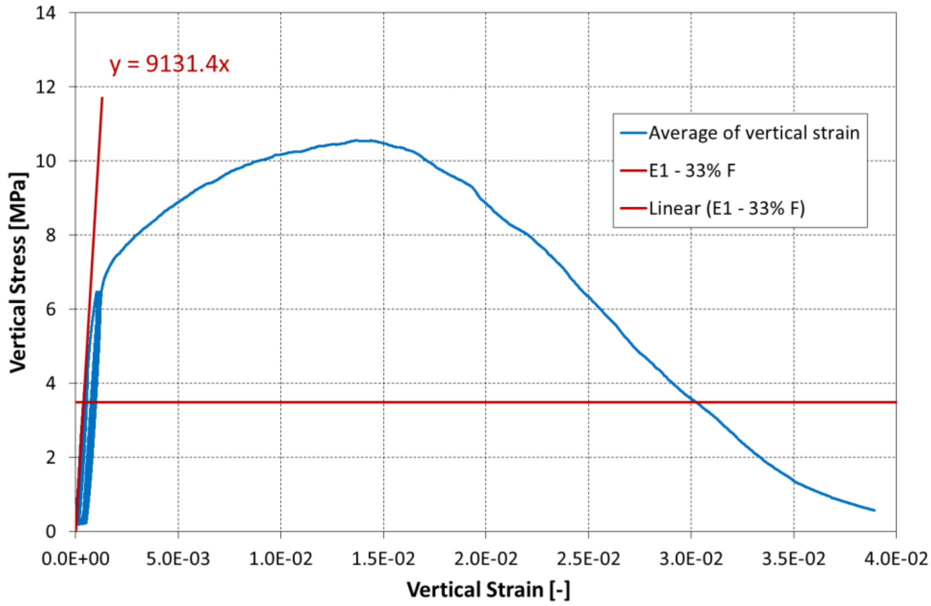

Figure 8.106 Vertical stress vs. vertical strain and determination of the modulus of elasticity for double wallette CTBSCL_5D.

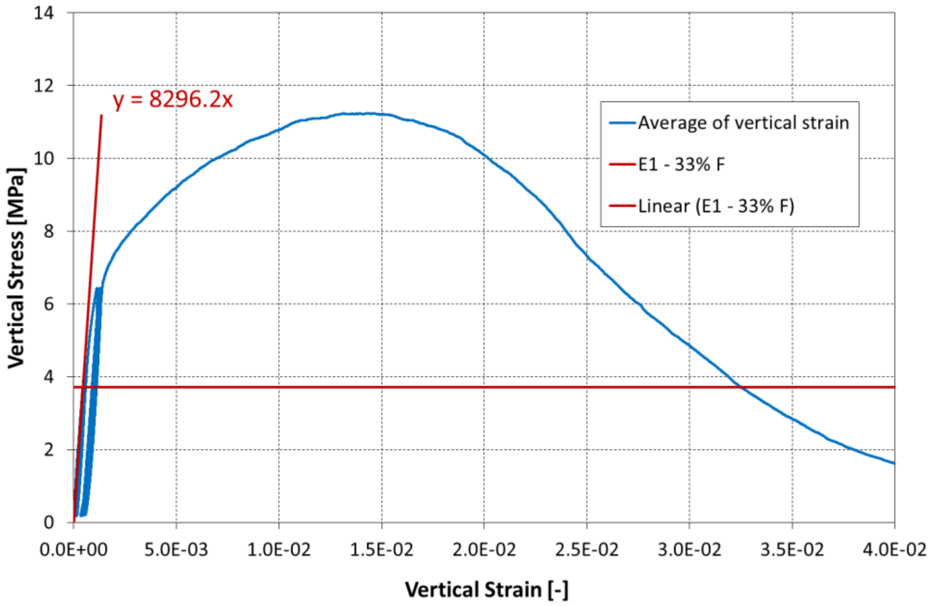

Figure 8.107 Vertical stress vs. vertical strain and determination of the modulus of elasticity for double wallette CTBSCL_6D.

The results obtained for the modulus of elasticity E_1 for each double *wallette* are summarised in Table 8.35, while Figure 8.108 shows the distribution of the moduli of elasticity obtained.

Table 8.35 Summary of the modulus of elasticity for double wallettes.

Specimen	Compressive strength [MPa]	E_1 (33% F_{max}) [MPa]
CTBSCL_1D	12.68	7706
CTBSCL_2D	12.56	8572
CTBSCL_3D	10.52	10567
CTBSCL_4D	11.13	10447
CTBSCL_5D	10.55	9131
CTBSCL_6D	11.24	8296
Average [MPa]	**11.45**	**9120**
Standard deviation [MPa]	0.96	1169
Coefficient of variation [-]	0.083	0.128

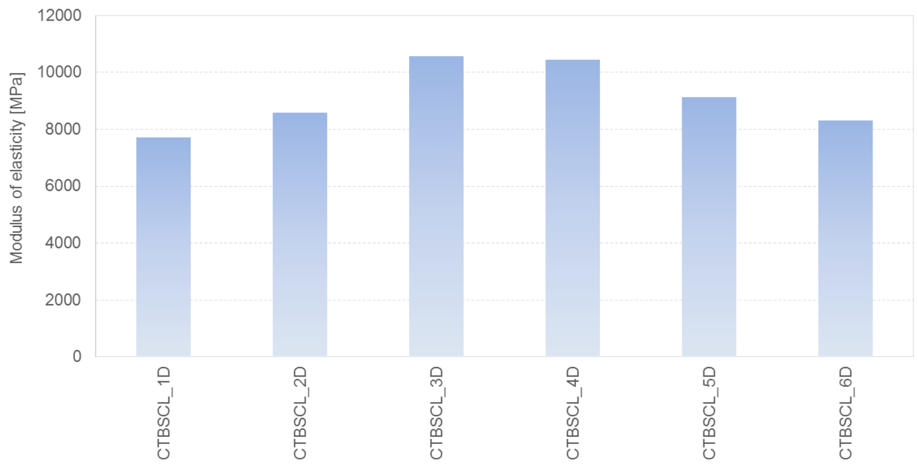

Figure 8.108 Distribution of moduli of elasticity obtained for double wallettes.

8.4.3 Tests for the determination of bond strength

The purpose of this section is to describe the complementary destructive tests that were carried out on 26 masonry *triplets*, as shown in Figure 8.109, to determinate the bond strength of their horizontal bed-joints at different maturation ages using the bond wrench method described in the standard EN 1052-5:2005 "Methods of test for masonry – Part 5: Determination of bond strength by the bond wrench method" (EN 1052-5, 2005).

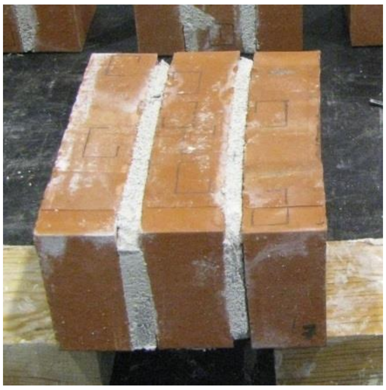

Figure 8.109 Type of specimens subjected to bond strength test.

The main idea of the test is to keep the specimen rigidly held while a clamp is applied to its top unit, see Figure 8.110. A bending moment is applied to the clamp by a lever until the top unit is torn from the remaining part of the specimen. From the stresses achieved by the specimen, the bond strength of the masonry can be evaluated.

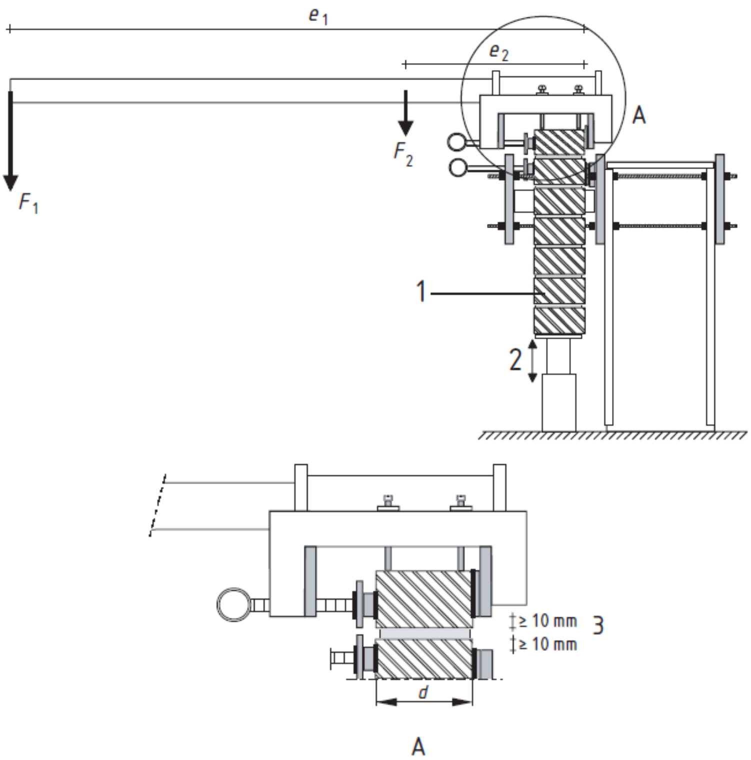

Figure 8.110 Example of a possible device for the test in accordance with EN 1052-5 (2005).

The device used to carry out this test was the same previously used on the triplets of the first and second campaigns of this work. This device allows the use of a torque wrench with a memory needle for moment recording. All tests performed in triplets that were referred in sub-chapter 8.4.2 were performed using this device, as illustrated in Figure 8.111.

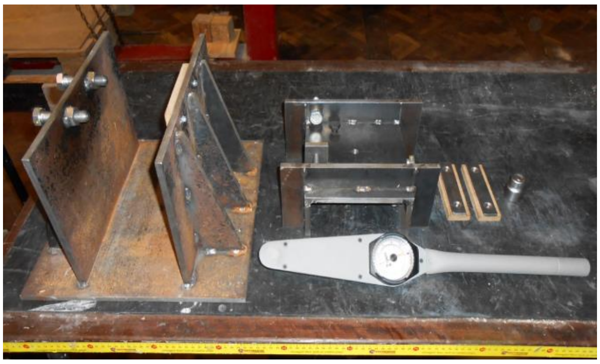

Figure 8.111 Test device used for bond-wrench test.

The device has two independent steel structures: a lower support frame with two side plates, reinforced with gussets, and welded to a base plate, which holds in place the unit beneath the top bed-joint of the specimen without applying any significant bending moment to any lower units; the upper structure is a lever with a clamp at one end, made up of three welded plates and a horizontal level steel rebar, which can be applied to the top unit of the *triplet*.

The test procedure was as follows:

1. The lower frame was attached to a rigid plate and a position for the *triplet* was defined, according with the standard. The screws were clamping approximately with equal torque (a ratchet torque wrench was used). Bricks and small pieces of timber were used with the thickness of the joints to ensure the same fixing height as defined in the standard. This was envisaged for two reasons: i) since the lower structure is common to the two types of *triplets* which have different heights; and ii) so that after the first failure of the connection the specimen could be raised to the required height, allowing the second connection to be tested, as shown in Figure 8.112;

First bed joint Second bed joint

Figure 8.112 Test of the two connections in triplets using the same test device.

2. The *triplet* was securely clamped in the retaining frame such that the second from top unit had a reasonable degree of restraint against rotation but the joint to be tested remained between 10 and 15 mm clear of the lower clamp. The clamp was intertwined with thin layers of a material such as plywood to ensure an even grip;

3. Fix the upper clamp with lever arm on the upper block to be tested, respecting the tightening location indicated by the standard (a distance equal to or greater than 10 mm from the test joint) and ensuring that the lever is horizontal, as shown in ;

4. Apply the vertical force on the torque wrench and read the value of the moment that leads to a bond failure, as shown in Figure 8.114;

5. Weighing of the top unit and the adherent mortar leading to a bond failure, as shown in Figure 8.115.

Figure 8.113 Application of vertical force until bond failure.

Figure 8.114 Application of vertical force until bond failure.

Figure 8.115 Measure of the weight of the top unit and adherent mortar.

Figure 8.81 present triplets during the bond wrench test after break the first and second bed joint.

Failure of second joint

Failure of second joint

Figure 8.116 Measure of the weight of the top unit and adherent mortar.

For each valid failure the bond strength was calculated using the following expression, which includes the effects of both applied bending moment and compression:

$$f_{wi} = \frac{F_1 e_1 + F_2 e_2 - \frac{2}{3} d\ (F1 + F2 + W/4)}{\frac{bd^2}{6}} \qquad (10)$$

where:

f_{wi} bond strength in masonry [MPa];

b width of the bed-joint tested [mm];

d depth of the specimen [mm];

e_1 distance from the applied load (F_1) to the tension face of the specimen [mm];

e_2 distance from the centre of gravity of the lower and upper clamp (F_2) from the tension face of the specimen [mm];

F_1 applied load [N];

F_2 weight of the bond wrench [N];

W weight of the masonry unit pulled off the specimen and any adherent mortar [N].

The modes of failure represented in Figure 8.117 were considered valid to calculate the bond strength, according to EN 1052-5:2005 "Methods of test for masonry – Part 5: Determination of bond strength by the bond wrench method" (EN 1052-5, 2005). The type of bond failure mechanisms obtained in the tests exemplified in Figure 8.118. In Appendix I, the pictures for tested specimens after 6 weeks are presented.

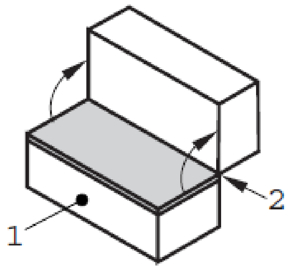

Failure at interface between mortar and upper unit.

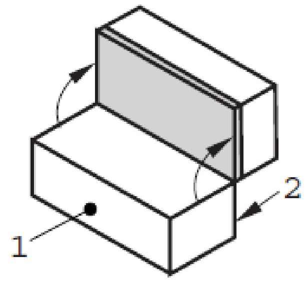

Failure at interface between mortar and lower unit

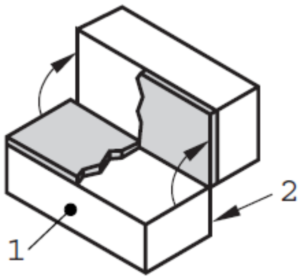

Failure at interface between mortar and both units

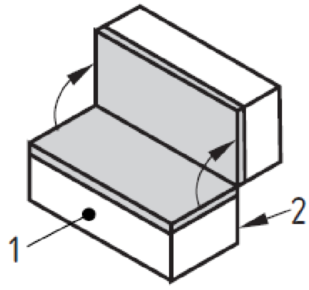

Tension failure within mortar bed

Figure 8.117 Admissible failure mechanisms for the bond wrench test.

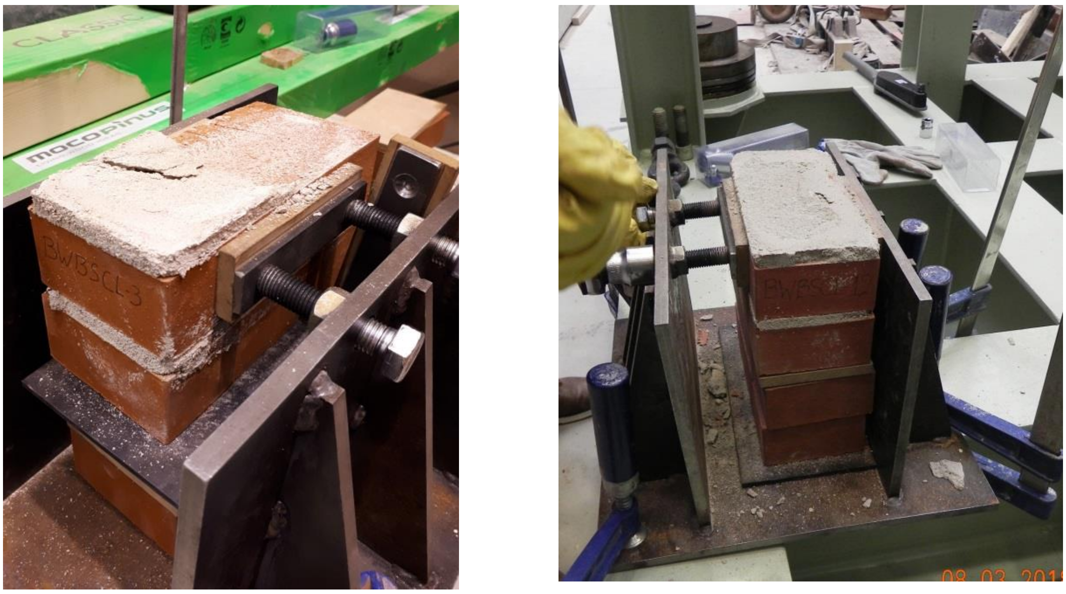

Figure 8.118 Example of failure mechanisms obtained for triplets in the bond wrench test.

Table 8.36 presents the results from tests carried out after two, three, four and six weeks of maturation. Each assembly included two mortar joints, termed as upper and lower joints, consequently, two estimates were obtained for every specimen. The average values are shown in Table 8.37.

Table 8.36 Results from bond wrench tests on triplets.

Triplet specimen ID / tested joint		Testing age	Mass of detached unit [g]	Maximum attainable moment [Nm]	Flexural bond strength [MPa]
BWBSCL-1	Upper joint	2 weeks	2182	112	0.248
	Lower joint		2469	68	0.145
BWBSCL-2	Upper joint	2 weeks	2429	166	0.376
	Lower joint		2449	134	0.300
BWBSCL-3	Upper joint	2 weeks	2466	108	0.239
	Lower joint		2348	113	0.251
BWBSCL-4	Upper joint	2 weeks	2240	99	0.218
	Lower joint		2427	120	0.267
BWBSCL-5	Upper joint	3 weeks	2448	70	0.149
	Lower joint		2513	70	0.149
BWBSCL-6	Upper joint	3 weeks	2146	107	0.237
	Lower joint		2154	101	0.223
BWBSCL-7	Upper joint	3 weeks	2365	124	0.277
	Lower joint		2482	131	0.293
BWBSCL-8	Upper joint	3 weeks	2264	132	0.296
	Lower joint		2589	102	0.225
BWBSCL-9	Upper joint	3 weeks	2140	110	0.244
	Lower joint		2202	208	0.475
BWBSCL-10	Upper joint	4 weeks	2208	205	0.468
	Lower joint		2234	100	0.220
BWBSCL-11	Upper joint	4 weeks	2186	157	0.355
	Lower joint		2533	127	0.284
BWBSCL-12	Upper joint	4 weeks	2140	155	0.350
	Lower joint		2553	171	0.388
BWBSCL-13	Upper joint	4 weeks	2142	141	0.317
	Lower joint		2565	166	0.376
BWBSCL-14	Upper joint	6 weeks	2366	242.5	0.556
	Lower joint		2267	185	0.421
BWBSCL-15	Upper joint	6 weeks	2262	122.5	0.273
	Lower joint		2450	172.5	0.391
BWBSCL-16	Upper joint	6 weeks	2188	105	0.232
	Lower joint		2454	192.5	0.438
BWBSCL-17	Upper joint	6 weeks	2110	30	0.055
	Lower joint		2734	123	0.274
BWBSCL-18	Upper joint	6 weeks	2102	153	0.345
	Lower joint		2565	112.5	0.249
BWBSCL-19	Upper joint	6 weeks	2086	83	0.180
	Lower joint		2587	297.5	0.686
BWBSCL-20	Upper joint	6 weeks	2225	127.5	0.285
	Lower joint		2459	275	0.633
BWBSCL-21	Upper joint	6 weeks	2124	117.5	0.261
	Lower joint		2647	183	0.416
BWBSCL-22	Upper joint	6 weeks	2108	165	0.374
	Lower joint		2460	117.5	0.261
BWBSCL-23	Upper joint	6 weeks	2193	175	0.397
	Lower joint		2458	275	0.633
BWBSCL-24	Upper joint	6 weeks	2186	172.5	0.391
	Lower joint		2513	187.5	0.426
BWBSCL-25	Upper joint	6 weeks	2284	185	0.421
	Lower joint		2340	182.5	0.415
BWBSCL-26	Upper joint	6 weeks	2337	190	0.432
	Lower joint		2360	160	0.362

Table 8.37 Summary of bond strength tests on triplets.

Age of specimen in moment of test	Bond strength		
	Average [MPa]	Standard deviation [MPa]	Coefficient of variation [-]
2 weeks	0.256	0.066	0.259
3 weeks	0.257	0.092	0.360
4 weeks	0.345	0.074	0.214
6 weeks	0.365	0.131	0.360

The average estimate of the bond tensile strength, as obtained from the tests carried out the week of the shake-table tests (i.e. week six) is 0.365 MPa, with standard deviation, σ = 0.13 MPa (C.o.V. = 0.36), after removing outliers (i.e. lower joint of BWBSCL_19).

Figure 8.25 shows the maturation curve over time for the flexural bond strengths of triplets.

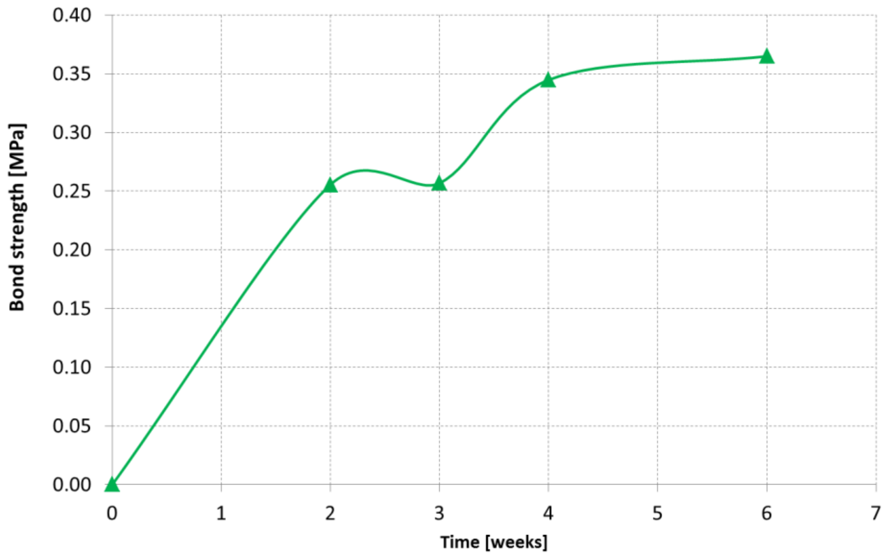

Figure 8.119 Maturation curve over time for the flexural bond strengths of triplets.

8.4.4 Tests for the determination of shear strength

The test for determination of shear strength was performed according to an adaptation of the standard method described in the standard EN 1052-3 (2005). The principle of this test is the determination of the initial shear strength in the plane of the horizontal joints, the characteristic value of the cohesion and the coefficient of friction.

This test was carried out on the *triplets* already mentioned. With the objective of recording the evolution of the displacements in the specimens during the tests, two displacement transducers were used on one side with the purpose of analysing the behaviour of the brick / mortar interface, thus registering the vertical displacement differential between rows. This displacement ratio was defined by a small plate, fixed to the central block, thus allowing to determine the displacements in the end blocks relative to the central block. Two deformeters (1 and 2) were also placed on each side of the joint to measure the horizontal displacements in these joints, thus allowing them to be measured during the test. Figure 8.120 presents the instrumentation placed on *triplets.* An example of the location of the instrumentation on specimens is shown in Figure 8.121 (the schematics with the instrumentation locations for all tested *triplets* are given in Appendix H)

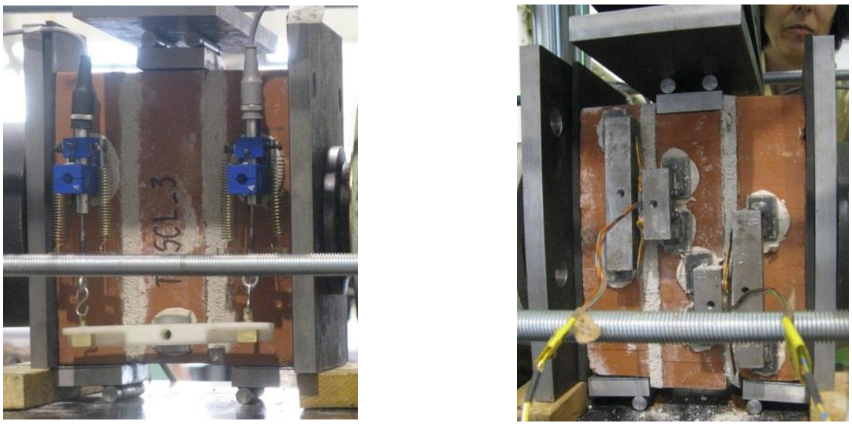

Front Back

Figure 8.120 Instrumentation placed on the triplets.

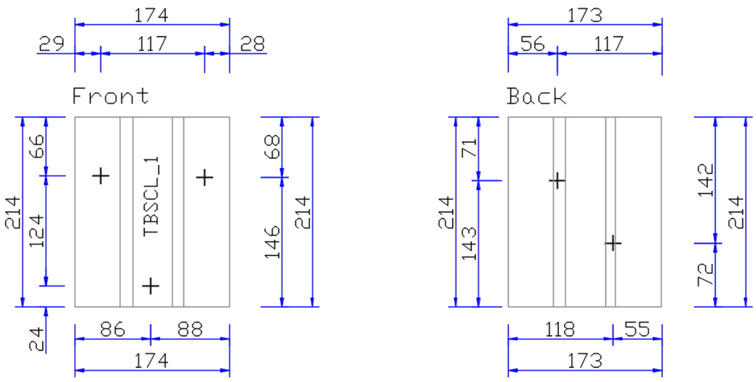

Front Back

Figure 8.121 Location of the instrumentation placed on the triplets (dimensions in mm).

Since the blocks present a strength greater than 10 N/mm^2, the pre-compression stress F_{pi} to be applied on the specimens should be 0,2 N/mm^2, 0,6 N/mm^2 and 1,0 N/mm^2. The pre-compression force should be uniform and well distributed on the faces of the specimen.

The compression force was read by a load cell with a capacity of 25 kN while the shear force was measured by the load cell of the actuator of the testing machine itself, with a maximum capacity of 1000 kN. The use of an auxiliary pumping system with an accumulator ensured that the various pre-compression levels remained constant during the test, even though some dilatancy is to be expected.

Given the existence of small irregularities on the lateral sides of the *triplets* (areas to be pre-compressed) a neoprene rubber was placed between the specimen and the plates of the hydraulic jacks that apply the pre-compression.

The shear strength test consisted on the application of a vertical force in the central block, a shear force, and an horizontal force applied to the geometric center of the specimen, a pre-compression force. The shear force was applied with displacement-control at a speed of 0.01 mm/s and a sampling frequency of 25 Hz. The test scheme is shown in Figure 8.122.

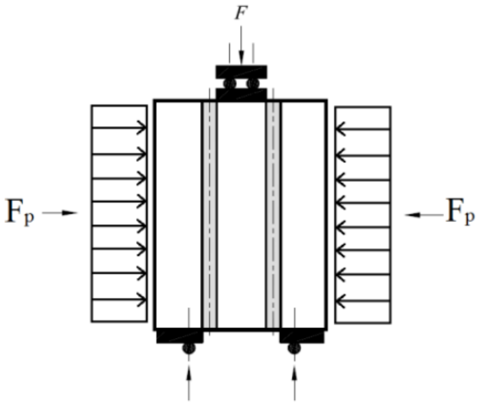

Figure 8.122 Test scheme for the determination of shear strength.

The device used to perform this test was the same already used in the first campaign and is shown in Figure 8.123.

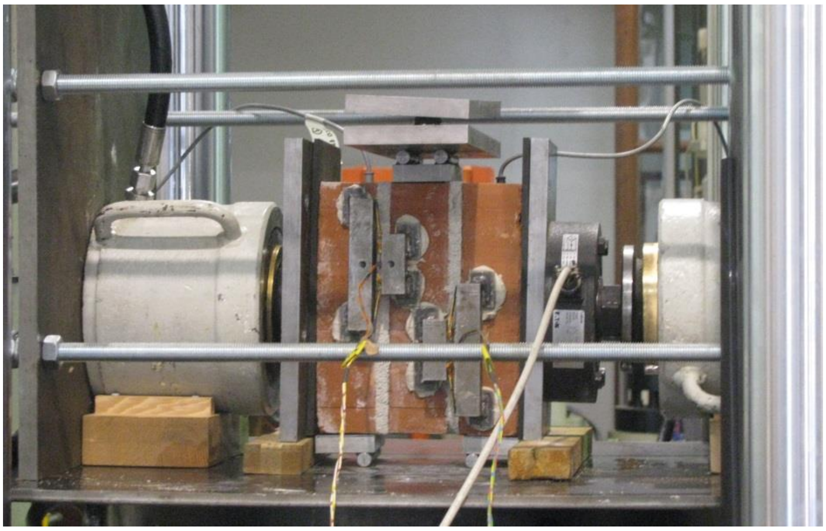

Figure 8.123 Device used in shear test.

The initial shear strength of the masonry was determined with a shear action defined by three points of application of load parallel to the horizontal joints and with the simultaneous application of a pre-compression force perpendicular to the horizontal joints. The tests were carried out, recording the load and deformation values, identifying the representative values upon failure, and the test was finalised after confirmation of the significant reduction of the shear force and measurement of the deformation for the various pre-compression levels.

Cohesion and shear stress were determined on at least three specimens at each pre-compression level (0,2 N/mm^2, 0,6 N/mm^2 and 1,0 N/mm^2). The friction was then determined for the two remaining pre-compression levels different from the initial one, as exemplified in the plots of Figure 8.124, Figure 8.125 and Figure 8.126.

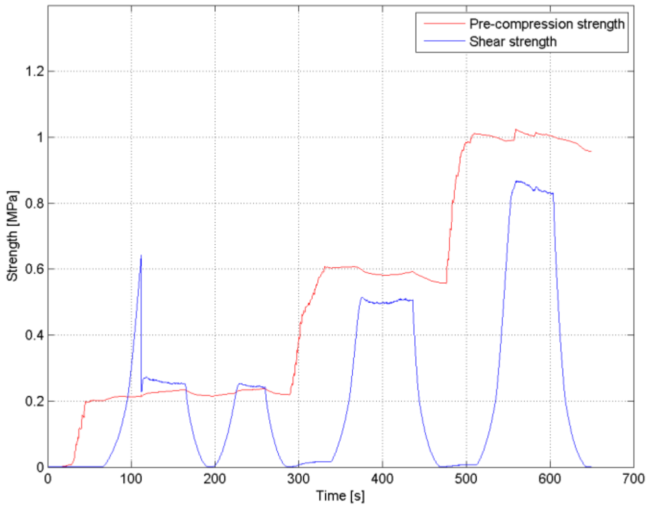

Figure 8.124 Application of the pre-compression and shear stresses throughout the test starting with the lowest pre-compression level (TBSCL_2).

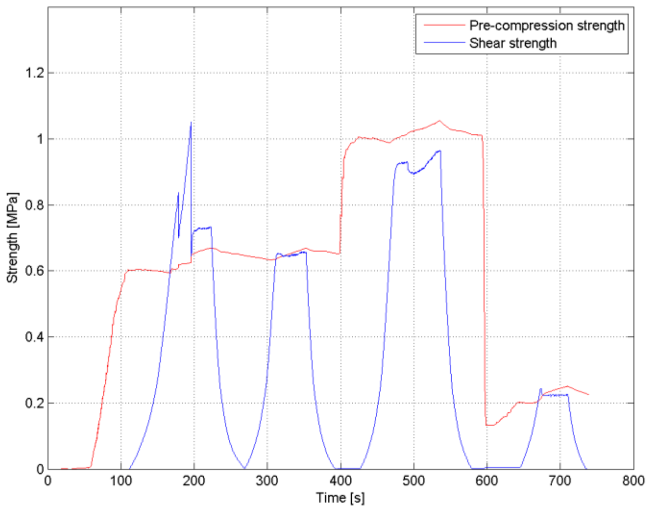

Figure 8.125 Application of the pre-compression and shear stresses throughout the test initiated with the intermediate pre-compression level (TBSCL_5).

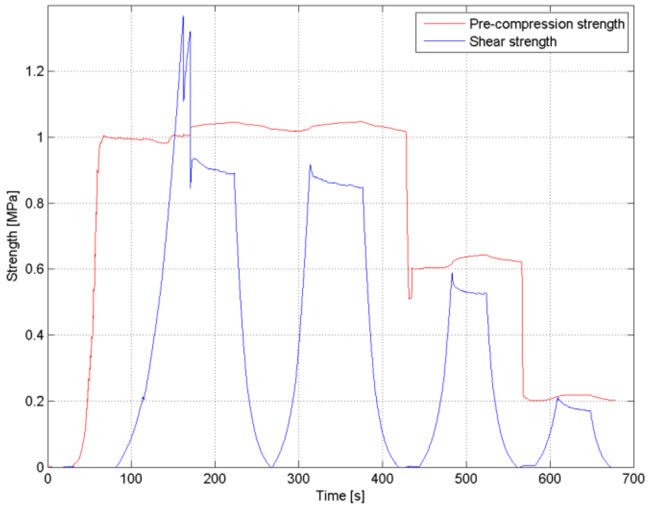

Figure 8.126 Application of pre-compression and shear stresses throughout the test started at the highest pre-compression level (TBSCL_8).

For each specimen the pre-compression stress and the shear stress were calculated according to the following formulas:

$$f_{pi} = \frac{F_{pi}}{A_{ei}} \tag{11}$$

$$f_{vi} = \frac{F_{i,máx.}}{2 \times A_{ei}} \tag{12}$$

where:
f_{pi} is the pre-compression stress [MPa];
F_{pi} is the pre-compression force [N];
A_{ei} is the effective area of contact [mm^2];
f_{vi} is the shear failure stress [MPa];
$F_{i,máx.}$ is the shear failure force [N].

For each pair of values (f_{pi}, f_{vi}) it is possible to obtain a plot like the one shown in Figure 8.127. Coulomb's law is the most representative of the results. The shear strength of the bedding mortar of the specimens (f_v) depends on three parameters: cohesion, coefficient of friction and transversal compression. Cohesion contributes to the force only if the bedding mortar is not cracked, while the frictional force also acts after cracking, as long as there is contact between the two materials. The shear strength (f_v), according to Coulomb's law, is linearly depending on the pre-compression stress (f_p):

$$f_v = f_{v0} + \mu \times f_p \tag{13}$$

where:
f_{v0} is the cohesion [MPa];
μ is the angle of friction with dimensionless units [-].

For each specimen, the cohesion and internal friction angle were calculated, as shown in the plot of Figure 8.128.

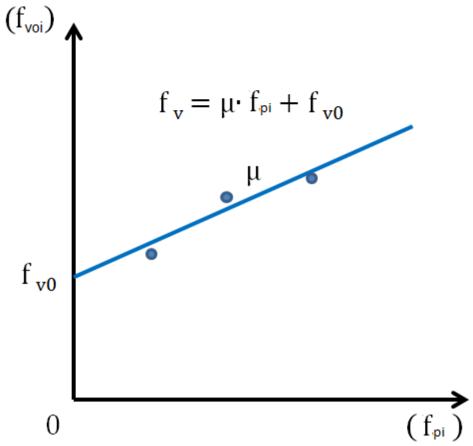

Figure 8.127 Theoretical determination of cohesion and angle of friction in the shear strength test.

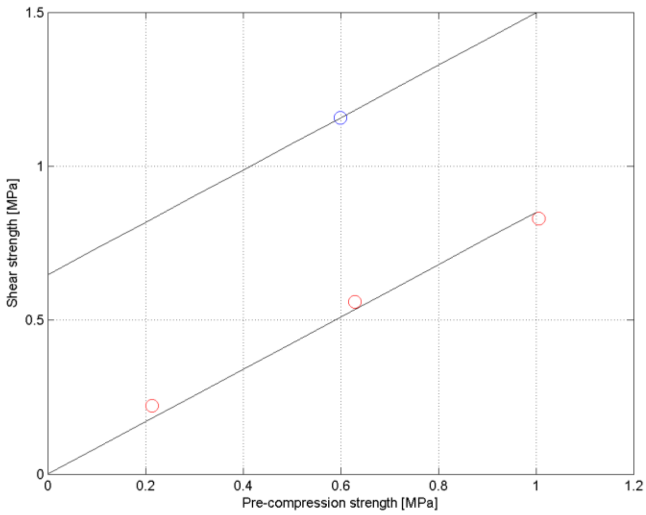

Figure 8.128 Determination of cohesion and friction angle for specimen TS_3.

The acceptable collapse mechanisms for the test to be considered valid are shown in Figure 8.129.

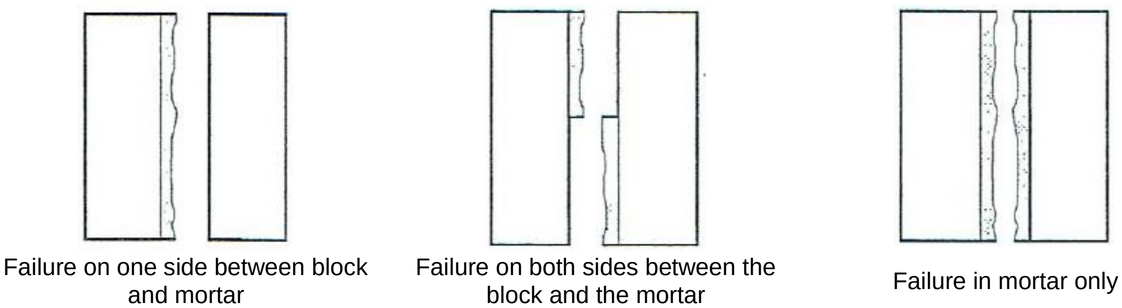

Figure 8.129 Acceptable collapse mechanisms for the shear strength test.

The test is finished upon the measurement of the friction after fracture formations, while there is contact between the two materials, as shown in Figure 8.130.

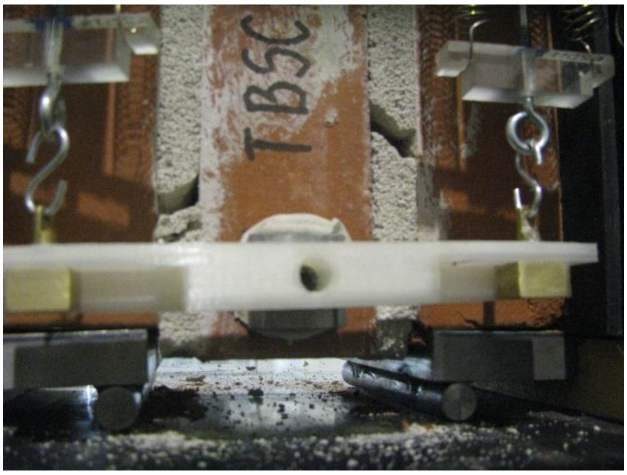

Figure 8.130 Completion of the test for the triplets tested.

The type of failure mechanisms obtained in the various tests are as exemplified in Figure 8.131. Appendix I presents further details on the obtained fractures for all the specimens tested.

Figure 8.131 Example of one of the failure mechanisms obtained for each triplet in the shear strength test.

The shear strength results obtained in the tests for the all specimens are summarised in Table 8.38.

Table 8.38 Summary of the shear strength obtained for all solid clay triplets tested.

Specimen	Date of test	Contact area A_{ei} [mm^2]	Pre-compression stress f_{pi} [MPa]	Shear strength f_{vi} [MPa]
TBSCL_1	26-04-2018	21477.48	0.2003	0.5503
TBSCL_2	26-04-2018	21409.11	0.2137	0.6437
TBSCL_3	26-04-2018	21514.99	0.2148	0.5717
TBSCL_4	26-04-2018	21513.79	0.6218	0.9445
TBSCL_5	26-04-2018	21483.71	0.6261	1.0520
TBSCL_6	26-04-2018	21527.14	0.5995	1.1576
TBSCL_7	30-05-2018	21445.00	1.0330	1.1583
TBSCL_8	30-05-2018	21473.56	1.0023	1.3691
TBSCL_9	30-05-2018	21342.36	1.0175	1.3372
TBSCL_10	30-05-2018	21557.22	1.0012	1.1783
TBSCL_11	30-05-2018	21548.20	0.9955	1.2521
TBSCL_12	30-05-2018	21424.24	0.5842	0.9643
TBSCL_13	30-05-2018	21491.45	0.6065	0.9697
TBSCL_14	30-05-2018	21620.67	0.1875	0.6475
TBSCL_15	30-05-2018	21329.64	0.1995	0.6573
TBSCL_16	30-05-2018	21523.89	0.2170	0.5854

The plot in Figure 8.132 relate the individual value of the failure stress to the shear strength and the individual pre-compression stress value of each *triplet*, according to point 10 of standard EN 1052-3 (2005). The plots for all specimens are shown in Appendix J.

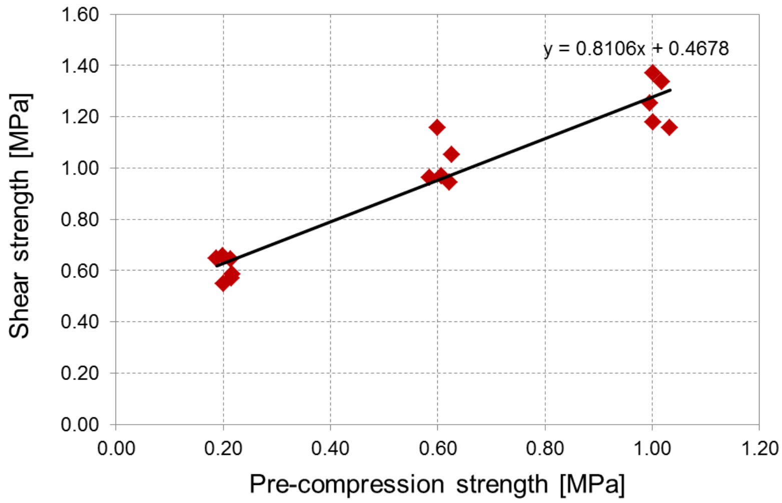

Figure 8.132 Shear strength, cohesion and internal friction angle for the solid clay triplets tested.

By plotting a line of linear regression with all points and through the equation that translates this line we can derive the mean values of cohesion (f_{v0}) and angle of internal friction (μ), presented in Table 8.39 for the two types of *triplets*.

Table 8.39 Summary of average cohesion values and internal friction angles for the solid clay triplets tested.

Specimen	f_{v0} [MPa]	μ [-]
Solid Clay *triplets*	0.47	0.81

8.4.5 Tests for the determination of torsional shear strength

A test setup for the evaluation of the torsional shear strength of the bed joints under combined torsion and compression was developed, based on the experimental study of Graziotti *et al.* (2018).

This test setup is under construction and the tests will be performed in the coming weeks. A Coulomb-type friction law will approximate the test results, with an initial shear strength in torsion, $f_{v0,tor}$, and a coefficient of friction, μ_{tor}.

8.4.6 Tests for the determination of out-of-plane bending strength

Four-point out-of-plane bending tests on eight single-wythe wallettes (EN 1052-2, 1999) were carried out to evaluate the out-of-plane flexural strength of the masonry, f_{x2}. The test setup is represented in Figure 8.133. Being the first time that this type of test was performed, some tests were used in a learning curve and only five of the tests were deemed as having produced acceptable results.

Figure 8.133 Test setup for four-point out-of-plane bending tests.

The failure mechanisms of these tests may correspond to a line failure, through bricks and vertical mortar joints, a stepped failure, following the joint geometry when its resistance is clearly lower than the brick flexural strength, or a mixture of both. The observed failure mechanisms correspond to a mixed failure, with some tendency to a line failure, as can be observed in Figure 8.134.

The stress-displacement curves of the specimens are represented in Figure 8.135, with the results being summarised in Table 8.40.

Table 8.40 Summary of flexural strength from out-of-plane bending tests.

Specimen	Flexural strength [MPa]
3	2.13
4	2.24
5	2.01
6	2.40
8	1.86
Average [MPa]	**2.13**
Standard deviation [MPa]	0.21
Coefficient of variation [-]	0.097

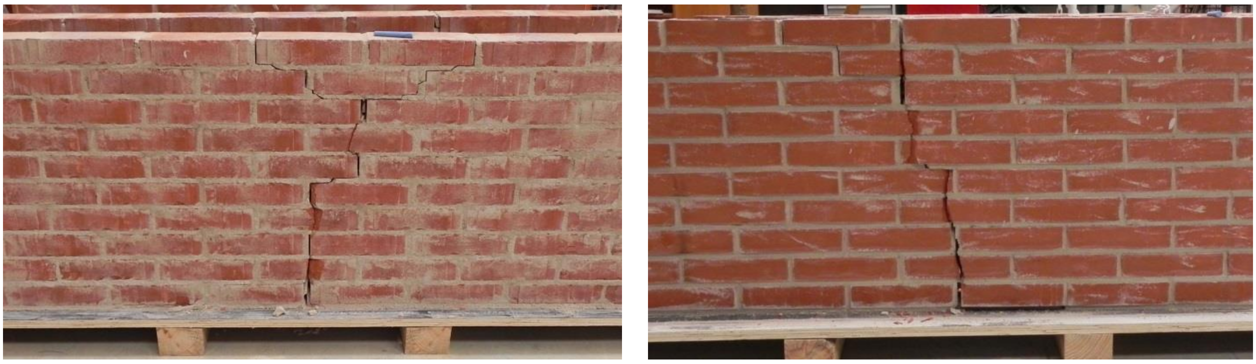

Figure 8.134 Failure mechanisms in out-of-plane bending tests.

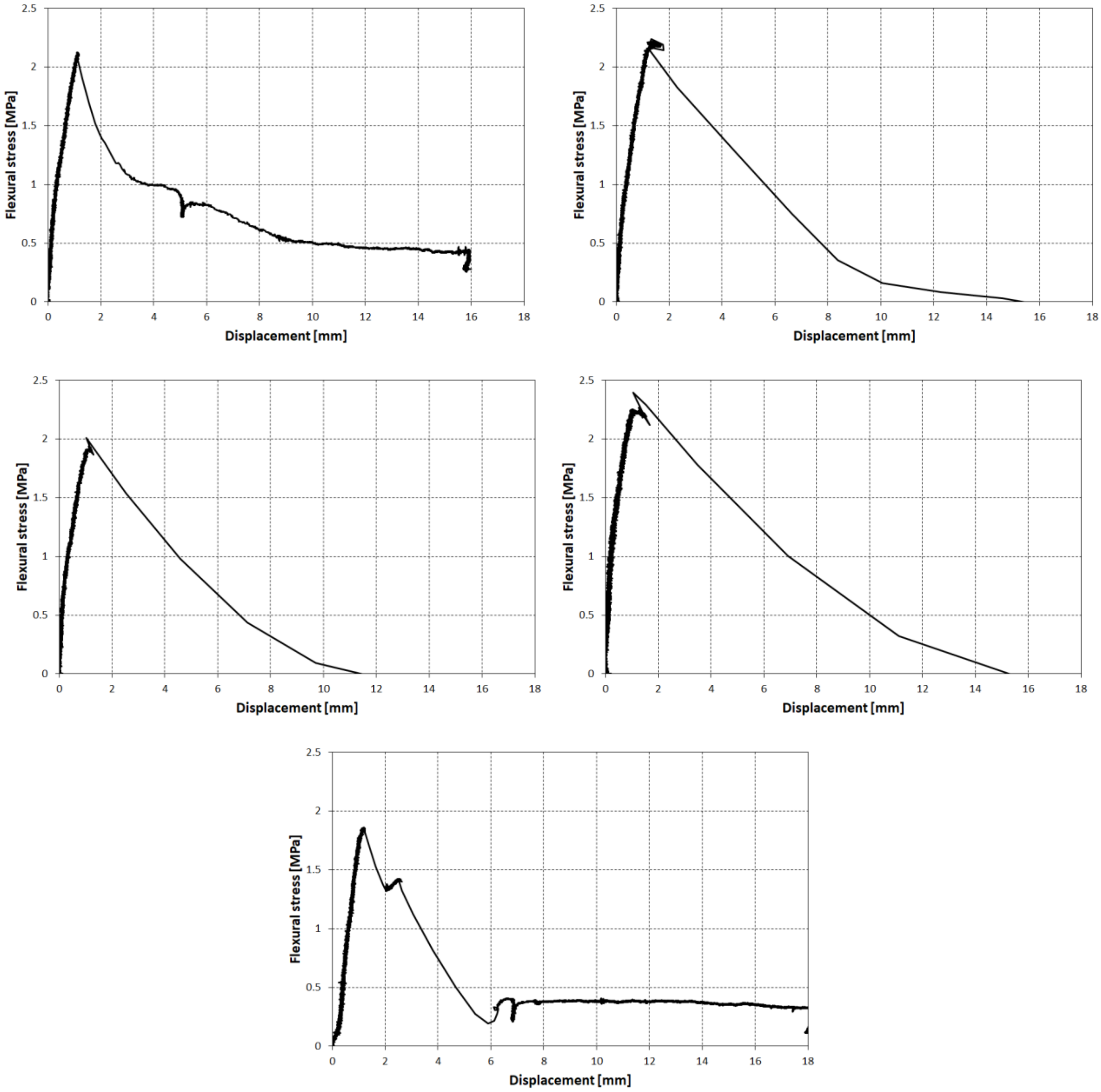

Figure 8.135 Four-point out-of-plane bending test response curves.

9 CONCLUSIONS

A testing campaign was designed including unidirectional shake-table tests on a full-scale building prototype up to collapse. The structure was a single-storey clay-URM building that embodied construction details of typical detached houses found in the Groningen province of the Netherlands. The absence of seismic considerations in the design of the local URM buildings, in combination with the scarcity of damage data due to the unprecedented exposure to seismic actions, underlines the necessity for lab testing at full scale to investigate the overall dynamic response of such structures and the most prevalent collapse mechanisms.

The general testing strategy was kept consistent with past tests, to allow the comparison of the response characteristics of the building with previously tested full-scale specimens. A considerable number of tests were performed comprising realistic induced-seismicity earthquakes at increasing shaking intensity, and random vibrations to quantify any changes in the natural frequencies of the building as a result of damage accumulation. The dynamic tests were complemented by a series of small-scale tests to characterise the employed masonry.

The results obtained from these test are aligned with the results of the shake-table tests on EUC-BUILD-2. Some of the main outcomes are summarised below:

- The building did not suffer any visible damage up to input motion with *PGA* of 0.21 g and reached its near-collapse state for a *PGA* of 0.68 g when the squat chimney collapsed. Under seismic input with *PGA* equal to 1.0 g, debris fell in the interior of the building, and a considerable percentage of the walls had lost their load-bearing capacity. Significant out-of-plane damage was observed in zones of high acceleration response and absence of wall-to-diaphragm connections (i.e. West wall). Damage due to wall in-plane response was mostly associated with rocking of slender piers.
- The tests confirmed the main behavioural trends observed in the shake-table tests on building EUC-BUILD-2, such as substantial hysteretic energy dissipation and inelastic deformations, and high floor-diaphragm flexibility. In particular, the flexible wooden diaphragms allowed the East and West walls to lean and bow excessively out of their plane, while providing little coupling between parallel walls (i.e. North and South), resulting in significant differential displacements. As the floor diaphragm bent sideways, it caused severe damage to the interior wall.
- The floor girder provided a considerable lateral restraint to the East wall, favouring the overall stability against overturning while the high vertical compression prevented the formation of a hinge at mid-height of the wall. The timber plates installed on the external faces of the gables proved essential in preventing the walls from leaning too far and collapsing.
- The test results also confirmed the evident hazardous nature of the free-standing parts of chimneys in earthquakes, albeit for input motions much larger than the ones expected to occur in the Netherlands. The chimneys proved to be of the most vulnerable parts of the structure, prone to fail under shaking intensity well below the one required to cause structural collapse.
- Among other aspects, the new tests allowed refining the definition of damage limit states for URM walls; correlating the observed damage with quantitative engineering parameters for the performance-based assessment of URM buildings.
- An overarching objective of the experiments was to acquire adequate data for the development of numerical models with high predictive accuracy. The enhanced capabilities of the ever-increasing available options in numerical modelling of complex structures offer the opportunity to employ such experimental information for further model validation and improvements in predicting progressive damage and collapse. In this regard, the test provided abundant information for constraining the numerical response of such models.

REFERENCES

Allemang, R.J., Brown, D.L. [1982] "A correlation coefficient for modal vector analysis", *Proceedings of the 1st International Modal Analysis Conference*, Orlando, United States, 8-10 November 1982.

Arias, A. [1970] "A measure of earthquake intensity", In: Hansen, R.J. (ed), *Seismic Design of Nuclear Power Plants*, MIT Press, Cambridge, Massachusetts, United States; 1970, pp. 438-483.

Applied Science International (ASI). *Extreme Loading for Structures v5*, Applied Science International LLC, Durham, North Carolina, United States, 2017.

Bendat, J.S., Piersol, A.G. [2010] *Random Data: Analysis and Measurement Procedures* (4th Edition), Wiley Series in Probability and Statistics.

Bianchini, M., Diotallevi, P., Baker, J.W. [2009] "Prediction of inelastic structural response using an average of spectral accelerations", *Proceedings of 10th International Conference on Structural Safety and Reliability (ICOSSAR09)*, Osaka, Japan, 13-17 September 2009.

Bommer, J.J., Crowley, H., Pinho, R., Polidoro, B. [2015] "Selection of acceleration time-series for shake table testing of Groningen masonry building at the EUCENTRE, Pavia", *Report - Groningen field seismic hazard and risk assessment project*, EUCENTRE, Pavia, Italy.

Bourne, S.J., Oates, S.J., Bommer, J.J., Dost, B., van Elk, J., Doornhof, D. [2015] "A Monte Carlo method for probabilistic hazard assessment of induced seismicity due to conventional natural gas production", *Bulletin of the Seismological Society of America*, 105(3), 1721-1738. https://doi.org/10.1785/0120140302.

Bradley, B.A. [2011] "Correlation of significant duration with amplitude and cumulative intensity measures and its use in ground motion selection", *Journal of Earthquake Engineering*; 15(6), 809-832. https://doi.org/10.1080/13632469.2011.557140.

Brincker, R., Ventura, C., Andersen, P. [2001] "Damping estimation by frequency domain decomposition", *Proceedings of the 19th International Modal Analysis Conference*, Hyatt Orlando, Kissimmee, Florida, United States, 5-8 February 2001.

Brown, D. *Tracker 5.0: Video analysis and modelling tool*, Open Source Physics, 2018. Available at https://physlets.org/tracker.

Campbell, K.W., Bozorgnia, Y. [2010] "A ground motion prediction equation for the horizontal component of cumulative absolute velocity (CAV) based on the PEER-NGA strong motion database", *Earthquake Spectra*, 26(3), 635-650. https://doi.org/10.1193/1.3457158.

Centre Scientifique et Technique du Batiment (CSTB) [1993] *Certification CSTB des enduits monocouches d'imperméabilisation. Modalités d'essais*. Cahiers du CSTB 2669-4, Livrasion 341, Paris, Fance.

Correia, A.A., Tomassetti, U., Campos Costa, A., Penna, A., Magenes, G., Graziotti, F. [2018] "Collapse shake-table test on a URM-timber roof substructure", *Proceedings of the 16th European Conference on Earthquake Engineering (ECEE)*, Thessaloniki, Greece, 18-21 June 2018.

Eads, L., Miranda, E., Lignos, D. [2015] "Average spectral acceleration as an intensity measure for collapse risk assessment", *Earthquake Engineering & Structural Dynamics*, 44(12), 2057-2073. https://doi.org/10.1002/eqe.2575.

Electrical Power Research Institute (EPRI) [1991] "Standardization of the cumulative absolute velocity", *Report EPRI TR-100082-T2*, EPRI, Palo Alto, California, United States.

EUCENTRE. *Videos of shake-table tests on a full-scale detached URM house with chimneys at LNEC in Portugal*, EUCENTRE, Pavia, Italy, 2018. Available at www.youtube.com/playlist.

European Committee for Standardization (CEN) [1999] *Methods of test for masonry units - Part 1: Determination of compressive strength*, European Standard EN 772-1, CEN/TC 125, Brussels, Belgium.

European Committee for Standardization (CEN) [1999] *Methods of test for masonry units - Part 10: Determination of moisture content of calcium silicate and autoclaved aerated concrete units*, European Standard EN 772-10, CEN/TC 125, Brussels, Belgium.

European Committee for Standardization (CEN) [2011] *Methods of test for masonry units - Part 11: Determination of water absorption of aggregate concrete, autoclaved aerated concrete*, European Standard EN 772-11, CEN/TC 125, Brussels, Belgium.

European Committee for Standardization (CEN) [1999] *Methods of test for mortar for masonry - Part 3: Determination of consistency of fresh mortar (by flow table*), European Standard EN 1015-3, CEN/TC 125, Brussels, Belgium.

European Committee for Standardization (CEN) [1998] *Methods of test for mortar for masonry - Part 6: Determination of bulk density of fresh mortar*, European Standard EN 1015-6, CEN/TC 125, Brussels, Belgium.

European Committee for Standardization (CEN) [1999] *Methods of test for mortar for masonry - Part 11: Determination of flexural and compressive strength of hardened mortar*, European Standard EN 1015-11, CEN/TC 125, Brussels, Belgium.

European Committee for Standardization (CEN) [1998] *Methods of test for masonry - Part 1: Determination of compressive strength*, European Standard EN 1052-1, CEN/TC 125, Brussels, Belgium.

European Committee for Standardization (CEN) [1999] *Methods of test for masonry - Part 2: Determination of flexural strength*, European Standard EN 1052-2, CEN/TC 125, Brussels, Belgium.

European Committee for Standardization (CEN) [2002] *Methods of test for masonry - Part 3: Determination of initial shear strength*, European Standard EN 1052-3, CEN/TC 125, Brussels, Belgium.

European Committee for Standardization (CEN) [2005] *Methods of test for masonry - Part 5: Determination of bond strength by the bond wrench method*, European Standard EN 1052-5, CEN/TC 125, Brussels, Belgium.

Giaretton, M., Ingham, J.M., Dizhur, D. [2017] "Experimental validation of seismic retrofit solutions for URM chimneys", *Bulletin of Earthquake Engineering*. 16(1), 295-313. https://doi.org/10.1007/s10518-017-0200-0.

Graziotti, F., Penna, A., Magenes, G. [2018] "A comprehensive in-situ and laboratory testing programme in support of seismic risk analysis of URM buildings subjected to induced earthquakes", *Bulletin of Earthquake Engineering*, In review.

Graziotti, F., Tomassetti, U., Rossi, A., Marchesi, B., Kallioras, S., Mandirola, M., Fragomeli, A., Mellia, E., Peloso, S., Cuppari, F., Guerrini, G., Penna, A., Magenes, G. [2016] "Shaking table tests on a full-scale clay-brick masonry house representative of the Groningen building stock and related characterization tests", *Technical Report EUC128/2016U*, EUCENTRE, Pavia, Italy. Available at www.eucentre.it/nam-project.

Graziotti, F., Tomassetti, U., Sharma, S., Grottoli, L., Magenes, G. [2018] "Experimental response of URM single leaf and cavity walls in out-of-plane two-way bending generated by seismic excitation", *Construction and Building Materials*. Accepted for publication.

Graziotti, F., Penna, A., Magenes, G. [2016] "A nonlinear SDOF model for the simplified evaluation of the displacement demand of low-rise URM buildings", *Bulletin of Earthquake Engineering*, 14(6), 1589-1612. https://doi.org/10.1007/s10518-016-9896-5.

Grünthal, G. (ed) [1998] *European Macroseismic Scale 1998 (EMS-98)*, Cahiers du Centre Européen de Géodynamique et de Séismologie 15, Centre Européen de Géodynamique et de Séismologie, Luxembourg, 1998.

Housner, G.W. [1952] "Intensity of ground motion during strong earthquakes", *Caltech Technical Report*, California Institute of Technology, California, United States. Available at http://authors.library.caltech.edu.

Instituto Português da Qualidade (IPQ) [2011] *Test for mechanical and physical properties of aggregates. Part 5: Determination of water content by drying in a ventilated oven*, Portuguese Standard NP EN 1097-5, Lisbon, Portugal.

Instituto Português da Qualidade (IPQ) [2006] *Test methods for natural stone. Determination of dynamic modulus of elasticity (by measuring fundamental resonance frequency),* Portuguese Standard NP EN 14146, Lisbon, Portugal.

Kallioras, S., Guerrini, G., Tomassetti, U., Marchesi, B., Penna, A., Graziotti, F., Magenes, G. [2018] "Experimental seismic performance of a full-scale unreinforced clay-masonry building with flexible timber diaphragms", *Engineering Structures*, 161, 231-249. https://doi.org/10.1016/j.engstruct.2018.02.016.

Kempton, J.J., Stewart, J.P. [2006] "Prediction equations for significant duration of earthquake ground motions considering site and near-source effects", *Earthquake Spectra*, 22(4), 985-1013. https://doi.org/10.1193/1.2358175.

Magenes, G., Penna, A., Senaldi, I.E., Rota, M., Galasco, A. [2014] "Shaking table test of a strengthened full-scale stone masonry building with flexible diaphragms", *International Journal of Architectural Heritage: Conservation, Analysis, and Restoration*, 8(3), 349-375. https://doi.org/10.1080/15583058.2013.826299.

Meguro, K., Tagel-Din, H. [2000] "Applied element method for structural analysis: theory and application for linear materials", *Proceedings of Japan Society of Civil Engineering (JSCE)*, 17(1), 21-35.

Mendes, L., Campos Costa, A. [2007] "LNEC-SPA: Signal processing and analysis tool for civil engineers - Version 1.0 - Build 12", *Report DE/NESDE*, LNEC, Lisbon, Portugal.

Mitchell, C.F., Mitchel, G.A. *Building Construction and Drawing - Part 1: First Stage or Elementary Course* (2nd Edition - Revised), B.T. Batsford, 52 High Holborn. 1889, pp. 37.

Netherlands Standardization Institute (NEN) [2017] NPR 9998: Assessment of structural safety of buildings in case of erection, reconstruction and disapproval - Basic rules for seismic actions: induced earthquakes. Dutch Standards, NEN, Delft, The Netherlands. The code response spectra are available at http://seismischekrachten.nen.nl/webtool.php.

Pinho, R., Malomo, D., Brunesi, E. [2017] "Nonlinear dynamic analysis of index buildings for v5 fragility and consequence models", *Deliverable D8 - Project title: Advanced modelling of URM buildings in support of fragility/consequence functions derivation*, Mosayk, Pavia, Italy. Available at www.nam.nl/feiten-en-cijfers.

Tondelli, M., Graziotti, F., Rossi, A., Magenes, G. [2015] "Characterization of masonry materials in the Groningen area by means of in situ and laboratory testing", *EUCENTRE Technical Report*, EUCENTRE, Pavia, Italy. Available at www.eucentre.it/nam-project.

Tomassetti, U., Correia, A.A., Candeias, P.X., Graziotti, F., Campos Costa, A. [2018] "Two-way bending out-of-plane collapse of a full-scale URM building tested on a shake-table", *Bulletin of Earthquake Engineering*. In review.

Travasarou, T., Bray, J.D., Abrahamson, N.A. [2003] "Empirical attenuation relationship for Arias intensity", *Earthquake Engineering & Structural Dynamics*, 32(7), 1133-1155. https://doi.org/10.1002/eqe.270.

Vaculik, J., Griffith, M.C. [2018] "Out-of-plane shake table testing of unreinforced masonry walls in two-way bending", *Bulletin of Earthquake Engineering*, 16(7), 2839-2876. https://doi.org/10.1007/s10518-017-0282-8.

Van Elk, J., Doornhof, D., Bommer, J.J., Bourne, S.J., Oates, S.J., Pinho, R., Crowley, H. [2017] "Hazard and risk assessments for induced seismicity in Groningen", *Netherlands Journal of Geosciences*, 96(5):259-269. https://doi.org/10.1017/njg.2017.37.

APPENDIX A. DYNAMIC IDENTIFICATION ANALYSIS RESULTS

CHAR#0

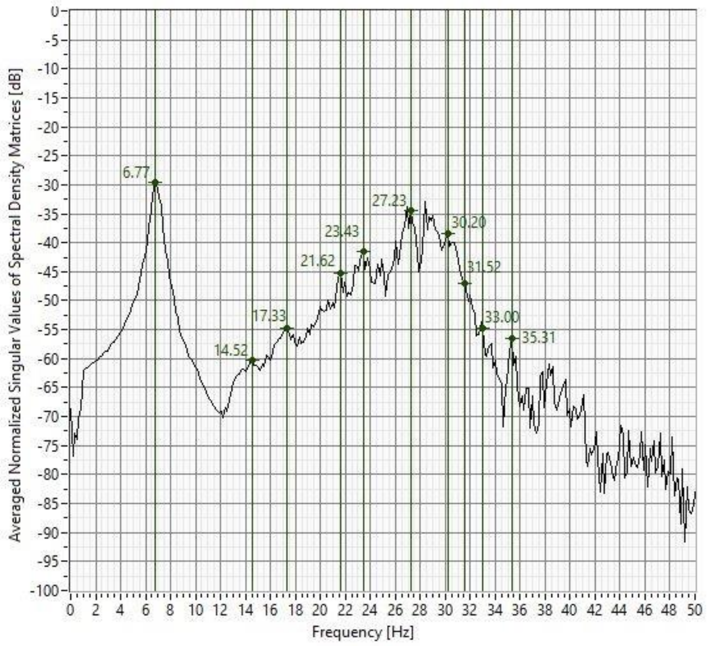

Frequency domain decomposition for dynamic identification CHAR#0

Vibration modes characteristics for dynamic identification CHAR#0

Mode	FDD Frequency [Hz]	EFDD Frequency [Hz]	Damping [%]
1	6.77	6.82	4.04
2	14.52	14.53	2.36
3	17.33	17.38	1.70
4	21.62	21.66	0.41
5	23.43	23.43	1.00
6	27.23	27.12	1.04
7	30.20	30.27	0.95
8	31.52	31.49	0.91
9	33.00	33.03	0.25
10	35.31	35.26	0.24

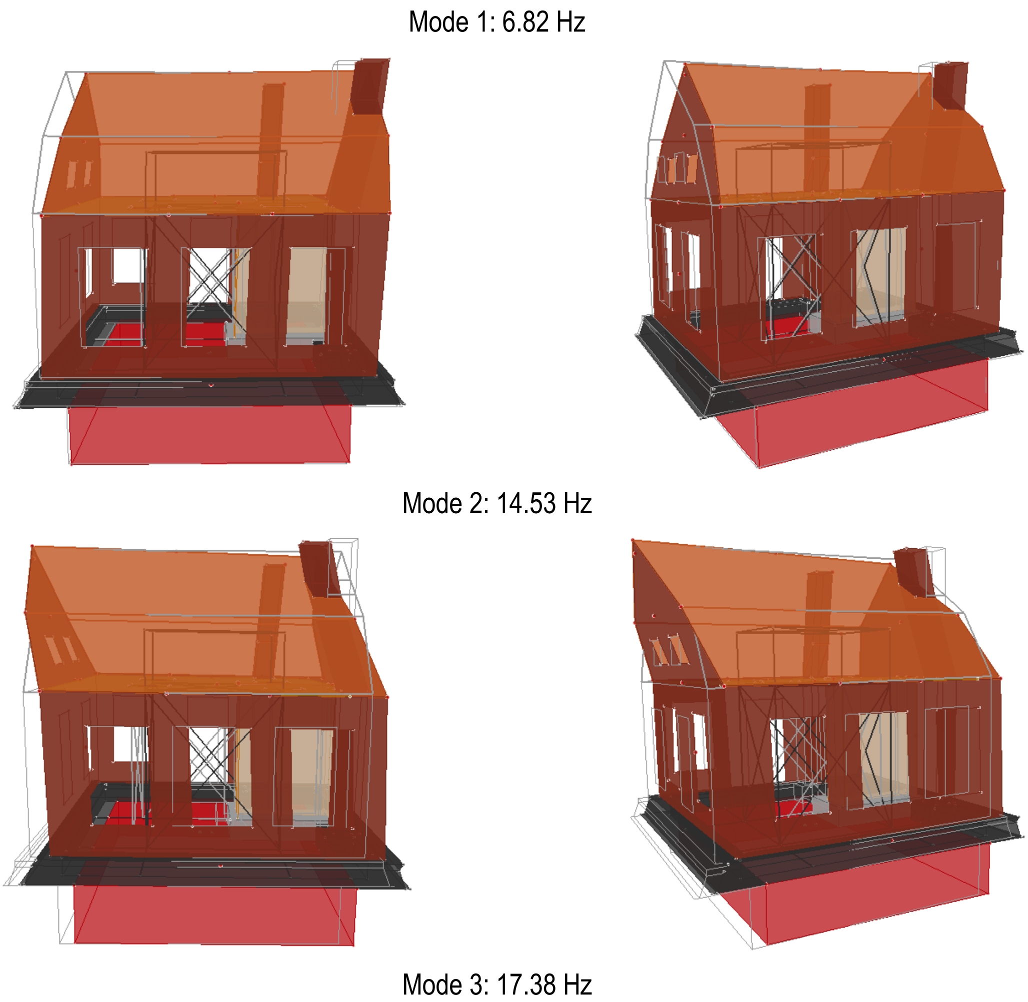

EFDD dynamic identification (CHAR#0)

CHAR#1

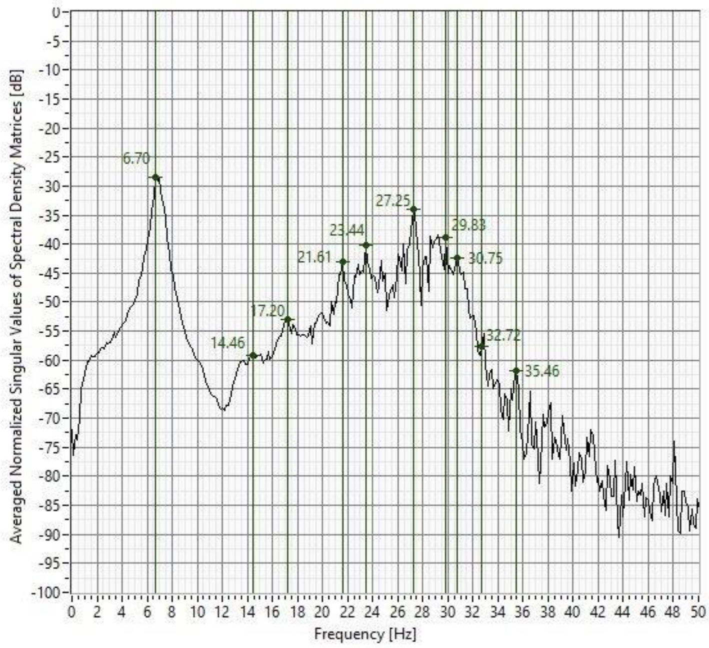

Frequency domain decomposition for dynamic identification CHAR#1

Vibration modes characteristics for dynamic identification CHAR#1

Mode	FDD Frequency [Hz]	EFDD Frequency [Hz]	Damping [%]
1	6.70	6.80	3.95
2	14.46	14.46	2.15
3	17.20	17.23	1.57
4	21.61	21.64	0.38
5	23.44	23.44	0.89
6	27.25	27.25	0.96
7	29.83	29.65	0.92
8	30.75	30.71	0.96
9	32.73	32.56	0.40
10	35.46	35.54	0.74

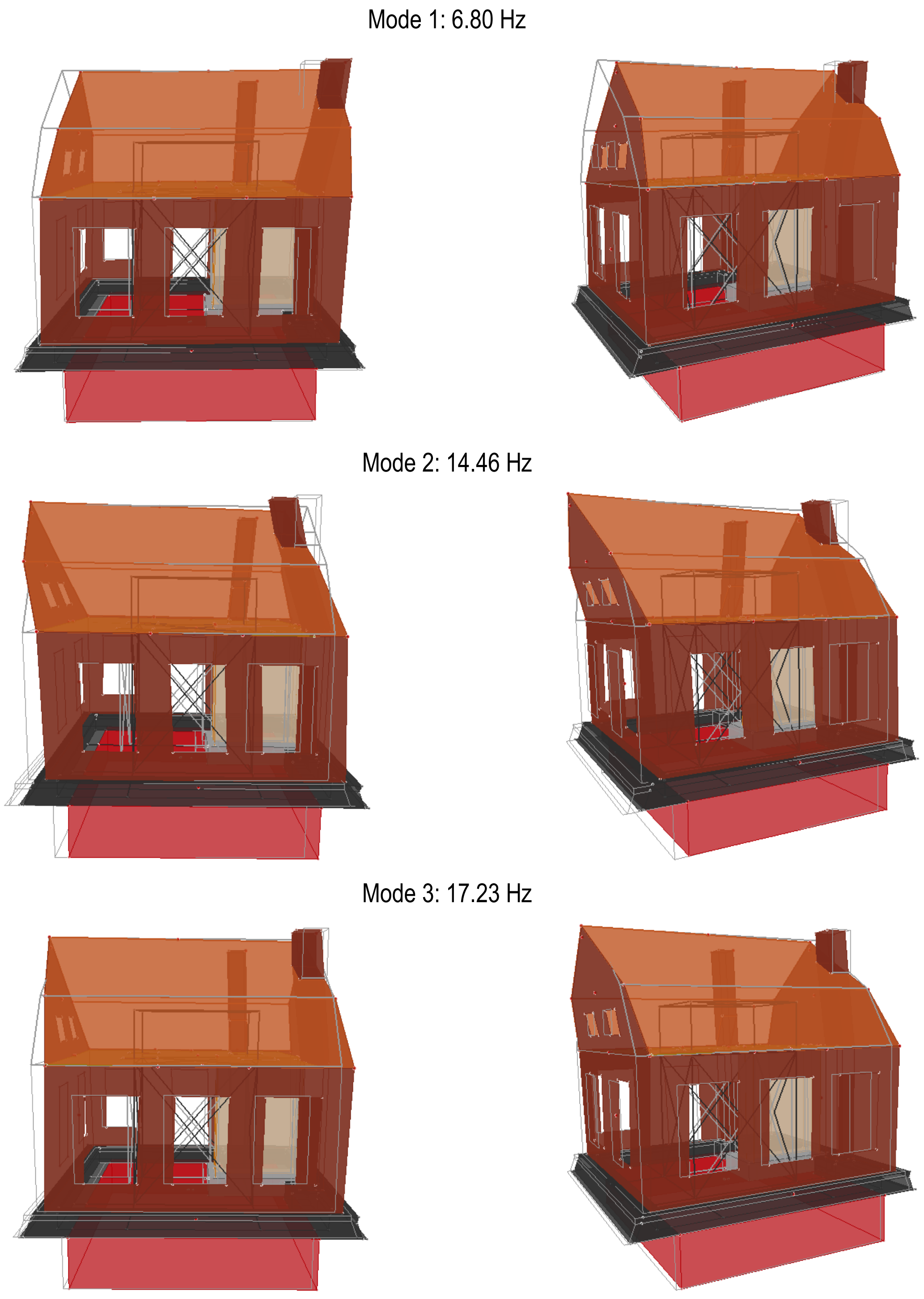

EFDD dynamic identification (CHAR#1)

CHAR#2

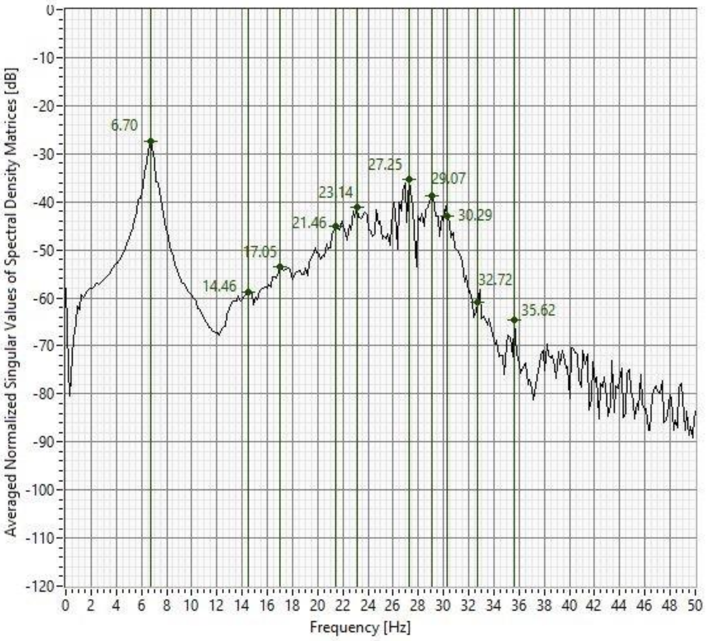

Frequency domain decomposition for dynamic identification CHAR#2

Vibration modes characteristics for dynamic identification CHAR#2

Mode	FDD Frequency [Hz]	EFDD Frequency [Hz]	Damping [%]
1	6.70	6.69	3.97
2	14.46	14.45	2.03
3	17.05	17.13	1.52
4	21.46	21.59	0.61
5	23.14	23.18	0.74
6	27.25	27.14	0.97
7	29.07	29.03	0.98
8	30.29	30.39	0.86
9	32.73	32.47	0.59
10	35.62	35.63	0.50

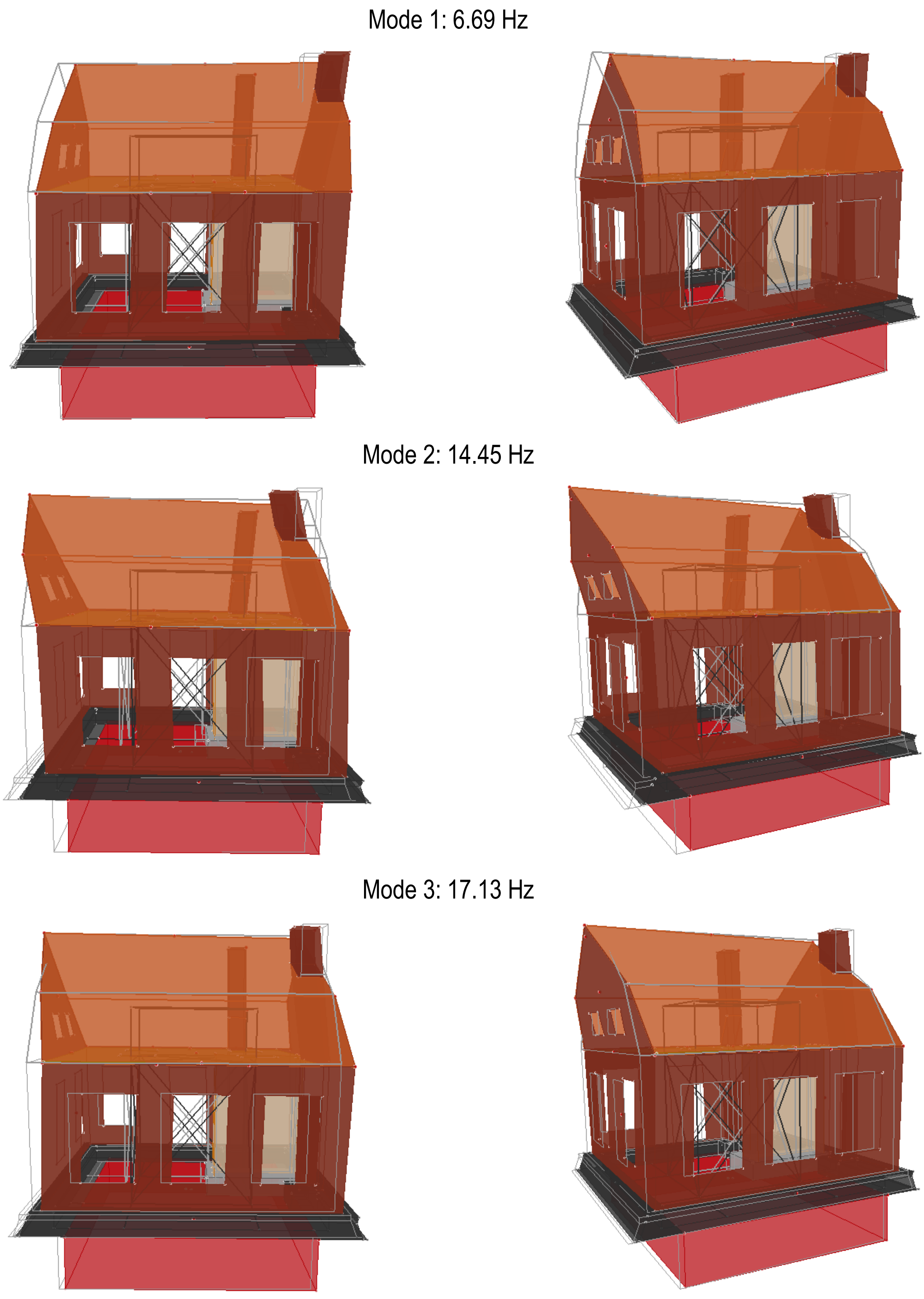

EFDD dynamic identification (CHAR#2)

CHAR#3

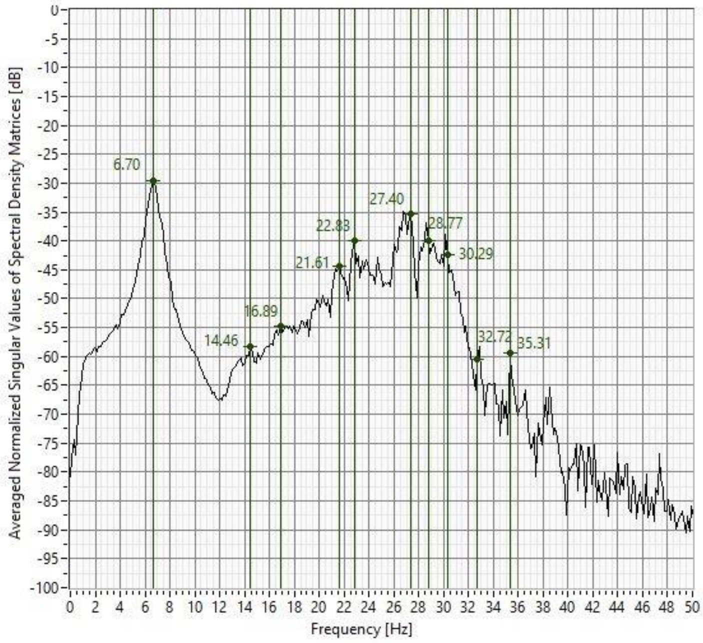

Frequency domain decomposition for dynamic identification CHAR#3

Vibration modes characteristics for dynamic identification CHAR#3

Mode	FDD Frequency [Hz]	EFDD Frequency [Hz]	Damping [%]
1	6.70	6.67	4.46
2	14.46	14.44	2.05
3	16.90	16.97	1.58
4	21.61	21.60	0.60
5	22.83	22.85	0.36
6	27.40	27.30	0.67
7	28.77	28.84	0.82
8	30.29	30.42	0.85
9	32.73	32.69	0.24
10	35.31	35.29	0.08

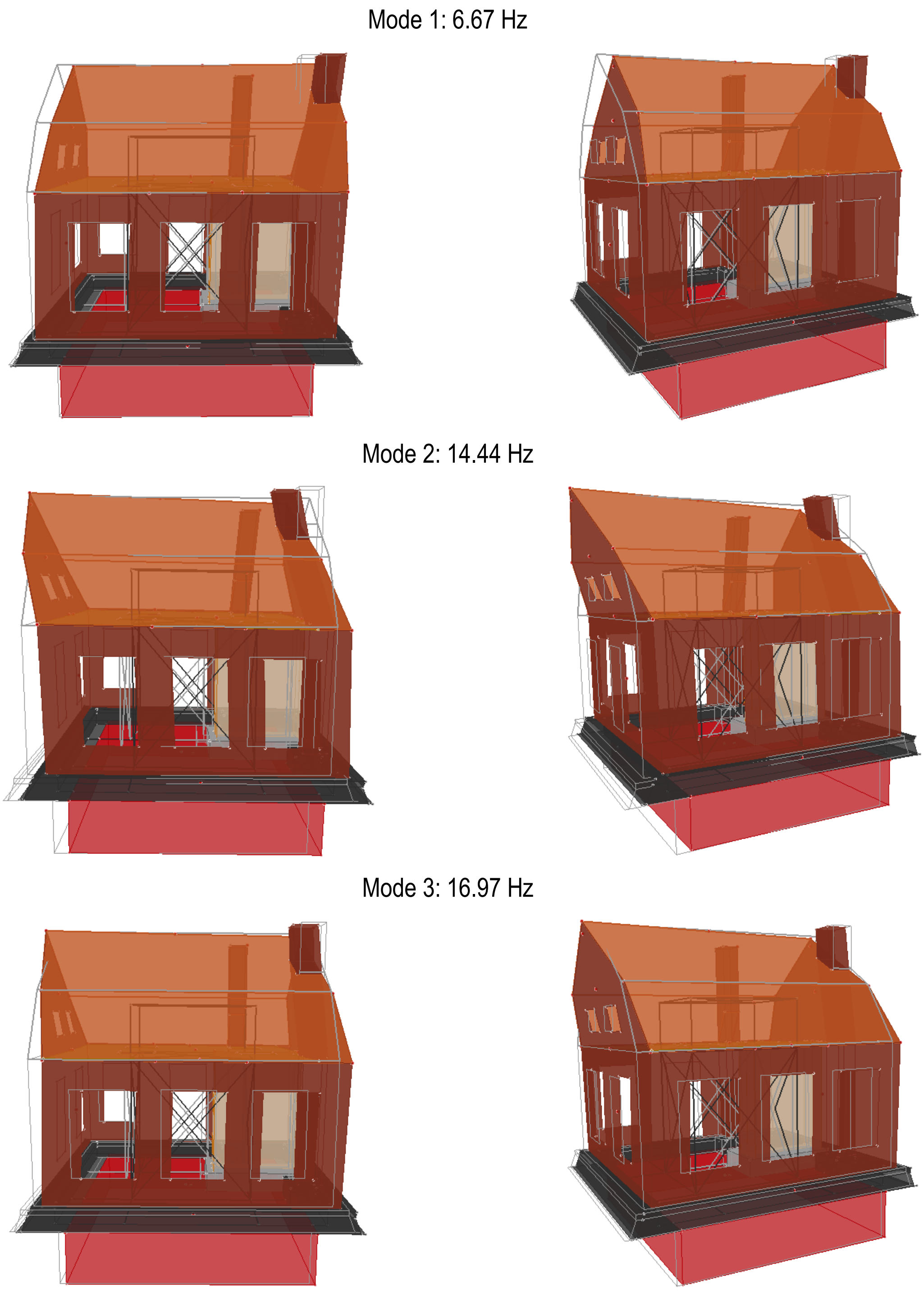

EFDD dynamic identification (CHAR#3)

CHAR#4

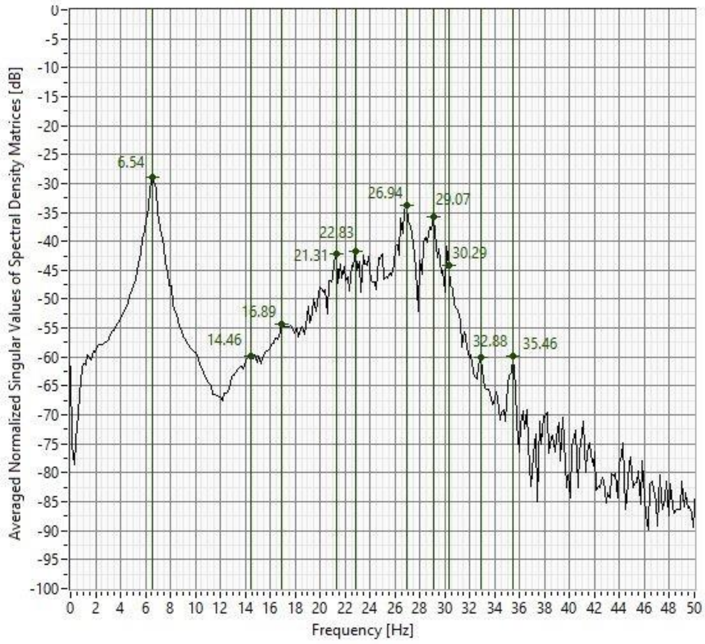

Frequency domain decomposition for dynamic identification CHAR#4

Vibration modes characteristics for dynamic identification CHAR#4

Mode	FDD Frequency [Hz]	EFDD Frequency [Hz]	Damping [%]
1	6.55	6.59	4.19
2	14.46	14.45	2.13
3	16.90	16.99	1.56
4	21.31	21.31	0.37
5	22.83	22.94	0.60
6	26.94	26.85	0.94
7	29.07	29.03	0.84
8	30.29	30.28	1.07
9	32.88	32.95	0.38
10	35.46	35.42	0.36

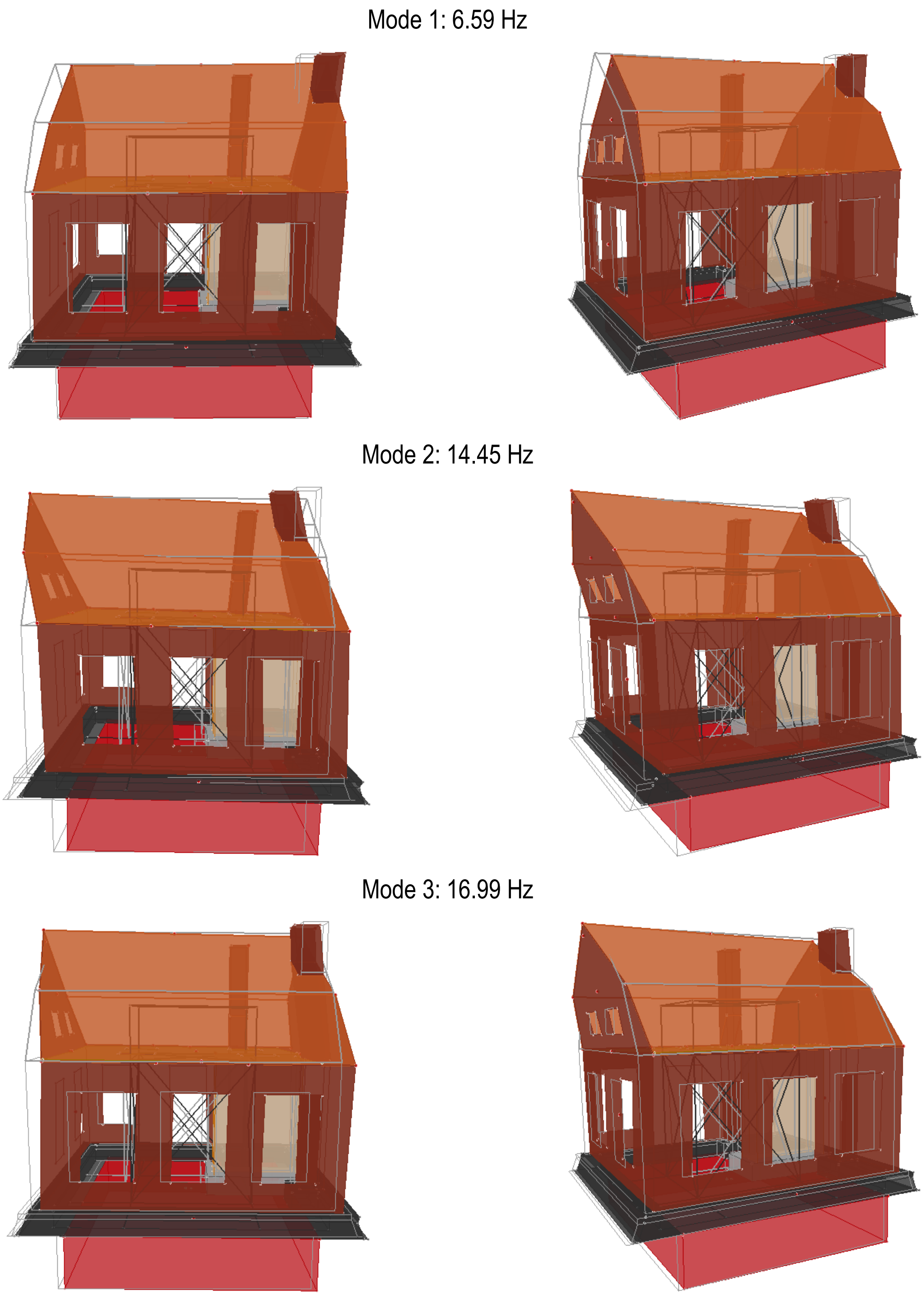

EFDD dynamic identification (CHAR#4)

CHAR#5

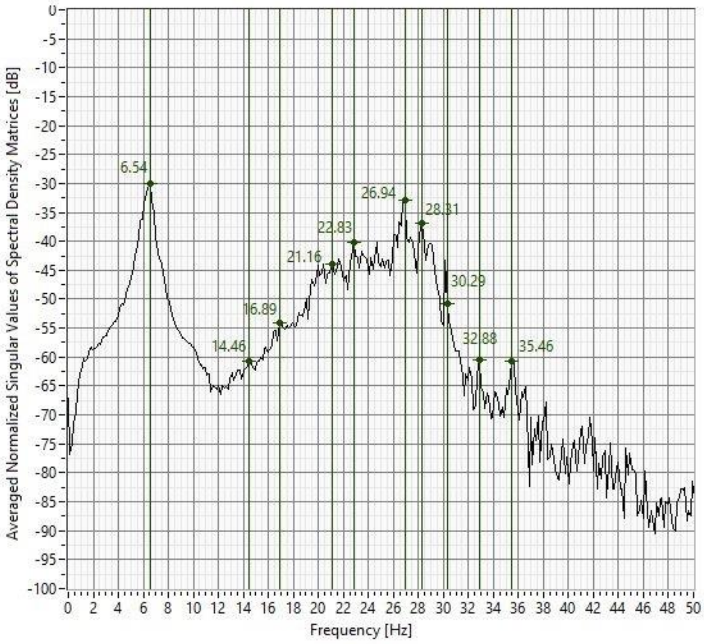

Frequency domain decomposition for dynamic identification CHAR#5

Vibration modes characteristics for dynamic identification CHAR#5

Mode	FDD Frequency [Hz]	EFDD Frequency [Hz]	Damping [%]
1	6.55	6.44	3.90
2	14.46	14.46	2.05
3	16.90	16.92	1.77
4	21.16	21.07	0.81
5	22.83	22.87	1.09
6	26.94	26.81	0.85
7	28.31	28.32	0.28
8	30.29	30.41	0.57
9	32.88	32.93	0.40
10	35.46	35.54	0.33

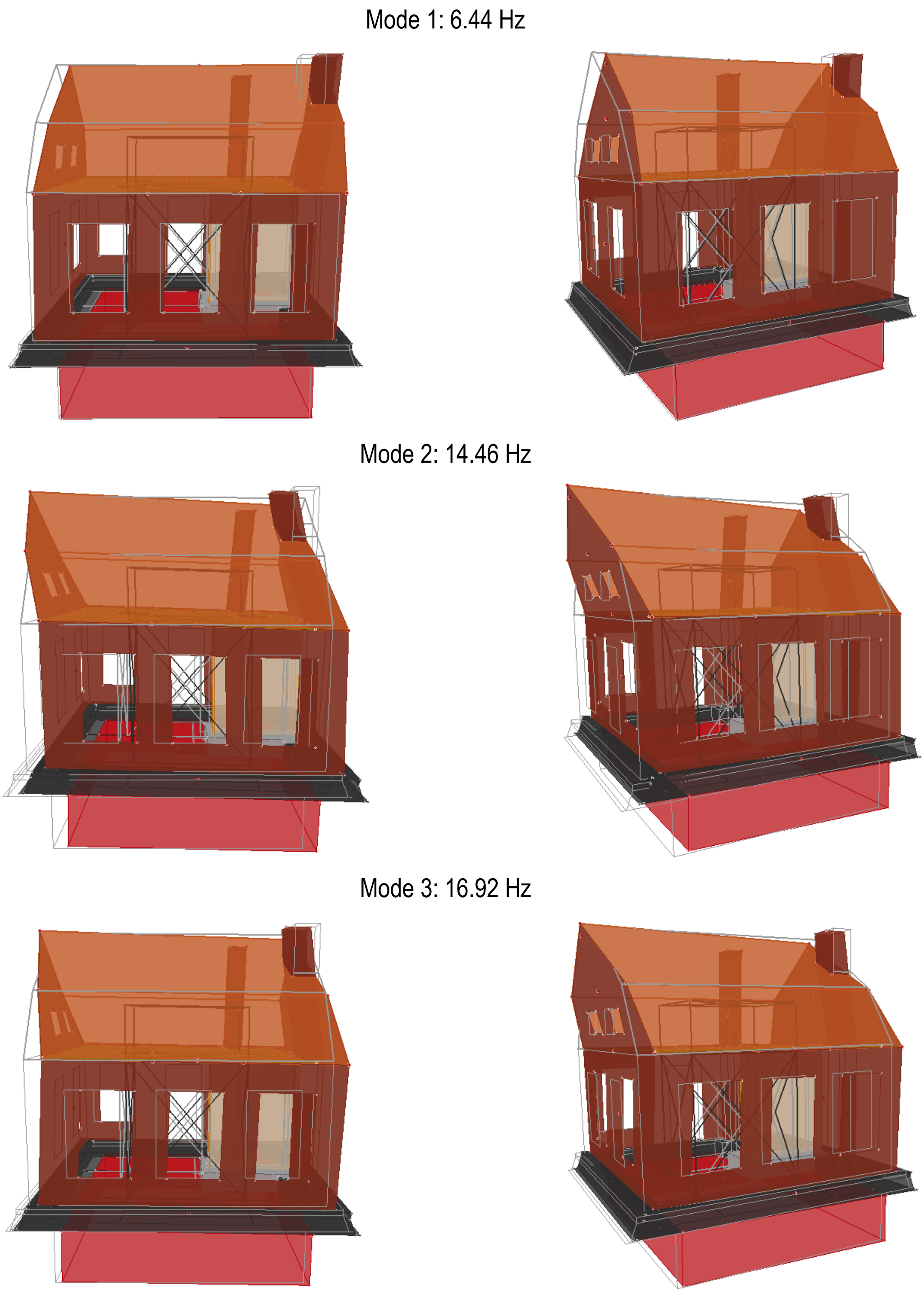

EFDD dynamic identification (CHAR#5)

CHAR#6

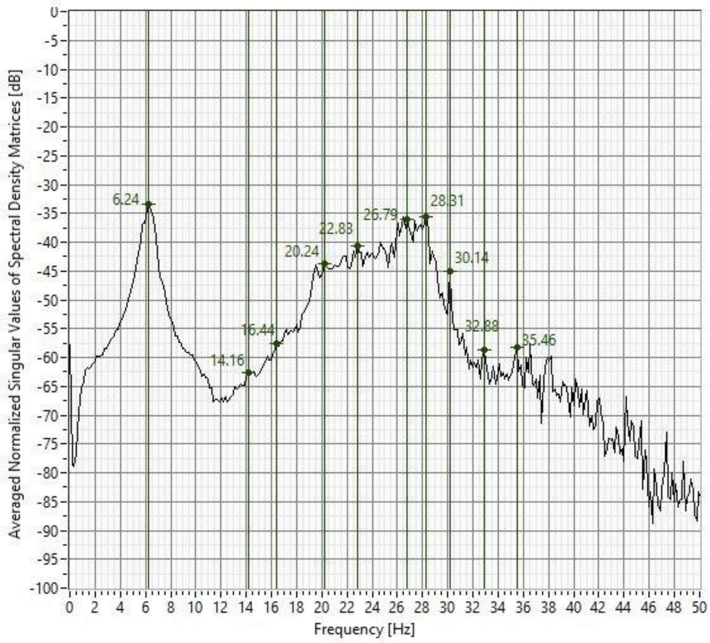

Frequency domain decomposition for dynamic identification CHAR#6

Vibration modes characteristics for dynamic identification CHAR#6

Mode	FDD Frequency [Hz]	EFDD Frequency [Hz]	Damping [%]
1	6.24	6.24	4.68
2	14.16	14.20	2.17
3	16.44	16.49	1.89
4	20.24	20.19	1.31
5	22.83	22.82	1.27
6	26.79	26.71	1.15
7	28.31	28.22	0.59
8	30.14	30.09	0.23
9	32.88	32.66	0.56
10	35.46	35.60	0.49

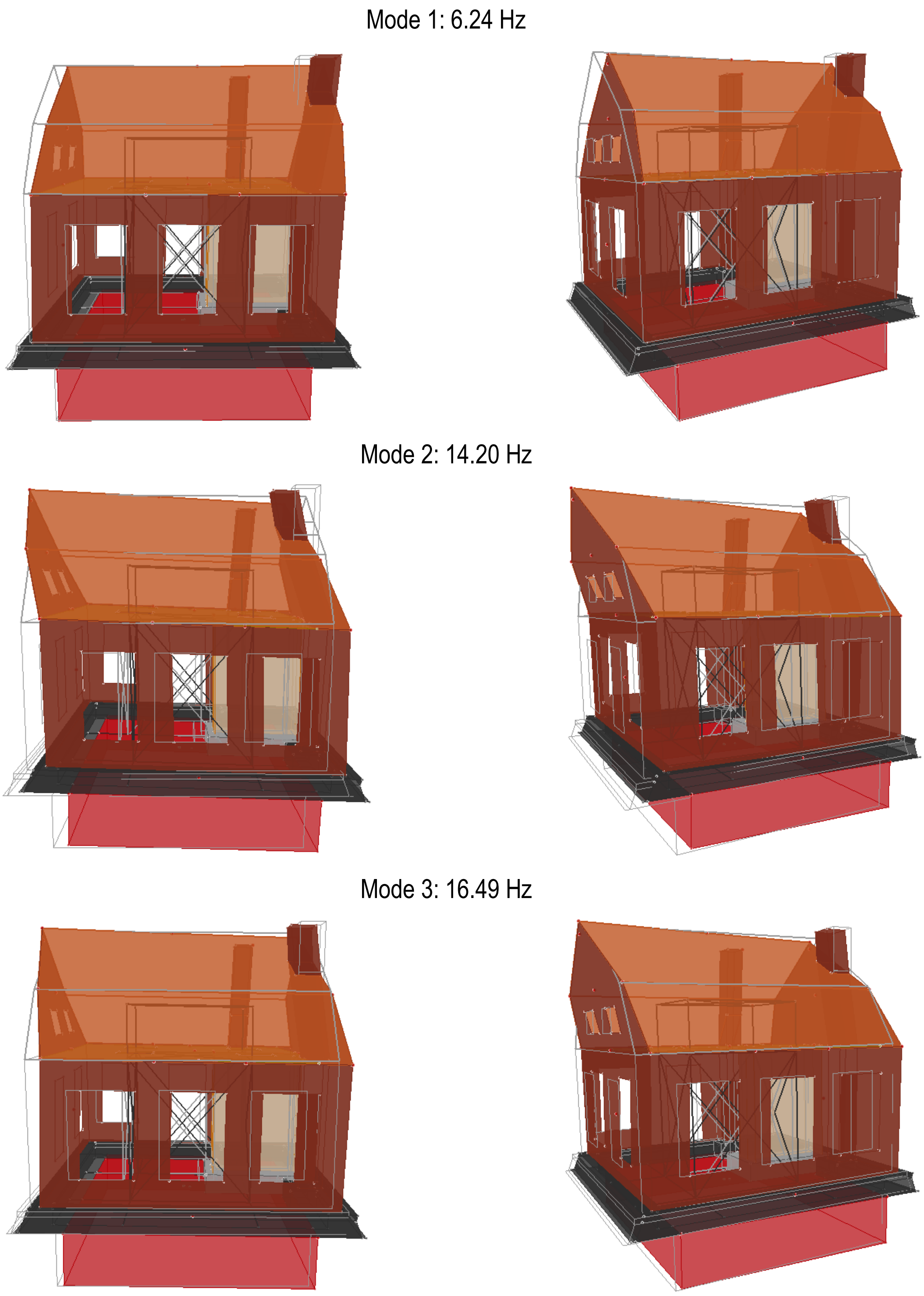

EFDD dynamic identification (CHAR#6)

CHAR#7

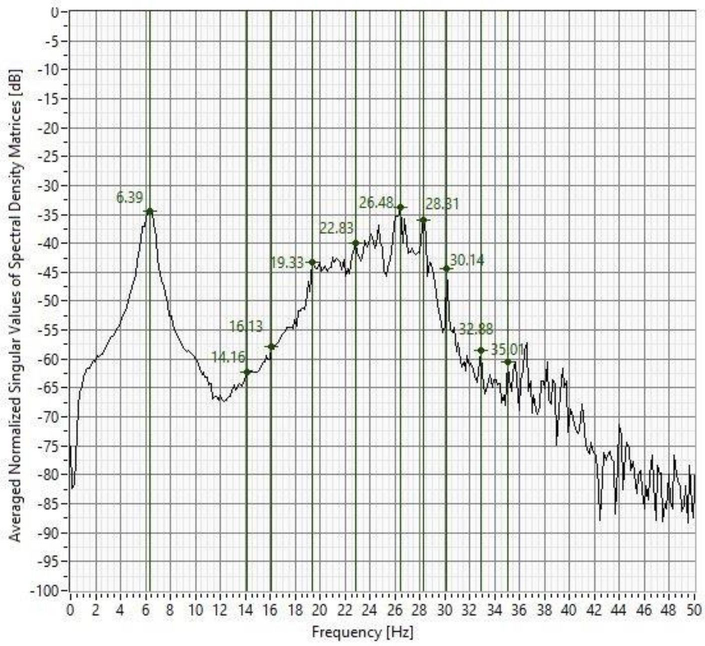

Frequency domain decomposition for dynamic identification CHAR#7

Vibration modes characteristics for dynamic identification CHAR#7

Mode	FDD Frequency [Hz]	EFDD Frequency [Hz]	Damping [%]
1	6.39	6.33	4.04
2	14.16	14.20	2.16
3	16.13	16.19	1.96
4	19.33	19.28	1.09
5	22.83	22.78	1.08
6	26.48	26.46	0.98
7	28.31	28.28	0.44
8	30.14	30.18	0.87
9	32.88	32.70	0.55
10	35.01	34.98	0.17

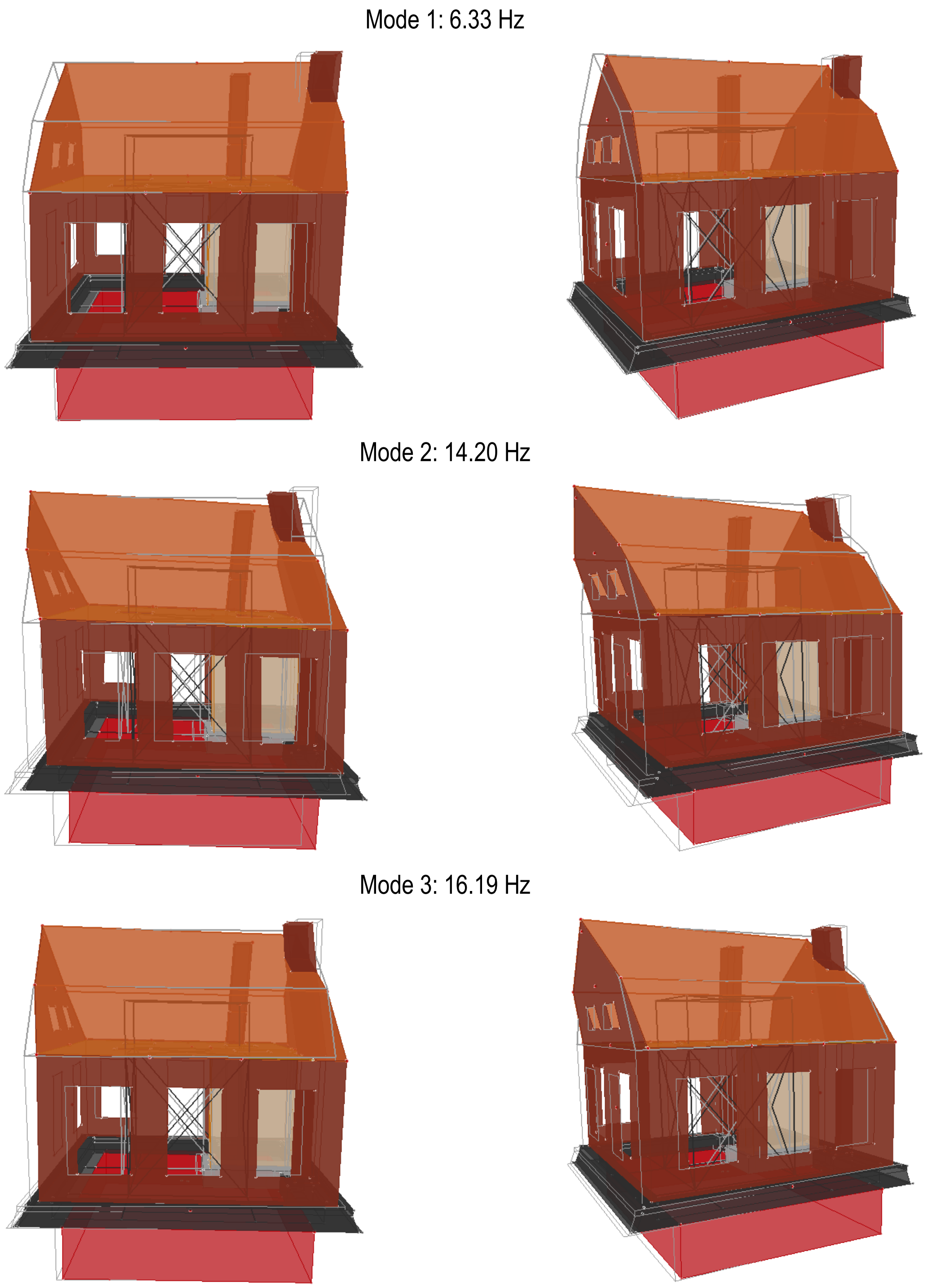

EFDD dynamic identification (CHAR#7)

CHAR#8

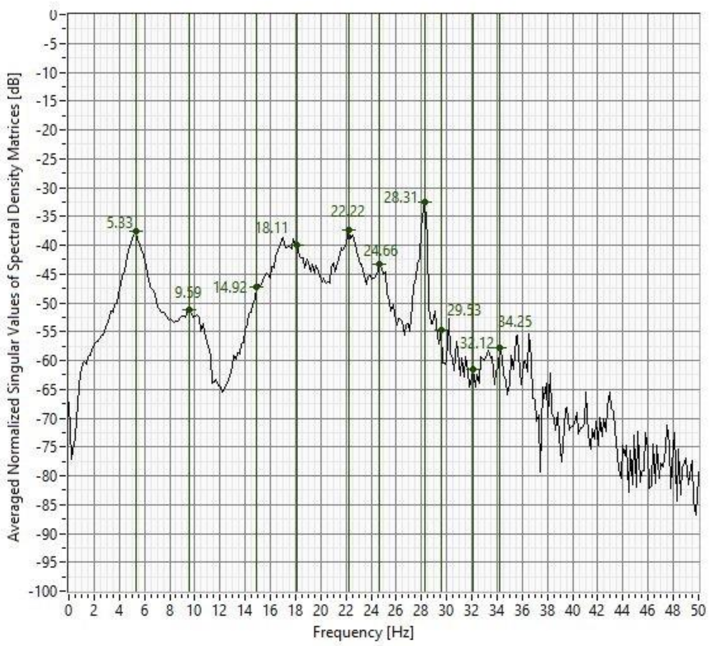

Frequency domain decomposition for dynamic identification CHAR#8

Vibration modes characteristics for dynamic identification CHAR#8

Mode	FDD Frequency [Hz]	EFDD Frequency [Hz]	Damping [%]
1	5.33	5.20	4.42
2	9.59	9.51	2.64
3	14.92	15.14	1.22
4	18.11	18.20	1.24
5	22.22	22.19	0.18
6	24.66	24.65	0.88
7	28.31	28.24	0.41
8	29.53	29.21	0.63
9	32.12	32.01	0.51
10	34.25	34.31	0.59

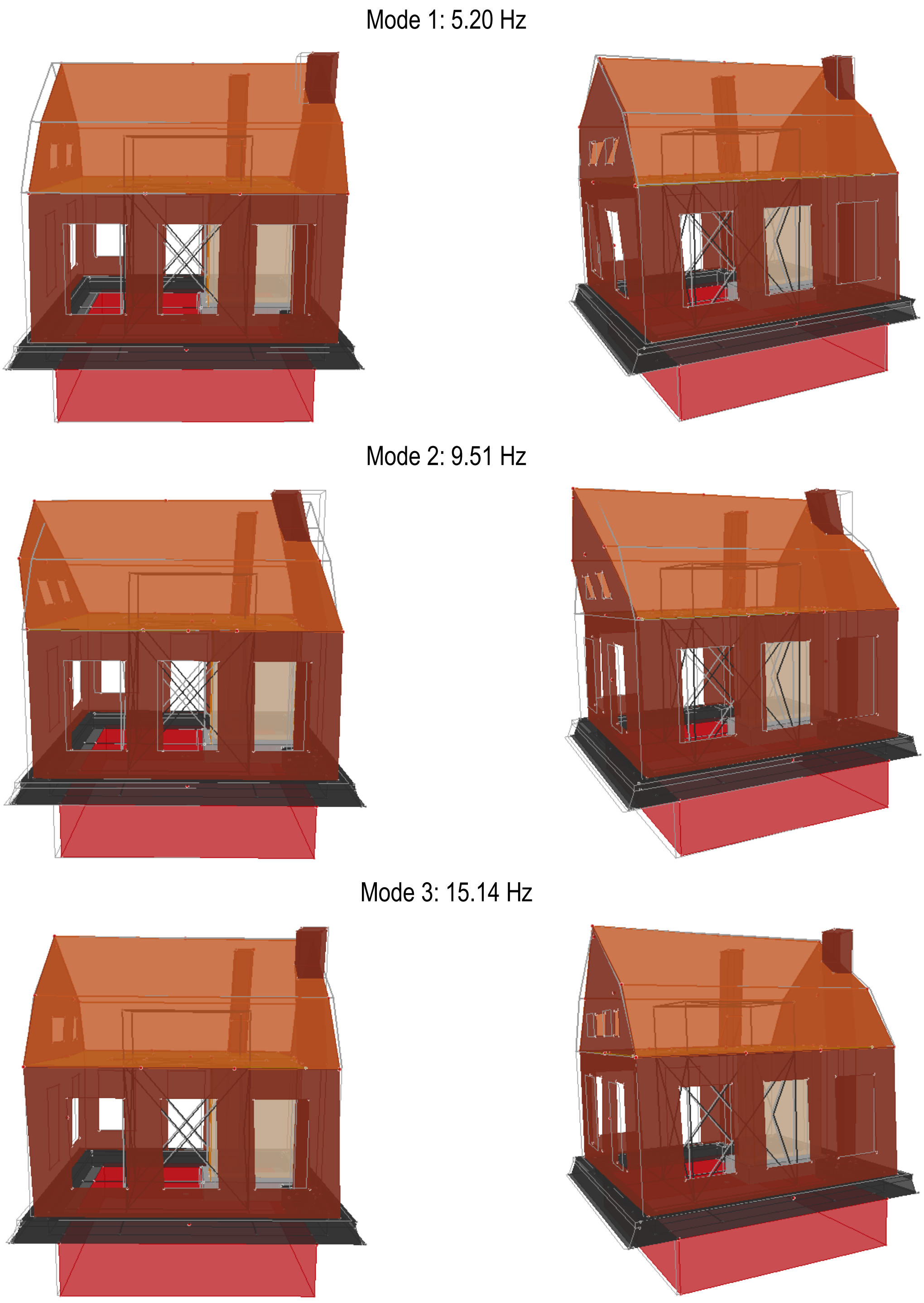

EFDD dynamic identification (CHAR#8)

CHAR#9

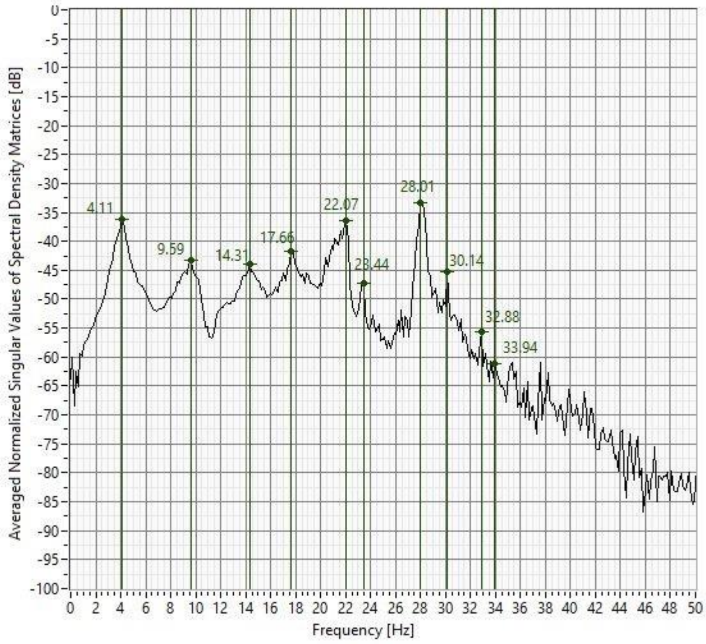

Frequency domain decomposition for dynamic identification CHAR#9

Vibration modes characteristics for dynamic identification CHAR#9

Mode	FDD Frequency [Hz]	EFDD Frequency [Hz]	Damping [%]
1	4.11	3.99	3.44
2	9.59	9.57	3.11
3	14.31	14.36	0.59
4	17.66	17.68	1.65
5	22.07	22.09	0.49
6	23.44	23.37	0.51
7	28.01	28.11	0.70
8	30.14	30.07	0.52
9	32.88	32.69	0.55
10	33.94	33.82	0.72

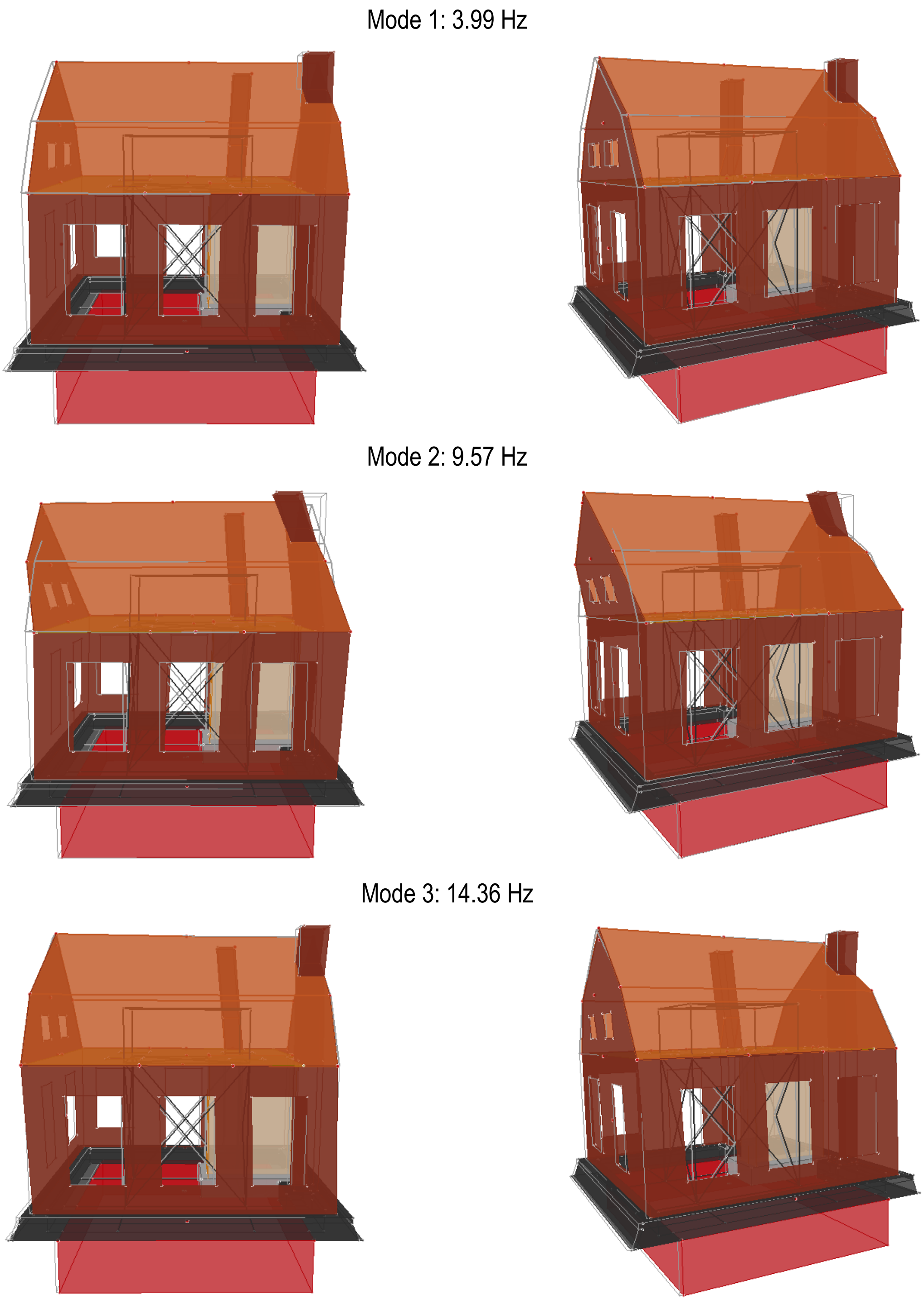

EFDD dynamic identification (CHAR#9)

CHAR#10

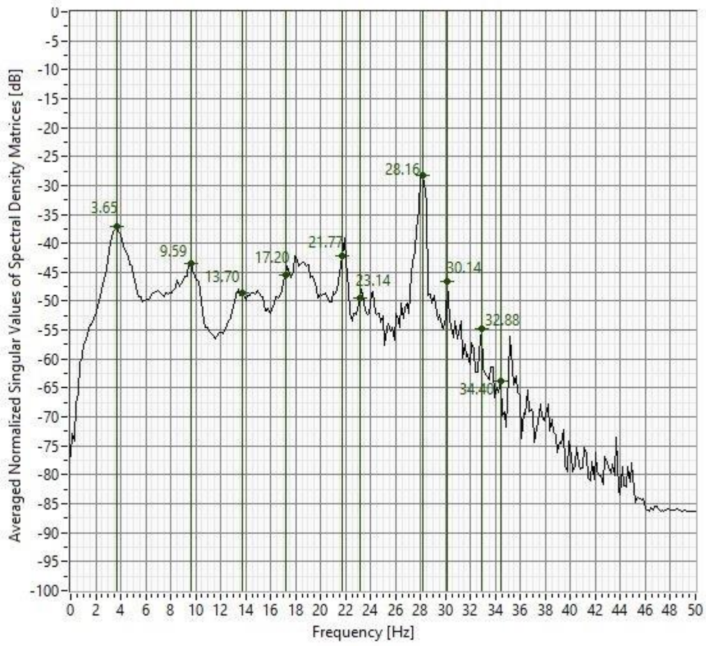

Frequency domain decomposition for dynamic identification CHAR#10

Vibration modes characteristics for dynamic identification CHAR#10

Mode	FDD Frequency [Hz]	EFDD Frequency [Hz]	Damping [%]
1	3.65	3.58	2.41
2	9.59	9.56	3.20
3	13.70	13.83	1.62
4	17.20	17.20	1.46
5	21.77	21.61	0.80
6	23.14	23.06	0.36
7	28.16	28.16	0.60
8	30.14	30.15	9.06
9	32.88	32.73	0.62
10	34.40	34.171	0.52

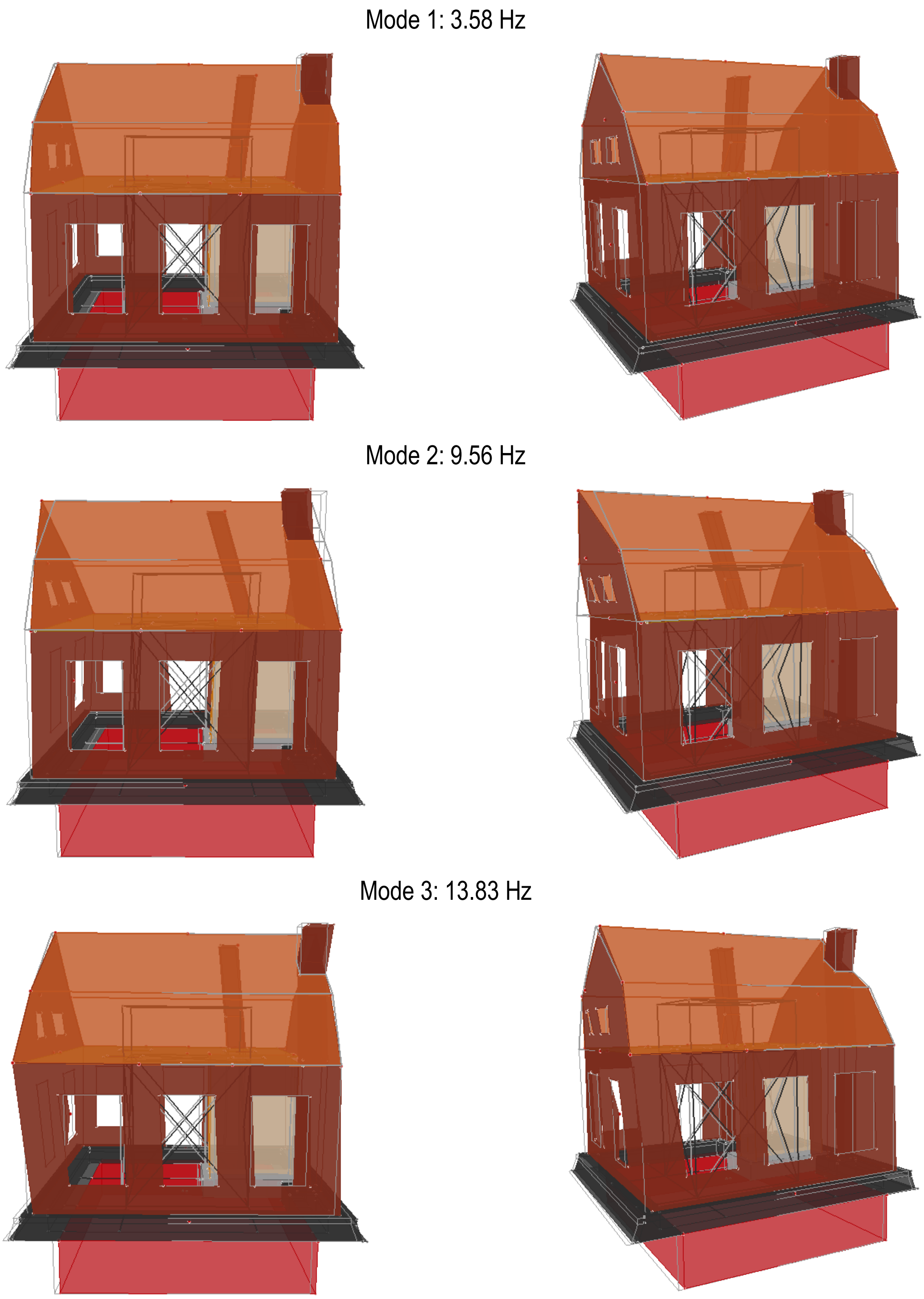

EFDD dynamic identification (CHAR#10)

CHAR#11

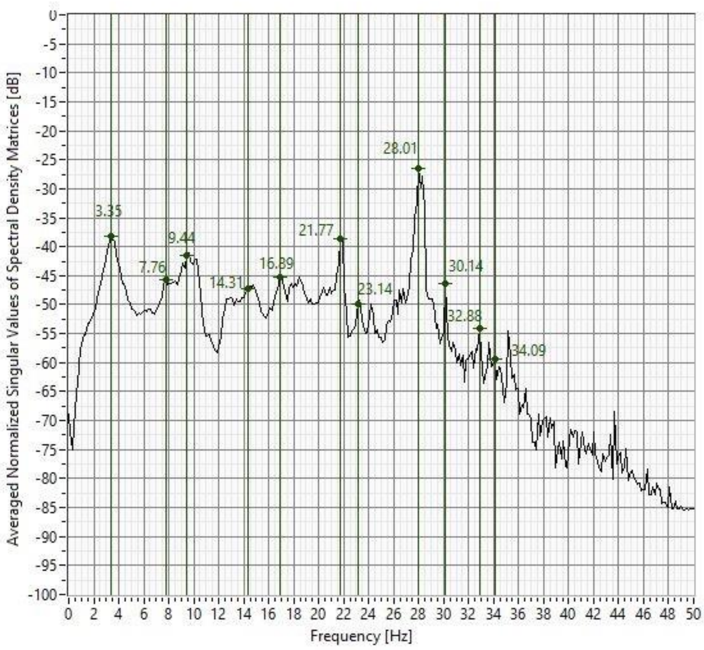

Frequency domain decomposition for dynamic identification CHAR#11

Vibration modes characteristics for dynamic identification CHAR#11

Mode	FDD Frequency [Hz]	EFDD Frequency [Hz]	Damping [%]
1	3.35	3.18	5.38
2	7.76	7.66	2.66
3	9.44	9.39	1.89
4	14.31	14.35	2.19
5	16.90	16.93	1.73
6	21.77	21.65	0.78
7	23.14	23.08	0.36
8	28.01	28.16	0.61
9	30.14	30.08	0.15
10	32.88	32.70	0.51
11	34.09	34.05	0.64

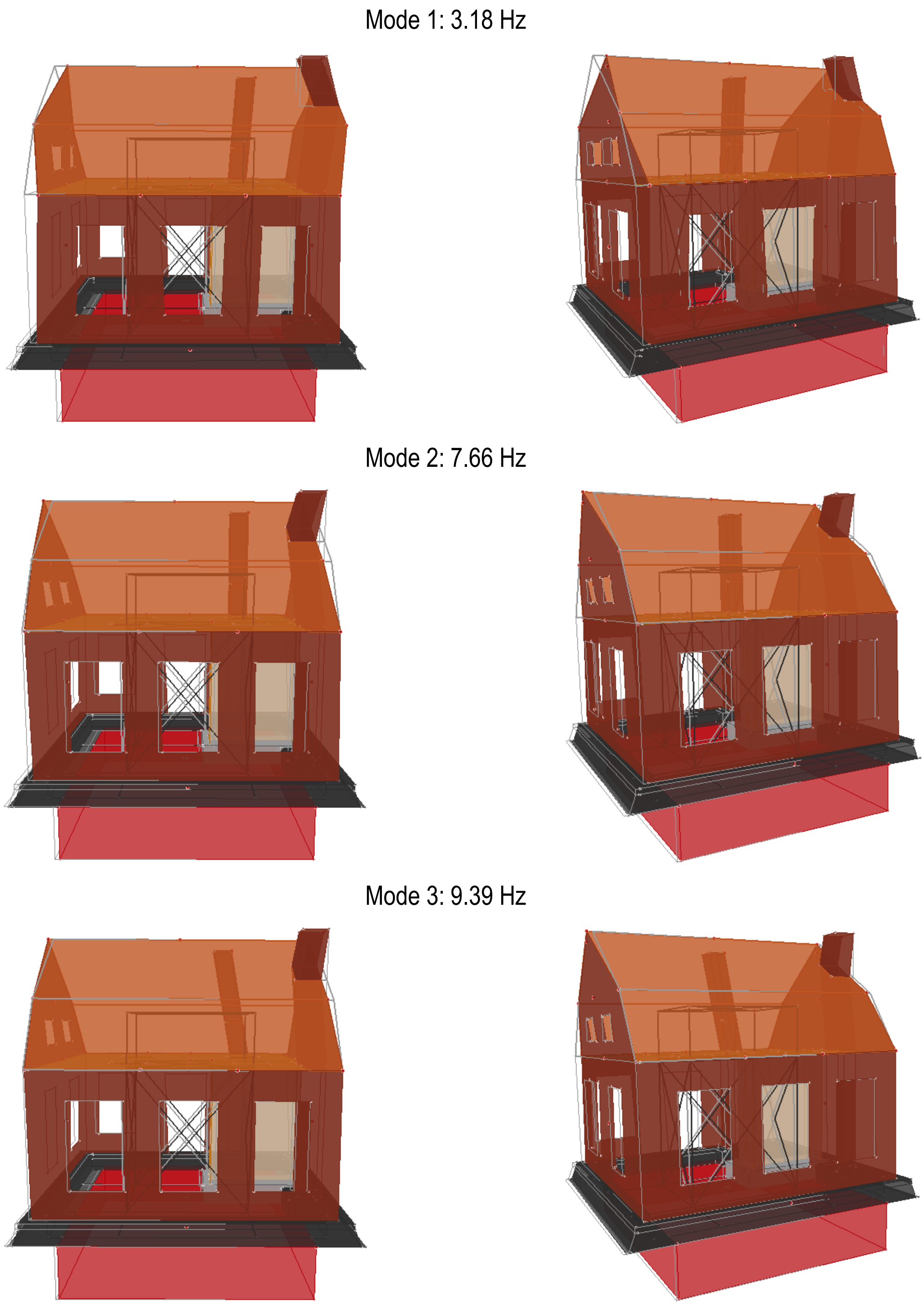

EFDD dynamic identification (CHAR#11)

CHAR#12

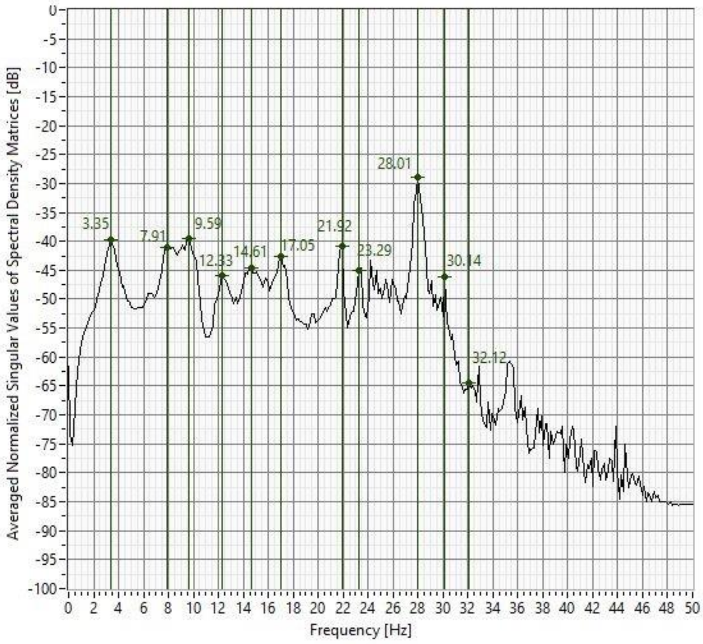

Frequency domain decomposition for dynamic identification CHAR#12

Vibration modes characteristics for dynamic identification CHAR#12

Mode	FDD Frequency [Hz]	EFDD Frequency [Hz]	Damping [%]
1	3.35	3.18	5.44
2	7.35	7.91	1.68
3	9.59	9.55	3.14
4	12.33	12.39	1.44
5	14.61	14.67	1.80
6	17.05	17.02	0.76
7	21.92	21.87	0.23
8	23.29	23.26	0.68
9	28.01	27.98	0.81
10	30.14	30.12	0.63
11	32.12	32.08	0.66

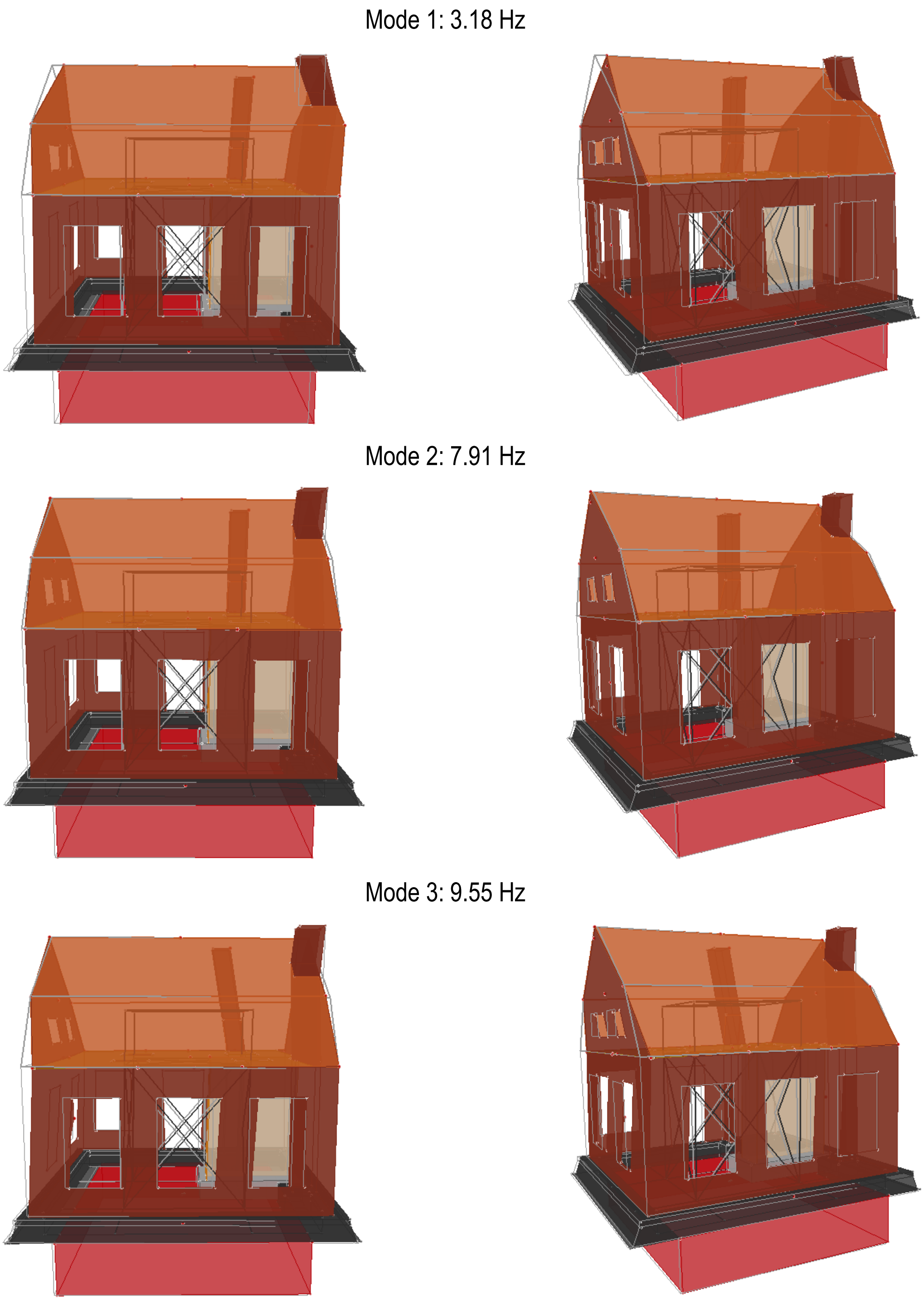

EFDD dynamic identification (CHAR#12)

APPENDIX B. CUMULATIVE DISPLACEMENTS FROM SHAKE TABLE TESTS

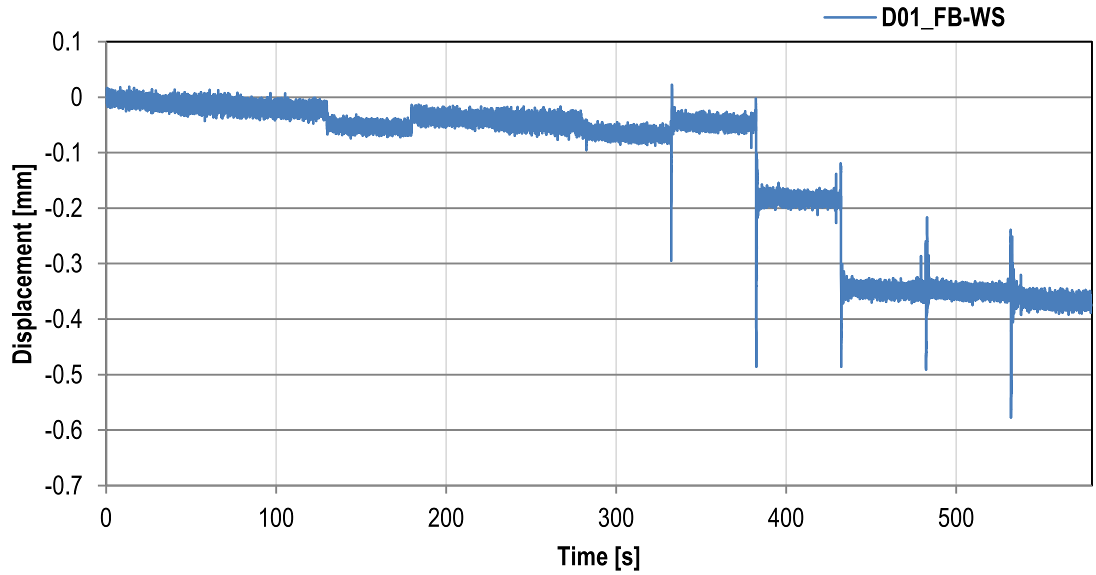

Channel D01_FB-WS – Relative displacement

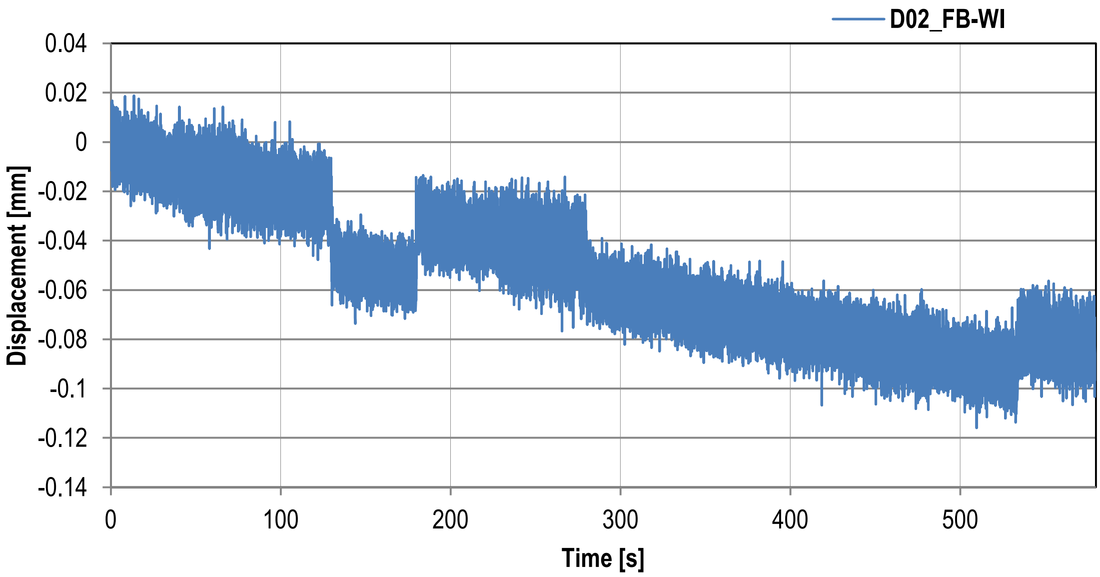

Channel D02_FB-WI – Relative displacement

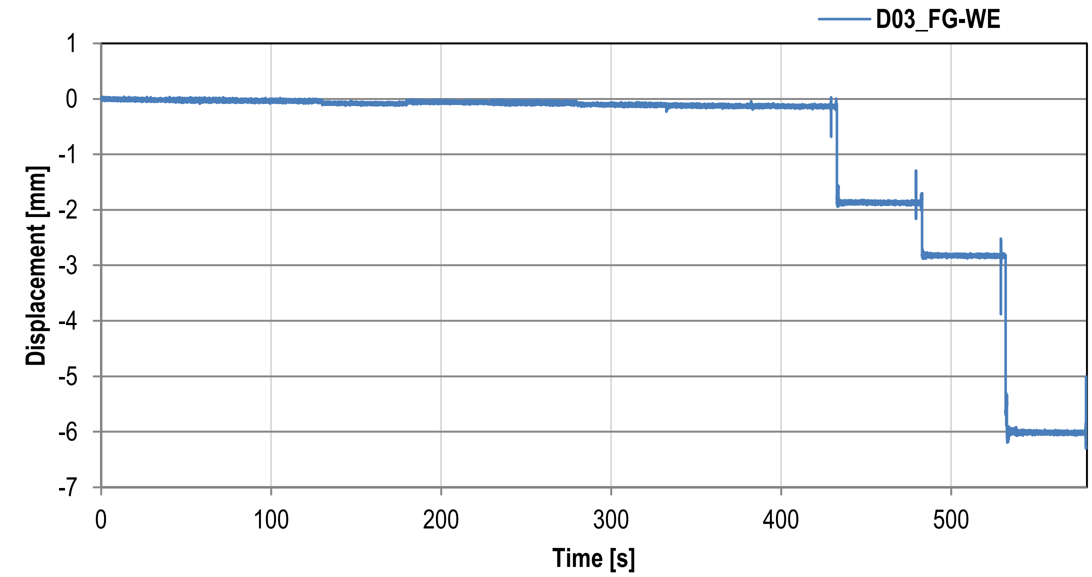

Channel D03_FG-WE – Relative displacement

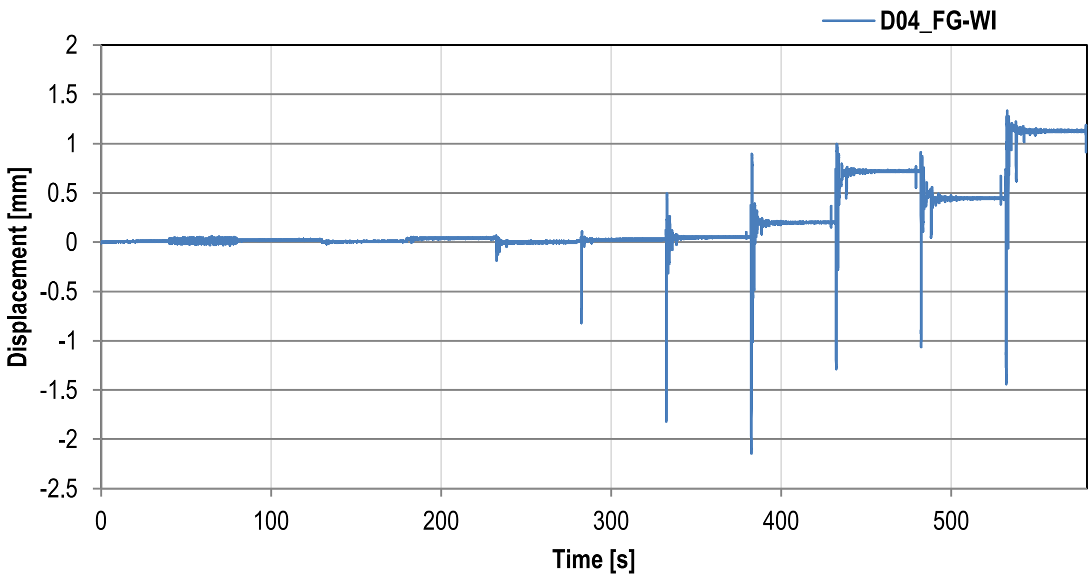

Channel D04_FG-WI – Relative displacement

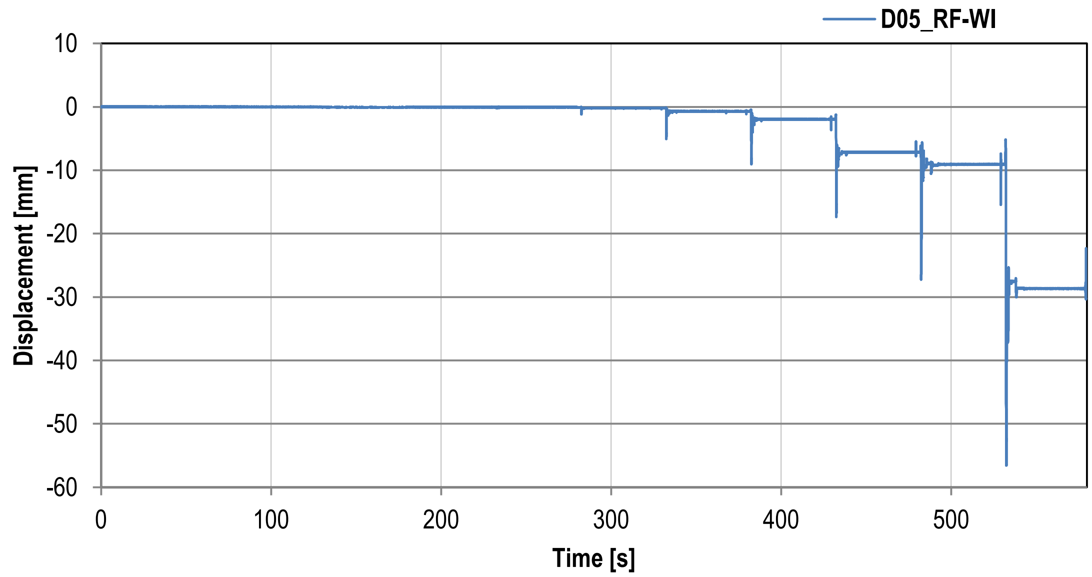

Channel D05_RF-WI – Relative displacement

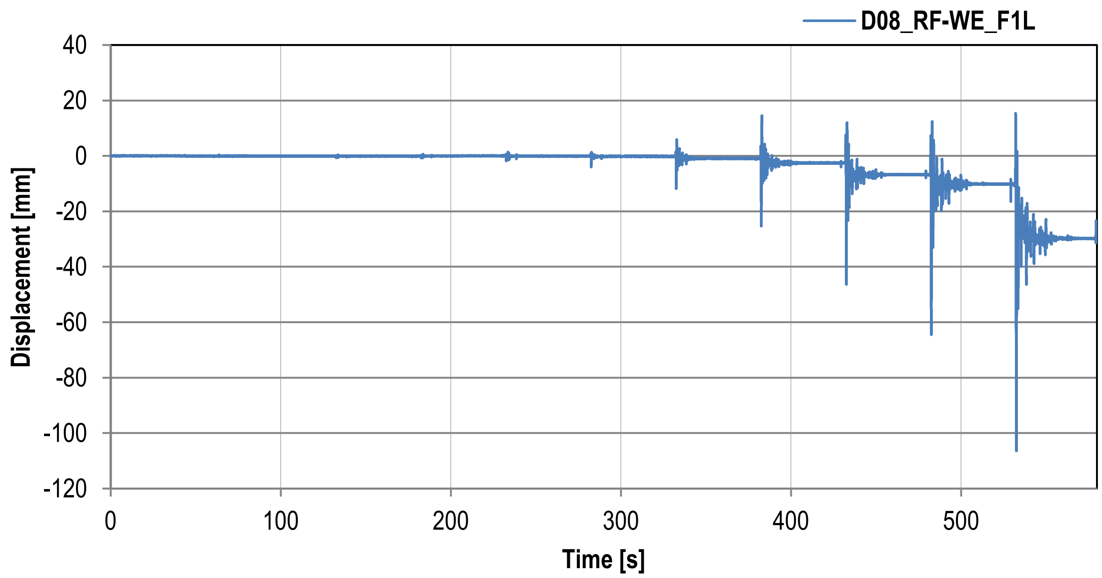

Channel D08_RF-WE_F1L – Relative displacement

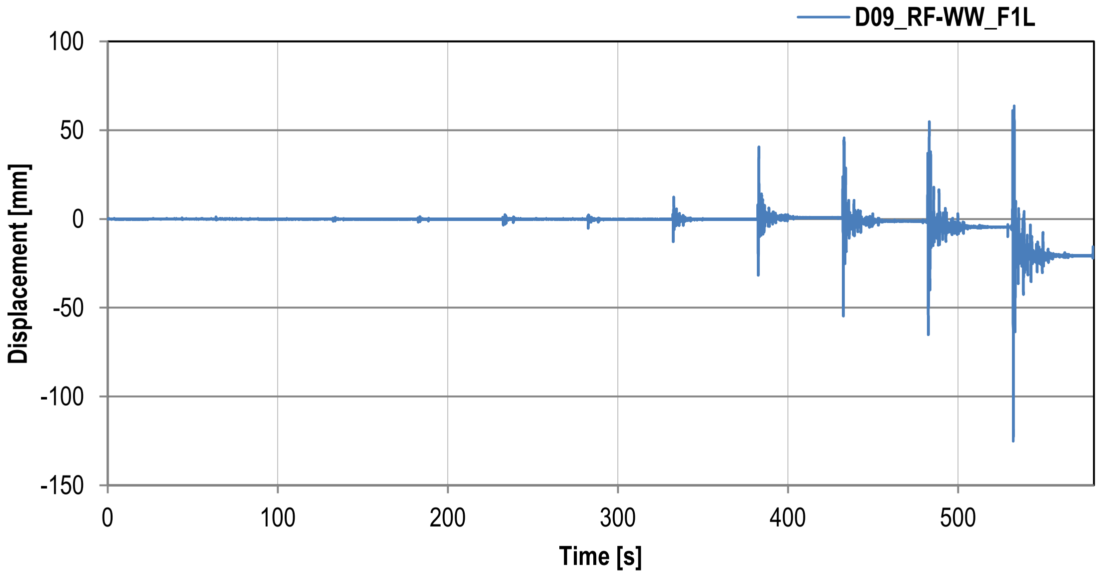

Channel D09_RF-WW_F1L – Relative displacement

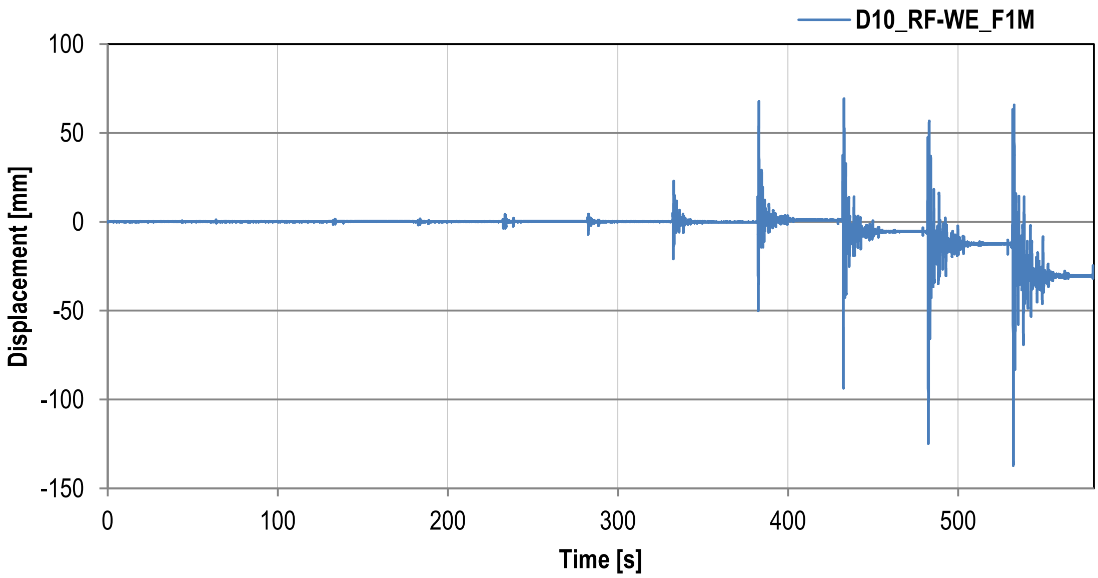

Channel D10_RF-WE_F1M – Relative displacement

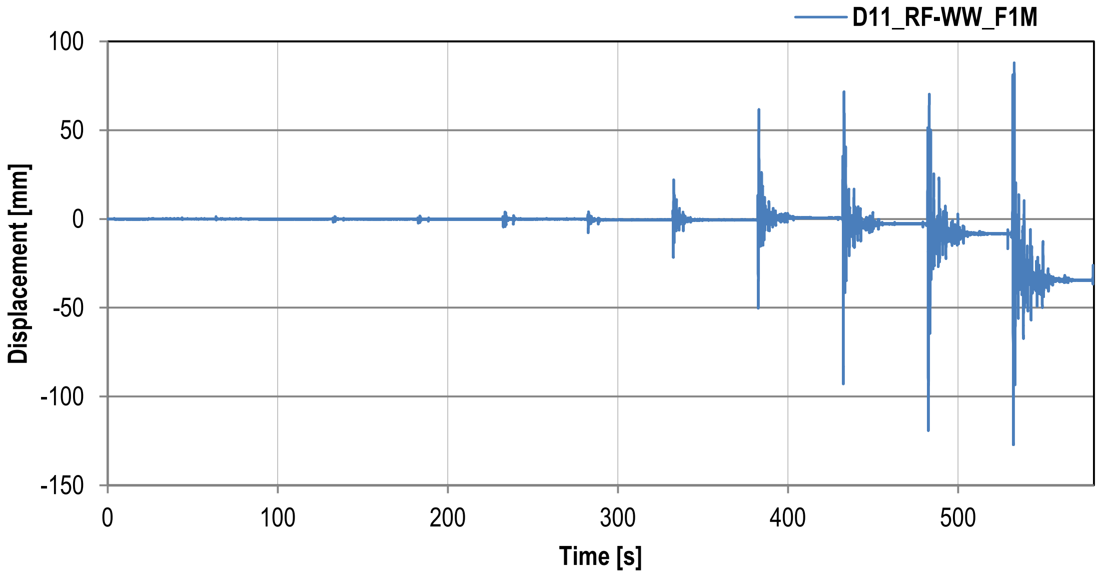

Channel D11_RF-WW_F1M – Relative displacement

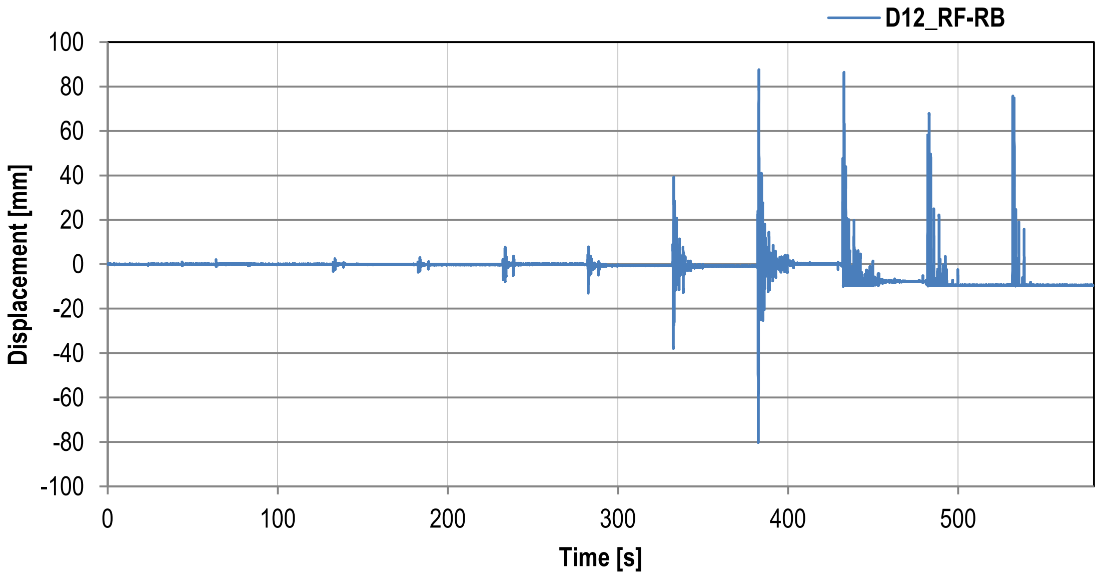

Channel D12_RF-RB – Relative displacement

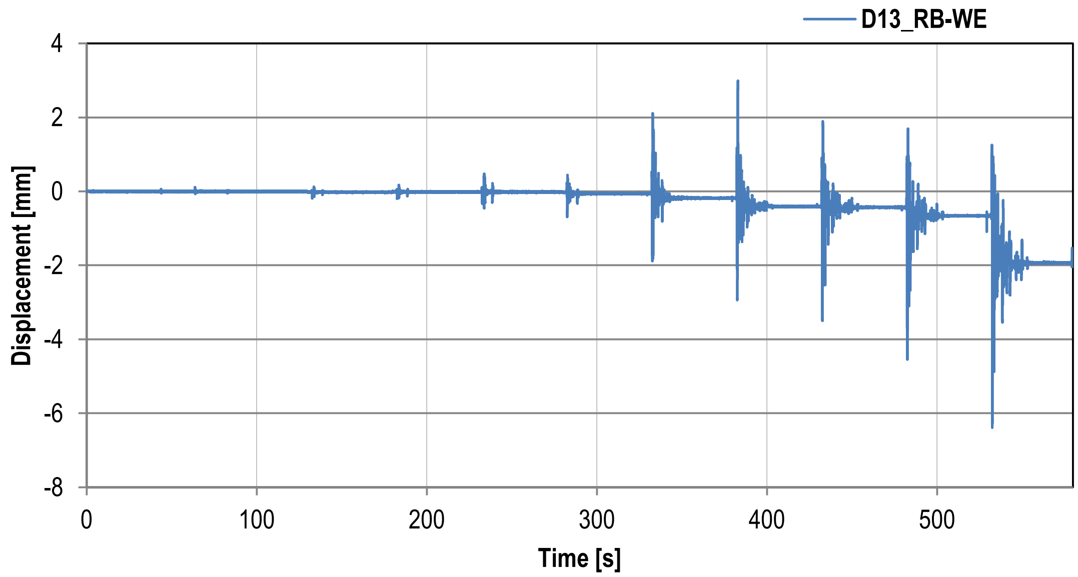

Channel D13_RB-WE – Relative displacement

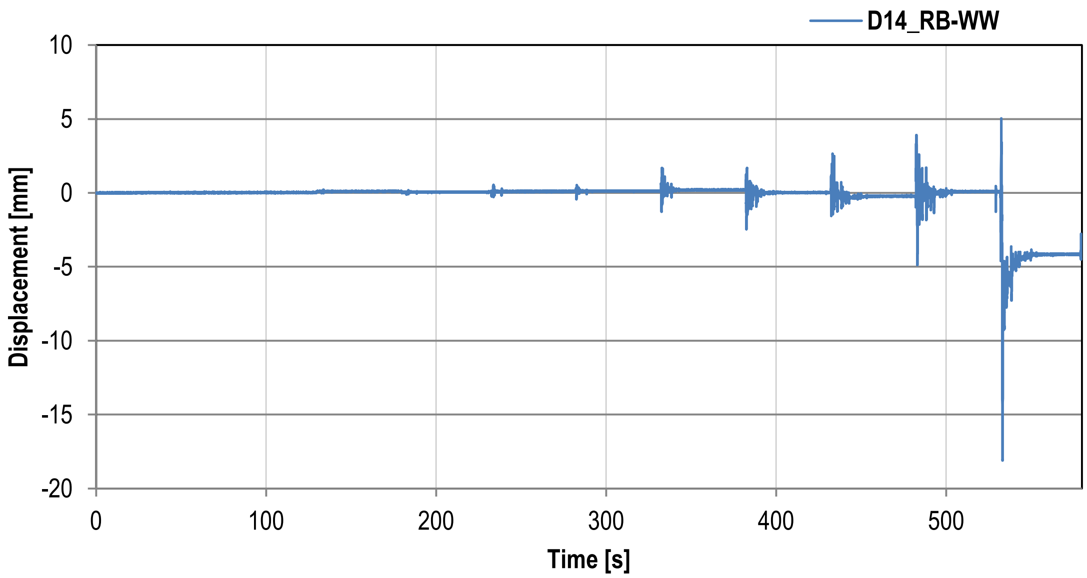

Channel D14_RB-WW – Relative displacement

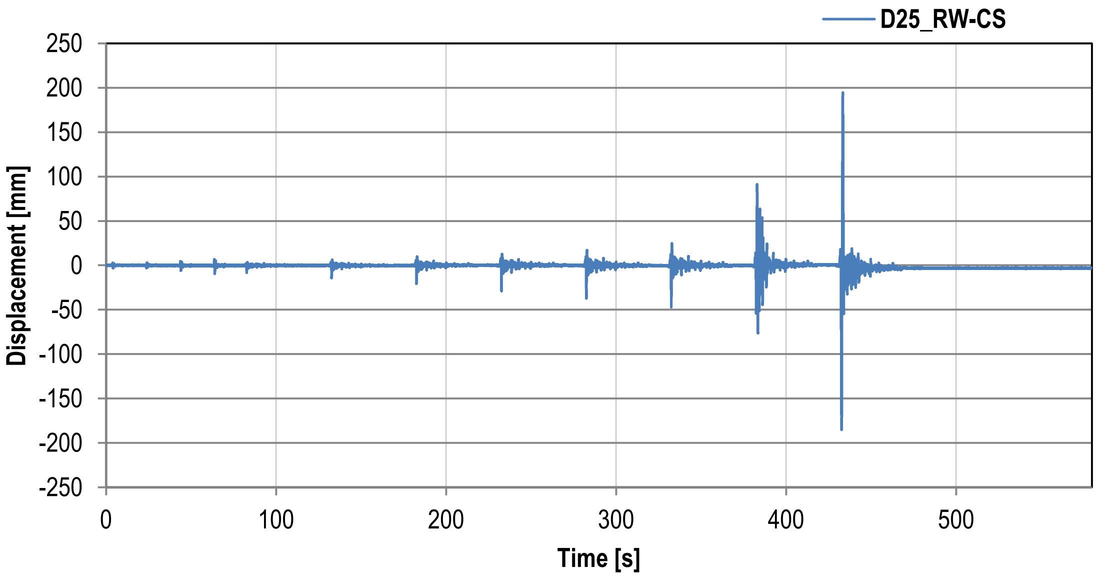

Channel D25_RW-CS – Relative displacement

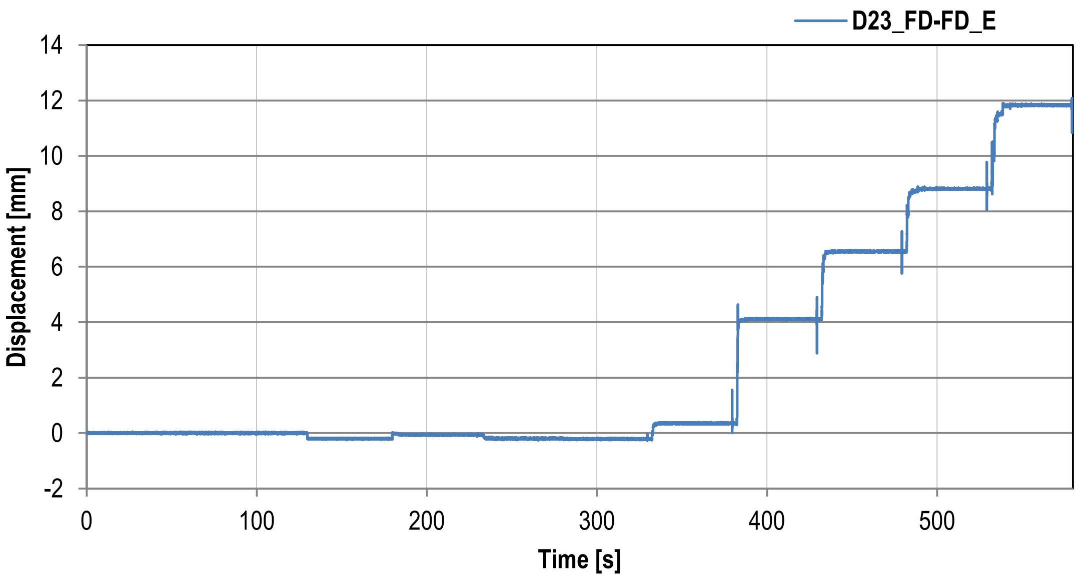

Channel D23_FD-FD_E – Relative displacement

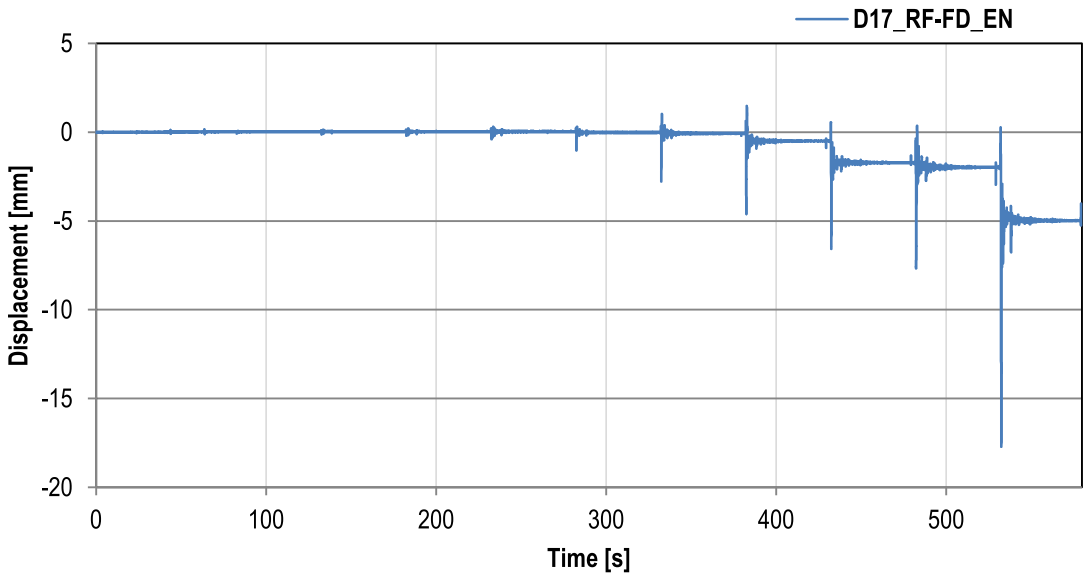

Channel D17_RF-FD_EN – Relative displacement

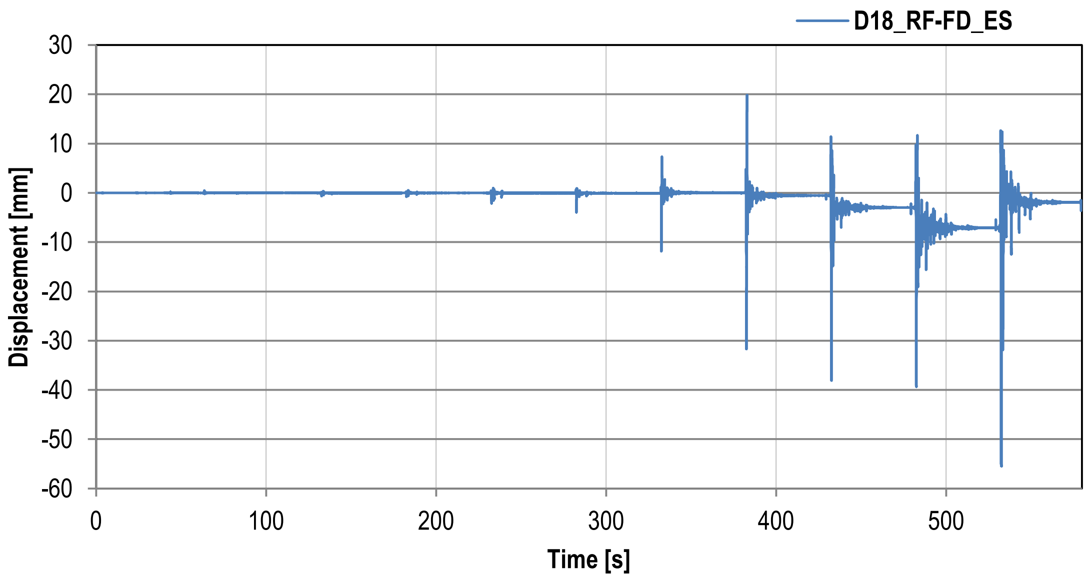

Channel D18_RF-FD_ES – Relative displacement

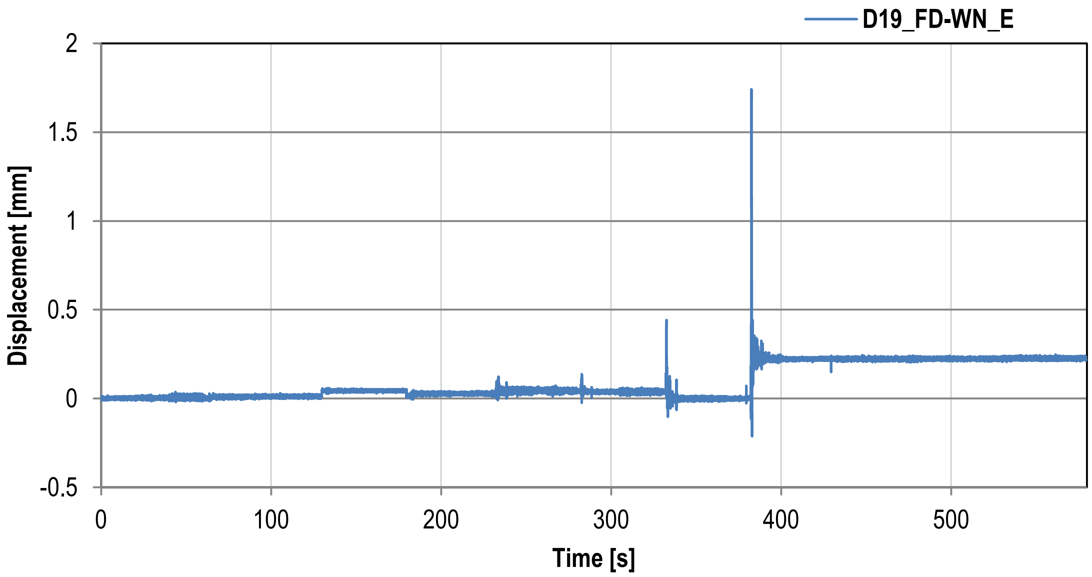

Channel D19_FD-WN_E – Relative displacement

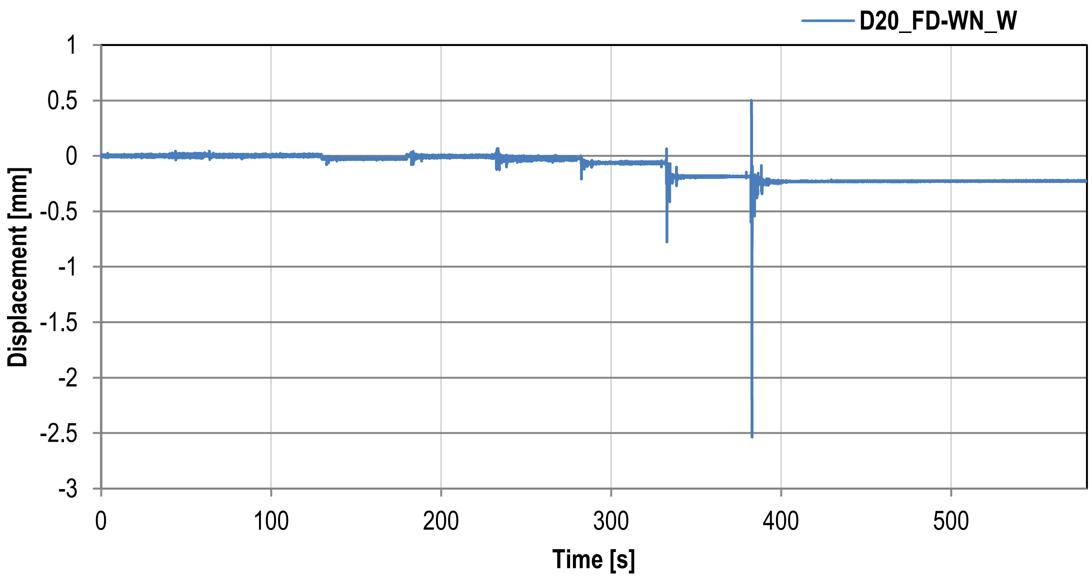

Channel D20_FD-WN_W – Relative displacement

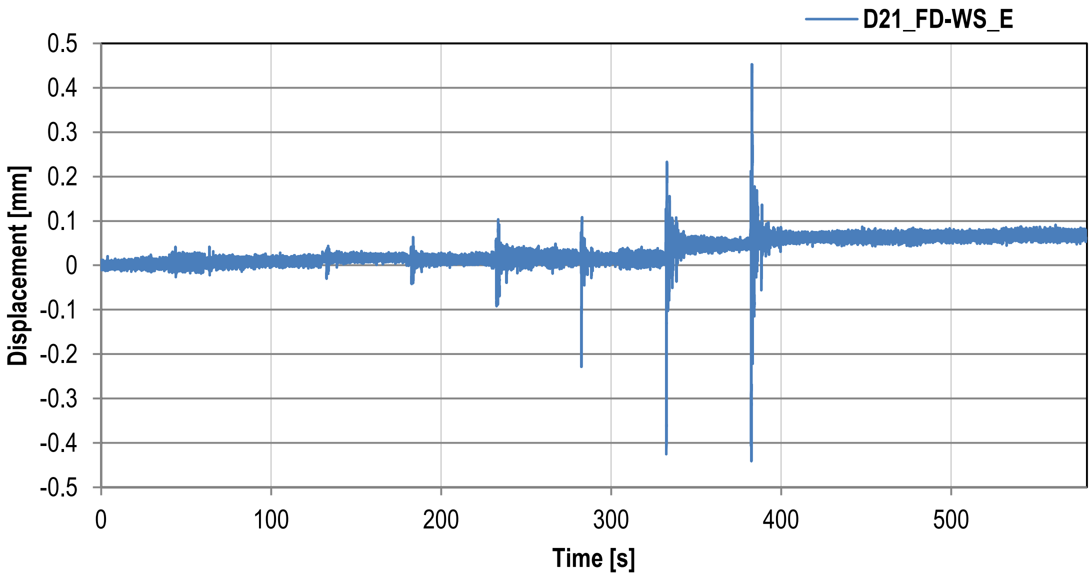

Channel D21_FD-WS_E – Relative displacement

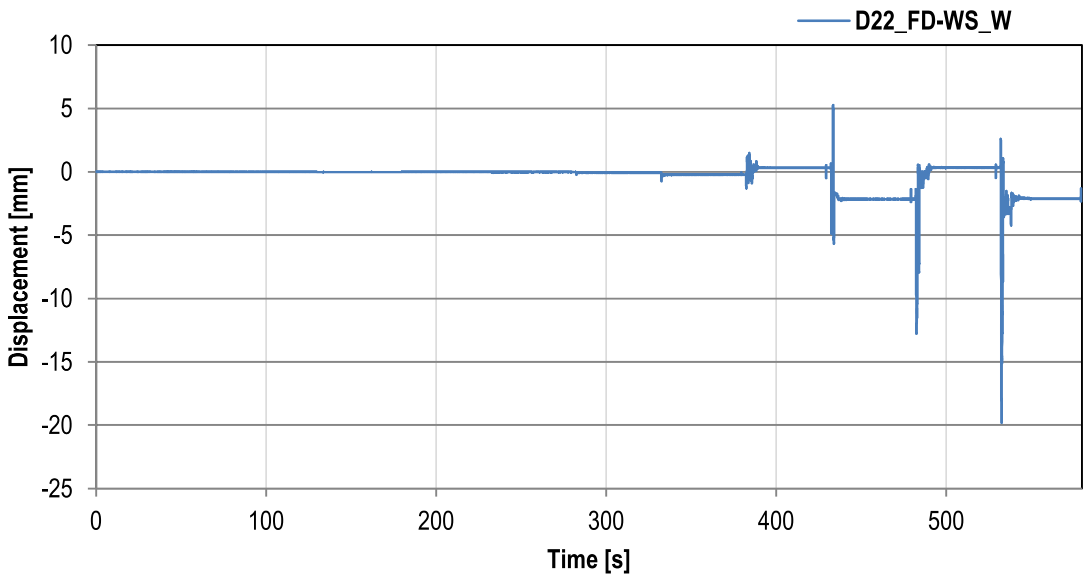

Channel D22_FD-WS_W – Relative displacement

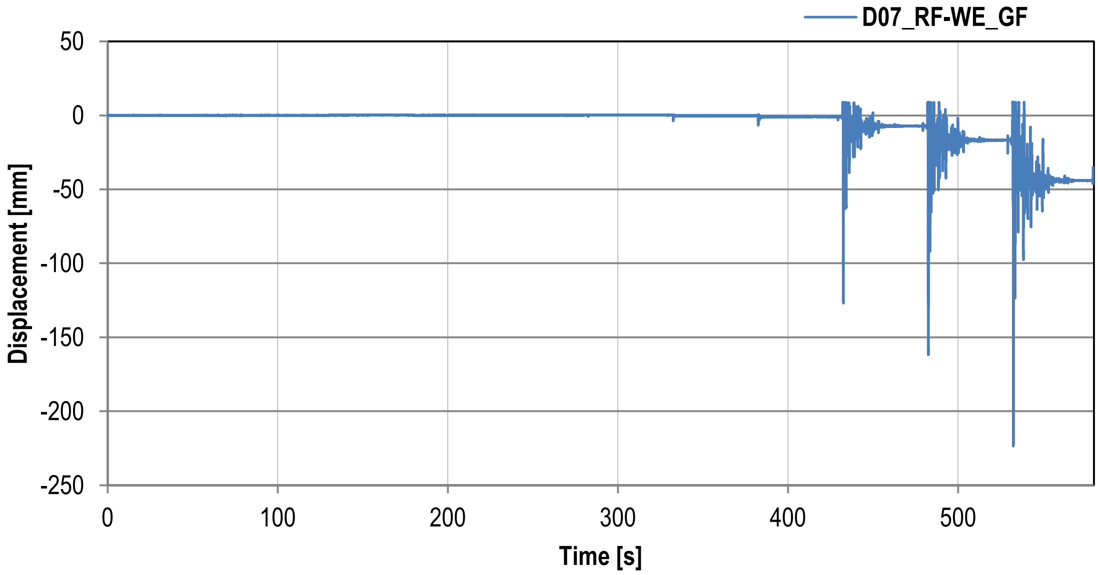

Channel D07_RF-WE_GF – Relative displacement

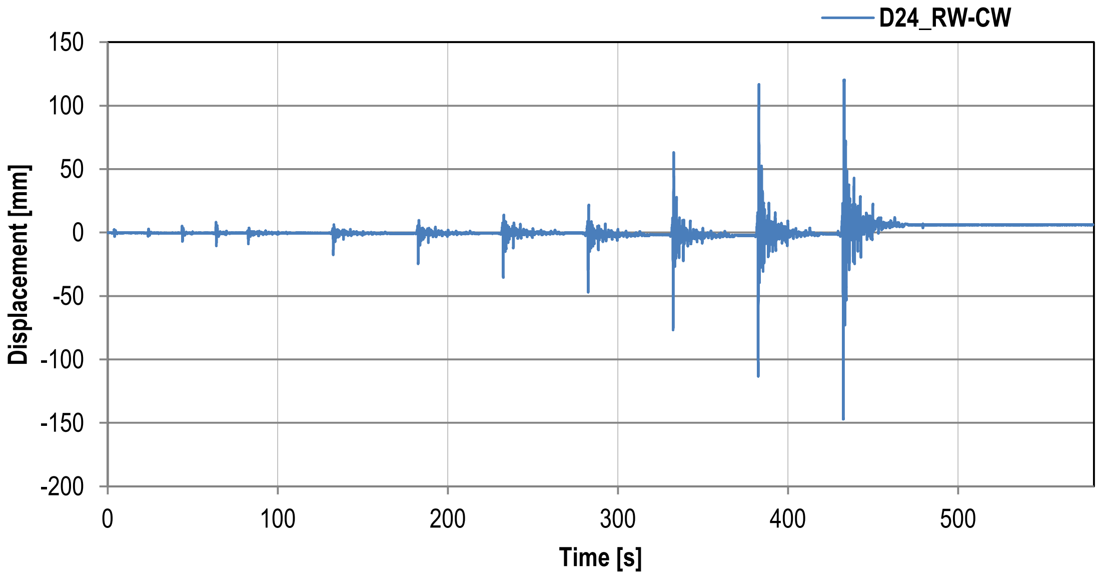

Channel D24_RW-CW– Relative displacement

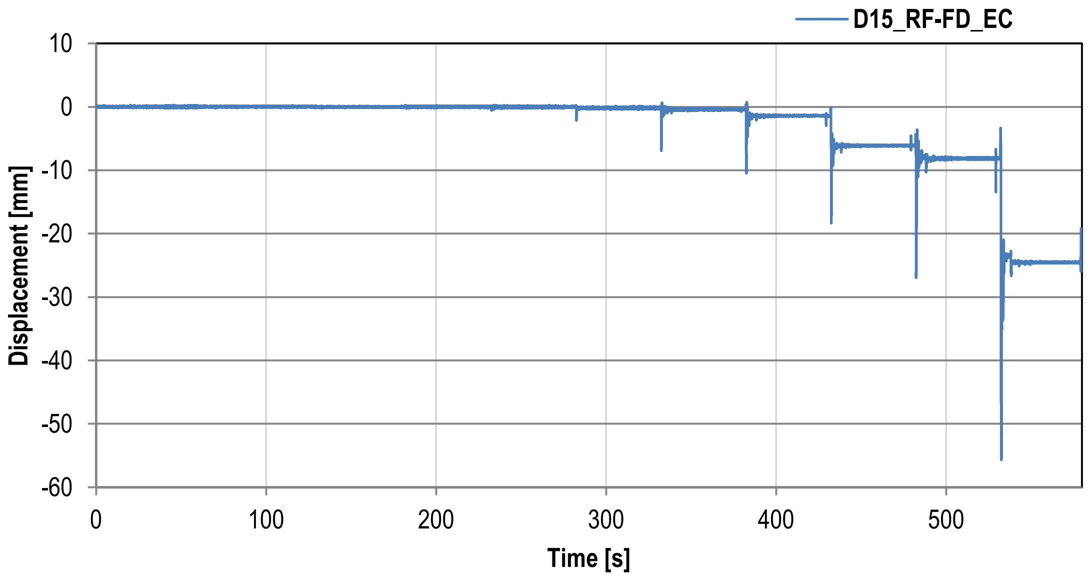

Channel D15_RF-FD_EC– Relative displacement

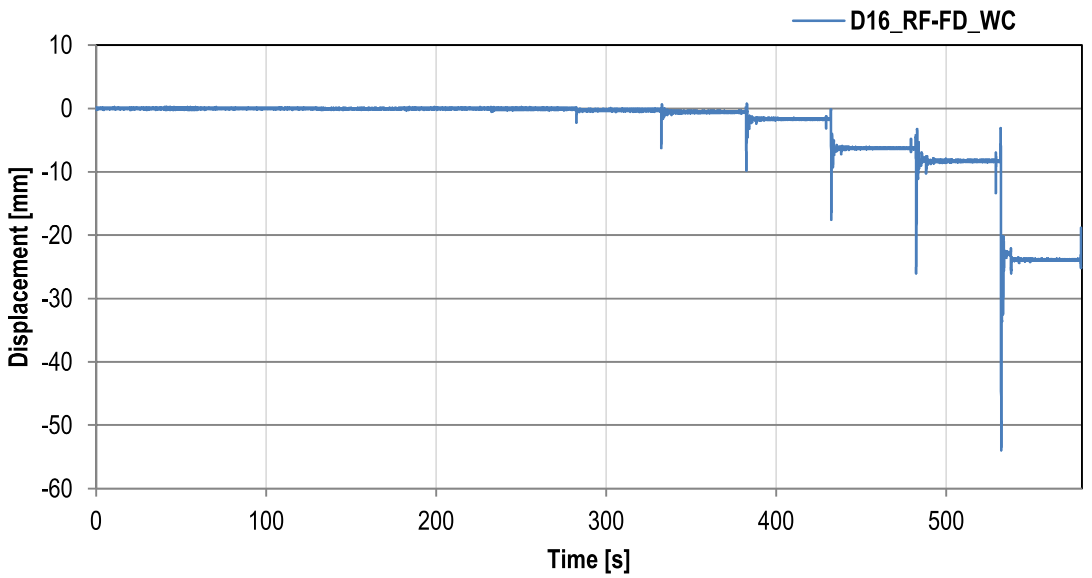

Channel D16_RF-FD_WC– Relative displacement

APPENDIX C. TRANSDUCERS' READINGS FOR SC1-100%

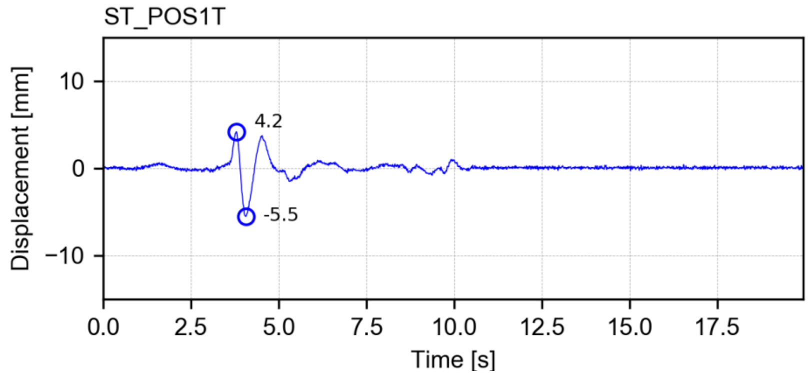

Channel ST_POS_T – Transverse displacement of the LNEC 3D shake table motion control

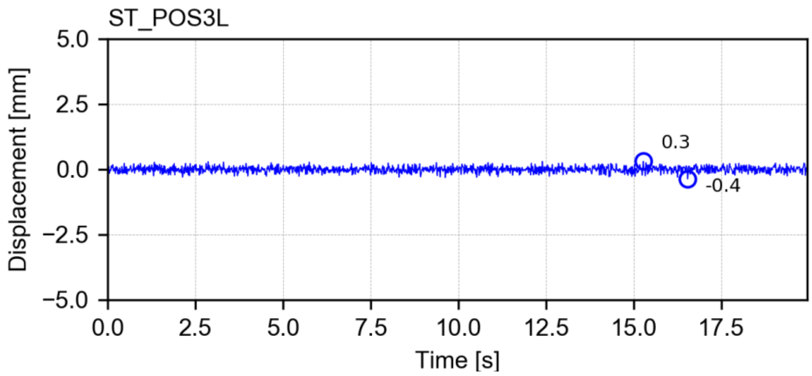

Channel ST_POS_L – Vertical displacement of the LNEC 3D shake table motion control

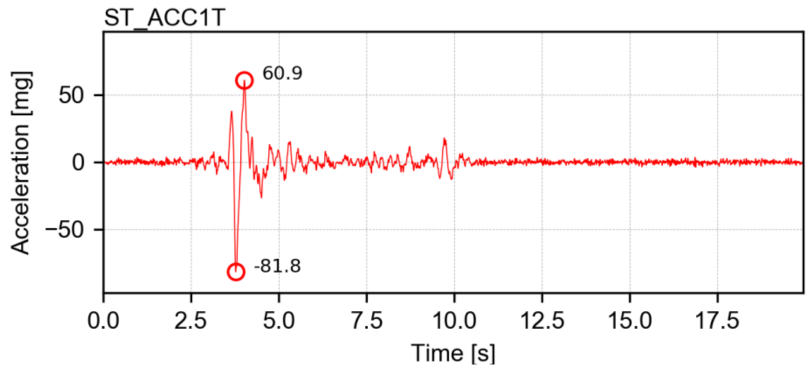

Channel ST_ACC_T – Transverse acceleration of the LNEC 3D shake table motion control

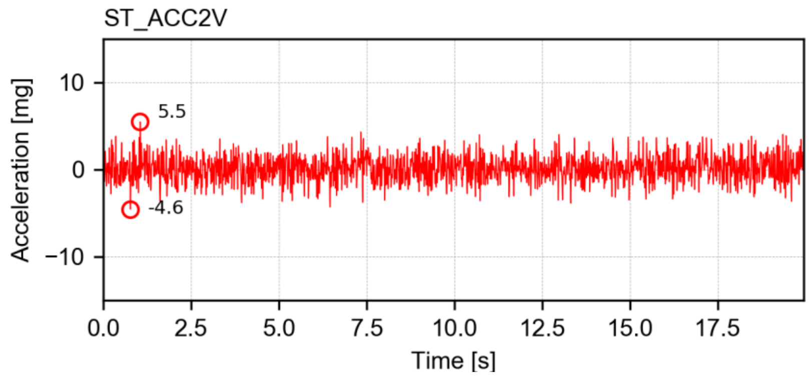

Channel ST_ACC_L – Vertical acceleration of the LNEC 3D shake table motion control

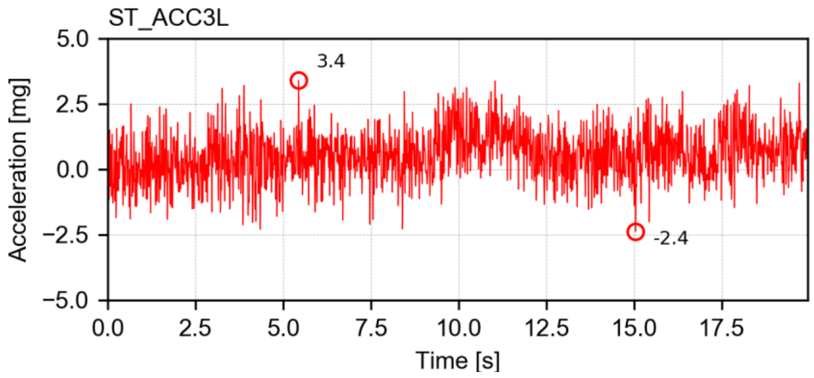

Channel ST_ACC_V – Longitudinal acceleration of the LNEC 3D shake table motion control

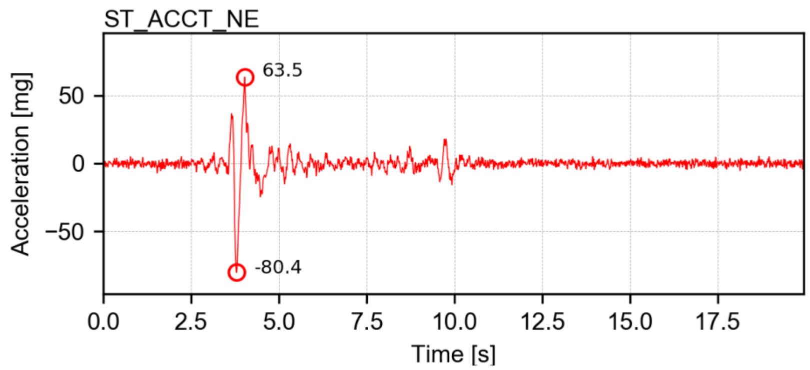

Channel ST_ACCT_NE – Transverse acceleration of the North-East LNEC 3D shake table platform

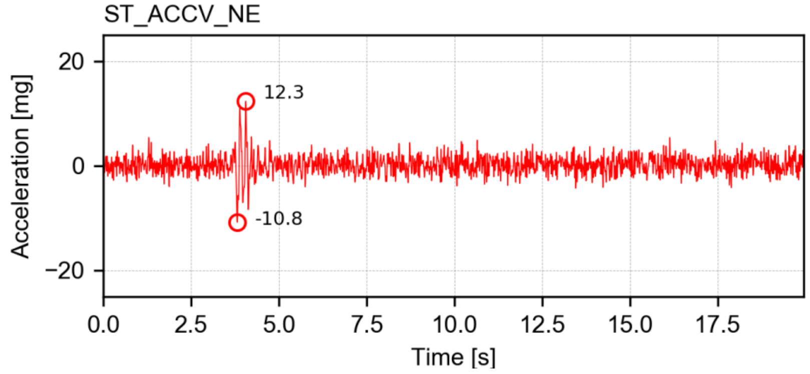

Channel ST_ACCV_NE – Vertical acceleration of the North-East LNEC 3D shake table platform

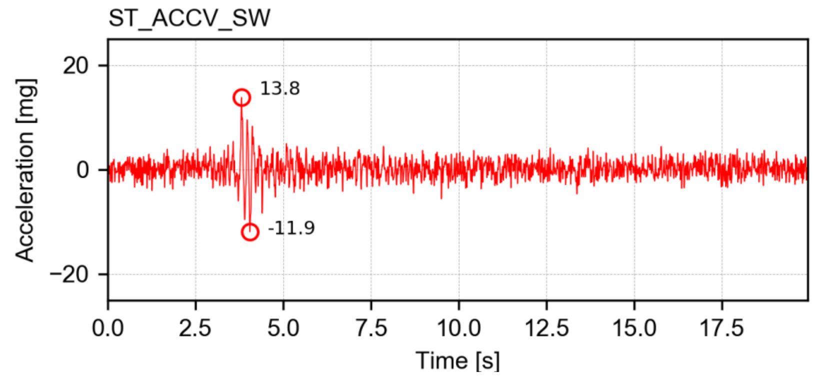

Channel ST_ACCV_SW – Vertical acceleration of the South-West LNEC 3D shake table platform

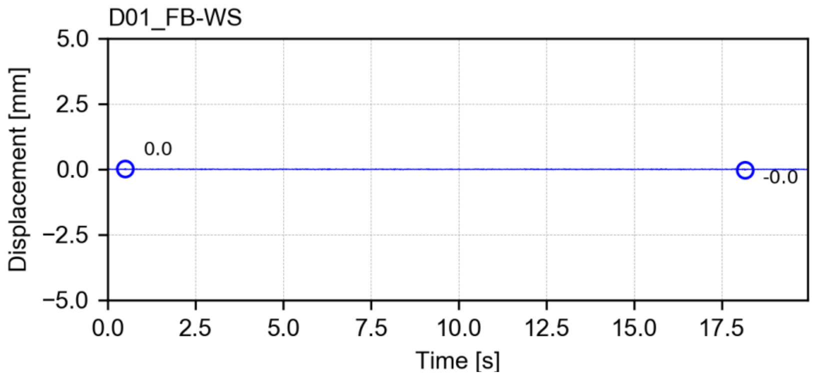

Channel D01_FB-WS – displacement

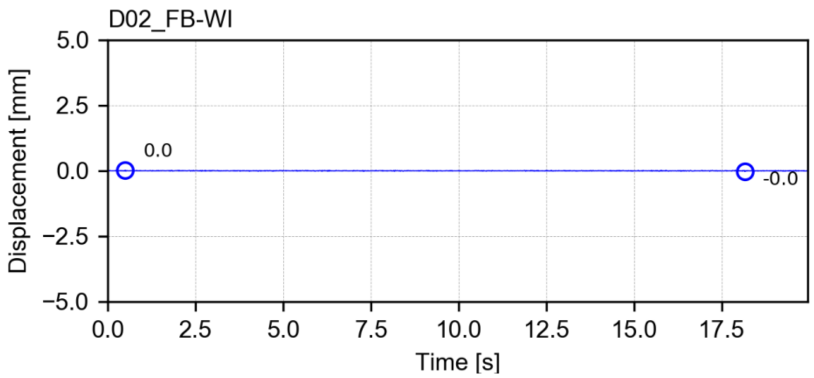

Channel D02_FB-WI – displacement

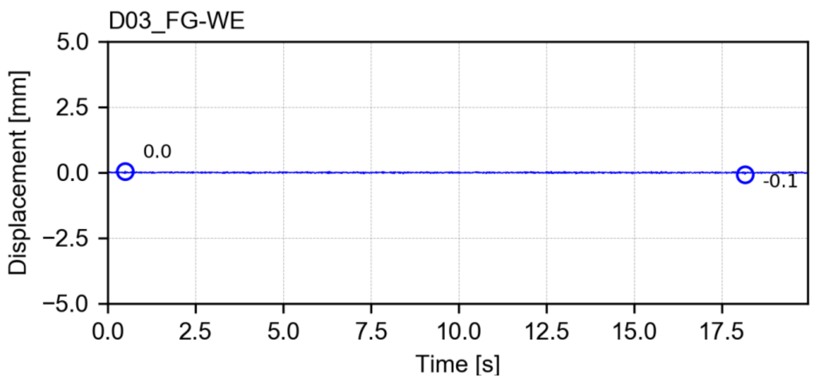

Channel D03_FG-WE – displacement

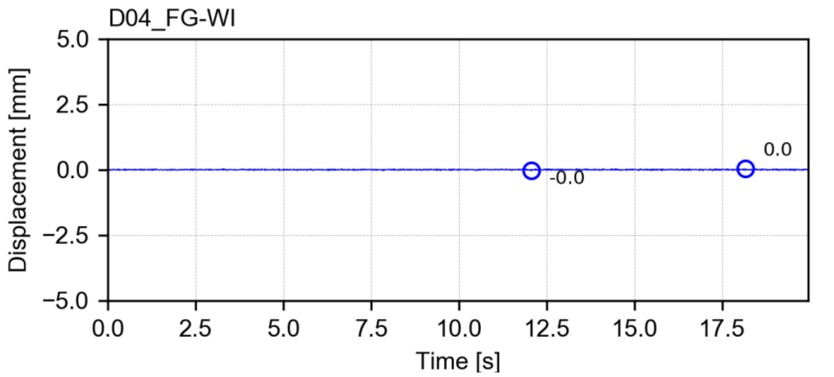

Channel D04_FG-WI – displacement

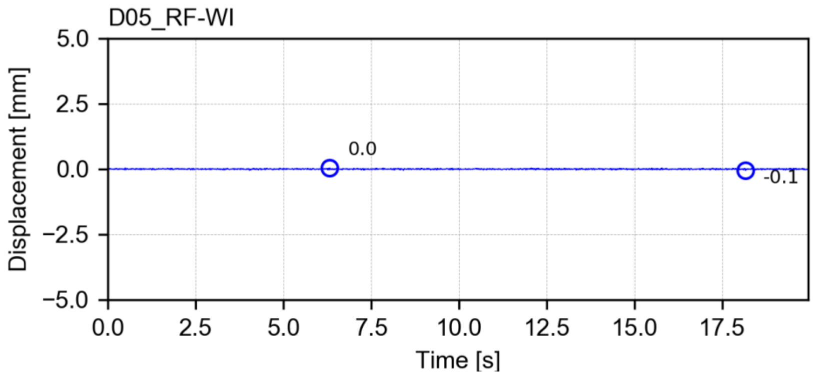

Channel D05_RF-WI – displacement

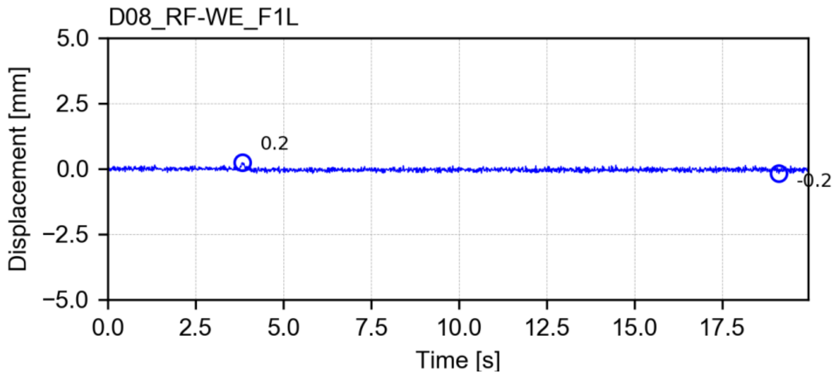

Channel D08_RF-WE_F1L – displacement

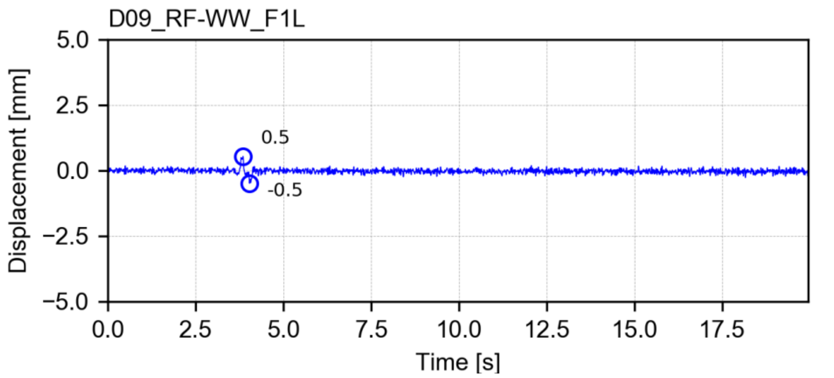

Channel D09_RF-WW_F1L – displacement

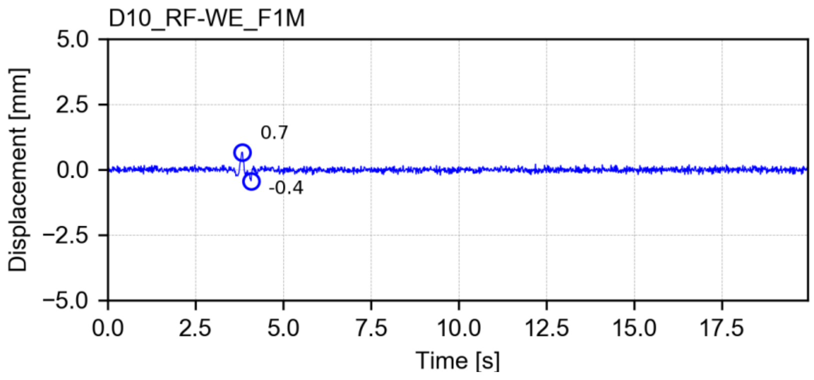

Channel D10_RF-WE_F1M – displacement

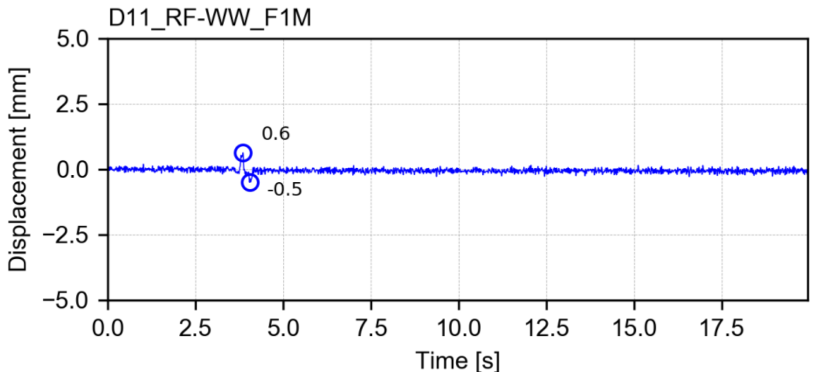

Channel D11_RF-WW_F1M – displacement

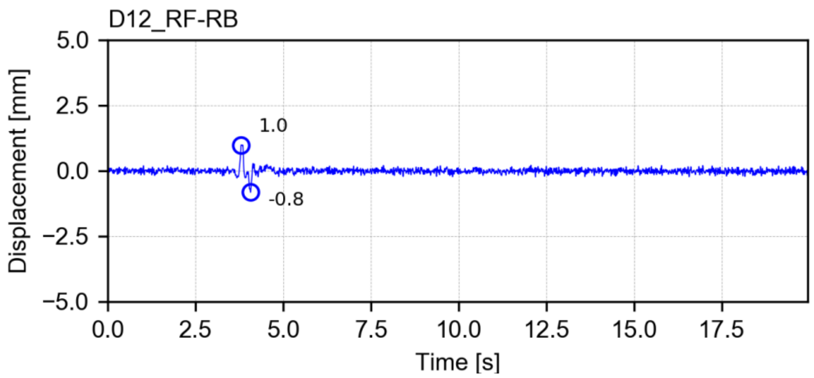

Channel D12_RF-RB – displacement

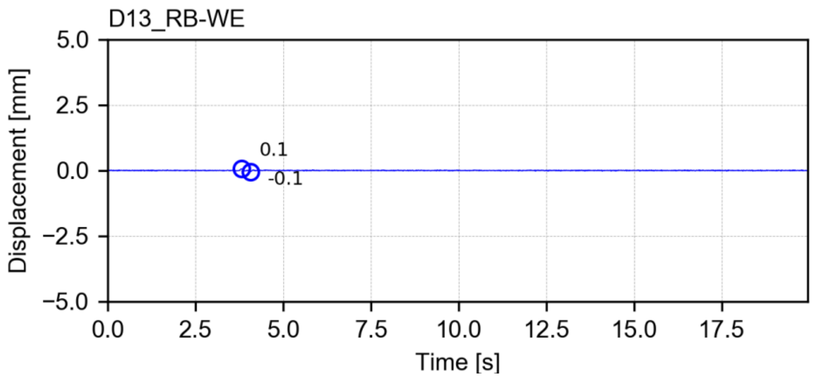

Channel D13_RB-WE – displacement

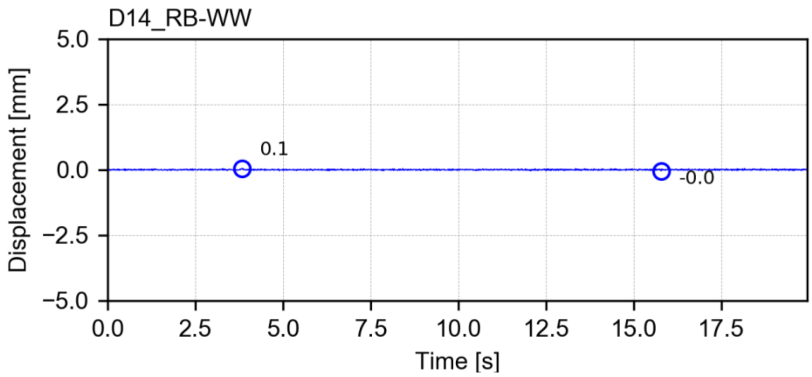

Channel D14_RB-WW – displacement

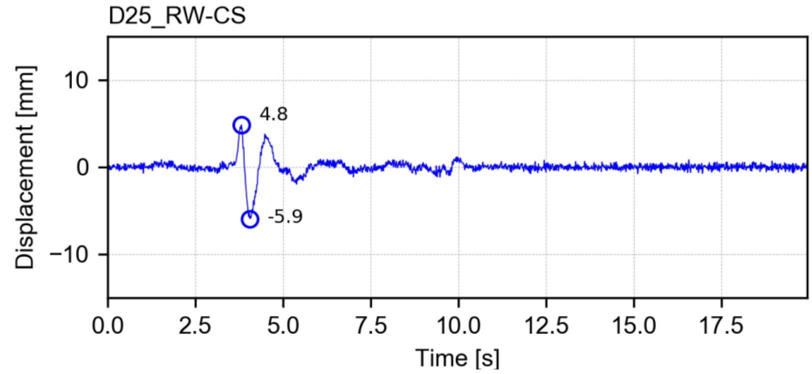

Channel D25_RW-CS – displacement

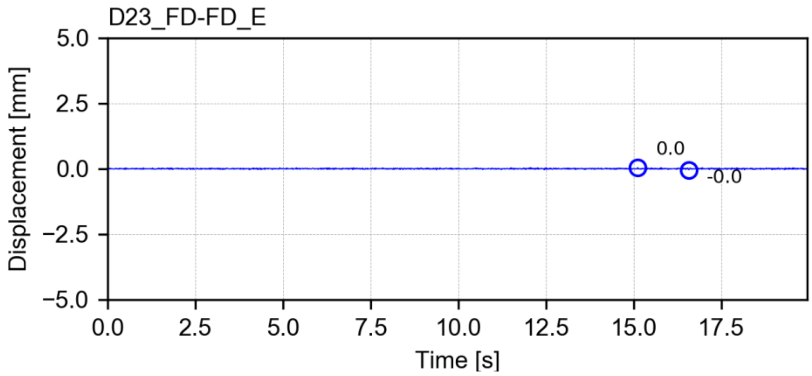

Channel D23_FD-FD_E – displacement

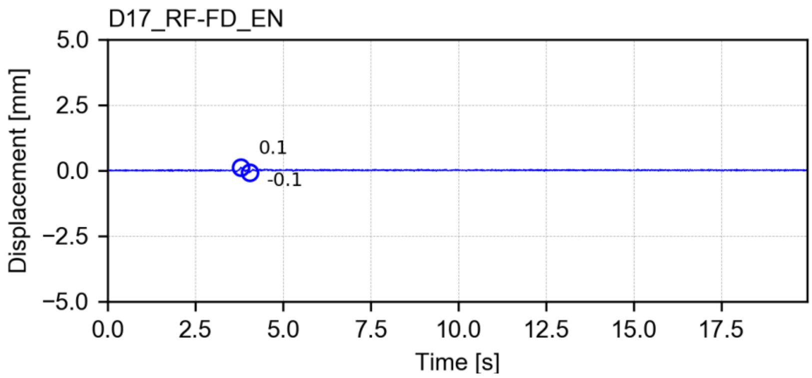

Channel D17_RF-FD_EN SC – displacement

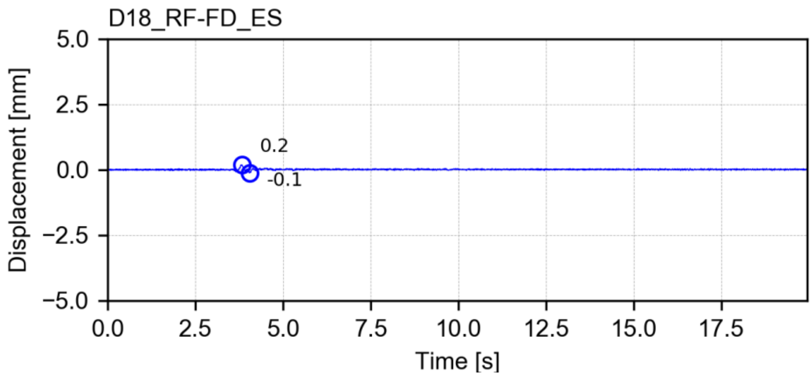

Channel D18_RF-FD_ES – displacement

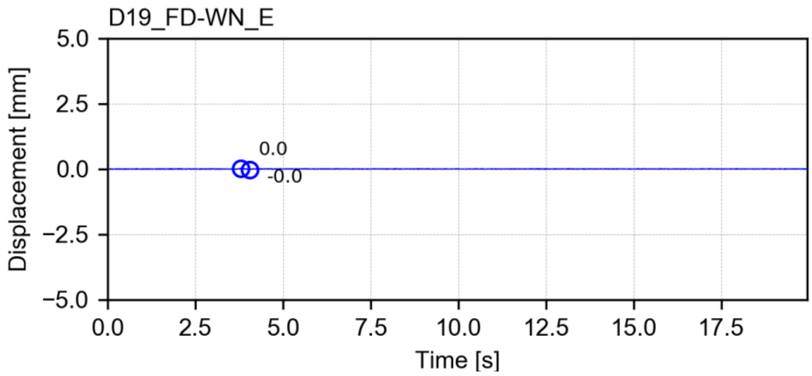

Channel D19_FD-WN_E – displacement

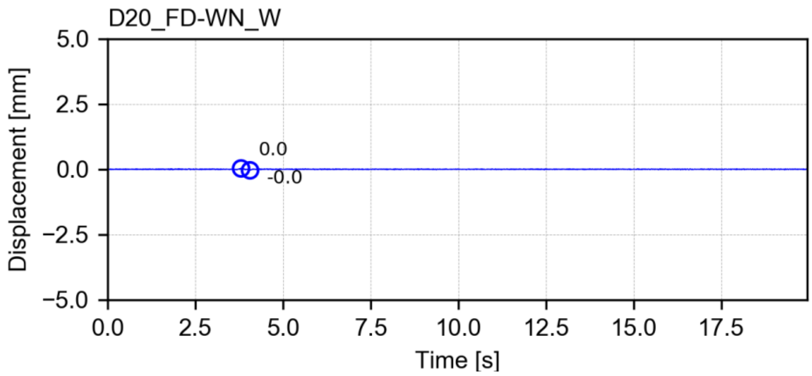

Channel D20_FD-WN_W – displacement

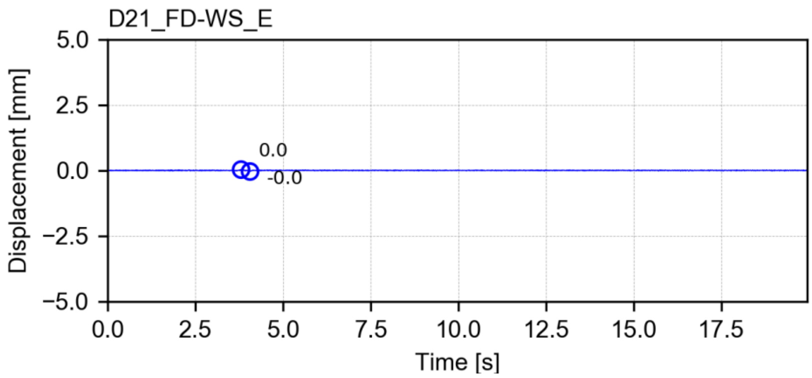

Channel D21_FD-WS_E – displacement

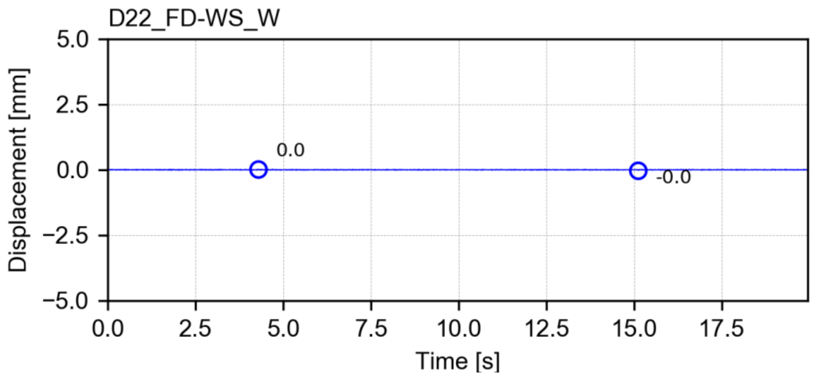

Channel D22_FD-WS_W – displacement

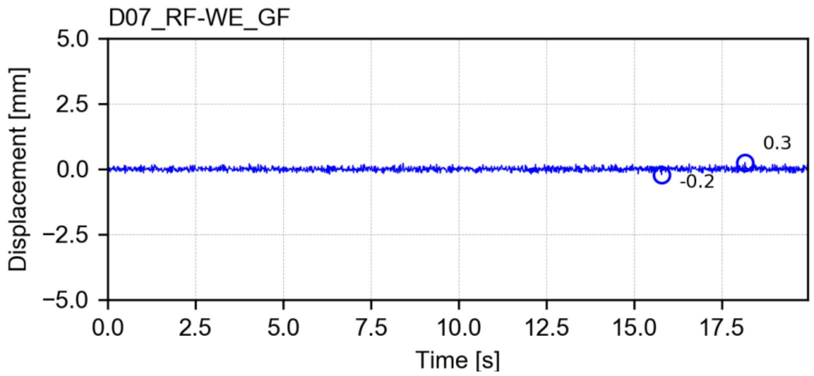

Channel D07_RF-WE_GF – displacement

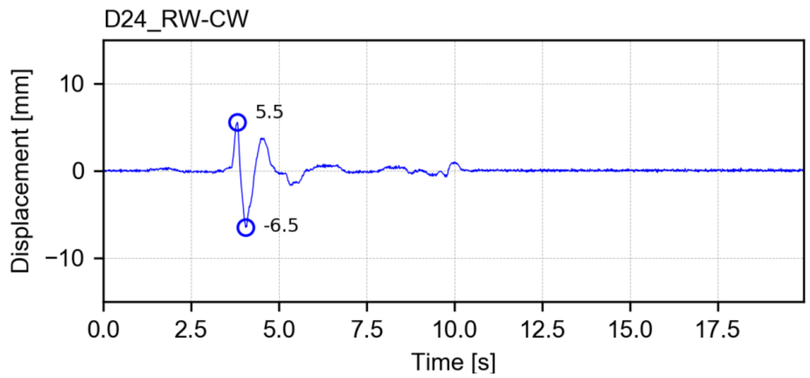

Channel D24_RW-CW– displacement

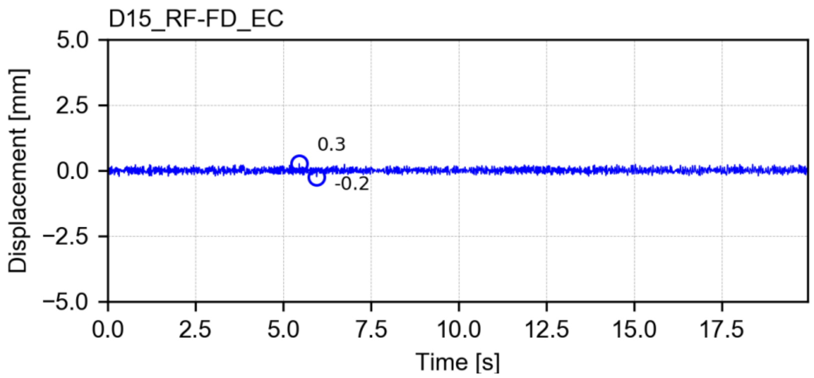

Channel D15_RF-FD_EC – displacement

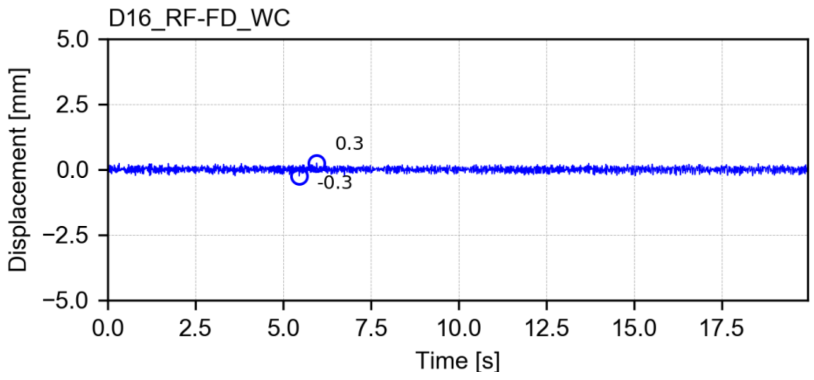

Channel D16_RF-FD_WC – displacement

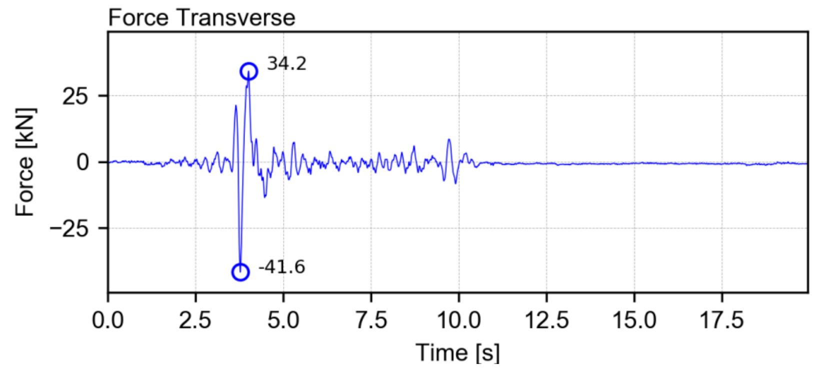

Channel Force Transverse – force

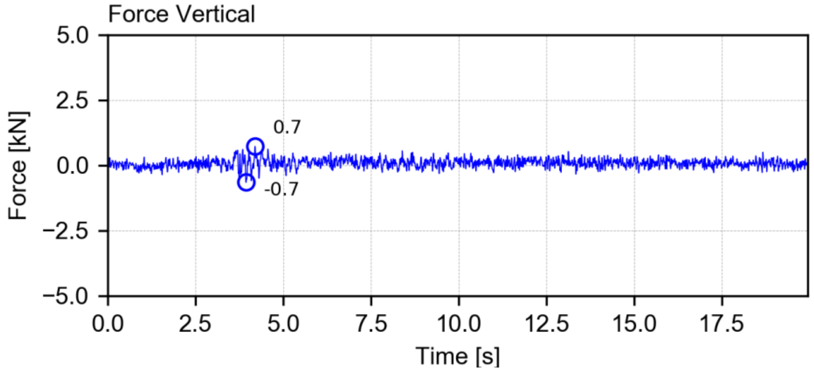

Channel Force Vertical – force

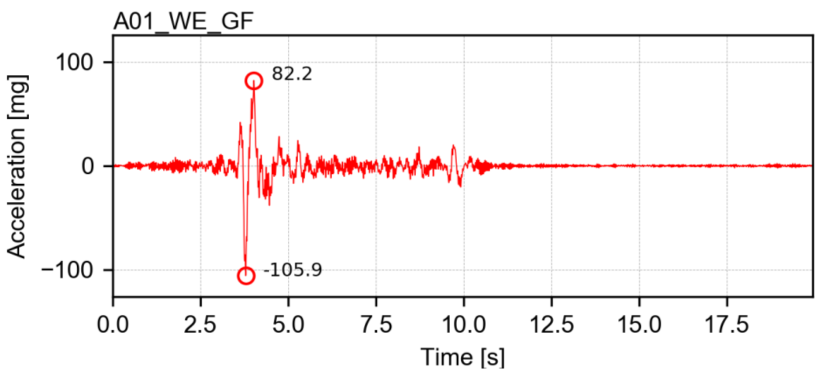

Channel A01_WE_GF –acceleration

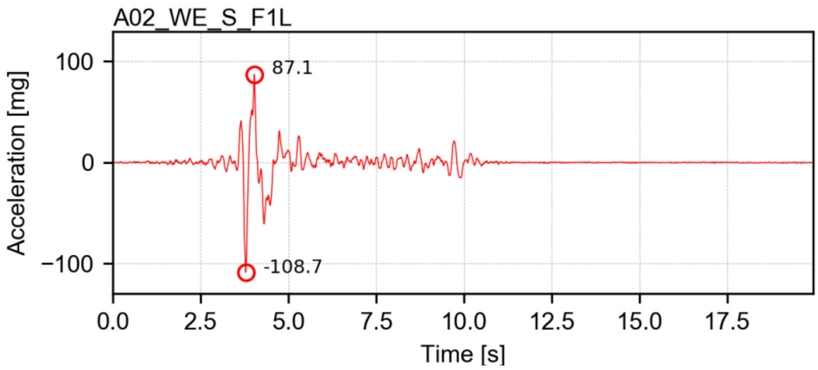

Channel A02_WE_S_F1L – acceleration

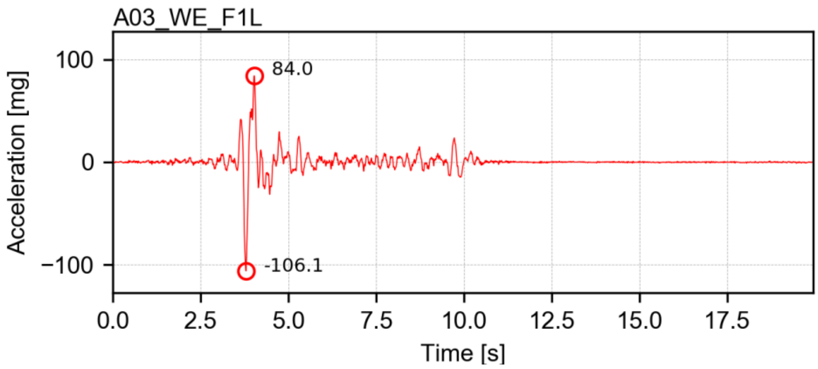

Channel A03_WE_F1L – acceleration

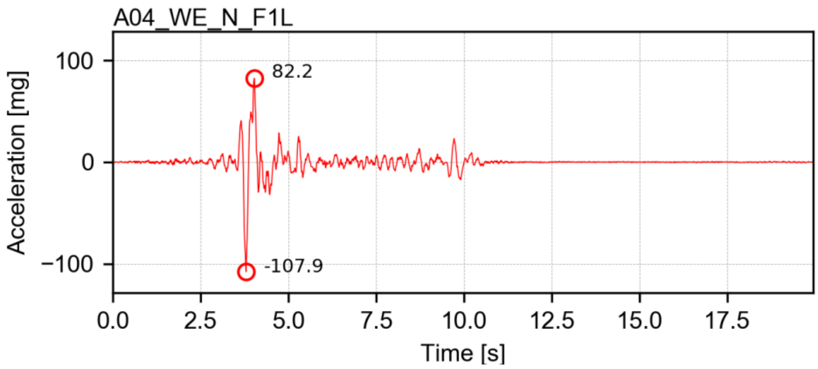

Channel A04_WE_N_F1L – acceleration

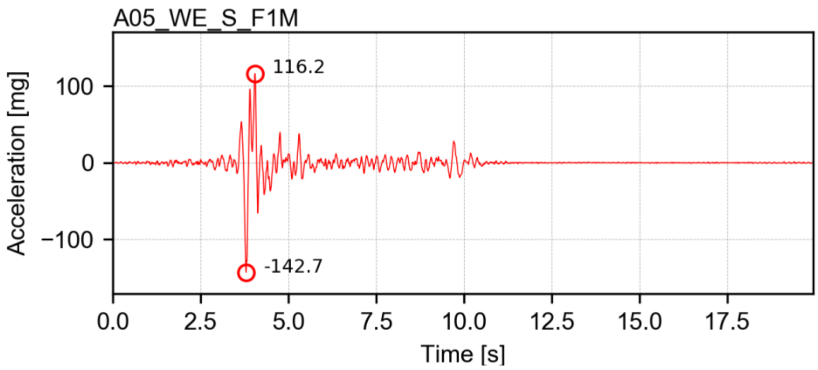

Channel A05_WE_S_F1M – acceleration

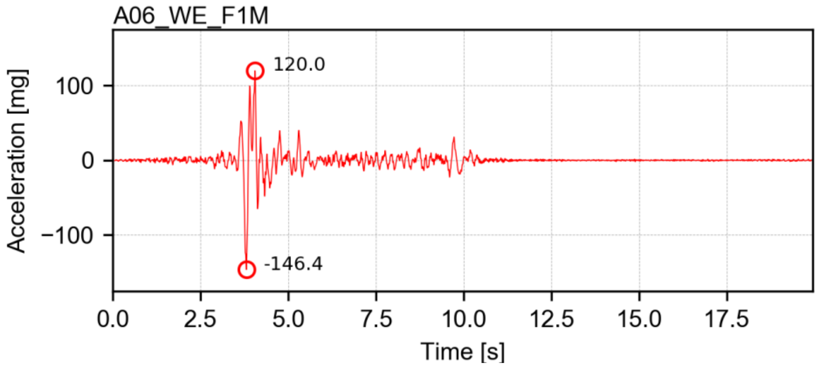

Channel A06_WE_F1M – acceleration

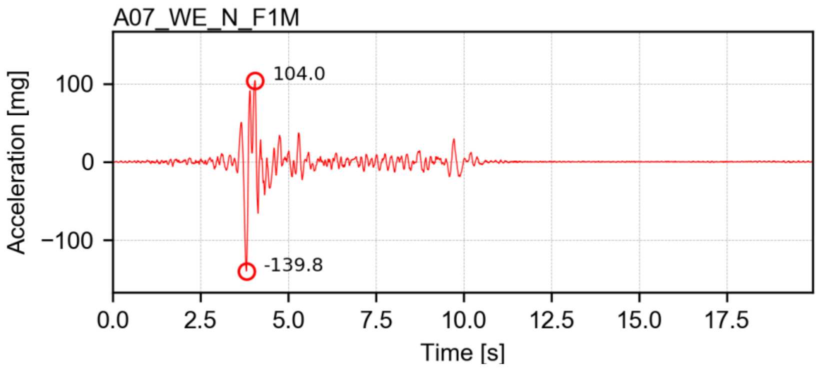

Channel A07_WE_N_F1M – acceleration

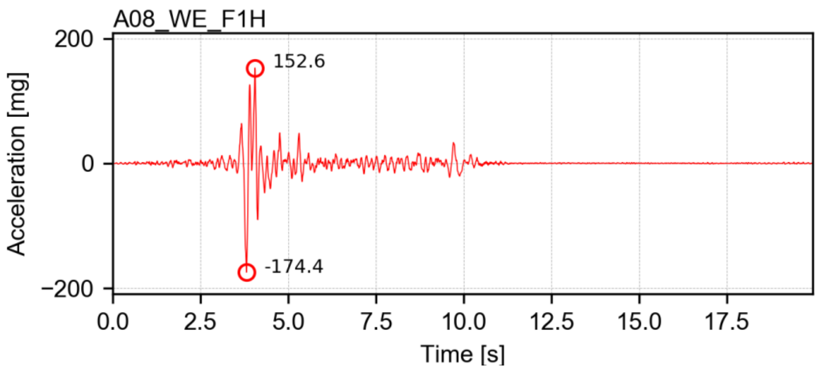

Channel A08_WE_F1H – acceleration

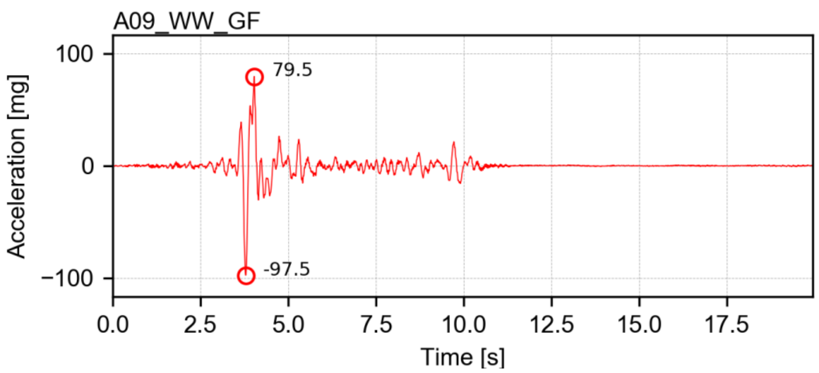

Channel A09_WW_GF – acceleration

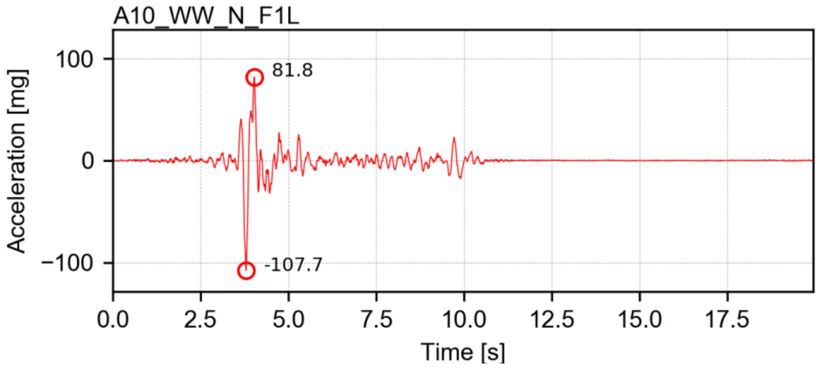

Channel A10_WW_N_F1L – acceleration

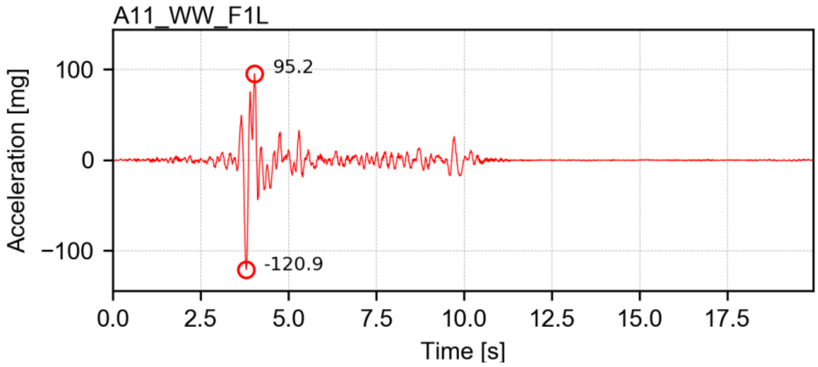

Channel A11_WW_F1L – acceleration

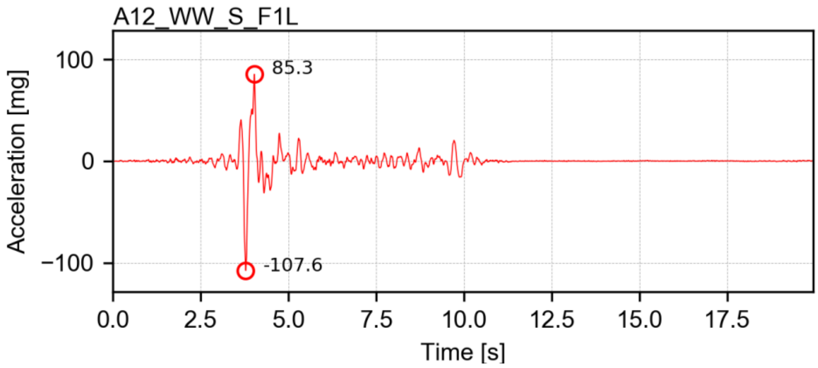

Channel A12_WW_S_F1L – acceleration

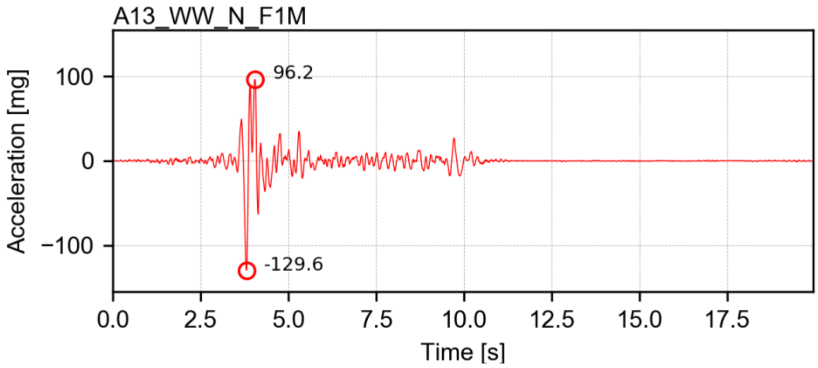

Channel A13_WW_N_F1M – acceleration

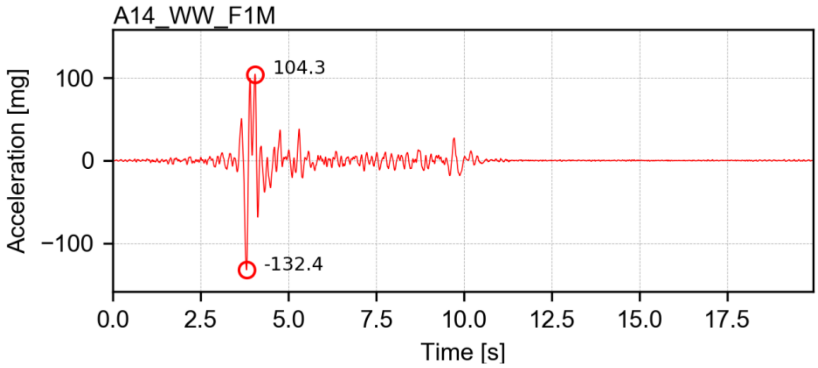

Channel A14_WW_F1M – acceleration

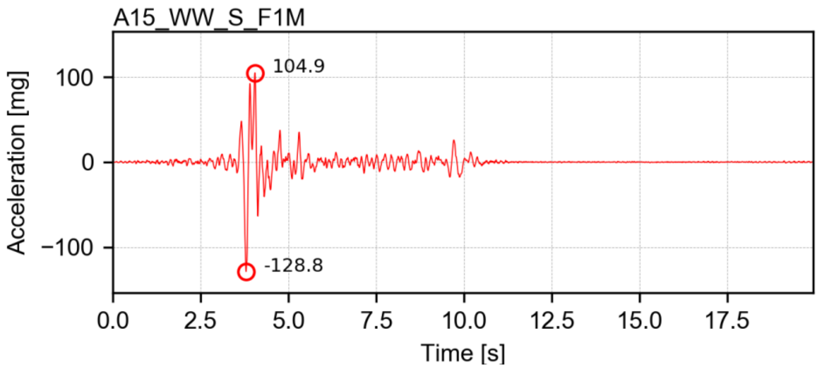

Channel A15_WW_S_F1M – acceleration

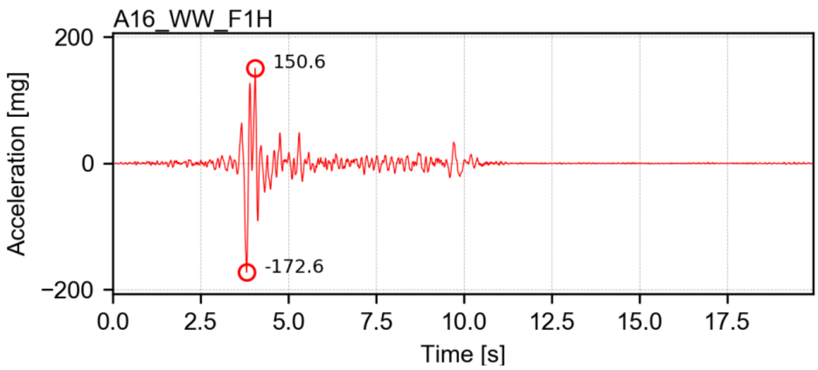

Channel A16_WW_F1H – acceleration

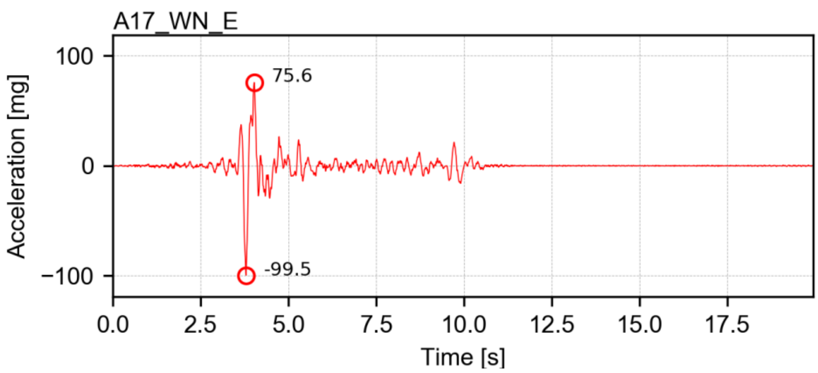

Channel A17_WN_E – acceleration

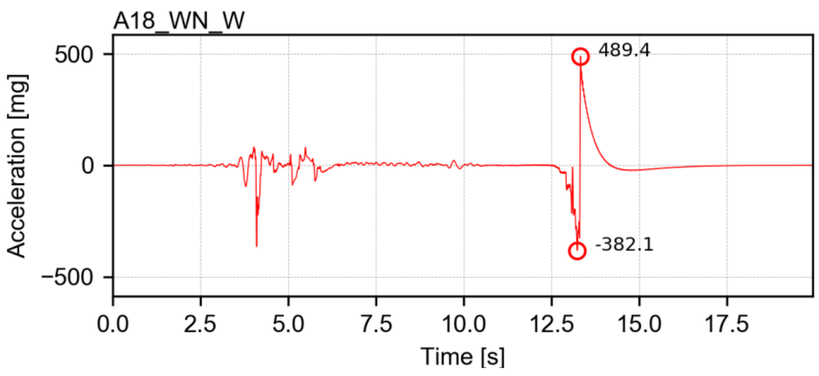

Channel A18_WN_W – acceleration

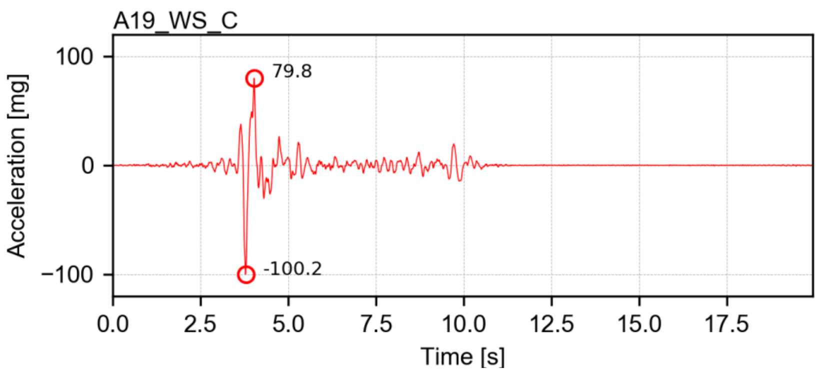

Channel A19_WS_C – acceleration

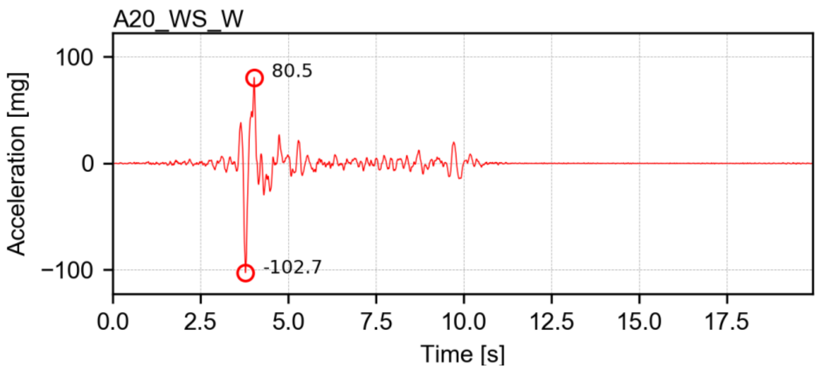

Channel A20_WS_W – acceleration

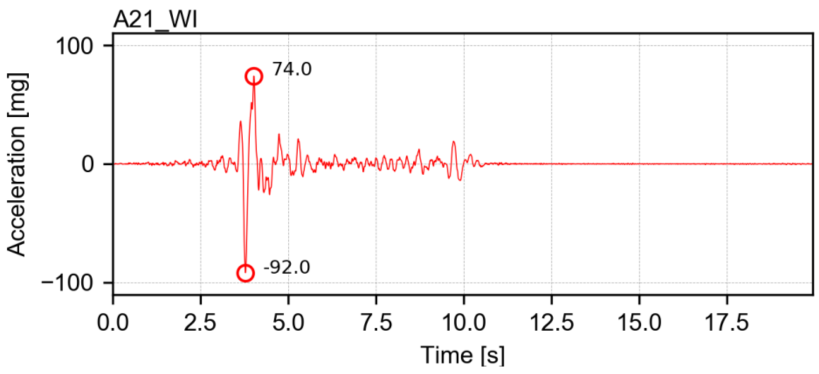

Channel A21_WI – acceleration

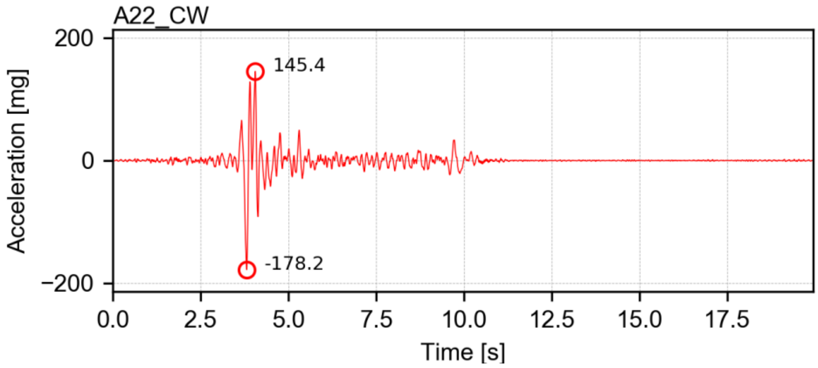

Channel A22_CW – acceleration

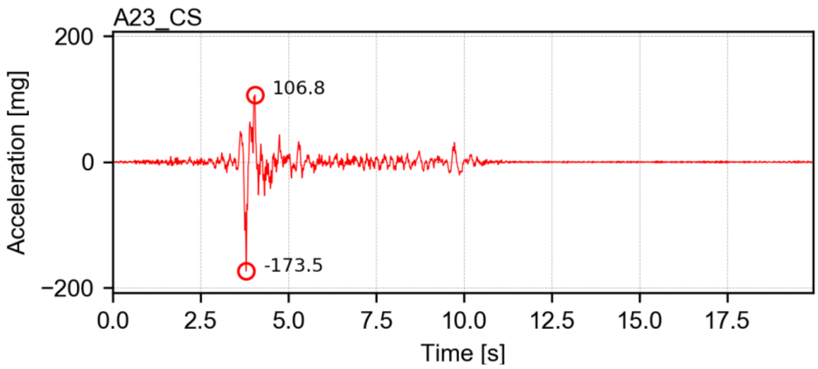

Channel A23_CS – acceleration

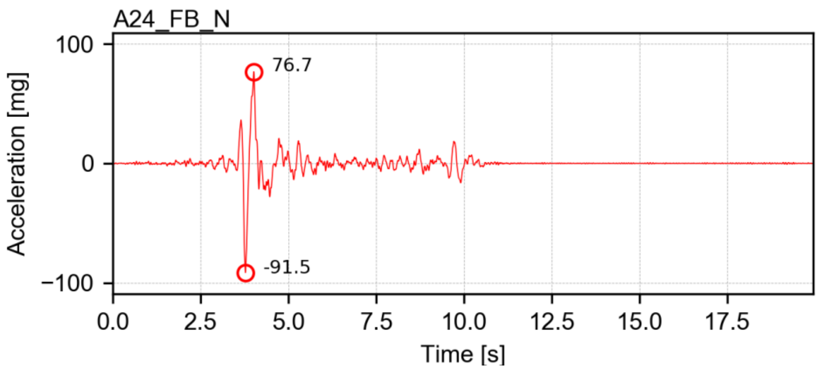

Channel A24_FB_N – acceleration

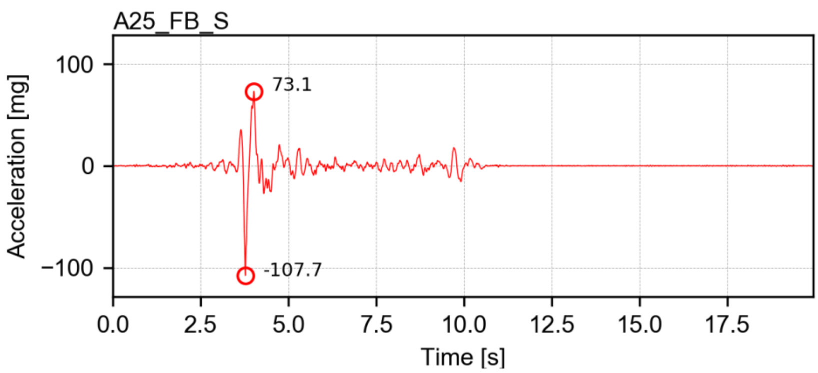

Channel A25_FB_S – acceleration

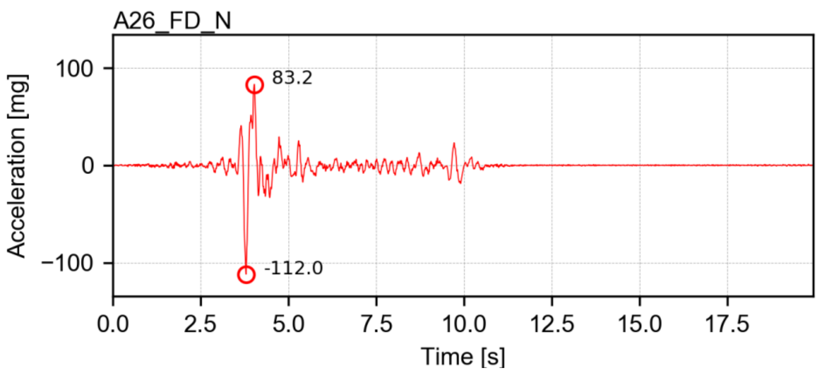

Channel A26_FD_N – acceleration

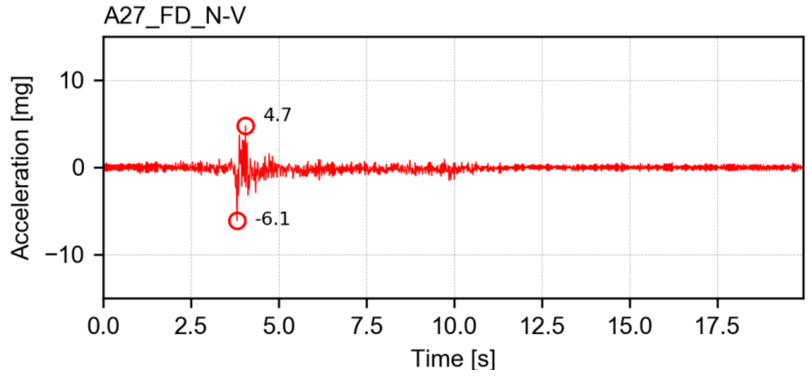

Channel A27_FD_N-V – acceleration

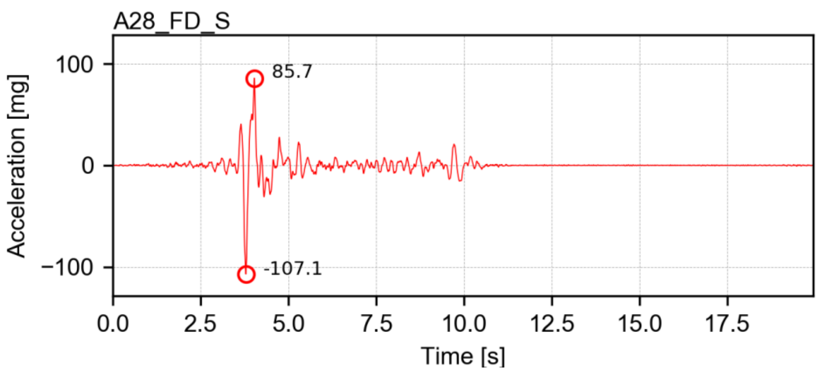

Channel A28_FD_S – acceleration

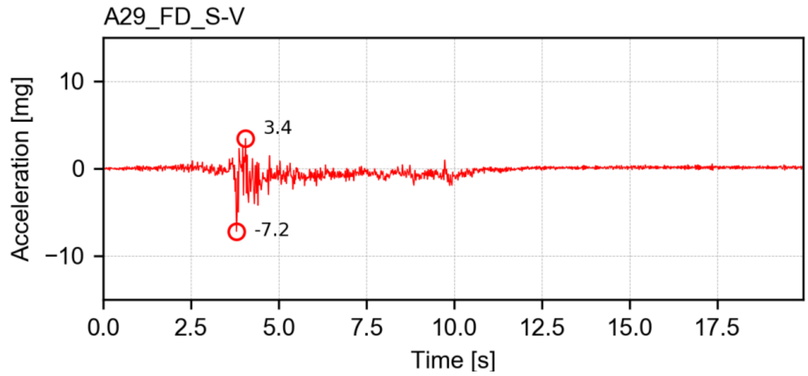

Channel A29_FD_S-V – acceleration

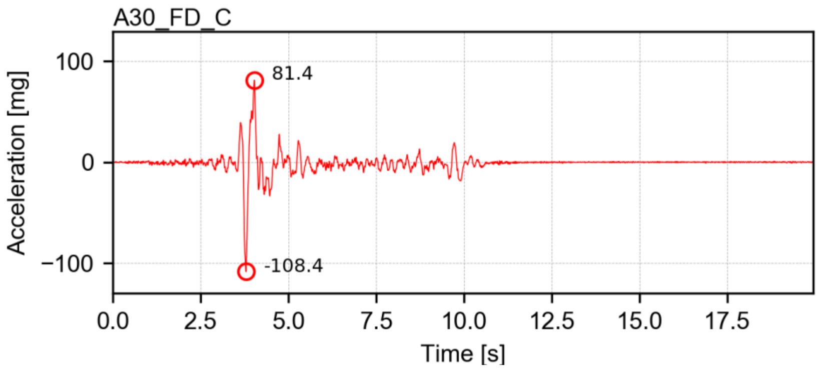

Channel A30_FD_C – acceleration

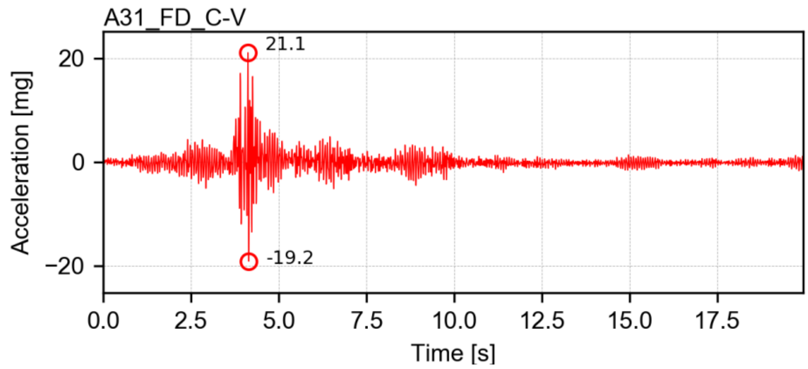

Channel A31_FD_C-V – acceleration

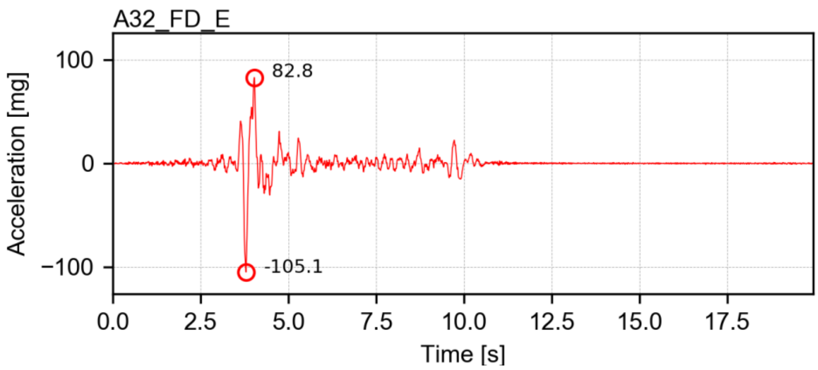

Channel A32_FD_E – acceleration

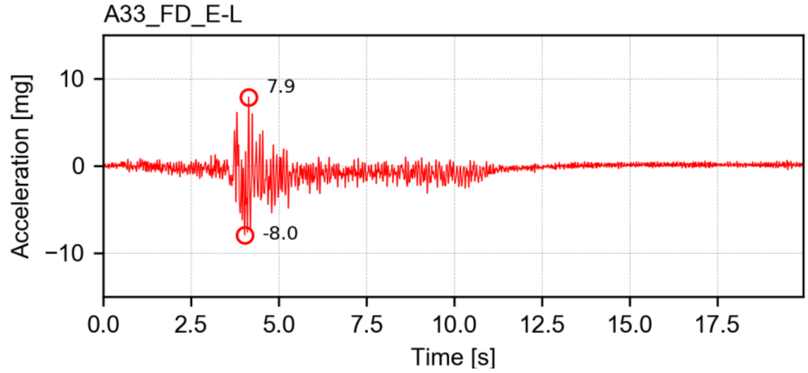

Channel A33_FD_E-L – acceleration

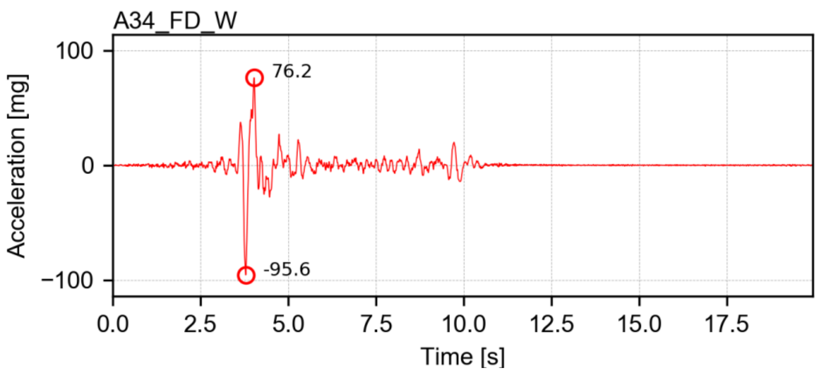

Channel A34_FD_W – acceleration

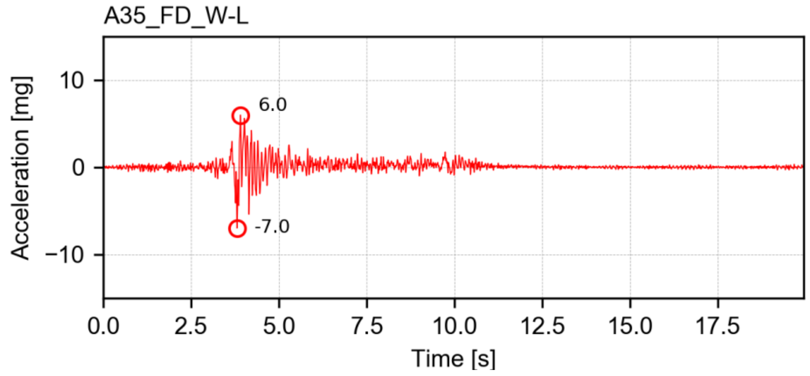

Channel A35_FD_W-L – acceleration

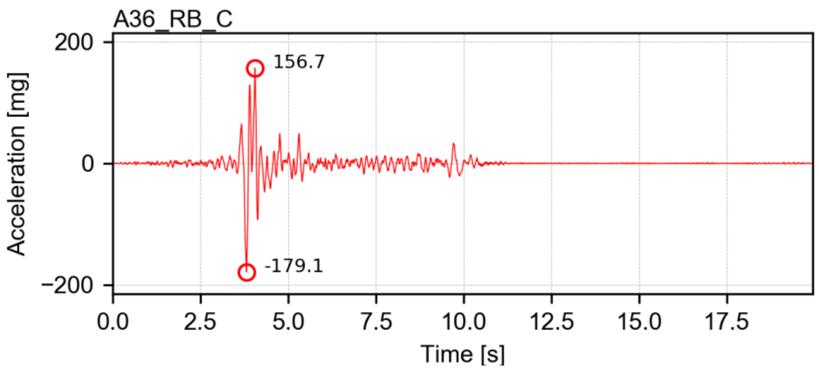

Channel A36_RB_C – acceleration

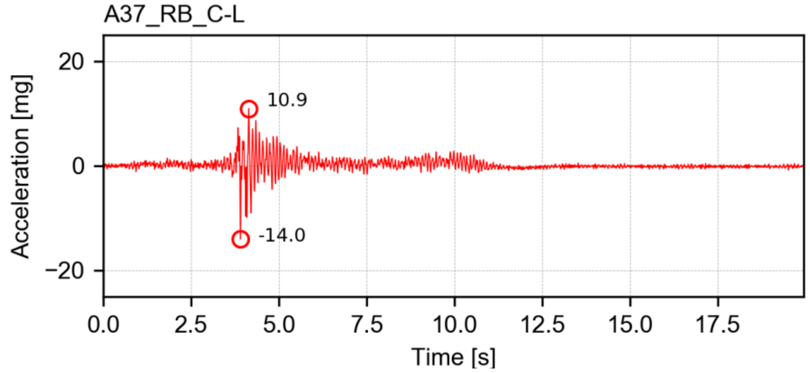

Channel A37_RB_C-L – acceleration

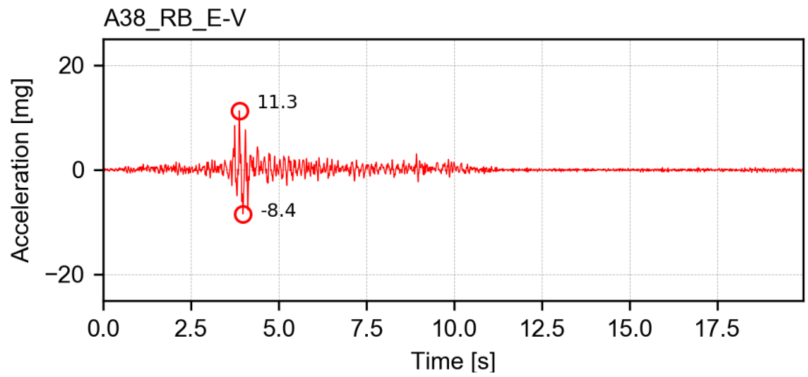

Channel A38_RB_E-V – acceleration

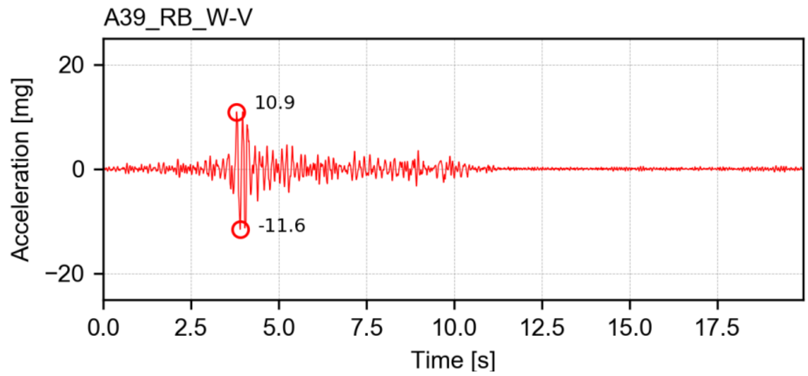

Channel A39_RB_W-V – acceleration

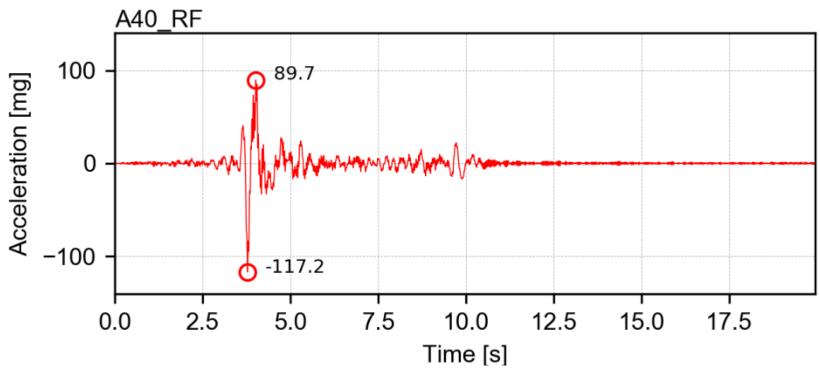

Channel A40_RF – acceleration

APPENDIX D. TRANSDUCERS' READINGS FOR SC2-100%

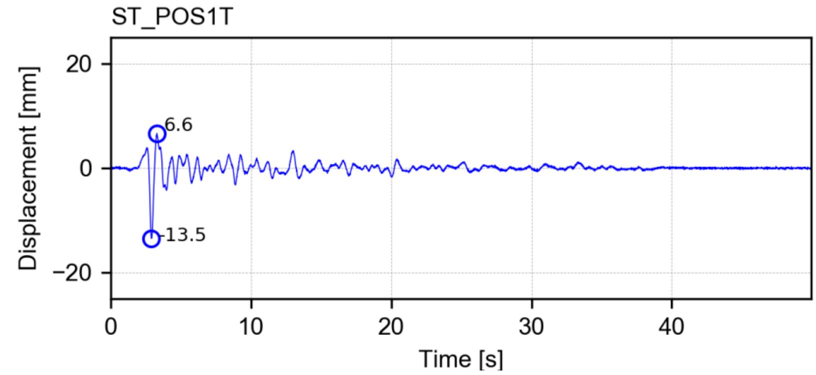

Channel ST_POS_T – Transverse displacement of the LNEC 3D shake table motion control

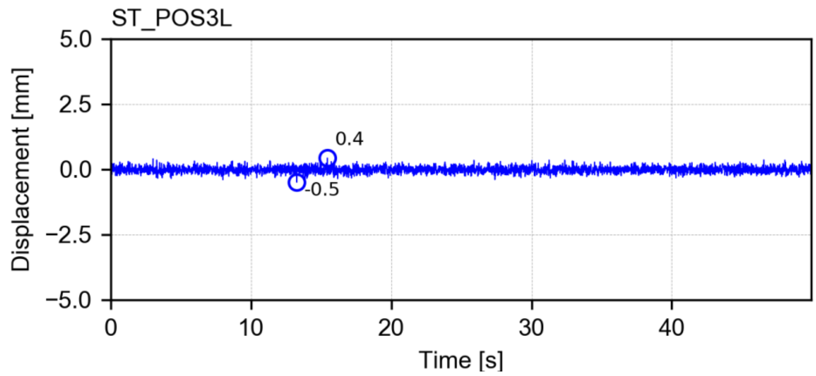

Channel ST_POS_L – Vertical displacement of the LNEC 3D shake table motion control

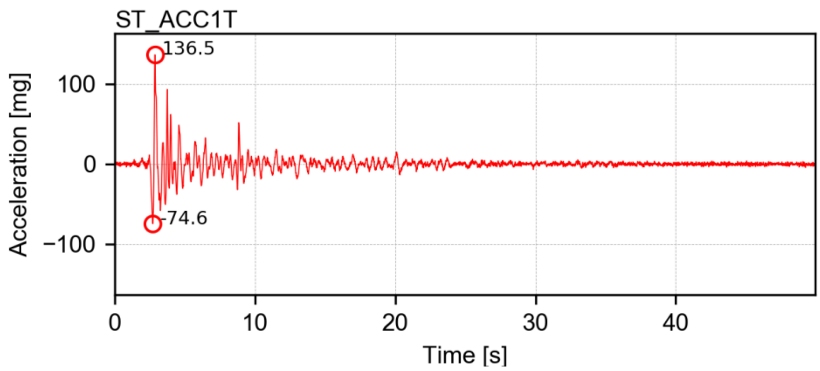

Channel ST_ACC_T – Transverse acceleration of the LNEC 3D shake table motion control

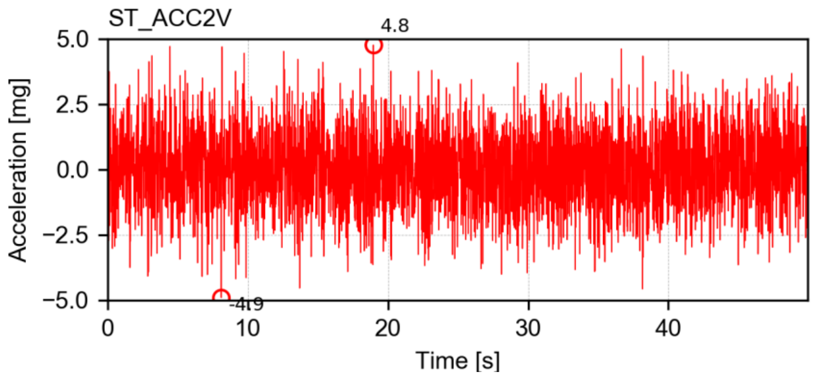

Channel ST_ACC_L – Vertical acceleration of the LNEC 3D shake table motion control

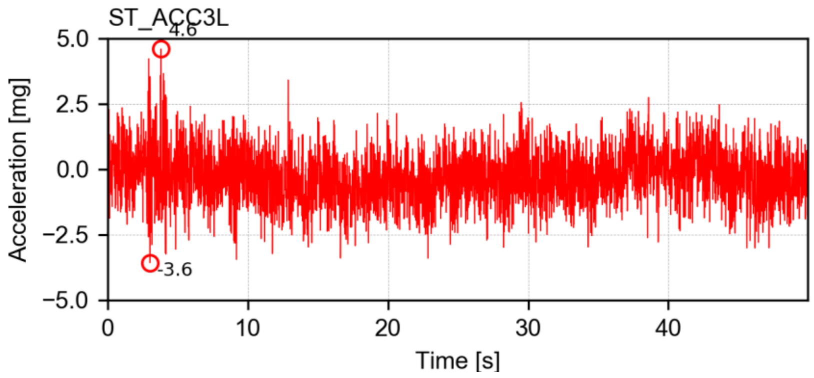

Channel ST_ACC_V – Longitudinal acceleration of the LNEC 3D shake table motion control

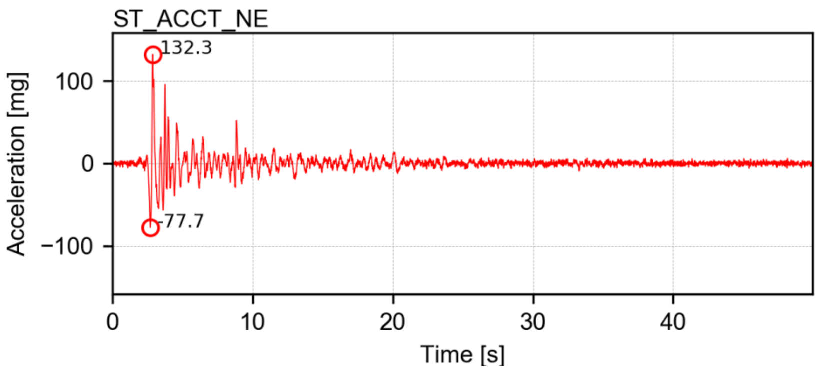

Channel ST_ACCT_NE – Transverse acceleration of the North-East LNEC 3D shake table platform

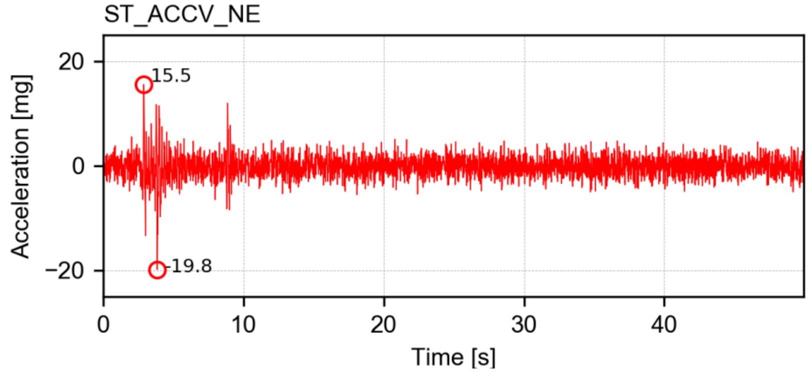

Channel ST_ACCV_NE – Vertical acceleration of the North-East LNEC 3D shake table platform

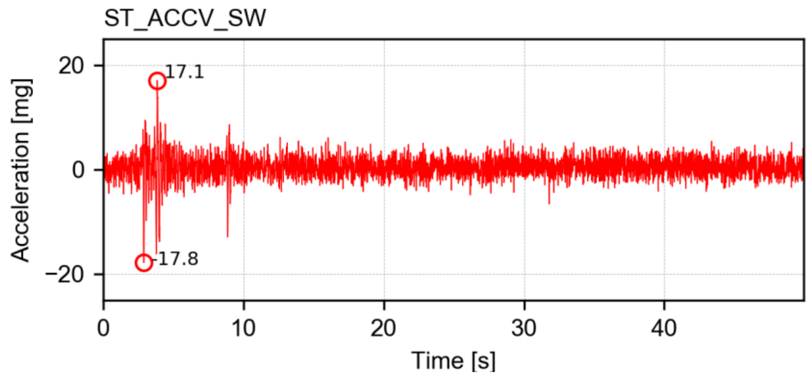

Channel ST_ACCV_SW – Vertical acceleration of the South-West LNEC 3D shake table platform

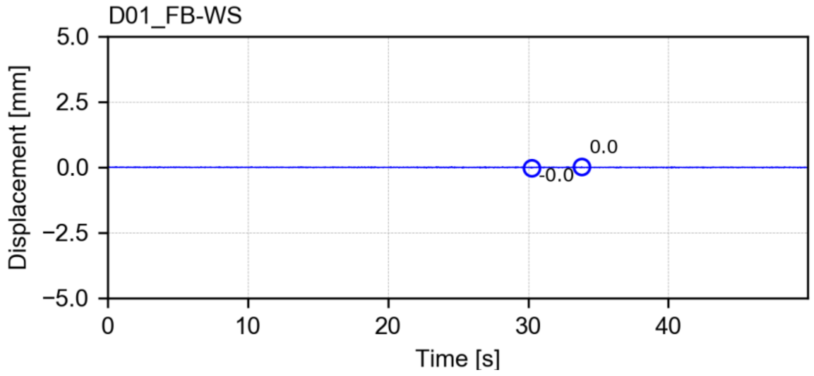

Channel D01_FB-WS – displacement

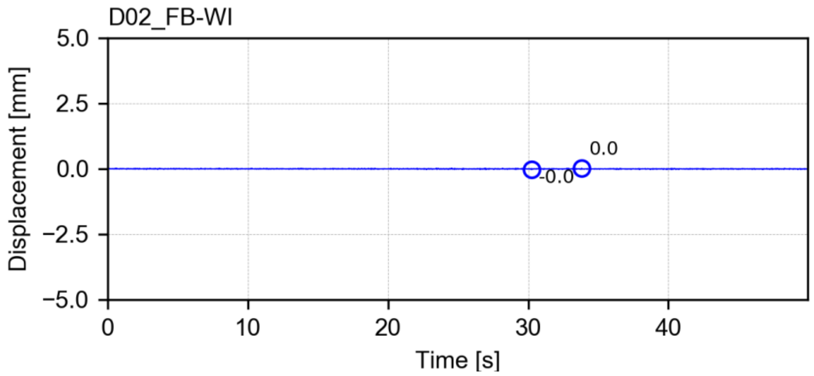

Channel D02_FB-WI – displacement

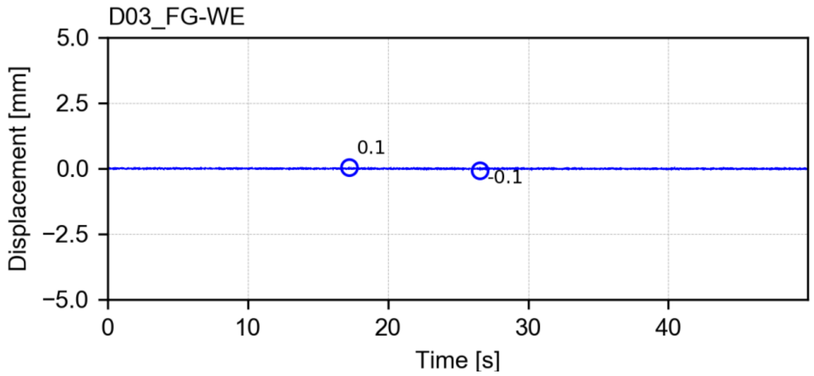

Channel D03_FG-WE – displacement

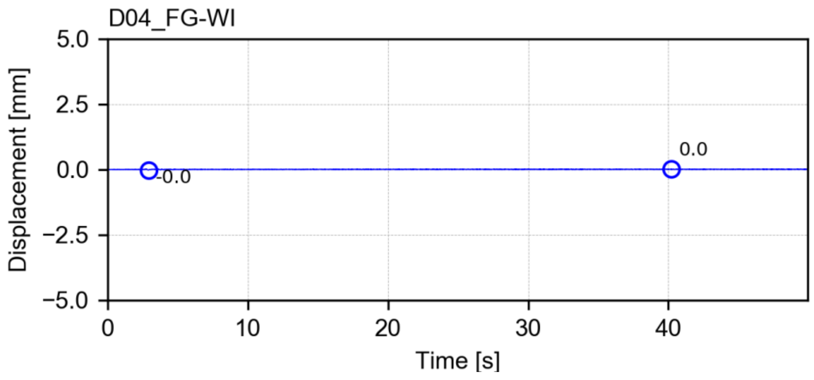

Channel D04_FG-WI – displacement

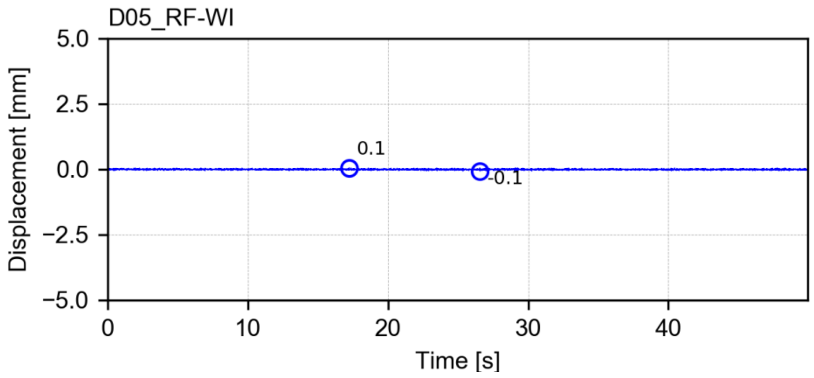

Channel D05_RF-WI – displacement

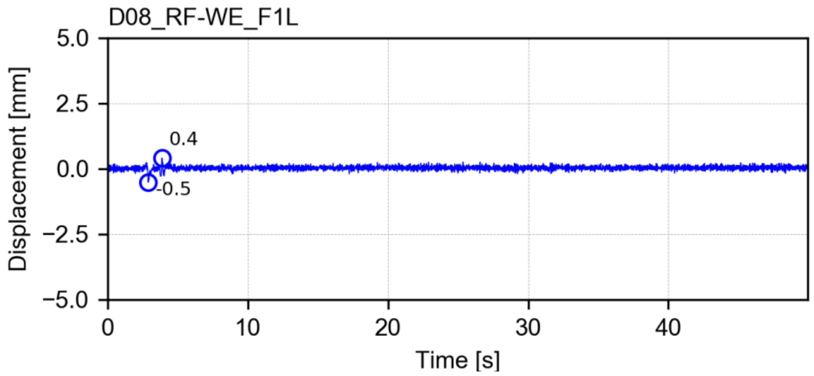

Channel D08_RF-WE_F1L – displacement

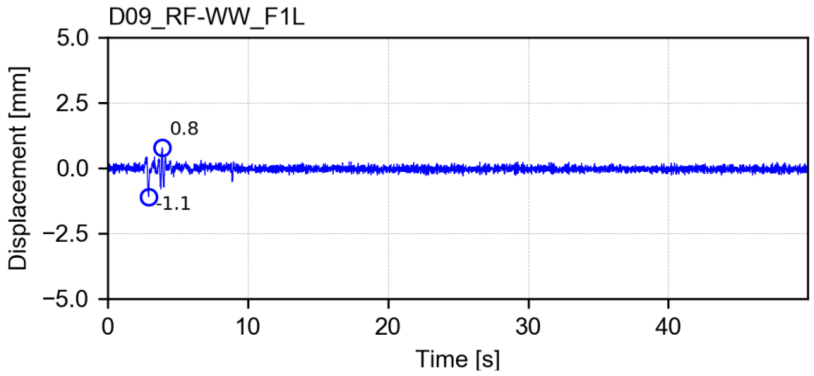

Channel D09_RF-WW_F1L – displacement

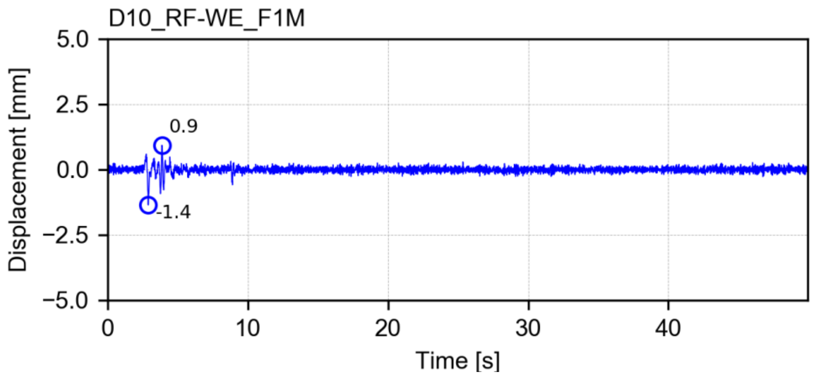

Channel D10_RF-WE_F1M – displacement

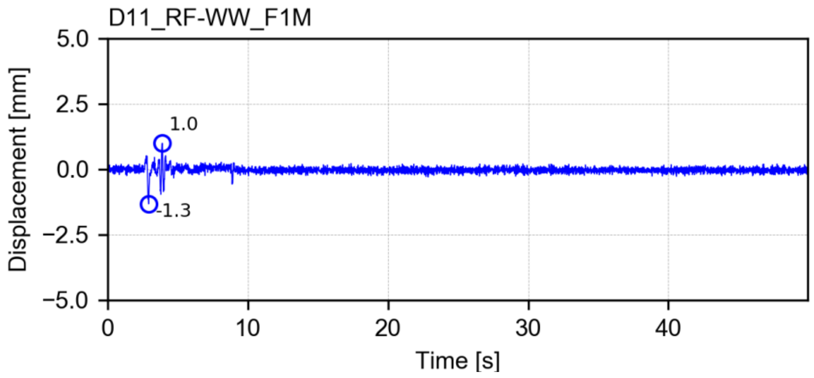

Channel D11_RF-WW_F1M – displacement

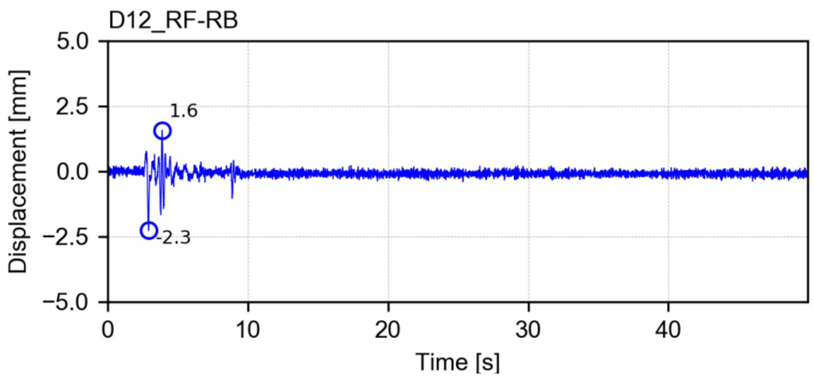

Channel D12_RF-RB – displacement

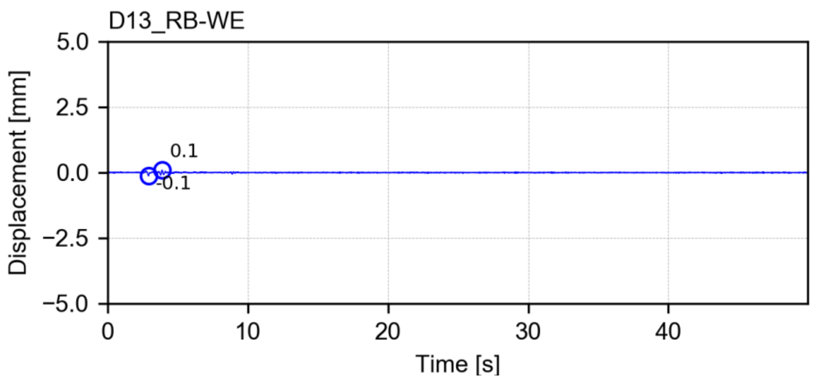

Channel D13_RB-WE – displacement

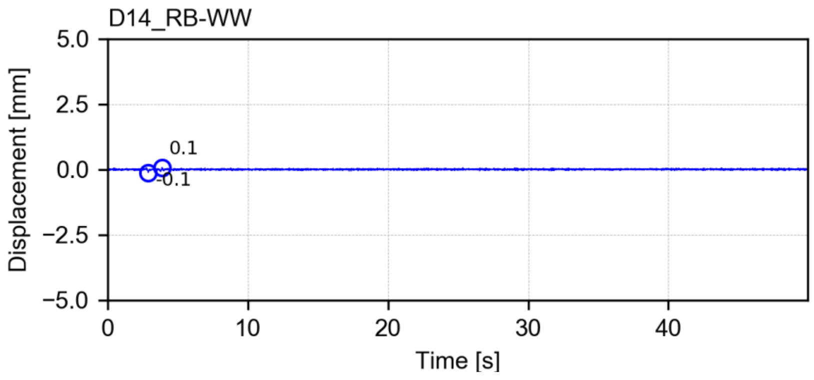

Channel D14_RB-WW – displacement

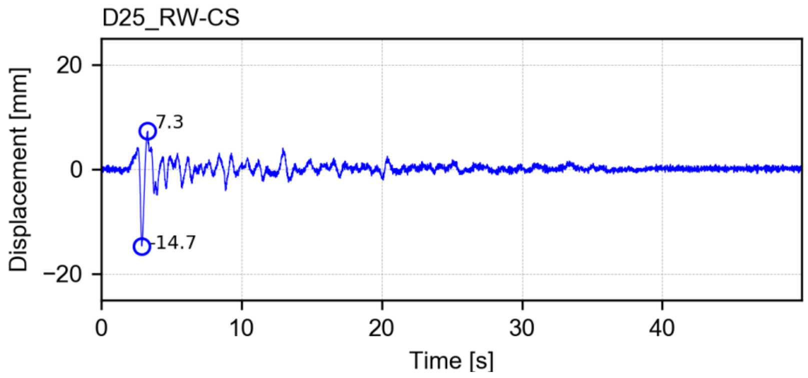

Channel D25_RW-CS – displacement

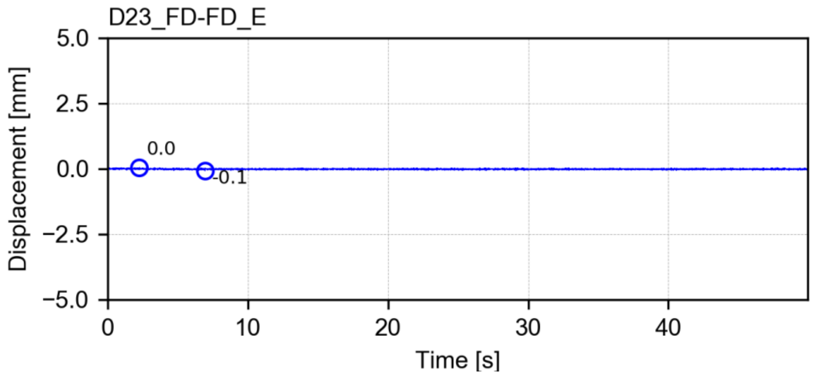

Channel D23_FD-FD_E – displacement

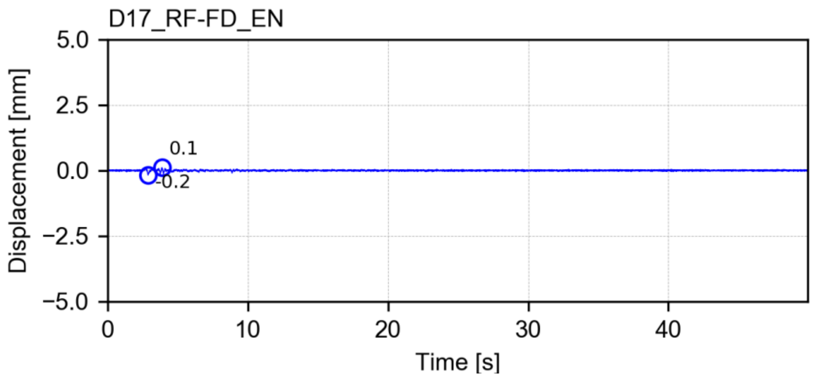

Channel D17_RF-FD_EN SC – displacement

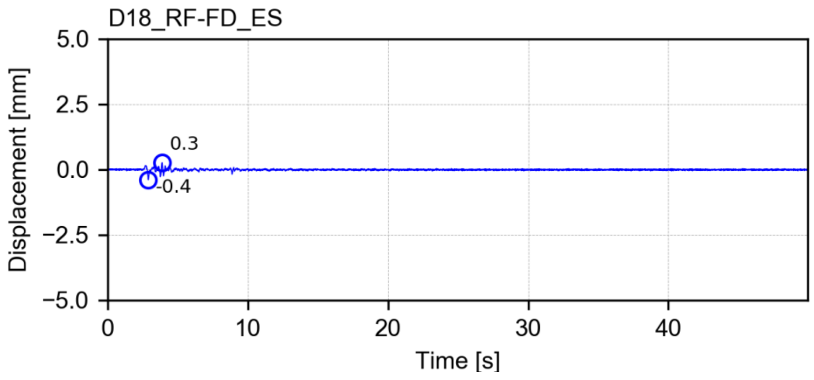

Channel D18_RF-FD_ES – displacement

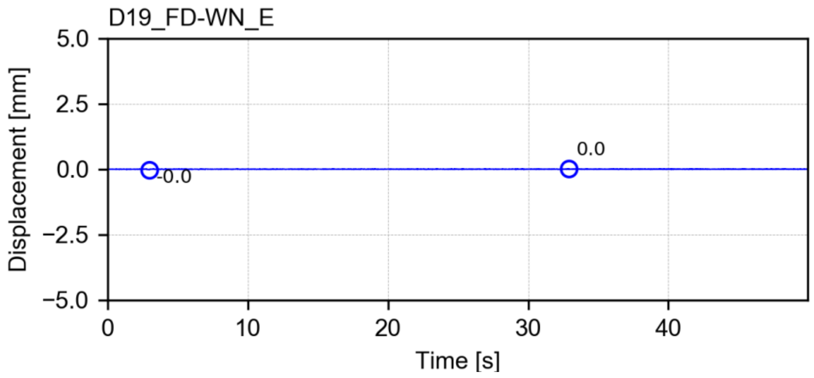

Channel D19_FD-WN_E – displacement

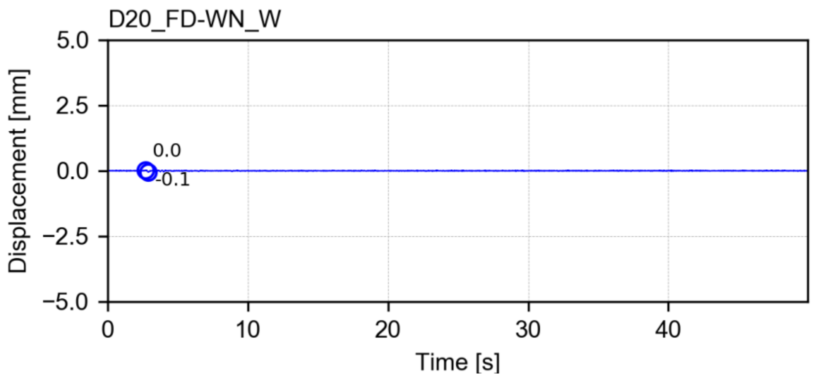

Channel D20_FD-WN_W – displacement

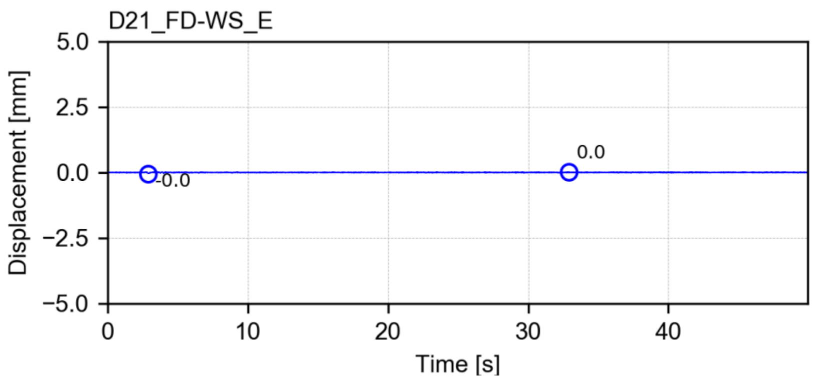

Channel D21_FD-WS_E – displacement

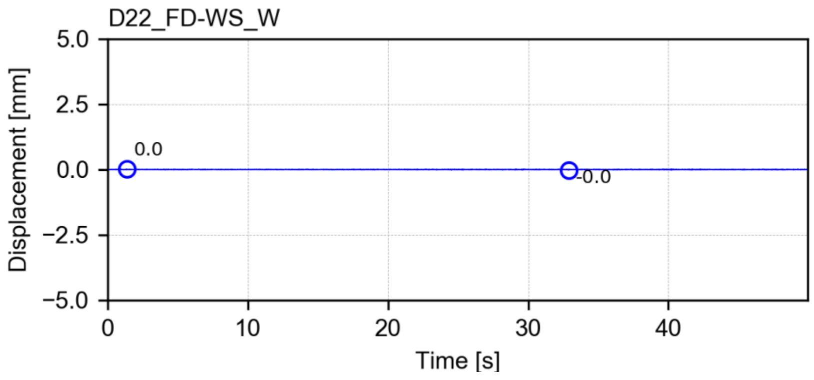

Channel D22_FD-WS_W – displacement

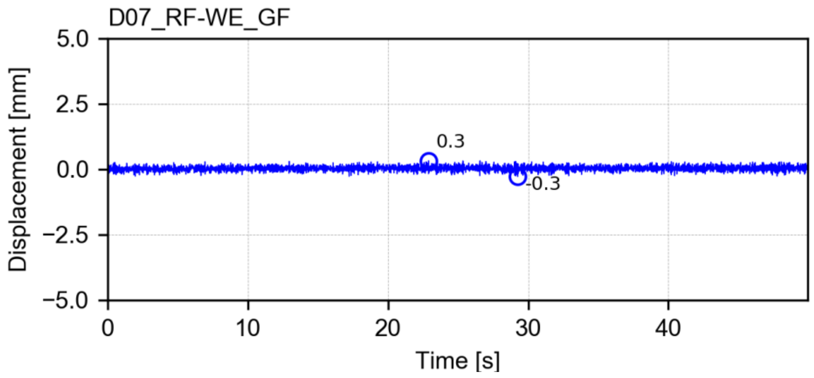

Channel D07_RF-WE_GF – displacement

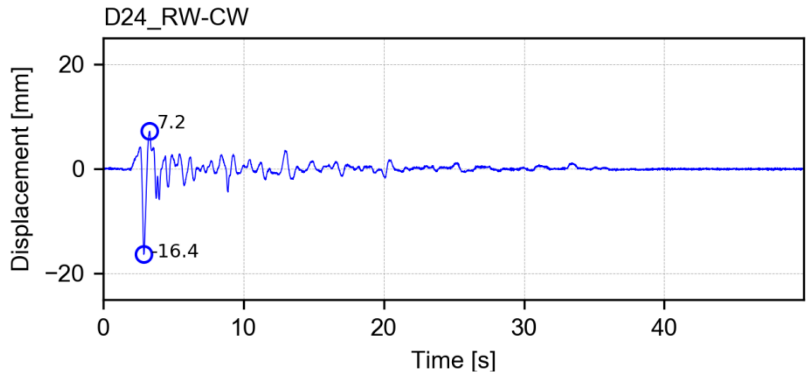

Channel D24_RW-CW– displacement

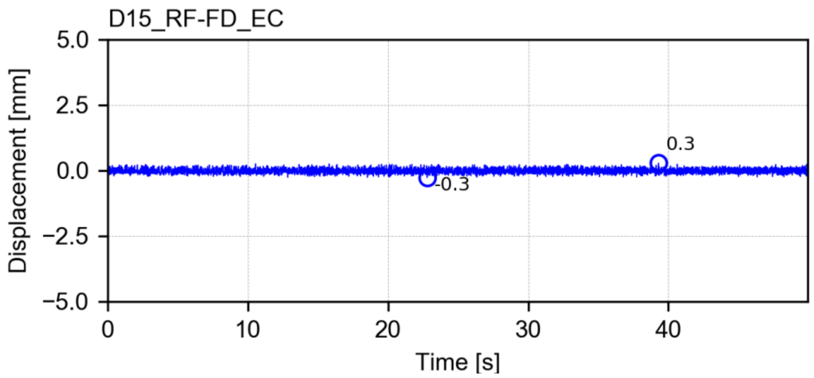

Channel D15_RF-FD_EC – displacement

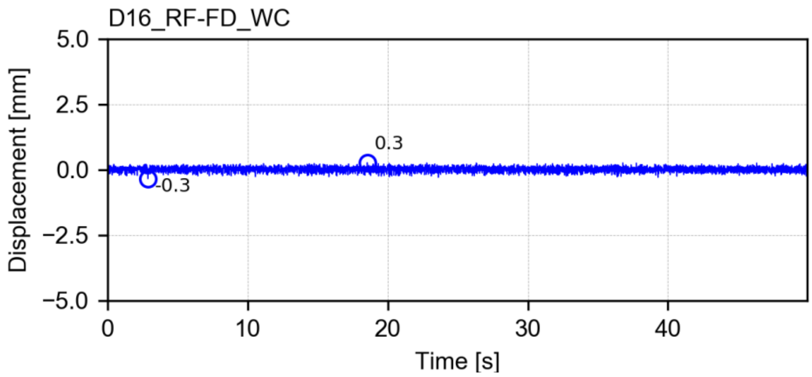

Channel D16_RF-FD_WC – displacement

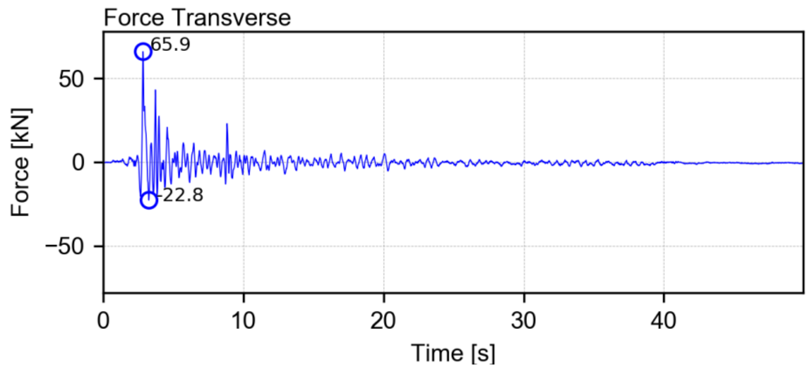

Channel Force Transverse – force

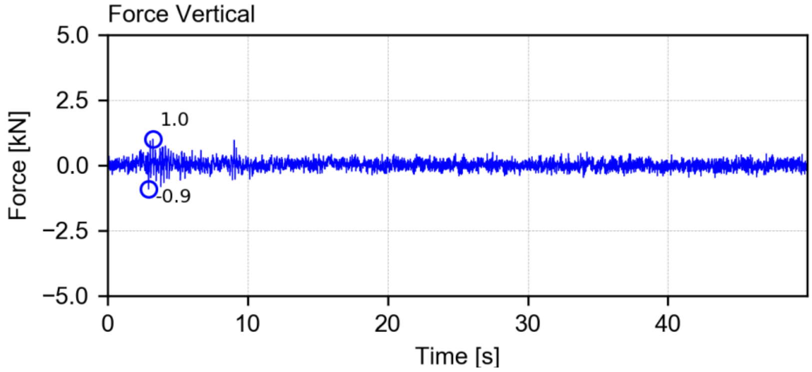

Channel Force Vertical – force

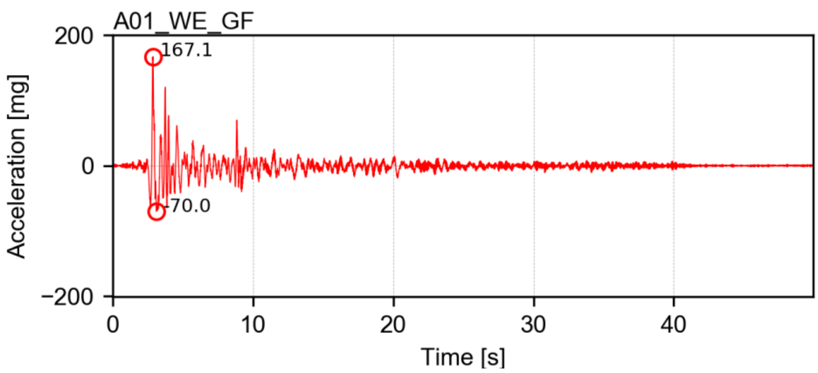

Channel A01_WE_GF –acceleration

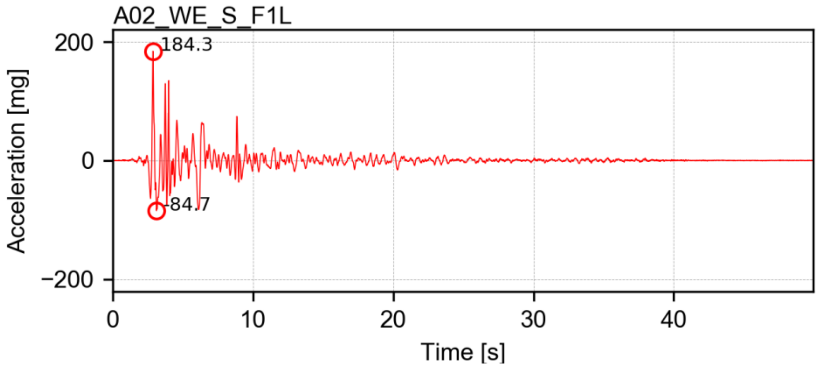

Channel A02_WE_S_F1L – acceleration

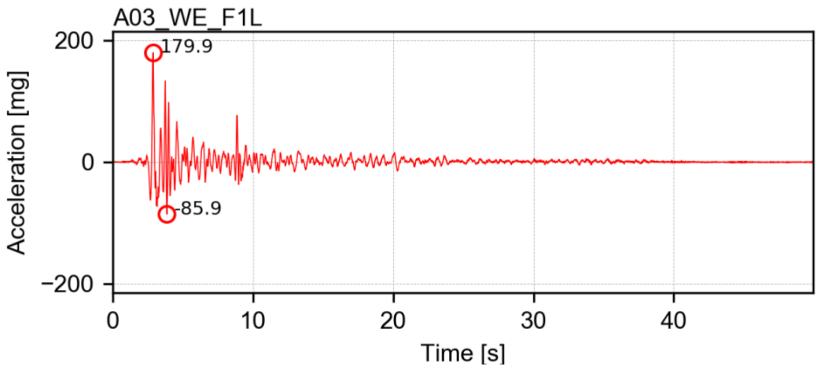

Channel A03_WE_F1L – acceleration

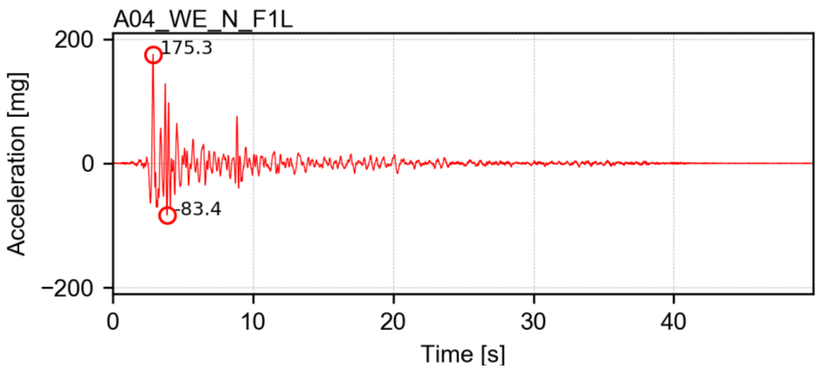

Channel A04_WE_N_F1L – acceleration

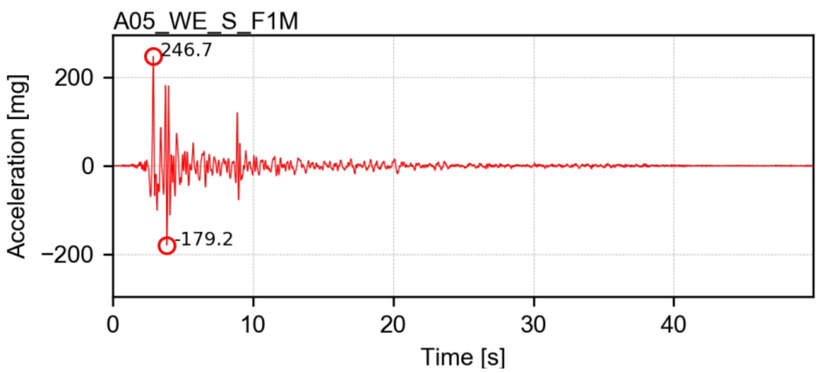

Channel A05_WE_S_F1M – acceleration

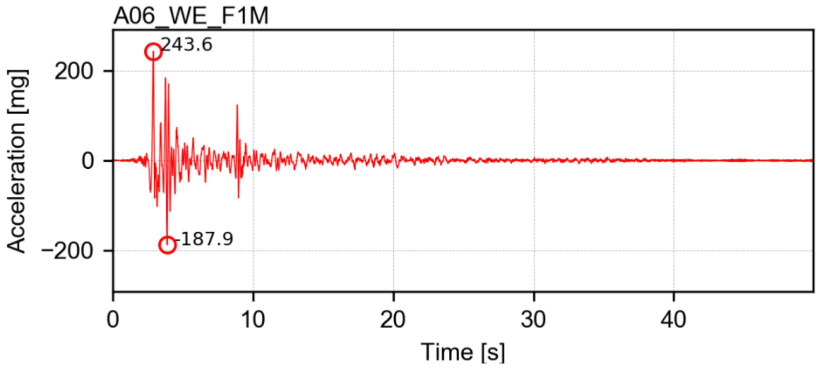

Channel A06_WE_F1M – acceleration

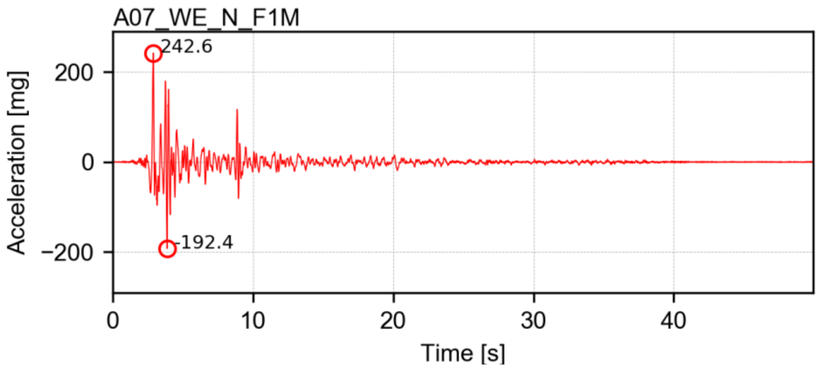

Channel A07_WE_N_F1M – acceleration

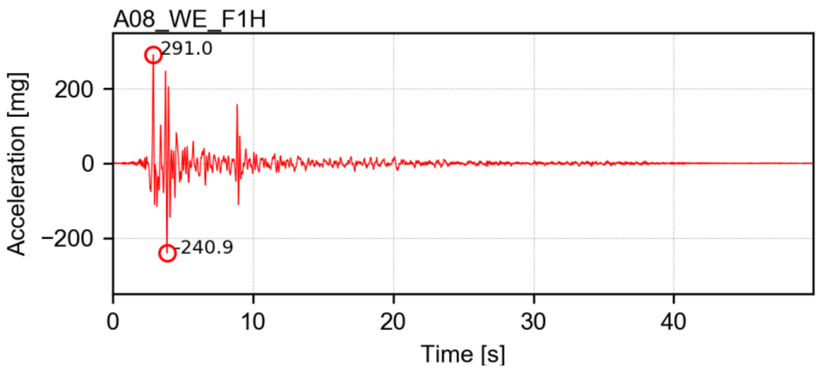

Channel A08_WE_F1H – acceleration

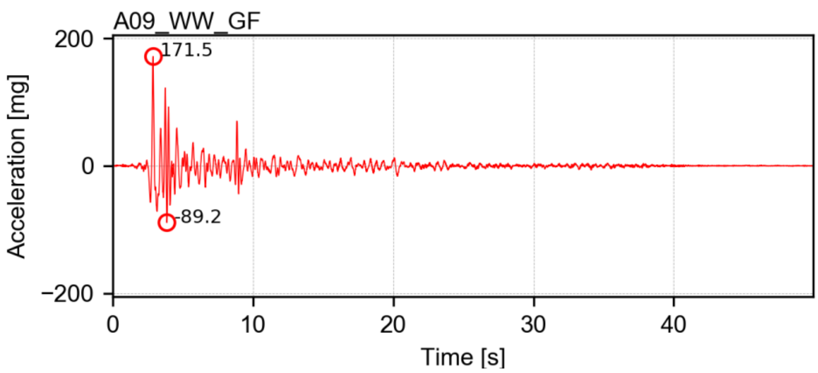

Channel A09_WW_GF – acceleration

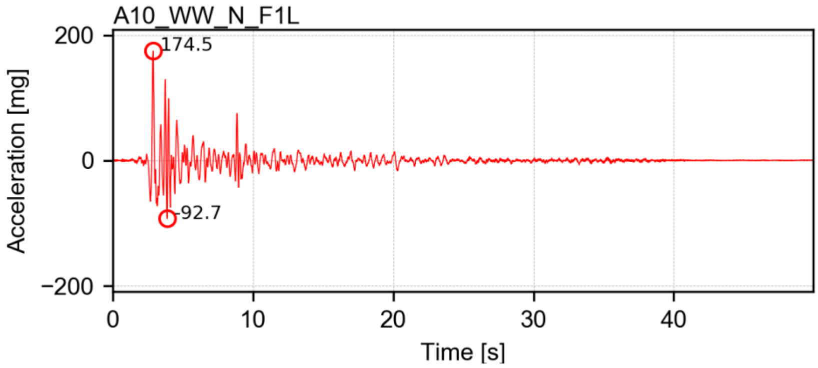

Channel A10_WW_N_F1L – acceleration

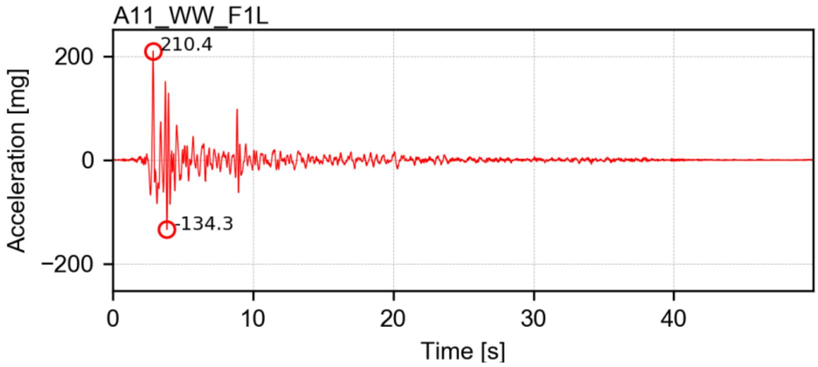

Channel A11_WW_F1L – acceleration

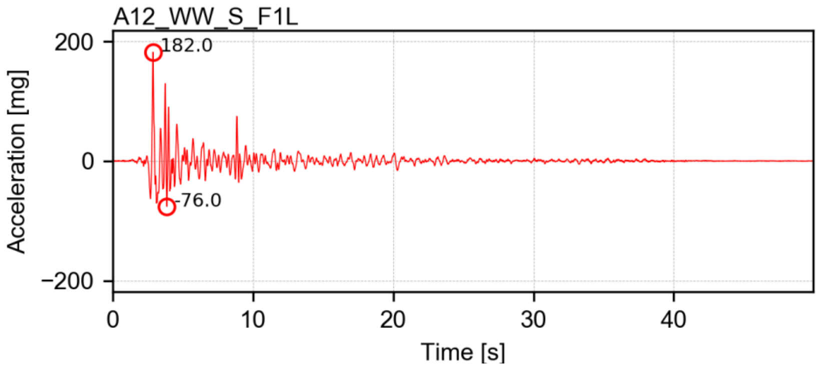

Channel A12_WW_S_F1L – acceleration

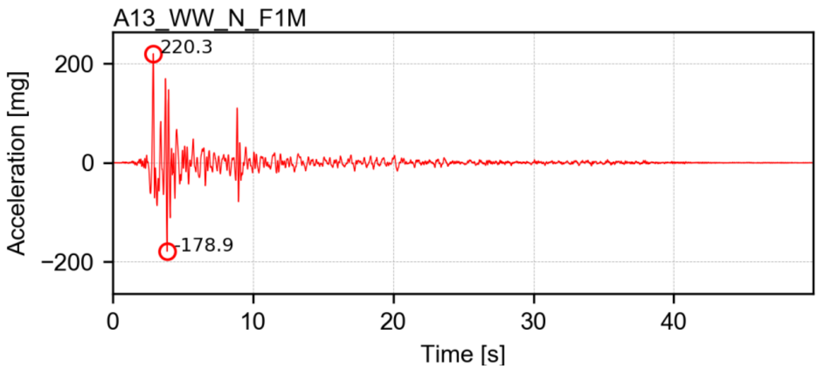

Channel A13_WW_N_F1M – acceleration

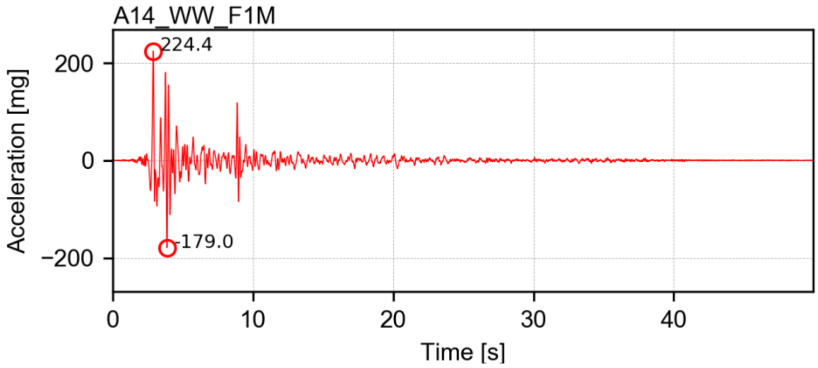

Channel A14_WW_F1M – acceleration

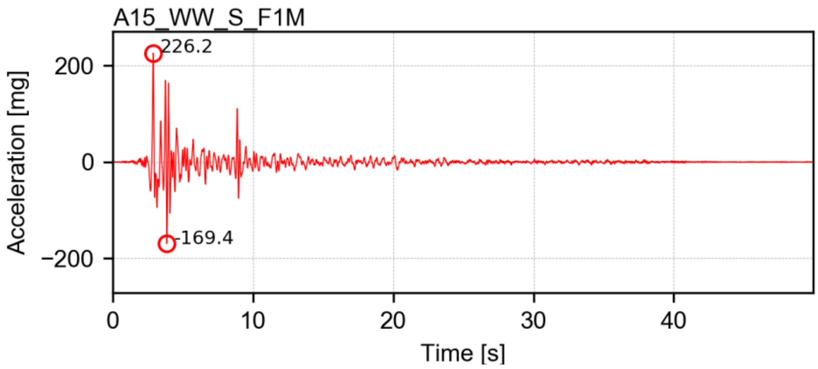

Channel A15_WW_S_F1M – acceleration

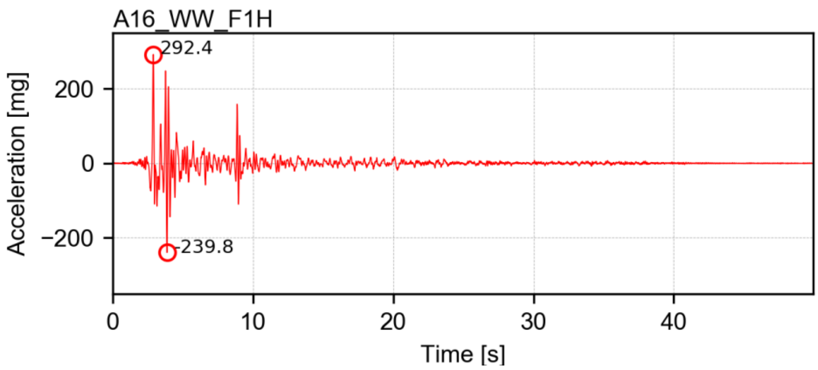

Channel A16_WW_F1H – acceleration

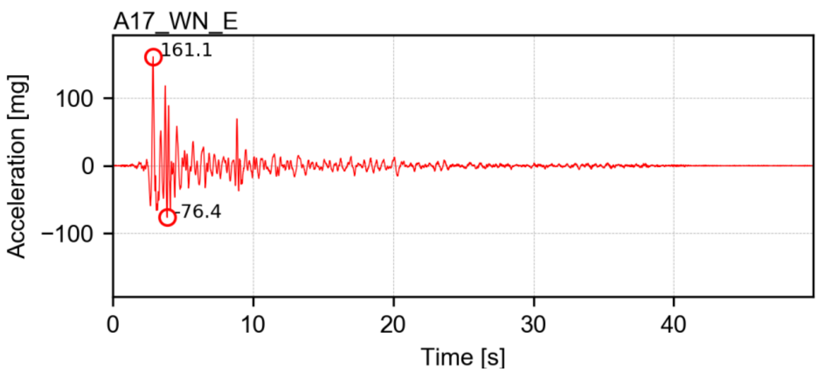

Channel A17_WN_E – acceleration

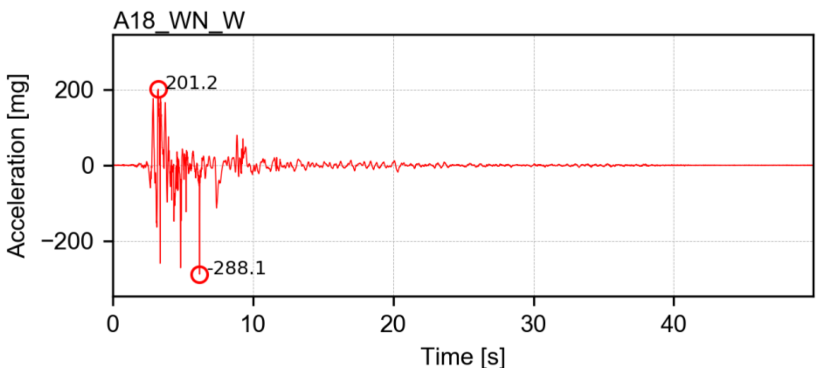

Channel A18_WN_W – acceleration

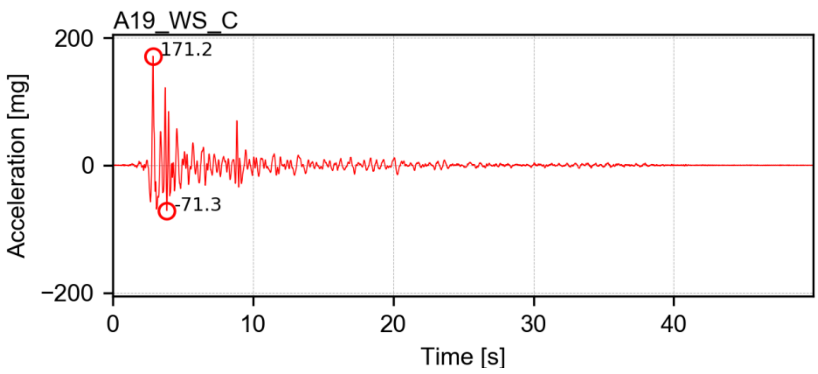

Channel A19_WS_C – acceleration

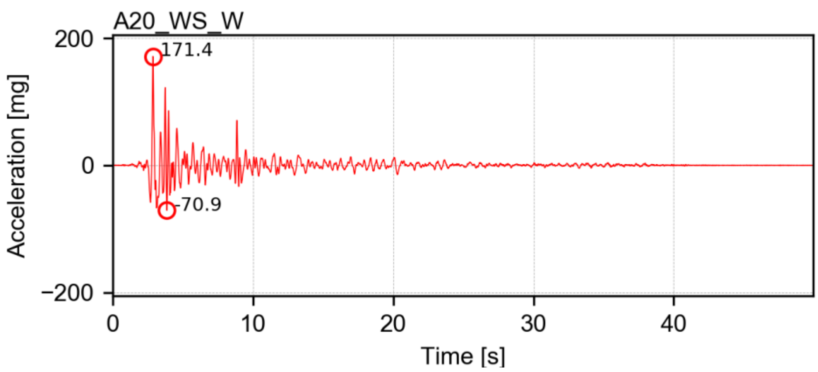

Channel A20_WS_W – acceleration

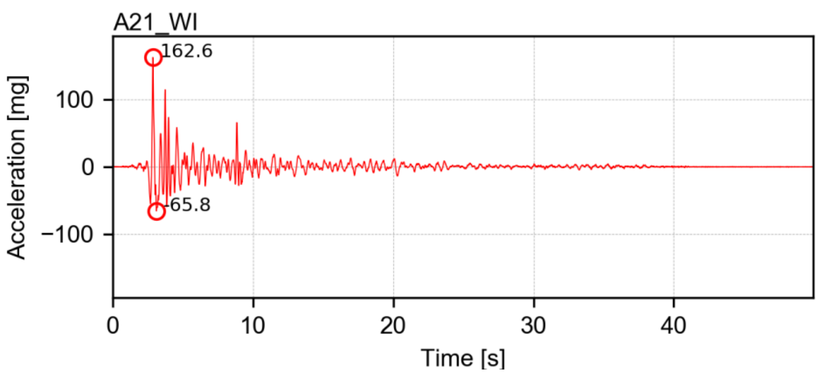

Channel A21_WI – acceleration

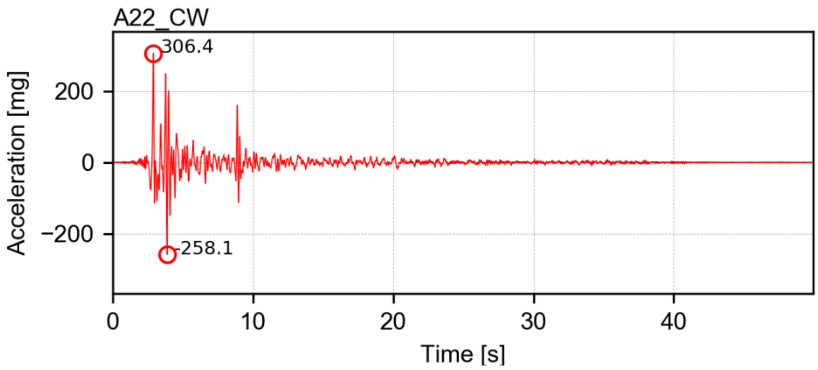

Channel A22_CW – acceleration

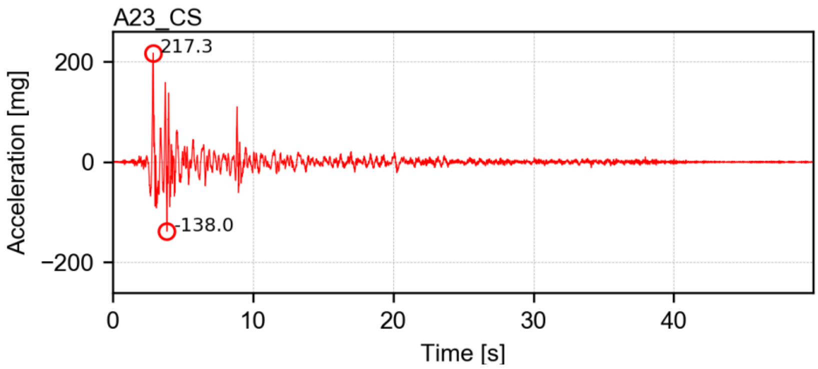

Channel A23_CS – acceleration

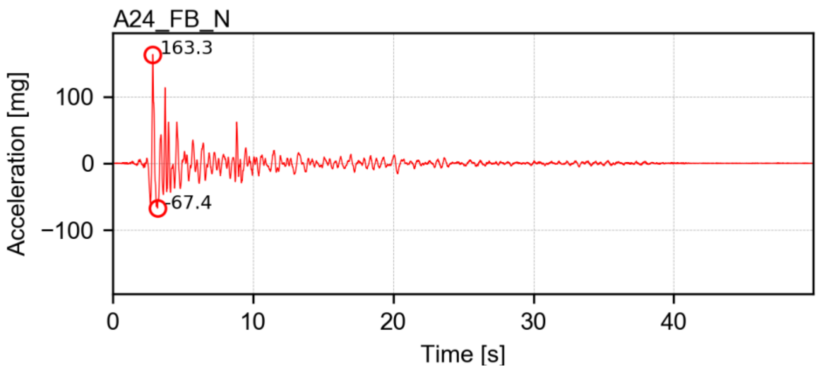

Channel A24_FB_N – acceleration

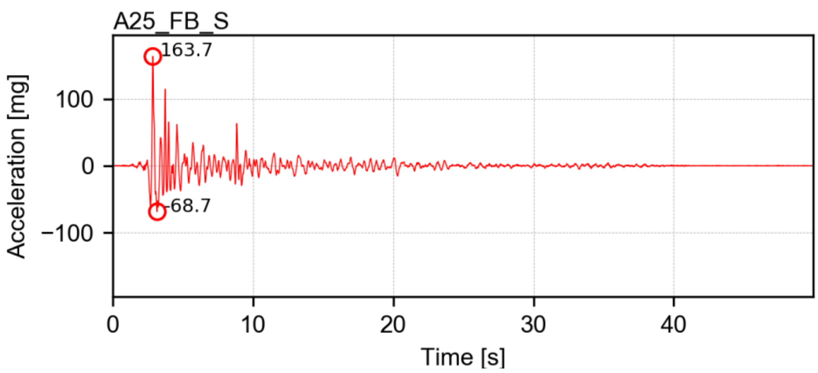

Channel A25_FB_S – acceleration

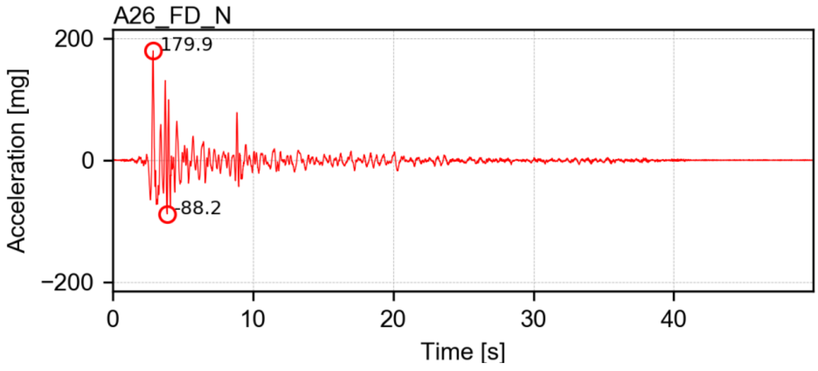

Channel A26_FD_N – acceleration

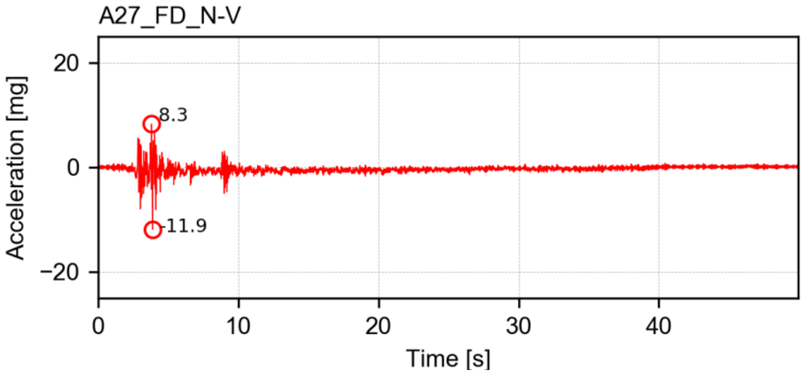

Channel A27_FD_N-V – acceleration

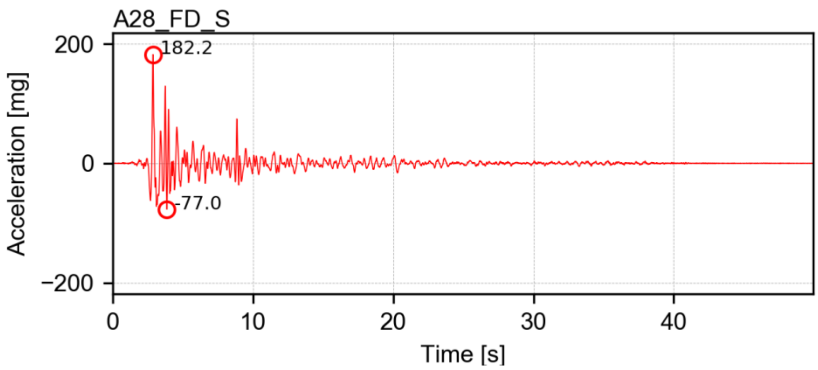

Channel A28_FD_S – acceleration

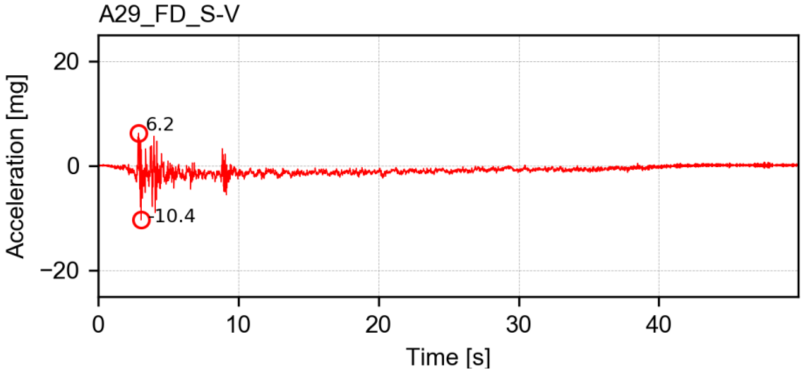

Channel A29_FD_S-V – acceleration

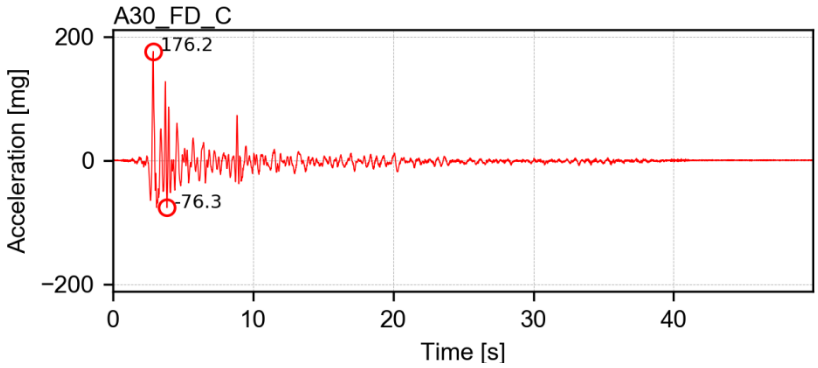

Channel A30_FD_C – acceleration

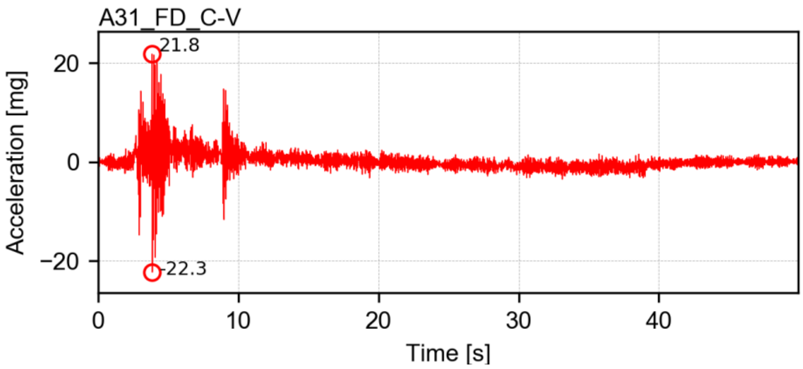

Channel A31_FD_C-V – acceleration

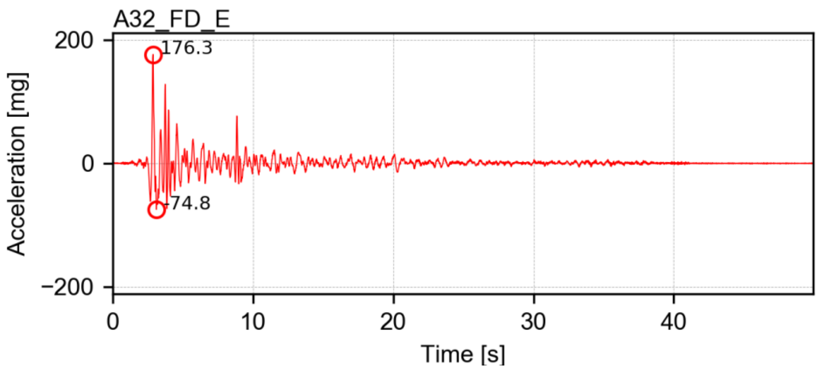

Channel A32_FD_E – acceleration

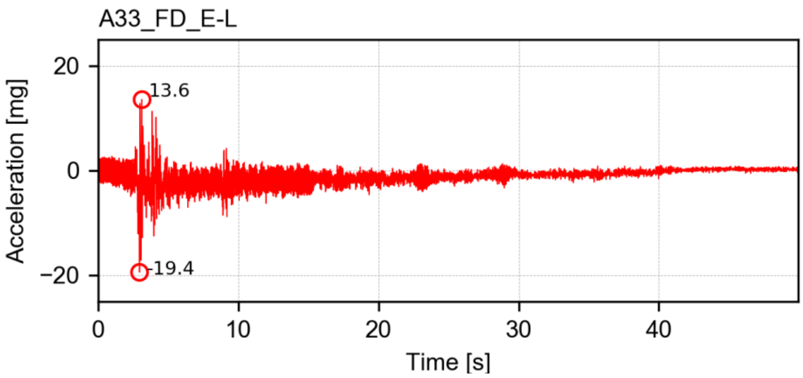

Channel A33_FD_E-L – acceleration

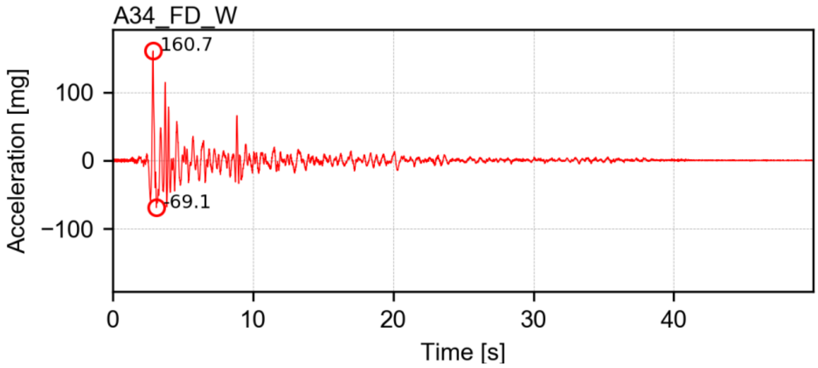

Channel A34_FD_W – acceleration

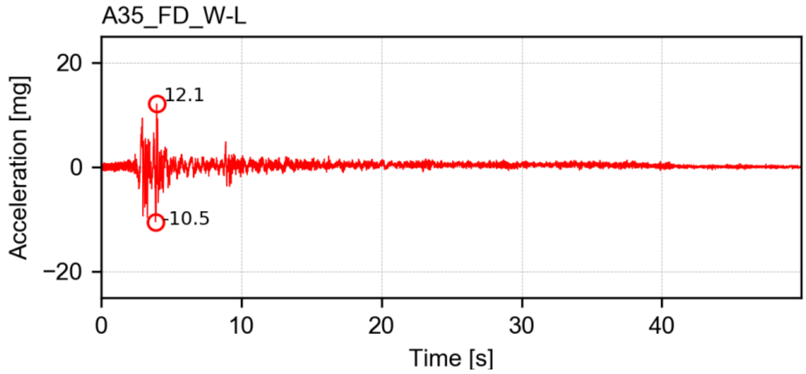

Channel A35_FD_W-L – acceleration

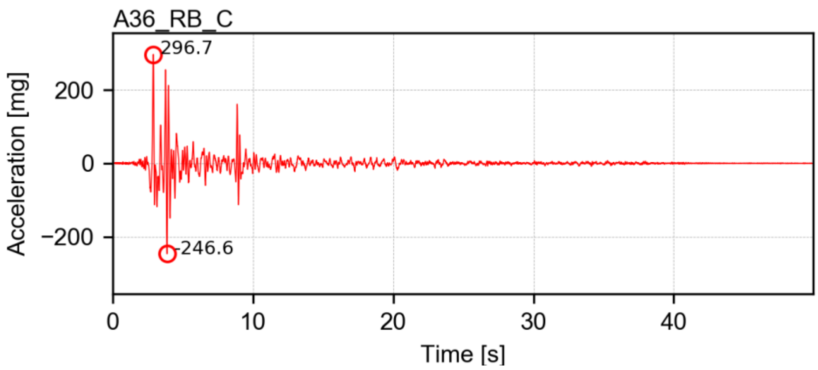

Channel A36_RB_C – acceleration

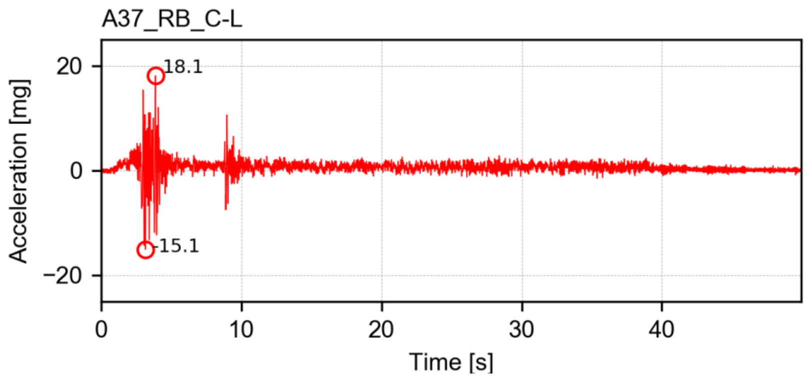

Channel A37_RB_C-L – acceleration

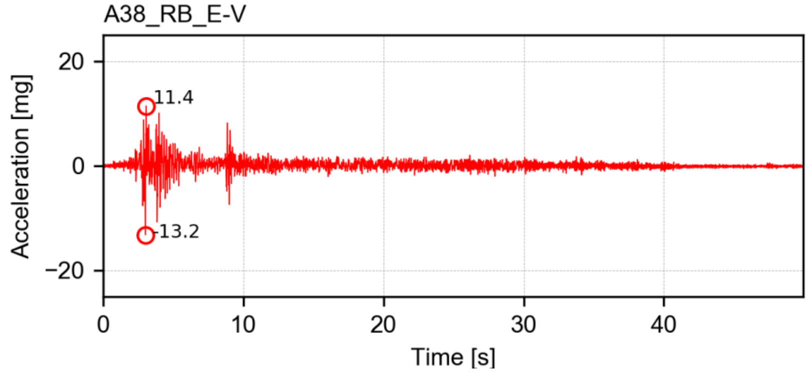

Channel A38_RB_E-V – acceleration

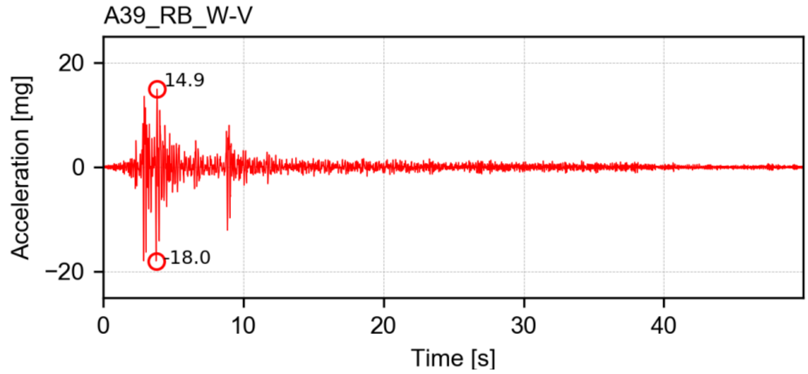

Channel A39_RB_W-V – acceleration

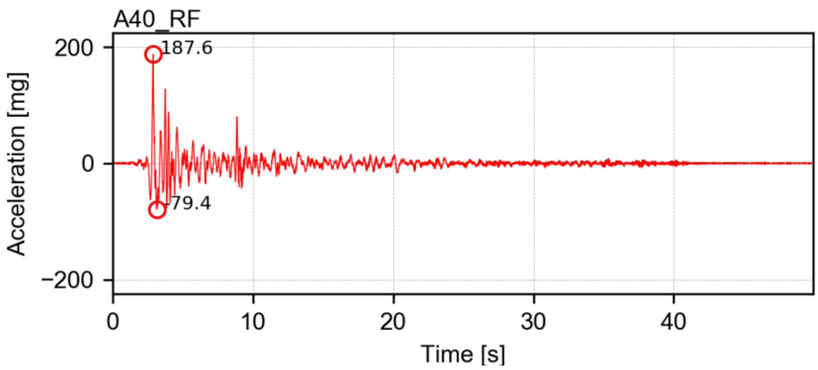

Channel A40_RF – acceleration

APPENDIX E. TRANSDUCERS' READINGS FOR SC2-300%

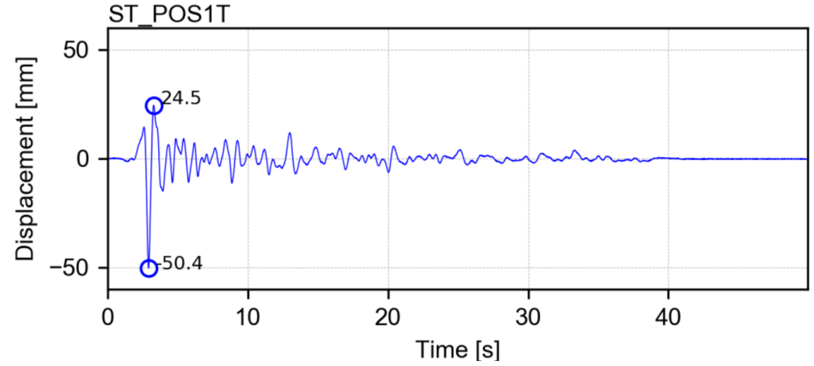

Channel ST_POS_T – Transverse displacement of the LNEC 3D shake table motion control

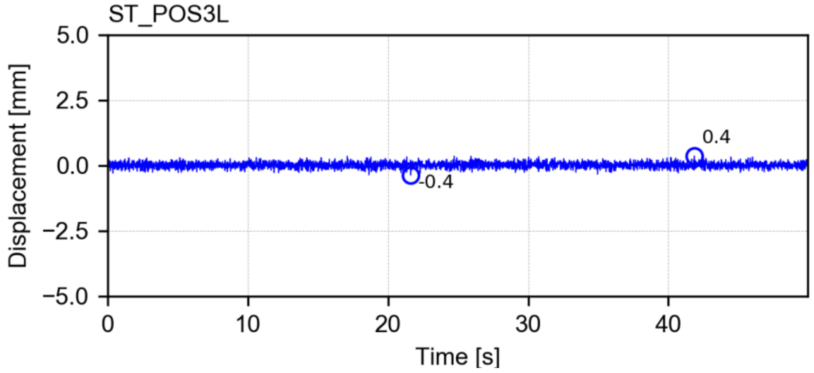

Channel ST_POS_L – Vertical displacement of the LNEC 3D shake table motion control

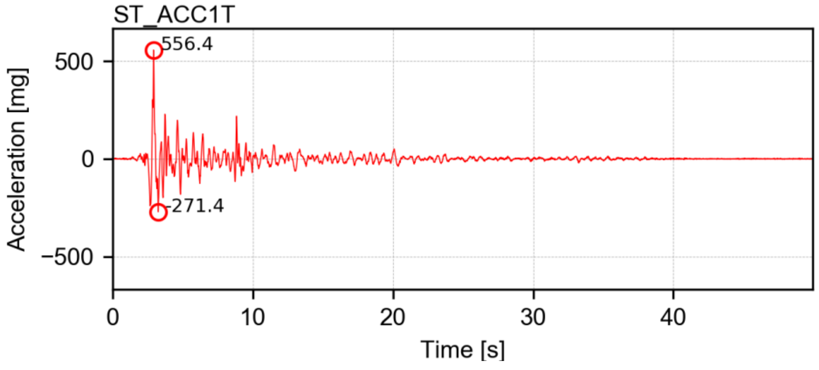

Channel ST_ACC_T – Transverse acceleration of the LNEC 3D shake table motion control

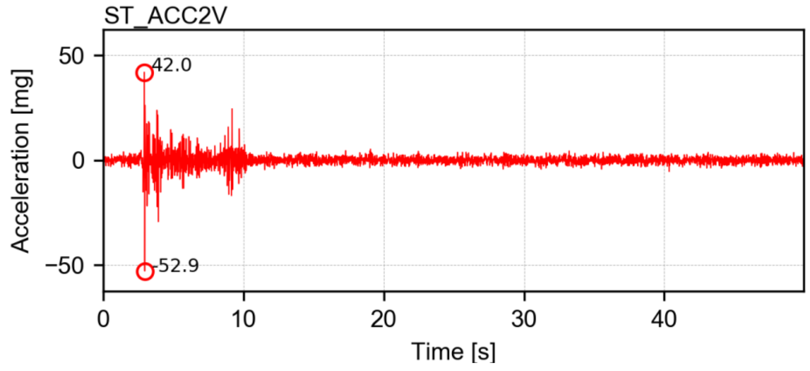

Channel ST_ACC_L – Vertical acceleration of the LNEC 3D shake table motion control

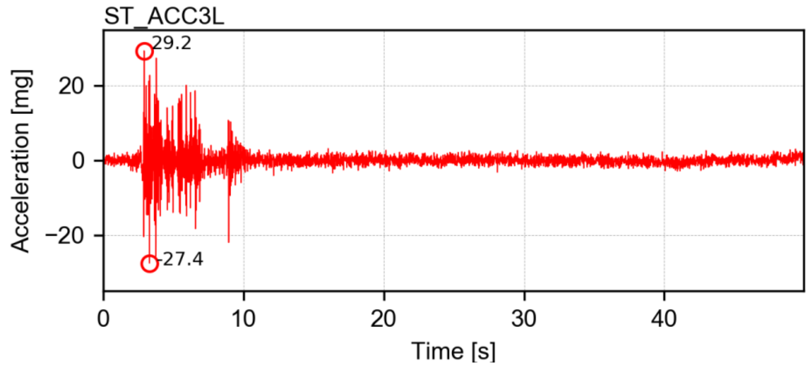

Channel ST_ACC_V – Longitudinal acceleration of the LNEC 3D shake table motion control

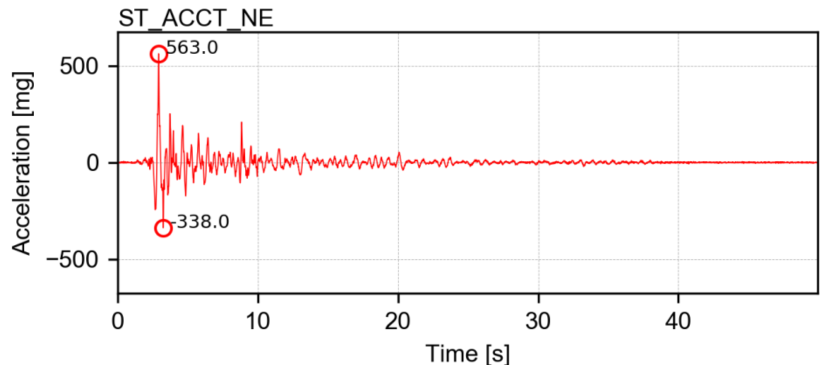

Channel ST_ACCT_NE – Transverse acceleration of the North-East LNEC 3D shake table platform

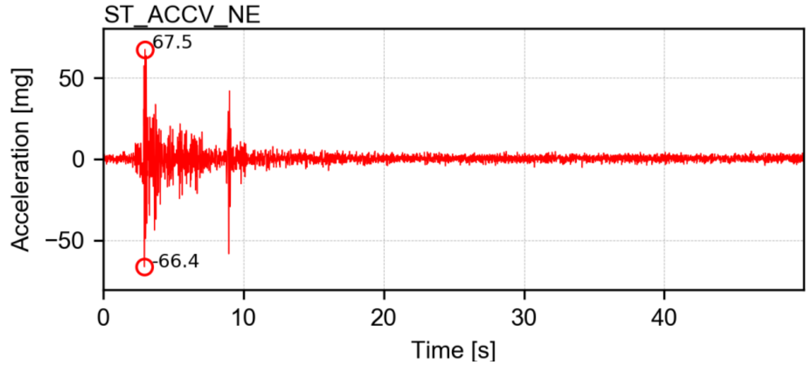

Channel ST_ACCV_NE – Vertical acceleration of the North-East LNEC 3D shake table platform

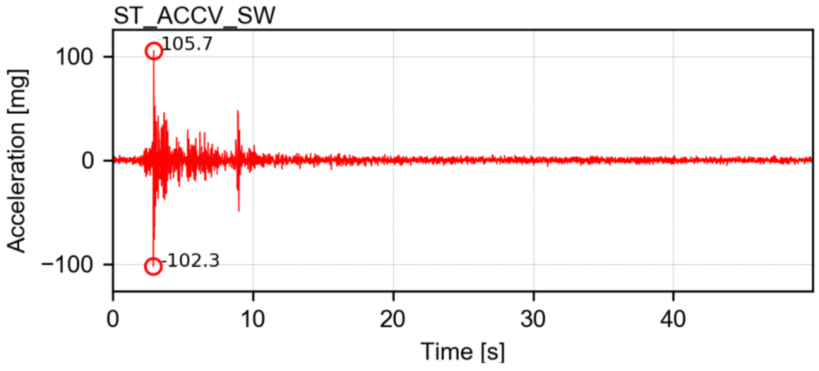

Channel ST_ACCV_SW – Vertical acceleration of the South-West LNEC 3D shake table platform

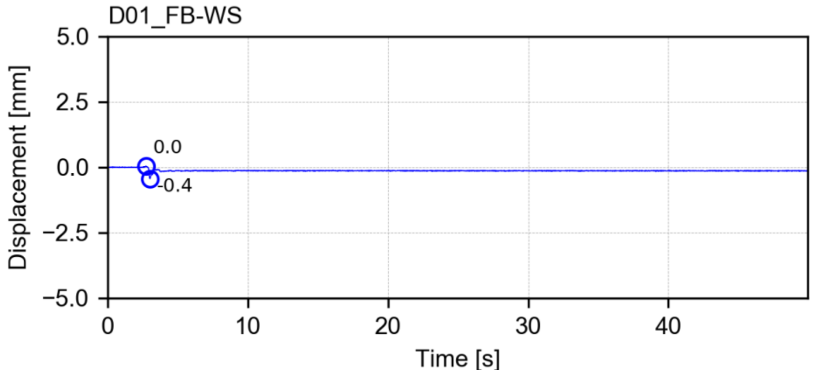

Channel D01_FB-WS – displacement

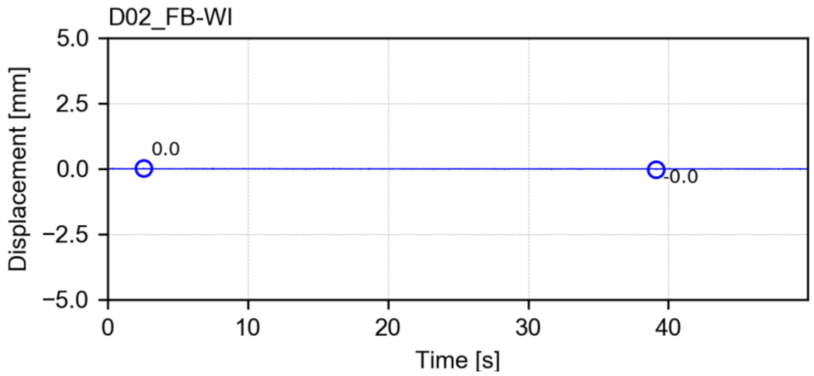

Channel D02_FB-WI – displacement

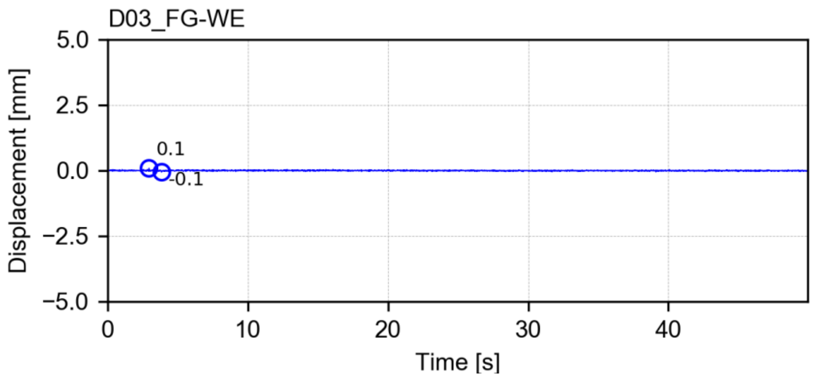

Channel D03_FG-WE – displacement

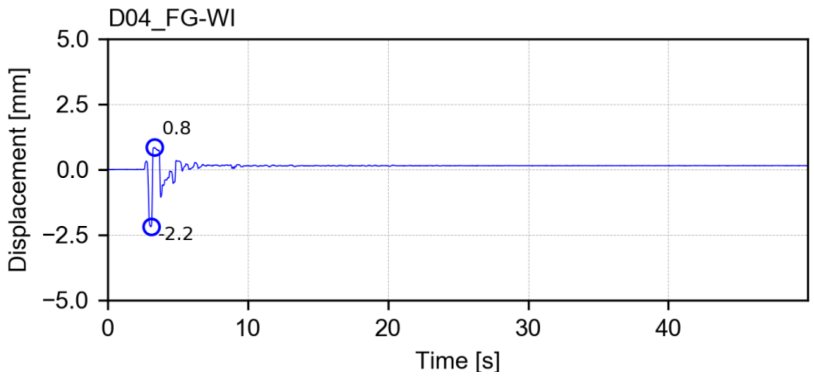

Channel D04_FG-WI – displacement

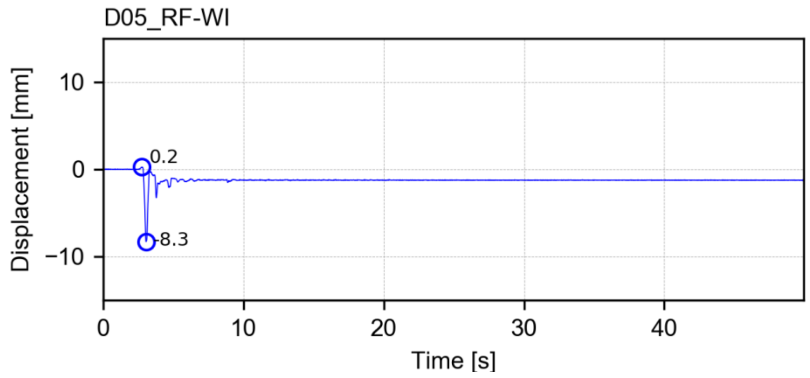

Channel D05_RF-WI – displacement

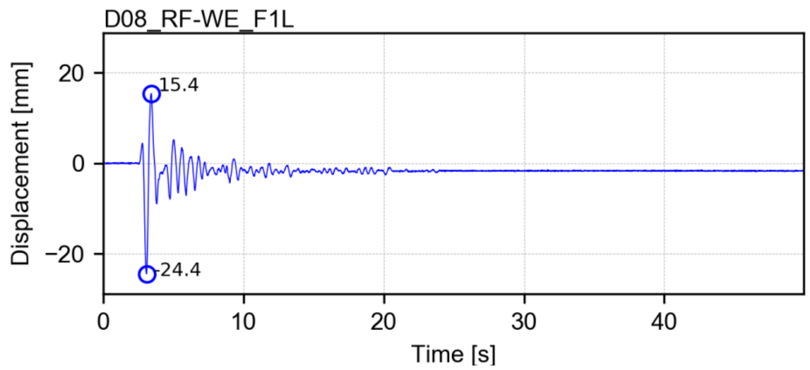

Channel D08_RF-WE_F1L – displacement

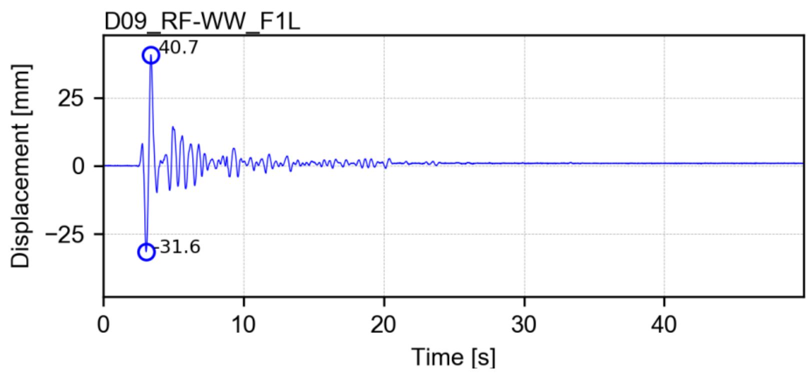

Channel D09_RF-WW_F1L – displacement

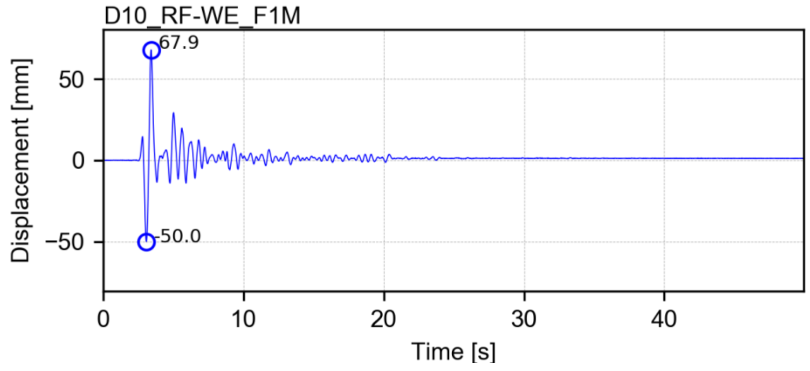

Channel D10_RF-WE_F1M – displacement

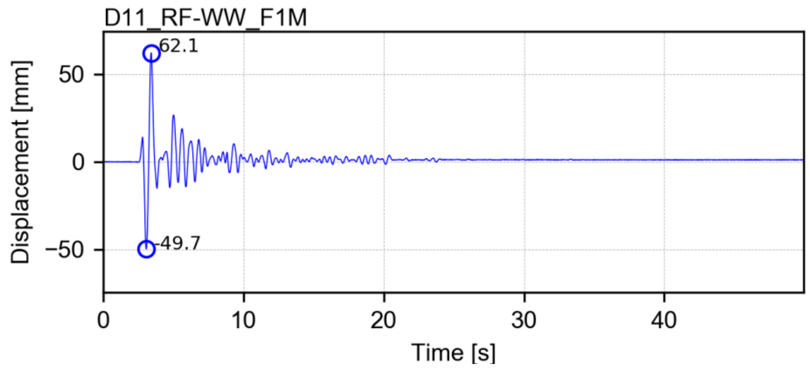

Channel D11_RF-WW_F1M – displacement

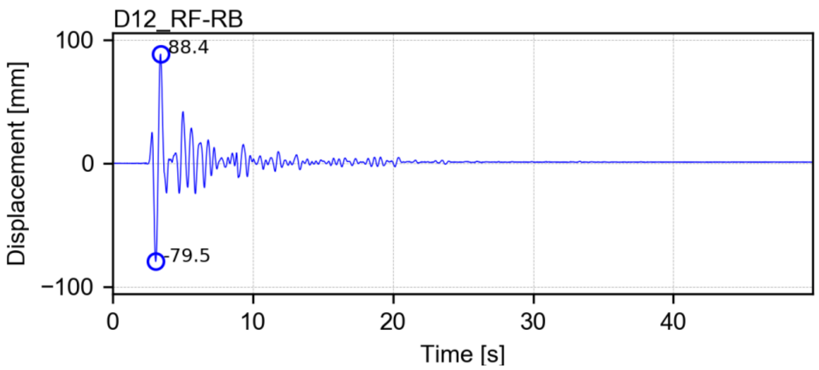

Channel D12_RF-RB – displacement

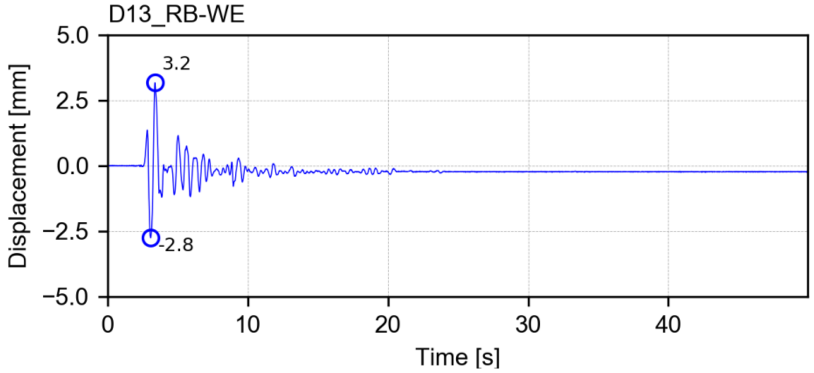

Channel D13_RB-WE – displacement

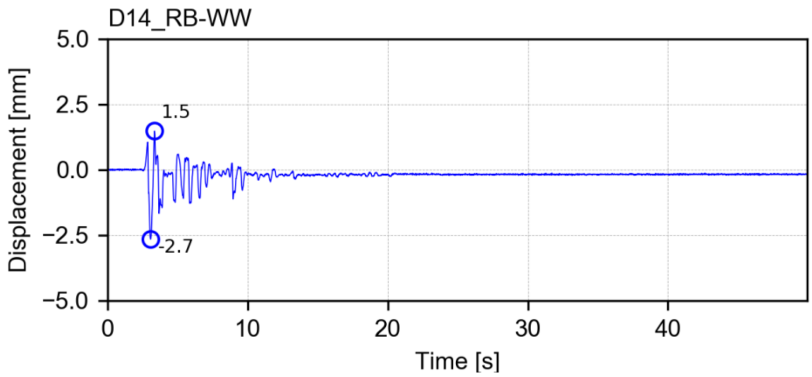

Channel D14_RB-WW – displacement

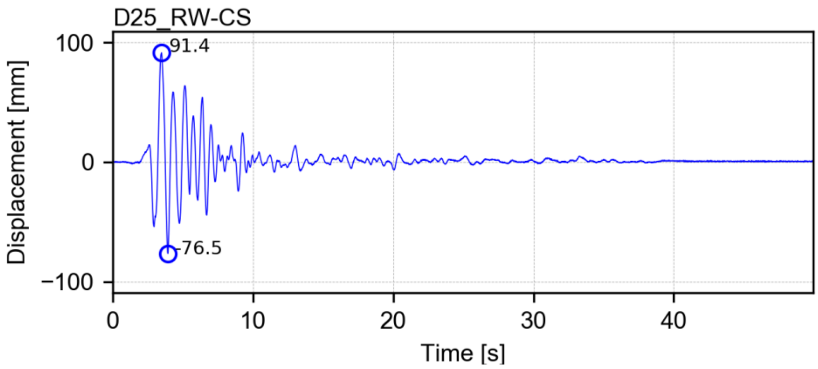

Channel D25_RW-CS – displacement

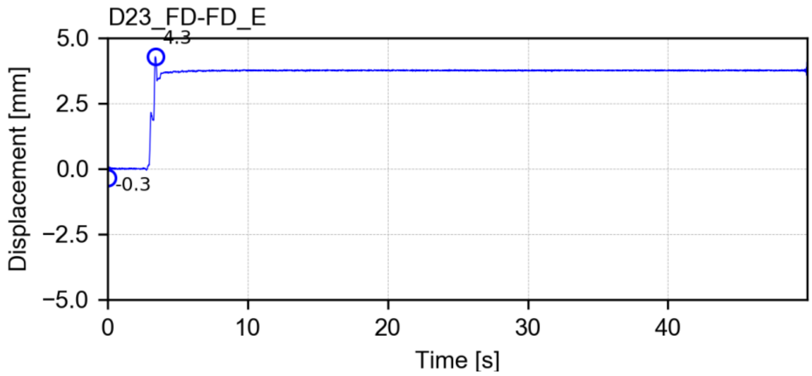

Channel D23_FD-FD_E – displacement

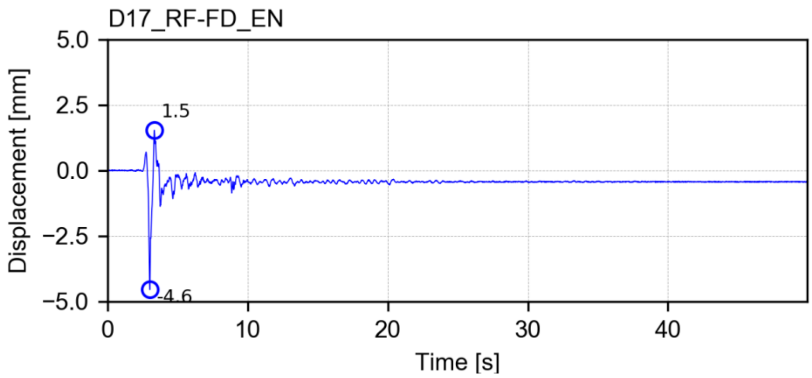

Channel D17_RF-FD_EN SC – displacement

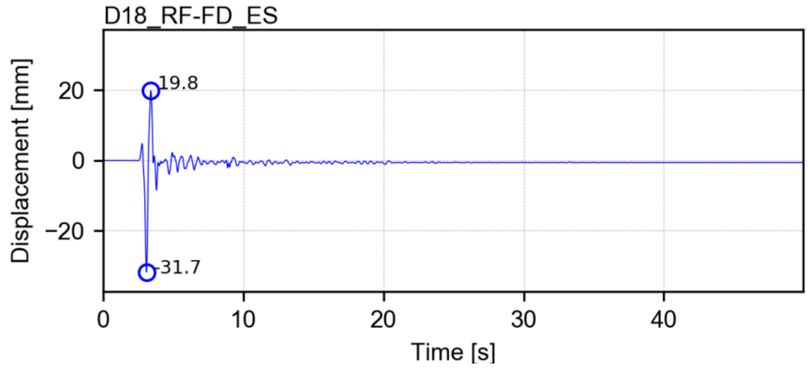

Channel D18_RF-FD_ES – displacement

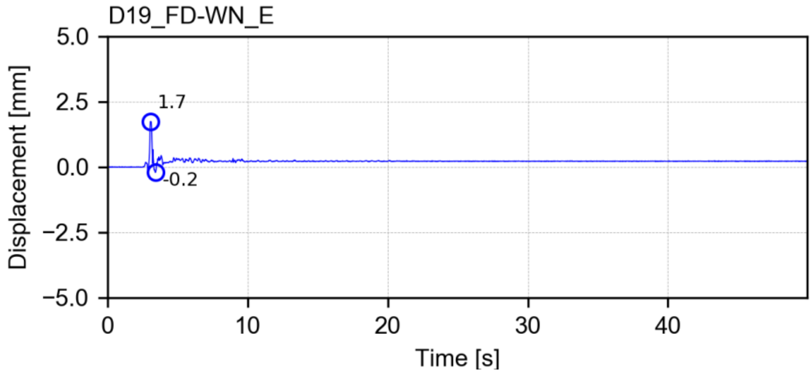

Channel D19_FD-WN_E – displacement

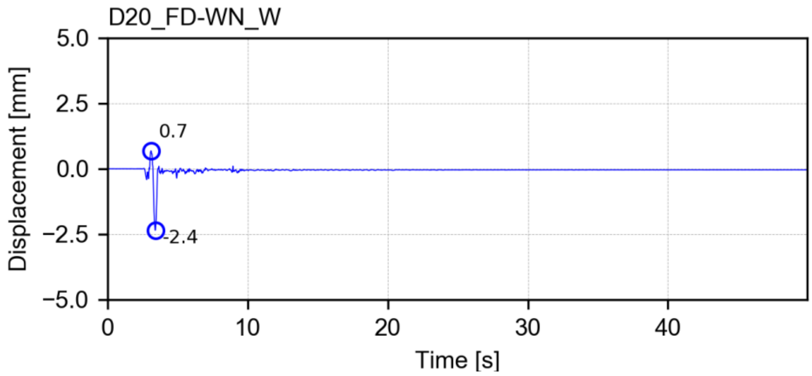

Channel D20_FD-WN_W – displacement

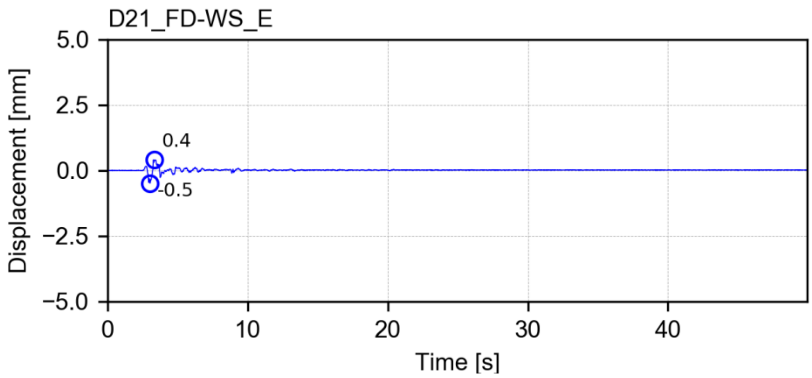

Channel D21_FD-WS_E – displacement

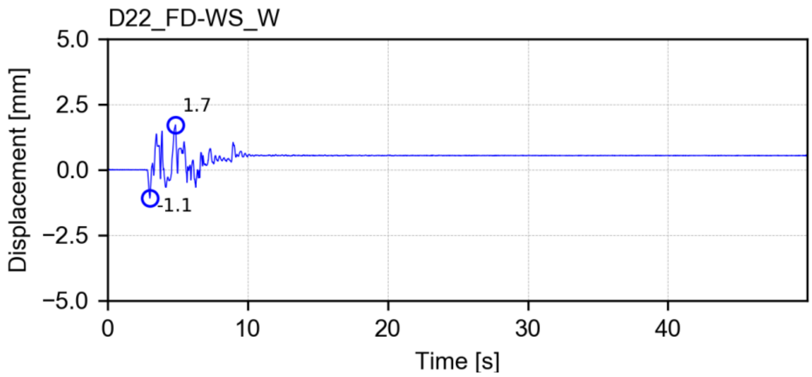

Channel D22_FD-WS_W – displacement

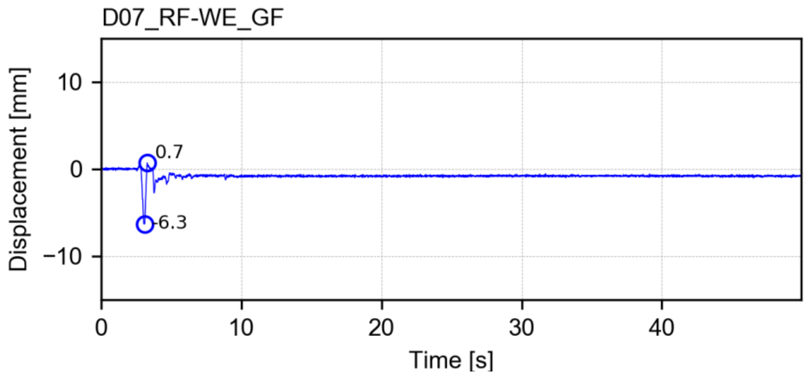

Channel D07_RF-WE_GF – displacement

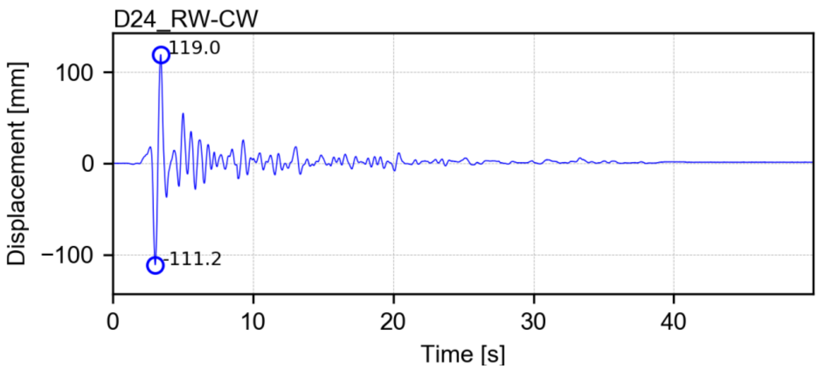

Channel D24_RW-CW– displacement

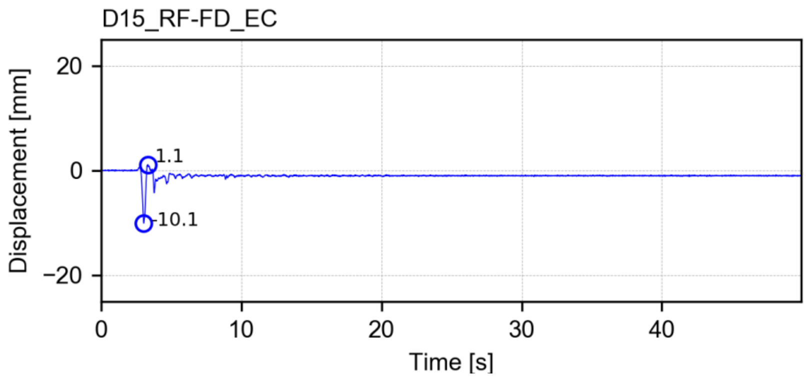

Channel D15_RF-FD_EC – displacement

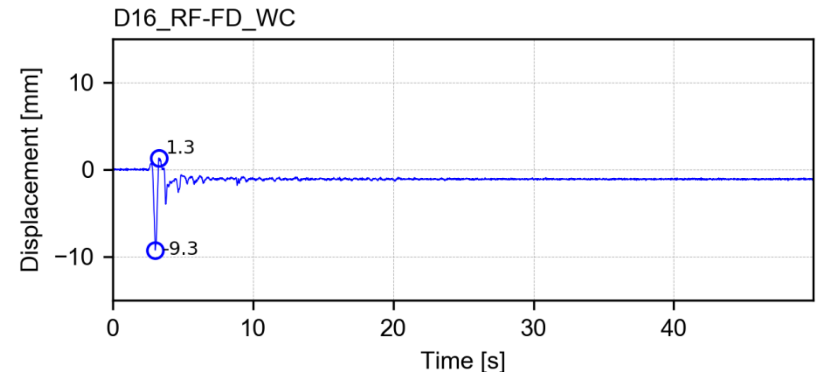

Channel D16_RF-FD_WC – displacement

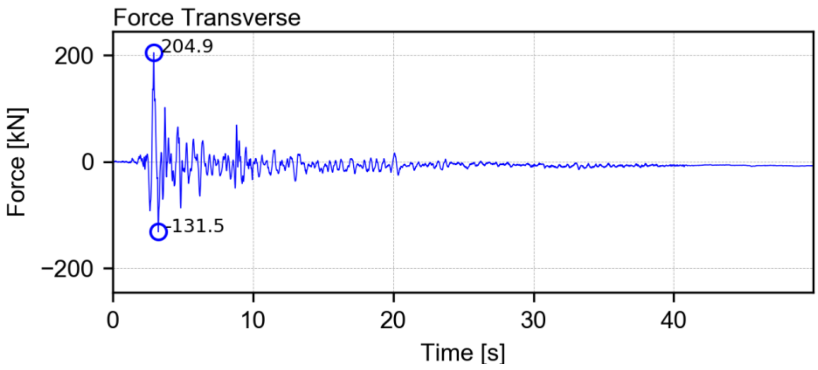

Channel Force Transverse – force

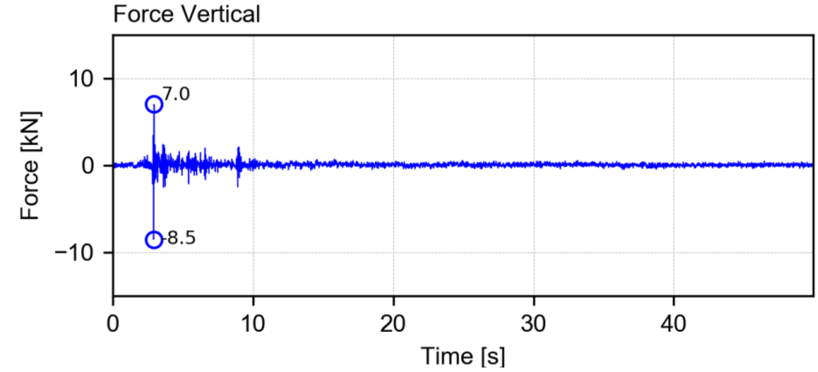

Channel Force Vertical – force

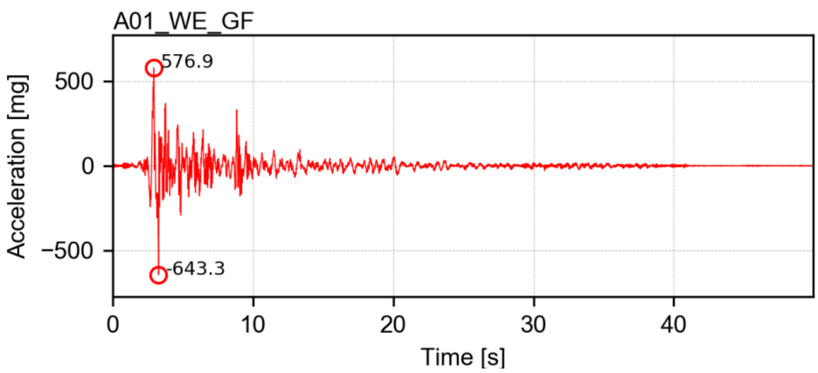

Channel A01_WE_GF –acceleration

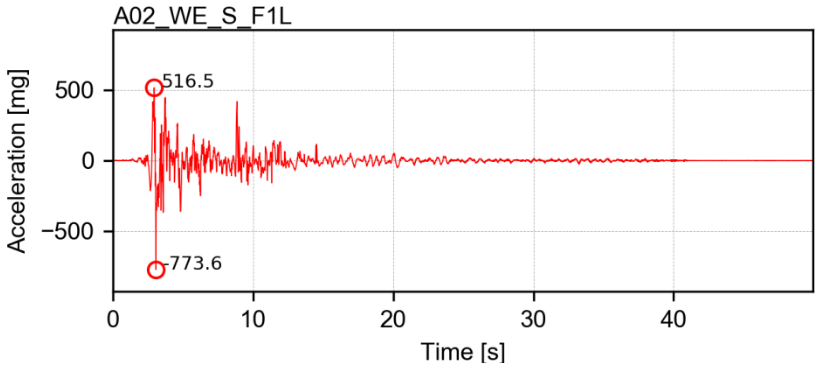

Channel A02_WE_S_F1L – acceleration

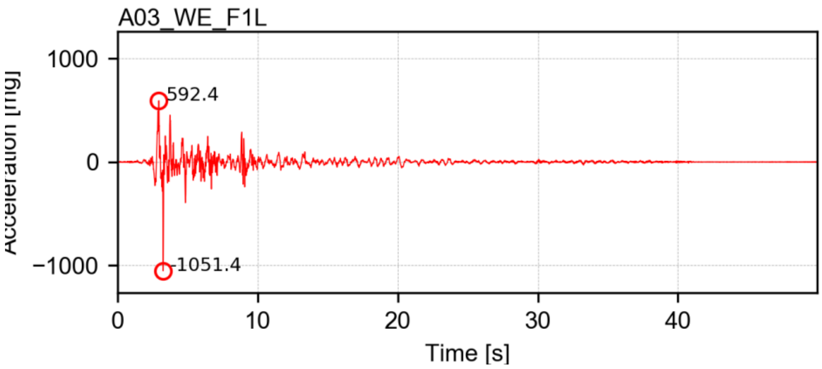

Channel A03_WE_F1L – acceleration

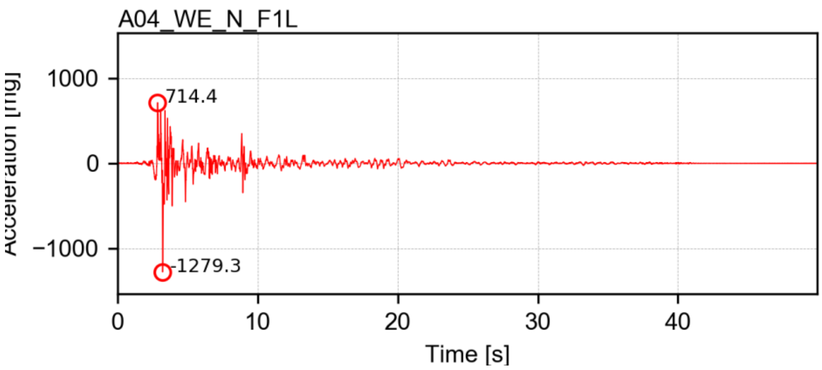

Channel A04_WE_N_F1L – acceleration

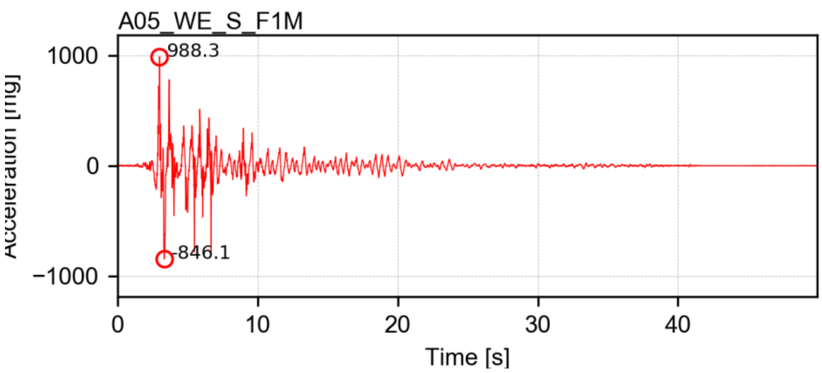

Channel A05_WE_S_F1M – acceleration

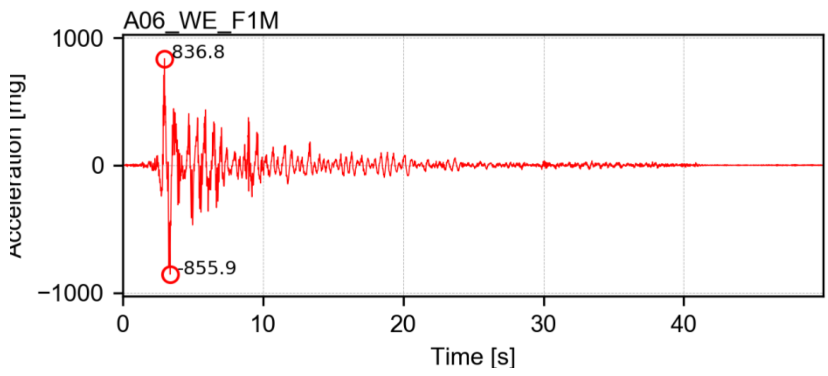

Channel A06_WE_F1M – acceleration

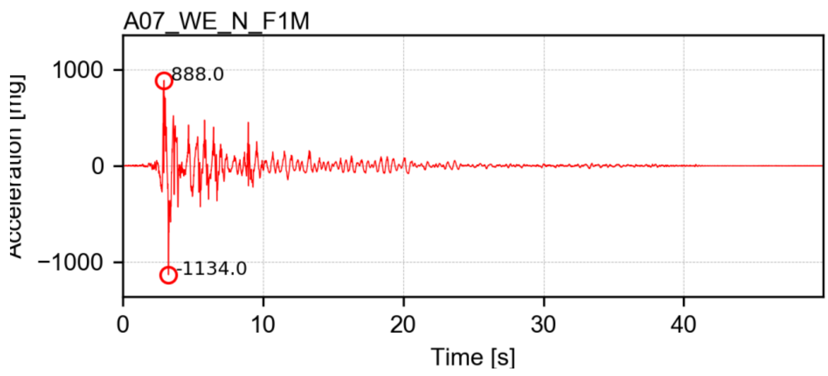

Channel A07_WE_N_F1M – acceleration

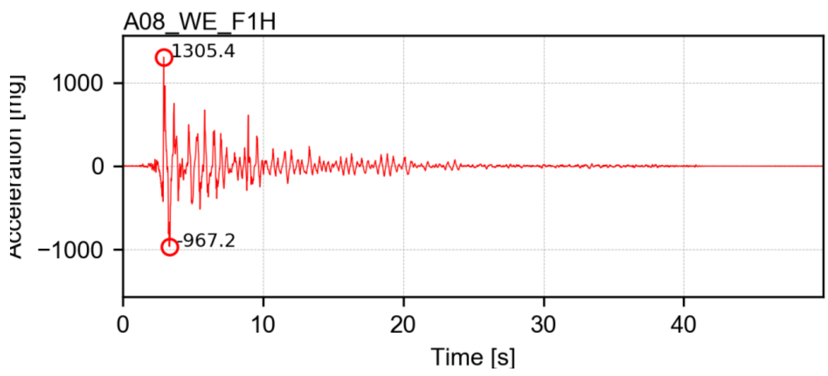

Channel A08_WE_F1H – acceleration

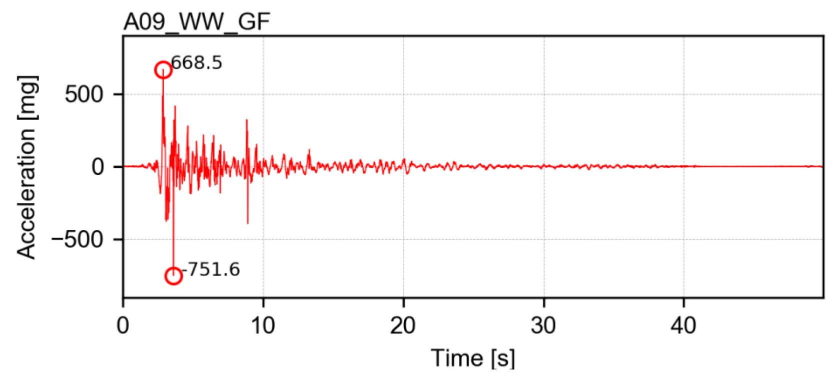

Channel A09_WW_GF – acceleration

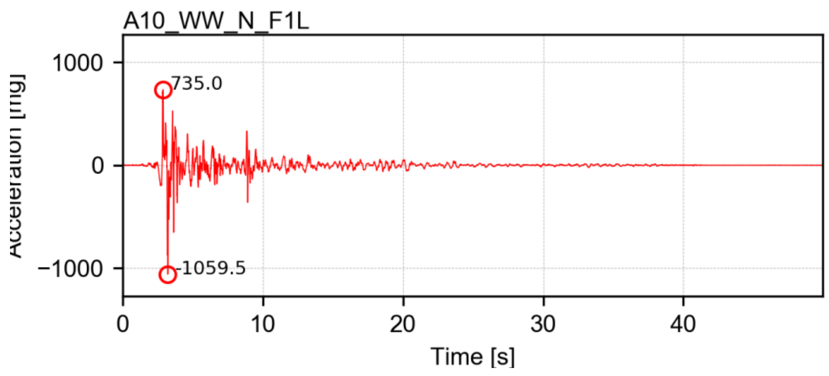

Channel A10_WW_N_F1L – acceleration

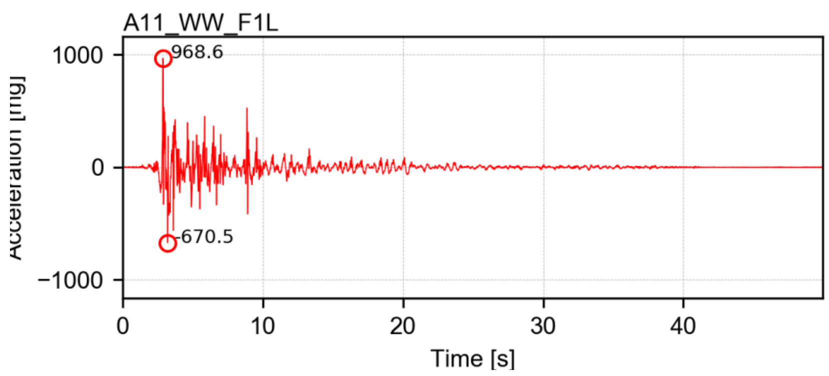

Channel A11_WW_F1L – acceleration

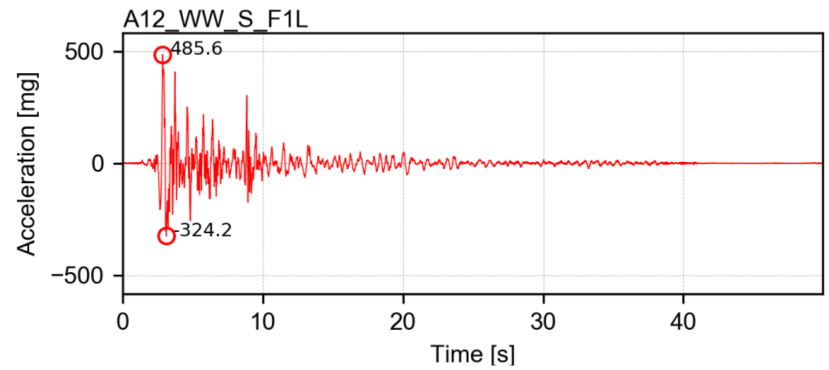

Channel A12_WW_S_F1L – acceleration

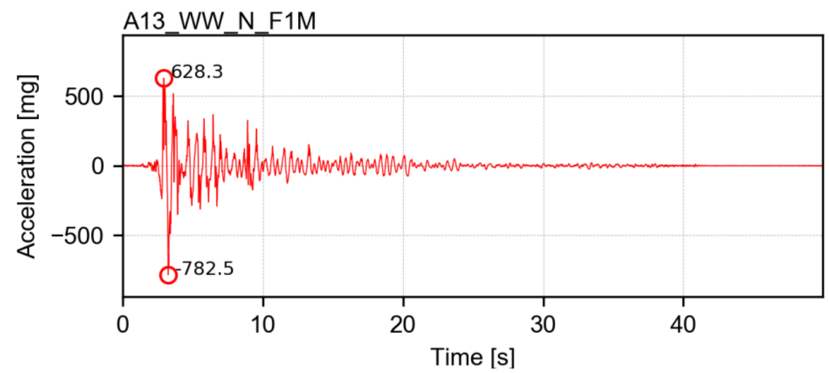

Channel A13_WW_N_F1M – acceleration

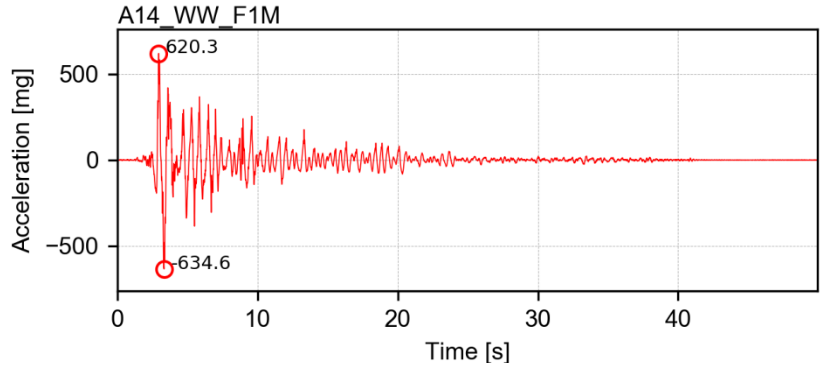

Channel A14_WW_F1M – acceleration

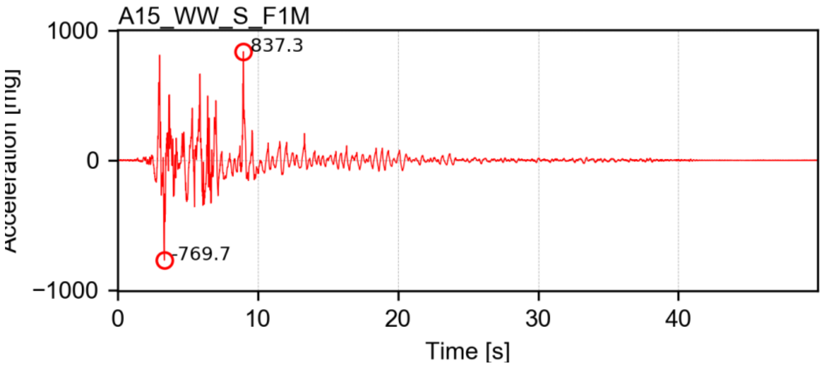

Channel A15_WW_S_F1M – acceleration

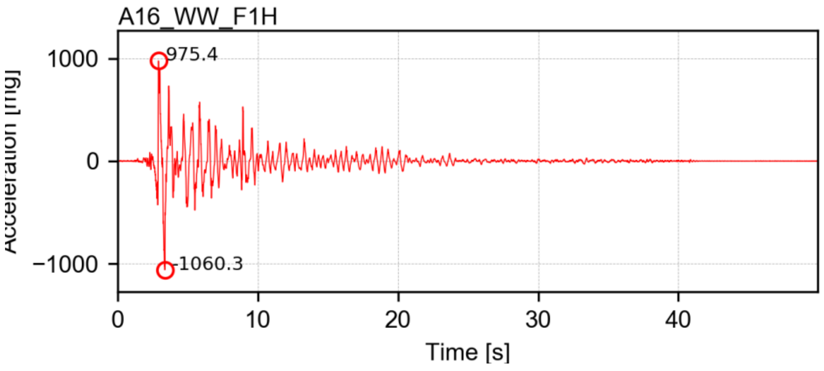

Channel A16_WW_F1H – acceleration

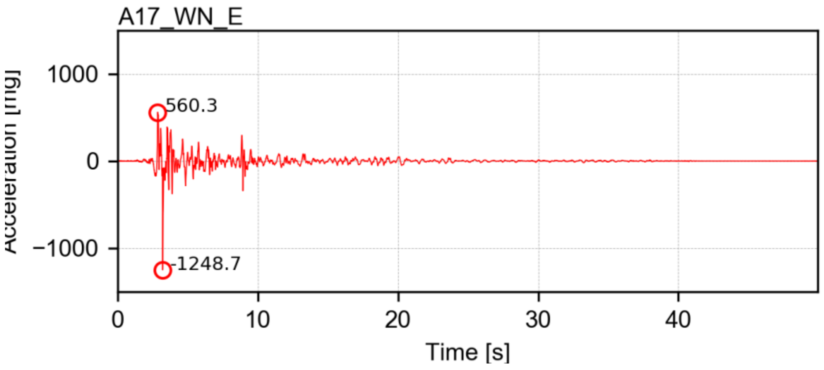

Channel A17_WN_E – acceleration

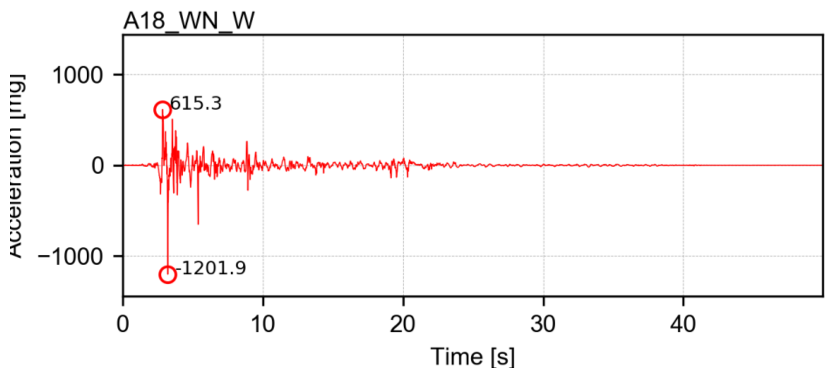

Channel A18_WN_W – acceleration

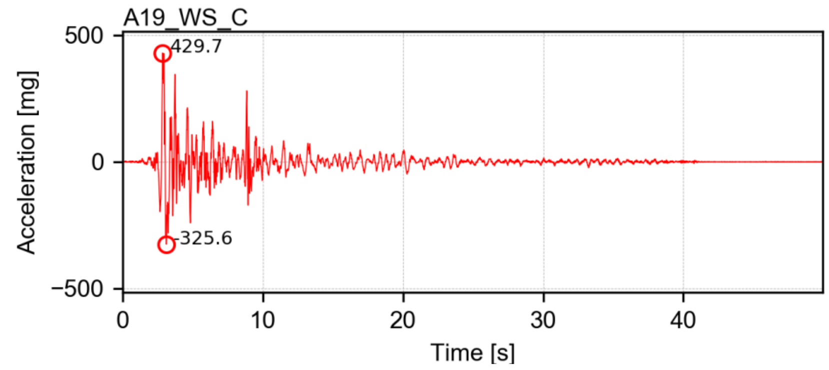

Channel A19_WS_C – acceleration

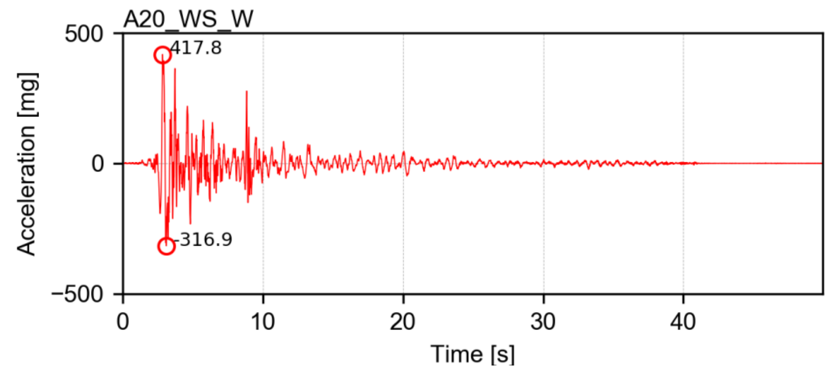

Channel A20_WS_W – acceleration

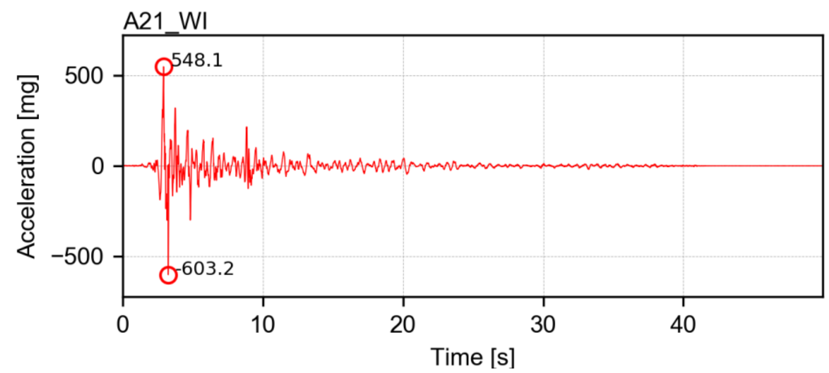

Channel A21_WI – acceleration

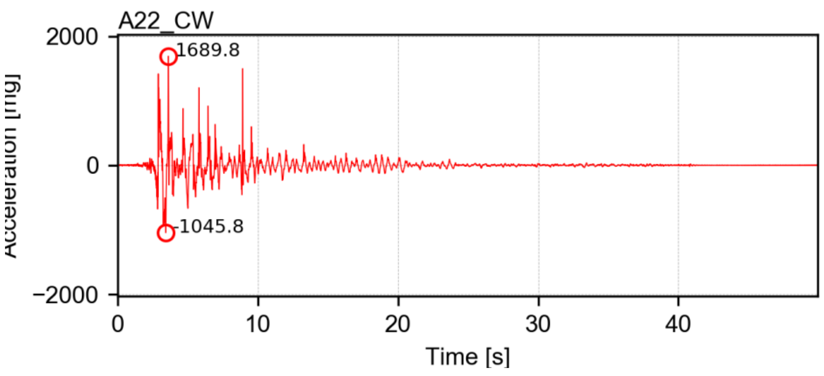

Channel A22_CW – acceleration

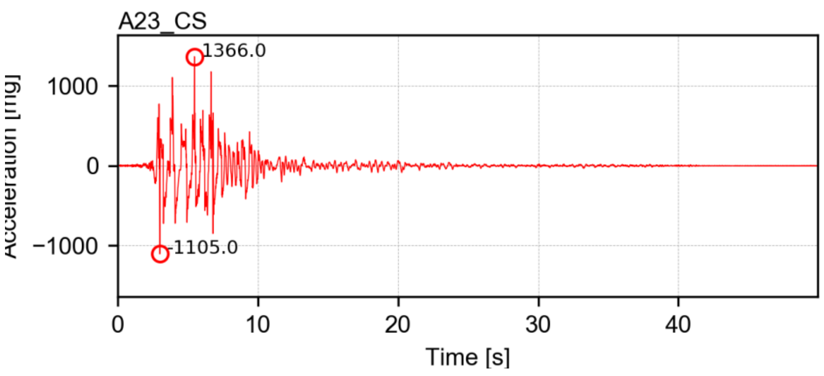

Channel A23_CS – acceleration

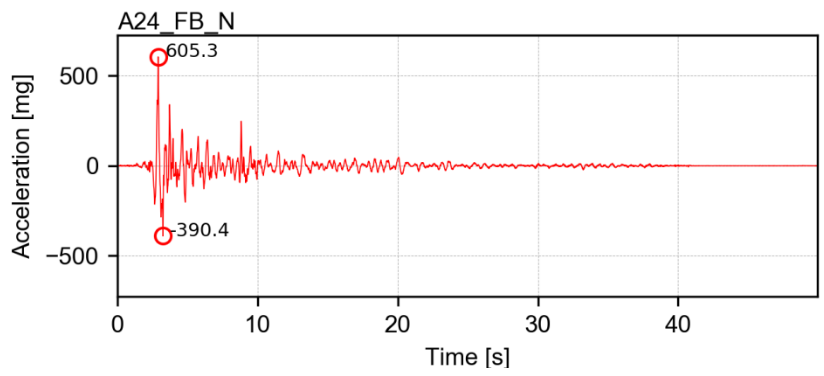

Channel A24_FB_N – acceleration

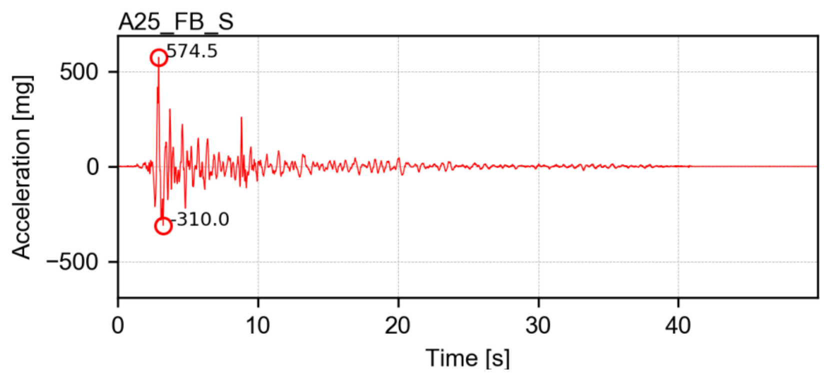

Channel A25_FB_S – acceleration

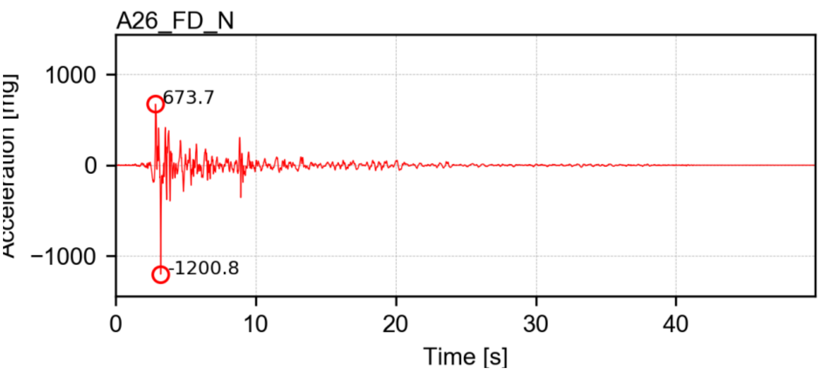

Channel A26_FD_N – acceleration

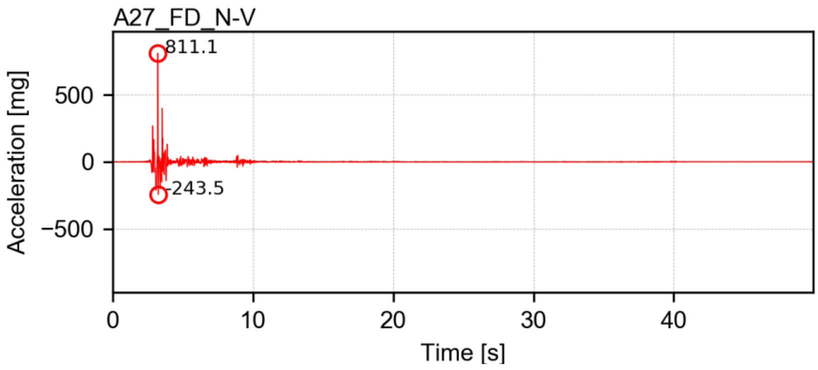

Channel A27_FD_N-V – acceleration

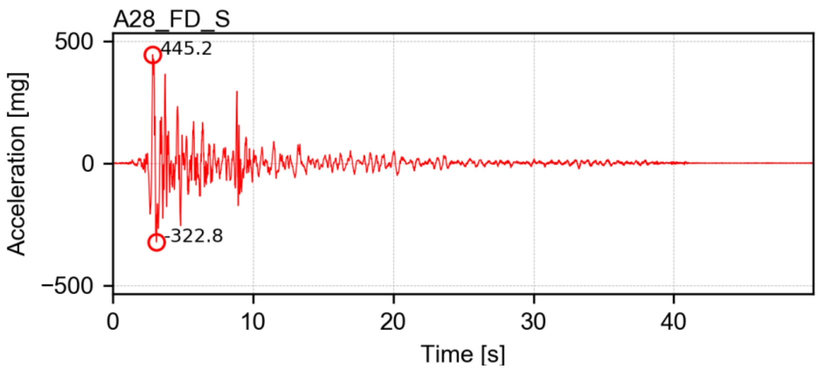

Channel A28_FD_S – acceleration

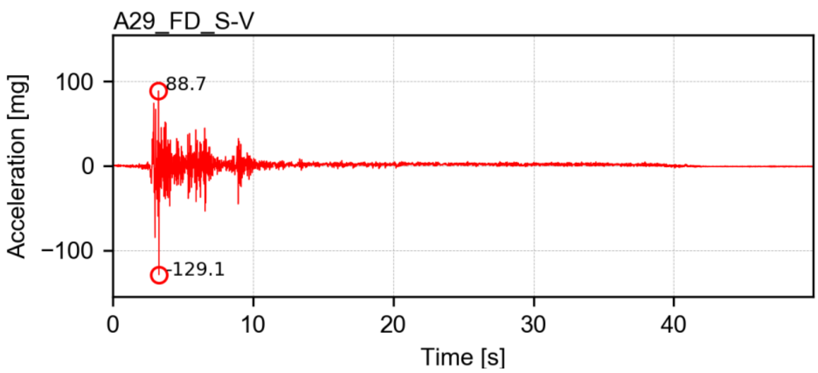

Channel A29_FD_S-V – acceleration

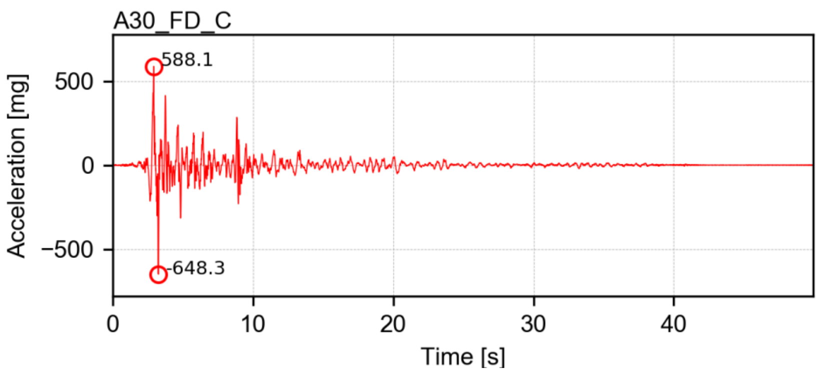

Channel A30_FD_C – acceleration

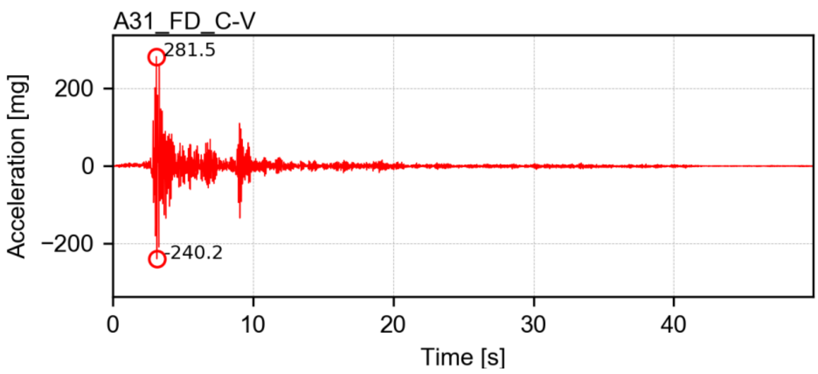

Channel A31_FD_C-V – acceleration

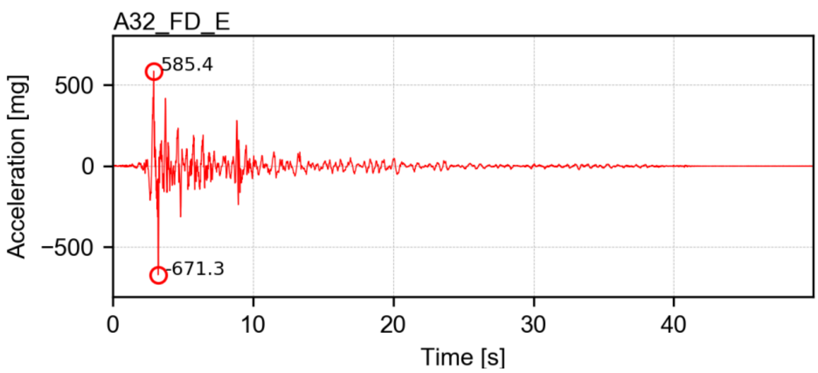

Channel A32_FD_E – acceleration

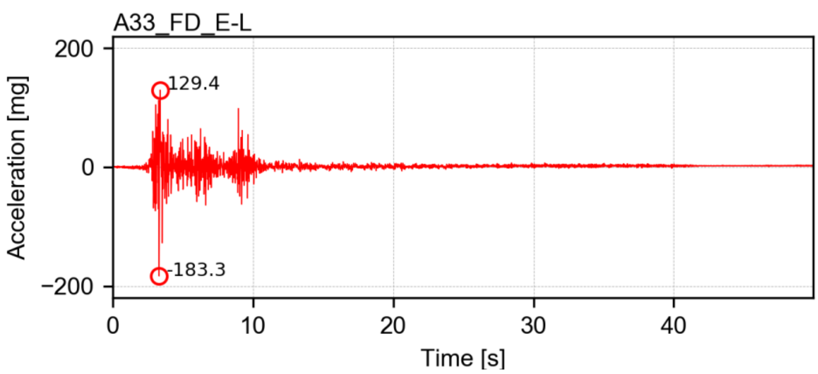

Channel A33_FD_E-L – acceleration

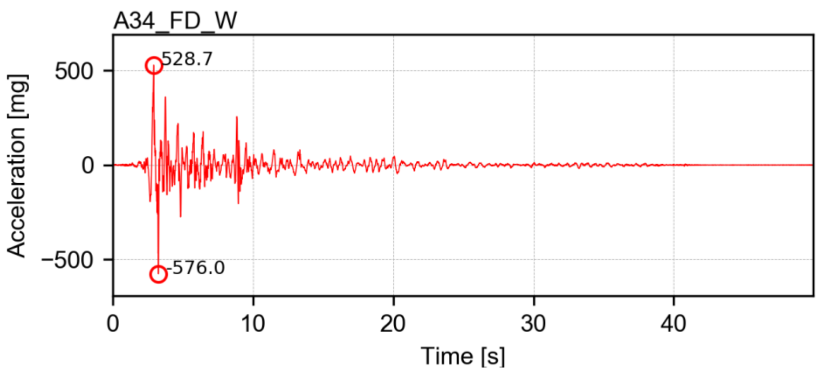

Channel A34_FD_W – acceleration

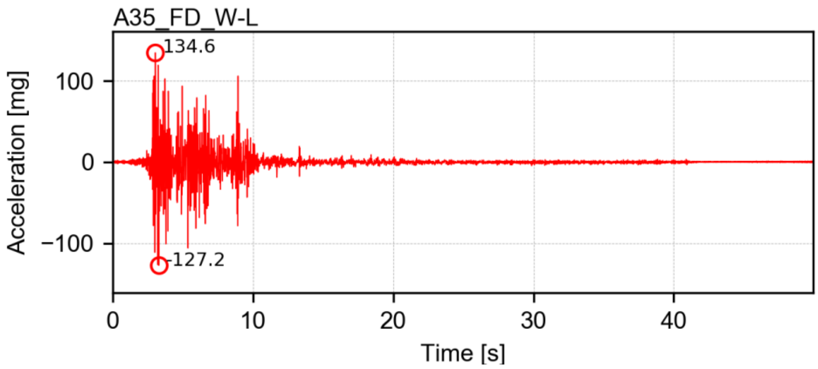

Channel A35_FD_W-L – acceleration

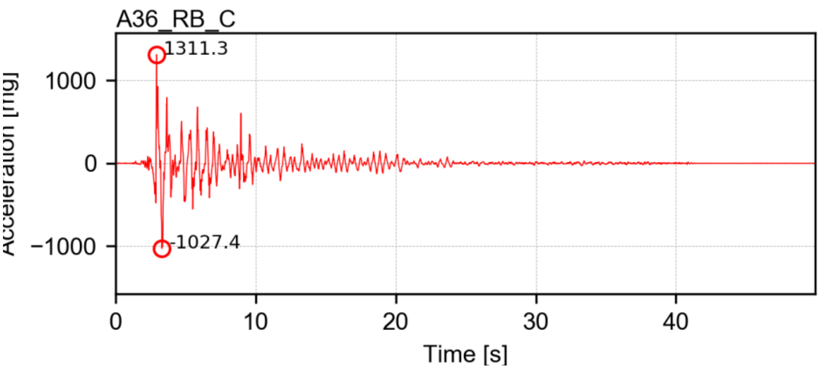

Channel A36_RB_C – acceleration

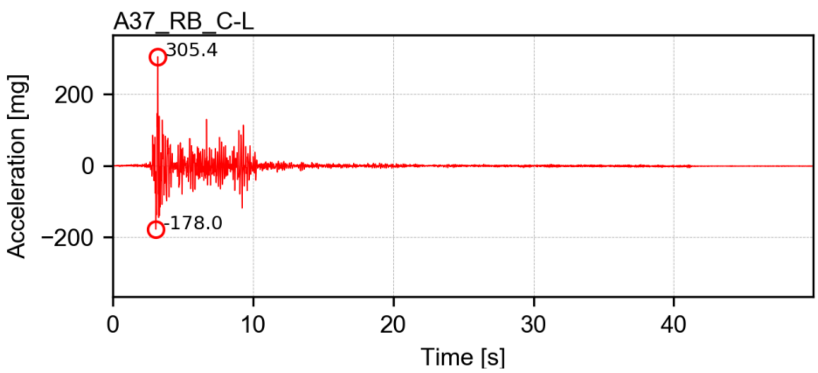

Channel A37_RB_C-L – acceleration

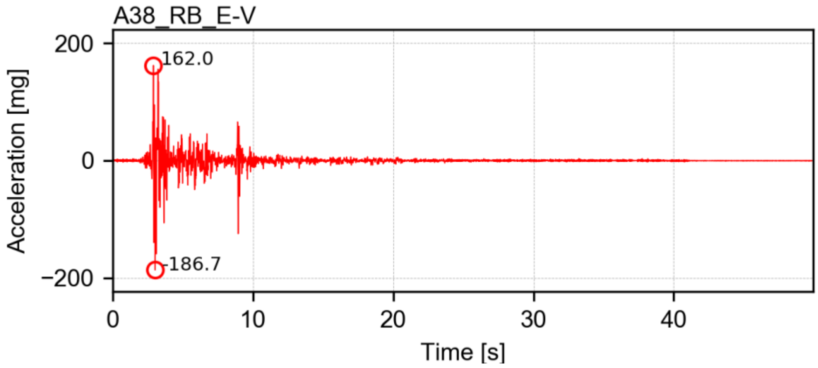

Channel A38_RB_E-V – acceleration

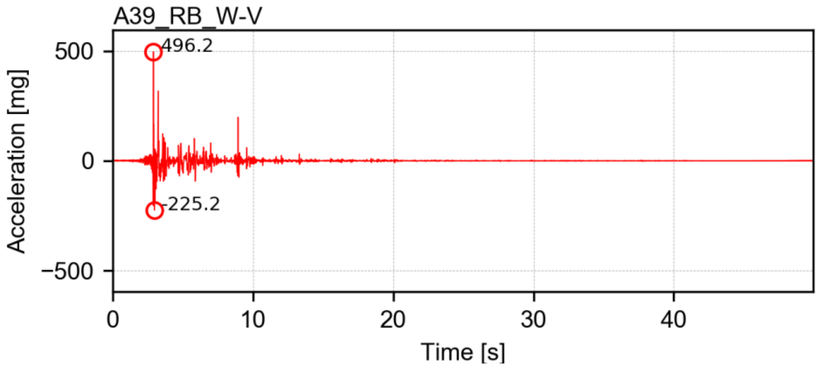

Channel A39_RB_W-V – acceleration

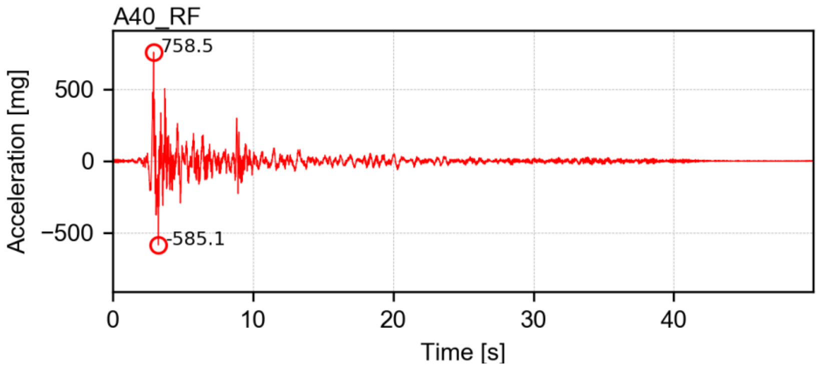

Channel A40_RF – acceleration

APPENDIX F. ADDITIONAL INFORMATION ON MORTAR CHARACTERISATION TESTS

Characteristics of mortar test specimens (MT_0%, MT_20% and MT_40%):

Sample	Specimen	Age [days]	Length [mm]	Width [mm]	Height [mm]	Mass [g]
MT0%	MT0%_1	6	160.04	39.98	40.91	400.67
	MT0%_2		160.13	40.10	40.58	401.27
	MT0%_3		160.09	39.96	40.72	401.14
MT20%	MT20%_4	6	159.90	40.06	40.64	381.56
	MT20%_5		160.02	39.98	40.87	376.49
	MT20%_6		159.92	40.01	40.53	376.96
MT40%	MT40%_7	6	158.86	39.98	40.81	374.79
	MT40%_8		160.10	40.03	41.04	374.78
	MT40%_9		160.13	39.93	40.69	370.68

Characteristics of mortar for maturation curve specimens (MMC_0%, MMC_20% and MMC_40%):

Sample	Specimen	Age [days]	Length [mm]	Width [mm]	Height [mm]	Mass [g]
MMC0%	MMC0%_1	9	160.02	40.23	41.08	436.37
	MMC0%_2		160.11	40.09	40.92	437.08
	MMC0%_3		159.95	40.12	40.00	440.74
MMC0%	MMC20%_4	9	160.11	40.08	40.00	416.72
	MMC20%_5		160.22	39.82	40.47	414.60
	MMC20%_6		160.27	40.26	40.53	417.92
MMC0%	MMC40%_7	9	160.17	39.95	41.00	392.10
	MMC40%_8		160.37	40.14	41.09	393.50
	MMC40%_9		160.36	40.18	40.82	394.91
MMC20%	MMC0%_10	20	160.89	40.17	40.49	415.88
	MMC0%_11		160.11	40.18	41.26	420.30
	MMC0%_12		160.31	40.11	40.66	413.11
MMC20%	MMC20%_13	20	160.42	39.68	40.90	381.12
	MMC20%_14		161.12	40.01	40.39	377.08
	MMC20%_15		160.64	39.98	40.49	373.86
MMC20%	MMC40%_16	20	160.03	40.27	40.12	376.65
	MMC40%_17		160.09	40.13	40.25	374.82
	MMC40%_18		160.60	40.03	40.16	376.32
MMC40%	MMC0%_19	28	159.93	40.16	40.80	412.07
	MMC0%_20		160.01	40.05	40.84	408.34
	MMC0%_21		160.04	39.94	40.58	408.31

MMC40%	MMC20%_22	28	160.00	39.94	40.74	380.50
	MMC20%_23		159.90	40.01	40.61	380.99
	MMC20%_24		160.13	40.12	40.76	381.46
MMC40%	MMC40%_25	28	160.04	39.89	40.73	367.36
	MMC40%_26		160.06	40.14	40.47	365.07
	MMC40%_27		159.99	40.21	40.75	368.62

Characteristics of collected mortar specimens (MC_1 to MC11):

+	Specimen	Age [days]	Length [mm]	Width [mm]	Height [mm]	Mass [g]
MC1	MC1_1	10	160.14	40.00	40.83	431.06
	MC1_2		160.32	40.10	41.27	434.35
	MC1_3		160.16	39.92	40.93	431.31
MC1	MC1_4	21	160.38	40.08	41.22	431.38
	MC1_5		160.42	40.01	41.27	431.92
	MC1_6		160.17	39.99	40.79	427.00
MC1	MC1_7	28	159.98	40.03	40.96	428.63
	MC1_8		160.12	40.07	40.94	426.54
	MC1_9		159.94	40.11	40.96	427.49
MC1	MC1_10	52	160.50	36.77	36.05	433.69
	MC1_11		160.10	40.26	40.64	440.27
	MC1_12		161.01	40.19	40.84	436.51
MC2	MC2_13	10	160.26	40.19	41.07	424.64
	MC2_14		160.20	40.00	40.73	420.16
	MC2_15		160.09	40.22	40.83	426.33
MC2	MC2_16	21	160.10	40.03	41.11	422.17
	MC2_17		160.26	39.98	41.13	420.10
	MC2_18		160.09	40.04	40.75	420.38
MC2	MC2_19	28	160.02	40.06	40.93	418.52
	MC2_20		159.95	40.00	40.77	417.85
	MC2_21		160.10	40.00	40.69	417.68
MC2	MC2_22	52	160.68	39.93	40.53	421.32
	MC2_23		160.55	40.30	40.99	421.03
	MC2_24		160.47	40.10	40.63	420.03
MC3	MC3_25	10	160.03	40.18	40.86	422.34
	MC3_26		159.94	41.33	40.12	423.01
	MC3_27		159.92	40.90	40.00	422.21
MC3	MC3_28	20	159.56	40.04	40.60	417.48
	MC3_29		159.60	40.09	40.66	419.57
	MC3_30		159.61	40.08	40.96	415.73
MC3	MC3_31	27	159.66	40.11	40.62	419.28
	MC3_32		159.64	39.98	40.66	418.62
	MC3_33		159.64	40.04	40.45	417.87

+	Specimen	Age [days]	Length [mm]	Width [mm]	Height [mm]	Mass [g]
MC3	MC3_34	51	159.99	40.06	40.59	423.79
	MC3_35		159.98	40.48	40.66	424.91
	MC3_36		159.98	40.09	40.54	424.91
MC4	MC4_37	10	160.05	39.98	41.47	434.12
	MC4_38		160.41	40.02	41.04	432.38
	MC4_39		160.13	40.02	41.49	433.56
MC4	MC4_40	20	159.93	40.12	41.35	424.23
	MC4_41		160.01	39.95	40.74	421.18
	MC4_42		160.02	40.04	40.78	423.51
MC4	MC4_43	27	160.12	40.01	40.78	429.50
	MC4_44		160.09	40.05	40.72	427.91
	MC4_45		160.11	39.84	40.97	426.81
MC4	MC4_46	51	159.73	40.04	40.62	427.57
	MC4_47		159.71	40.09	40.59	428.70
	MC4_48		159.91	40.11	40.69	428.71
MC5	MC5_49	12	159.90	40.16	40.47	405.77
	MC5_50		160.03	39.79	40.71	406.11
	MC5_51		160.13	40.16	40.60	409.80
MC5	MC5_52	19	159.53	40.06	40.71	409.69
	MC5_53		159.71	40.18	40.82	410.06
	MC5_54		159.59	40.16	40.50	408.35
MC5	MC5_55	28	160.03	40.05	40.70	412.40
	MC5_56		160.21	40.18	41.20	415.49
	MC5_57		160.28	40.39	41.04	416.24
MC5	MC5_58	50	159.72	40.04	40.29	410.09
	MC5_59		159.94	40.49	40.18	413.83
	MC5_60		160.88	40.20	40.81	414.32
MC6	MC6_61	12	159.94	40.04	40.76	418.73
	MC6_62		160.41	40.03	40.74	418.14
	MC6_70		160.51	40.12	40.11	412.27
MC6	MC6_64	19	159.85	39.99	40.91	415.98
	MC6_65		160.16	40.05	40.66	415.63
	MC6_66		159.85	40.08	40.67	416.77
MC6	MC6_67	28	160.70	39.94	40.58	413.25
	MC6_68		160.30	40.11	40.75	416.16
	MC6_69		159.98	40.26	40.58	416.33
MC6	MC6_71	50	162.31	40.39	39.62	421.19
	MC6_72		159.83	40.29	41.96	422.08
MC7	MC7_73	11	160.30	39.98	41.12	431.27
	MC7_74		160.21	39.96	40.94	427.09
	MC7_75		160.46	40.03	40.65	432.50
MC7	MC7_76	18	160.08	39.98	40.71	430.17

+	Specimen	Age [days]	Length [mm]	Width [mm]	Height [mm]	Mass [g]
	MC7_77		159.99	40.11	40.76	431.00
	MC7_78		159.99	39.99	40.53	428.02
MC7	MC7_79	28	160.10	39.95	40.31	427.88
	MC7_80		160.05	40.22	40.40	431.66
	MC7_81		160.18	40.24	40.35	429.61
MC7	MC7_82	49	159.96	40.00	40.74	434.04
	MC7_83		160.94	39.91	41.03	436.51
	MC7_84		160.20	40.06	41.15	437.73
MC8	MC8_85	11	159.31	40.31	40.94	402.63
	MC8_86		159.98	40.02	40.91	402.52
	MC8_87		159.70	40.14	40.83	403.33
MC8	MC8_88	18	159.54	40.00	41.13	403.84
	MC8_89		159.58	40.03	41.20	403.47
	MC8_90		159.67	40.00	40.81	401.56
MC8	MC8_91	28	160.15	40.03	40.86	406.64
	MC8_92		159.94	39.97	41.14	406.72
	MC8_93		159.86	40.11	40.95	405.48
MC8	MC8_94	49	160.01	40.06	40.48	406.87
	MC8_95		159.64	39.92	40.39	406.19
	MC8_96		159.58	40.11	40.73	408.37
MC9	MC9_97	10	159.96	40.27	40.93	431.10
	MC9_98		160.23	40.08	40.92	432.72
	MC9_99		160.42	40.08	40.00	428.35
MC9	MC9_100	20	160.20	40.00	41.06	432.98
	MC9_101		160.05	40.12	41.10	433.64
	MC9_102		160.05	40.14	41.22	433.00
MC9	MC9_103	28	160.17	40.06	41.00	432.81
	MC9_104		160.11	40.00	41.01	434.00
	MC9_105		160.03	39.97	40.87	431.87
MC9	MC9_106	48	160.15	39.99	41.24	439.65
	MC9_107		160.42	40.12	41.23	442.53
	MC9_108		160.15	40.07	41.00	438.46
MC10	MC10_109	10	160.41	40.02	40.00	401.84
	MC10_110		160.40	40.08	40.00	403.78
	MC10_111		160.25	39.75	40.64	402.60
MC10	MC10_112	20	159.86	40.04	41.87	416.66
	MC10_113		160.08	40.10	41.25	410.35
	MC10_114		159.64	40.25	40.72	407.63
MC10	MC10_115	28	160.04	40.29	41.02	410.48
	MC10_116		160.05	39.96	40.91	405.72
	MC10_117		160.11	40.17	40.81	408.95

+	Specimen	Age [days]	Length [mm]	Width [mm]	Height [mm]	Mass [g]
MC10	MC10_118	48	159.91	40.22	40.71	409.81
	MC10_119		160.09	40.14	40.80	408.63
	MC10_120		161.12	40.01	40.90	410.37
MC11	MC11_121	9	160.30	40.15	41.57	452.69
	MC11_122		160.45	39.91	41.91	453.59
	MC11_123		160.02	39.98	41.36	449.43
MC11	MC11_124	20	159.94	40.05	40.45	431.55
	MC11_125		159.95	40.13	40.72	431.51
	MC11_126		160.06	40.40	41.14	437.65
MC11	MC11_127	30	159.98	39.99	41.64	445.20
	MC11_128		159.80	40.08	40.84	441.07
	MC11_129		159.98	39.93	41.24	440.55
MC11	MC11_130	47	159.80	40.06	41.71	450.07
	MC11_131		160.68	40.13	41.16	445.38
	MC11_132		160.15	40.02	41.25	443.71

Test results for the determination of the dynamic modulus of elasticity after 10 days, 20 days and 28 days of mortar for maturation curve specimens (MMC_0%, MMC_20% and MMC_40%):

Specimen	Date of test	Age of specimen [days]	Density [kg/m^3]		Frequency of resonance [Hz]		Dynamic modulus of elasticity [MPa]	
			Individual values	Average	Individual values	Average	Individual values	Average
MMC0%_1	09-02-2018	9	1650	1677	6558	6516	7267	7294
MMC0%_2			1664		6436		7066	
MMC0%_3			1717		6554		7548	
MMC20%_4	09-02-2018	9	1623	1610	5822	5854	5642	5660
MMC20%_5			1606		5814		5574	
MMC20%_6			1598		5925		5764	
MMC40%_7	09-02-2018	9	1494	1494	4602	4597	3248	3246
MMC40%_8			1488		4584		3216	
MMC40%_9			1501		4604		3272	
MMC0%_10	20-02-2018	20	1589	1584	6226	6253	6378	6377
MMC0%_11			1584		6263		6369	
MMC0%_12			1580		6270		6385	
MMC20%_13	20-02-2018	20	1464	1450	5089	5094	3902	3887
MMC20%_14			1448		5104		3917	
MMC20%_15			1437		5089		3842	
MMC40%_16	20-02-2018	20	1457	1455	4743	4748	3357	3369
MMC40%_17			1450		4743		3342	

MMC40%_18			1458		4760		3407	
MMC0%_19	28-02-2018	28	1573	1569	6076	6004	5941	5792
MMC0%_20			1560		5982		5717	
MMC0%_21			1574		5954		5718	
MMC20%_22	28-02-2018	28	1461	1460	4918	4916	3619	3618
MMC20%_23			1467		4895		3594	
MMC20%_24			1457		4937		3642	
MMC40%_25	28-02-2018	28	1413	1408	4294	4301	2670	2668
MMC40%_26			1404		4244		2592	
MMC40%_27			1406		4364		2742	

Test results for the determination of the dynamic modulus of elasticity after 10 days of collected mortar specimens (MC_1 to MC11):

Specimen	Date of test	Age of specimen [days]	Density [kg/m^3]		Frequency of resonance [Hz]		Dynamic modulus of elasticity [MPa]	
			Individual values	Average	Individual values	Average	Individual values	Average
MC_1_1	15-02-2018	10	1648	1644	5799	5762	5684	5605
MC_1_2			1637		5777		5616	
MC_1_3			1648		5711		5516	
MC_2_13	15-02-2018	10	1605	1610	5515	5604	5016	5198
MC_2_14			1610		5632		5242	
MC_2_15			1622		5665		5336	
MC_3_25	16-02-2018	10	1608	1605	5555	5544	5082	5051
MC_3_26			1595		5513		4961	
MC_3_27			1614		5563		5109	
MC_4_37	16-02-2018	10	1636	1640	5577	5571	5213	5213
MC_4_38			1641		5622		5340	
MC_4_39			1630		5514		5085	
MC_5_49	19-02-2018	12	1561	1566	5317	5309	4514	4521
MC_5_50			1567		5293		4497	
MC_5_51			1570		5317		4551	
MC_6_61	19-02-2018	12	1604	1600	5384	5295	4759	4611
MC_6_62			1598		5357		4721	
MC_6_70			1596		5144		4352	
MC_8_85	19-02-2018	11	1531	1540	5104	5127	4049	4118
MC_8_86			1537		5129		4139	
MC_8_87			1541		5149		4167	
MC_10_109	19-02-2018	10	1565	1560	4827	4846	3753	3777
MC_10_110			1570		4819		3753	
MC_10_111			1555		4892		3824	
MC_11_121	19-02-2018	9	1692	1694	5666	5625	5584	5505
MC_11_122			1690		5660		5575	

MC_11_123			1698		5549		5356	

Test results for the determination of the dynamic modulus of elasticity after 20 days of collected mortar specimens (MC_1 to MC11):

Specimen	Date of test	Age of specimen [days]	Density [kg/m^3]		Frequency of resonance [Hz]		Dynamic modulus of elasticity [MPa]	
			Individual values	Average	Individual values	Average	Individual values	Average
MC_1_4	26-02-2018	21	1628	1631	5907	5999	5844	6035
MC_1_5			1631		6057		6159	
MC_1_6			1634		6033		6103	
MC_2_16	26-02-2018	21	1603	1600	5808	5859	5542	5642
MC_2_17			1594		5866		5635	
MC_2_18			1609		5904		5749	
MC_3_28	26-02-2018	20	1610	1603	5757	5771	5433	5439
MC_3_29			1613		5838		5601	
MC_3_30			1587		5717		5284	
MC_4_40	26-02-2018	20	1599	1610	5910	5853	5714	5655
MC_4_41			1617		5859		5685	
MC_4_42			1621		5791		5567	
MC_5_52	26-02-2018	19	1575	1571	5531	5512	4903	4864
MC_5_53			1566		5509		4848	
MC_5_54			1573		5496		4841	
MC_6_64	26-02-2018	19	1591	1590	5367	5372	4682	4710
MC_6_65			1594		5358		4695	
MC_6_66			1599		5392		4753	
MC_8_88	26-02-2018	18	1539	1540	5217	5265	4263	4342
MC_8_89			1533		5275		4345	
MC_8_90			1541		5302		4417	
MC_10_112	01-03-2018	20	1554	1550	4965	4967	3918	3919
MC_10_113			1550		4893		3803	
MC_10_114			1558		5042		4038	
MC_11_124	02-03-2018	20	1666	1654	5527	5492	5207	5108
MC_11_125			1651		5484		5081	
MC_11_126			1645		5465		5035	

Test results for the determination of the dynamic modulus of elasticity after 28 days of collected mortar specimens (MC_1 to MC11):

Specimen	Date of test	Age of specimen [days]	Density [kg/m^3]		Frequency of resonance [Hz]		Dynamic modulus of elasticity [MPa]	
			Individual values	Average	Individual values	Average	Individual values	Average
MC_1_7	05-03-2018	28	1634	1628	5981	5997	5985	5998

MC_1_8			1624		5992		5979	
MC_1_9			1627		6017		6028	
MC_2_19	05-03-2018	28	1595	1600	5706	5706	5319	5335
MC_2_20			1602		5699		5324	
MC_2_21			1603		5712		5363	
MC_3_31	05-03-2018	27	1612	1614	5725	5784	5386	5503
MC_3_32			1613		5827		5582	
MC_3_33			1616		5799		5542	
MC_4_43	05-03-2018	27	1644	1640	5807	5810	5686	5672
MC_4_44			1639		5850		5751	
MC_4_45			1633		5772		5579	
MC_5_55	07-03-2018	28	1581	1571	5649	5661	5167	5167
MC_5_56			1567		5699		5224	
MC_5_57			1567		5634		5111	
MC_6_67	07-03-2018	28	1587	1590	5503	5539	4963	5013
MC_6_68			1588		5526		4985	
MC_6_69			1593		5588		5091	
MC_8_91	08-03-2018	28	1552	1550	5316	5305	4500	4460
MC_8_92			1546		5303		4450	
MC_8_93			1544		5297		4429	
MC_10_115	09-03-2018	28	1552	1550	5044	5023	4045	4018
MC_10_116			1551		4979		3940	
MC_10_117			1558		5047		4070	
MC_11_127	12-03-2018	30	1671	1677	5589	5556	5344	5294
MC_11_128			1687		5565		5335	
MC_11_129			1672		5514		5204	

Test results for the determination of the flexural and compressive strengths after 6 days of mortar test specimens (MT_0%, MT_20% and MT_40%):

Specimen	Date of test	Age of specimen [days]	Density [kg/m³]		Compressive strength [MPa]			Flexural strength [MPa]	
			Individual values	Average	Individual values		Average	Individual values	Average
MT0%_1	05-02-2018	6	1530	1154	1.95	2.00	1.93	0.90	0.83
MT0%_2			1540		2.05	1.80		0.90	
MT0%_3			1540		1.90	1.90		0.70	
MT20%_4	05-02-2018	6	1470	1092	1.35	1.40	1.33	0.60	0.65
MT20%_5			1440		1.25	1.25		0.75	
MT20%_6			1450		1.40	1.35		0.60	
MT40%_7	05-02-2018	6	1450	1074	1.00	1.10	1.00	0.75	0.67
MT40%_8			1420		0.95	1.00		0.70	
MT40%_9			1420		0.95	1.00		0.55	

Test results for the determination of the flexural and compressive strengths after 10 days, 20 days and 28 days of mortar for maturation curve specimens (MMC_0%, MMC_20% and MMC_40%):

Specimen	Date of test	Age of specimen [days]	Density [kg/m³]		Compressive strength [MPa]			Flexural strength [MPa]	
			Individual values	Average	Individual values		Average	Individual values	Average
MMC0%_1	09-02-2018	9	1650	1677	3.60	3.70	3.53	2.00	1.82
MMC0%_2			1664		3.55	3.20		1.90	
MMC0%_3			1717		3.70	3.40		1.55	
MMC20%_4	09-02-2018	9	1623	1610	2.45	2.45	2.33	1.25	1.33
MMC20%_5			1606		2.35	1.60		1.05	
MMC20%_6			1598		2.55	2.60		1.70	
MMC40%_7	09-02-2018	9	1494	1494	1.10	1.20	1.22	0.75	0.65
MMC40%_8			1488		1.20	1.20		0.60	
MMC40%_9			1501		1.40	1.20		0.60	
MMC0%_10	20-02-2018	20	1589	1584	3.20	3.45	3.29	1.45	1.65
MMC0%_11			1584		3.50	3.25		1.60	
MMC0%_12			1580		3.30	3.05		1.90	
MMC20%_13	20-02-2018	20	1464	1450	1.25	1.45	1.43	1.10	0.97
MMC20%_14			1448		1.50	1.50		0.95	
MMC20%_15			1437		1.65	1.25		0.85	
MMC40%_16	20-02-2018	20	1457	1455	1.20	1.25	1.30	0.80	0.82
MMC40%_17			1450		1.40	1.35		0.70	
MMC40%_18			1458		1.15	1.45		0.95	
MMC0%_19	28-02-2018	28	1573	1569	2.65	3.20	3.03	1.55	1.43
MMC0%_20			1560		3.40	3.15		1.45	
MMC0%_21			1574		3.05	2.75		1.30	
MMC20%_22	28-02-2018	28	1461	1460	1.80	1.95	1.76	0.90	0.85
MMC20%_23			1467		1.85	1.80		0.80	
MMC20%_24			1457		1.60	1.55		0.85	
MMC40%_25	28-02-2018	28	1413	1408	1.30	1.35	1.31	0.70	0.63
MMC40%_26			1404		1.30	1.30		0.60	
MMC40%_27			1406		1.35	1.25		0.60	

Test results for the determination of the flexural and compressive strengths after 10 days of collected mortar specimens (MC_1 to MC11):

Specimen	Date of test	Age of specimen [days]	Density [kg/m³]		Compressive strength [MPa]			Flexural strength [MPa]	
			Individual values	Average	Individual values		Average	Individual values	Average
MC_1_1	15-02-2018	10	1648	1644	2.55	2.60	2.46	1.75	1.47
MC_1_2			1637		2.45	2.30		1.40	
MC_1_3			1648		2.55	2.30		1.25	

MC_2_13			1605		2.15	2.30		1.50	
MC_2_14	15-02-2018	10	1610	1610	2.20	2.20	2.13	1.30	1.47
MC_2_15			1622		1.55	2.35		1.60	
MC_3_25			1608		2.00	2.20		1.05	
MC_3_26	16-02-2018	10	1595	1605	1.95	1.75	2.03	1.05	0.98
MC_3_27			1614		1.75	2.50		0.85	
MC_4_37			1636		2.10	2.45		1.10	
MC_4_38	16-02-2018	10	1641	1640	2.45	2.40	2.36	1.40	1.23
MC_4_39			1630		2.50	2.25		1.20	
MC_5_49			1561		1.80	2.15		0.60	
MC_5_50	19-02-2018	12	1567	1566	2.45	2.25	2.19	0.45	0.70
MC_5_51			1570		2.40	2.10		1.05	
MC_6_61			1604		2.50	2.50		0.45	
MC_6_62	19-02-2018	12	1598	1600	2.30	2.50	2.45	0.90	0.67
MC_6_70			1596		2.55	2.35		0.65	
MC_7_73			1636		3.45	3.40		1.75	
MC_7_74	19-02-2018	11	1629	1641	3.30	3.05	3.28	1.50	1.52
MC_7_75			1656		3.25	3.25		1.30	
MC_8_85			1531		2.05	2.20		1.10	
MC_8_86	19-02-2018	11	1537	1540	2.10	2.15	2.07	0.95	1.05
MC_8_87			1541		2.05	1.85		1.10	
MC_9_97			1635		2.80	2.60		1.20	
MC_9_98	19-02-2018	10	1647	1654	2.70	2.80	2.73	1.55	1.30
MC_9_99			1682		2.80	2.65		1.15	
MC_10_109			1565		1.45	1.75		0.80	
MC_10_110	19-02-2018	10	1570	1560	1.70	1.55	1.53	0.95	0.92
MC_10_111			1555		1.55	1.20		1.00	
MC_11_121			1692		2.40	2.35		0.70	
MC_11_122	19-02-2018	9	1690	1694	2.50	2.25	2.34	1.15	0.98
MC_11_123			1698		2.35	2.20		1.10	

Test results for the determination of the flexural and compressive strengths after 20 days of collected mortar specimens (MC_1 to MC11):

Specimen	Date of test	Age of specimen [days]	Density [kg/m^3]		Compressive strength [MPa]			Flexural strength [MPa]	
			Individual values	Average	Individual values		Average	Individual values	Average
MC_1_4			1628		3.40	3.35		1.35	
MC_1_5	26-02-2018	21	1631	1631	3.35	3.30	3.25	1.30	1.33
MC_1_6			1634		3.10	3.00		1.35	
MC_2_16			1603		2.90	2.75		1.25	
MC_2_17	26-02-2018	21	1594	1600	2.90	2.95	2.83	1.50	1.42
MC_2_18			1609		2.75	2.75		1.50	

MC_3_28			1610		2.75	2.80		1.40	
MC_3_29	26-02-2018	20	1613	1603	3.05	2.75	2.76	1.30	1.35
MC_3_30			1587		2.80	2.40		1.35	
MC_4_40			1599		2.75	2.80		1.55	
MC_4_41	26-02-2018	20	1617	1610	2.60	2.85	2.74	1.25	1.28
MC_4_42			1621		2.60	2.85		1.05	
MC_5_52			1575		2.80	2.50		1.15	
MC_5_53	26-02-2018	19	1566	1571	2.60	2.85	2.69	1.10	1.12
MC_5_54			1573		2.70	2.70		1.10	
MC_6_64			1591		2.60	2.60		0.95	
MC_6_65	26-02-2018	19	1594	1590	2.60	2.40	2.60	0.95	0.95
MC_6_66			1599		2.65	2.75		0.95	
MC_7_76			1651		4.00	3.75		1.70	
MC_7_77	26-02-2018	18	1648	1650	3.95	3.90	3.93	1.60	1.67
MC_7_78			1651		3.85	4.15		1.70	
MC_8_88			1539		2.20	2.35		1.15	
MC_8_89	26-02-2018	18	1533	1540	2.35	2.30	2.20	1.10	1.07
MC_8_90			1541		2.45	1.55		0.95	
MC_9_100			1645		2.95	3.20		1.60	
MC_9_101	01-03-2018	20	1643	1641	3.35	3.15	3.20	1.40	1.48
MC_9_102			1635		3.35	3.20		1.45	
MC_10_112			1554		1.90	2.10		0.90	
MC_10_113	01-03-2018	20	1550	1550	1.75	1.70	1.94	0.95	0.93
MC_10_114			1558		2.10	2.10		0.95	
MC_11_124			1666		3.00	2.90		1.35	
MC_11_125	02-03-2018	20	1651	1654	2.95	2.85	2.95	1.30	1.28

Test results for the determination of the flexural and compressive strengths after 28 days of collected mortar specimens (MC_1 to MC11):

Specimen	Date of test	Age of specimen [days]	Density [kg/m^3]		Compressive strength [MPa]			Flexural strength [MPa]	
			Individual values	Average	Individual values		Average	Individual values	Average
MC_1_7			1634		3.15	3.40		1.55	
MC_1_8	05-03-2018	28	1624	1628	3.30	2.80	3.20	1.45	1.48
MC_1_9			1627		3.20	3.35		1.45	
MC_2_19			1595		2.75	2.70		1.20	
MC_2_20	05-03-2018	28	1602	1600	2.90	2.80	2.79	1.30	1.23
MC_2_21			1603		2.80	2.80		1.20	
MC_3_31			1612		2.95	3.10		1.25	
MC_3_32	05-03-2018	27	1613	1614	3.15	2.60	2.93	1.40	1.32
MC_3_33			1616		2.80	2.95		1.30	

MC_4_43	05-03-2018	27	1644	1640	3.05	0.60	2.58	1.50	1.40
MC_4_44			1639		2.95	2.90		1.30	
MC_4_45			1633		3.10	2.90		1.40	
MC_5_55	07-03-2018	28	1581	1571	2.45	2.60	2.68	1.25	1.32
MC_5_56			1567		2.55	2.75		1.50	
MC_5_57			1567		2.75	2.95		1.20	
MC_6_67	07-03-2018	28	1587	1590	2.50	2.30	2.37	1.20	1.07
MC_6_68			1588		2.00	2.35		1.05	
MC_6_69			1593		2.55	2.50		0.95	
MC_7_79	08-03-2018	28	1660	1657	3.90	4.00	3.80	1.35	1.27
MC_7_80			1660		3.80	3.95		1.20	
MC_7_81			1652		3.75	3.40		1.25	
MC_8_91	08-03-2018	28	1552	1550	2.40	1.75	2.23	0.85	0.87
MC_8_92			1546		2.15	2.40		0.85	
MC_8_93			1544		2.20	2.50		0.90	
MC_9_103	09-03-2018	28	1645	1650	3.40	3.35	3.34	1.55	1.53
MC_9_104			1653		3.60	3.30		1.45	
MC_9_105			1652		3.15	3.25		1.60	
MC_10_115	09-03-2018	28	1552	1550	2.10	2.15	2.05	1.10	1.07
MC_10_116			1551		1.90	2.05		1.00	
MC_10_117			1558		1.95	2.15		1.10	
MC_11_127	12-03-2018	30	1671	1677	3.10	3.10	3.03	1.30	1.20
MC_11_128			1687		3.20	2.95		1.20	
MC_11_129			1672		2.95	2.90		1.10	

APPENDIX G. ADDITIONAL INFORMATION ON MASONRY BRICKS' CHARACTERISATION TESTS

Characteristics of the bricks selected for the tests:

Specimen	Mass [kg]	Length (L1) [mm]			Width (L2) [mm]			Height (H) [mm]		
		L1 (top)	L1 (down)	Average	L2 (Top)	L2 (down)	Average	H1 (left)	H2 (right)	Average
BSCL_1	2.1536	0.2123	0.2122	**0.2122**	0.1020	0.1007	**0.1014**	0.0469	0.0473	**0.0471**
BSCL_2	2.1372	0.2128	0.2132	**0.2130**	0.1027	0.1015	**0.1021**	0.0457	0.0462	**0.0460**
BSCL_3	2.1272	0.2128	0.2171	**0.2150**	0.1018	0.1017	**0.1018**	0.0459	0.0464	**0.0461**
BSCL_4	2.1432	0.2135	0.2134	**0.2135**	0.1010	0.1018	**0.1014**	0.0466	0.0471	**0.0469**
BSCL_5	2.1117	0.2133	0.2139	**0.2136**	0.1013	0.1011	**0.1012**	0.0465	0.0474	**0.0469**
BSCL_6	2.1194	0.2125	0.2133	**0.2129**	0.1018	0.1018	**0.1018**	0.0457	0.0461	**0.0459**
BSCL_7	2.1268	0.2133	0.2130	**0.2132**	0.1015	0.1018	**0.1016**	0.0459	0.0465	**0.0462**
BSCL_8	2.1059	0.2129	0.2126	**0.2127**	0.1019	0.1012	**0.1015**	0.0466	0.0466	**0.0466**
BSCL_9	2.1138	0.2114	0.2122	**0.2118**	0.1024	0.1022	**0.1023**	0.0457	0.0463	**0.0460**
BSCL_10	2.1017	0.2132	0.2131	**0.2131**	0.1016	0.1022	**0.1019**	0.0463	0.0464	**0.0463**
BSCL_11	2.1295	0.2120	0.2120	**0.2120**	0.1021	0.1014	**0.1018**	0.0465	0.0458	**0.0461**
BSCL_12	2.1030	0.2120	0.2115	**0.2118**	0.1018	0.1012	**0.1015**	0.0457	0.0463	**0.0460**
BSCL_13	2.0875	0.2120	0.2110	**0.2115**	0.1018	0.1011	**0.1014**	0.0469	0.0457	**0.0463**
BSCL_14	2.1486	0.2120	0.2130	**0.2125**	0.1013	0.1011	**0.1012**	0.0487	0.0491	**0.0489**
BSCL_15	2.1279	0.2120	0.2115	**0.2118**	0.1014	0.1009	**0.1011**	0.0497	0.0485	**0.0491**
BSCL_16	2.1050	0.2120	0.2120	**0.2120**	0.1014	0.1012	**0.1013**	0.0478	0.0465	**0.0472**
BSCL_17	2.1236	0.2125	0.2120	**0.2123**	0.1001	0.1005	**0.1003**	0.0467	0.0476	**0.0472**

Determination of bulk density for bricks selected for the tests:

Specimen	Length (L1)	Width (L2)	Height (H)	Mass	Bulk density
	[m]	[m]	[m]	[kg]	[kg/m^3]
BSCL_1	0.2122	0.1014	0.0471	2.1536	2126.30
BSCL_2	0.2130	0.1021	0.0460	2.1372	2139.14
BSCL_3	0.2150	0.1018	0.0461	2.1272	2107.52
BSCL_4	0.2135	0.1014	0.0469	2.1432	2111.93
BSCL_5	0.2136	0.1012	0.0469	2.1117	2081.91
BSCL_6	0.2129	0.1018	0.0459	2.1194	2130.67
BSCL_7	0.2132	0.1016	0.0462	2.1268	2124.48
BSCL_8	0.2127	0.1015	0.0466	2.1059	2094.29
BSCL_9	0.2118	0.1023	0.0460	2.1138	2119.29
BSCL_10	0.2131	0.1019	0.0463	2.1017	2088.63
BSCL_11	0.2120	0.1018	0.0461	2.1295	2140.43
BSCL_12	0.2118	0.1015	0.0460	2.1030	2127.61

BSCL_13	0.2115	0.1014	0.0463	2.0875	2101.41
BSCL_14	0.2125	0.1012	0.0489	2.1486	2042.84
BSCL_15	0.2118	0.1011	0.0491	2.1279	2023.88
BSCL_16	0.2120	0.1013	0.0472	2.1050	2078.32
BSCL_17	0.2123	0.1003	0.0472	2.1236	2115.57

Failure mechanisms of solid clay bricks for compressive strength tests:

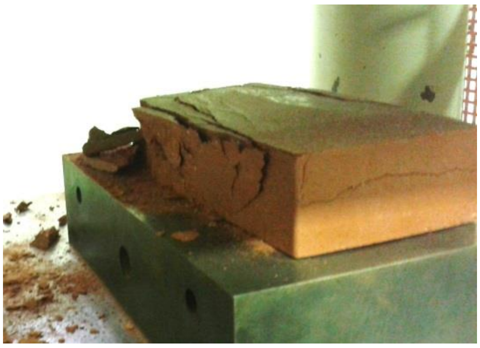

BSCL_1

BSCL_2

BSCL_3

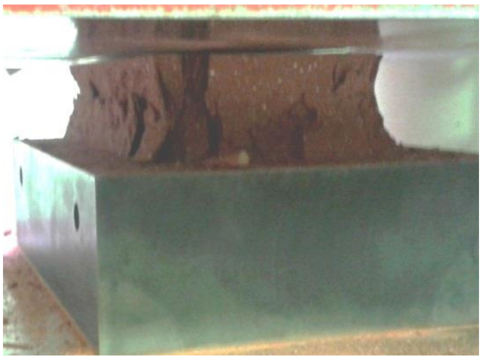

BSCL_4

BSCL_5

BSCL_6

BSCL_7

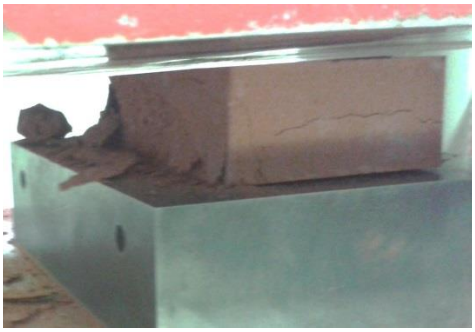

BSCL_8

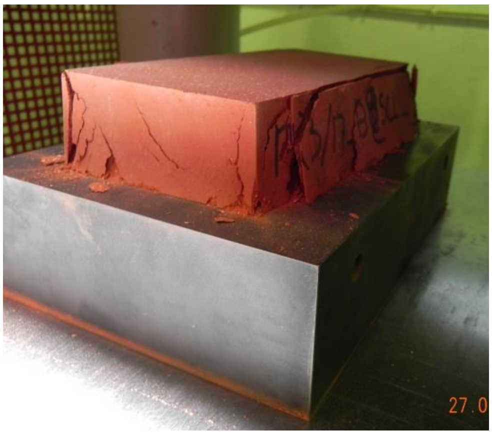

BSCL_9

BSCL_10

BSCL_11

APPENDIX H. GEOMETRY, INSTRUMENTATION LAYOUT AND ADDITIONAL INFORMATION ON WALLETTES AND TRIPLETS FOR MATERIAL CHARACTERISATION TESTS

Dimensions and masses of the two types of wallettes (simple and double) constructed for the compression strength tests:

Specimen	Length [mm]				Width [mm]				Height [mm]			Mass [kg]
		Up	Down	Average		Top	Bottom	Average		Center	Average	
CTBSCL_1S	Front	433.00	433.00	433.50	Left	101.00	100.00	100.75	Left	471.00	471.00	40.500
	Back	434.00	434.00		Right	101.00	101.00		Rigth	471.00		
CTBSCL_2S	Front	433.00	433.00	433.75	Left	101.00	101.00	101.00	Left	473.00	473.00	40.750
	Back	434.00	435.00		Right	101.00	101.00		Rigth	473.00		
CTBSCL_3S	Front	438.00	436.00	437.75	Left	101.00	101.00	100.00	Left	473.00	472.50	41.100
	Back	439.00	438.00		Right	98.00	100.00		Rigth	472.00		
CTBSCL_4S	Front	440.00	435.00	437.75	Left	99.00	100.00	99.50	Left	473.00	473.00	40.800
	Back	440.00	436.00		Right	99.00	100.00		Rigth	473.00		
CTBSCL_5S	Front	437.00	436.00	436.50	Left	101.00	100.00	100.00	Left	473.00	471.50	40.800
	Back	438.00	435.00		Right	100.00	99.00		Rigth	470.00		
CTBSCL_6S	Front	434.00	434.00	434.50	Left	100.00	101.00	100.00	Left	472.00	471.00	40.600
	Back	435.00	435.00		Right	99.00	100.00		Rigth	470.00		
CTBSCL_7S	Front	440.00	436.00	437.50	Left	101.00	100.00	100.75	Left	477.00	475.00	40.650
	Back	438.00	436.00		Right	101.00	101.00		Rigth	473.00		
CTBSCL_8S	Front	439.00	432.00	437.25	Left	99.00	99.00	99.25	Left	470.00	470.00	40.900
	Back	441.00	437.00		Right	100.00	99.00		Rigth	470.00		
CTBSCL_1D	Front	542.00	545.00	540.00	Left	211.00	214.00	212.00	Left	651.00	650.50	145.100
	Back	539.00	534.00		Right	210.00	213.00		Rigth	650.00		
CTBSCL_2D	Front	544.00	538.00	543.00	Left	211.00	208.00	211.00	Left	653.00	651.50	146.600
	Back	545.00	545.00		Right	218.00	207.00		Rigth	650.00		
CTBSCL_3D	Front	540.00	537.00	541.75	Left	210.00	218.00	212.75	Left	650.00	652.00	145.700
	Back	543.00	547.00		Right	209.00	214.00		Rigth	654.00		
CTBSCL_4D	Front	548.00	540.00	545.75	Left	208.00	208.00	210.25	Left	653.00	650.00	145.600
	Back	550.00	545.00		Right	213.00	212.00		Rigth	647.00		
CTBSCL_5D	Front	552.00	540.00	546.75	Left	210.00	210.00	210.50	Left	645.00	646.00	146.000
	Back	553.00	542.00		Right	210.00	212.00		Rigth	647.00		
CTBSCL_6D	Front	545.00	541.00	543.25	Left	215.00	213.00	213.00	Left	648.00	648.50	145.600
	Back	550.00	537.00		Right	212.00	212.00		Rigth	649.00		
CTBSCL_7D	Front	541.00	537.00	539.75	Left	210.00	209.00	209.75	Left	649.00	650.00	146.500
	Back	542.00	539.00		Right	210.00	210.00		Rigth	651.00		
CTBSCL_8D	Front	545.00	545.00	547.50	Left	210.00	212.00	211.25	Left	653.00	651.50	148.850
	Back	550.00	550.00		Right	212.00	211.00		Rigth	650.00		

Dimensions and masses of triplets built for the bond wrench tests:

Specimen	Height [mm]			Width [mm]			Length [mm]			Thickness of bed joint [mm]				Mass [kg]
										Bed joint 1		Bed joint 2		
	Left	Right	Average	Top	Bottom	Average	Top	Bottom	Average	Front	Back	Front	Back	
BWBSCL_14	163.06	164.41	**163.74**	100.93	101.44	**100.93**	212.32	211.23	**211.78**	9.99	10.39	7.89	5.32	6.957
										10.61	9.68	9.28	4.38	
BWBSCL_15	170.02	170.76	**170.39**	101.31	101.61	**101.61**	211.39	210.92	**211.16**	12.26	12.32	12.36	9.02	7.108
										12.10	13.50	13.59	8.01	
BWBSCL_16	164.41	165.07	**164.74**	101.41	101.32	**101.32**	212.83	211.18	**212.01**	9.40	9.38	8.93	5.62	6.971
										9.64	8.62	8.46	6.93	

BWBSCL_17	165.58	164.89	**165.24**	101.70	101.63	**101.63**	212.09	211.99	**212.04**	9.69	9.88	9.09	5.60	6.960
										9.65	10.38	8.84	7.03	
BWBSCL_18	168.35	169.73	**169.04**	101.13	101.49	**101.49**	211.74	210.28	**211.01**	10.52	10.17	11.51	8.50	7.097
										10.84	11.29	13.08	7.97	
BWBSCL_19	162.68	165.87	**164.28**	101.39	101.50	**101.50**	212.18	211.26	**211.72**	8.87	10.18	7.53	7.30	6.926
										12.57	7.90	9.70	5.76	
BWBSCL_20	164.66	166.35	**165.51**	102.00	101.78	**101.78**	212.62	211.64	**212.13**	8.84	9.54	9.19	5.33	7.006
										10.25	11.09	9.48	4.40	
BWBSCL_21	168.25	167.26	**167.76**	101.71	101.95	**101.95**	212.25	210.08	**211.17**	10.08	13.68	11.58	5.23	7.061
										12.05	12.16	9.35	6.45	
BWBSCL_22	165.62	166.92	**166.27**	101.41	101.45	**101.45**	212.77	211.14	**211.96**	10.88	12.79	10.43	6.02	7.009
										12.30	10.51	9.64	6.69	
BWBSCL_23	165.15	165.17	**165.16**	102.13	102.07	**102.07**	211.87	212.03	**211.95**	9.36	7.30	9.83	5.38	6.987
										10.67	9.10	8.34	5.02	
BWBSCL_24	167.03	168.65	**167.84**	101.67	101.47	**101.47**	212.01	211.66	**211.84**	9.59	12.83	11.13	8.23	7.061
										12.22	10.22	10.52	9.28	
BWBSCL_25	166.50	167.66	**167.08**	101.22	101.46	**101.46**	212.54	210.45	**211.78**	9.54	8.58	10.08	9.94	7.026
										10.00	8.78	11.43	7.37	
BWBSCL_26	167.72	168.93	**168.33**	100.58	100.99	**100.99**	210.07	210.88	**211.16**	10.78	12.90	10.90	7.72	7.023
										11.53	12.50	11.87	6.87	

Dimensions and masses of triplets built for the shear strength tests:

Specimen	Block	Length [mm]			Block	Width [mm]				Height [mm]			Thickness of bed joint [mm]				Mass
		Front	Back	Average		TOP	Middle	LOW	Average	Individual values		Average	Bed joint 1		Bed joint 2		[kg]
										L	R		Front	Back	Front	Back	
TBSCL_1	1	173.53	173.48	173.61	1	99.56	100.73	99.68	100.55	213.12	214.08	213.60	15.05	14.01	13.32	11.48	7.450
	2	173.83	173.56		2	102.09		101.36					13.63	13.13	13.01	11.46	
	3	173.93	173.31		3	99.42	100.64	99.74									
TBSCL_2	1	172.76	170.46	172.85	1	98.93	100.53	99.98	100.55	212.30	213.54	212.92	14.21	13.86	11.36	9.66	7.450
	2	173.90	174.41		2	101.52		102.32					14.42	13.01	10.86	10.18	
	3	173.02	172.56		3	99.47	100.49	99.79									
TBSCL_3	1	173.01	171.00	172.91	1	100.22	100.97	99.47	100.82	213.51	213.29	213.40	12.40	9.89	12.02	10.07	7.400
	2	174.12	173.32		2	102.51		101.81					13.10	11.78	13.14	10.36	
	3	173.65	172.36		3	99.76	101.12	99.33									
TBSCL_4	1	172.86	171.78	171.90	1	100.10	101.14	99.49	100.72	213.66	213.53	213.60	13.13	11.76	13.80	11.40	7.350
	2	172.63	171.63		2	102.26		101.74					13.20	12.19	11.91	9.85	
	3	171.87	170.62		3	100.23	100.13	99.36									
TBSCL_5	1	171.67	170.68	171.41	1	100.07	101.10	99.59	101.00	212.69	212.72	212.71	13.47	10.71	9.69	10.84	7.350
	2	171.88	171.45		2	102.28		102.42					14.03	10.65	10.95	10.28	
	3	172.00	170.77		3	100.18	100.90	100.13									
TBSCL_6	1	171.97	170.03	171.78	1	100.37	100.79	99.59	101.00	214.06	212.22	213.14	14.46	11.55	11.58	11.03	7.350
	2	171.80	170.41		2	102.72		101.79					15.71	13.17	11.97	9.96	

Specimen	Block	Length [mm]			Block	Width [mm]				Height [mm]			Thickness of bed joint [mm]				Mass
		Front	Back	Average		TOP	Middle	LOW	Average	Individual values L	Individual values R	Average	Bed joint 1 Front	Bed joint 1 Back	Bed joint 2 Front	Bed joint 2 Back	[kg]
	3	173.60	172.88		3	100.32	100.91	100.25									
TBSCL_7	1	173.88	172.93		1	100.58	101.10	99.61		212.03	211.91	211.97	16.11	14.40	11.59	10.76	
	2	172.32	170.56	172.58	2	102.85		102.06	101.17				14.71	12.06	11.78	10.73	7.350
	3	173.31	172.47		3	100.76	101.24	99.88									
TBSCL_8	1	170.91	170.04		1	99.46	101.19	99.90		213.02	213.78	213.37	14.14	9.73	10.83	10.64	
	2	171.57	170.71	171.01	2	102.13		101.12	100.64				13.55	10.52	11.90	10.02	7.300
	3	172.20	170.64		3	99.74	100.80	99.78									
TBSCL_9	1	171.38	169.84		1	99.37	102.01	99.66		212.96	210.91	211.94	13.88	9.66	11.03	11.11	
	2	171.90	171.41	170.67	2	101.10		102.49	100.70				13.11	9.62	10.50	10.28	7.300
	3	170.16	169.31		3	99.31	100.83	99.72									
TBSCL_10	1	170.84	171.20		1	99.33	101.64	100.84		213.30	213.28	213.88	12.65	11.52	10.57	11.58	
	2	171.52	172.23	171.72	2	101.15		103.27	101.07				14.34	11.46	10.67	11.52	7.350
	3	172.30	172.21		3	99.49	100.57	101.14									
TBSCL_11	1	172.72	173.07		1	99.63	101.67	100.35		213.04	212.93	212.99	13.60	10.59	12.14	13.04	
	2	172.96	173.82	173.15	2	101.73		103.34	101.17				15.36	12.46	11.28	11.84	7.400
	3	173.15	173.18		3	99.45	100.49	101.36									
TBSCL_12	1	171.40	171.46		1	99.34	101.62	99.91		213.16	212.60	212.88	14.35	8.66	12.43	12.52	
	2	171.40	171.98	171.55	2	101.55		101.79	100.64				13.69	10.58	10.71	10.90	7.350
	3	171.41	171.63		3	99.22	100.63	100.04									
TBSCL_13	1	169.54	168.50		1	99.85	101.60	99.71		213.21	213.24	213.23	10.93	7.19	11.23	10.87	
	2	170.89	170.54	170.16	2	102.09		101.46	100.79				10.99	10.60	10.44	11.33	7.300
	3	171.82	169.68		3	100.17	100.68	99.78									
TBSCL_14	1	171.34	171.98		1	100.17	101.51	101.00		213.58	213.20	213.39	11.76	9.15	11.53	12.07	
	2	170.95	171.99	171.96	2	101.89		103.45	101.32				14.76	12.08	12.61	12.57	7.350
	3	172.39	173.08		3	99.91	100.44	100.88									
TBSCL_15	1	171.73	171.68		1	99.97	101.69	99.51		212.77	211.11	211.94	14.04	11.36	10.28	11.36	
	2	171.34	172.13	171.66	2	100.65		102.22	100.64				12.83	11.03	12.39	11.46	7.300
	3	171.64	171.44		3	99.71	101.25	99.36									
TBSCL_16	1	170.78	171.11		1	99.75	101.59	100.25		213.26	213.04	213.15	11.80	9.02	10.77	12.26	
	2	171.05	170.84	170.81	2	100.95		103.11	100.98				12.99	9.68	12.22	14.15	7.300
	3	170.79	170.26		3	99.83	100.98	100.32									

Determination of bulk density for simple and double wallettes:

Specimen	Length [m]	Width [m]	Height [m]	Mass [kg]	Bulk density [kg/m^3]
CTBSCL_1S	0.43350	0.10075	0.47100	40.5	1968.79
CTBSCL_2S	0.43375	0.10100	0.47300	40.75	1966.55
CTBSCL_3S	0.43775	0.10000	0.47250	41.1	1987.07
CTBSCL_4S	0.43775	0.09950	0.47300	40.8	1980.39
CTBSCL_5S	0.43650	0.10000	0.47150	40.8	1982.41
CTBSCL_6S	0.43450	0.10000	0.47100	40.6	1983.88
CTBSCL_7S	0.43750	0.10075	0.47500	40.65	1941.53
CTBSCL_8S	0.43725	0.09925	0.47000	40.9	2005.23
				Average	**1976.98**
CTBSCL_1D	0.54000	0.21200	0.65050	145.1	1948.46
CTBSCL_2D	0.54300	0.21100	0.65150	146.6	1963.98
CTBSCL_3D	0.54175	0.21275	0.65200	145.7	1938.85
CTBSCL_4D	0.54575	0.21025	0.65000	145.6	1952.17
CTBSCL_5D	0.54675	0.21050	0.64600	146	1963.72
CTBSCL_6D	0.54325	0.21300	0.64850	145.6	1940.31
CTBSCL_7D	0.53975	0.20975	0.65000	146.5	1990.81
CTBSCL_8D	0.54750	0.21125	0.65150	148.85	1975.39
				Average	**1959.21**

Determination of bulk density for triplets for bond wrench tests:

Specimen	Length [m]	Width [m]	Height [m]	Mass [kg]	Bulk density [kg/m^3]
BWBSCL_14	0.21178	0.10093	0.16374	6.957	1987.96
BWBSCL_15	0.21116	0.10161	0.17039	7.108	1944.41
BWBSCL_16	0.21201	0.10132	0.16474	6.971	1970.05
BWBSCL_17	0.21204	0.10163	0.16524	6.96	1954.74
BWBSCL_18	0.21101	0.10149	0.16904	7.097	1960.56
BWBSCL_19	0.21172	0.10150	0.16428	6.926	1961.93
BWBSCL_20	0.21213	0.10178	0.16551	7.006	1960.72
BWBSCL_21	0.21117	0.10195	0.16776	7.061	1955.25
BWBSCL_22	0.21196	0.10145	0.16627	7.009	1960.41
BWBSCL_23	0.21195	0.10207	0.16516	6.987	1955.48
BWBSCL_24	0.21184	0.10147	0.16784	7.061	1957.30
BWBSCL_25	0.21150	0.10146	0.16708	7.026	1959.70
BWBSCL_26	0.21048	0.10099	0.16833	7.023	1962.98
				Average	**1960.88**

Determination of bulk density for triplets for shear strength tests:

Specimen	Length [m]	Width [m]	Height [m]	Mass [kg]	Bulk density [kg/m^3]
TBSCL_1	0.17361	0.10055	0.21360	7.450	1998.01
TBSCL_2	0.17285	0.10055	0.21292	7.450	2013.21
TBSCL_3	0.17291	0.10082	0.21340	7.400	1989.16
TBSCL_4	0.17190	0.10072	0.21360	7.350	1987.44
TBSCL_5	0.17141	0.10100	0.21271	7.350	1995.91
TBSCL_6	0.17178	0.10100	0.21314	7.350	1987.60
TBSCL_7	0.17258	0.10117	0.21197	7.350	1985.96
TBSCL_8	0.17101	0.10064	0.21337	7.300	1987.91
TBSCL_9	0.17067	0.10070	0.21194	7.300	2004.12

Specimen	Length	Width	Height	Mass	Bulk density
TBSCL_10	0.17172	0.10107	0.21388	7.350	1980.04
TBSCL_11	0.17315	0.10117	0.21299	7.400	1983.34
TBSCL_12	0.17155	0.10064	0.21288	7.350	1999.82
TBSCL_13	0.17016	0.10079	0.21323	7.300	1996.18
TBSCL_14	0.17196	0.10132	0.21339	7.350	1976.93
TBSCL_15	0.17166	0.10064	0.21194	7.300	1993.75
TBSCL_16	0.17081	0.10098	0.21315	7.300	1985.59
				Average	**1991.56**

Geometry and instrumentation layout in simple wallettes for compressive strength tests:

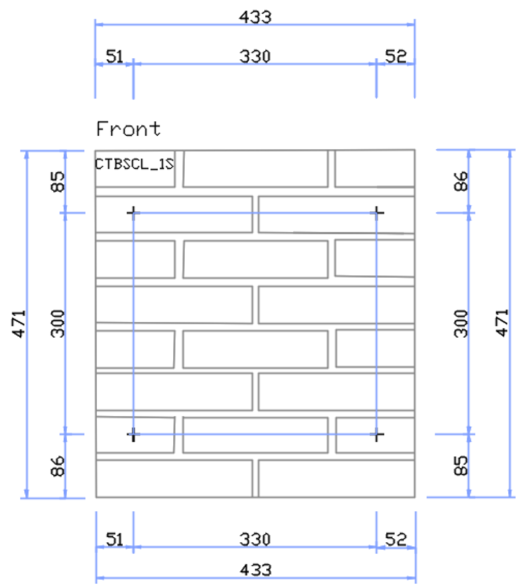

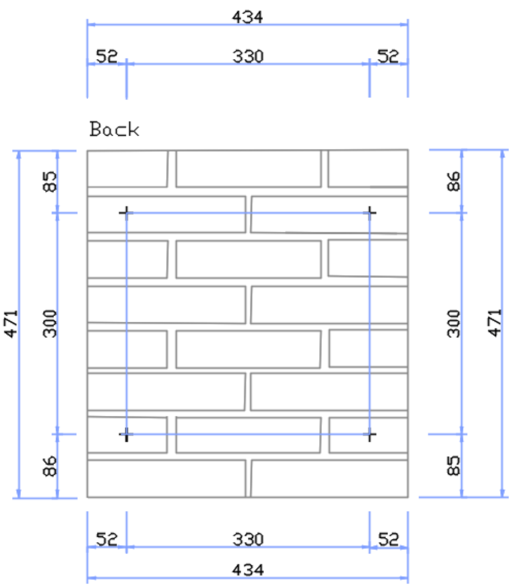

.

Wallette CTBSCL_1S – front side

Wallette CTBSCL_1S – back side

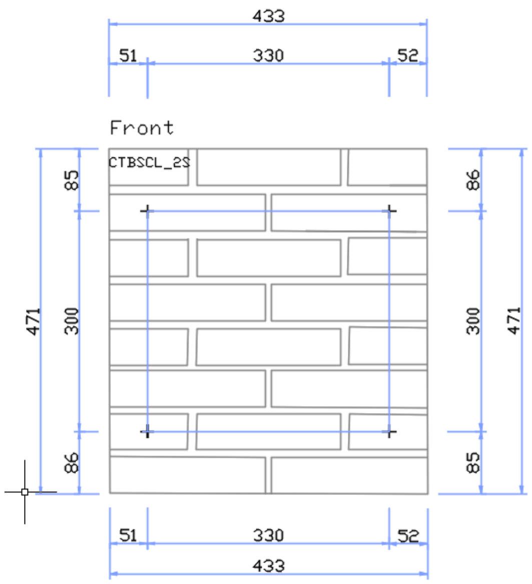

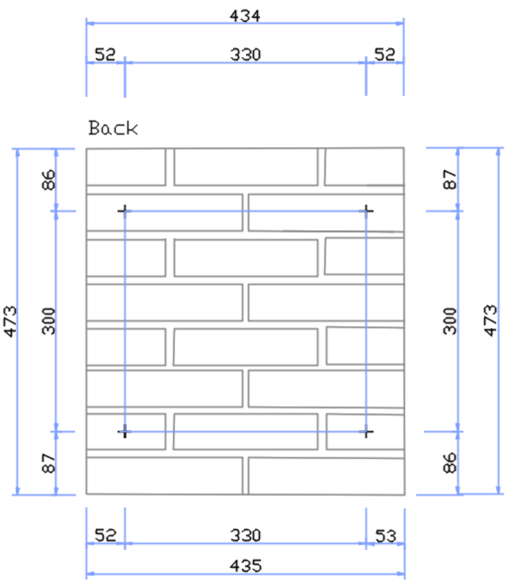

Wallette CTBSCL_2S – front side

Wallette CTBSCL_2S – back side

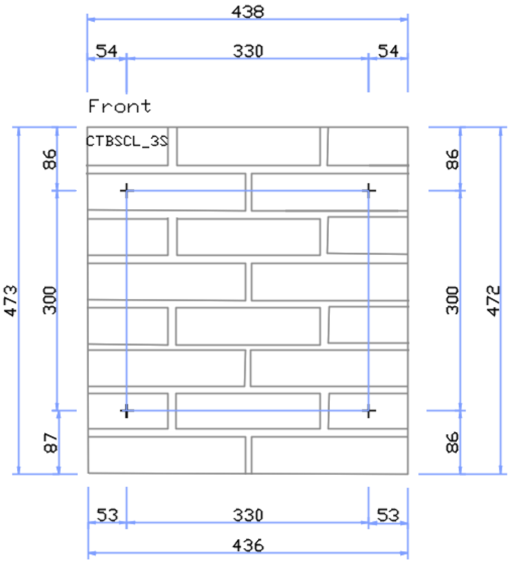

Wallette CTBSCL_3S – front side

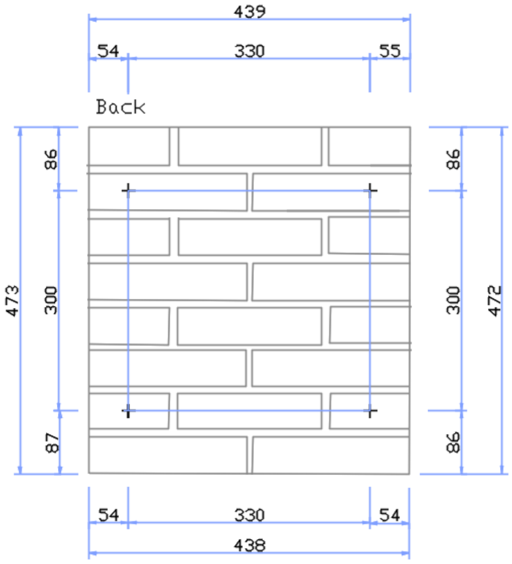

Wallette CTBSCL_3S – back side

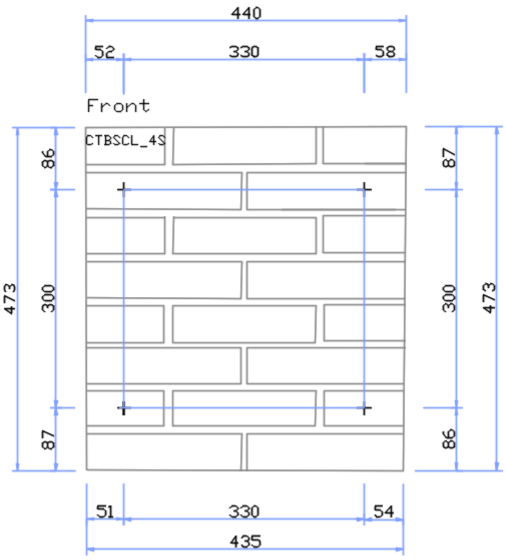

Wallette CTBSCL_4S – front side

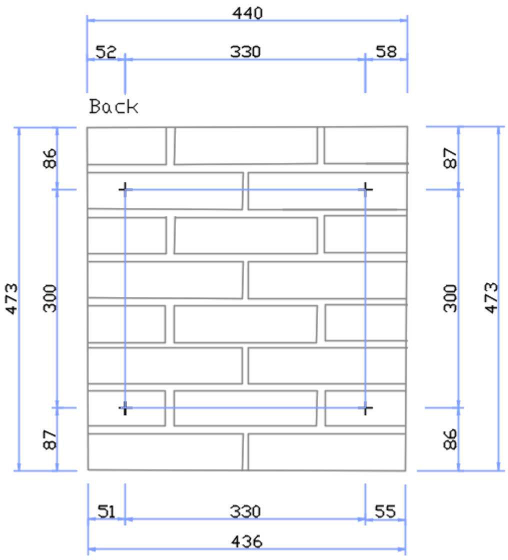

Wallette CTBSCL_4S – back side

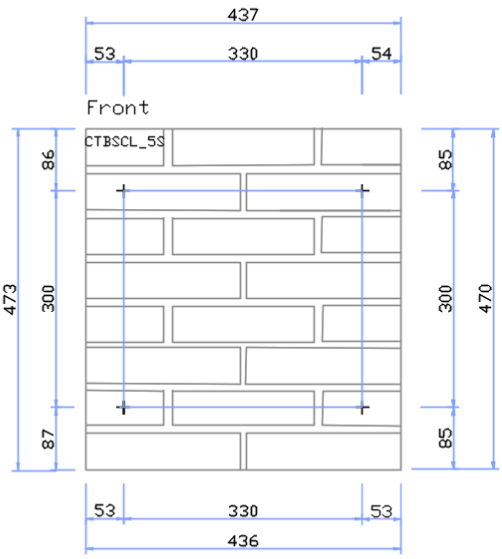

Wallette CTBSCL_5S – front side

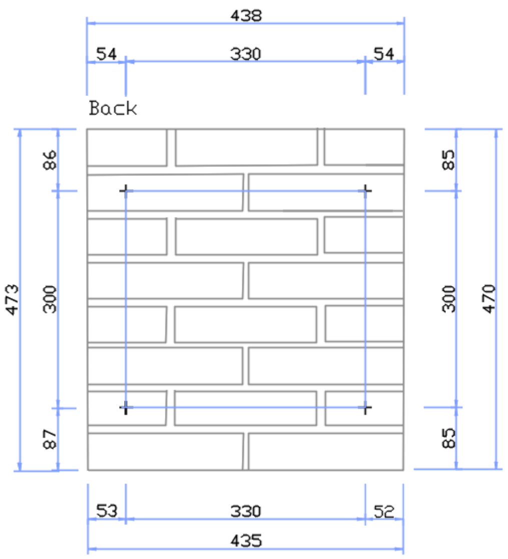

Wallette CTBSCL_5S – back side

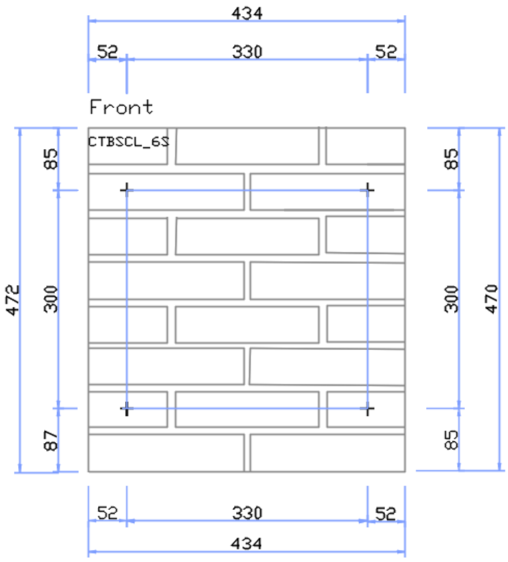

Wallette CTBSCL_6S – front side

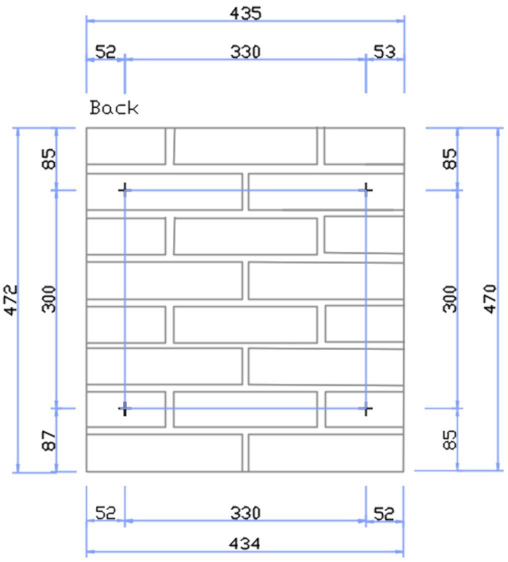

Wallette CTBSCL_6S – back side

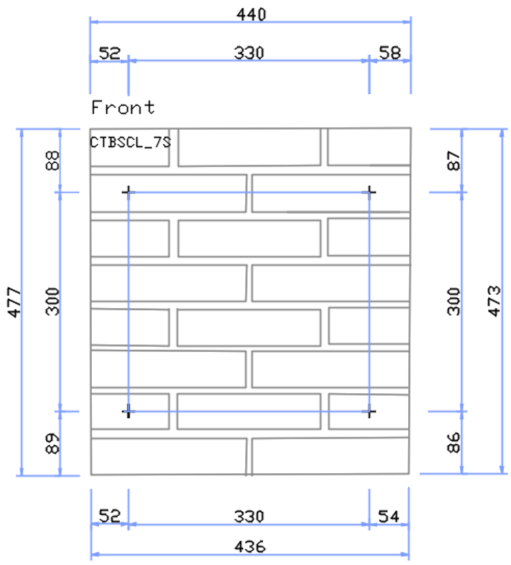

Wallette CTBSCL_7S – front side

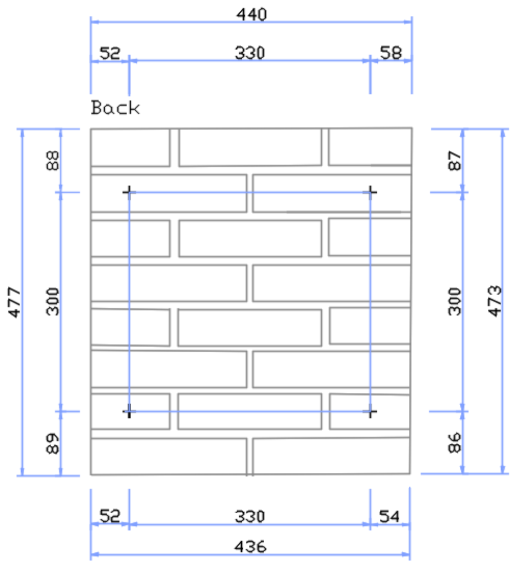

Wallette CTBSCL_8S – back side

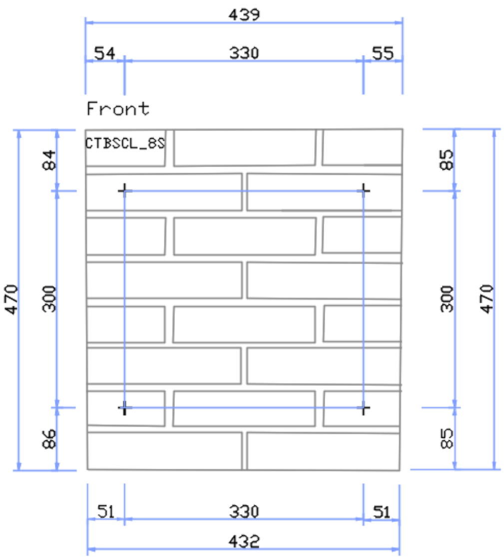

Wallette CTBSCL_8S – front side

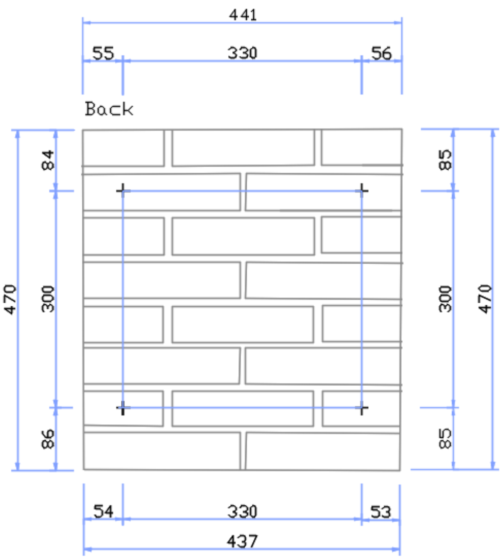

Wallette CTBSCL_8S – back side

Geometry and instrumentation layout in double wallettes for compressive strength tests:

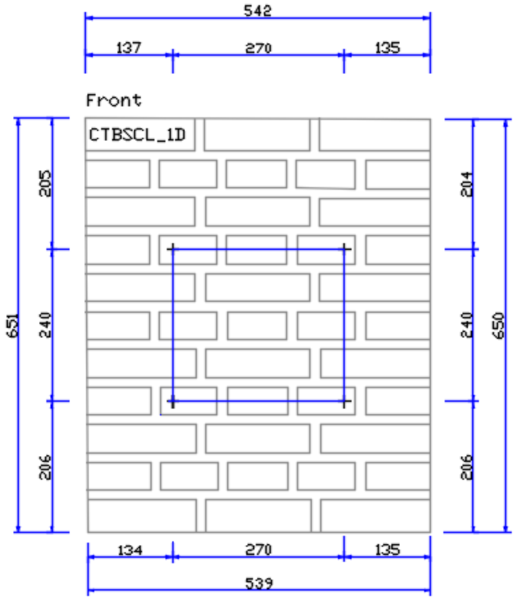

Wallette CTBSCL_1D – front side

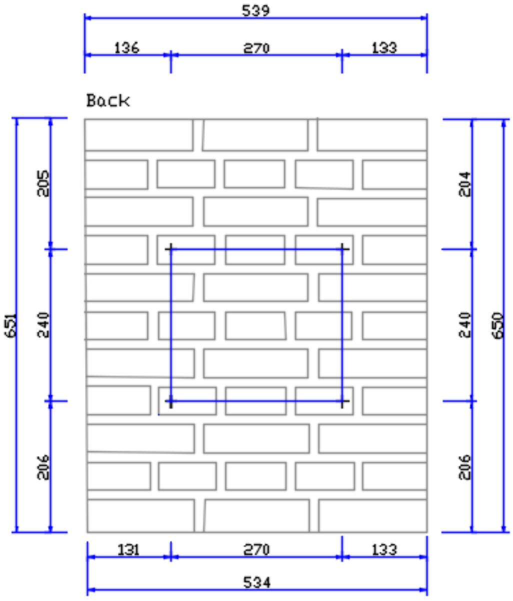

Wallette CTBSCL_1D – back side

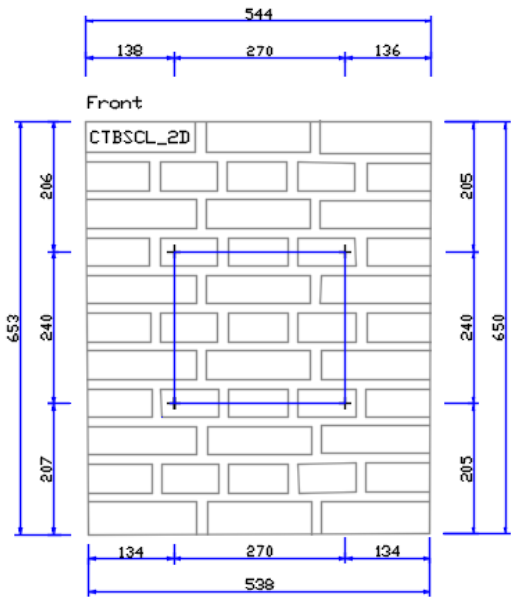

Wallette CTBSCL_2D – front side

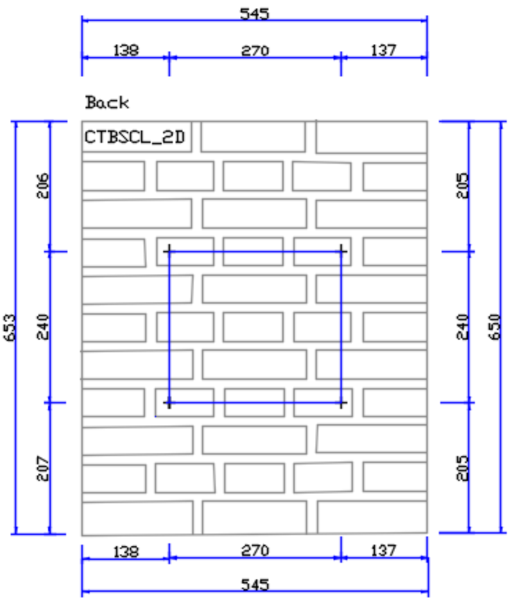

Wallette CTBSCL_2D – back side

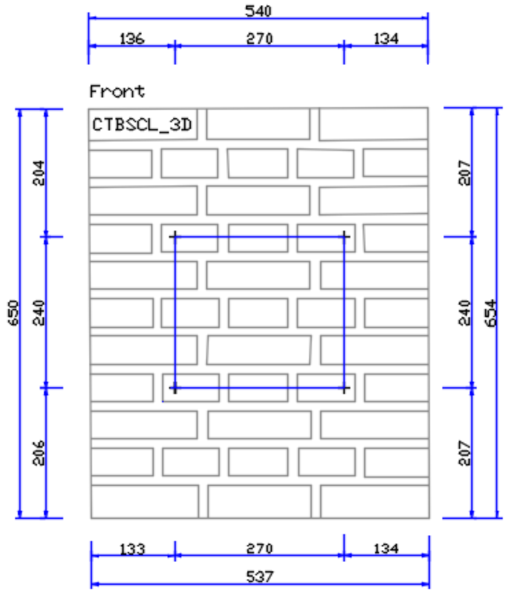

Wallette CTBSCL_3D – front side

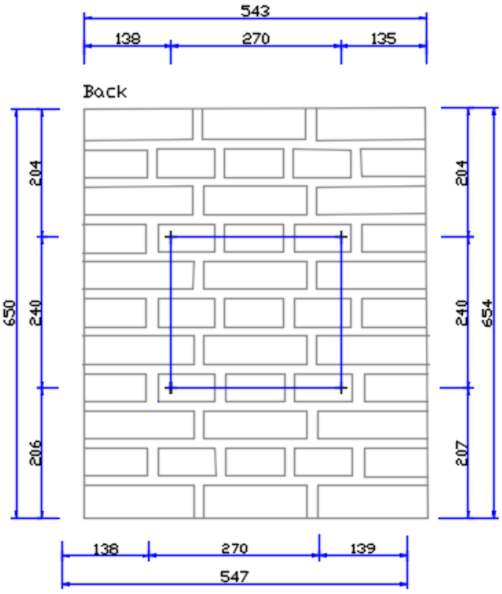

Wallette CTBSCL_3D – back side

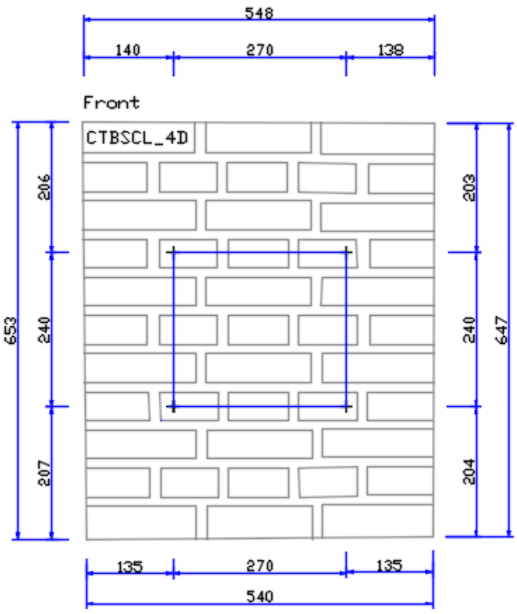

Wallette CTBSCL_4D – front side

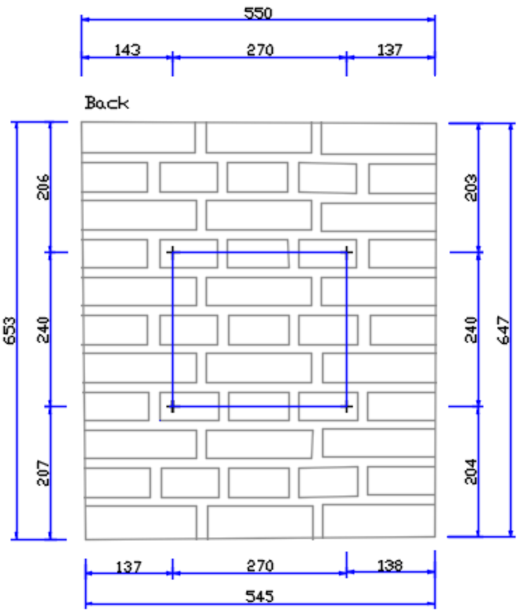

Wallette CTBSCL_4D – back side

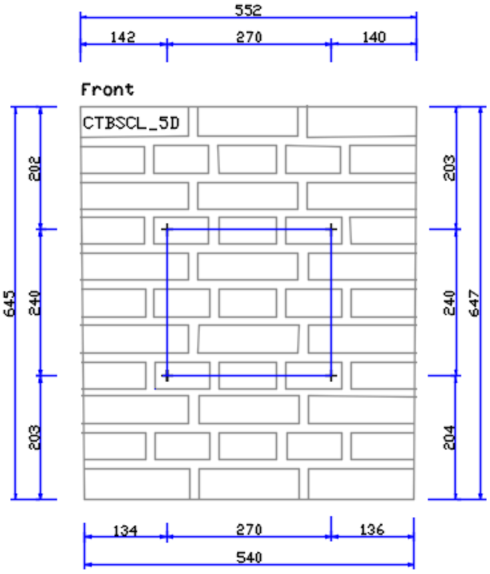

Wallette CTBSCL_5D – front side

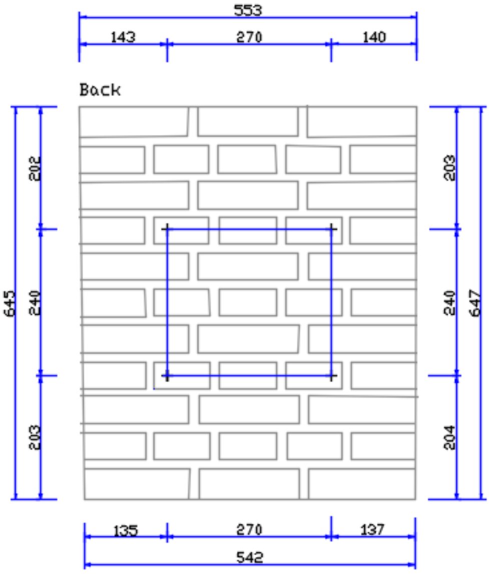

Wallette CTBSCL_5D – back side

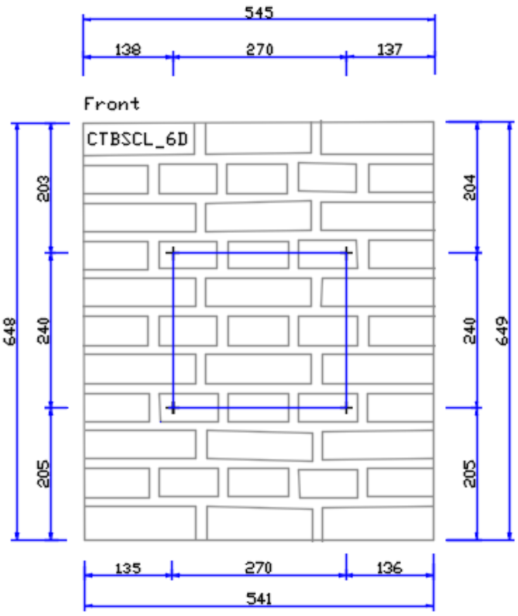

Wallette CTBSCL_6D – front side

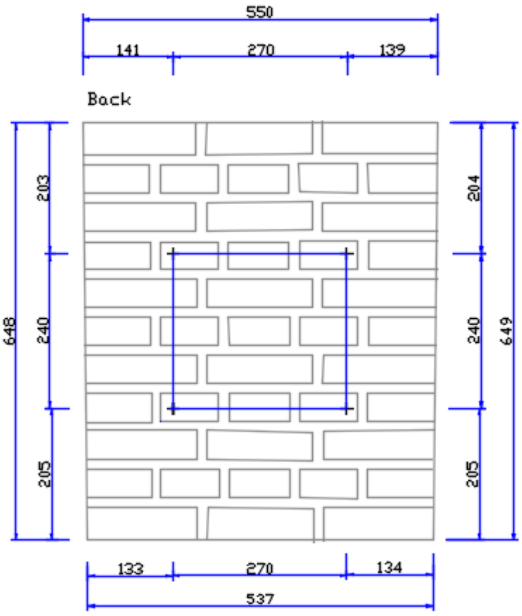

Wallette CTBSCL_6D – back side

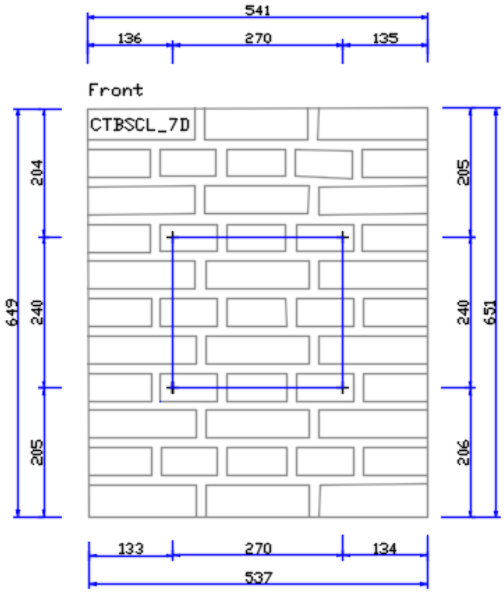

Wallette CTBSCL_7D – front side

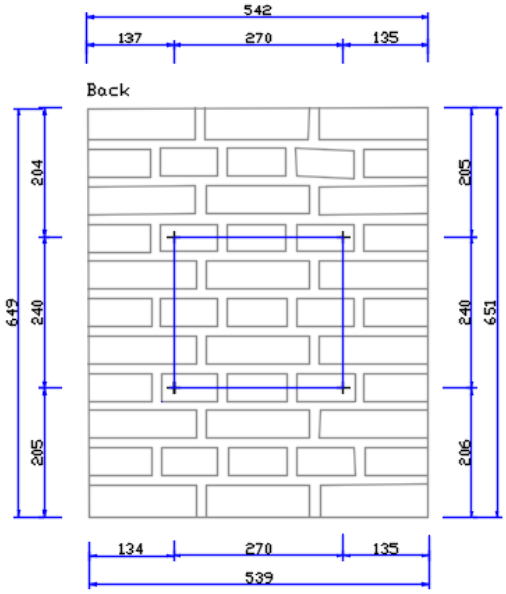

Wallette CTBSCL_7D – back side

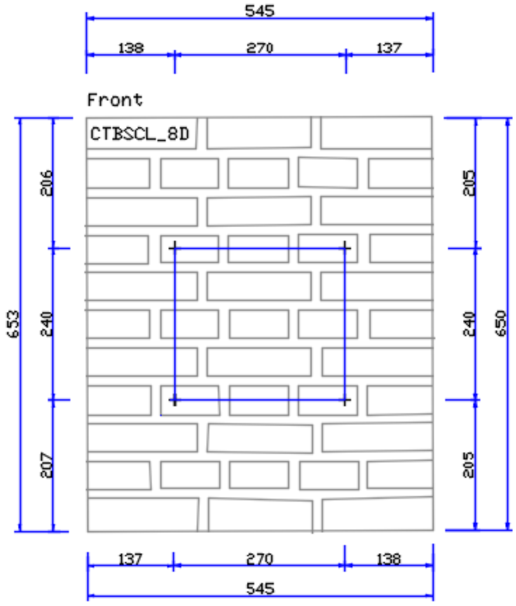

Wallette CTBSCL_8D – front side

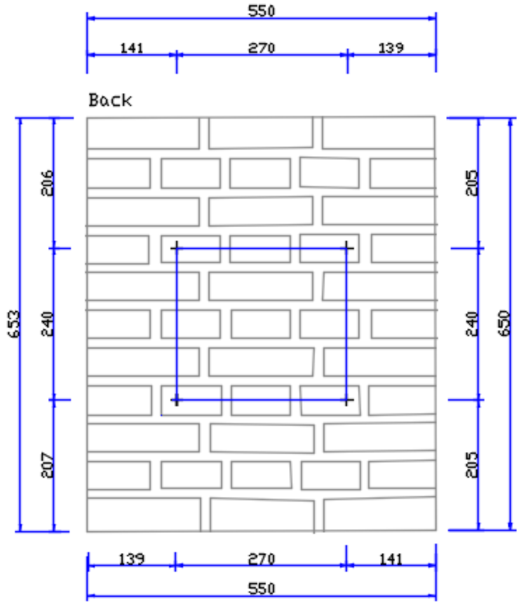

Wallette CTBSCL_8D – back side

Geometry and instrumentation layout in triplets for shear strength tests:

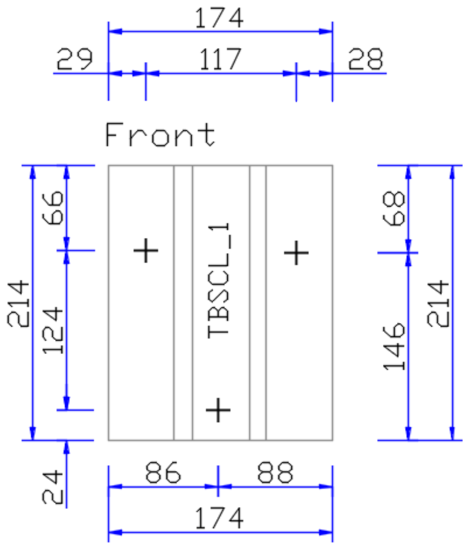

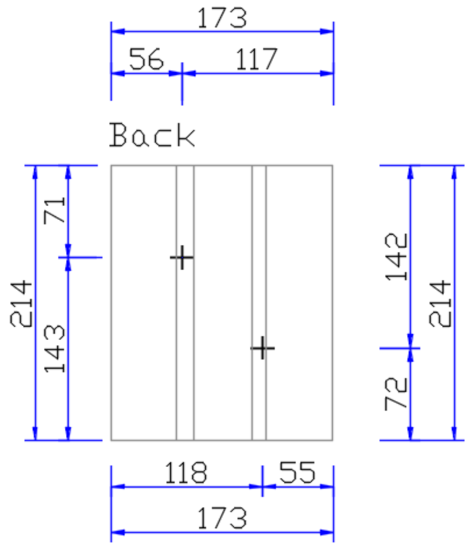

Triplet TBSCL_1 – front side

Triplet TBSCL_1 – back side

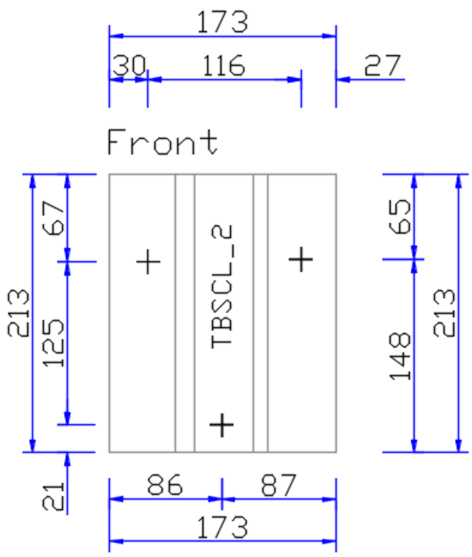

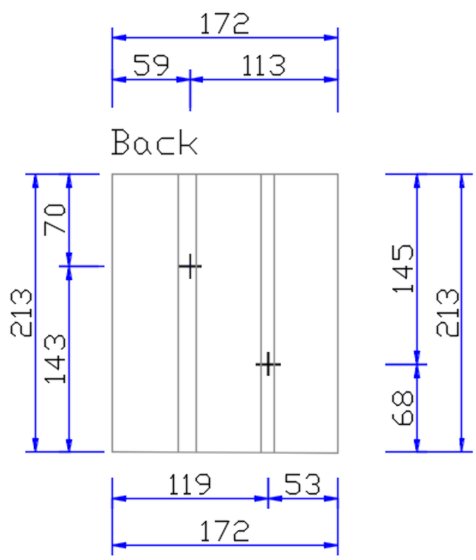

Triplet TBSCL_2 – front side

Triplet TBSCL_2 – back side

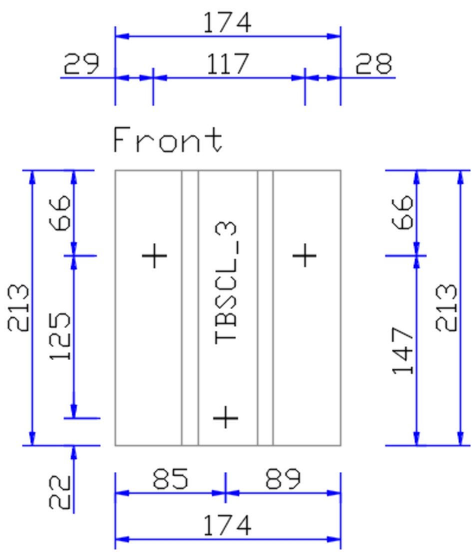

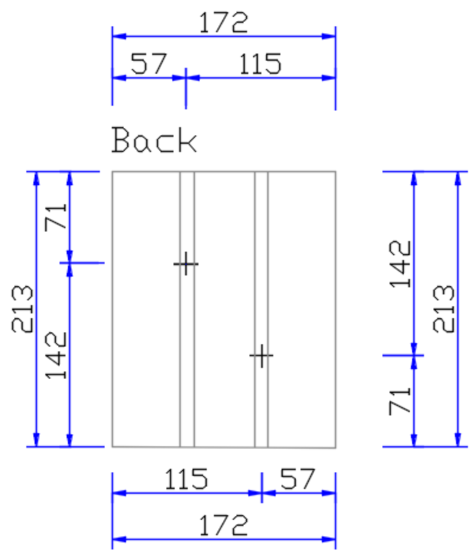

Triplet TBSCL_3 – front side

Triplet TBSCL_3 – back side

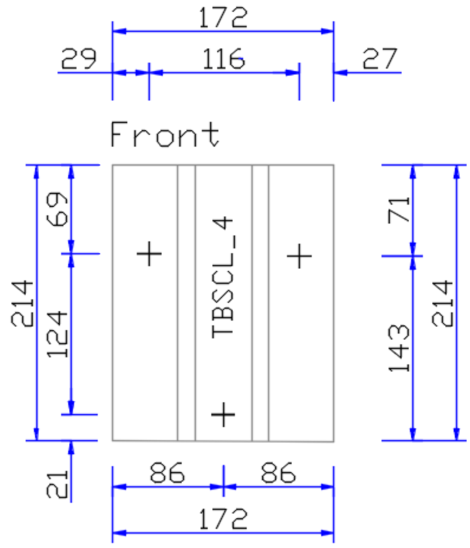

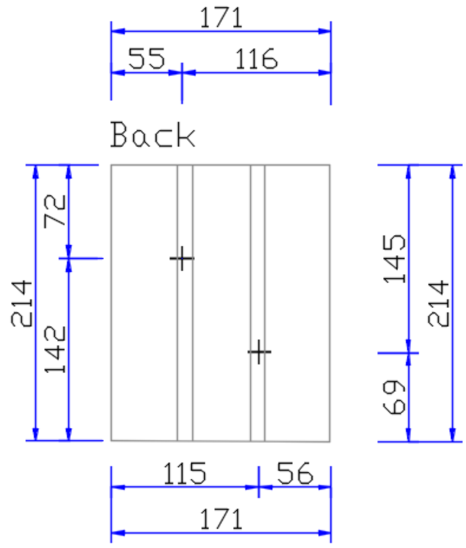

Triplet TBSCL_4 – front side

Triplet TBSCL_4 – back side

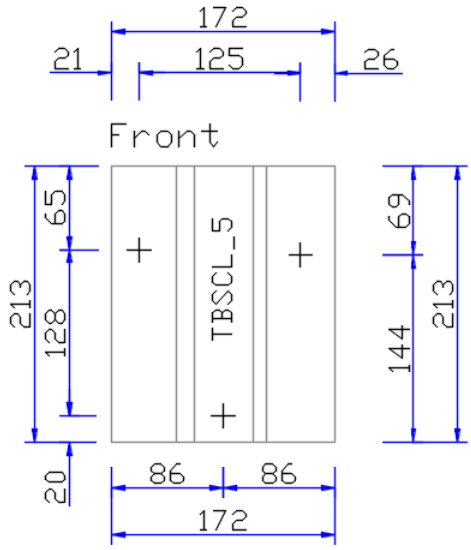

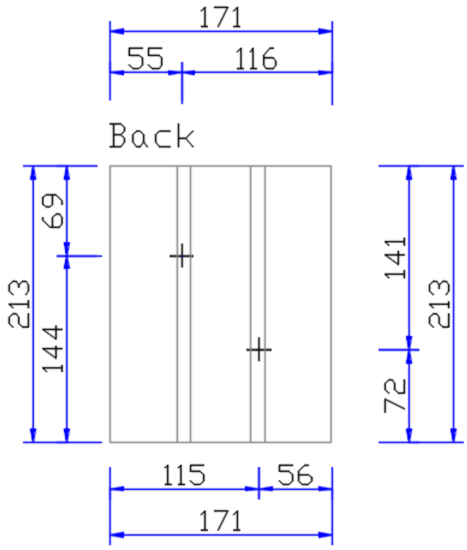

Triplet TBSCL_5 – front side

Triplet TBSCL_5 – back side

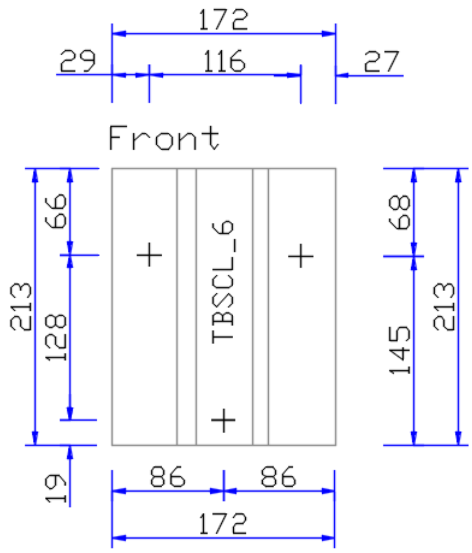

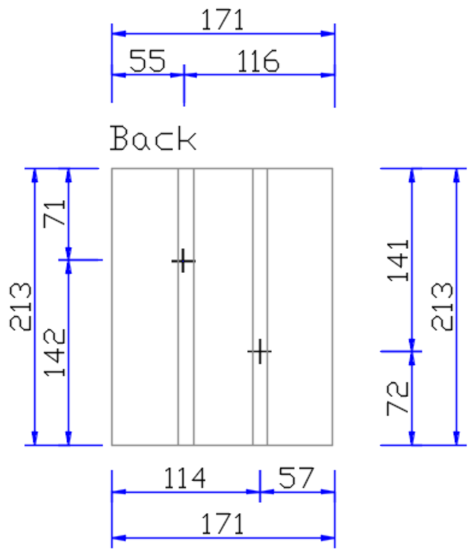

Triplet TBSCL_6 – front side

Triplet TBSCL_6 – back side

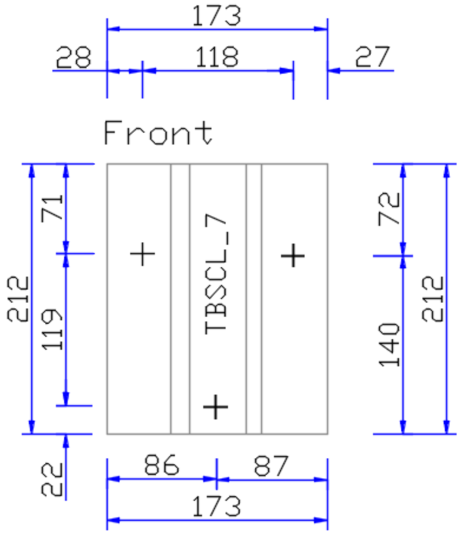

Triplet TBSCL_7 – front side

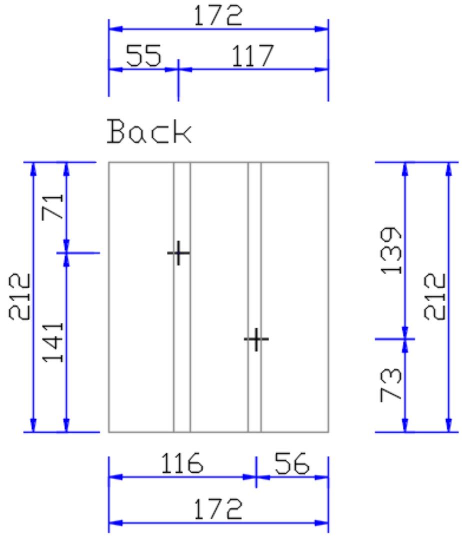

Triplet TBSCL_7 – back side

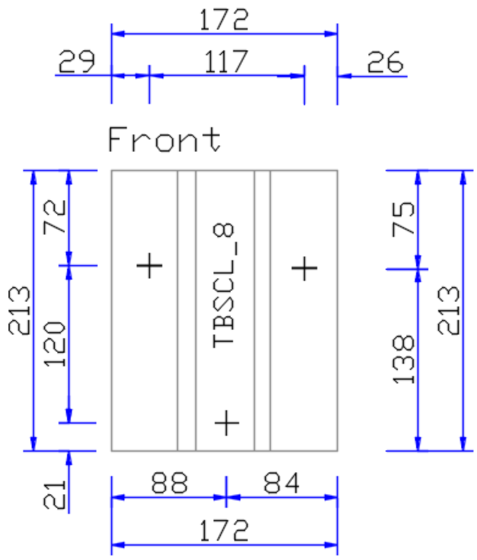

Triplet TBSCL_8 – front side

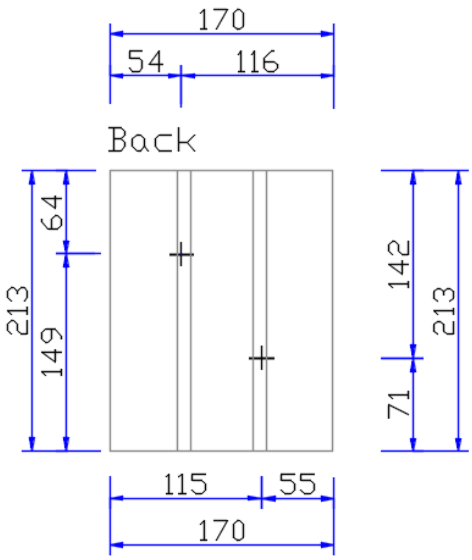

Triplet TBSCL_8 – back side

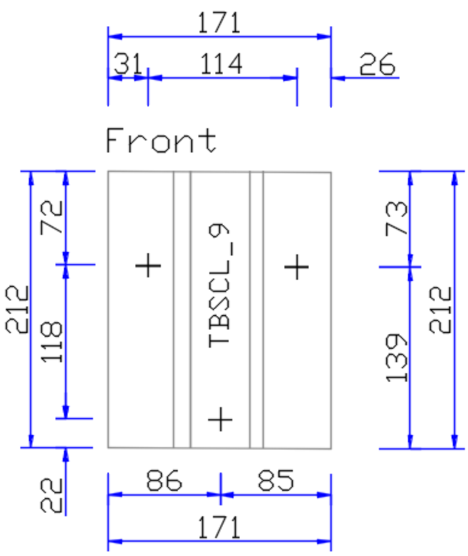

Triplet TBSCL_9 – front side

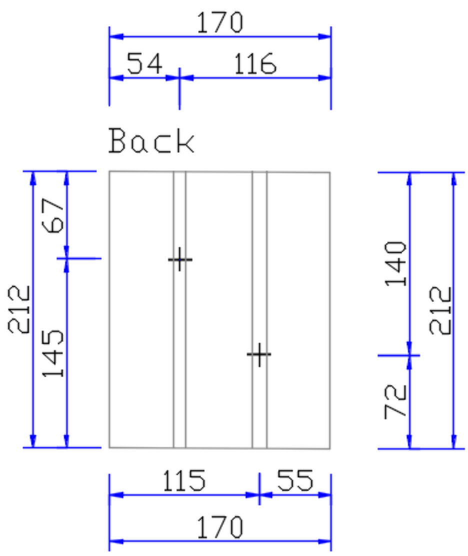

Triplet TBSCL_9 – back side

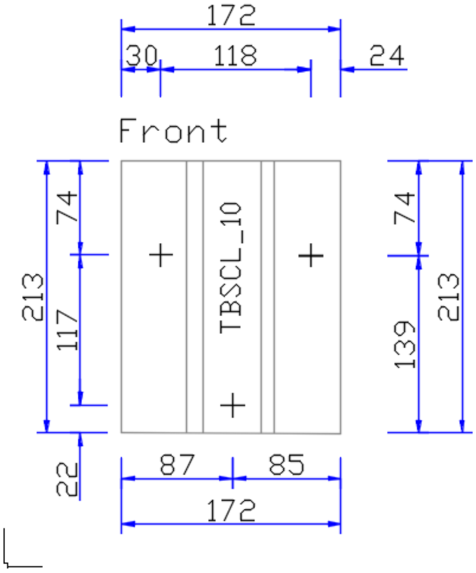

Triplet TBSCL_10 – front side

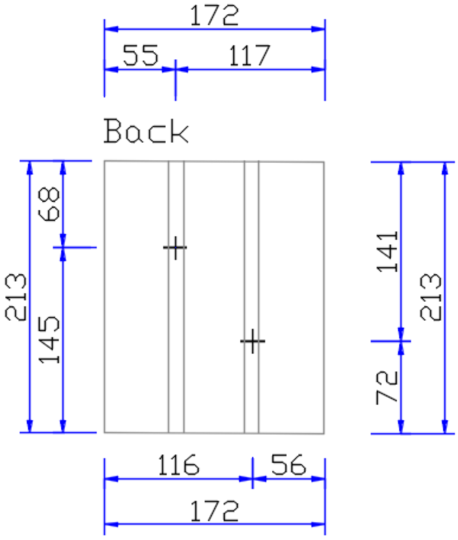

Triplet TBSCL_10 – back side

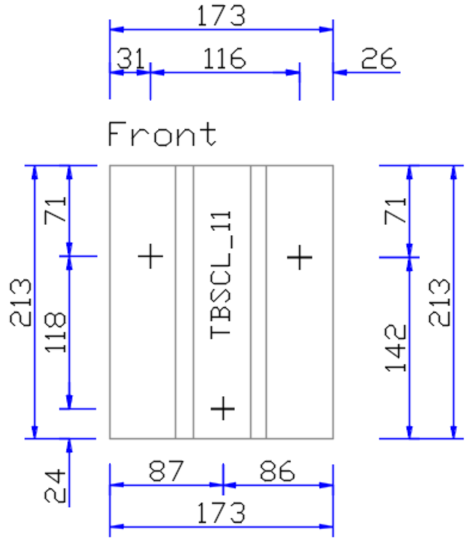

Triplet TBSCL_11 – front side

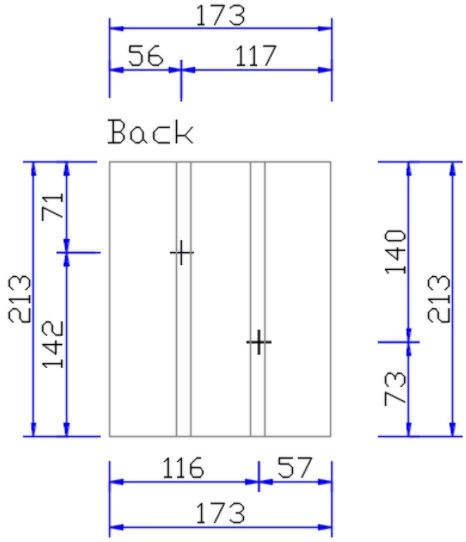

Triplet TBSCL_11– back side

wireframe)

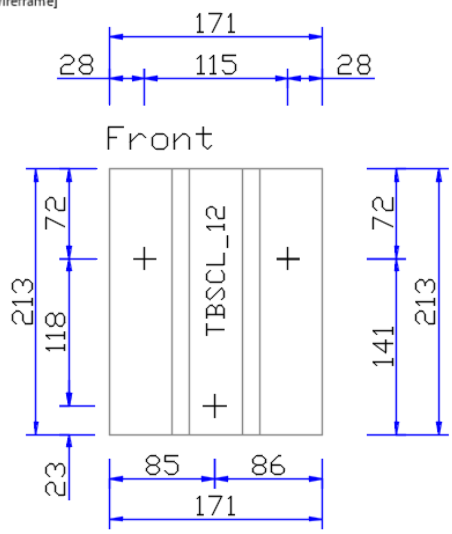

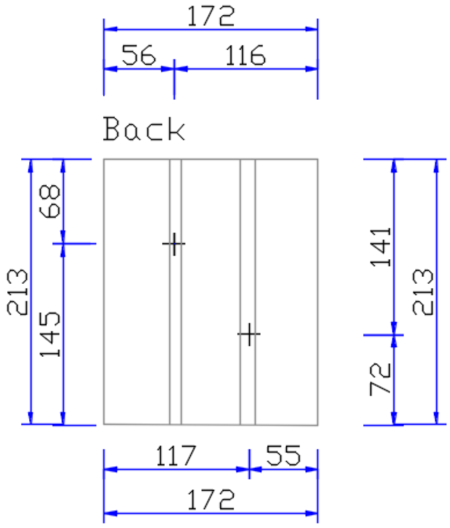

Triplet TBSCL_12 – front side

Triplet TBSCL_12 – back side

APPENDIX I. COLLAPSE MECHANISMS ON WALLETTES AND TRIPLETS FROM MATERIAL CHARACTERISATION TESTS

Failure mechanisms of triplets for shear strength tests:

Wallette CTBSCL_1S – front side

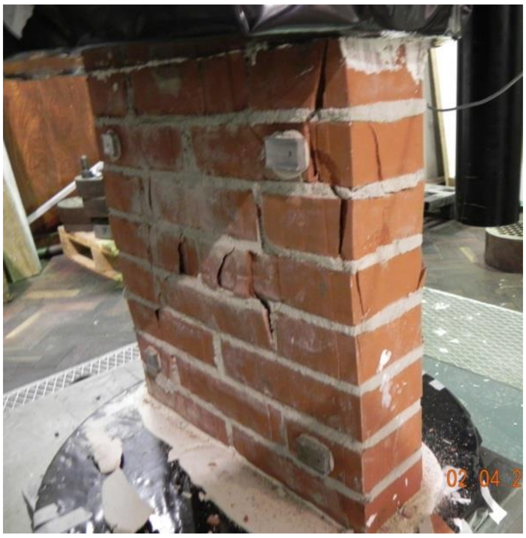

Wallette CTBSCL_1S – back side

Wallette CTBSCL_2S – front side

Wallette CTBSCL_2S – back side

Wallette CTBSCL_3S – front side

Wallette CTBSCL_3S – back side

Wallette CTBSCL_4S – front side

Wallette CTBSCL_4S – back side

Wallette CTBSCL_5S – front side

Wallette CTBSCL_5S – back side

Wallette CTBSCL_6S – front side

Wallette CTBSCL_6S – back side


Wallette CTBSCL_7S – front side


Wallette CTBSCL_7S – back side


Wallette CTBSCL_8S – front side


Wallette CTBSCL_8S – back side

Failure mechanisms of double wallettes for compressive strength tests:

Wallette CTBSCL_1D – front side

Wallette CTBSCL_1D – back side

Wallette CTBSCL_2D – front side

Wallette CTBSCL_2D – back side

Wallette CTBSCL_3D – front side

Wallette CTBSCL_3D – back side

Wallette CTBSCL_4D – front side

Wallette CTBSCL_4D – back side

Wallette CTBSCL_5D – front side

Wallette CTBSCL_5D – back side

Wallette CTBSCL_6D – front side

Wallette CTBSCL_6D – back side

Wallette CTBSCL_7D – front side

Wallette CTBSCL_7D – back side

Wallette CTBSCL_8D – front side

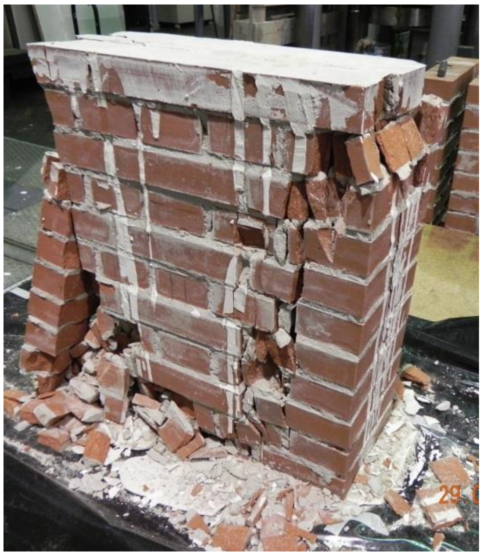

Wallette CTBSCL_8D – back side

Failure mechanisms of triplets for bond wrench tests after 6 weeks:

Triplet BWBSCL_14

Triplet BWBSCL_15

Triplet BWBSCL_16

Triplet BWBSCL_17

Triplet BWBSCL_18

Triplet BWBSCL_19

Triplet BWBSCL_20

Triplet BWBSCL_21

Triplet BWBSCL_22

Triplet BWBSCL_23

Triplet BWBSCL_24

Triplet BWBSCL_25

Triplet BWBSCL_26

Failure mechanisms of triplets for shear tests:

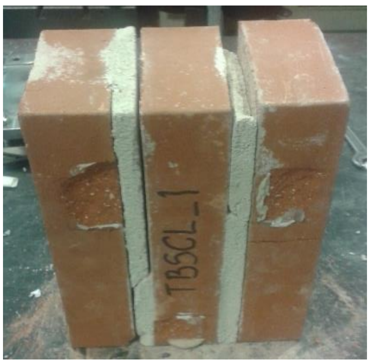

Triplet TBSCL_1

Triplet TBSCL_2

Triplet TBSCL_3

Triplet TBSCL_4

Triplet TBSCL_5

Triplet TBSCL_6

Triplet TBSCL_7

Triplet TBSCL_8

Triplet TBSCL_9

Triplet TBSCL_10

Triplet TBSCL_11

Triplet TBSCL_12

Triplet TBSCL_13

Triplet TBSCL_14

Triplet TBSCL_15

APPENDIX J. INDIVIDUAL RESULTS FROM SHEAR STRENGTH TESTS

Results for solid clay triplets from shear strength tests:

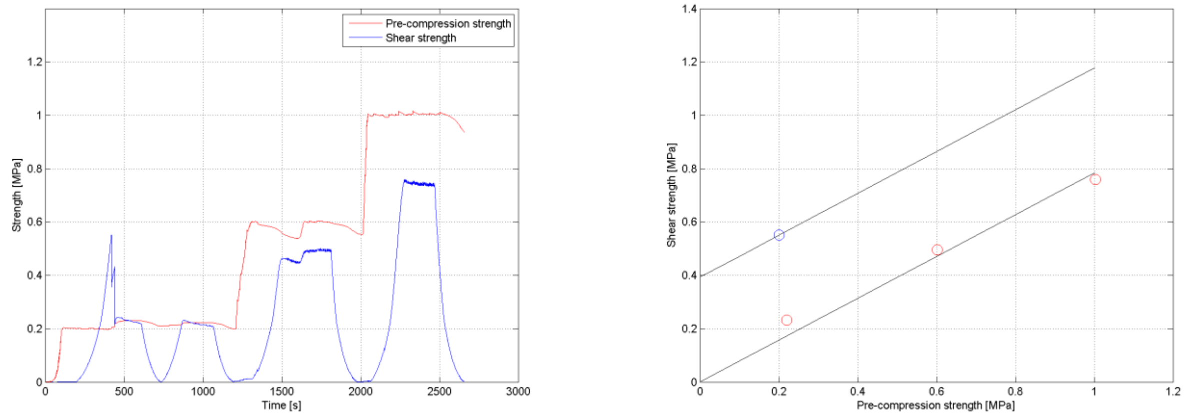

Triplet TBSCL_1

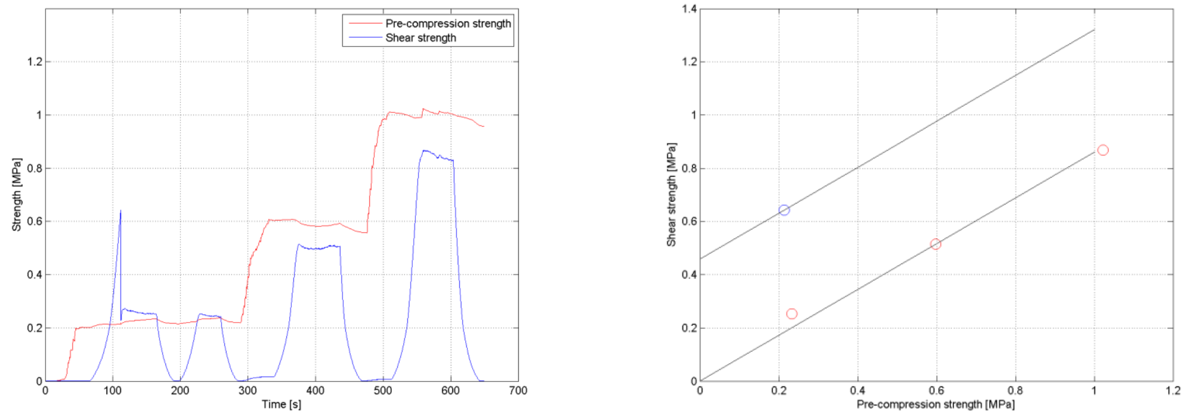

Triplet TBSCL _2

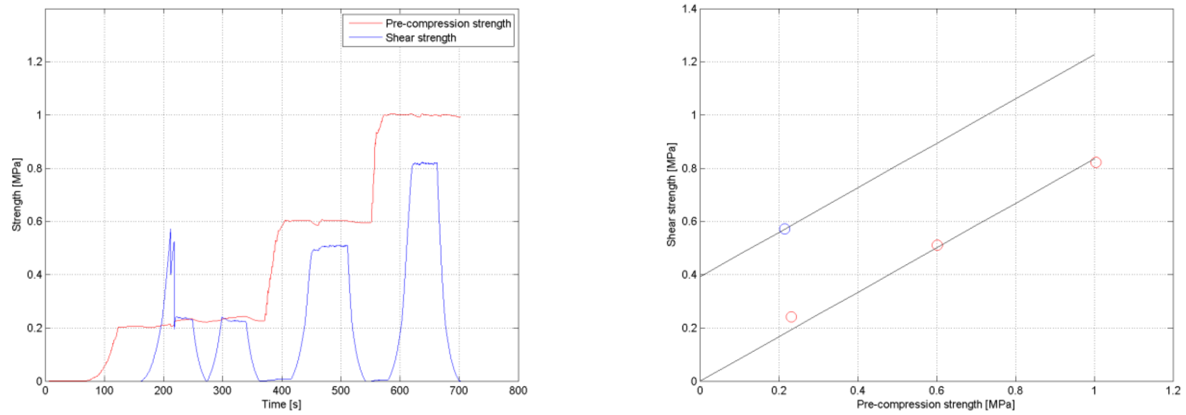

Triplet TBSCL _3

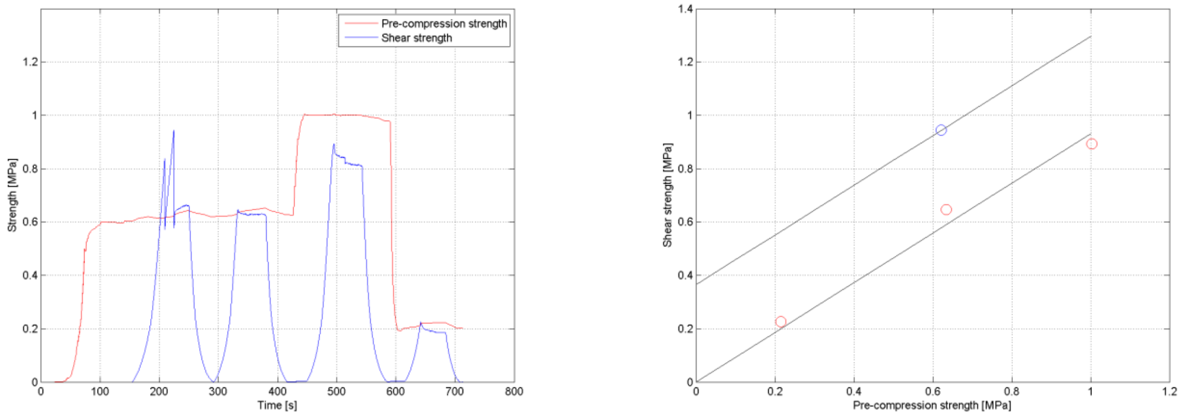

Triplet TBSCL _4

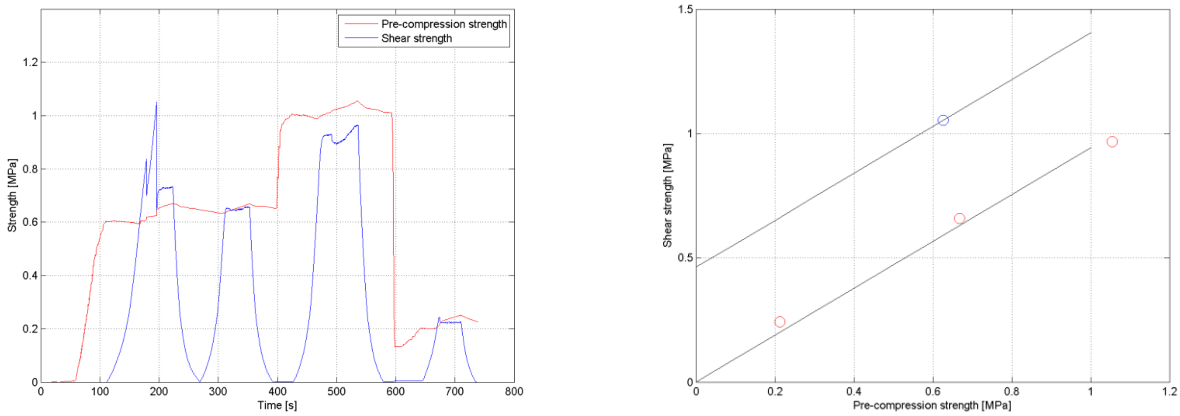

Triplet TBSCL _5

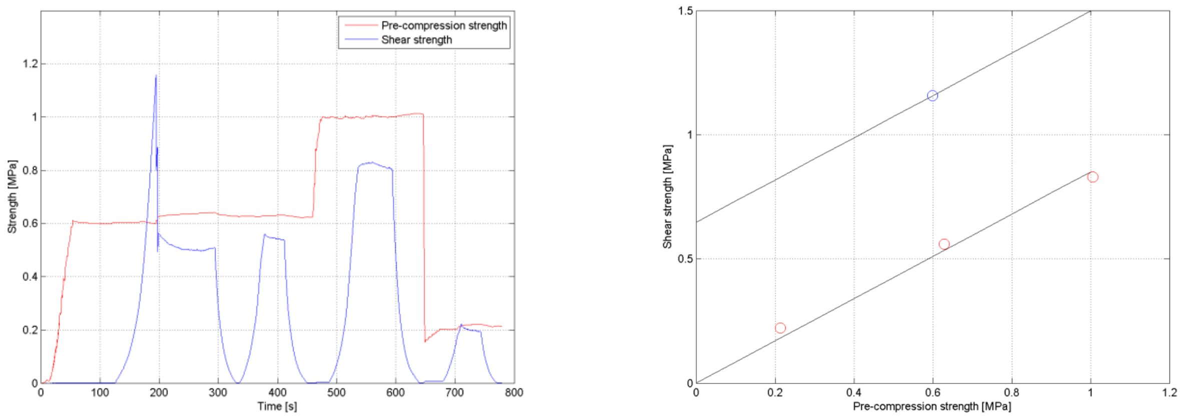

Triplet TBSCL _6

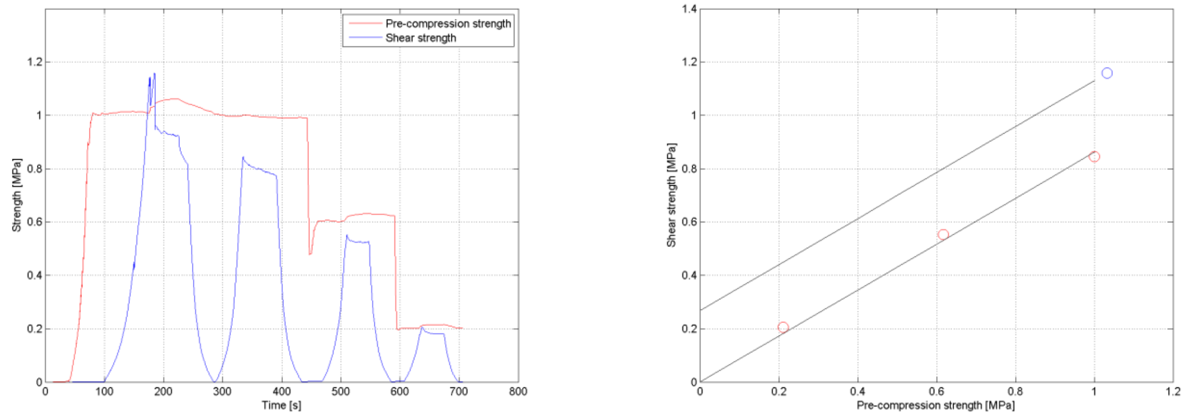

Triplet TBSCL _7

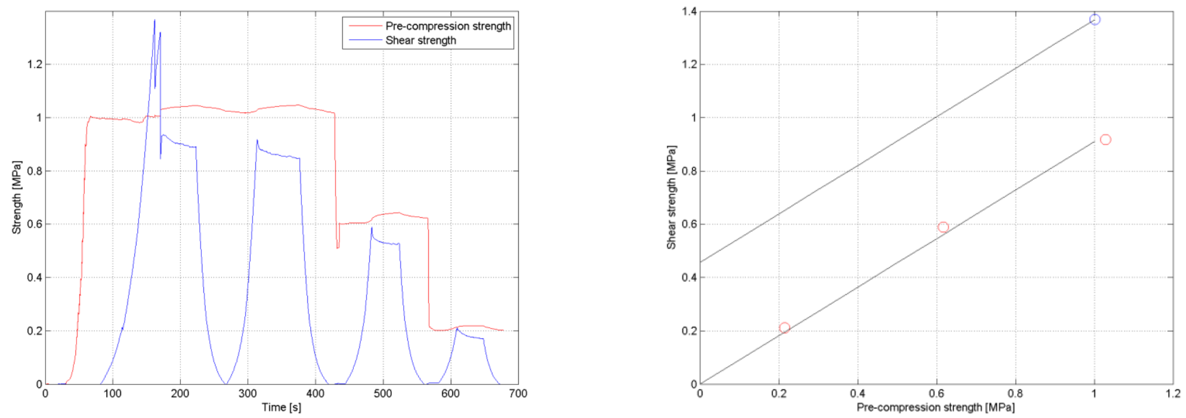

Triplet TBSCL _8

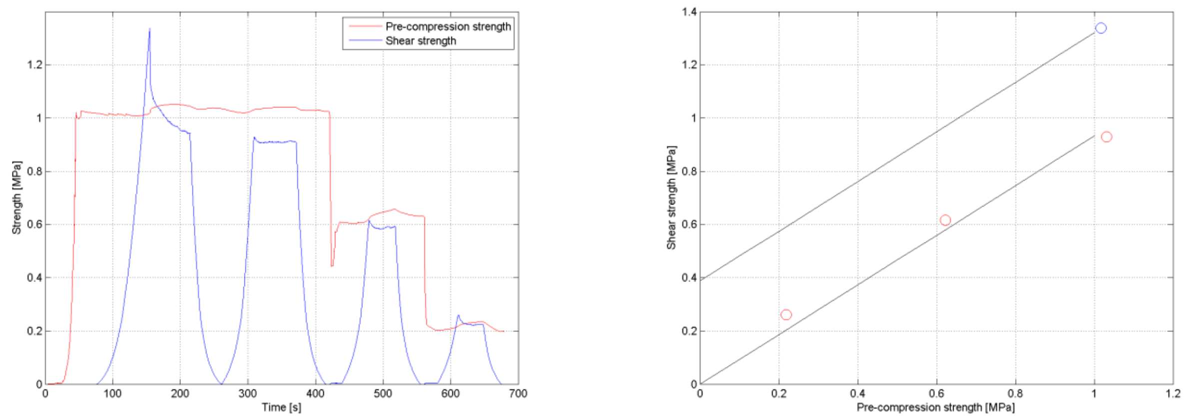

Triplet TBSCL _9

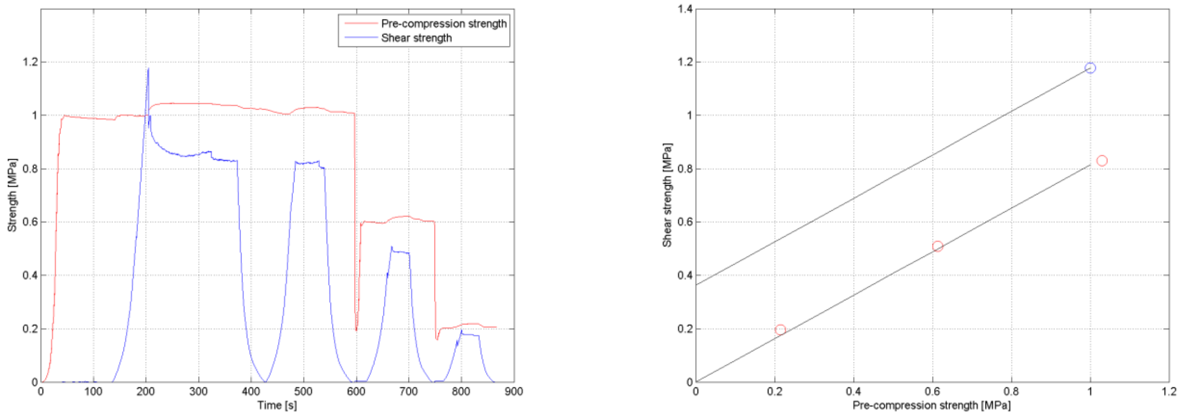

Triplet TBSCL _10

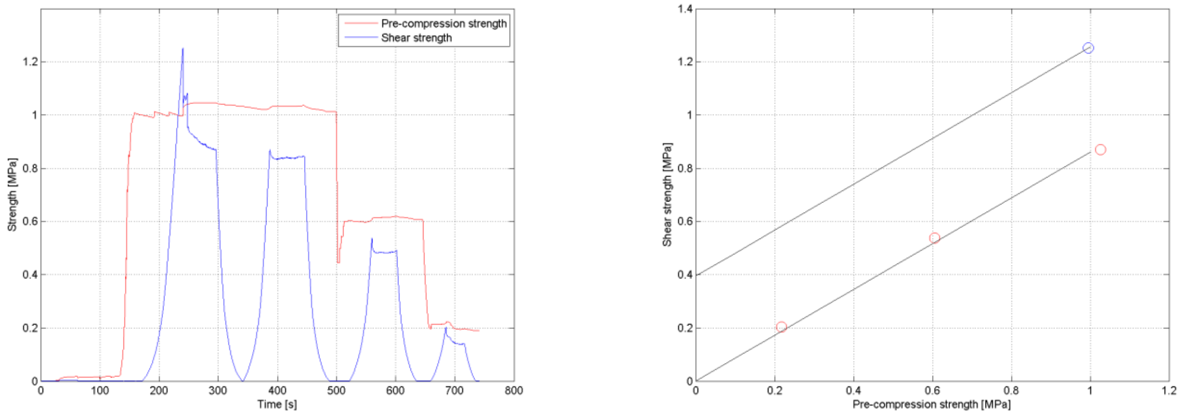

Triplet TBSCL _11

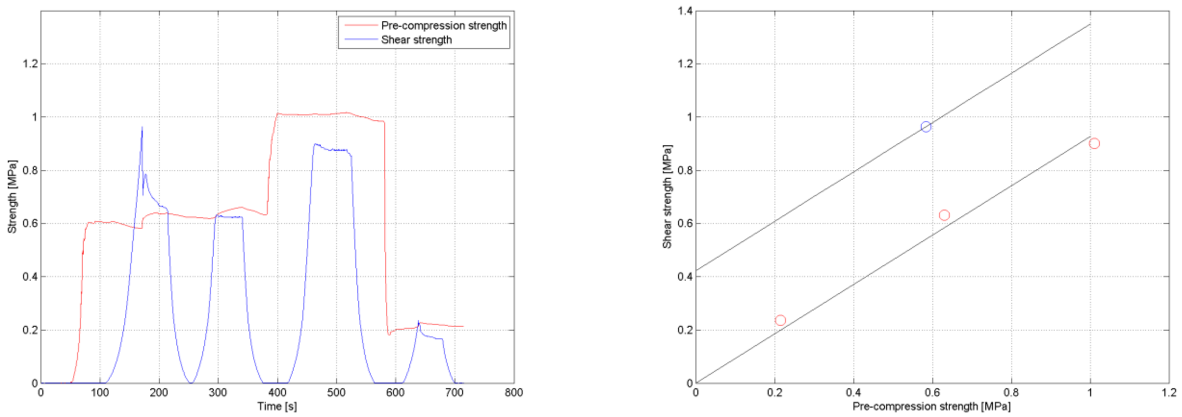

Triplet TBSCL _12

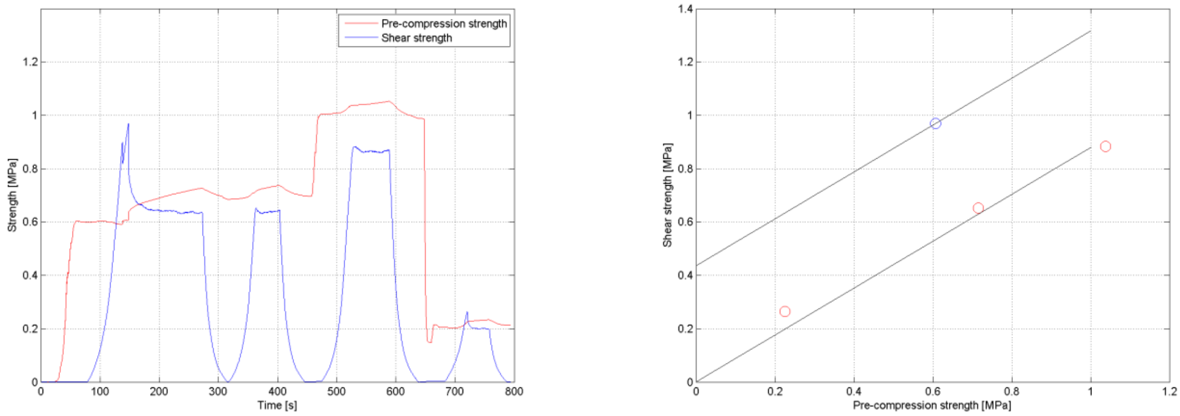

Triplet TBSCL _13

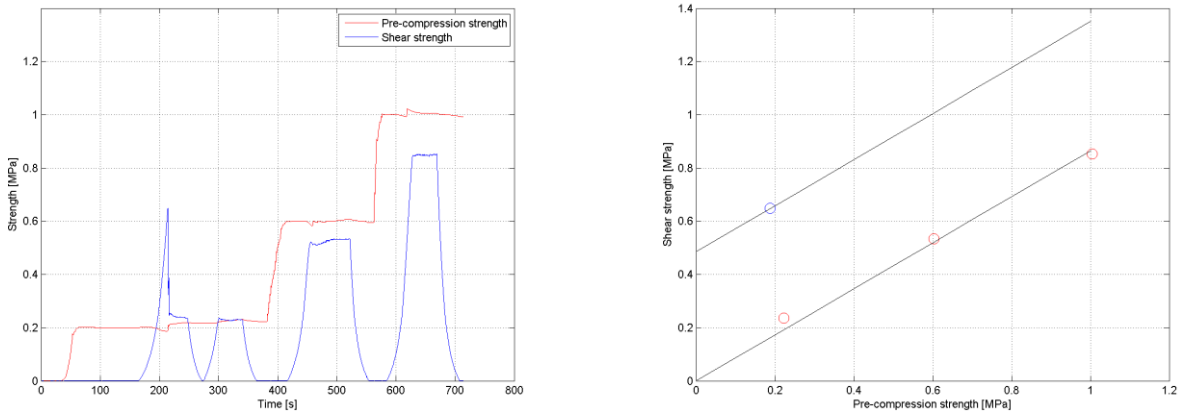

Triplet TBSCL _14

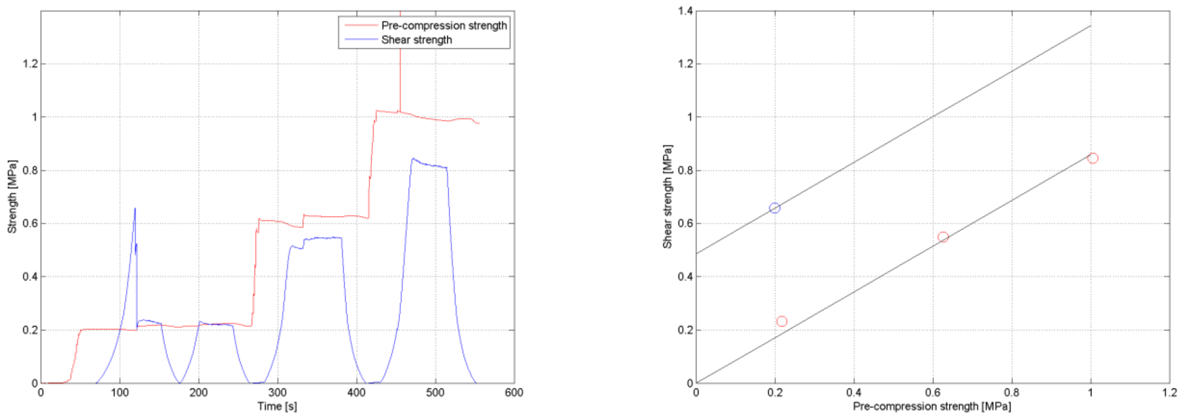

Triplet TBSCL _15

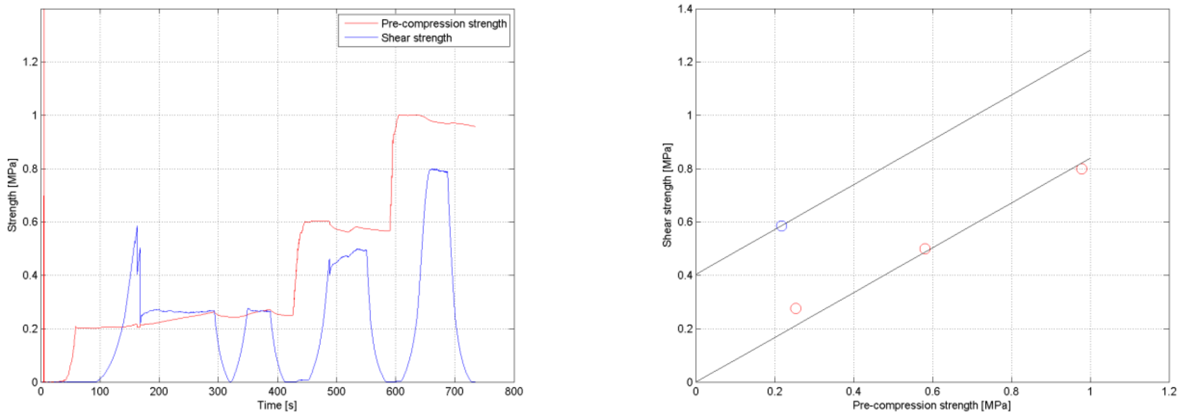

Triplet TBSCL _16

EUCENTRE
Research Report

ABSTRACT

With the aim of investigating the seismic behaviour and failure modes of residential unreinforced masonry construction of the Groningen region in the Netherlands, a unidirectional shake-table test was performed on a full-scale building model up to collapse conditions. The tests were carried out at the testing facilities of the Structural Dynamics Laboratory of LNEC in Lisbon, Portugal.

The specimen embodied construction details representative of old detached single-storey houses of the Groningen region of the Netherlands, without any specific seismic detailing. The house featured a typical Dutch gambrel roof that allowed for living space above the attic floor, with high gables that were vulnerable to out-of-plane excitation. The floor was made of timber joists and planks, resulting in a flexible diaphragm. Two clay-brick chimneys were included to investigate the performance of falling non-structural masonry elements in earthquakes. An incremental dynamic test was carried out up to collapse conditions of the specimen, using input ground motions compatible with induced-seismicity scenarios for the examined region. Structural and non-structural damage was surveyed in detail at the end of every earthquake simulation. Low-intensity random vibration tests were additionally performed to assess the effect of the cumulative damage on the dynamic properties of the structure. The specimen was sufficiently instrumented with sensors that recorded the dynamic response at various locations. The mechanical properties of the employed masonry were determined through complementary strength tests on small masonry assemblies.

This report describes the key characteristics of the specimen, including the as-built geometry, the construction details and the mechanical characteristics of the materials, as well as the adopted instrumentation plan, the seismic input and the testing protocol. It also summarises the observations from the shake-table tests, illustrating the evolution of the structural and non-structural damage, and the global and by-parts dynamic response of the building. The attainment of significant damage limit states is correlated with experimentally defined engineering demand parameters and ground-motion intensity measures for the performance-based assessment of URM buildings. The tests produced experimental data that constitutes a valuable addition to the current state of knowledge on the seismic response of masonry building chimneys and the global structural masonry collapse. All data, including photographs and video recordings taken during the construction and the testing phases, are available upon request on www.eucentre.it/nam-project. The authors make this information available to assist in the development of analytical and numerical models to simulate the earthquake response of unreinforced masonry buildings and chimneys.

Protocol EUC203/2018U